polymers

Special Issue Reprint

Polymeric Materials in Energy Conversion and Storage, 2nd Edition

Edited by
Md Najib Alam and Vineet Kumar

mdpi.com/journal/polymers

MDPI

Polymeric Materials in Energy Conversion and Storage, 2nd Edition

Polymeric Materials in Energy Conversion and Storage, 2nd Edition

Guest Editors

Md Najib Alam
Vineet Kumar

MDPI

Basel • Beijing • Wuhan • Barcelona • Belgrade • Novi Sad • Cluj • Manchester

Guest Editors

Md Najib Alam
School of Mechanical Engineering
Yeungnam University
Gyeongsan
Republic of Korea

Vineet Kumar
School of Mechanical Engineering
Yeungnam University
Gyeongbuk
Republic of Korea

Editorial Office
MDPI AG
Grosspeteranlage 5
4052 Basel, Switzerland

This is a reprint of the Special Issue, published open access by the journal *Polymers* (ISSN 2073-4360), freely accessible at: https://www.mdpi.com/journal/polymers/special_issues/7D98VRJ20Q.

For citation purposes, cite each article independently as indicated on the article page online and as indicated below:

Lastname, A.A.; Lastname, B.B. Article Title. *Journal Name* **Year**, *Volume Number*, Page Range.

ISBN 978-3-7258-6001-2 (Hbk)
ISBN 978-3-7258-6002-9 (PDF)
https://doi.org/10.3390/books978-3-7258-6002-9

Contents

About the Editors

Md Najib Alam

Md Najib Alam obtained his B.Sc. and M.Sc. degrees from the University of Kalyani, India, in 2006 and 2008, respectively. He completed his Ph.D. at the same university in 2014, where he addressed numerous challenges related to rubber vulcanization chemistry. Following his Ph.D., Dr. Alam pursued postdoctoral research at Chulalongkorn University, Thailand, from 2015 to 2019. From 2019 to 2022, he served as a research fellow at the School of Mechanical Engineering, Yeungnam University, Republic of Korea. In 2022, he transitioned to the role of assistant professor at the same institution. Throughout his research career, Dr. Alam has published over 50 original research articles in internationally recognized peer-reviewed journals, including the *Journal of Industrial and Engineering Chemistry*, *Composites Science and Technology*, and *Composites Part B: Engineering*. Currently, he is serving as a Guest Editor for various Special Issues in *Polymers* (MDPI). His research focuses on rubber vulcanization, novel rubber composites, stretchable sensors, and smart materials.

Vineet Kumar

Vineet Kumar has been an Assistant Professor since 2016 at the Department of Mechanical Engineering, Yeungnam University, Gyeongsan-si, Republic of Korea. He completed his Ph.D. in the Department of Materials Science at the University of Milan-Bicocca, Milan, Italy, in 2014. He finished his Master of Science in Environment Management from the Forest Research Institute, Dehradun, India, in 2008. He has co-authored more than 75 peer-reviewed articles in reputed SCI journals. He has also served as a Topic Editor for *Polymers* (MDPI) since 2021. Moreover, he served as a Guest Editor for more than six Special Issues in *Polymers* (MDPI) and *Frontiers in Materials*.

Preface

Energy is the fundamental driver of all physical phenomena. Per relativistic principles, energy forms are interconvertible, enabling diverse key conversion processes. In modern civilization, harvesting diverse energy sources is critical for long-term sustainable development. Thermodynamics dictates that all energy dissipates as thermal energy, but optimizing conversion pathways cuts waste heat significantly. For instance, biomass combustion emits CO_2, contributing notably to global warming; wind, hydropower, and ocean waves offer clean, renewable, economical alternatives. Rapid microelectronics/portable tech advances have spiked demand for small-scale sustainable power, met by harvesting mechanical, thermal, and ambient effects. Continuous materials science progress positions polymers as indispensable for next-gen energy conversion/storage. Their diverse structures, tunable physical/chemical properties, and excellent processability let them fulfill key functional roles across energy device components. This reprint delivers comprehensive insights into recent polymer-based energy harvesting/storage advances: materials design, fabrication, characterization, conversion mechanisms in polymers/composites, plus eco-friendly polymers/hybrids for better efficiency and sustainability. Each chapter is organized into conceptual, experimental, and concluding sections to aid clear understanding and knowledge transfer. We are confident this reprint, like previous editions, equips readers with advanced practical knowledge to foster continued innovation in polymer-based energy materials.

Md Najib Alam and Vineet Kumar
Guest Editors

polymers

MDPI

Editorial

Polymeric Materials in Energy Conversion and Storage, 2nd Edition

Md Najib Alam and Vineet Kumar *

School of Mechanical Engineering, Yeungnam University, 280, Daehak-ro, Gyeongsan 38541, Republic of Korea; mdnajib.alam3@gmail.com
* Correspondence: vineetfri@gmail.com

1. Introduction

At present, the utilization of electronic devices is rapidly increasing due to the growing demand for a more sophisticated and convenient lifestyle. Consequently, the global demand for electrical energy is continuously rising. In general, mechanical and chemical energy sources serve as the two primary means of electrical energy generation. Although chemical energy can produce a substantial amount of electricity, it is often associated with environmental and safety concerns, prompting researchers to explore more sustainable and eco-friendly alternatives. Mechanical energy, which naturally exists in the form of wind or water flow, can be effectively converted into electrical energy through mechanical-to-electrical conversion systems such as wind turbines or hydroelectric generators. Likewise, renewable sources such as solar radiation and waste heat can be transformed into electricity using photovoltaic cells or thermoelectric generators, respectively, offering environmentally benign solutions. Moreover, efficient storage of electrical energy plays a crucial role in ensuring the continuous and stable operation of remote or portable electronic devices. Therefore, the development of advanced energy harvesting and storage systems has become an essential focus in modern energy research and technology.

The choice of materials plays a critical role in achieving efficient electrical energy conversion and storage. In this context, polymers have garnered significant attention due to their diverse range of physical and chemical properties. These materials exhibit remarkable versatility, with characteristics that vary from rigid to flexible, degradable to non-degradable, and stable under both low- and high-temperature conditions. Additionally, polymers offer tunable flow behavior, solvent swelling capacity, electrical conductivity or dielectric nature, chemical reactivity, and optical transparency. Their lightweight nature, ease of processing, and economic availability from both synthetic routes and natural sources further enhance their appeal. Owing to this unique combination of attributes, polymers have emerged as highly suitable candidates for energy generation and storage applications across a wide range of environmental and operational conditions.

Li et al. [1], in their review, discussed various polymers utilized in flexible energy storage devices. Polymer materials can serve multiple functions in these systems, acting as electrodes, electrolytes, separators, and packaging layers [1–7]. Similarly, Wang et al. [8] systematically described the role of polymers in self-powered energy conversion systems. Polymer-based energy harvesters have demonstrated broad applicability across diverse fields, including biomedical and electronic devices [8–11].

Several notable studies were reported in the previous Special Issue entitled "Polymeric Materials in Energy Conversion and Storage" [12]. Alam et al. [13,14] developed

hybrid rubber composites using nano carbon black/MoS_2 in silicone rubber and natural rubber/CNT–diatomaceous earth systems, achieving up to a 184% increase in fracture toughness and over a 100% enhancement in output voltage (3.2 mV), as well as a 484% improvement in toughness and a 25 mV output voltage for CNT-filled samples. Jeżowski et al. [15] fabricated a biopolymer membrane exhibiting a capacitance of 30 F/g and an output voltage of 1.6 V, while Guo et al. [16] synthesized redox-active polymers capable of generating up to 7.14×10^{-4} C of charge. Zappia et al. [17] employed silver nanoparticles to develop water-processable anodes, and Alshammari et al. [18] enhanced the electrical conductivity of PVA films by nearly an order of magnitude. Muñoz et al. [19] achieved 96.12% capacitance recovery in PVA/H_3PO_4-based supercapacitors, while Surisetty et al. [20] and Yuan et al. [21] investigated the aging and electrothermal behavior of polymers. Xu et al. [22] and Liu et al. [23] demonstrated ionogel actuators and PEDOT-based thermoelectric materials with a conductivity of 62.91 S/cm. Tameev et al. [24] reported that incorporating electron acceptor molecules such as PCBM into poly-TPD significantly enhanced charge carrier mobility, increasing electronic mobility from approximately 4.2×10^{-6} $cm^2/V{\cdot}s$ for pure poly-TPD to 8.3×10^{-6} $cm^2/V{\cdot}s$ for the poly-TPD:PCBM composite. Furthermore, Cho et al. [25] fabricated durable Zn–MnO_2 batteries, and Hrostea et al. [26] along with Wei et al. [27] explored optoelectronic and light-actuated elastomer systems, demonstrating significant performance enhancements.

2. Overview of Published Articles

The continuous evolution of advanced materials for energy harvesting, conversion, and storage has accelerated the development of multifunctional devices and systems that merge mechanical robustness, structural adaptability, and high energy efficiency. Recent works [28–36] demonstrate substantial progress in these domains, spanning from structural design optimization in polymeric cellular architectures to hybrid and composite systems for triboelectric, piezoelectric, photovoltaic, and electrochemical applications. Collectively, these studies contribute to the growing body of knowledge focused on the design, processing, and multifunctional performance of next-generation materials.

Monkova et al. [28] investigated the mechanical behavior and energy absorption capacity of thermoplastic cellular structures based on triply periodic minimal surfaces (TPMS) such as Primitive, Diamond, and Gyroid architectures. Using Nylon CF12 fabricated via Fused Filament Fabrication (FFF), the study systematically evaluated the impact of volume fraction (30–55%) on bending properties, stiffness, yield strength, and effective modulus. The results highlighted the direct influence of cell topology and wall thickness on mechanical response and ductility indices, which are crucial for impact absorption and damping applications. Such findings underscore the promise of TPMS-based cellular structures in automotive, aerospace, and protective systems, where lightweight materials must exhibit high energy dissipation and durability.

Alam et al. [29] presented a highly efficient stretchable triboelectric nanogenerator (TENG) based on styrene–butadiene rubber (SBR) composites incorporating barium titanate (BT) and carbon nanotubes (CNTs). The study emphasizes the synergistic influence of dielectric and conductive fillers, particularly when BT is modified with stearic acid to enhance nanoscale dispersion. The resulting composites demonstrated superior power density (8.258 mW/m^3) and charge efficiency (0.146 nC/N) under low compressive strain (2%), with stable performance under cyclic loading. Additionally, the TENG exhibited excellent handwriting recognition capabilities with high repeatability (<5% deviation), highlighting its potential in wearable electronics, low-pressure sensors, and human–machine interfaces. This work provides critical insights into achieving balance between mechanical flexibility and electrical performance in elastomer-based energy harvesters.

Li et al. [30] advanced the field of flexible piezoelectric sensors through the fabrication of ZnO nanorod (NR)-reinforced P(VDF-TrFE) nanofiber membranes. Employing electrospinning with a high-speed rotating drum, the researchers achieved uniform alignment and controlled nanorod incorporation. The optimal composition yielded a piezoelectric coefficient (d33) of -62.4 pC/N, nearly ten times higher than that of neat P(VDF-TrFE). The enhanced piezoelectric response facilitated effective bending and finger-tapping detection, demonstrating the potential of such nanocomposite membranes for wearable electronics, motion sensors, and self-powered devices. The study reinforces the efficacy of nanostructure–matrix interactions in tuning electromechanical coupling and offers a scalable route for the development of high-sensitivity piezoelectric materials.

Kim et al. [31] focused on self-powered perovskite-based photovoltaic photodiodes (PVPDs), integrating a poly(amic acid)-polyimide (PAA-PI) interfacial layer within $MAPbI_3$ perovskite devices. The introduction of PAA-PI effectively reduced charge carrier recombination at the perovskite/PEDOT:PSS interface, yielding an improved power conversion efficiency (PCE) of 11.8%, compared to 10.4% for control samples. The devices exhibited significantly enhanced specific detectivity (7.82×10^{10} Jones) and rapid response times (61 μs rise; 18 μs decay). These improvements demonstrate the critical role of interfacial engineering in enhancing the optoelectronic properties of perovskite systems. Such design strategies pave the way for weak-light detection and high-sensitivity photodetectors, suitable for advanced imaging and sensing applications.

The study by Taouali et al. [32] employed density functional theory (DFT) and time-dependent DFT (TD-DFT) to explore novel donor–π–acceptor (D–π–A) organic compounds for solar cell applications. By modifying phenothiazine-based donors and introducing brominated thienyl-fused indanone-cyano (IC) acceptor groups, the researchers tailored six molecular systems (M1–M6) exhibiting HOMO–LUMO energy gaps between 2.14 and 2.30 eV and open-circuit voltages (Voc) exceeding 1.5 V. Enhanced dipole moments and strong charge transfer characteristics were achieved through halogen substitution, indicating potential for improved light absorption and charge separation. These computational insights serve as a roadmap for the rational design of high-efficiency organic photovoltaic materials, particularly those incorporating halogenated functionalities for better stability and tunability.

Feng et al. [33] provided an in-depth molecular-level understanding of proton exchange membranes (PEMs) by constructing semicrystalline and crystalline models of perfluoro sulfonic acid (PFSA) systems. Using molecular dynamics (MD) and energy-conserving dissipative particle dynamics (DPD) simulations, they revealed that crystalline regions exhibit 5–10 times higher proton transport efficiency and 1–3 times higher thermal conductivity compared to amorphous regions. The study introduced a proportionality coefficient dependent on temperature and hydration level to describe proton mobility, bridging computational predictions with experimental validation. The findings offer valuable insights into microstructure–transport relationships, facilitating the rational optimization of PEMs in fuel cells and hydrogen-based energy systems.

Fischer et al. [34] explored cellulose acetate butyrate (CAB) microspheres as a precursor for porous carbon materials, introducing an alternative to traditional cellulose acetate routes. CAB-based carbon microspheres exhibited high specific surface areas (567 m^2/g) and tunable pore structures even without chemical activation. When employed as electrodes in symmetric supercapacitors (6 M KOH electrolyte), the activated carbons achieved energy densities of 12 Wh/kg at a power density of 0.9 kW/kg. These results highlight CAB-derived carbons as promising sustainable electrode materials with controllable morphology, bridging the gap between biopolymer chemistry and electrochemical energy storage.

Huang et al. [35] reviewed electrically conductive functional polymers (ECFPs)—notably conjugated and radical polymers—for applications in batteries, flexible electronics, and solid-state devices. The review detailed limitations such as low conductivity, dopant instability, and poor environmental resistance, and proposed strategies including molecular design, self-doping side chains, hydrophobic modifications, and 2D material composites. These approaches enhance electronic transport and mechanical resilience while promoting eco-friendly and renewable synthesis routes. The study underscores that tailoring the structure–function relationships in ECFPs is pivotal to achieving high-performance, sustainable energy storage materials.

Finally, Annu et al. [36] presented a comprehensive review of cobalt oxide composites with conducting polymers such as polypyrrole (PPy) and polyaniline (PANI) as electrode materials for supercapacitors, batteries, and hybrid "supercapatteries". The synergy between cobalt oxide's high theoretical capacitance and the polymers' pseudocapacitive and conductive properties yields enhanced charge transport, ion diffusion, and cycling stability. Despite challenges in scalability and long-term durability, these hybrid systems show strong potential for next-generation electrochemical energy storage devices, bridging the functionality of batteries and supercapacitors.

3. Summary and Future Outlook

Collectively, these studies highlight a cross-disciplinary progression in the design, synthesis, and performance optimization of advanced materials across structural, electronic, and energy domains. From TPMS-based lightweight architectures to hybrid nanocomposites for triboelectric and piezoelectric energy harvesting and from molecularly engineered solar cells and photodiodes to biopolymer-derived carbons and conductive polymers for energy storage, a unifying trend becomes evident—namely, the convergence of multifunctionality, scalability, and sustainability. These collective innovations provide a strong foundation for the next generation of smart materials and devices capable of efficiently harvesting, storing, and utilizing energy while maintaining mechanical adaptability and environmental compatibility. Future research should focus on the development of functional polymers and filler systems with enhanced physical, chemical, and interfacial properties to further expand the potential of next-generation energy materials.

Author Contributions: Conceptualization: M.N.A.; validation: M.N.A. and V.K.; writing—original draft preparation: M.N.A.; writing—review and editing: M.N.A. and V.K.; visualization: M.N.A.; supervision: V.K.; project administration: M.N.A. and V.K. All authors have read and agreed to the published version of the manuscript.

Acknowledgments: The authors thank all the contributors and reviewers for their valuable contributions and the section editors of this Special Issue for their support.

Conflicts of Interest: The authors declare no conflicts of interest.

References

1. Li, C.; Zhang, K.; Cheng, X.; Li, J.; Jiang, Y.; Li, P.; Wang, B.; Peng, H. Polymers for flexible energy storage devices. *Prog. Polym. Sci.* **2023**, *143*, 101714. [CrossRef]
2. Li, S.; Lorandi, F.; Wang, H.; Liu, T.; Whitacre, J.F.; Matyjaszewski, K. Functional polymers for lithium metal batteries. *Prog. Polym. Sci.* **2021**, *122*, 101453. [CrossRef]
3. Xiao, B.H.; Xiao, K.; Li, J.X.; Xiao, C.F.; Cao, S.; Liu, Z.Q. Flexible electrochemical energy storage devices and related applications: Recent progress and challenges. *Chem. Sci.* **2024**, *15*, 11229–11266. [CrossRef]
4. Chattopadhyay, J.; Pathak, T.S.; Santos, D.M. Applications of polymer electrolytes in lithium-ion batteries: A review. *Polymers* **2023**, *15*, 3907. [CrossRef] [PubMed]
5. Mecerreyes, D.; Casado, N.; Villaluenga, I.; Forsyth, M. Current trends and perspectives of polymers in batteries. *Macromolecules* **2024**, *57*, 3013–3025. [CrossRef] [PubMed]

6. Chen, S.; Li, Y.; Feng, Y.; Feng, W. Thermally responsive polymers for overcoming thermal runaway in high-safety electrochemical storage devices. *Mater. Chem. Front.* **2023**, *7*, 1562–1590. [CrossRef]
7. Wan, X.; Mu, T.; Yin, G. Intrinsic self-healing chemistry for next-generation flexible energy storage devices. *Nano-Micro Lett.* **2023**, *15*, 99. [CrossRef]
8. Wang, Q.; Zhang, Q.; Mao, L.; Zheng, G.; Song, M.; Liu, Z.; Wu, D.; Wu, M. Recent advances in flexible high polymer-based self-powered systems for energy conversion. *Mater. Today Chem.* **2024**, *42*, 102384. [CrossRef]
9. Parvin, N.; Joo, S.W.; Jung, J.H.; Mandal, T.K. Electroactive polymers for self-powered actuators and biosensors: Advancing biomedical diagnostics through energy harvesting mechanisms. *Actuators* **2025**, *14*, 257. [CrossRef]
10. Zhou, Y.; Li, L.; Han, Z.; Li, Q.; He, J.; Wang, Q. Self-healing polymers for electronics and energy devices. *Chem. Rev.* **2022**, *123*, 558–612. [CrossRef]
11. Yang, Y.; Li, H.; Xu, Z.; Luo, S.; Chen, L. Wearable self-powered devices based on polymer thermoelectric materials. *Moore More* **2025**, *2*, 3803–3812. [CrossRef]
12. Kumar, V.; Alam, M.N. Polymeric materials in energy conversion and storage. *Polymers* **2024**, *16*, 3132. [CrossRef] [PubMed]
13. Alam, M.N.; Kumar, V.; Jeong, T.; Park, S.S. Nanocarbon black and molybdenum disulfide hybrid filler system for the enhancement of fracture toughness and electromechanical sensing properties in the silicone rubber-based energy harvester. *Polymers* **2023**, *15*, 2189. [CrossRef] [PubMed]
14. Alam, M.N.; Kumar, V.; Jung, H.S.; Park, S.S. Fabrication of high-performance natural rubber composites with enhanced filler–rubber interactions by stearic acid-modified diatomaceous earth and carbon nanotubes for mechanical and energy harvesting applications. *Polymers* **2023**, *15*, 3612. [CrossRef]
15. Jeżowski, P.; Kowalczewski, P.Ł. Isinglass as an alternative biopolymer membrane for green electrochemical devices: Initial studies of application in electric double-layer capacitors and future perspectives. *Polymers* **2023**, *15*, 3557. [CrossRef]
16. Guo, H.X.; Takemura, Y.; Tange, D.; Kurata, J.; Aota, H. Redox-active ferrocene polymer for electrode-active materials: Step-by-step synthesis on gold electrode using automatic sequential polymerization equipment. *Polymers* **2023**, *15*, 3517. [CrossRef]
17. Zappia, S.; Alloisio, M.; Valdivia, J.C.; Arias, E.; Moggio, I.; Scavia, G.; Destri, S. Silver Nanoparticle–PEDOT: PSS Composites as Water-Processable Anodes: Correlation between the Synthetic Parameters and the Optical/Morphological Properties. *Polymers* **2023**, *15*, 3675. [CrossRef]
18. Alshammari, K.; Alashgai, T.; Alshammari, A.H.; Abdelhamied, M.M.; Alotibi, S.; Atta, A. Effects of Nd_2O_3 nanoparticles on the structural characteristics and dielectric properties of PVA polymeric films. *Polymers* **2023**, *15*, 4084. [CrossRef] [PubMed]
19. Muñoz, B.K.; González-Banciella, A.; Ureña, D.; Sánchez, M.; Ureña, A. Electrochemical comparison of 2D-flexible solid-state supercapacitors based on a matrix of PVA/H_3PO_4. *Polymers* **2023**, *15*, 4036. [CrossRef]
20. Surisetty, J.; Sharifian, M.; Lucyshyn, T.; Holzer, C. Investigating the aging behavior of high-density polyethylene and polyketone in a liquid organic hydrogen carrier. *Polymers* **2023**, *15*, 4410. [CrossRef]
21. Yuan, Z.; Liu, J.; Qian, G.; Dai, Y.; Li, K. Self-rotation of electrothermally responsive liquid crystal elastomer-based turntable in steady-state circuits. *Polymers* **2023**, *15*, 4598. [CrossRef]
22. Xu, J.; Hu, H.; Zhang, S.; Cheng, G.; Ding, J. Flexible actuators based on conductive polymer ionogels and their electromechanical modeling. *Polymers* **2023**, *15*, 4482. [CrossRef] [PubMed]
23. Liu, F.; Gao, L.; Duan, J.; Li, F.; Li, J.; Ge, H.; Li, M. A novel and green method for preparing highly conductive PEDOT: PSS films for thermoelectric energy harvesting. *Polymers* **2024**, *16*, 266. [CrossRef] [PubMed]
24. Tameev, A.R.; Aleksandrov, A.E.; Sayarov, I.R.; Pozin, S.I.; Lypenko, D.A.; Dmitriev, A.V.; Nekrasova, N.V.; Chernyadyev, A.Y.; Tsivadze, A.Y. Charge carrier mobility in poly (N, N′-bis-4-butylphenyl-N, N′-bisphenyl) benzidine composites with electron acceptor molecules. *Polymers* **2024**, *16*, 570. [CrossRef] [PubMed]
25. Cho, J.; Turney, D.E.; Yadav, G.G.; Nyce, M.; Wygant, B.R.; Lambert, T.N.; Banerjee, S. Use of hydrogel electrolyte in Zn-MnO_2 rechargeable batteries: Characterization of safety, performance, and Cu^{2+} ion diffusion. *Polymers* **2024**, *16*, 658. [CrossRef]
26. Hrostea, L.; Oajdea, A.; Leontie, L. Impact of PCBM as a third component on optical and electrical properties in ternary organic blends. *Polymers* **2024**, *16*, 1324. [CrossRef]
27. Wei, L.; Hu, J.; Wang, J.; Wu, H.; Li, K. Theoretical analysis of light-actuated self-sliding mass on a circular track facilitated by a liquid crystal elastomer fiber. *Polymers* **2024**, *16*, 1696. [CrossRef]
28. Monkova, K.; Monka, P.P.; Godec, D.; Torokova, M. Research into the Influence of Volume Fraction on the Bending Properties of Selected Thermoplastic Cellular Structures from a Mechanical and Energy Absorption Perspective. *Polymers* **2025**, *17*, 2795. [CrossRef]
29. Alam, M.N.; Kumar, V.; Kim, Y.; Lee, D.-J.; Park, S.-S. High-Performance Barium Titanate, Carbon Nanotube, and Styrene–Butadiene Rubber-Based Single Composite TENG for Energy Harvesting and Handwriting Recognition. *Polymers* **2025**, *17*, 2016. [CrossRef]
30. Li, X.; Zhang, Z.; Ye, J.; Li, Y.; Li, Q.; Wang, H.; Zhang, X.; Guo, Y. Enhanced Piezoelectric Performance of Highly-Aligned ZnO Nanorods Embedded in P(VDF-TrFE) Nanofiber Membranes. *Polymers* **2025**, *17*, 585. [CrossRef]

31. Kim, W.; Park, J.; Jeong, H.; Lee, K.; Yang, S.; Choi, E.H.; Park, B. Poly(amic acid)-Polyimide Copolymer Interfacial Layers for Self-Powered $CH_3NH_3PbI_3$ Photovoltaic Photodiodes. *Polymers* **2025**, *17*, 163. [CrossRef] [PubMed]
32. Taouali, W.; Azazi, A.; Hassani, R.; EL-Araby, E.H.; Alimi, K. Exploring the Impact of Structural Modifications of Phenothiazine-Based Novel Compounds for Organic Solar Cells: DFT Investigations. *Polymers* **2025**, *17*, 115. [CrossRef]
33. Feng, C.; Luo, C.; Ming, P.; Zhang, C. Exploring Crystal Structure Features in Proton Exchange Membranes and Their Correlation with Proton and Heat Transport. *Polymers* **2024**, *16*, 3250. [CrossRef] [PubMed]
34. Fischer, J.; Thümmler, K.; Zlotnikov, I.; Mikhailova, D.; Fischer, S. Synthesis of Cellulose Acetate Butyrate Microspheres as Precursor for Hard Carbon-Based Electrodes in Symmetric Supercapacitors. *Polymers* **2024**, *16*, 2176. [CrossRef] [PubMed]
35. Huang, Z.; Lyu, M.; Meng, N.; Cao, J.; Xiong, C.; Lian, F. Electrically Conductive Functional Polymers and Application Progress in Lithium Batteries. *Polymers* **2025**, *17*, 778. [CrossRef]
36. Annu; Park, S.-S.; Alam, M.N.; Yewale, M.; Shin, D.K. Unraveling the Electrochemical Insights of Cobalt Oxide/Conducting Polymer Hybrid Materials for Supercapacitor, Battery, and Supercapattery Applications. *Polymers* **2024**, *16*, 2907. [CrossRef]

polymers

MDPI

Article

Research into the Influence of Volume Fraction on the Bending Properties of Selected Thermoplastic Cellular Structures from a Mechanical and Energy Absorption Perspective

Katarina Monkova [1,2,*], Peter Pavol Monka [1,2], Damir Godec [3] and Monika Torokova [1]

[1] Faculty of Manufacturing Technologies with a seat in Presov, Technical University of Kosice, Sturova 31, 080 01 Presov, Slovakia; peter.pavol.monka@tuke.sk (P.P.M.); monika.torokova@tuke.sk (M.T.)
[2] Faculty of Technology, Tomas Bata University in Zlin, Vavreckova 5669, 760 01 Zlin, Czech Republic
[3] Faculty of Mechanical Engineering and Naval Architecture, University of Zagreb, HR-10000 Zagreb, Croatia; damir.godec@fsb.unizg.hr
* Correspondence: katarina.monkova@tuke.sk

Abstract: The aim of the manuscript is to study the effect of volume fraction on the bending properties of selected thermoplastic cellular structures (Primitive, Diamond, and Gyroid) from a mechanical and energy absorption perspective, with a view to their promising prospects and use not only for bumpers, but also for various vehicle and aircraft components, or other applications. Samples belonging to the group of so-called complex structures with Triply Periodic Minimal Surfaces, dimensions of 20 × 20 × 250 mm, and volume fractions of 30, 35, 40, 45, and 55%, were prepared by PTC Creo 10.0 software and produced using the Fused Filament Fabrication technique from Nylon CF12 material, while the basic cell size of 10 × 10 × 10 mm was maintained for all samples and the volume fraction was controlled by the wall thickness of the structure. Experimental bending tests were performed on a Zwick 1456 machine and based on recorded data; in addition to the maximum forces, the stiffness, yield strength, and effective modulus of elasticity in bending were evaluated for individual structures and volume fractions. Furthermore, the amount of energy absorbed until reaching the maximum force and until failure was compared, as well as the ductility indices μ_d and μ_U (derived from deformation and absorbed energy, respectively), as an important dissipation factor in absorbers, based on which it is also possible to predict which of the structures will have better damping.

Keywords: bending; energy; cellular structures; additive manufacturing; thermoplastic; mechanical properties

1. Introduction

The development of science and technology affects the progress of various sectors and industries. It allows components to be produced faster, more efficiently, and more reliably. Not only new technologies and materials, but also computer-aided design and simulations play a key role. Technologies that are advancing by leaps and bounds today include 3D printing, which reduces the consumption of materials for the fabrication of a component, since the processes for removing unnecessary material from the semi-finished product that were necessary in conventional production are no longer needed [1,2].

The main advantage of 3D printing is the possibility of manufacturing a part with a complex shape that cannot be manufactured conventionally. A special area of components is the so-called lightweight components with regularly spaced structures inside the component body. From a certain point of view, this lightweight material is a three-dimensional

(3D) reticulated "foam" with a special structure, but the pore support is connected and oriented according to certain rules in porous materials. This means that the pores are not randomly shaped and distributed, so their properties are better controlled [3–5].

Porous materials can give certain products specific exceptional properties. In addition to making the component lighter and having exceptional mechanical properties per unit volume of material, they can also absorb a lot of energy and therefore serve as good "absorbers". This makes them very promising for application in various industrial sectors, from aerospace through to civil and automotive industries to biomedicine [6].

For example, in cars, bumpers play a very important role in terms of safety. They must be deformable, elastic, absorb impacts, and prevent permanent damage. Car manufacturers use a variety of materials to make bumpers, with aluminum, fiberglass, and composites often used, as well as thermoplastic materials [7,8].

To compare the quasi-static bending from an energetic point of view, the authors selected three types of structures, so-called Primitive, Diamond, and Gyroid, made of thermoplastic Nylon CF12, as a promising perspective for their use not only for bumpers, but also for other components of vehicles, aircrafts, or for other applications.

2. State of the Art

In recent years, intensive research has been conducted worldwide on the various properties of cellular structures and their application possibilities. There are also several studies specifically focused on the mechanical properties of thermoplastic materials and porous structures evaluated from an energy point of view. These include, for example, the following studies.

Bernard [9] hypothesized that cellular solids absorb energy more efficiently than monolithic materials. Lattice materials are particularly valuable for their predictable behavior and adaptability through additive manufacturing. His study investigated the strength of multi-layer multi-topology lattices (MLMTs) made from nylon and carbon fiber composites. The material properties were tuned by the orientation of the struts, and single- and three-layer cubic and octet lattices were compared at 30% relative density. The results show that the unique MLMT designs do not exceed the energy absorption of their combined layers, but that modifying the layer interfaces can improve the results. The cubic-octet-cubic MLMT lattice outperformed the octet lattice in mass-specific energy absorption, while the octet-cubic-octet lattice improved the plateau voltage over its MLMT counterpart, although the cubic lattices had higher absorption overall.

The study of Sahu [10] examined how honeycomb cell size affects compressive strength, flexural strength, beam deflection, and impacts behavior. TPE nylon cores showed both in-plane cushioning and out-of-plane energy absorption. Smaller cells (<15 mm) failed by crushing but absorbed more energy, while 15–36 mm cells offered the best in-plane cushioning with lower flexural strength. Larger cells reduced overall beam deflection due to plastic buckling. Drop impact tests confirmed that smaller cells (10 mm) absorbed more energy, which decreased with larger cell sizes. Experimental results matched FEM simulations. Cells under 15 mm are ideal for energy absorption, while 15–36 mm cells excel at cushioning. TPE filament's flexibility makes it suitable for use as a backing layer in bulletproof vests, helping absorb energy and reduce blunt trauma.

The bending performance of 3D-printed lattice beams, focusing on octet and cube structures, was examined by Yalçın [11] Results showed that energy absorption, specific energy absorption (SEA), and specific load capacity (SLC) depend on lattice type, layer count, and arrangement. Octet beams consistently outperformed cube beams; for instance, in a triple-layer double column set up, the octet beam absorbed 38% more energy and had a higher SEA (0.39 J/g vs. 0.29 J/g). Force–displacement analysis revealed that the

octet specimen also supported 43% greater maximum load. While mixed-lattice beams like octet-cube-octet showed benefits, uniform octet lattices achieved the best energy absorption and load capacity. The study also identified two deformation regions—stretch-dominated and compressive-dominated—where vertical struts contributed less to load-bearing in the former, explaining the lower capacity of cube beams compared to octet ones. However, vertical struts were more effective in compressive-dominated regions.

Calignano [12] investigated mechanical properties of components fabricated with a low-cost printer utilizing carbon fiber-reinforced nylon filament. The results showed that components produced in the XY plane exhibit higher hardness than those manufactured in the XZ plane. Within the XZ orientation, samples with 80% and 100% infill demonstrate similar hardness; however, at 100% infill, the hardness of XZ plane specimens is substantially lower than that of their XY counterparts. Specimens printed along the XZ axis are stiffer than those printed along the XY axis, as evidenced by higher Young's modulus and stress at break, while energy at break is greater for samples from the XY plane. As previously noted, the relationship between mechanical properties and filing factors remains nonlinear.

Additively manufactured (AM) nylon matrix composites reinforced with short and continuous carbon fibers under tensile loading were tested by Islam and his team [13]. It also compares how fiber volume fraction affects mechanical properties using both experimental results and literature. Tensile tests show that nylon with 5% continuous carbon fiber achieves higher tensile strength and Young's modulus, but lower elongation at break than nylon with 20% short carbon fiber, due to the advantages of continuous fibers. Fracture surfaces indicate brittle failure and fiber pull-outs in the continuous fiber composite, suggesting weak matrix–fiber bonding. Mechanical property trends are presented for varying fiber content, showing a near-linear increase in strength and stiffness for continuous fibers at high volume fractions, while short fibers at low content display no clear relationship.

Monkova [14] investigated how loading and layering directions affect the flexural properties of 3D-printed Nylon CF12, with implications for lightweight sports equipment like pole vault poles. Full-volume and porous samples (Diamond, Primitive, Gyroid) at fixed volume fractions of 30% underwent three-point bending tests. Results revealed that full-volume beams' flexural properties depend heavily on loading direction and printing strategy, whereas porous cellular beams show minimal differences. At the given volume fraction, the Diamond structure exhibited the highest yield strength among porous designs, while Gyroid had the lowest. Layer adhesion and material deposition paths likely influence these outcomes.

The article of Alfouneh [15] has presented a topology optimization approach for multi-layer, multi-material composite structures under static loads. The method extends moving iso-surface threshold optimization with a physical response function discrepancy scheme and integrates an alternating active-phase algorithm. Three objective functions are addressed: minimizing compliance, maximizing mutual strain energy, and minimizing full-stress (von Mises stress) designs. Benchmark examples demonstrate that the approach yields effective, stiffer, and highly optimized layouts compared to the existing literature, and using multiple materials in layered plates can enhance compliant mechanism performance. All objectives show smooth convergence during optimization, and fully stressed designs have layouts similar to those minimizing compliance.

Xie and Shen [16] investigated the effect of hole shape, size, and distribution on the impact response of porous materials by comparing a spherical hole array model and a square hole model using both an experimental approach and a finite element method. They found that the specific energy absorption capacity correlated with the hole shape, size, and

deformation mode, and that, unlike spherical holes, the deformation in square holes was always caused by compression dominance, either with open or closed cells.

There are certainly several other studies that dealt with the mechanical properties of some cellular materials [17–23], as well as a small number of studies that compare energy absorption between structures [24–27], but a study that would investigate the effect of volume fraction on the bending properties of complex structures of the Gyroid, Primitive, and Diamond type made of Nylon CF12, and at the same time compare their behavior from a mechanical and energetic point of view as presented in this research, has so far been absent. The obtained results can contribute to the expansion of knowledge not only in the field of material behavior of the thermoplastic Nylon CF12 during bending, but also in the field of investigating cellular structures from an energetic point of view, given their prospective application in many industrial and consumer sectors.

3. Materials and Methods

3.1. The Samples Design and Production

To investigate bending properties from energetic point of view, three types of cellular structures were used—Diamond, Primitive and Gyroid—which belong to the category of Triply Periodic Minimal Surfaces (TPMSs). They are based on three-dimensional surfaces that minimize surface area for a given boundary. Additionally, they are triply periodic, repeating in three independent spatial directions, resulting in crystallographic symmetry. They have a zero-mean curvature at every point, indicating that the surfaces are locally flat and lack sharp edges [28]. The basic unit cells of the above structures designed in PTC Creo 10.0 software, similarly to the whole samples, are shown in Figure 1.

(**a**) (**b**) (**c**)

Figure 1. Basic cells of the investigated structures: (**a**) Diamond; (**b**) Primitive; (**c**) Gyroid.

The selection of the structures, as well as the Nylon CF12 material, was based not only on their promising energy absorption properties and possible applications in the automotive and aerospace industries, but also on ongoing research into the behavior of cellular structures, which has been conducted at the authors' home institution for several years, while the technological conditions of 3D printing were also optimized.

Nylon CF12 is a carbon-filled thermoplastic, featuring 35% short carbon fibers by weight in a Nylon 12 matrix. It offers superior flexural strength and stiffness-to-weight ratio among FDM thermoplastics. Ideal for strong yet lightweight tooling, functional prototypes, and end-use parts in aerospace, automotive, and industrial sectors, it resists heavy mechanical stress and harsh conditions while maintaining structural integrity. Its stability, strength, lightness, and vibration resistance also make it suitable, e.g., for drone frames or components requiring damping properties [29,30].

Physical properties of Nylon CF12 are listed in Table 1.

Table 1. Physical properties of Nylon CF12 [29].

Property	Unit	Value
Density	g/cm^3	1.19
Melting point	°C	180–190
Tensile modulus of elasticity *	GPa	3–9.46
Ultimate tensile strength *	MPa	32.7–83.5
Elongation at break	%	1.2–2.4
Toughness	J/m^2	50

* Depends on printing orientation.

The material in the form of a filament with a diameter of 1.75 mm was delivered wound on a spool and vacuum-packed, suitable for direct use without the need for drying, and its properties were verified in ongoing tests, confirming the specifications given in the material sheet.

Given the manufacturability of the 10 × 10 × 10 mm basic cell of all selected structures from Nylon CF12, established based on previous research [31], a minimum material volume fraction (defined as the ratio of the volume of the material required to create the structure inside the cell to the total volume of the cell space [32]) of Vr = 30% was chosen to determine the effect of volume fraction on bending properties. Subsequent volume fractions of 35, 40, 45, and 55% were established to examine their respective effects, with the highest fraction selected to ensure a discernible reduction in the weight of the final products, while the volume fraction was controlled by the wall thickness of the structure.

Three identical samples were produced from each series specified by volume fraction and structure type, so a total of 45 samples were manufactured (3 structures × 5 volume fractions × 3 pieces). Samples' total sizes of 20 × 20 × 250 mm (2 × 2 × 25 cells) were printed using the Fused Filament Fabrication (FFF) technique employing a MarkerBot Method X printer (MakerBot, New York, NY, USA) with MarkerBot Cloud software 3.10.1 with the following production parameters set up based on preliminary research [33]: filament diameter, 1.75 mm; nozzle diameter, 0.4 mm; temperature in the printer chamber, 65 °C; extruder temperature, 260 °C; printing speed, 35 mm/s; travel speed, 80 mm/s; layer height, 0.15 mm; bed temperature, 65 °C; printing technique, stripes with 45° degree angle and 90° degree rotation for every second layer.

An example of produced samples with 35% volume fraction is in Figure 2.

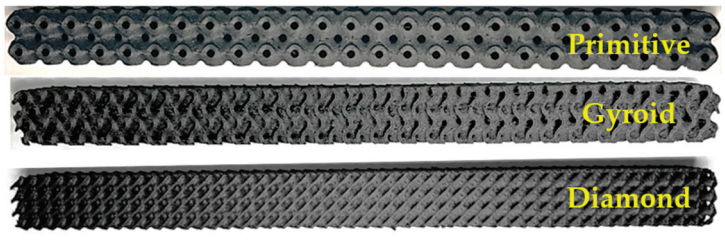

Figure 2. Example of produced samples with 35% volume fraction.

3.2. Testing and Evaluation Methodology

Experimental bending tests were performed on a Zwick 1456 machine (Ulm, Germany) according to ISO 178:2019 [34] standard at a temperature of 20 °C and a humidity of 50%. The support span distance of l = 200 mm was set symmetrically around the center of the specimen; the pressure thumb had a radius of 10 mm and operated at a crosshead loading rate of 10 mm/min. The experimental set up is shown in Figure 3.

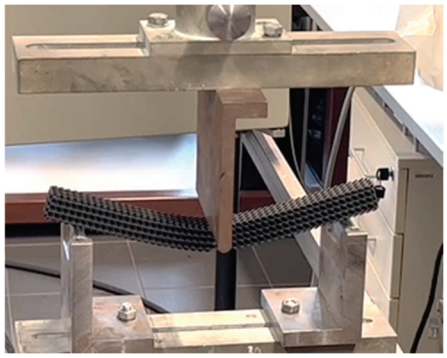

Figure 3. Sample during testing when placed in the experimental set up of the testing machine.

The crosshead speed of 10 mm/min was set up based on the standards of ASTM D790 (3-point flexural test for plastics) [35] and ISO 178 (plastics—determination of flexural properties) [34].

ASTM D790 has Procedure A (for materials that break at comparatively small deflections, it uses a strain rate of 0.01 mm/mm/min) and Procedure B (for materials that yield large deflections, it uses 0.10 mm/mm/min). ASTM D790 gives the formula for crosshead speed (displacement rate) calculation. For the material Carbon fiber-reinforced Nylon (i.e., thermoplastic composite, moderately stiff and brittle) used in our case, with a support span of 200 mm and cross-section (width × depth) of 20 mm × 20 mm, the target crosshead speed was calculated based on the standard recommendation as 66.7 mm/min. This keeps strain rate at 0.01 mm/mm/min, matching quasi-static requirements.

ISO 178 recommends 1 %/min strain rate for rigid plastics that also leads to a crosshead speed of 66.7 mm/min. So, both the ASTM D790 and ISO 178 standards are essentially the same in the crossbar speed prescription.

For 70% porosity (Vf = 30%), the effective modulus is reduced which means that material stiffness behaves much more flexibly, so calculated crosshead speed was close to 30 mm/min. The authors decided to use a crosshead speed of 10 mm/min, which is much slower than the standards prescribe, to be sure that they are in the quasi-static loading region.

The central position of the pressure finger relative to the supports was ensured by the test machine fixtures (checked before the experiments were run, Figure 4a), and the symmetrical position of the sample relative to the push thorn was checked before each experiment by aligning the marked center of the sample with the center of the push thorn, as well as with respect to the marked center between the supports (Figure 4b).

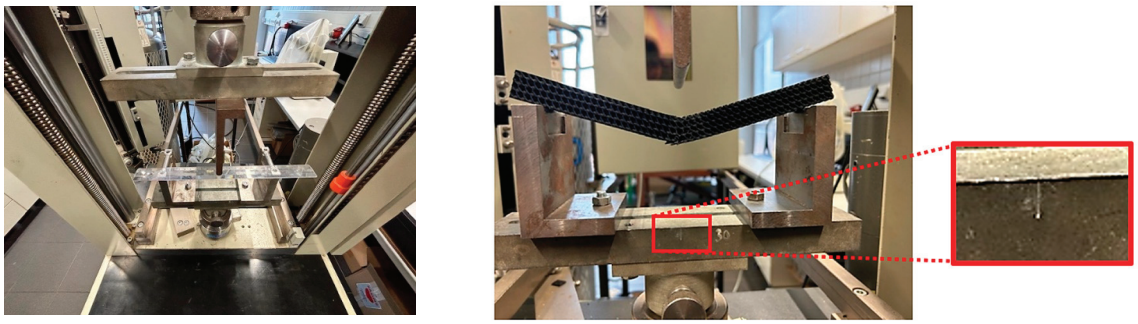

(**a**) (**b**)

Figure 4. Central position of a sample checking (**a**) before experiments were run; (**b**) aligning the marked center of the sample with the center of the push thorn.

Outliers from further measurements and calculations were excluded by statistical processing, while the recorded differences in results between identical samples within one series were in all cases less than 5%.

Several outcomes were assessed using recorded data and load–deflection curves based on the fundamental theory of the three-point bending test.

The bending load has its highest value in the cross-section of the maximum deflection, i.e., in the middle of the specimen, as is seen in Figure 5. The material is subjected to compressive stress on the inside and tensile stress on the outside side, while the stress values are highest at the surface layer of the material due to the maximum compression or strain. In so-called neutral axis, the tensile and compressive stresses are distributed identically over the cross-section.

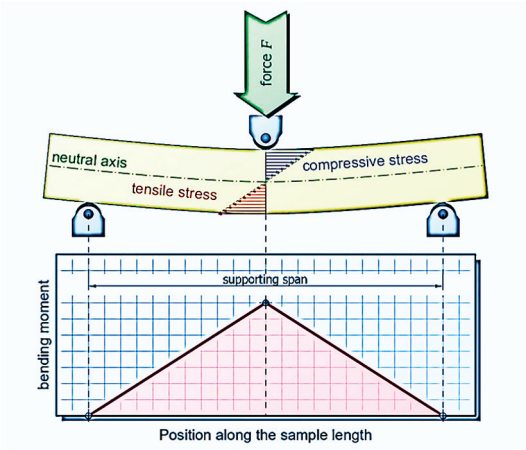

Figure 5. Three-point bending test in theory—bending moment distribution.

Assuming a linear stress distribution, the bending moment M relates to the stress σ (Pa) at a distance "z" from the neutral axis, based on the specimen's cross-sectional geometry defined by the area moment of inertia I (also referred to as the second moment of area) [36].

$$\sigma = \frac{M}{I} z \,, \tag{1}$$

The limit to which the materials can be stressed at a given bending load without permanent deformations is called flexural yield strength. The induced bending moment M_y (Nm) at the onset of plastic deformation can be determined with the yield force F_y according to the equation

$$M_y = \frac{F_y l}{4} \,, \tag{2}$$

where l is a supporting span.

During loading, the energy is stored in the structure. It can be said that a structure's energy is its capacity to do work. In linear elasticity, the entire deformation work is converted into elastic tension energy and strain energy is the internal energy in the structure because of its deformation [37]. By the principle of conservation of energy,

$$Wi = U \tag{3}$$

where U denotes the strain energy and Wi represents the work done by internal forces. For linearly elastic structures, the partial derivative of the strain energy concerning an applied force F is equal to the displacement u of the force along its line of action [38,39]:

$$u = \frac{\partial U}{\partial F} \tag{4}$$

The strain energy of a beam can be expressed by the equation [40]:

$$U = \int_0^l \frac{M^2}{2EI} dx. \tag{5}$$

where E is flexural elastic modulus (Pa) of the beam material. Finding the partial derivative of this expression will give the equations of Castigliano's deflection and rotation of beams.

According to elementary beam theory, the applied bending moment M is given as follows [41]:

$$M = EI \frac{\mathrm{d}^2 w}{\mathrm{d}x^2}, \tag{6}$$

where x is the distance along the beam. Then, double integration of Equation (6) results in the beam's deflection.

Based on the energy approach, the flexural modulus of elasticity E can also be determined. If the elastic deflection w_e (m) is expressed by Equation (7)

$$w_e = \frac{F_e l^3}{48EI}, \tag{7}$$

then flexural elastic modulus can be expressed

$$E = \frac{F_e l^3}{48 w_e I}, \tag{8}$$

where F_e denotes the applied elastic force (N).

It becomes apparent from Equation (7) that the greater the product of flexural modulus E (material property) and area moment of inertia I (geometric property), the less the specimen deflects. For this reason, this product EI is often referred to as flexural rigidity R_f (Nm^2) which refers to the ability of a material to maintain its shape under stress or load, while bending stiffness k_b (N/m) refers to the ability of a material to resist deformation when subjected to an external load, and it comes from the relation [42]

$$k_b = \frac{F_e}{w_e} \tag{9}$$

The sample can continue to be plastically deformed with tough materials as the load increases. Compared to ductile materials, brittle ones break without any noticeable deformation [43].

When evaluating results from an energetic point of view, total energy absorption can be found by integrating the force–deflection curve. Subsequently, based on energy, the ductility of the beams can also be accessed through two indices, μ_d and μ_U, that are given by Formulas (9) and (10) [44,45]:

$$\mu_d = \frac{w_u}{w_e} \tag{10}$$

$$\mu_U = \frac{1}{2}\left(\frac{U_{tot}}{U_e} + 1\right) \tag{11}$$

where w_u (mm) is the deflection at the ultimate load and w_u (mm) is the deflection at the elastic limit; U_{tot} (J) is the total energy absorbed by the sample during bending; and U_e (J) is the elastic energy absorbed up to the elastic limit.

4. Results and Discussions

4.1. Experimental Results

In order to determine the behavior of samples of Nylon CF12 material with the selected topology characterized by the type of structure and volume fraction while maintaining the cell size of 10 × 10 × 10 mm, experimental testing was carried out using a three-point bend. During testing, curves of the dependence of the applied force on the deformation of the beam were recorded. Examples of recorded dependencies of three identical samples, which were subjected to testing with respect to repeatability and statistical data processing for three different structure topologies, are shown in Figure 6.

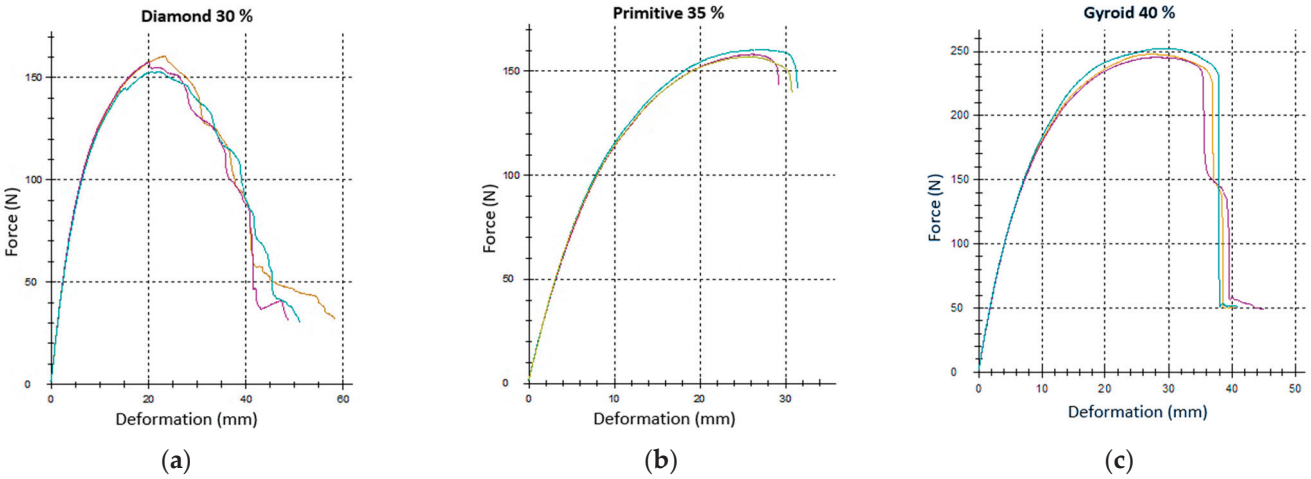

(**a**) (**b**) (**c**)

Figure 6. Load–deformation curves recorded during experimental testing for repeated measurements of identical samples within a single series: (**a**) Diamond 30%; (**b**) Primitive 35%; (**c**) Gyroid 40%. (The results of three samples of the same type, tested for repeatability and statistical processing, are inserted into one graph, while the recorded dependencies are shown in the graph with a different line color for clarity).

As is evident from the displayed dependencies, the samples in each series showed good agreement of the measured data and the reliability of repeated measurements, which was also confirmed by the results of statistical processing focusing on the Grubbs' test, with only one outlier found, which was excluded from further data processing.

An example of one collection of post-failure samples divided by structure type and arranged in ascending order of volume fraction is shown in Figure 7. According to the assumption, failure occurred at the point of highest stress in the middle of the lower part of the specimens and crack propagation proceeded by breaching the intercellular walls upwards.

For structures with a volume fraction of 30%, failures occurred approximately in the middle of the beam, around the point of the largest bending moment, but at the locations of the highest stress concentration. In the Diamond structure (V_f = 30%), two crack propagations were observed after failure, which proceeded obliquely upwards perpendicular to the cell walls (Figure 8a); in the Gyroid (Figure 8b), this was similar, but due to the larger pore size, the propagation was steeper. In the Primitive structure (Figure 8c), the deflection of the crack propagation was caused by the perpendicular orientation of the cell wall of the internal pore, which in this case acted as a reinforcing element.

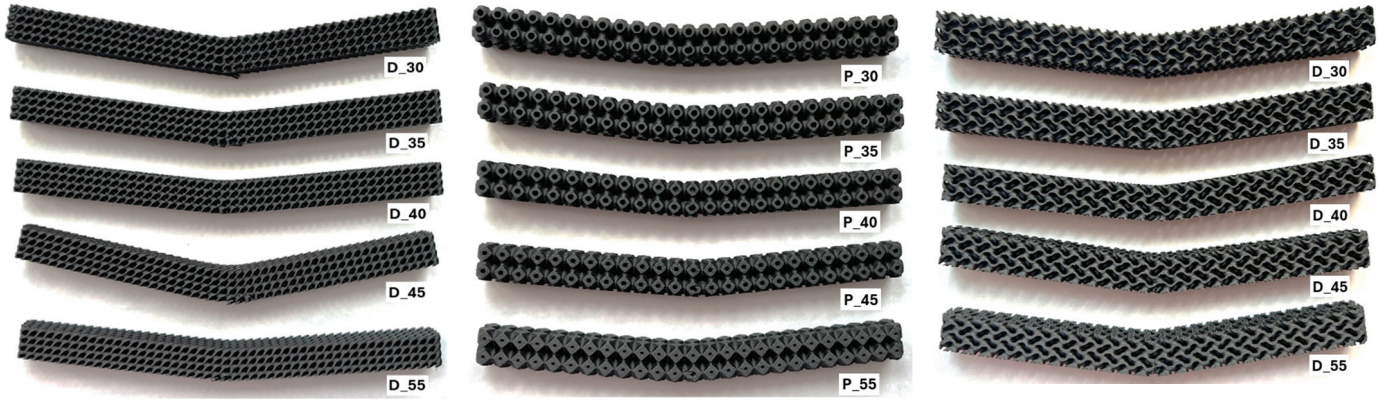

Figure 7. An example of damaged samples with different volume fractions: (**a**) Diamond; (**b**) Primitive; (**c**) Gyroid.

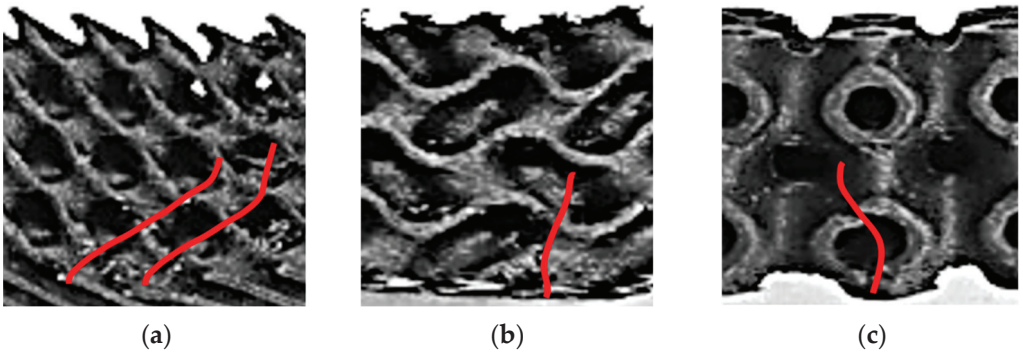

Figure 8. An example of crack propagation (red lines) at the samples with V_f = 30%, magnification 2:1: (**a**) Diamond; (**b**) Gyroid; (**c**) Primitive.

As volume fraction/wall thickness increased, a shift could be seen as slender elements that could previously buckle or bend plastically were at some stages comparatively rigid; the load carried by the walls was higher and local stresses likely reached levels that caused fracture instead of allowing stable plastic deformation. Also, increased wall thickness reduced slenderness; increased stiffness reduced the amplitude of buckling but increased stress concentration at defects, etc.

The threshold volume fraction (or relative density), at which the failure mechanism transitions (from buckling/ductile to brittle), depends not only on the geometry (topology), but also on the material and the quality (defects, etc.). For our observed samples, those volume fractions, 40% for Gyroid and 45% for Diamond, are plausible thresholds, which are related to the material Nylon CF12 and print/processing conditions.

To assess the influence of volume fraction V_f on the behavior of samples during bending loading, the measured data were processed and grouped by type of structures. The average values of measured maximal forces are listed in Table 2, while representative curves of one of the series of samples for each structure type are shown in Figure 9.

As expected, with increasing volume fraction, the maximum measured force also increased; however, its increase was not regular regarding the volume fraction, but for different types of structures the behavior was different, and similarly with regard to the deflection achieved at sample failure. Therefore, examining the behavior of structures from various perspectives, including energetic viewpoint, could provide a more comprehensive understanding.

Table 2. Measured maximal forces F_{max} (N).

	V_f	Structure Type		
		Diamond	**Primitive**	**Gyroid**
Maximal Force F_{max} (N)	30%	163 ± 6.67	141 ± 5.33	110 ± 4.67
	35%	190 ± 2.67	151 ± 4.67	227 ± 2.33
	40%	213 ± 2.00	158 ± 5.33	242 ± 4.67
	45%	279 ± 4.67	179 ± 4.00	252 ± 6.67
	55%	317 ± 6.67	314 ± 6.33	283 ± 0.50

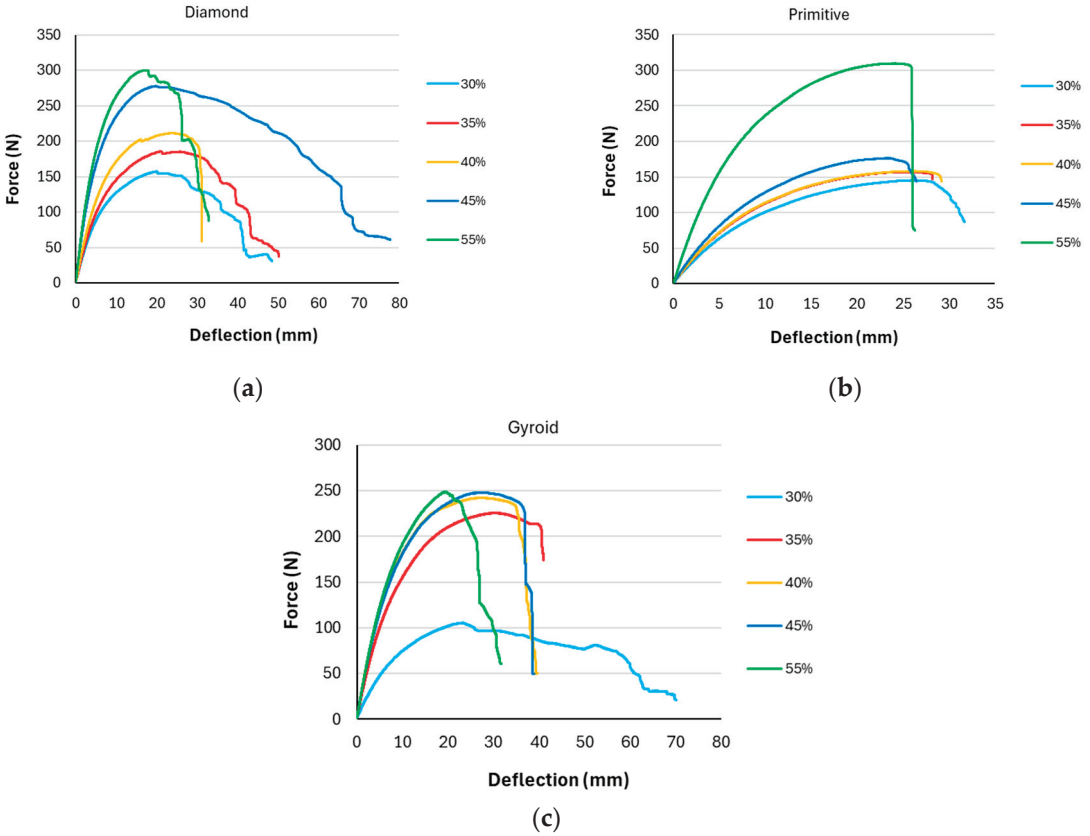

Figure 9. Representative force–deflection curves with different volume fraction for individual structures: (**a**) Diamond; (**b**) Primitive; (**c**) Gyroid.

4.2. Evaluation of Research Results from Mechanical and Energy Absorption Perspective

When evaluating the measured data and dependencies, at first, the bending stiffness was calculated for each structure topology given by the type of structure and the volume fraction.

From the histogram in Figure 10, it is clear that stiffness increases with increasing volume fraction, which was expected. However, it is possible to observe different ways of increasing stiffness with increasing volume fraction for different structures. For the Primitive structure, the increase in stiffness is slow, and only at a volume fraction of 55% is a sudden change evident, while the values for the studied area were in the range of 13.2–28.4 N/mm.

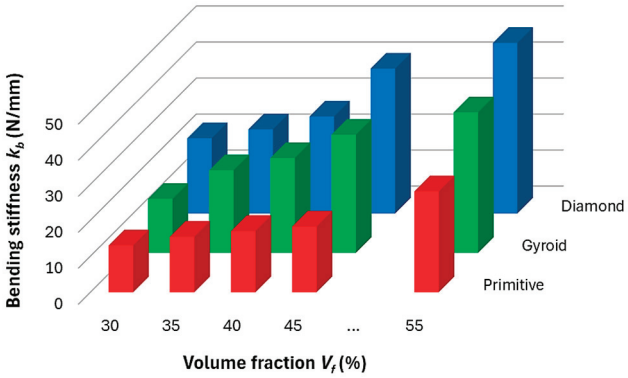

Figure 10. Bending stiffness.

For Gyroid, the dependence of k_b on V_f appears to be linearly increasing with values from 15 to 39.3 N/mm for extreme values of volume fraction of 30 and 55%, while the highest stiffness values (20.9–47.3 N/mm) within the investigated range of volume fraction were shown by the Diamond structure and the increase trend is related to an exponential function.

The irregular growth of stiffness occurs because cellular materials have a nonlinear response as they approach a more rigid mass-like structure. This transition depends on the architecture of the unit cells and the mechanical properties of the material used. It can be said that as the volume fraction in a cellular structure increases, the relative thickness of the cell walls also increases, which affects the stiffness due to the bending and stretching of the material in the structure. Thicker walls contribute more to the overall stiffness, while thinner walls make the structure more flexible, as described in the studies [46,47]. Cellular materials are also prone to stress concentrations at the intersections of cell walls and pores, which act as notches [48]. Higher volume fraction can lead to a transition where the material becomes less porous and more rigid, which affects both stress transfers.

The authors therefore made a quick overview of the dependence of the wall thickness of the structure on the volume fraction, and found that the differences between the wall thicknesses of the structure are relatively large for the same volume fraction of the samples. Below, in Figure 11, the authors generated dependence of the wall thickness on the volume fraction for all three types of structures with a basic cell size of a = 10 mm.

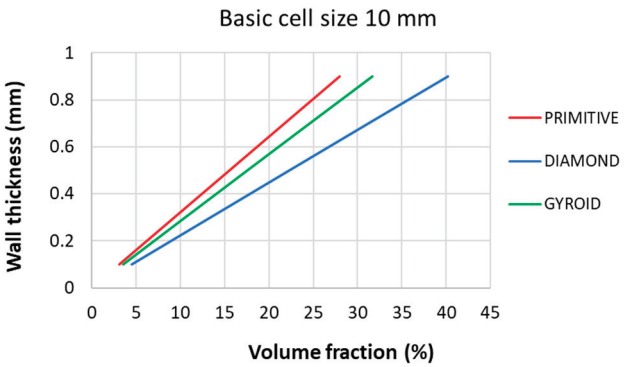

Figure 11. Dependencies of wall thickness on volume fraction for all three studied structures with a basic cell size of a = 10 mm.

It is possible to obtain wall thickness values for higher volume fractions based on the trend of the dependencies given by the equations (with coefficient $R^2 = 1$ in all three cases):

Diamond:

$$y = 0.0224x + 0.001 \quad (12)$$

Gyroid:

$$y = 0.0284x + 0.0012 \quad (13)$$

Primitive:

$$y = 0.0322x + 0.0001 \quad (14)$$

The graph in Figure 11 explains why the Primitive structure exhibits the lowest mechanical properties and the Diamond structure the highest, and demonstrates that wall thickness is a significant factor influencing the properties of the structures if the volume fraction (i.e., the amount of solid phase material used in the production of samples) is set as a criterion for comparing the behavior of the structures.

Analysis of the results suggests that the stiffness mutation observed at 55% volume fraction in the Primitive structure could be due to an increase in cell wall thickness, which causes the material to transition from a "porous support" structure to a "quasi-rigid" structure, where the structure is more continuous and the material can carry a greater load. This transition is likely to lead to a shift in the mechanical properties of the material.

The Gibson-Ashby model [49] describes the mechanical behavior of cellular solids by relating their effective modulus to their relative density (volume fraction). The model predicts the stiffness of the structure based on geometric factors (such as cell wall thickness) and material properties. However, the Gibson-Ashby model assumes isotropic structures, which may not be applicable to more complex, anisotropic lattice structures such as Gyroid or Diamond, which may require more sophisticated models to account for their geometric anisotropy as well as realistic manufacturing conditions and the influence of technological parameters.

For practical applications, it is essential to know the behavior of samples within elastic regions to ensure that components function within a safe range, thereby preventing plastic deformation and potential damage. By means of Equations (2) and (8), and entering the geometric characteristics of the structure using software in which the 3D models of the samples were generated, the yield strength σ_y and effective modulus of elasticity E were calculated, implementing the average value of the force at the elastic point for a specific sample topology, and these are presented in Figure 12. Since the experiments were not directly aimed at specifying Young's modulus following the necessary standards, the term "effective modulus of elasticity E_{ef}" is applied in the manuscript for the purpose of presenting the obtained results, which represent the real behavior of the sample under the given conditions.

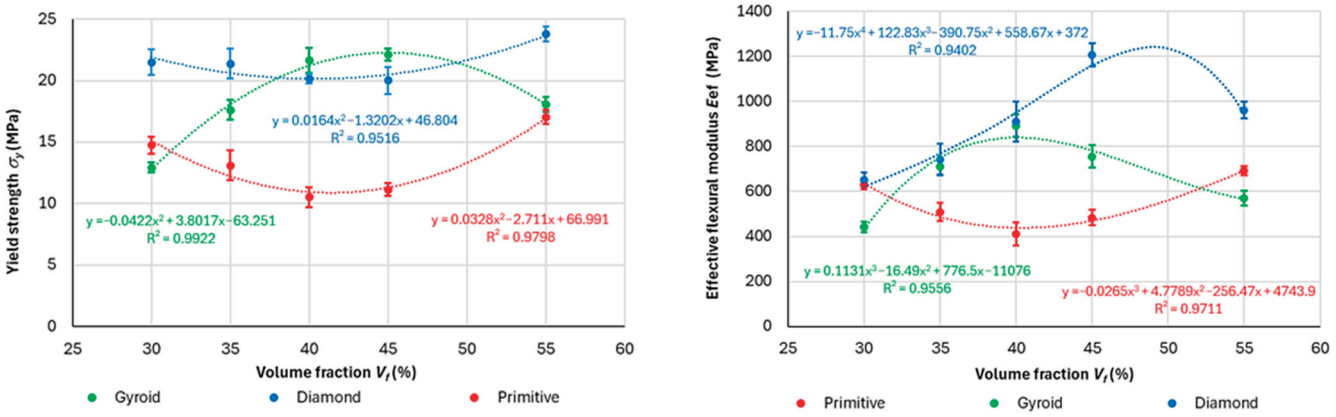

(**a**) (**b**)

Figure 12. Dependence of: (**a**) yield strength; (**b**) effective flexural modulus of elasticity, on volume fraction.

The effective elastic modulus in bending varied within the range of investigated volume fraction V_f for individual structures according to the trends described by the following equations:

Diamond: ($R^2 = 0.9516$)

$$y = 0.0164x^2 - 1.3202x + 46.804 \quad (15)$$

Gyroid: ($R^2 = 0.9922$)

$$y = -0.0422x^2 + 3.8017x - 63.251 \quad (16)$$

Primitive: ($R^2 = 0.9798$)

$$y = 0.0328x^2 - 2.711x + 66.991 \quad (17)$$

It is clear that in the investigated volume fraction range of 30–55% (limited by manufacturability and meaningful applicable material lightweighting) there is a region (minimum for Primitive and Diamond structures, respectively; maximum for Gyroid structure) in which the stresses become extreme, which can mean that this combination of material, structure, technological conditions, cell size, skin thickness, and volume fraction (controlled by wall thickness) is the most suitable (respectively, the most unsuitable) for use when considering the behavior of the sample in the elastic region.

With a high coefficient of determination R^2, which states how well the statistical model predicts the outcomes [50], it is possible to calculate a more accurate volume fraction in which the function takes an extreme. For example, in the Gyroid structure, where a second-order polynomial describes the behavior of the structure in terms of yield strength with respect to volume fraction with relatively high reliability ($R^2 = 0.9922$ is high, close to 1), it is possible to determine through computation that the extremum of the function (maximum value of yield strength) will be at a volume fraction of $V_f = 45.044\%$.

Similarly, the dependence functions of the effective modulus of elasticity E_{ef} on the volume fraction V_f for individual structures were generated, while to describe the dependencies with relatively good reliability of predicting the outputs, it was necessary to use polynomials of a higher degree (third order for Gyroid and Primitive, and fourth order for Diamond). The obtained dependency equations are as follows:

Diamond, $R^2 = 0.9402$

$$y = -11.75x^4 + 122.83x^3 - 390.75x^2 + 558.67x + 372 \quad (18)$$

Gyroid, $R^2 = 0.9534$

$$y = 0.1139x^3 - 16.604x^2 + 781.62x - 11149 \quad (19)$$

Primitive, $R^2 = 0.9711$

$$y = -0.0265x^3 + 4.7789x^2 - 256.47x + 4743.9 \quad (20)$$

In this case, it also appears that the functions in a given range of volume fractions reach an extreme at which the configuration of input parameters for the effective modulus of elasticity E_{ef} ($E_{ef} = \sigma_y / \varepsilon$) is the most (or the least) appropriate. On the basis of the dependencies, it is also inversely possible to determine the necessary volume fraction of the material for the required modulus of elasticity, since sometimes in practice, for low-

stressed components, the yield strength values are not the most important, but the strain is more important.

A measure of the energy dissipation capacity of a structure is given by ductility, which is the deformation capacity of a structure after the first yield [51]. Energy dissipation is desirable for structures in many applications since it refers to the loss of energy in a system in quasi-static loading, and materials with high static energy dissipation tend to also have high damping capabilities under oscillatory motion [52].

Based on the methodology presented in Section 3.2, the values of absorbed energy $U_{F\max}$ (J) up to the maximum force $F_{\max}$ (N), energy required to break the sample U_{break} (J), and consequently the values of the ductility indices μ_d and μ_E were calculated for individual samples. The average values achieved from three measurements of identical samples' topologies are shown in the graphs in Figures 13–15, while the deviation of the evaluated variable did not exceed 5% in all cases.

Both histograms in Figure 13 show similar behavior in samples of the same type. In Gyroid and Diamond structures, the values of absorbed energy (both $U_{F\max}$ until reaching $F_{\max}$ and U_{break} until break) increased. Gyroid reached maximum values of absorbed energy at V_f = 40%, unlike the Diamond structure, in which the values were highest at 45% volume fraction, after which the values decreased in both structures. The Primitive structure also showed a gradual increase in absorbed energy with increasing volume fraction, reaching a maximum at the highest volume fraction examined of 55%, but the further development trend (increase or decrease in energy) is difficult to predict from the measured results.

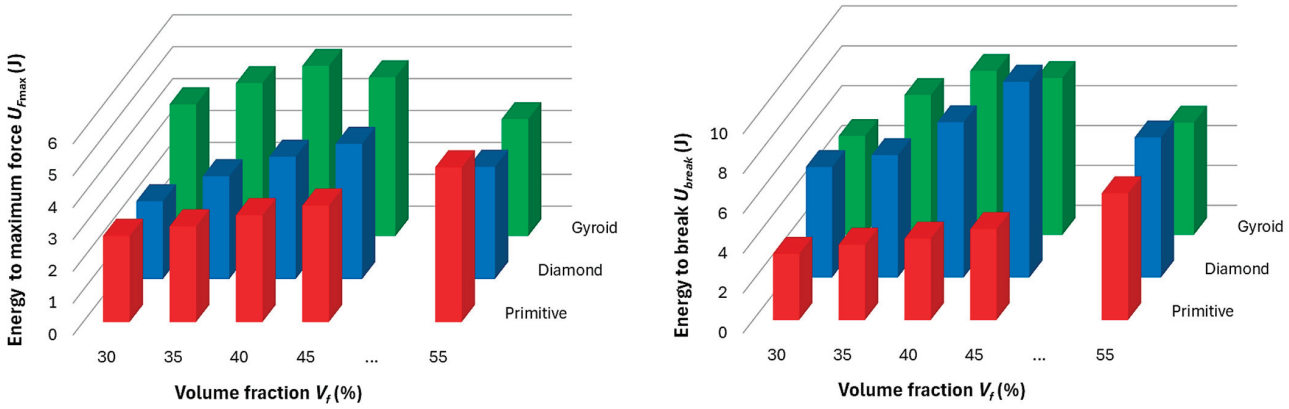

Figure 13. Histograms showing amount of energy (**a**) absorbed up to the maximum force $F_{\max}$ (N); (**b**) required to break the sample.

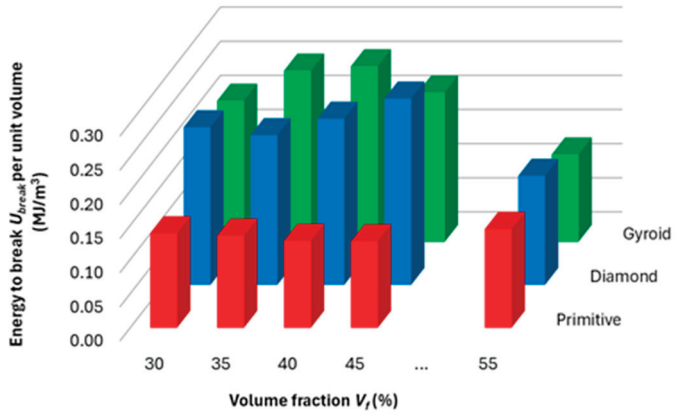

Figure 14. Energy absorption to break per mass unit.

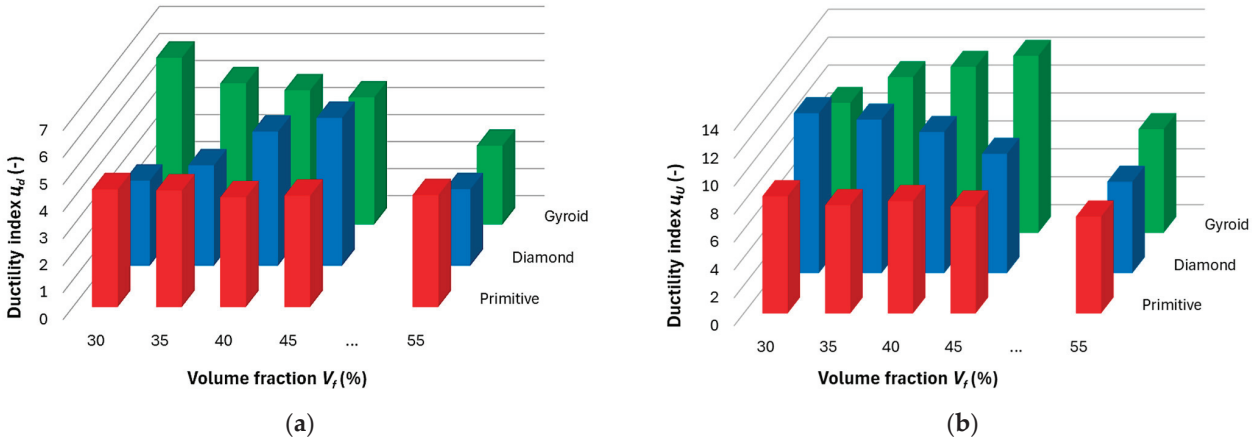

Figure 15. Ductility indices derived from (**a**) deformation and (**b**) absorbed energy for the investigated topologies of the structures.

In order to compare the efficiency of material use, and for the purpose of comparing performance with other materials (results of other researchers), the amount of energy absorbed (until the sample breaks) per unit volume of the solid phase was calculated and plotted in the histogram in Figure 14, and the values achieved for energy absorption to break per a unit mass were tabled (Table 3).

Table 3. Average values of energy absorption to break per unit mass (J/g) for individual structures.

Structure Type	Volume Fraction V_f (%)				
	30	35	40	45	55
Gyroid	0.1737	0.2107	0.2161	0.1837	0.1075
Diamond	0.1940	0.1843	0.2046	0.2292	0.1343
Primitive	0.1162	0.1134	0.1071	0.1064	0.1215

It is clear from the graph in Figure 14 that the highest absorbed energy normalized to a unit volume of material is achieved by structures at different volume fractions; while for Gyroid it is at 40% of the Nylon CF12 used and the value of U_{break} per unit volume reaches 0.257 MJ/m^3, for the Diamond structure it is at a volume fraction of V_f = 45%, U_{break} per unit volume = 0.273 MJ/m^3, and for Primitive it is 0.145 MJ/m^3 at a volume fraction of 55%. Interesting values of material utilization efficiency for evaluating the amount of absorbed energy were shown by the Diamond structure, which at 30% volume fraction reached a value of 0.231 MJ/m^3, which is higher than the Gyroid structure at V_f = 45%, and than the Diamond structure at V_f = 35%.

After recalculating with the specific gravity of the material (1.19 g/cm^3) [29], the Diamond and Gyroid structures in our research achieved energy absorption values in the range of 0.174–0.229 J/g, which is in line with the available study by Feng et al. [53], which focused on CFRP tubes filled with bio-inspired stepped lattices and achieved an amount of absorbed energy in the range of 1.33–3.19 J/g. On the other hand, our energy absorption values are about half the results achieved by Ma [54], who dealt with a reinforced star-shaped sandwich beam with auxetic honeycomb (RSSAH) reinforced with hollow thin-walled tubes of the polymer material PLA. Zhou [55] evaluated energy absorption performances of novel auxetic honeycomb circular tubes under different impact loading, made of PLA and designed with a gradient auxetic circular tube (ACT) by adjusting the number of radial honeycomb layers. The amount of energy absorbed reached a value of around 1 J/g for their structures.

In these mentioned cases, the skin covering the structures and its thickness played an important role, as well as the volume fraction of the material and the shape of the samples, which affect the section modulus of inertia to a large extent. The authors of the presented research did not use any skin because they wanted to know the properties of the structures themselves without the influence of the outer skin since their previous research [5] showed that the influence of the outer surface layer of a continuous material (so-called skin) is very large.

Energy absorption performances of hybrid thin-walled tubes with BCC and BCC-Z lattice structures investigated by Cetin [56], which were made of AlSi10Mg, reached 35 J/g under axial impact loading conditions. In this case, the metal material and the method of loading play the most important role.

The ductility indices, μ_d (based on deformation, Figure 15a) and μ_U (based on absorbed energy, Figure 15b), show inverse behavioral trends for individual structures with increasing volume fraction compared to the trend of energy absorption dependences on volume fraction (Figure 13). If the values of one of the indices decrease with increasing volume fraction, the values of the other index increase, while for the Primitive structure the trend is almost constant in both cases.

As mentioned above, in the experimental analysis of structures with Gyroid and Diamond topologies, an inverse relationship was observed between the ductility indices (μ_d, μ_u) and the ability of the material to absorb energy during deformation. With increasing energy absorption, the ductility of the material decreases, which at first glance seems paradoxical, since a higher rate of absorbed energy is often associated with a greater deformation capacity. However, this phenomenon can be explained in terms of the dominant mechanisms of plastic dissipation and the nature of the deformation of the cellular structure itself.

In structures with a higher volume fraction, i.e., denser topologies, more elastic deformation occurred during loading, while the proportion of plastic energy dissipation was limited. The thicker and stiffer cell walls of these structures showed increased resistance to plastic flow and were more prone to elastic buckling or local deformations, which allowed for a more efficient distribution of the loaded energy without permanent damage to the material. This led to a higher value of absorbed energy, but at the cost of reduced ductility, because plastic deformation—and therefore the ability of the material to change its shape without immediate failure—was significantly limited.

In contrast, structures with a lower volume fraction had thinner cell walls, which were more sensitive to plastic mechanisms such as permanent buckling, local fractures, or friction between elements. In such cases, the energy during deformation was absorbed predominantly by plastic work, thereby increasing the ductility of the structure. However, this higher deformation capacity was achieved at the cost of lower overall energy absorption, as the structure was not able to effectively resist sudden or intense loads in an elastic manner alone.

This correlation between ductility, energy absorption, and structural safety has a fundamental impact on the selection of the appropriate topology for a particular application. In cases where impact protection is a priority, such as in automotive deformation zones or protective elements, structures with a higher volume fraction and higher energy absorption are more suitable, even at the cost of lower ductility. Conversely, in applications where high ductility or flexibility is required—such as in biomechanical implants or soft damping components—structures with lower density are more advantageous, allowing for greater plastic deformations. In cases where a compromise between energy absorption and ductility is needed, such as in vibration dampers or multipurpose technical components,

solutions with structural gradation, or a combination of different topologies or materials, appear promising.

It follows from the above that the inverse relationship between energy absorption and ductility is not just an empirical observation, but reflects deeper connections between microstructural geometry, deformation mechanisms, and energy dissipation. In the future, when designing functional structures from advanced topologies such as Gyroid and Diamond, it will be therefore essential for the authors to consider not only their static strength, but also their dynamic and plastic behavior in terms of the requirements of the given application.

In connection with the tested material, questions arise regarding its limits in use for specific applications. One of the most important environmental factors that can affect the performance of Nylon CF12 is temperature. Since Nylon, as a synthetic fiber-based polymer, is known for its susceptibility to change in mechanical properties at elevated temperatures, in real practice, where materials are exposed to high temperatures, its thermal degradation can occur. High temperatures can lead to softening of the material, a decrease in its strength and elasticity, and thus a decrease in its ability to withstand mechanical loads [57]. This effect can be particularly critical in applications where the requirements for long-term stability of the material at operating temperatures are high. On the other hand, low temperatures can also affect the performance of the material, especially if Nylon CF12 operates in aerospace applications or in places with extreme winter conditions. At temperatures below freezing, the material can become more brittle and less able to withstand shock or impact loads, which could lead to structural failure [58]. These temperature changes can have a negative impact on the overall service life of components made from this material.

Another factor to consider when selecting Nylon CF12 for a given application is the effect of humidity. Nylon, as a hygroscopic material, tends to absorb moisture from the surrounding environment. In the case of high humid conditions (e.g., in humid environments or when the material is exposed to rain), mechanical properties can degrade, such as a decrease in strength and elastic modulus. Humidity causes water molecules to bind to the polymer chains, which can lead to their swelling and a decrease in intermolecular forces between the chains [59]. This process can ultimately affect not only the strength of the material, but also its resistance to wear and fatigue damage.

Possible improvements in the material properties include, for example, modifying the material mixture to increase moisture resistance and improve stability at high temperatures, or implementing protective coatings or composite materials to provide additional protection against external influences.

For later practical applications, it will be important to find a compromise (using multi-criteria optimization) between the performance characteristics of the sample and the material consumption, while of course it will be necessary to take into account other safety and reliability factors.

5. Conclusions

Porous materials can be an effective tool for saving material and reducing the weight of a component while maintaining its desired properties. The aim of the presented research was to determine the effect of volume fraction on the properties of Nylon CF12 in terms of mechanical properties and energy absorption to assess their dissipative properties and damping potential. At the same time, the behavior of three types of complex porous structures (Diamond, Gyroid, and Primitive) was compared when changing the volume fraction, while the same basic cell size was maintained for all samples. The most important findings of the research are as follows:

- The stiffness of the structure increased with increasing volume fraction, and the highest stiffness was shown by the Diamond structure with values from 20.9 to 47.3 N/mm, followed by Gyroid in the range of 15–39.3 N/mm, and finally by the Primitive structure with values of 13.2–28.4 N/mm in the investigated volume fraction range of 30–55%.
- When assessing the behavior of the sample in the elastic region, the results of yield strength and effective elastic modulus showed that within the investigated volume fraction range of 30–55%, there is an area in which the individual structures show the best/worst properties, which may mean that this specific combination of material, structure, technological conditions, cell size, and volume fraction is the most suitable (or least suitable). The dependencies of the above variables on V_f can be described by polynomial functions with relatively good reliability, but the resulting equations and coefficients will need to be verified in the future by testing with a larger number of samples.
- Thicker and stiffer cell walls of these structures have shown increased resistance to plastic flow and are more susceptible to elastic buckling or local deformations, which allow for a more efficient distribution of the loaded energy without permanent damage to the material. This leads to a higher value of absorbed energy, but at the cost of reduced ductility, since plastic deformation—and therefore the ability of the material to change its shape without immediate failure—is significantly limited.
- Until reaching maximum force, the Gyroid structure is best able to absorb energy, and in terms of the total energy that the samples were able to absorb until failure, the Gyroid and Diamond structures were comparable; however, the highest values of absorbed energy were achieved by the Gyroid structure at 40% volume fraction, and the Diamond structure at V_f = 45%.
- The inverse relationship between energy absorption and ductility reflects deeper connections between microstructural geometry, deformation mechanisms, and energy dissipation.
- In terms of ductility, the structures show different behavior. In the area up to the maximum load, the ductility index μ_d based on deflection shows for the Gyroid structure a decreasing character with increasing volume fraction, and, conversely, for the Diamond structure it increases, while at V_f = 55% a significant decrease was already recorded at the Diamond structure.

  In the area of the behavior of the samples up to failure, the ductility index derived on the basis of energy has the opposite trend; for the Gyroid it increases with volume fraction and for the Diamond it decreases.

  The Primitive structure shows stable values with the smallest influence of volume fraction in both ductility indices.
- Based on the research, it can be stated that both Gyroid and Diamond structures appear to be suitable static energy dissipators and the choice of structure will depend on the application and the area in which energy absorption is required (i.e., whether it is a stress area up to maximum load or to total failure). The damping properties during oscillation or impact will be verified and compared in the authors' research in the near future.

Author Contributions: Conceptualization, K.M.; methodology, K.M.; software, K.M.; validation, K.M., P.P.M. and D.G.; formal analysis, K.M. and M.T.; investigation, K.M., P.P.M. and D.G.; resources, K.M. and M.T.; data curation, K.M., P.P.M. and D.G.; writing—original draft preparation, K.M.; writing—review and editing, P.P.M. and D.G.; visualization, K.M.; supervision, K.M. and P.P.M.; project administration, K.M. and P.P.M.; funding acquisition, K.M. All authors have read and agreed to the published version of the manuscript.

Funding: This research was funded by the Ministry of Education, Science, Research and Sport of the Slovak Republic by the grants APVV-19-0550 and KEGA 042TUKE-4/2025, as well as the CEEPUS agency within the network SK-2026-01-2526.

Institutional Review Board Statement: Not applicable.

Data Availability Statement: The data are contained within the article.

Acknowledgments: The authors would like to express their gratitude to the Ministry of Education, Science, Research and Sports of the Slovak Republic for research support provided through the grants APVV-19-0550, KEGA 042TUKE-4/2025 and APVV SK-AT-23-0008, as well as the CEEPUS agency within the network SK-2026-01-2526.

Conflicts of Interest: The authors declare no conflicts of interest.

References

1. Arshad, A.; Kovaļčuks, V. Computational Investigations for the Feasibility of Passive Flow Control Devices for Enhanced Aerodynamics of Small-Scale UAVs. *Aerospace* **2024**, *11*, 473. [CrossRef]
2. Hreha, P.; Hloch, S.; Monka, P.; Monkova, K.; Knapčikova, L.; Hlavaček, P.; Zeleňák, M.; Samardžić, I.; Kozak, D. Investigation of sandwich material surface created by abrasive water jet (AWJ) via vibration emission. *Metalurgija* **2014**, *53*, 29–32.
3. Kadkhodapour, J.; Montazerian, H.; Darabi, A.; Anaraki, A.; Ahmadi, S.; Zadpoor, A.; Schmauder, S. Failure mechanisms of additively manufactured porous biomaterials. *J. Mech. Behav. Biomed. Mater.* **2015**, *50*, 180–191. [CrossRef]
4. Plessis, A.D.; Razavi, S.M.J.; Benedetti, M.; Murchio, S.; Leary, M.; Watson, M.; Bhate, D.; Berto, F. Properties and applications of additively manufactured metallic cellular materials: A review. *Prog. Mater. Sci.* **2022**, *125*, 100918. [CrossRef]
5. Monkova, K.; Monka, P.P.; Koroľ, M.; Torok, J.; Beňo, P. The Effect of a Face Wall on a Cellular Structure During Bending. In *Smart Cities: Importance of Management and Innovations for Sustainable Development. Mobility IoT 2023. EAI/Springer Innovations in Communication and Computing*; Springer: Cham, Switzerland, 2024.
6. Kinik, D.; Gánovská, B.; Hloch, S.; Monka, P.; Monková, K.; Hutyrová, Z. On-line monitoring of technological process of material abrasive water jet cutting. *Tech. Vjesn.-Tech. Gaz.* **2015**, *22*, 351–357. [CrossRef]
7. Khosravani, M.R.; Reinicke, T. Effects of fiber on the fracture behavior of 3D-printed fiber reinforced nylon. *Procedia Struct. Integr.* **2022**, *35*, 59–65. [CrossRef]
8. Grbović, A.; Kastratović, G.; Božić, Ž.; Božić, I.; Obradović, A.; Sedmak, A.; Sedmak, S. Experimental and numerical evaluation of fracture characteristics of composite material used in the aircraft engine cover manufacturing. *Eng. Fail. Anal.* **2022**, *137*, 106286. [CrossRef]
9. Bernard, A.R.; Yalcin, M.M.; ElSayed, M.S. Crashworthiness investigations for 3D printed multi-layer multi-topology carbon fiber nylon lattice materials. *J. Reinf. Plast. Compos.* **2024**, *44*, 634–649. [CrossRef]
10. Sahu, S.K.; Badgayan, N.D.; Samanta, S.; Sreekanth, P.S.R. Evaluation of Cell Parameter Variation on Energy Absorption Characteristic of Thermoplastic Honeycomb Sandwich Structure. *Arab. J. Sci. Eng.* **2021**, *46*, 12487–12507. [CrossRef]
11. Yalçın, M.M. Flexural Behavior of 3D-Printed Carbon Fiber-Reinforced Nylon Lattice Beams. *Polymers* **2024**, *16*, 2991. [CrossRef]
12. Calignano, F.; Lorusso, M.; Roppolo, I.; Minetola, P. Investigation of the Mechanical Properties of a Carbon Fibre-Reinforced Nylon Filament for 3D Printing. *Machines* **2020**, *8*, 52. [CrossRef]
13. Islam, N.; Baxevanakis, K.P.; Silberschmidt, V.V. Mechanical characterisation of AM nylon-matrix carbon-fibre-reinforced composite in tension. *Mater. Today Proc.* **2022**, *70*, 50–54. [CrossRef]
14. Monkova, K.; Monka, P.P.; Burgerova, J.; Szabo, G. Investigating the Flexural Properties of 3D-Printed Nylon CF12 with Respect to the Correlation Between Loading and Layering Directions. *Polymers* **2025**, *17*, 788. [CrossRef]
15. Alfouneh, M.; Hoang, V.N.; Luo, Z.; Luo, Q. Topology optimization for multi-layer multi-material composite structures. *Eng. Optim.* **2022**, *55*, 773–790. [CrossRef]
16. Xie, K.; Li, M.; Shen, J. Dynamic Behavior and Energy Absorption of Typical Porous Materials under Impacts. *Materials* **2024**, *17*, 5035. [CrossRef]
17. Taylor, S.V.; Moustafa, A.R.; Cordero, Z.C. Architectured Chain Lattices with Tailorable Energy Absorption in Tension. *arXiv* **2020**, arXiv:2008.07402. [CrossRef]
18. Zhao, X.; Li, X.; Su, Y. Origami-inspired viscoelastic lattice structures for energy absorption. *Adv. Mater.* **2023**, *35*, 2304–10238.
19. Lee, C.S.; Park, Y.J. Mechanical behavior of octet-truss lattices with variable strut geometries. *Mater. Des.* **2023**, *234*, 111944. [CrossRef]
20. Zhou, S.; Li, Y. Mechanical properties of FFF-printed hybrid lattice structures: A comparison of design strategies. *J. Manuf. Process.* **2023**, *75*, 358–368. [CrossRef]

21. Wang, W.; Lee, D. Energy absorption and mechanical performance of flexible TPU lattice structures. *Polym. Eng. Sci.* **2020**, *60*, 1405–1417. [CrossRef]
22. Zia, A.A.; Tian, X.; Liu, T.; Zhou, J.; Ghouri, M.A.; Yun, J.; Li, W.; Zhang, M.; Li, D.; Malakhov, A.V. Mechanical and energy absorption behaviors of 3D printed continuous carbon/Kevlar hybrid thread reinforced PLA composites. *Compos. Struct.* **2023**, *303*, 116386. [CrossRef]
23. Farshbaf, S.; Dialami, N.; Cervera, M. Large deformation and collapse analysis of re-entrant auxetic and hexagonal honeycomb lattice structures subjected to tension and compression. *Mech. Mater.* **2025**, *210*, 105457. [CrossRef]
24. Li, D.; Liao, W.; Dai, N.; Xie, Y.M. Comparison of Mechanical Properties and Energy Absorption of Sheet-Based and Strut-Based Gyroid Cellular Structures with Graded Densities. *Materials* **2019**, *12*, 2183. [CrossRef]
25. Kahraman, M.F.; İriç, S.; Genel, K. Comparative failure behavior of metal honeycomb structures under bending: A finite element-based study. *Eng. Fail. Anal.* **2024**, *157*, 107963. [CrossRef]
26. Sun, Q.; Sun, J.; Guo, K.; Wang, L. Compressive mechanical properties and energy absorption characteristics of SLM fabricated Ti6Al4V triply periodic minimal surface cellular structures. *Mech. Mater.* **2022**, *166*, 104241. [CrossRef]
27. Benedetti, M.; du Plessis, A.; Ritchie, R.O.; Dallago, M.; Razavi, S.M.J.; Berto, F. Architected cellular materials: A review on their mechanical properties towards fatigue-tolerant design and fabrication. *Mater. Sci. Eng. R* **2021**, *144*, 100606. [CrossRef]
28. Simsek, U.; Akbulut, A.; Gayir, C.E.; Basaran, C.; Sendur, P. Modal characterization of additively manufactured TPMS structures: Comparison between different modeling methods. *Int. J. Adv. Manuf. Technol.* **2021**, *115*, 657–674. [CrossRef]
29. FDM Nylon 12 Carbon Fiber Data Sheet; Stratasys Ltd. 2018. Available online: https://www.stratasys.com/siteassets/materials/materials-catalog/fdm-materials/nylon-12cf/mds_fdm_nylon-12cf_0921a.pdf?v=48e2e4 (accessed on 15 June 2025).
30. Christodoulou, T.I.; Alexopoulou, V.E.; Markopoulos, A.P. An experimental investigation of the mechanical properties of fused filament fabricated nylon-carbon fiber composites. *Cut. Tools Technol. Syst.* **2024**, *100*, 148–167. [CrossRef]
31. Korol, M. Research on the Adaptation of the Characteristics of Cellular Structures for the Distribution of Stress in the Components. Ph.D. Thesis, Faculty of Manufacturing Technologies with a seat in Presov, Technical University in Kosice, Kosice, Slovakia, 2024.
32. Guo, K.; Ren, Y.; Han, G.; Xie, T.; Jiang, H. Hygrothermal aging and durability prediction of 3D-printed hybrid fiber composites with continuous carbon/Kevlar-fiber and short carbon-fiber. *Eng. Fail. Anal.* **2025**, *167 Pt A*, 108958. [CrossRef]
33. Korol, M.; Török, J.; Monka, P.P.; Baron, P.; Mrugalska, B.; Monkova, K. Researching on the Effect of Input Parameters on the Quality and Manufacturability of 3D-Printed Cellular Samples from Nylon 12 CF in Synergy with Testing Their Behavior in Bending. *Polymers* **2024**, *16*, 1429. [CrossRef]
34. *ISO 178:2019*; Plastics Determination of Flexural Properties. ISO: Geneva, Switzerland, 2019.
35. *ASTM D790*; Standard Test Methods for Flexural Properties of Unreinforced and Reinforced Plastics and Electrical Insulating Materials. ASTM: West Conshohocken, PA, USA, 2017. [CrossRef]
36. Mitrovic, N.; Milosevic, M.; Momcilovic, N.; Petrovic, A.; Miskovic, Z.; Sedmak, A.; Popovic, P. Local Strain and Stress Analysis of Globe Valve Housing Subjected to External Axial Loading. In *Key Engineering Materials*; Trans Tech Publications Ltd.: Zurich, Switzerland, 2014; Volume 586, pp. 214–217.
37. Kumar, R.; Lal, A.; Sutaria, B.M. Numerical and experimental investigation for flexural response of Kevlar short fiber tissue/carbon fiber belts toughened honeycomb sandwich plate. *Forces Mech.* **2023**, *12*, 100222. [CrossRef]
38. Guo, Y.; Zhang, J.; Chen, L.; Du, B.; Liu, H.; Chen, L.; Li, W.; Liu, Y. Deformation behaviours and energy absorption of auxetic lattice cylindrical structures under axial crushing load. *Aerosp. Sci. Technol.* **2020**, *98*, 105662. [CrossRef]
39. Zhang, X.; Jin, H.; Yu, S.; Bi, X.; Zhou, S. Analysis of bending deflection of tunnel segment under load- and corrosion-induced cracks by improved XFEM. *Eng. Fail. Anal.* **2022**, *140*, 106576. [CrossRef]
40. Ribeiro, V.; Correia, J.; Mourão, A.; Lesiuk, G.; Gonçalves, A.; De Jesus, A.; Berto, F. Fatigue crack growth modelling by means of the strain energy density-based Huffman model considering the residual stress effect. *Eng. Fail. Anal.* **2022**, *140*, 106543. [CrossRef]
41. Montazeri, A.; Bahmanpour, E.; Safarabadi, M. Three-Point Bending Behavior of Foam-Filled Conventional and Auxetic 3D-Printed Honeycombs. *Adv. Eng. Mater.* **2023**, *25*, 2300273. [CrossRef]
42. Monkova, K.; Monka, P.P.; Božić, Ž.; Rački, I. Comparison of the stiffnesses of three types of porous structures. *Procedia Struct. Integr.* **2025**, *68*, 588–591. [CrossRef]
43. Djordjevic, B.; Sedmak, A.; Mastilovic, S.; Popovic, O.; Kirin, S. History of ductile-to-brittle transition problem of ferritic steels. *Procedia Struct. Integr.* **2022**, *42*, 88–95. [CrossRef]
44. Subhani, M.; Globa, A.; Al-Ameri, R.; Moloney, J. Flexural strengthening of LVL beam using CFRP. *Constr. Build. Mater.* **2017**, *150*, 480–489. [CrossRef]
45. Naaman, A.E.; Jeong, S.M. Structural Ductility of Concrete Beams Prestressed with FRP Tendons. In *Non-Metallic (FRP) Reinforcement for Concrete Structures, Proceedings of the 2nd International RILEM Symposium (FRPRXS-2), Ghent, Belgium, 23–25 August 1995*; RILEM: Bagneus, France, 1995; pp. 379–386.

46. Burnett, C.; Graninger, G.; Eren, Z.; Fazlan, B.G.; Kazanci, Z. Tensile performance of carbon fibre-reinforced 3D-printed polymers: Effect of printing parameters. *Eng. Fail. Anal.* **2025**, *152*, 107436. [CrossRef]
47. Marşavina, L.; Valean, C.; Marghitas, M.; Linul, E.; Razavi, N.; Berto, F.; Brighenti, R. Effect of the manufacturing parameters on the tensile and fracture properties of FDM 3D-printed PLA specimens. *Eng. Fract. Mech.* **2022**, *274*, 108766. [CrossRef]
48. Monkova, K.; Monka, P.P.; Žaludek, M.; Beňo, P.; Hricová, R.; Šmeringaiová, A. Experimental Study of the Bending Behaviour of the Neovius Porous Structure Made Additively from Aluminium Alloy. *Aerospace* **2023**, *10*, 361. [CrossRef]
49. Gibson, L.J.; Ashby, M.F. *Cellular Solids: Structure and Properties*; Cambridge University Press: Cambridge, UK, 1997; ISBN 9781139878326. [CrossRef]
50. Bazios, P.; Tserpes, K.; Pantelakis, S. Modelling and Experimental Validation of the Porosity Effect on the Behaviour of Nano-Crystalline Materials. *Metals* **2020**, *10*, 821. [CrossRef]
51. Mohabeddine, A. Comparison between brittle and ductile adhesives in CFRP/steel joints. *Procedia Struct. Integr.* **2022**, *37*, 1043–1048. [CrossRef]
52. Hu, Y.; Liu, Y.; Xi, J.; Jiang, J.; Wang, Y.; Chen, A.; Nikbin, K. Energy dissipation-based LCF model for additive manufactured alloys with dispersed fatigue properties. *Eng. Fail. Anal.* **2024**, *159*, 108139. [CrossRef]
53. Feng, J.; Zhu, G.; Niu, X.; Lv, R.; Wang, Z.; Guo, B. Energy absorption of CFRP tubes filled with bio-inspired graded lattices under bending load. *Eng. Struct.* **2025**, *336*, 120309. [CrossRef]
54. Ma, Y.; Zhang, D.; Liu, Z.; Xu, P.; Lu, F.; Fei, Q. Bending response and energy absorption of sandwich beams with combined reinforced auxetic honeycomb core. *Mech. Adv. Mater. Struct.* **2024**, *32*, 4993–5005. [CrossRef]
55. Zhou, Q.; Xu, Z.; Cui, Y.; Wang, K.; Wang, B.; Wang, B. Evaluations of three-point bending and energy absorption performances of novel auxetic honeycomb circular tubes under different impact loading. *Constr. Build. Mater.* **2025**, *475*, 141132. [CrossRef]
56. Cetin, E.; Baykasoğlu, C. Energy absorption of thin-walled tubes enhanced by lattice structures. *Int. J. Mech. Sci.* **2019**, *157–158*, 471–484. [CrossRef]
57. Lin, S.; Peng, C.; Deng, F.; Yin, D.; Ye, B. Influence of structural geometry on tensile properties and fracture toughness in 3D printed novel structures. *Eng. Fail. Anal.* **2024**, *161*, 108277. [CrossRef]
58. Luo, J.; Luo, Q.; Zhang, G.; Sun, G. On strain rate and temperature dependent mechanical properties and constitutive models for additively manufactured polylactic acid (PLA) materials. *Thin-Walled Struct.* **2022**, *179*, 109624. [CrossRef]
59. Najafi, M.; Ahmadi, H.; Liaghat, G. Experimental investigation on energy absorption of auxetic structures. *Mater. Today Proc.* **2021**, *34*, 350–355. [CrossRef]

polymers

MDPI

Article

High-Performance Barium Titanate, Carbon Nanotube, and Styrene–Butadiene Rubber-Based Single Composite TENG for Energy Harvesting and Handwriting Recognition

Md Najib Alam, Vineet Kumar , Youjung Kim, Dong-Joo Lee and Sang-Shin Park *

School of Mechanical Engineering, Yeungnam University, 280, Daehak-ro, Gyeongsan 38541, Republic of Korea; mdnajib.alam3@gmail.com (M.N.A.); vineetfri@gmail.com (V.K.); msyzlmc@naver.com (Y.K.); djlee@yu.ac.kr (D.-J.L.)

* Correspondence: pss@ynu.ac.kr

Abstract: In this research, a single composite-type stretchable triboelectric nanogenerator (TENG) is proposed for efficient energy harvesting and handwriting recognition. The composite TENGs were fabricated by blending dielectric barium titanate (BT) and conductive carbon nanotubes (CNTs) in varying amounts into a styrene–butadiene rubber matrix. The energy harvesting efficiency depends on the type and amount of fillers, as well as their dispersion within the matrix. Stearic acid modification of BT enables near-nanoscale filler distribution, resulting in high energy conversion efficiencies. The composite achieved power efficiency, power density, charge efficiency, and charge density values of 1.127 nW/N, 8.258 mW/m^3, 0.146 nC/N, and 1.072 mC/m^3, respectively, under only 2% cyclic compressive strain at 0.85 Hz. The material performs better at low stress–strain ranges, exhibiting higher charge efficiency. The generated charge in the TENG composite is well correlated with the compressive stress, which provides a minimum activation pressure of 0.144 kPa, making it suitable for low-pressure sensing applications. A flat composite with dimensions of 0.02 × 6 × 5 cm^3 can produce a power density of 26.04 W/m^3, a charge density of 0.205 mC/m^3, and an output voltage of 10 V from a single hand pat. The rubber composite also demonstrates high accuracy in handwriting recognition across different individuals, with clear differences in sensitivity curves. Repeated attempts by the same person show minimal deviation (<5%) in writing time. Additionally, the presence of reinforcing fillers enhances mechanical strength and durability, making the composite suitable for long-term cyclic energy harvesting and wearable sensor applications.

Keywords: triboelectric nanogenerator; barium titanate; carbon nanotubes; rubber nanocomposite; energy harvesting; handwriting recognition

1. Introduction

Electrical energy derived from physical processes has become increasingly viable due to advancements in materials and technology. Although the energy produced through these processes is comparatively low, it does not have the harmful environmental impacts associated with chemical processes. Recently, nanogenerators have been developed to generate energy on both small and large scales from mechanical motion or temperature gradients [1]. Among various types of nanogenerators, triboelectric nanogenerators (TENGs) have gained significant attention for their ability to harvest energy from mechanical motion [2]. However, several challenges remain, including low power density, material degradation due to friction, low stretchability, environmental sensitivity, limitations in

large-scale production, irregular output, charge retention issues, fabrication complexity, and compatibility with existing systems [3–8]. Overcoming these challenges could enable TENGs to provide scalable energy solutions that can be utilized across a wide range of intelligent and commercial applications [9–14].

Material selection and fabrication techniques are crucial for achieving high-power TENGs. Ideally, the selected materials should possess high dielectric constants, wide electron affinity differences, and large surface areas [15–18]. Since TENGs rely on contact and separation mechanisms to generate electrical energy, significant physical interaction between the interfaces is essential. This interaction leads to higher frictional forces, which, in turn, generate more triboelectric charges [19,20]. The materials used in triboelectric nanogenerators are diverse, including metals as conductors, dielectric polymers, and inorganic materials [21]. Several parameters must be considered for practical applications, including power efficiency, stretchability, mechanical stability, and material compatibility.

Among various electrically conductive materials, carbon nanotubes (CNTs) have emerged as attractive components in TENGs. Okochi et al. [22] found that carbon nanotube composite papers can serve as TENGs with promising output voltages. In another study, Kınas et al. [23] demonstrated that a 3 wt% CNT-based polyacrylonitrile nanofiber TENG composite (4×4 cm^2) could generate 960 V and had a charge capacity of 260 nC under a 14.6 MΩ load resistance and a 0.022 μF capacitive load, respectively. Wang et al. [24] developed a TENG incorporating 0.5% CNTs into a supramolecular polyrotaxane matrix, achieving a power density of 385 mW/m^2 at a 20 MΩ load resistance. Although polymer-based composites [22–24] show significant output power densities, they may exhibit limitations in mechanical properties such as stretchability. To address this, Lee et al. [25] developed a poly (dimethylsiloxane) (PDMS)-based TENG using surface-modified CNTs via pulsed laser ablation, achieving excellent power density. Similarly, Matsunaga et al. [26] demonstrated a transparent and stretchable TENG fabricated with a thin CNT film over a PDMS substrate, achieving excellent power output suitable for soft wearable applications.

Dielectric ceramic materials play a significant role in enhancing the dielectric properties of TENG components, thereby improving charge accumulation and polarization, which leads to higher energy harvesting efficiencies [17,27–29]. Barium titanate, a ceramic material with a high dielectric constant and excellent binding capability with polymers, is an attractive choice for TENG composites [30–34]. Pandey et al. [30] fabricated a Nafion-functionalized barium titanate and polyvinylidene fluoride composite, which demonstrated several times higher output voltage, current density, and power density compared to pristine polyvinylidene fluoride. Sun et al. [31] achieved a high-performance TENG by using aminated barium titanate and functionalized graphite oxide with polyimide as a substrate, aimed at the early detection of Parkinson's disease. Yan et al. [32] demonstrated a TENG with a polyimide nanofiber and a piezoelectric carbon nanotube/barium titanate hybrid filler-based composite, resulting in three times higher energy output compared to pristine polyimide. They also achieved a maximum power density of 5.3 W/m^2 at a 5 MΩ loading resistance and a maximum charge of approximately 80 nC with 25 N of applied force. Shuai-Bo et al. [33] developed a paper-based TENG using barium titanate and bamboo cellulose, achieving 13.51 μA of current, 118.5 V output voltage, and a maximum power density of 0.36 W/m^2 at a 5 MΩ load resistance, significantly outperforming pure cellulose paper. Similarly, Patil et al. [34] achieved 103 V output voltage, 3.6 μA current, and a maximum power density of 32 μW/cm^2 at 40 N of applied force with a copy paper and barium titanate-based composite. From this discussion, it is evident that TENG performance varies significantly with material properties, and thus, the choice of materials is critical for achieving higher energy conversion efficiency.

Recently, rubber has emerged as a viable candidate for flexible and stretchable TENG applications [35–39]. As a tribo-negative material, rubber can be combined with tribo-positive materials to enhance TENG efficiency. Unlike other polymeric materials, rubber offers a wide elasticity range and robust stretchability. Additionally, due to stronger physical and chemical interactions with various fillers, the mechanical properties of rubber-based composites can be significantly improved. As a result, rubber composite-based TENGs are suitable for use in durable electronic and energy-harvesting systems.

Appamato et al. [35] fabricated natural rubber-Ag nanocomposites with different surfactants, finding that cationic surfactant CTAB-capped Ag nanoparticles resulted in higher power densities compared to anionic SDS-modified composites, due to better filler dispersion and dielectric enhancements. These composites achieved a maximum output voltage of 120 V and a power density of 0.83 W/m^2, which is six times higher than unfilled natural rubber. The composites also exhibited antibacterial activity and demonstrated energy harvesting from walking using a TENG film integrated into a shoe insole. In another study, Chomjun et al. [36] obtained a maximum power density of 0.242 W/m^2 and an output voltage of 89.6 V using a natural rubber and activated carbon composite. Candido et al. [37] fabricated all-silicone rubber-based TENGs, achieving a maximum power density of 197.2 $\mu W/cm^2$ and an output voltage of 308.7 V with graphite-impregnated electrodes. Lu et al. [38] developed a TENG with carboxyl-functionalized nitrile butadiene rubber, achieving a maximum power density of 6.14 W/m^2. Gao et al. [39] created a TENG from a special rubber prepared by grafting acrylamide and hydroxyethyl acrylate to carboxylated nitrile butadiene rubber, obtaining an open-circuit voltage of 723 V and a power density of 3.25 W/m^2. These results highlight that output voltage, current, and power density vary with different rubber composites, likely due to differences in electron affinity values and measurement techniques. A TENG composite with higher resistivity may produce higher peak voltage and current according to Ohm's law. Similarly, maximum power density can be achieved at an optimum loading resistance. However, charge generation primarily depends on the electron affinity differences and the interfacial areas of interaction between the materials. Therefore, for high-performance TENGs, the composite should exhibit a high electron affinity difference and large interfacial areas of interaction.

Although the separated triboelectric interfaces in a TENG provide better peak voltages due to the non-conducting nature of the films, the peaks are often non-symmetric and irregular with mechanical loads. This could be attributed to the non-homogeneous mechanical load transfer caused by distinctly separated triboelectric interfaces in the two-electrode-based TENG system, which limits its application as a physical sensor. Another disadvantage of the two-electrode TENG system is the lower mechanical stability when sufficiently thin films are used to enhance performance. In contrast, a single-electrode type TENG produces lower output currents and voltages but exhibits more symmetric responses to mechanical loads due to the homogeneous distribution of the triboelectric interfaces in the composite. Considering these challenges, we have proposed a single-electrode type TENG fabricated by incorporating conducting carbon nanotubes (CNTs) and high-dielectric barium titanate (BT) into a styrene–butadiene rubber (SBR) matrix. SBR is a synthetic rubber known for its high industrial value due to its elasticity, stretchability, abrasion resistance, and ability to be reinforced with various fillers through physical and chemical interactions [40–43]. Moreover, SBR contains a large number of benzene rings as π-electron systems, which strongly interact with carbon materials such as carbon nanotubes through π–π interactions. This significantly improves the mechanical, electrical, and electromechanical properties of the rubber composite [43]. Unlike other diene rubbers, SBR also has a lower number of reactive unsaturations in its molecular chains, providing better

aging resistance [44] and making it more suitable for harsh environments. Furthermore, SBR belongs to the tribo-negative side, while barium titanate belongs to the tribo-positive side in the triboelectric series, facilitating higher triboelectric charge generation. Given these properties, SBR and the selected fillers were deliberately chosen to formulate a new TENG composite aimed at achieving higher performance.

Here, we propose a single-electrode TENG composite, where electrically conducting networks in the rubber matrix act as the electrode, and rubber and barium titanate interfaces serve as triboelectric layers, forming numerous hypothetical triboelectric cells within the rubber composite. Upon the application of mechanical energy, even at very low deformation, these cells generate a significant amount of triboelectric charge due to internal friction between the rubber and barium titanate particles. This TENG offers several advantages, including symmetric output voltage and current, possibly due to the homogeneous distribution of the filler, which results in smooth mechanical load transfer. Moreover, due to the strong reinforcing abilities of the filler materials, the composite becomes more robust and gains higher mechanical stability, which is essential for a durable energy-harvesting system. To understand the triboelectric behaviors of different rubber composites with varying filler amounts, power efficiency, power density, charge efficiency, and charge density were measured. In a triboelectric cell, both the interactive area and the electrode area are critical factors; thus, optimal conductivity and an optimal filler–rubber interfacial area can result in the highest triboelectric charge generation. To investigate the triboelectric interactions between barium titanate and the rubber phases, barium titanate was modified with stearic acid, with the belief that, at an optimal concentration, it would enhance filler dispersion in the rubber matrix, thereby resulting in higher triboelectric charge generation. Beyond the optimum concentration, excess unreacted stearic acid may remain between the triboelectric layers, reducing triboelectric efficiencies. The results support this hypothesis. Finally, the optimum TENG composite was demonstrated for longer energy-harvesting cycles and personal handwriting recognition.

2. Materials and Methods

2.1. Materials

Styrene–butadiene rubber (SBR-1502, approximately 23.5% styrene monomer content) was procured from Kumho Petrochemicals, Seoul, Republic of Korea. A masterbatch of unvulcanized rubber was formulated using a two-roll mixing mill, incorporating curing ingredients such as zinc oxide, stearic acid, tetramethyl thiuram disulfide, N-tert-butylbenzothiazole sulfonamide, and sulfur in the amounts of 5, 2, 1, 1.75, and 1.5 g, respectively, per 100 g of raw rubber, as described elsewhere [42,43]. Barium titanate (BT), with a primary particle size of 100 nm, was purchased from US Research Nanomaterials, Inc., Houston, TX, USA. Multiwalled carbon nanotubes (CNT, CNT-100), with a specific surface area of 250 m^2/g, were purchased from Hanwha Nanotech Corporation Ltd., Seoul, Republic of Korea. Both fillers were further characterized by X-ray diffraction (XRD, PANalytical XpertPro, Malvern, Worcestershire, UK) and scanning electron microscopy (SEM, S-4800, Hitachi, Tokyo, Japan) to examine their crystal structures and morphology. The results are provided in Figure 1a–d. Figure 1a shows the cubic crystalline structure of barium titanate, according to the ICDD-PDF#01-084-9618 [45]. The SEM image in Figure 1b indicates that the primary particle dimensions range within 100 nm, although the agglomerated filler structures vary from a few micrometers to several micrometers (as shown in the inset of Figure 1b). The XRD result in Figure 1c confirms that CNTs exhibit a hexagonal graphitic crystal structure, according to the reference JCPDS PDF#00-008-0415. The SEM image reveals that the CNTs have tubular morphologies, with individual tube diameters of less than 50 nm and lengths extending to a few micrometers.

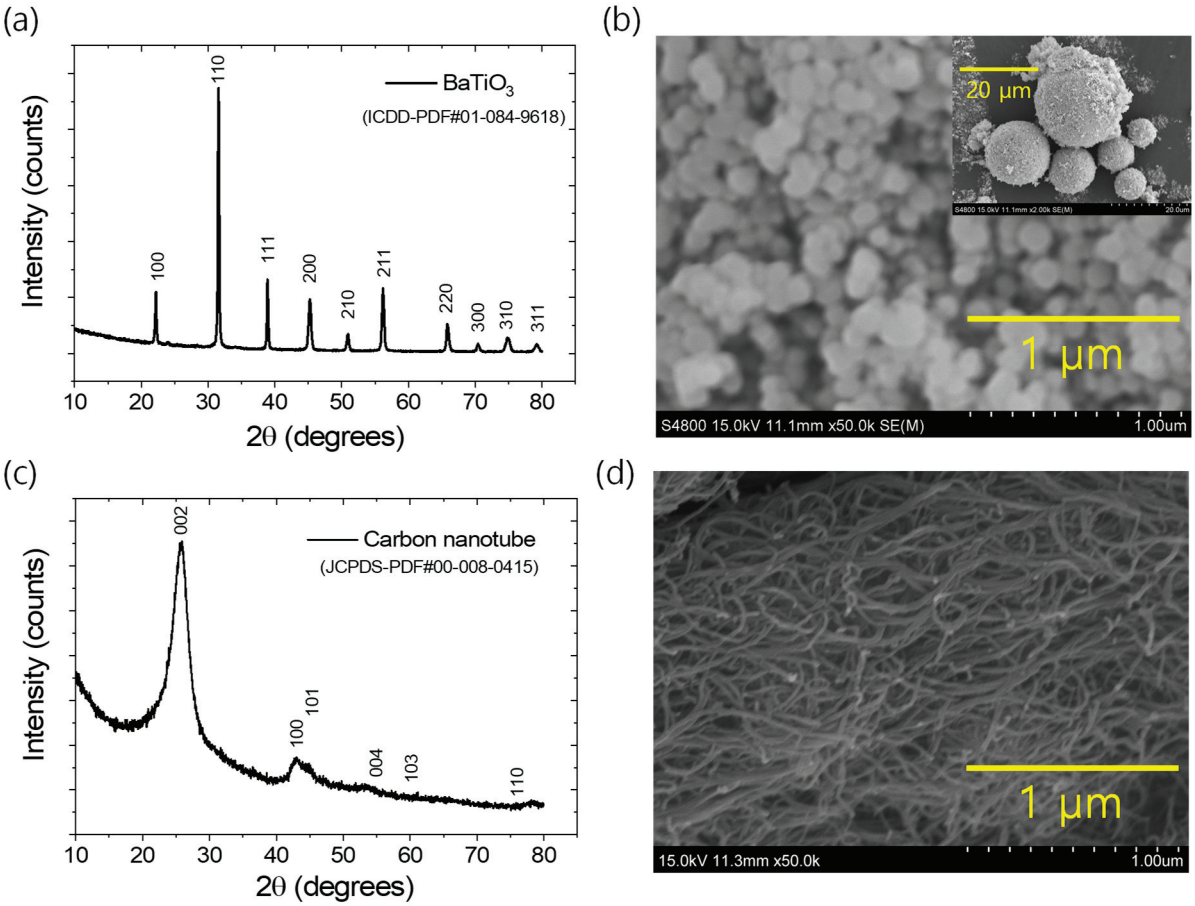

Figure 1. (**a**) XRD plot $BaTiO_3$, (**b**) SEM image images of $BaTiO_3$, (**c**) XRD plot of CNT, and (**d**) SEM image of CNT.

2.2. Fabrication of Rubber Composites

Before preparing the vulcanized rubber composites, the filler materials were mixed with the unvulcanized masterbatch rubber using a solvent blending technique. This method offers several advantages, including uniform filler dispersion, efficient wetting of fillers by rubber chains, and enhanced electrical properties in the resulting rubber composites. Additionally, it minimizes environmental impact when the solvent is used in a controlled manner, as described previously [42,43,46].

First, 25 g of masterbatch rubber was taken in a glass jar, and 80 mL of toluene was added and left to soak for about 18–20 h. After soaking, the rubber was converted into a slurry by mechanical stirring. In another glass container, the requisite amount of barium titanate from Table 1 was dispersed in 100 mL of toluene and sonicated for 1 h. The container was then placed in an oven at 100 °C to evaporate the solvent, reducing the total volume by half. For stearic acid-modified barium titanate-filled composites, the required amount of stearic acid from Table 1 was first dissolved in toluene before adding the barium titanate, followed by sonication. After removing the barium titanate solution from the oven, the requisite amount of CNTs was added to the solution, and the entire mixture was further sonicated for another 30 min. In the next step, the rubber slurry and the solvent-blended fillers were mixed by vigorous mechanical stirring for about 10 min. The final slurry was then placed in a flat tray and dried in an oven at 80 °C for about 24 h. The dried rubber compounds were subsequently cured (vulcanized) into sheet and cylindrical shapes, as presented in Figure S1a (Supporting Information), using a hot press molding machine at 150 °C for 15 min [42,43].

Table 1. Mixing compositions of different fillers and modifier per hundred grams of masterbatch rubber (phr).

Formulation	Amount of Masterbatch Rubber (g)	Amount of $BaTiO_3$ (g)	Amount of CNTs (g)	Amount of Stearic Acid Modifier (g)
BT-50/CNT-1.5/	100	50	1.5	-
BT-50/CNT-2	100	50	2.0	-
BT-50/CNT-2.5/	100	50	2.5	-
BT-100/CNT-2.5	100	100	2.5	-
BT-50/CNT-2/SA-1	100	50	2	1
BT-50/CNT-2/SA-3	100	50	2	3
BT-50/CNT-2/SA-5	100	50	2	5

2.3. Measurements of Mechanical Properties

Mechanical properties, including compressive and tensile behavior, were investigated using a Universal Testing Machine (Lloyd UTM, Westminster, UK) equipped with a 1 kN load cell. For compressive tests, cylindrical samples (height = 10 mm, diameter = 20 mm) were compressed up to 20% strain at a motor speed of 2 mm/min. For tensile tests, dumbbell-shaped specimens (ISO-37 [47], Type-2) were used, with the motor speed set to 300 mm/min. To determine the average value of each specific property, four consecutive tests were conducted.

2.4. Filler Dispersion of Rubber Composites

The dispersion of fillers in the rubber matrix was studied using the aforementioned SEM instrument. Tensile fracture surfaces of the rubber composites were used for SEM analysis. Prior to imaging, the samples were sputter-coated with gold.

2.5. Measurements of Triboelectric Properties

A digital multimeter (Keysight 34461A, Keysight, Santa Rosa, CA, USA) and a loading machine (UTM) were used to measure the triboelectric performance in terms of power efficiency, power density, charge efficiency, and charge density under a 2% compressive loading–unloading cycle of cylindrical specimens (height = 10 mm, diameter = 20 mm). These parameters were calculated using the following equations (Equations (1)–(4)) at a frequency of 0.85 Hz, based on the average of ten cycles:

$$Power\ efficiency = \frac{\Delta I \cdot \Delta V}{\mathrm{N}} \quad (1)$$

$$Power\ density = \frac{\Delta I \cdot \Delta V}{\mathrm{V_n}} \quad (2)$$

$$Charge\ efficiency = \frac{\int_0^{\mathrm{t}} \mathrm{I(t)dt}}{\mathrm{N}} \quad (3)$$

$$Charge\ density = \frac{\int_0^{\mathrm{t}} \mathrm{I(t)dt}}{\mathrm{V_n}} \quad (4)$$

where ΔI is the difference between the maximum and minimum current values, ΔV is the difference between the maximum and minimum voltage values, N is the applied force, V_n is the volume of the cylindrical sample, and I(t) is the time-dependent current.

It is well known that electrical charge is the product of current and time, which corresponds to the area under the current–time curve. In this case, the total electrical

charge per cycle is obtained by integrating both the negative and positive areas under the current–time plot over the full cycle duration from 0 to t.

Figure S1b illustrates the components of the triboelectric nanogenerator (TENG), while Figure S1c,d show the experimental setup with the actual sample.

3. Results and Discussion

3.1. Mechanical Properties of the Rubber Composites

Mechanical properties are critical parameters for ensuring stable TENG applications. Therefore, it is important to describe the mechanical behavior of the rubber composites before discussing their TENG performance. Various compressive mechanical behaviors are illustrated in Figure 2a–d. The compressive stress–strain curves in Figure 2a,b indicate that compressive stress increases with increasing strain. As shown in Figure 2a, increasing the amount of carbon nanotubes (CNTs) or barium titanate (BT) results in steeper stress–strain slopes, suggesting enhanced stiffness. In contrast, Figure 2b shows that, at a constant BT content, increasing the amount of stearic acid modifiers does not significantly affect the slope. From the Young's modulus values presented in Figure 2c,d, it can be observed that the addition of CNTs or BT increases the modulus, while the inclusion of stearic acid as a filler modifier decreases the modulus. This indicates that CNTs and BT act as reinforcing fillers, whereas stearic acid reduces the reinforcing capability of the filler materials. Several interactions contribute to the enhancement of compressive modulus in filled rubber composites [48]. Among them, occluded rubber chains within the filler structures significantly reduce the effective volume of soft rubber domains, and the higher stress transfer through rigid filler networks results in increased stiffness or Young's modulus. On the other hand, stearic acid promotes the deagglomeration of filler particles into primary particles, thereby reducing the effectiveness of stress transfer and leading to decreased stiffness or modulus values compared to unmodified composites. This observation is supported by the SEM studies discussed in later sections. Interestingly, although at the lowest amount of stearic acid the Young's modulus is lower than that of the unmodified composite, the modified composite maintains a similar modulus, as observed from the stress–strain curves in Figure 2b. This may be attributed to improved filler–polymer interactions, possibly due to the increased effective surface area of the BT particles in the rubber composites following filler modification [48,49]. For easier reference of load values corresponding to different strain levels, Figure S2a,b are provided in the Supporting Information section.

Tensile mechanical properties are important for the stretchable applications of rubber composites. It has been reported that CNT-based rubber composites exhibit excellent strain sensitivity [43,50,51]. For high-performance strain sensors, mechanical stability and stretchability are crucial parameters, along with linearity in strain sensitivity [43,50,51]. Various tensile properties of the rubber composites are presented in Figure 3a–d. From the stress–strain curves in Figure 3a, it is evident that increasing the filler content enhances the tensile strength. Unlike CNT, increasing the amount of BT leads to an improvement in the elongation at break. Figure 3b further shows that the addition of stearic acid, up to an optimal amount, results in increased tensile strength as well as elongation at break. The stress–strain curves in Figure 3b also reveal smoother profiles for stearic acid-modified composites, which can be attributed to improved filler distribution within the rubber matrix. Fracture toughness, which is directly related to the mechanical stability of rubber composites, is shown in Figure 3c,d. These figures indicate that fracture toughness improves with increasing filler content, with BT-rich composites demonstrating particularly high values. Since fracture toughness is influenced by both tensile strength and elongation at break, a significant increase in elongation can contribute to enhanced toughness. As shown in Figure 3d, stearic acid modification of the filler significantly increases the fracture tough-

ness and overall stability of the composites. Due to the smooth stress–strain response and improved mechanical stability, the stearic acid-modified composite demonstrates excellent potential for strain sensing applications, exhibiting a fracture toughness of 12.1 MJ/m^3 and an elongation at break of approximately 337%, which surpass previously reported values for similar CNT content in SBR composites [43]. The variation in tensile load with strain is provided in Figure S3a,b in the Supporting Information section.

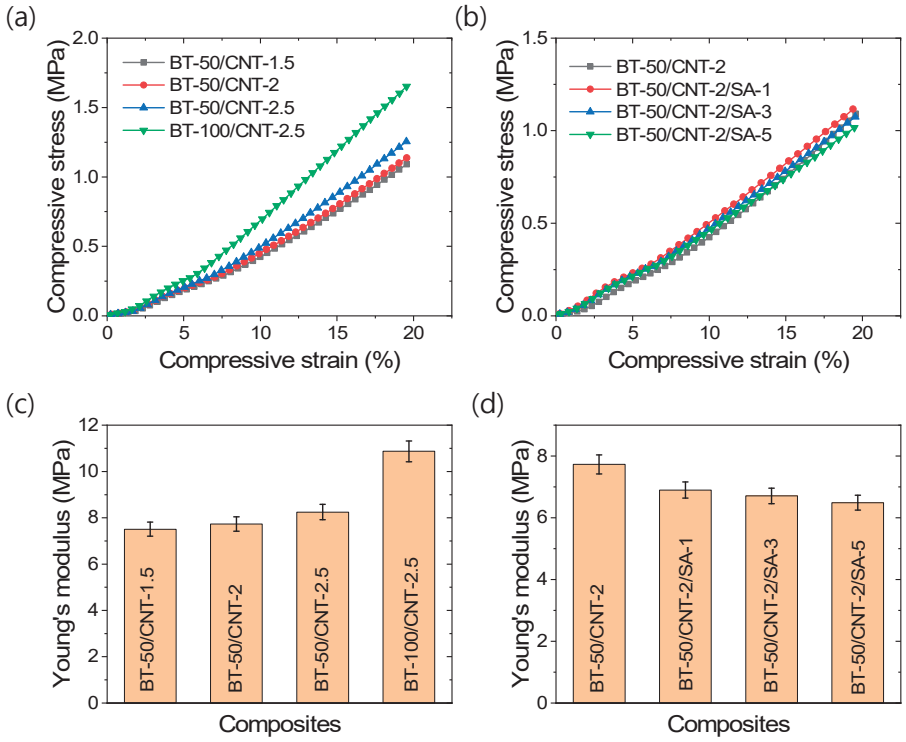

Figure 2. Compressive mechanical properties of rubber composites; (**a**,**b**) Stress–strain curves, and (**c**,**d**) Young's modulus.

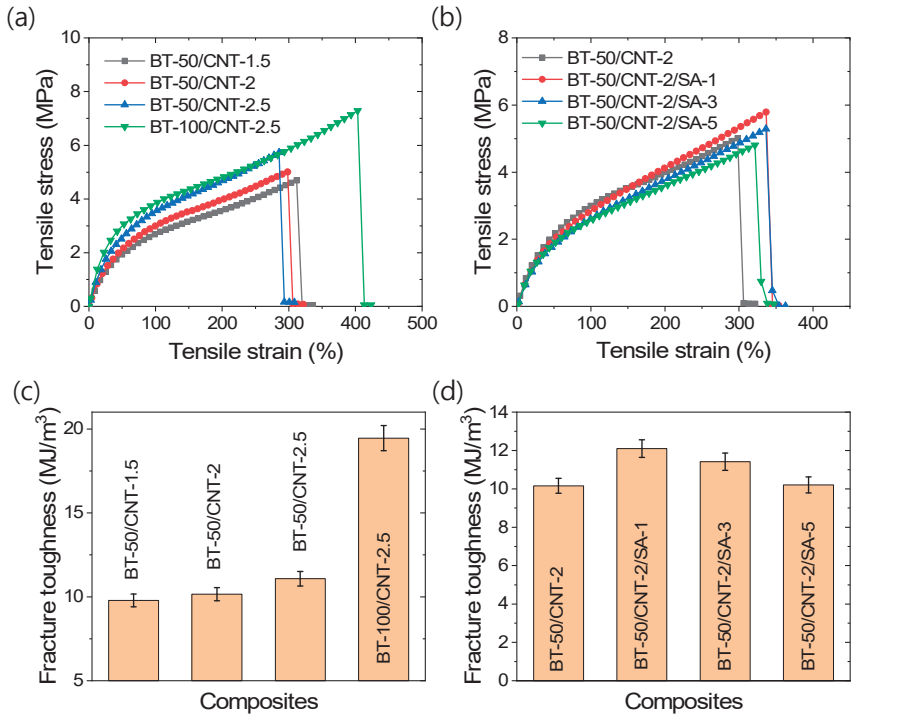

Figure 3. Tensile mechanical properties of rubber composites; (**a**,**b**) stress–strain curves and (**c**,**d**) fracture toughness values.

SEM images of different rubber composites are presented in Figure 4a–l. Figure 4a–c reveal that, without stearic acid modification, BT particles exhibit poor dispersibility in the rubber matrix, with many remaining in the form of agglomerated filler structures. However, increasing the filler content, whether CNT or BT, slightly improves filler distribution homogeneity, contributing to the enhanced mechanical properties observed with higher filler loading. When stearic acid is introduced as a filler modifier, a significantly improved dispersion of filler particles is achieved, with predominantly primary filler structures, as observed in Figure 4d–f. Specifically, Figure 4d shows no visible agglomeration of BT particles, unlike the structures seen in Figure 4a–c. In Figure 4e,f, both BT and CNT particles appear more uniformly dispersed throughout the matrix. This improved dispersion contributes to a marginal increase in fracture toughness when an optimal amount of stearic acid is used. Similarly, other stearic acid-modified composites also demonstrate excellent BT particle distribution, as seen in Figure 4g–l. However, when the stearic acid content exceeds 1 phr, the excess modifier—beyond the level required for optimal filler surface coverage—may deposit on the rubber matrix. Since unreacted stearic acid has low compatibility with the rubber, it does not further enhance fracture toughness and may even reduce it at higher concentrations. Although stearic acid substantially improves BT filler dispersion, no significant increase in Young's modulus is observed. This suggests that the Young's modulus is primarily governed by the integrity of the filler network structures [48]. In stearic acid-modified composites, these networks are largely broken down, resulting in reduced modulus values. However, the more homogeneous, nanoscale distribution of fillers in these modified composites can enhance elongation properties. As there is no notable improvement in tensile strength following filler modification, it can be inferred that BT particles have relatively weak physical interactions with rubber chains, possibly due to a large polarity mismatch. Overall, stearic acid modification results in softer composites with enhanced elongation at break, which may lead to improved fracture toughness compared to unmodified systems.

3.2. Triboelectric Behaviors of the Rubber Composites

The output voltage generation behavior of the triboelectric rubber composites is presented in Figure 5a–g. Figure 5a–c demonstrate that the output voltage significantly increases with increasing CNT content from 1.5 to 2 phr. However, beyond 2 phr CNT, only a marginal improvement in voltage output is observed. Similarly, at a fixed CNT content, increasing the BT concentration further enhances the output voltage. This indicates that the composite-based TENG achieves maximum output voltage when both the conductive network formed by CNTs and the interfacial interaction area between rubber and BT particles are optimized. At low conductivity, a portion of the generated charge may not be effectively extracted, while at high conductivity continuous conductive pathways may form between the rubber and BT particles, reducing triboelectric charge generation or enhancing charge relaxation due to direct connections between the triboelectric layers by conducting CNTs. Interestingly, when the BT content is doubled at a fixed CNT level, no significant improvement in output voltage is observed compared to the composite with lower BT content (Figure 5d). This initially suggested poor BT filler dispersion, which was later confirmed by SEM analysis. SEM studies revealed that the dispersion of BT fillers can be significantly enhanced by modifying them with stearic acid. The output voltages of the composites containing stearic acid-modified fillers are shown in Figure 5e–g. Notably, up to an optimal amount, stearic acid modification improves both filler dispersion and output voltage. However, exceeding the optimal quantity results in a decline in output voltage, despite maintaining good filler dispersion. It is believed that, at lower concentrations, stearic acid efficiently modifies the BT particle surfaces,

reducing particle size and weakening strong filler–filler interactions, while any excess stearic acid may dissolve in the rubber matrix. This results in a larger triboelectric surface area and the highest output voltage, as seen in Figure 5e. Beyond the optimal level, excess stearic acid may remain undissolved and precipitate within the matrix, as observed in SEM images. The presence of this layer between the triboelectric interfaces can hinder effective charge generation, leading to reduced output voltage, as shown in Figure 5f,g. Another possible explanation is that higher levels of stearic acid cause over-coating of filler particles, which may reduce the electrical conductivity. Therefore, an optimal stearic acid content of 1 phr appears to provide the best balance between filler distribution and triboelectric voltage output.

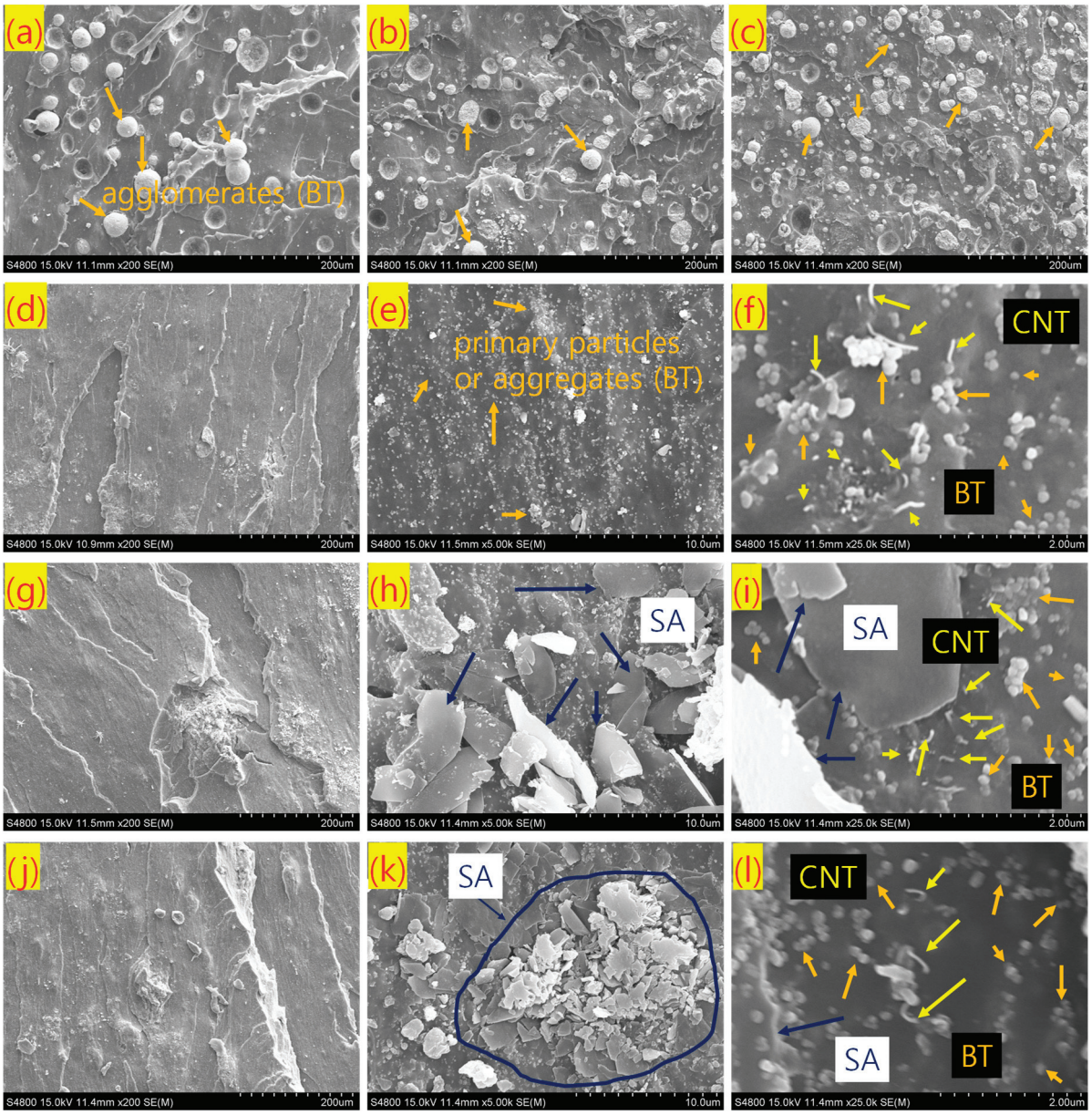

Figure 4. SEM images of tensile fractured rubber composites with different magnification; (**a**) BT-50/CNT-2 at 200×, (**b**) BT-50/CNT-2.5 at 200×, (**c**) BT-100/CNT-2.5 at 200×, (**d**) BT-50/CNT-2/SA-1 at 200×, (**e**) BT-50/CNT-2/SA-1 at 5.0k×, (**f**) BT-50/CNT-2/SA-1 at 25.0k×, (**g**) BT-50/CNT-2/SA-3 at 200×, (**h**) BT-50/CNT-2/SA-3 at 5.0k×, (**i**) BT-50/CNT-2/SA-3 at 25.0k×, (**j**) BT-50/CNT-2/SA-5 at 200×, (**k**) BT-50/CNT-2/SA-5 at 5.0k×, and (**l**) BT-50/CNT-2/SA-5 at 25.0k×.

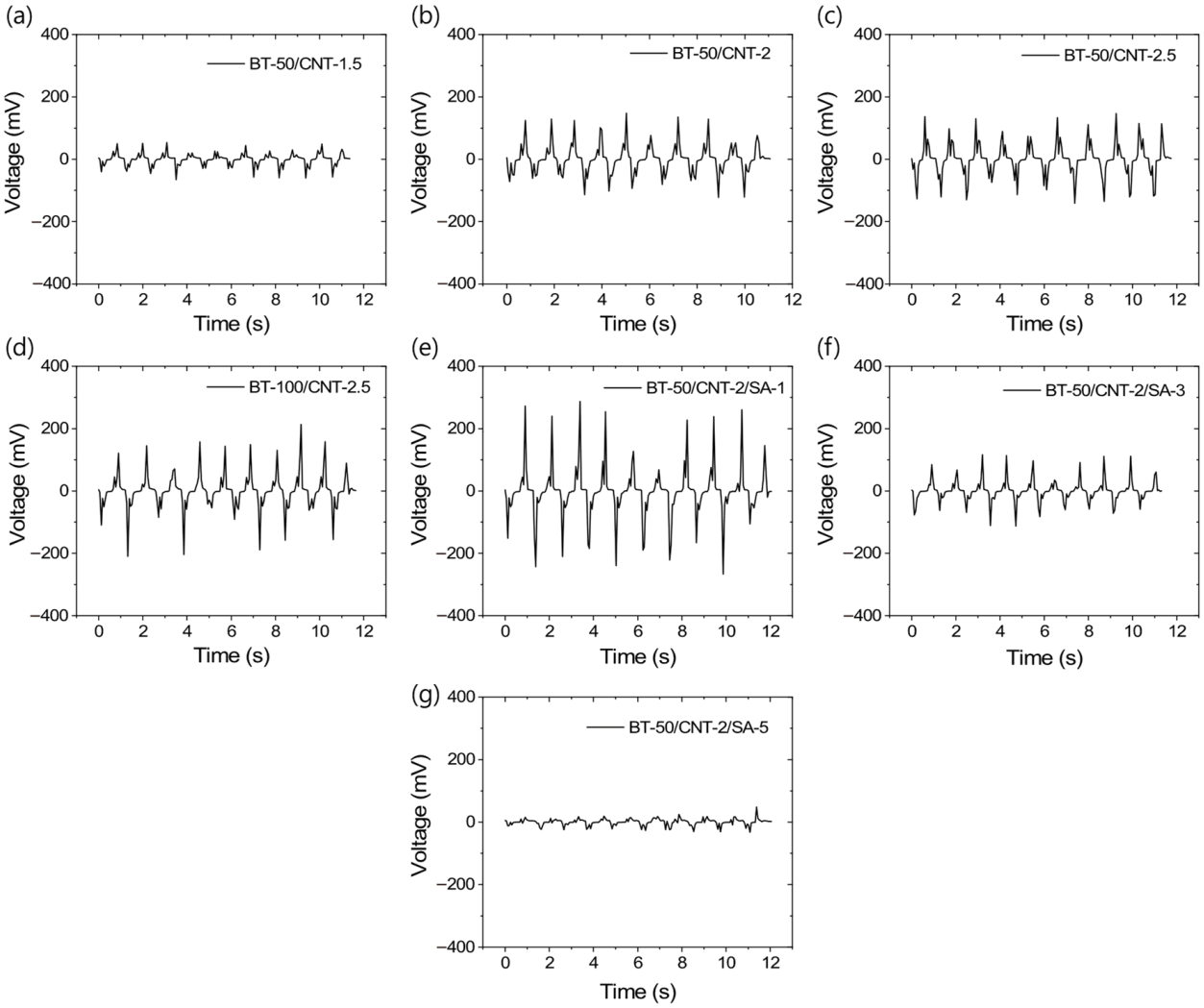

Figure 5. TENG output voltage profiles for different rubber composites at 2% dynamic strain and 10 loading–unloading cycles; (**a**) BT-50/CNT-1.5, (**b**) BT-50/CNT-2, (**c**) BT-50/CNT-2.5, (**d**) BT-100/CNT-2.5, (**e**) BT-50/CNT-2/SA-1, (**f**) BT-50/CNT-2/SA-3, and (**g**) BT-50/CNT-2/SA-5.

Similar to the voltage outputs, the output current values also follow the same trend, as shown in Figure 6a–g. These figures indicate that, at higher concentrations of stearic acid, the current outputs are significantly reduced, even falling below those of the unmodified composites. Figure S4a–d in the Supporting Information section present the average voltage and current responses under 2% compressive deformation cycles, which are useful for evaluating triboelectric efficiency. From these data, it is evident that the composite modified with 1 phr stearic acid (BT-50/CNT-2/SA-1) exhibits the best performance, achieving output values of approximately 500 mV and 50 nA under 2% compressive strain—significantly higher than all other composites tested.

Different types of TENG efficiencies are presented in Figure 7a–h. Regarding the maximum power efficiency and power density under a 2% deformation cycle, Figure 7a–d show that the addition of CNTs or BT leads to improvements in both parameters. Furthermore, improved filler dispersion—achieved with up to 1 phr of stearic acid—also enhances power efficiency and power density. However, at stearic acid contents above this optimum level, both metrics decline. The BT-50/CNT-2/SA-1 composite exhibits the highest performance, with a power efficiency of 1.127 nW/N and a power density of 8.258 mW/m^3 at a frequency of 0.85 Hz under a 2% compressive loading–unloading cycle of the cylindrical sample. These values represent improvements of approximately 290% and 400%, respec-

tively, compared to the corresponding unmodified composite (BT-50/CNT-2). Figure 7e–h illustrate the trends in charge efficiency and charge density. These figures reveal that increasing the CNT content up to an optimum of 2 phr enhances both charge efficiency and charge density. Beyond this point, further increases in CNTs reduce these values, likely due to the formation of continuous conductive networks between triboelectric interfaces, which promotes charge neutralization. This effect becomes clearer when BT content is increased at a fixed CNT level, as the enhanced triboelectric layer formation contributes to improved charge efficiencies. Since triboelectric efficiency is strongly influenced by the interfacial area between the filler and the rubber matrix, enhanced filler dispersion significantly boosts overall efficiency. The BT-50/CNT-2/SA-1 composite achieves a charge efficiency of 0.146 nC/N and a charge density of 1.072 mC/m^3—approximately 27% and 62% higher, respectively, than those of the unmodified composite (BT-50/CNT-2). Although filler dispersion plays a critical role in enhancing TENG efficiencies, excessive stearic acid beyond the optimal amount reduces efficiency, likely due to the presence of a surface layer that interferes with effective triboelectric charge generation. Therefore, using a minimal, optimized amount of stearic acid is essential for achieving superior TENG performance.

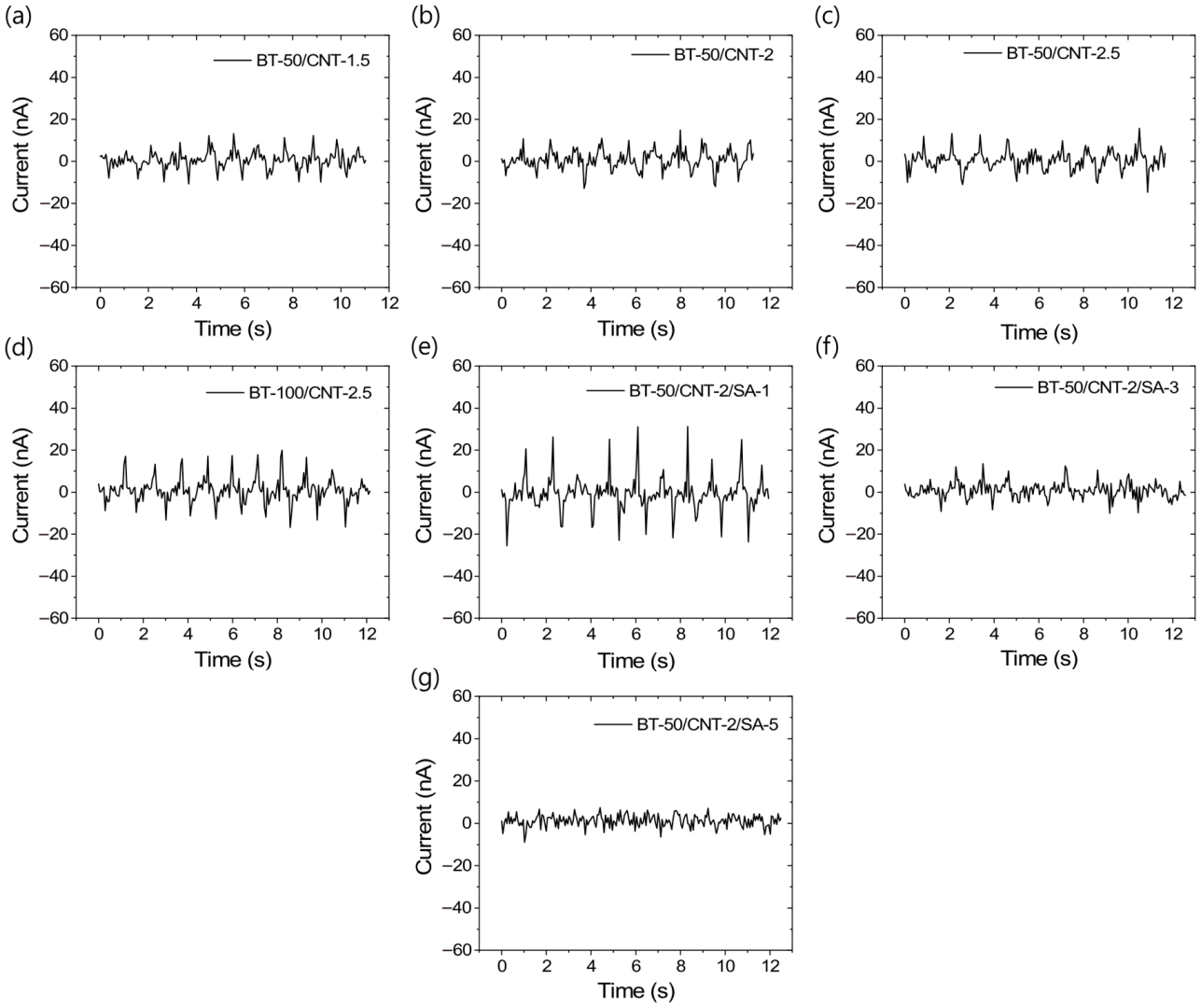

Figure 6. TENG output current profiles for different rubber composites at 2% dynamic strain and 10 loading–unloading cycles; (**a**) BT-50/CNT-1.5, (**b**) BT-50/CNT-2, (**c**) BT-50/CNT-2.5, (**d**) BT-100/CNT-2.5, (**e**) BT-50/CNT-2/SA-1, (**f**) BT-50/CNT-2/SA-3, and (**g**) BT-50/CNT-2/SA-5.

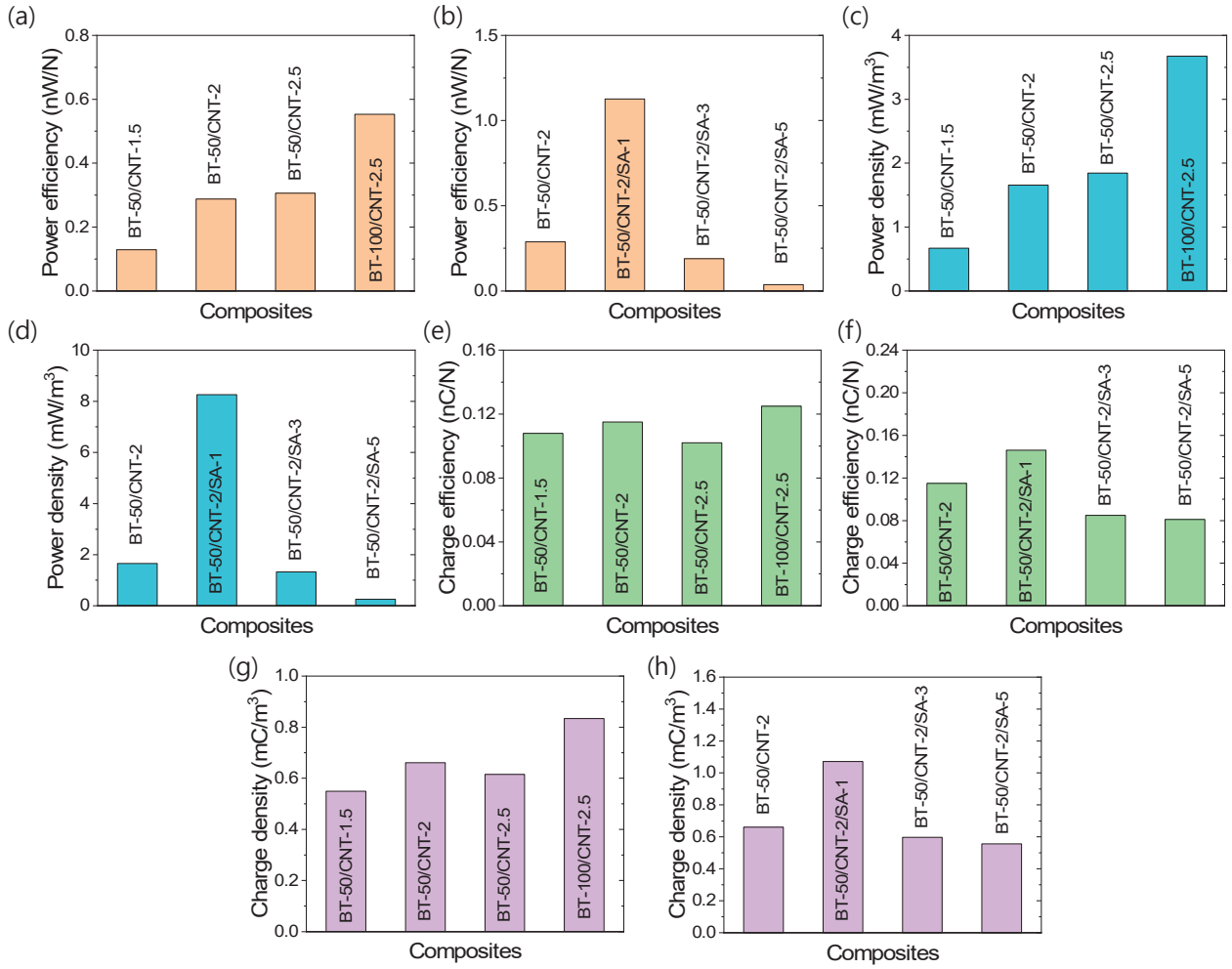

Figure 7. TENG efficiencies of the rubber composites under 2% compressive cyclic strain; (**a**,**b**) maximum power efficiency, (**c**,**d**) maximum power density, (**e**,**f**) charge efficiency, and (**g**,**h**) charge density.

To explore potential correlations between resistivity and TENG performance, the resistivities of various composites were investigated, as shown in Figure 8a,b. These figures clearly demonstrate that the resistivity of the composites decreases with increasing CNT content, due to the formation of more conductive pathways. Conversely, increasing the amount of dielectric BT results in higher resistivity. At a fixed BT content, increasing the CNT content improves TENG performance, despite the associated reduction in resistivity. On the other hand, at a fixed CNT level, increasing the BT content enhances both TENG performance and resistivity. A similar trend is observed with improved filler dispersion—higher dispersion levels lead to enhanced TENG performance, even when the overall resistivity is higher compared to unmodified composites. These observations suggest that an optimal balance between the conductive (CNT) and dielectric (BT) components is essential for achieving high energy conversion efficiency in rubber-based TENGs. Specifically, a sufficient level of conductive network formation is necessary to support effective charge transport, while an appropriate amount of dielectric filler ensures efficient charge generation and storage.

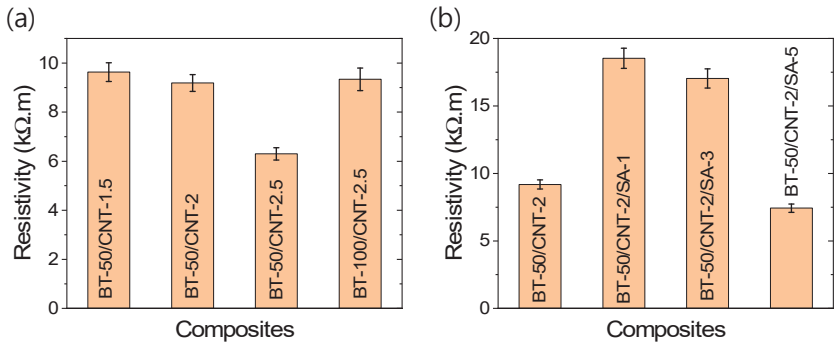

Figure 8. (**a**,**b**) Electrical resistivity of the rubber composites.

Based on the above results and discussion, it is evident that the BT-50/CNT-2/SA-1 composite exhibits the best triboelectric performance among all studied formulations. Therefore, this composite was further evaluated for its energy harvesting behavior under various stress–strain conditions, extended cyclic loading–unloading tests, and biomechanical force applications. Figure 9a–l illustrate the energy harvesting characteristics of the BT-50/CNT-2/SA-1 composite under these different mechanical conditions. From Figure 9a–c, it can be observed that the amount of generated current or charge increases with increasing compressive strain and stress values. Figure 9a shows the current outputs at different cyclic strains ranging from 1% to 5%. The fitted curves in Figure 9b,c follow Arrhenius-type logarithmic equations, suggesting that triboelectric energy generation requires a minimum activation energy to initiate the energy conversion process. Since both mechanical deformation and pressure are related to the input mechanical energy, they exhibit clear correlations with the charge values through these equations. By extrapolating the curve to a charge value of zero, a minimum pressure of 0.144 kPa was obtained. Notably, the minimum pressure required to activate the BT-50/CNT-2/SA-1 composite is 0.144 kPa, which is considerably lower than common biomechanical pressures, such as systolic (16 kPa) and diastolic (11 kPa) blood pressures. This highlights the potential of the composite for future applications in physiological sensing, such as blood pressure monitoring. Interestingly, Figure 9d indicates that charge efficiencies are higher at lower strains, suggesting that applying a lower mechanical pressure is more efficient for energy conversion than a higher pressure. At elevated strain levels, the frictional interactions between the rubber matrix and BT particles are likely to increase, as is evident from the increased amount of generated charge. However, due to extended filler percolation, the generated charge may relax more rapidly as a result of increased conductivity. For this reason, the charge generation efficiency decreases at higher strains. These findings suggest that, rather than increasing the applied load on a thick TENG sample, expanding the surface area under a similar load could lead to enhanced energy output.

Figure 9e–i represent the energy harvesting behavior up to 3000 loading–unloading cycles with 2% applied strain in the cylindrical sample. From the load values in Figure 9e, there is no significant loss in mechanical load from the beginning to the end of the cycles. However, the output voltage shown in Figure 9f exhibits some degradation at higher cycle numbers. It can be seen from Figure S5a–d that, after approximately 2000 s of cyclic loading, there is no significant further decrease in the output voltage. From Figure 9g, it is clearly observed that, even at higher cycle times, the voltage output remains relatively stable. Similarly, Figure 9h,i show that the current output also remains stable at higher cycle times. The decrease in output voltage or current at higher cycles is believed to be due to the increase in the temperature of the sample caused by internal friction between different materials, particularly the friction between similar filler particles. Such friction does not produce triboelectric charges due to the absence of electronic affinity gaps but

generates heat within the TENG. Although the resulting temperature increase is relatively low and does not significantly affect the bulk mechanical properties, it can have a notable effect on the charge generation efficiency depending on the temperature sensitivity of the TENG composite [52]. Although the durability was tested up to 3000 cycles, the degradation trends in output voltage and current suggest that the TENG composite can continue harvesting energy for many more cycles while maintaining similar efficiency, as observed after 2000 cycles.

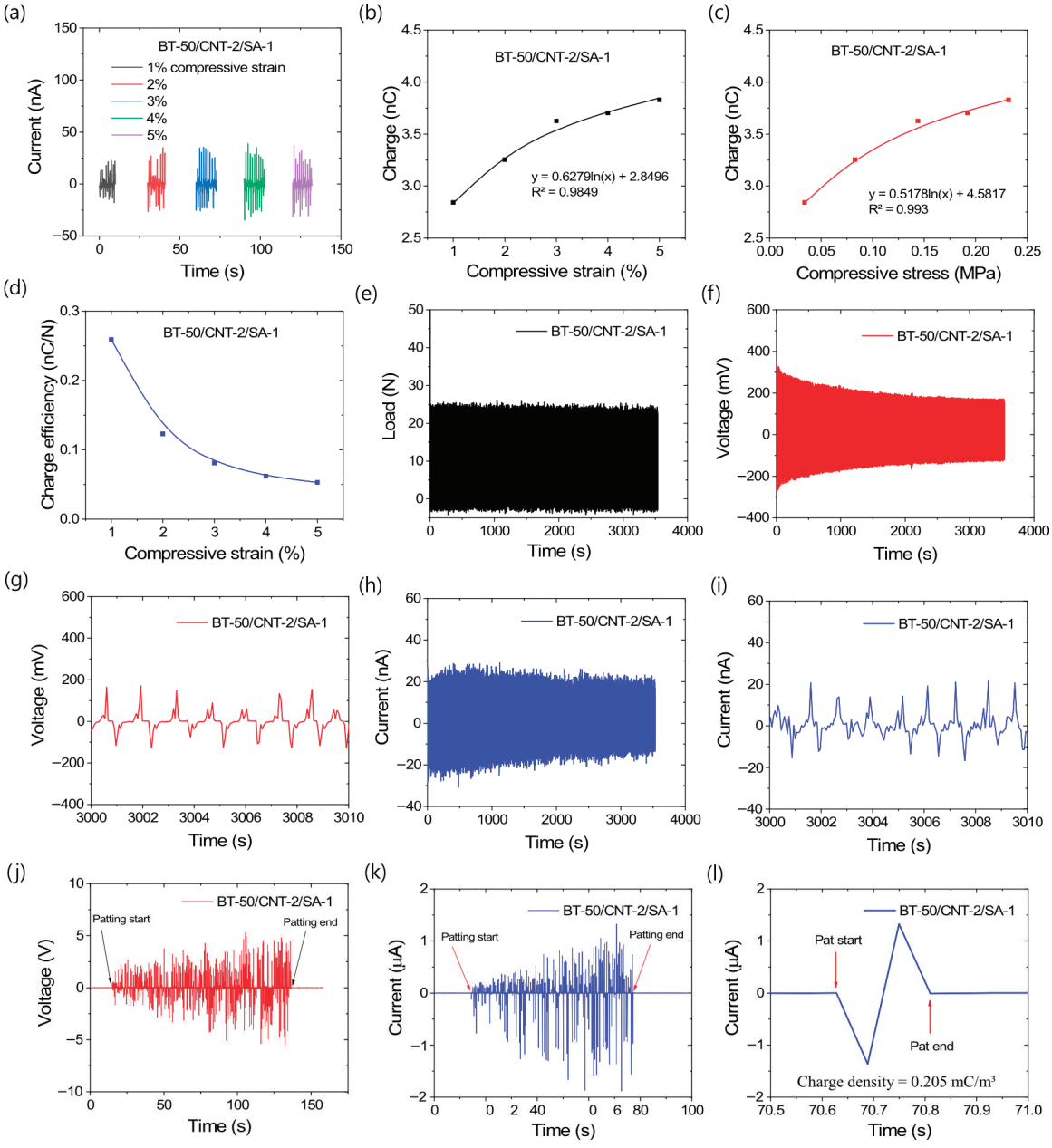

Figure 9. Triboelectric behavior of BT-50/CNT-2/SA-1 composite under different mechanical energy input systems; (**a**) current output with different cyclic compressive strains, (**b**) correlation of generated charge with compressive strains, (**c**) correlation of generated charge with compressive stress, (**d**) charge generation efficiencies under different compressive strain, (**e**) mechanical load profiles up to 3000 cycles, (**f**) voltage outputs up to 3000 cycles, (**g**) voltage outputs at higher cycles, (**h**) current outputs up to 3000 cycles, (**i**) current outputs at higher cycles, (**j**) voltage generation by patting, (**k**) current generation by patting, and (**l**) output current by a single pat.

As concluded previously, a thin TENG composite is expected to have higher energy conversion efficiency; therefore, a 0.02 cm-thick composite with an area of 6×5 cm^2 was investigated for energy harvesting through patting. The voltage and current generation behaviors under biomechanical force are shown in Figure 9j–l. From Figure 9j,l, it can be seen that the voltage and current outputs reach approximately 10 V and 2 μA, respectively. Consequently, the power density for this sample can reach as high as 26.04 W/m^3. Figure 9l shows that the calculated charge density for a single hand pat is as high as 0.205 mC/m^3. The power density achieved by hand patting is comparatively better than other rubber-based TENG composites [35–39], despite their higher voltage outputs. Previous studies on different rubber composites [35–39] reported high triboelectric voltages, but the corresponding power densities were not significantly high relative to the high voltage values. Since power is the product of current and voltage, these earlier results indicate lower current densities or reduced charge generation. This behavior may be attributed to the sensitivity of the load measurement systems used, which can capture current or voltage with high temporal resolution. As total charge or energy output depends on both current and the duration of flow, higher power efficiencies do not necessarily correspond to higher charge efficiencies. For example, Appamato et al. [35] obtained a maximum power density of 0.83 W/m^2 and a maximum output voltage of 120 V in natural rubber–Ag nanocomposites. The calculated current density was 6.92 mA/m^2, which is much lower than that of the BT-50/CNT-2/SA-1 composite (26.04 mA/m^2). Similarly, Gao et al. [39] reported a maximum voltage of 723 V and a power density of 3.25 W/m^2, corresponding to a current density of 4.5 mA/m^2. These data indicate that triboelectric charge extraction is more efficient in the BT-50/CNT-2/SA-1 composite due to its low resistivity or high conductivity. Moreover, the composite exhibits high stretchability and excellent fracture toughness. Considering all these factors, the BT-50/CNT-2/SA-1 composite demonstrates strong potential for effective energy harvesting from various forms of mechanical energy.

Since the TENG composite exhibits highly symmetric positive and negative output voltages under mechanical loading, it was further tested for personal handwriting recognition. The voltage patterns generated while writing "yu" by different individuals are shown in Figure 10a,b. From these figures, it is evident that, for the same person, the voltage patterns are similar in nature; however, for different individuals, the patterns are distinctly different. In addition to the visual distinction, the time taken to write the letters also varies significantly, with differences exceeding 500 ms, as shown in Figure 10c. Although the writing times differ considerably, it is interesting to note that the personal errors remain below 5%, as presented in Figure 10d. In a similar study, Alam et al. [53] showed that writing a single number or character produces a similar output voltage pattern if written in the same direction or style. However, when the same symbol is written in the other direction or style, the voltage patterns become significantly different due to changes in timing and force application. Generally, while there is only a small difference in time and pattern when writing a single character, this difference tends to increase progressively from a charecter to a word and then to a sentence. While visually similar signatures can be replicated through simple writing, replicating a signature while maintaining the same writing duration is extremely difficult. Based on this concept, the TENG composite shows great potential for future applications in handwriting recognition.

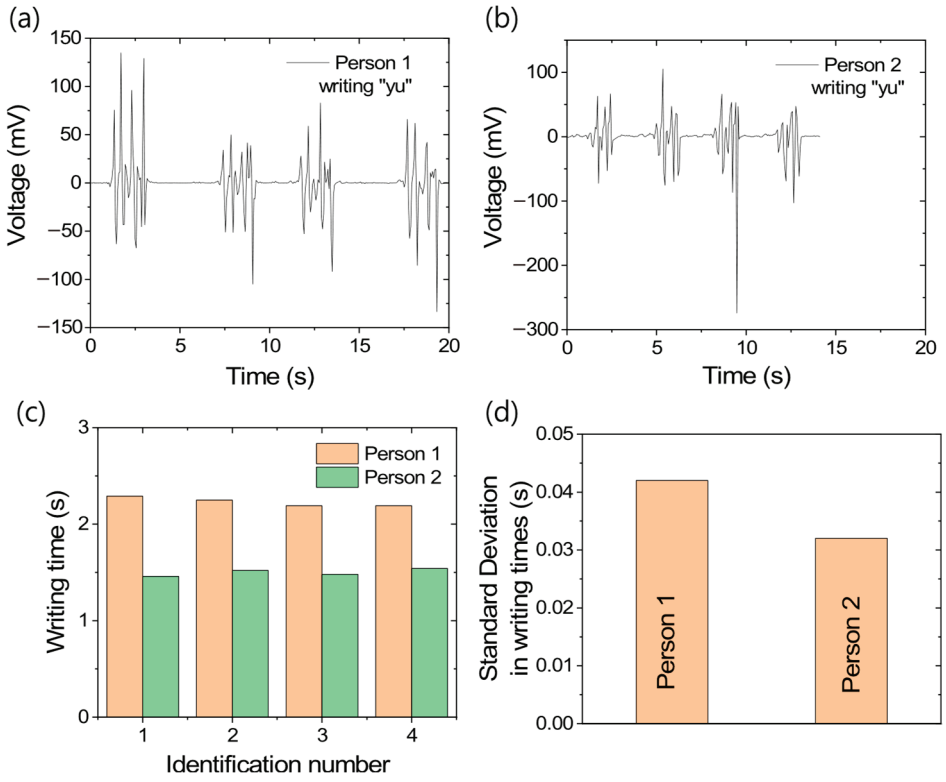

Figure 10. Handwriting recognition through TENG-based sensor; (**a**) output voltage patterns for Person 1, (**b**) output voltage patterns for Person 2, (**c**) writing times with different identification numbers, and (**d**) standard deviation in individual handwriting times.

4. Conclusions

In this research, single composite-type TENGs, where dispersed carbon nanotube networks act as electrodes and barium titanate–rubber interfaces act as triboelectric layers, were fabricated. Due to the reinforcing effects of the filler materials, the composites exhibit excellent mechanical properties, including high stretchability and toughness. These composites were evaluated for single-electrode-type TENG applications. Different triboelectric efficiencies suggest that TENG performance is strongly influenced by the optimum filler amounts and their dispersion behavior. It is evident that a rubber composite containing 2 phr CNTs and 50 phr barium titanate demonstrates better triboelectric efficiency than composites with higher CNT contents. Similarly, in composites with higher CNT content, increasing the amount of barium titanate leads to enhanced triboelectric effects. Although higher filler contents may sometimes result in increased triboelectric outputs, the associated enhancement in stiffness can negatively impact overall energy conversion efficiency. Due to dispersion challenges associated with polar barium titanate in a nonpolar rubber matrix, stearic acid was employed to improve filler dispersion. With improved filler dispersion, notable enhancements in both mechanical properties and triboelectric performance were observed. At an optimum amount of stearic acid, the composite exhibited increased toughness along with significant improvements in triboelectric efficiency. However, beyond the optimum stearic acid content, although mechanical properties may continue to improve due to better dispersion, the triboelectric efficiencies decline. This reduction is attributed to the presence of excess stearic acid-coated barium titanate particles that do not effectively participate in triboelectrification with the rubber matrix. Ultimately, the composite containing 50 phr barium titanate, 2 phr CNTs, and 1 phr stearic acid demonstrated the best performance, achieving power efficiency, power density, charge density, and charge efficiency values of 1.127 nW/N, 8.258 mW/m^3, 0.146 nC/N, and 1.072 mC/m^3, respec-

tively, under a 2% cyclic strain at 0.85 Hz frequency. Although a threshold pressure or deformation is required to activate the TENG, the device operates more efficiently under lower pressures. Therefore, a thin composite sheet ($0.02 \times 6 \times 5$ cm^3) was utilized for energy harvesting through hand patting, achieving significant power and charge densities of up to 26.04 W/m^3 and 0.205 mC/m^3, respectively, from a single hand pat. Due to its scalable energy generation efficiency, the composite also performed well in handwriting recognition, demonstrating high accuracy in time and sensitivity patterns. Therefore, this TENG composite shows strong potential for use in self-powered sensor devices with scalable energy generation capabilities.

Supplementary Materials: The following supporting information can be downloaded at: https://www.mdpi.com/article/10.3390/polym17152016/s1, Figure S1: (a) Sheet and cylindrical rubber specimens, (b) diagram of energy harvesting setup, (c,d) instrumental setup with original sample. Figure S2: (a,b) Variation in compressive load with % of strain for different rubber composites. Figure S3: (a,b) Variation in tensile load with % of strain for different rubber composites. Figure S4: Changes in voltage and current from lowest to highest outputs for different rubber composites at 2% deformative loading–unloading cycle; (a,b) change in voltage and (c,d) change in current. Figure S5: Degradation in output voltage of BT-50/CNT-2/SA-1 composite with loading–unloading cyclic time; (a) 0 s–10 s, (b) 1000 s–1010 s, (c) 2000 s–2010 s, and (d) 3530 s–end of cycles.

Author Contributions: Conceptualization, M.N.A.; methodology, M.N.A.; validation, M.N.A., V.K., Y.K., D.-J.L. and S.-S.P.; formal analysis, M.N.A., V.K. and Y.K.; investigation, M.N.A.; data curation, M.N.A.; writing—original draft preparation, M.N.A.; writing—review and editing, M.N.A., V.K., Y.K.,D.-J.L. and S.-S.P.; visualization, M.N.A. and S.-S.P.; supervision, S.-S.P.; project administration, S.-S.P.; funding acquisition, S.-S.P. All authors have read and agreed to the published version of the manuscript.

Funding: This research received no external funding.

Institutional Review Board Statement: Not applicable.

Data Availability Statement: The original contributions presented in this study are included in the article/Supplementary Material. Further inquiries can be directed to the corresponding authors.

Conflicts of Interest: The authors declare no conflicts of interest.

References

1. Sripadmanabhan Indira, S.; Aravind Vaithilingam, C.; Oruganti, K.S.P.; Mohd, F.; Rahman, S. Nanogenerators as a Sustainable Power Source: State of Art, Applications, and Challenges. *Nanomaterials* **2019**, *9*, 773. [CrossRef]
2. Kim, W.G.; Kim, D.W.; Tcho, I.W.; Kim, J.K.; Kim, M.S.; Choi, Y.K. Triboelectric Nanogenerator: Structure, Mechanism, and Applications. *ACS Nano* **2021**, *15*, 258–287. [CrossRef]
3. Lone, S.A.; Lim, K.C.; Kaswan, K.; Chatterjee, S.; Fan, K.P.; Choi, D.; Lee, S.; Zhang, H.; Cheng, J.; Lin, Z.H. Recent Advancements for Improving the Performance of Triboelectric Nanogenerator Devices. *Nano Energy* **2022**, *99*, 107318. [CrossRef]
4. Armitage, J.L.; Ghanbarzadeh, A.; Bryant, M.G.; Neville, A. Investigating the Influence of Friction and Material Wear on Triboelectric Charge Transfer in Metal–Polymer Contacts. *Tribol. Lett.* **2022**, *70*, 46. [CrossRef]
5. Nguyen, V.; Zhu, R.; Yang, R. Environmental Effects on Nanogenerators. *Nano Energy* **2015**, *14*, 49–61. [CrossRef]
6. Gao, X.; Xing, F.; Hang, X.; Guo, F.; Wen, J.; Sun, W.; Song, H.; Wang, Z.L.; Chen, B. Scalable-Produced Micro-Elastic Triboelectric Sensing Ground for All-Weather Large-Scale Applications. *Chem. Eng. J.* **2024**, *493*, 152645. [CrossRef]
7. Zhang, J.H.; Hao, X. Enhancing Output Performances and Output Retention Rates of Triboelectric Nanogenerators via a Design of Composite Inner-Layers with Coupling Effect and Self-Assembled Outer-Layers with Superhydrophobicity. *Nano Energy* **2020**, *76*, 105074. [CrossRef]
8. Li, Z.; Yu, A.; Zhang, Q.; Zhai, J. Recent Advances in Fabricating High-Performance Triboelectric Nanogenerators via Modulating Surface Charge Density. *Int. J. Extrem. Manuf.* **2024**, *6*, 052003. [CrossRef]
9. Niu, Z.; Cheng, W.; Cao, M.; Wang, D.; Wang, Q.; Han, J.; Long, Y.; Han, G. Recent Advances in Cellulose-Based Flexible Triboelectric Nanogenerators. *Nano Energy* **2021**, *87*, 106175. [CrossRef]

10. Zhao, W.; Li, N.; Liu, X.; Liu, L.; Yue, C.; Zeng, C.; Liu, Y.; Leng, J. 4D Printed Shape Memory Metamaterials with Sensing Capability Derived from the Origami Concept. *Nano Energy* **2023**, *115*, 108697. [CrossRef]
11. Peng, Z.; Niu, Z.; Zeng, C.; Zhao, W.; Leng, J.; Liu, Y. Design and Functional Verification of a Flexible Wireless Spinal Cord Stimulator with Spinal Motion Monitoring Function. *Nano Energy* **2025**, *139*, 110895. [CrossRef]
12. Cao, X.; Xiong, Y.; Sun, J.; Xie, X.; Sun, Q.; Wang, Z.L. Multidiscipline Applications of Triboelectric Nanogenerators for the Intelligent Era of Internet of Things. *Nano-Micro Lett.* **2023**, *15*, 14. [CrossRef]
13. Choi, D.; Lee, Y.; Lin, Z.H.; Cho, S.; Kim, M.; Ao, C.K.; Soh, S.; Sohn, C.; Jeong, C.K.; Lee, J.; et al. Recent Advances in Triboelectric Nanogenerators: From Technological Progress to Commercial Applications. *ACS Nano* **2023**, *17*, 11087–11219. [CrossRef] [PubMed]
14. Liu, Z.; Chen, X.; Wang, Z.L. Biopolymer and Biomimetic Techniques for Triboelectric Nanogenerators (TENGs). *Adv. Mater.* **2025**, *37*, 2409440. [CrossRef] [PubMed]
15. Hayat, K.; Shah, S.S.; Ali, S.; Shah, S.K.; Iqbal, Y.; Aziz, M.A. Fabrication and Characterization of $Pb(Zr_{0.5}Ti_{0.5})O_3$ Nanofibers for Nanogenerator Applications. *J. Mater. Sci. Mater. Electron.* **2020**, *31*, 15859–15874. [CrossRef]
16. Cui, S.; Zhou, L.; Liu, D.; Li, S.; Liu, L.; Chen, S.; Zhao, Z.; Yuan, W.; Wang, Z.L.; Wang, J. Improving Performance of Triboelectric Nanogenerators by Dielectric Enhancement Effect. *Matter* **2022**, *5*, 180–193. [CrossRef]
17. Li, Y.; Luo, Y.; Deng, H.; Shi, S.; Tian, S.; Wu, H.; Tang, J.; Zhang, C.; Zhang, X.; Zha, J.W.; et al. Advanced Dielectric Materials for Triboelectric Nanogenerators: Principles, Methods, and Applications. *Adv. Mater.* **2024**, *36*, 2314380. [CrossRef]
18. Li, Z.; Gan, W.C.; Tang, L.; Aw, K.C. Fundamental Understanding of Multicellular Triboelectric Nanogenerator with Different Electrical Configurations. *Micromachines* **2023**, *14*, 1333. [CrossRef]
19. Burgo, T.A.; Silva, C.A.; Balestrin, L.B.; Galembeck, F. Friction Coefficient Dependence on Electrostatic Tribocharging. *Sci. Rep.* **2013**, *3*, 2384. [CrossRef]
20. Zhang, W.; Bao, W.; Lü, X.; Diao, D. Friction Force Excitation Effect on the Sliding-Mode Triboelectric Nanogenerator. *Tribol. Int.* **2023**, *185*, 108504. [CrossRef]
21. Zhang, R.; Olin, H. Material Choices for Triboelectric Nanogenerators: A Critical Review. *EcoMat* **2020**, *2*, e12062. [CrossRef]
22. Okochi, K.; Oya, T. Unique Triboelectric Nanogenerator Using Carbon Nanotube Composite Papers. *Appl. Sci.* **2024**, *14*, 10030. [CrossRef]
23. Kınas, Z.; Karabiber, A.; Yar, A.; Ozen, A.; Ozel, F.; Ersöz, M.; Okbaz, A. High-Performance Triboelectric Nanogenerator Based on Carbon Nanomaterials Functionalized Polyacrylonitrile Nanofibers. *Energy* **2022**, *239*, 122369. [CrossRef]
24. Wang, J.; Ma, S.; Cheng, H.; Wang, Y.; Zhao, K.; Liu, C.; Liu, X. High-Performance Triboelectric Nanogenerator Based on Carbon Nanotube-Functionalized Supramolecular Polyrotaxane Composites. *ACS Appl. Polym. Mater.* **2025**, *7*, 1300–1306. [CrossRef]
25. Lee, K.; Mhin, S.; Han, H.; Kwon, O.; Kim, W.B.; Song, T.; Kang, S.; Kim, K.M. A High-Performance PDMS-Based Triboelectric Nanogenerator Fabricated Using Surface-Modified Carbon Nanotubes via Pulsed Laser Ablation. *J. Mater. Chem. A* **2022**, *10*, 1299–1308. [CrossRef]
26. Matsunaga, M.; Hirotani, J.; Kishimoto, S.; Ohno, Y. High-Output, Transparent, Stretchable Triboelectric Nanogenerator Based on Carbon Nanotube Thin Film toward Wearable Energy Harvesters. *Nano Energy* **2020**, *67*, 104297. [CrossRef]
27. Deng, H.-C.; Li, Y.; Tian, S.-S.; Zhang, X.-X.; Song, X. Dielectric Materials for High-Performance Triboelectric Nanogenerators. *Acta Phys. Sin.* **2024**, *73*, 070702. [CrossRef]
28. Xie, B.; Yin, R.; Miao, S.; Jia, H.; Ma, Y.; Liu, Y. Thermal-Stable and High-Dielectric $Ba(Cu_{0.5}W_{0.5})O_3$-Based Ceramic Powder/PDMS Films for Triboelectric Nanogenerator. *Ceram. Int.* **2024**, *50*, 12778–12786. [CrossRef]
29. Li, H.; Zhang, Y.; Yan, M.; Liu, Y.; Jia, M.; Xiang, S.; Gong, H.; Xu, Q.; Yuan, X.; Zhou, K.; et al. High-Performance Triboelectric Nanogenerator Based on High-Permittivity $BaZr_{0.2}Ti_{0.8}O_3$ Nanowires with Enhanced Surface Potential. *Ceram. Int.* **2025**, *51*, 11211–11219. [CrossRef]
30. Pandey, P.; Jung, D.H.; Choi, G.J.; Seo, M.K.; Lee, S.; Kim, J.M.; Park, I.K.; Sohn, J.I. Nafion-Mediated Barium Titanate-Polymer Composite Nanofibers-Based Triboelectric Nanogenerator for Self-Powered Smart Street and Home Control System. *Nano Energy* **2023**, *107*, 108134. [CrossRef]
31. Sun, W.; Wang, Y.; Lv, X.; Dong, J.; Zhang, Y.; Chen, B.; He, N.; Liu, J.; Nan, D. High-Performance Triboelectric Nanogenerator with Aminated Barium Titanate Composite Nanoparticles for Early Parkinson's Disease Diagnosis. *Chem. Eng. J.* **2024**, *500*, 156710. [CrossRef]
32. Yan, J.; Wang, K.; Wang, Y.; Lv, M.; Yang, G. Polyimide Nanofiber-Based Triboelectric Nanogenerators Using Piezoelectric Carbon Nanotube@Barium Titanate Nanoparticles. *ACS Appl. Nano Mater.* **2024**, *7*, 13156–13165. [CrossRef]
33. Liang, S.-B.; Yuan, T.; Qiu, Y.; Zhang, Z.; Miao, Y.-N.; Han, J.-F.; Liu, X.-T.; Yao, C.-L. Barium Titanate Dielectric Regulation Improved Output Performance of Paper-Based Triboelectric Nanogenerator. *Acta Phys. Sin.* **2022**, *71*, 077701. [CrossRef]
34. Patil, O.A.; Cheong, J.Y.; Lu, B.; Hwang, B.; Lim, S. High-Performance Screen-Printed Triboelectric Nanogenerator Based on $BaTiO_3$-Enhanced Copy Paper for Sustainable Energy Harvesting. *Chemosensors* **2025**, *13*, 76. [CrossRef]

35. Appamato, I.; Bunriw, W.; Harnchana, V.; Siriwong, C.; Mongkolthanaruk, W.; Thongbai, P.; Chanthad, C.; Chompoosor, A.; Ruangchai, S.; Prada, T.; et al. Engineering Triboelectric Charge in Natural Rubber–Ag Nanocomposite for Enhancing Electrical Output of a Triboelectric Nanogenerator. *ACS Appl. Mater. Interfaces* **2022**, *15*, 973–983. [CrossRef]
36. Chomjun, T.; Appamato, I.; Harnchana, V.; Amornkitbamrung, V. Eco-Friendly Triboelectric Material Based on Natural Rubber and Activated Carbon from Human Hair. *Polymers* **2022**, *14*, 1110. [CrossRef] [PubMed]
37. Candido, I.C.; Oliveira, G.D.S.; Lima, R.M.A.P.; Lima, J.J.I.D.; de Oliveira, H.P. All-Silicone Rubber Triboelectric Nanogenerators with Graphite-Impregnated Electrodes. *ACS Appl. Eng. Mater.* **2023**, *1*, 1069–1078. [CrossRef]
38. Lu, J.; He, Z.; Lin, Z.; Deng, X.; Huang, B.; Lin, B.; Fu, L.; Xu, C. Flexible, Wearable Triboelectric Rubber with Tunable Surface Charge Density Enabled by Regulation of Surface Functional Group Density and Permittivity. *Chem. Eng. J.* **2024**, *498*, 155315. [CrossRef]
39. Gao, W.; Pan, W.; Gao, X.; Xie, T.; Ou, F.; Ning, C.; Fu, Z.; Wang, F.; Gan, T.; Qin, Z.; et al. Special Rubber with Excellent Mechanical Strength, Environmental Stability, and Electrical Conductivity for Accordion-Structured High-Performance Triboelectric Nanogenerators. *Adv. Funct. Mater.* **2025**, *35*, 2425366. [CrossRef]
40. Sinclair, A.; Zhou, X.; Tangpong, S.; Bajwa, D.S.; Quadir, M.; Jiang, L. High-Performance Styrene-Butadiene Rubber Nanocomposites Reinforced by Surface-Modified Cellulose Nanofibers. *ACS Omega* **2019**, *4*, 13189–13199. [CrossRef]
41. Dhanorkar, R.J.; Mohanty, S.; Gupta, V.K. Synthesis of Functionalized Styrene Butadiene Rubber and Its Applications in SBR–Silica Composites for High Performance Tire Applications. *Ind. Eng. Chem. Res.* **2021**, *60*, 4517–4535. [CrossRef]
42. Alam, M.N.; Kumar, V.; Jo, C.R.; Ryu, S.R.; Lee, D.J.; Park, S.S. Mechanical and Magneto-Mechanical Properties of Styrene-Butadiene-Rubber-Based Magnetorheological Elastomers Conferred by Novel Filler-Polymer Interactions. *Compos. Sci. Technol.* **2022**, *229*, 109669. [CrossRef]
43. Alam, M.N.; Kumar, V.; Lee, D.J.; Park, S.S. Styrene–Butadiene Rubber-Based Nanocomposites Toughened by Carbon Nanotubes for Wide and Linear Electromechanical Sensing Applications. *Polym. Compos.* **2024**, *45*, 2485–2499. [CrossRef]
44. Osswald, K.; Reincke, K.; Schossig, M.; Sökmen, S.; Langer, B. Influence of Different Types of Antioxidants on the Aging Behavior of Carbon-Black Filled NR and SBR Vulcanizates. *Polym. Test.* **2019**, *79*, 106053. [CrossRef]
45. Pasuk, I.; Neațu, F.; Neațu, Ș.; Florea, M.; Istrate, C.M.; Pintilie, I.; Pintilie, L. Structural Details of $BaTiO_3$ Nano-Powders Deduced from the Anisotropic XRD Peak Broadening. *Nanomaterials* **2021**, *11*, 1121. [CrossRef]
46. Alam, M.N.; Azam, S.; Yun, J.; Park, S.S. Critical Role of Rubber Functionalities on the Mechanical and Electrical Responses of Carbon Nanotube-Based Electroactive Rubber Composites. *Polymers* **2025**, *17*, 127. [CrossRef] [PubMed]
47. *ISO-37*; Rubber, Vulcanized or Thermoplastic-Determination of Tensile Stress-Strain Properties. ISO: Geneva, Switzerland, 2017.
48. Fröhlich, J.; Niedermeier, W.; Luginsland, H.D. The Effect of Filler–Filler and Filler–Elastomer Interaction on Rubber Reinforcement. *Compos. Part A Appl. Sci. Manuf.* **2005**, *36*, 449–460. [CrossRef]
49. Alam, M.N.; Kumar, V.; Jung, H.S.; Park, S.S. Fabrication of High-Performance Natural Rubber Composites with Enhanced Filler–Rubber Interactions by Stearic Acid-Modified Diatomaceous Earth and Carbon Nanotubes for Mechanical and Energy Harvesting Applications. *Polymers* **2023**, *15*, 3612. [CrossRef]
50. Xue, S.S.; Tang, Z.H.; Zhu, W.B.; Li, Y.Q.; Huang, P.; Fu, S.Y. Stretchable and Ultrasensitive Strain Sensor from Carbon Nanotube-Based Composite with Significantly Enhanced Electrical and Sensing Properties by Tailoring Segregated Conductive Networks. *Compos. Commun.* **2022**, *29*, 100987. [CrossRef]
51. Alam, M.N.; Kumar, V.; Lee, D.J.; Choi, J. Synergistically Toughened Silicone Rubber Nanocomposites Using Carbon Nanotubes and Molybdenum Disulfide for Stretchable Strain Sensors. *Compos. Part B Eng.* **2023**, *259*, 110759. [CrossRef]
52. Lu, C.X.; Han, C.B.; Gu, G.Q.; Chen, J.; Yang, Z.W.; Jiang, T.; He, C.; Wang, Z.L. Temperature Effect on Performance of Triboelectric Nanogenerator. *Adv. Eng. Mater.* **2017**, *19*, 1700275. [CrossRef]
53. Alam, M.N.; Kim, Y.; Kumar, V.; Ryu, S.R.; Lee, D.J.; Park, S.S. Diatomaceous Earth and Carbon Nanotubes Toughened Advanced Rubber Composite for Triboelectric Nanogenerator and Sensor Applications. *Polym. Compos.* **2025**. [CrossRef]

polymers

MDPI

Review

Electrically Conductive Functional Polymers and Application Progress in Lithium Batteries

Zhe Huang †, Mengting Lyu †, Nan Meng, Jinxin Cao, Chenyu Xiong and Fang Lian *

School of Materials Science and Engineering, University of Science and Technology, Beijing 100083, China; zhehuang0722@163.com (Z.H.); 15052150017@163.com (M.L.); mengnan@ustb.edu.cn (N.M.); cjxys1998@163.com (J.C.); chenyuxiong_x@163.com (C.X.)

* Correspondence: lianfang@mater.ustb.edu.cn

† These authors contributed equally to this work.

Abstract: Electrically conductive functional polymers (ECFPs) have attracted much attention not only for their electron conductivity but also for their versatile properties, including redox activity, flexibility, and designability. These attributes are expected to enhance the energy density and mechanical compatibility of lithium batteries while mitigating the safety risks associated with such batteries. Furthermore, ECFPs are key candidates as active materials, current collectors, coatings, binders, and additives in energy storage and conversion systems, especially for the development of flexible batteries, dry electrodes, and solid-state batteries. However, their low electron conductivity, poor environmental stability, instability of dopants, and high costs limit their usage in production and large-scale applications. In this review, the two major electrically conductive functional polymer species with conjugated and radical structures are focused on to reveal their conductivity mechanisms. Moreover, the current strategies for improving the performance of these polymers are summarized, which include molecular design to optimize conjugated structures for enhanced conductivity, the addition of hydrophobic groups or protective coatings to improve environmental resistance, a side-chain design that is self-doping to introduce high-stability dopants, and the development of multifunctional systems through compositing with two-dimensional carbon-based materials. Additionally, green processes and renewable resource applications are also introduced with the aim of creating cost-effective and sustainable preparation technologies. The advancement of ECFPs in structural and performance engineering and optimization strategies will facilitate their potentially expansive applications in energy storage and conversion devices.

Keywords: lithium batteries; polymers; electrically conductive; multifunctional; redox activity; flexibility

1. Introduction

Polymers were thought of as insulators until Alan MacDiarmid et al. found conductive polyacetylene in 1977 [1]. Subsequently, various polymers such as polyaniline and polypyrrole were discovered to have electronic conductivity [2,3]. Electrically conductive functional polymers (abbreviated as ECFPs) refer to specialized polymer materials that not only possess the pros of conventional polymers but also the ability to conduct electricity. Importantly, regarding their applications, ECFPs also exhibit inherent flexibility, easy processing characteristics, and certain mechanical strength [4,5]. Therefore, they are usually employed to construct the elastic interface for lithium batteries with a higher energy density and degree of safety, especially for flexible energy storage devices. The

more important pros of ECFPs are their degradability, metal-free nature, and environmentally friendly usage. The degradability of ECFPs means that they are able to decompose naturally after completing their function, reducing environmental damage; the absence of metallic components reduces the long-term pollution of the environment compared to many traditional materials that rely on metal catalysts or additives; and the production process of ECFPs is generally greener, consuming less energy, emitting fewer emissions, and exhibiting environmental friendliness throughout their life cycle [6,7].

ECFPs are important in diverse energy and conversion systems, leveraging their redox properties. They find applications in lithium-ion batteries, lithium–sulfur batteries, sodium metal batteries, supercapacitors, and photovoltaic electrodes. Moreover, ECFPs are also utilized in the photovoltaic industry for imaging and organic solar cells, in the medical sector as magnetic resonance contrast agents and antioxidants, and in chemistry, where nitrogen–oxygen radical polymers are commonly employed as catalytic oxidants [8,9].

At present, the common preparation methods of ECFPs mainly include chemical oxidative polymerization [10], in situ polymerization [11], electrochemical polymerization methods [12], and copolymerization or composite strategies [13]. ECFPs exhibit a larger specific surface area compared to traditional carbon-based conductive agents, such as carbon black, thereby establishing extensive and continuous electron transport pathways in lithium batteries, both point-to-point and point-to-face. Consequently, ECFPs can form a stable layer at the interface between battery components, enhancing interface compatibility, reducing adverse reactions, decreasing interfacial resistance, and improving the safety and stability of the battery [14]. Moreover, ECFPs are modified to possess a dual-conductive capability and construct continuous electron and ion conduction networks in thick electrodes for high-energy-density batteries [15,16]. Additionally, some ECFPs substitute a portion of the binder, realizing the functional integration of battery materials and enhancing the mechanical strength of the electrodes. The inherent flexibility of polymers offers greater processing versatility, making them suitable for solvent-free electrode processes for the fabrication of flexible electrodes or electrolyte membranes [17–19]. Notably, their superior mechanical properties and high toughness enable them to effectively accommodate volume changes in electrode materials during charge and discharge cycles, mitigate stress impacts, and improve the cycling stability and lifespan of batteries.

Polymers are generally classified into two main categories: redox-active and non-redox-active. Redox-active polymers are widely used in lithium batteries because of their optimal molecular structure, great stability, good chemical and physical properties, and excellent electrochemical storage ability. According to their molecular structure, redox-active polymers can be further divided into conjugate and radical systems [20]. As shown in Figure 1, typical conductive functional polymers with a conjugated structure, including polyaniline (PANI), poly(3,4-ethylenedioxythiophene) (PEDOT), polybenzimidazole (PBI), and polypyrrole (PPy), exhibit electrical characteristics comparable to those of inorganic materials like semiconductors and metals [21]. The electronic conduction mechanism of conjugated polymers mainly depends on their molecular structural characteristics and electronic properties. These polymers often have alternating single- and double-bond structures that allow their π electrons to move freely along the polymer chain, thereby facilitating electron conductivity. Due to their low density, excellent processability, and high mechanical flexibility, they can be shaped into various forms, such as films and fibers, which are crucial for advancements in modern electronic and optoelectronic materials science and technology. Meanwhile, it is worth noting that some radical polymers have been reported with good intrinsic conductivity [22]. The electron transfer in radical polymers mainly happens through the redox reactions of free radical groups, involving electron exchanges with either intermolecular or intramolecular bonds. In some free radical poly-

mers, the presence of free radicals facilitates the formation of π-electron systems, which provide efficient pathways for electron migration. Although the π-π interactions in these polymers are generally weak, it is still possible to support electron migration under specific conditions [23–25]. In particular, radical polymers, characterized by a high density of redox-active sites, exhibit significant potential as electrode-active materials for energy storage and conversion devices [26]. For instance, poly(4-glycidyloxy-2,2,6,6-tetramethylpiperidine-1-oxyl) radical films with internal active sites for electron conduction are ultimately applied as anode materials in batteries [27]. Moreover, nitrogen–oxygen radicals are commonly used as catalytic oxidants in organic synthesis, catalysts in metal-based batteries, and active materials in redox flow batteries.

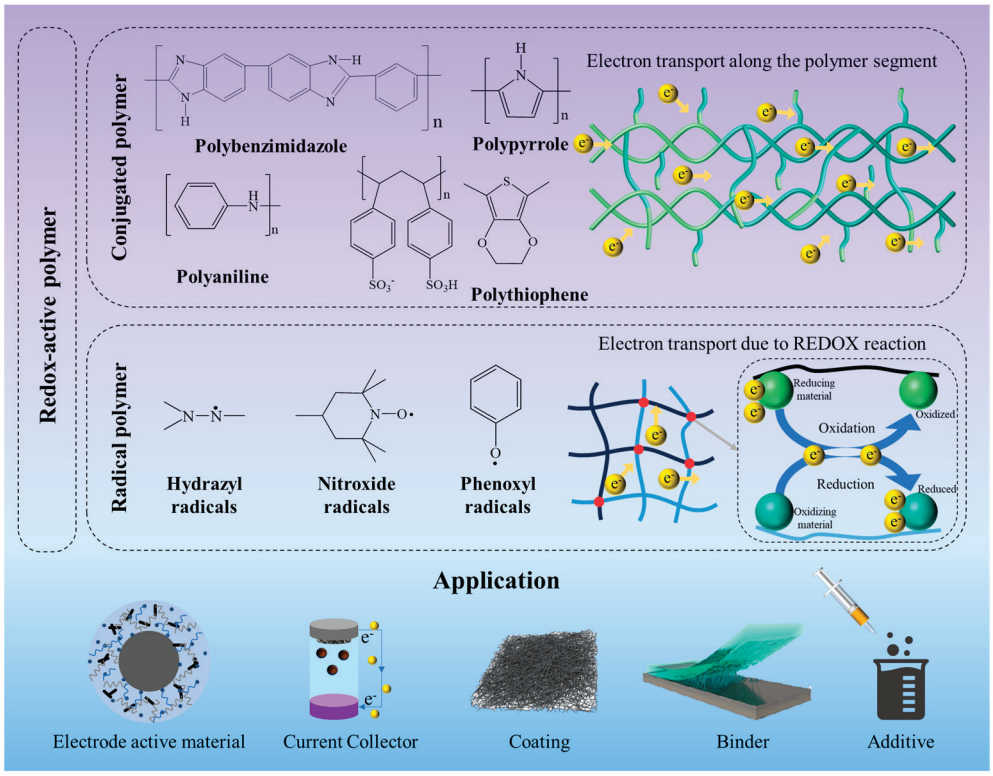

Figure 1. Typical electrically conducting polymers with conjugated and radical structures, their corresponding conduction mechanisms, and their applications in lithium batteries.

ECFPs possess conductivity, flexibility, and lightweight characteristics, which have garnered widespread attention. This review introduces and compares major conjugated polymers and radical polymer systems with their respective conduction mechanisms. In particular, the latest research advancements such as electrode active materials, binders, conductive agents, separator coatings, etc., in lithium batteries are reviewed in detail. Moreover, the current strategies employed to enhance electron conductivity and integrated performance are summarized, aiming to offer novel perspectives on the development and utilization of ECFPs in energy storage and conversion systems.

2. Conjugated Polymers

Conjugated polymers achieve conductive function from their long molecular chains with largely delocalized and polarized π-conjugated structures, which are composed of conjugated double bonds. Strategic molecular engineering of these π-conjugated backbones, particularly through π-orbital extension, significantly enhances charge transport capabilities [28,29]. In lithium battery systems, these polymers serve three principal functions: (i) As electrode active materials, their superior electrical conductivity facilitates efficient

charge transfer, thereby improving electrochemical utilization kinetics and boosting both specific capacity and rate performance; (ii) As conductive additives, they enable precise modulation of electrode conductivity; (iii) When employed as polymeric binders, they enhance electrode mechanical integrity while maintaining flexibility, ultimately extending their life cycle. The subsequent sections systematically elaborate on representative conjugated polymer systems and their optimization methodologies.

2.1. PANI

MacDiarmid made the discovery of PANI in the 1980s, and it is well known for its remarkable electrochemical and redox properties, environmental stability, and high conductivity [30,31]. While pure PANI demonstrates insulating behavior, its conductivity enhancement through chemical/electrochemical doping enables a theoretical capacity of 295 $mAh \cdot g^{-1}$ [32], positioning it as a competitive cathode candidate for high-performance lithium batteries. The stability of PANI is closely related to its various redox states, such as the fully reduced state, partially oxidized state, and fully oxidized state. Its electrochemical stability is influenced by its molecular structure and doping state, in detail, which can be significantly improved by doping with acids, carbon materials, metal oxides, etc. The electrochemical window under acidic conditions is approximately 1.0 V vs. SCE [33–36]. Additionally, compared to materials containing heavy metals, non-toxic PANI lowers environmental concerns during manufacture and disposal. The reliance on fossil fuels can be reduced by using sustainable biomass, such as lignin degradation products, as the raw material for PANI (aniline monomer). PANI is a viable option for green cathode materials due to its simple synthesis method, potential environmental friendliness, and capacity for pyrolytic recovery or chemical degradation.

As illustrated in Figure 2a, Guo et al. conducted a comprehensive investigation into the structure–performance relationship of various PANI forms, including emeraldine salt (ES) and emeraldine base (EB), with particular emphasis on the previously underexplored leucoemeraldine base (LB). Through quantitative structural analysis, they confirmed that LB exists in a fully reduced state. The researchers systematically re-evaluated the electrochemical performance of LB in non-aqueous lithium-ion batteries, achieving a remarkable reversible capacity of 197.2 $mAh \cdot g^{-1}$ through optimization of the cycling potential window (1.5–4.4 V) [37]. The optimized LB sample exhibited exceptional electrochemical properties, including a high average coulombic efficiency of 98%, superior rate performance (73.5 $mAh \cdot g^{-1}$ at 1800 $mA \cdot g^{-1}$), and excellent cycling stability with 76% capacity retention after 100 cycles at 20 $mA \cdot g^{-1}$. This groundbreaking study not only deepens the fundamental understanding of PANI's electrochemical properties and mechanisms but also represents a significant advancement in its development as a cost-effective, high-performance, and environmentally friendly cathode material for energy storage applications, marking a new milestone in this field. Furthermore, various doping strategies have been extensively explored to enhance the electrochemical performance of PANI as a cathode material in lithium batteries. A notable example is the work by Zou et al. [38], who developed a composite positive electrode comprising protonated polyaniline sulfide (SPANI) incorporated into a carbon black and polyvinylidene fluoride matrix (Figure 2b). Electrochemical analysis revealed that the reversible transition between protonated quinone imines (-NH^+=) and deprotonated quinone imines (-N=) during the charge–discharge process plays a crucial role in promoting lithium polysulfide (LiPS) adsorption and dissociation. This mechanism effectively suppresses the shuttle effect while simultaneously enhancing cycle stability and overall battery performance [39]. Additionally, the electron energy level of the quinone imide structure undergoes optimization through protonation-deprotonation state changes, leading to significantly improved electron conductivity. These investigations demonstrated

that protonated PANI sulfide exhibits exceptional electrochemical properties as a cathode-active material [40,41], characterized by superior rate capability, a high reversible specific capacity of 680 mAh·g^{-1} at 0.1 A·g^{-1}, and sustained coulombic efficiency approaching 100% during prolonged cycling.

As illustrated in Figure 2c,d, Fu et al. [42] developed an innovative solvent-free synthesis method for preparing graphene nanonetwork–PANI nanocomposites, which demonstrated superior electrical conductivity and enhanced lithium-ion storage capabilities. Acidic graphene oxide and PANI were ball-milled and treated at low temperatures to obtain chemically expanded graphene (CEG-PANI). This method provided sufficient active sites for lithium-ion storage because of the large specific surface area, mesoporous structure, and doping of the PANI conductive agent. In addition, PANI containing N heteroatoms significantly improved the electrochemical properties of CEG-PANI, and increased the reversible capacity to 664 mAh·g^{-1} in 150 cycles at 200 mA·g^{-1} and 253 mAh·g^{-1} in 350 cycles at 2000 mA·g^{-1}, respectively. Li et al. [43] implemented a wet etching strategy to introduce the modified PANI to construct a 3D holey graphene (HG)/nano-sulfur (NS)/photo-irradiated polyaniline (CPANI) composite as the cathode material. When PANI was integrated into the graphene structure, its amino groups bonded covalently with epoxy groups or formed hydrogen bonds with hydroxyl groups on the surface of HG. This interaction strengthened the connection between polysulfides and non-polar carbon, enhancing interface contact and improving the structural stability of PANI [44]. This configuration led to a high utilization rate of NS active materials and improved the electrochemical performance of lithium–sulfur batteries.

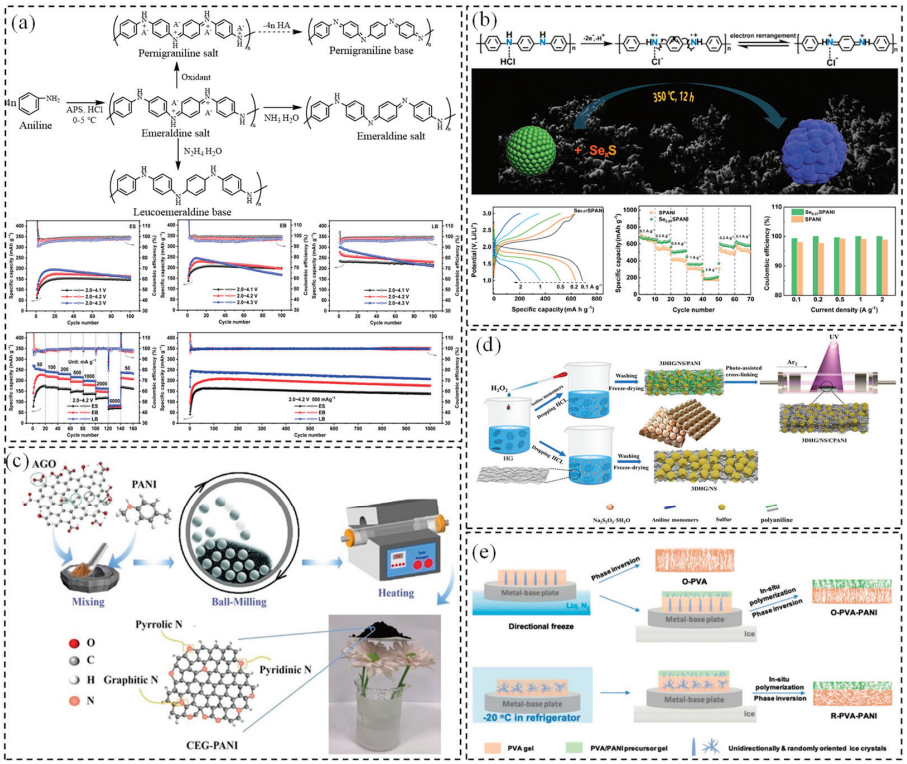

Figure 2. (**a**) Synthesis routes of ES, EB, LB, and their electrochemical performance in 1 M LiClO4/EC–DEC with 1 wt.% FEC [37]; copyright 2023, John Wiley and Sons. (**b**) The generation of quinoid imines, rate performance, coulombic efficiency, and GCD profiles of Se0.07SPANI compared with SPANI cathodes [38]; copyright 2023, Elsevier. (**c**) Synthesis process of CEG–PANI [42]; copyright 2023, Elsevier. (**d**) Preparation diagram of 3DHG/NS/CPANI composite [43]; copyright 2022, Elsevier. (**e**) Schematic illustration of fabrication processes of the oriented neat PVA separator and PVA–PANI Janus separators with oriented pores and random pores [45]. Copyright 2021, Royal Society of Chemistry.

As illustrated in Figure 2e, Xu et al. prepared a polymer unilateral conductive Janus separator featuring preferentially oriented pores using a water-soluble precursor solution of polyvinyl alcohol (PVA) and PANI through directional freezing and phase conversion [45]. The conductive PANI surface effectively alleviated the issue of localized current concentration and promoted the uniform and stable formation of the solid electrolyte interphase (SEI) layer, which effectively reduced local current density and minimized nucleation sites for lithium dendrite formation. Moreover, the Janus separator enhanced ionic conductivity while maintaining a balance between flexibility and rigidity, alongside superior wrinkle resistance and thermal stability. These contributed to the stable cycling performance and high coulombic efficiency of lithium metal batteries.

2.2. Polythiophene (PTH)—PEDOT:PSS

Compared to PANI, PTH exhibits superior flexibility and ductility, making it a preferred choice for conductive polymer composites in flexible electronic applications. Additionally, due to the delocalization of π electrons within its conjugated structure across the entire molecular chain, PTH possesses notable electrical conductivity, excellent stability, and favorable machinability [46]. Furthermore, PTH-PEDOT with a simple molecular structure, small energy gap, and higher conductivity is obtained by reducing the coupling effects of α-β and β-β during the oxidative polymerization process [47,48]. However, PTH-PEDOT is difficult to process and apply because of its poor solubility. To overcome this limitation, PEDOT:PSS is developed by blending PEDOT with the water-soluble polymer polystyrene sulfonic acid (PSS). This composite is widely utilized in energy storage and conversion devices due to its exceptional electron conductivity, high mechanical strength, excellent visible light transmittance, and superior stability [49]. It is worth mentioning that the conductivity of PEDOT:PSS is usually in the range of 10–1000 S cm^{-1}, depending on the preparation process and doping degree. By adding some organic solvents (such as DMSO) or using heat treatment, the electrical conductivity can be significantly improved to 10~100 S·cm^{-1}. Notably, advanced techniques such as multiple solvent displacement, interface engineering, or nanocomposite formation can enhance PEDOT:PSS conductivity to levels comparable with metals. PEDOT:PSS with doping of PSS exhibits excellent electrochemical stability and can remain stable in various electrolytes even after multiple cycles. Under pH = 7 conditions, its electrochemical window ranges from -1.0 V to 1.0 V vs. Ag/AgCl. Additionally, it remains stable at high potentials, but prolonged exposure to strong oxidizing environments can lead to performance degradation due to the loss of sulfonic acid groups [50,51]. Additionally, the preparation process of PEDOT:PSS typically occurs at low temperatures and pressures, resulting in lower energy consumption. If the use of organic solvents can be minimized, or water-based synthesis techniques are employed, they would be more environmentally friendly. Furthermore, recycling technologies for PEDOT:PSS are being developed to enhance its sustainability [52].

PEDOT:PSS is primarily utilized as a conductive agent and binder in lithium batteries. Zhang et al. [53] developed a standalone PEDOT-coated rhomboid sulfur/single-wall carbon nanotube (SWCNT) flexible composite cathode specifically for lithium–sulfur batteries. The rhomboid sulfur was encapsulated by PEDOT, which served as a shell to effectively capture polysulfides and limit their dissolution during charge/discharge cycles. Simultaneously, it facilitated efficient electron transport and enhanced the flexibility of the electrode. Chen et al. [54] designed a silicon-based negative electrode composite Si-PP-CA composed of PEDOT:PSS, citric acid, isopropanol, and silicon nanoparticles (Figure 3a). As a binder, linear PEDOT improves electron transport efficiency. Meanwhile, the hydroxyl groups in PSS can facilitate the rapid diffusion of Li^+ and form hydrogen and chemical bonds with citric acid and isopropyl alcohol at the interface, showing a tight interface effect and promot-

ing stable electrochemical performance. In addition, the PEDOT:PSS covered Si particles entirely due to its water-soluble property, which increased the Si content in the electrode. The composite electrode delivered more than 2200 mAh·g^{-1} capacity after 200 cycles at 0.2 A·g^{-1} and retained 89% even at a current density of 1.0 A·g^{-1} after 2000 cycles. As shown in Figure 3b, Li et al. [55] developed a water-soluble TA-PEDOT:PSS (TAPE) binder by mixing PEDOT:PSS with varying ratios of tannic acid (TA) to enhance the stability of $LiFePO_4$ cathodes in lithium-ion batteries. The sulfonic acid groups in PEDOT:PSS formed hydrogen bonds with the abundant hydroxyl groups in TA [56], altering the linear structure of PEDOT:PSS and establishing π-π stacking interactions between the conjugated π electrons in PEDOT and the aromatic rings in TA. Consequently, the PEDOT:PSS-TA composite exhibited excellent electrical conductivity, mechanical properties, adhesion, and stable electrochemical performance.

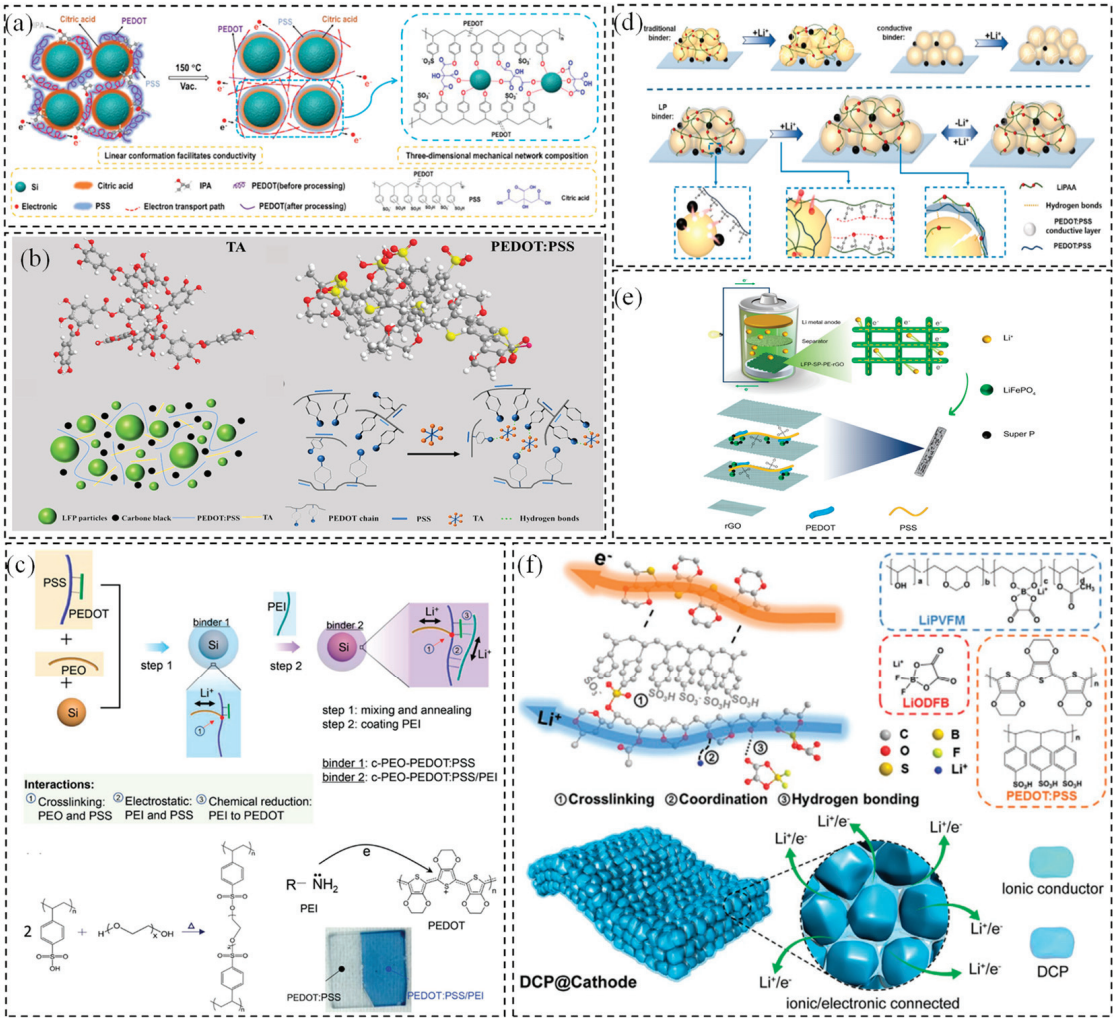

Figure 3. (**a**) Diagram of the preparation of a silicon–based anode electrode material Si/PP/CA from PEDOT:PSS, citric acid, isopropanol, and silicon nanoparticles [54]; copyright 2024, John Wiley and Sons. (**b**) Schematic diagram of PEDOT:PSS composited with TA [55]; copyright 2024, Elsevier. (**c**) PEO and PEI were assembled onto PEDOT:PSS to prepare polymeric adhesives with ionic and electronic conduction [57]; copyright 2018, John Wiley and Sons. (**d**) Schematic illustration of the function mechanism of the LP binder in a Si electrode [58]; copyright 2024, Elsevier. (**e**) Schematic of ions and electrons migration in the LFP–SP–PE–rGO electrodes/separator/Li metal battery system [59]; copyright 2024, Elsevier. (**f**) Sketch of interaction in electronic/ionic dual–conductive polymer between LiPVFM, LiODFB, and PEDOT:PSS, and illustration of Li^+/electron transportation of DCP–based cathode [60]. Copyright 2020, John Wiley and Sons.

In view of the adhesive effect, composite conductive multifunctional polymers were focused on by compositing PEDOT with other materials, for example, PAA, PEO, and graphene, as described in Figure 3c–e. Zeng et al. [57] developed a polymer binder with high ionic and electronic conductivity by integrating the ionic polymers polyethylene oxide (PEO) and polyethylene imine (PEI) into the conductive polymer PEDOT:PSS chain, which yielded a high modulus that helped to maintain the integrity of the Si anode. The lithium-ion diffusivity and electron conductivity of the developed polymer binder were found to be 14 and 90 times higher, respectively, compared to the widely used carboxymethyl cellulose (with acetylene black) binder. Geng et al. [58] introduced a multifunctional binder, LP19, by combining lithiated polyacrylic acid (LiPAA) with PEDOT:PSS. This binder exhibited high electronic and Li-ion conductivity, as well as improved mechanical properties. On a macroscopic scale, PEDOT:PSS facilitated electron transfer between conductive particles and active materials. On a microscopic scale, it established molecular-level electron coupling at the interface between the binder and active particles. This dual mechanism significantly enhanced the rate performance and energy density of the anode. Gao et al. [59] employed 3D printing technology to fabricate a composite electrode with a graded porous multidimensional conductive network. This network consisted of lithium iron phosphate, PEDOT:PSS, and graphene oxide (GO), where PEDOT:PSS and GO served dual roles as adhesive and conductive agents, respectively. The hierarchical porous structure allowed for efficient electrolyte infiltration, while the multidimensional conductive network enhanced electron and ion transport, optimizing the overall performance of the electrode [61,62]. Additionally, PEDOT:PSS and GO were strongly bonded through C-O-S linkages, which boosted mechanical strength and electron transfer efficiency, thereby significantly improving specific capacity and cycle performance. Furthermore, the PEDOT:PSS-based conductive multidimensional network mitigated polarization issues due to the close contact driven by surface negative groups and the enhanced electrical conductivity [63].

In previous work, our team developed an electronic/ionic dual-conductive polymer (DCP) [60] for the composite cathode in solid-state batteries. This polymer was synthesized through intermolecular interactions involving a lithiated polyvinyl formal-derived Li^+ single-ion conductor (LiPVFM), lithium difluoro borate (LiODFB), and PEDOT:PSS (Figure 3f). The sulfonic acid groups in PEDOT:PSS formed hydrogen bonds with the oxalate groups of LiODFB and the polar groups in LiPVFM, such as carbonyl and amide groups. Crosslinking, coordination, and hydrogen-bonding interactions endowed the DCP with excellent electronic conductivity (68.9 $S{\cdot}cm^{-1}$), Li-ion conductivity (2.76×10^{-4} $S{\cdot}cm^{-1}$), a broad electrochemical window exceeding 6 V, and a high modulus of 6.8 GPa. The DCP enabled the fabrication of self-standing composite cathodes with spatially and temporally stable interfaces, structural integrity, and efficient electronic/ionic transport. These properties enable solid-state batteries to achieve exceptional cycling performance, even under conditions of high active material loading and content.

2.3. PBI

PBI is a heterocyclic polymer characterized by a benzimidazole moiety as its repeating unit [64]. It possesses a rigid, rod-like structure with closely packed chain segments, stabilized by strong hydrogen bonding and π-π interactions between the polymer chains. These interactions endow PBI with excellent chemical and thermal stability [65,66]. The imidazole ring in PBI contributes to its electrochemical stability, enabling it to perform well in high-temperature and strongly acidic environments. Covalent organic frameworks (COFs) are materials linked by strong covalent bonds and composed of functional organic structural units [67,68]. PBI can be classified as a unique category of COF materials due to its two-dimensional structure, nitrogen-atom doping, physicochemical stability, and

programmable pore size. However, PBI lacks mobile electrons or holes as charge carriers, and its electrical conductivity is below 10^{-10} S·cm^{-1} at room temperature. To enhance its electronic transport capability, PBI can be doped with conductive fillers such as carbon nanotubes, graphene, and carbon black, or modified by introducing conductive units. As a result of these properties, PBI and its derivatives exhibit excellent high-temperature resistance, flame retardance, chemical stability, and mechanical strength, making them promising candidates for electrode materials in lithium batteries [69–71]. From an environmental sustainability perspective, the high durability of PBI can extend the lifespan of devices, thereby reducing resource consumption.

As shown in Figure 4a, Ren et al. [72] synthesized a microporous polybenzimidazole (MPBI) through a condensation reaction between 1,2,4,5-tetraaminobenzene and pyromellitic acid in a polyphosphate medium. Following treatment at 55 °C, MPBI formed a 2D graphene-like framework structure, which maintained a large surface area and preserved nitrogen-atom doping. This structure contributed to its excellent performance, including a remarkable long cycling life, a high reversible capacity of 700 mAh·g^{-1} (at 1 A·g^{-1}) after 500 cycles, and outstanding rate performance. Nie et al. [73] developed a pyrrole nitrogen-rich carbon source derived from PBI using an aerosol-assisted assembly and physical adsorption process. As an encapsulating coating for micro-sized silicon spheres, the carbon layers effectively prevented direct contact between the silicon and the electrolyte. This significantly suppressed the formation of an uncontrolled solid electrolyte interphase (SEI) film, thereby enhancing the stability and performance of the silicon-based anode. Furthermore, PBI contained a large number of nitrogen functional groups, which introduced numerous external defects and active sites for lithium storage, improving the specific capacity of the silicon anode [74]. As a result, the mesoporous Si-PBI carbon composite exhibited a high reversible specific capacity (2172 mAh·g^{-1}), excellent rate capability (1186 mAh·g^{-1} at 5 A·g^{-1}), and a long cycle life, as illustrated in Figure 4b.

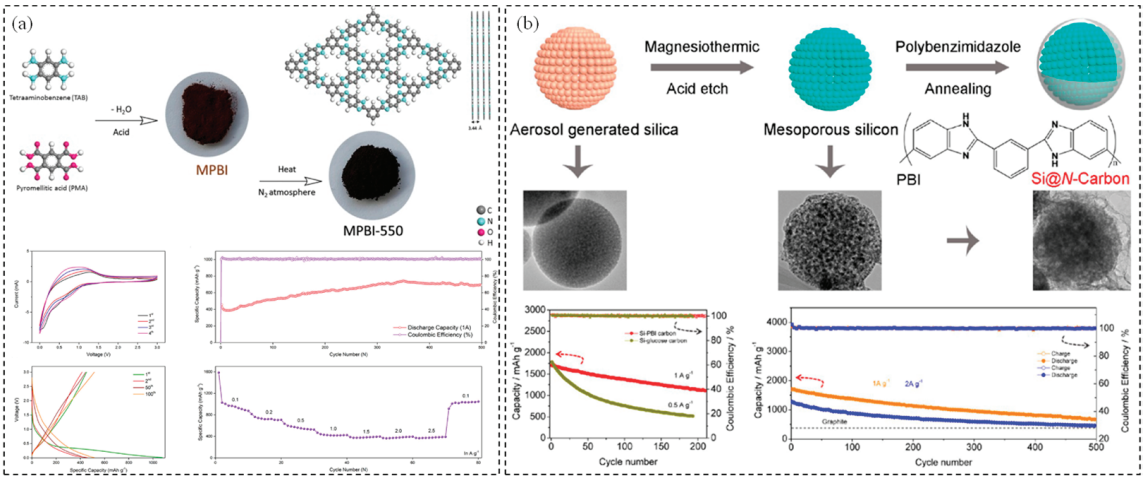

Figure 4. (**a**) Schematic diagram of the synthesis of 2D microporous polybenzimidazole MPBI and its electrochemical results [72]. Copyright 2021, Elsevier. (**b**) Mesoporous silicon anodes synthesized by using polybenzimidazole–derived pyrrolic N-enriched carbon [73]. Copyright 2017, American Chemical Society.

2.4. PPy

The conductive PPy with a conjugated chain oxidation and corresponding anion doping structure exhibits conductivity ranging from 10^2 to 10^3 S·cm^{-1} and demonstrates excellent electrochemical redox reversibility [75]. PPy shows good stability within a moderate potential range (0.76 V vs. Ag/Ag$^+$), but it is susceptible to over-oxidation at higher potentials, which can lead to degradation. Studies have shown that the electrochemical

stability of PPy can be enhanced by compositing it with carbon materials, metal oxides, and other conductive polymers. Notably, PPy can be produced industrially and applied across various fields due to its numerous advantages, including straightforward preparation methods, non-toxicity, excellent chemical stability, superior mechanical properties, and high conductivity [76,77]. Furthermore, it can be synthesized using electrochemical methods, which minimize the use of excessive chemical reagents and solvents, making it an eco-friendly material.

Due to its unique structure, PPy exhibits high electronic conductivity and mechanical strength [78,79]. Yi et al. [80] synthesized a sulfide polypyrrole (S-PPy) composite at a slightly elevated vulcanization temperature for application in solid-phase converted lithium–sulfur batteries. Unlike conventional mixtures of sulfur and polypyrrole, short-chain sulfur was incorporated into the PPy backbone to form the S-PPy composite. In this structure, PPy provides excellent electronic contact for the short-chain sulfur, enhancing its activity and promoting its conversion into Li_2S. Additionally, the PPy backbone mitigates the volume changes of sulfur during electrochemical reactions, ensuring the mechanical stability of the electrode and extending its cycling life, as illustrated in Figure 5a.

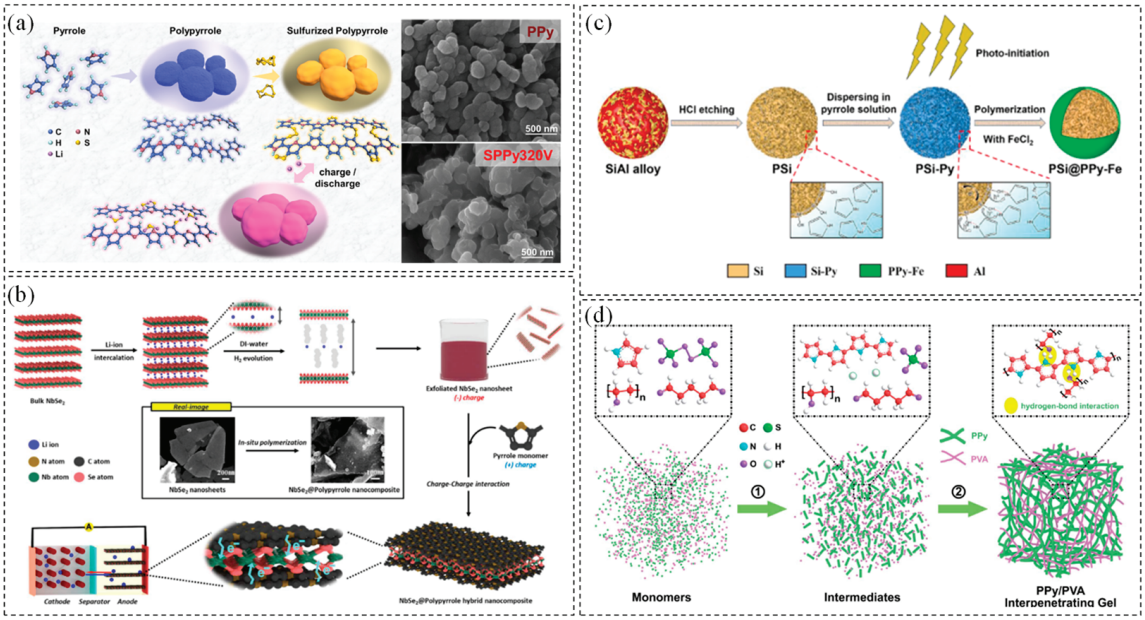

Figure 5. (**a**) Synthesis and discharging process of sulfurized polypyrrole [80]; copyright 2023, Elsevier. (**b**) Schematic illustrations of $NbSe_2$/PPy hybrid nanocomposite preparation [81]; copyright 2023, Royal Society of Chemistry. (**c**) Synthetic illustration for PSi/PPy–Fe composites [82]; copyright 2023, Elsevier. (**d**) Structural diagram of the PPy/PVA interpenetrating gel [83]. Copyright 2021, Royal Society of Chemistry.

Byung-Ho Kang et al. [81] demonstrated that $NbSe_2$, with its metallic properties, can be applied as an anode material by doping it with conductive polypyrrole (PPy), as illustrated in Figure 5b. The π-conjugated structure of PPy was bound to the two-dimensional surface layer of $NbSe_2$ through van der Waals interactions. Simultaneously, nitrogen-containing functional groups in PPy (such as -NH or -N= on the pyrrole ring) chemically adsorbed onto the surface of unsaturated metal atoms (Nb) or selenium atoms (Se) of $NbSe_2$. This interaction created a well-dispersed PPy layer on the $NbSe_2$ surface, enhancing the stability of the composite material. The $NbSe_2$-PPy hybrid nanocomposites exhibited a lithium storage capacity of 955 $mAh \cdot g^{-1}$, maintained over 300 cycles without capacity loss, and demonstrated excellent rate performance at 4 $A \cdot g^{-1}$. Leveraging the photoelectric effect of semiconductor silicon, Xu et al. [82] developed an eco-friendly and straightforward

photoinitiation synthesis approach to fabricate yolk–shell-structured polypyrrole–iron-coated porous silicon microspheres (PSi-PPy-Fe) for use as anode materials in lithium-ion batteries (Figure 5c). The polymerization of pyrrole monomers occurred exclusively at the interface of the silicon matrix, where vacancies were present, effectively preventing the formation of free PPy-Fe particles. Both hydrogen-bond interactions and covalent linkages were established between the PPy-Fe layer and silicon, playing a crucial role in maintaining strong contact and enhancing structural stability [84]. The PPy-Fe coating facilitated faster charge transfer and prevented the silicon-based material from detaching from the copper collector. More significantly, it effectively mitigated the severe structural expansion of the negative silicon electrode.

Additionally, Xia et al. [83] integrated an adhesive polymer into a conductive functional polymer network by mixing polyvinyl alcohol (PVA) and polypyrrole (PPy) to form an interpenetrating gel, as shown in Figure 5d. PPy formed numerous hydrogen bonds with the hydroxyl groups in PVA, enabling its uniform dispersion within the PVA matrix. This prevented agglomeration in the composite material and enhanced both the overall electrical conductivity and mechanical properties. Furthermore, glutaraldehyde promoted cross-linking with PPy at both intramolecular and intermolecular levels, creating stronger bonding effects. This method effectively addressed the brittleness of the electronic conductive polymer and its weak bonding force with the active material, thereby ensuring long-term stability and extending the cycling life of the electrode [85].

This section focuses on the application of typical electrically conductive functional polymers with conjugated structures, such as PANI, PEDOT:PSS, PBI, and PPy in lithium batteries. These conjugated polymers, renowned for their exceptional electrical conductivity, have been extensively utilized as active electrode materials, conductive additives, and/or binders in various battery systems.

PANI is a representative conjugated polymer, distinguished by its high electrical conductivity, excellent electrochemical stability, and environmental durability. Through careful structural and compositional design, PANI-based electrodes demonstrate significantly improved lithium-ion storage performance and electrochemical stability. For instance, PANI-based composites combined with graphene provide a larger specific surface area and a porous structure, which facilitate rapid lithium-ion transport. Additionally, the high conductivity of graphene enhances the charge transfer process. However, the volume expansion of PANI during charging and discharging may compromise the structural integrity of the electrode.

PEDOT:PSS-based multifunctional conductive polymers have been combined with other materials (e.g., tannic acid (TA), polyethylene oxide (PEO), graphene) to improve lithium-ion diffusion and electronic conductivity, thereby enhancing the mechanical integrity and cycling life of the electrode. A key challenge lies in balancing high conductivity with flexibility and stability during prolonged cycling. Through molecular structure design, nanocomposites, and cross-linked networks, it is possible to achieve an optimal balance between these properties. PPy combined with materials like polyvinyl alcohol (PVA) to form interpenetrating network gels demonstrates improved dispersion and conductivity. Additionally, intermolecular crosslinking enhances bond strength, addressing the issues of fragility in conductive polymers and weak binding forces with active materials, such as silicon negative electrode powders. However, PPy faces similar challenges to PANI, including volume expansion and degradation, which can lead to a decline in mechanical properties over prolonged cycling. PBI, as a special class of covalent organic framework (COF) materials, exhibits excellent high-temperature resistance, flame retardance, chemical stability, and mechanical properties, making it a promising candidate for lithium battery electrodes. Strategies such as material selection and composite formulation can mitigate

degradation issues during prolonged cycling and high-temperature conditions, thereby enhancing battery safety and performance stability.

In addition to the typical polymers discussed above, numerous other electrically conductive functional polymers (ECFPs) remain to be explored. For instance, polyaniline diamine (PPD) exhibits a high energy storage capacity and holds potential as an electrode material for lithium batteries. However, its poor mechanical properties make it difficult to withstand stress variations during prolonged cycling. Moreover, poly[(2-ethylhexyl) phenylene vinylene)] (MEH-PPV), poly[2,5-bis(3-hexylthiophene-2-yl) thiophene] (PBTTT), poly (triaryl amine) (PTAA), and poly(benzimidazobenzophenanthroline) (BBL) are conjugated polymers known for their excellent optical properties and are widely utilized in organic electronic devices. Because of their poor electrochemical stability under high-voltage operating conditions, the application of these materials in lithium batteries is currently limited. In the future, their mechanical properties could be improved through chemical cross-linking or by compounding with other materials. Additionally, their electrochemical stability may be enhanced by introducing stable side groups, such as fluorinated groups on the polymer backbone, or by doping with inorganic materials like lithium salts or other metal salts. With further optimization through molecular design, modification, and composite formation, a broader range of conjugated polymers is expected to meet the demands for high energy density and extended cycling life in lithium batteries.

3. Radical Polymers

Radical polymers are composed of flexible, non-conjugated backbones and functional side groups containing free radicals. These radical sites possess highly localized electrons, distinguishing their structure from that of conjugated conductive polymers. Electron transport in radical polymers is facilitated by the redox reaction processes of the free radicals [86]. This section provides a brief overview of recent advancements in the applications of organic radical polymers, including nitroxide radicals, phenoxy radicals, and others [87,88]. A notable nitroxide free radical species, 2,2,6,6-tetramethylpiperidinyl-n-oxyl (TEMPO), was first reported by Nakahara and his team in 2002 [89]. TEMPO exhibits excellent electrochemical properties, outstanding stability, and rapid redox reactions. Currently, poly (2,2,6,6-tetramethylpiperidinyl methyl acrylate) (PTMA) and poly(norbornene), both of which incorporate TEMPO, have been extensively studied and applied as polymer cathode materials [90,91]. These materials are characterized by low preparation costs, good hydrophilicity, and outstanding electrical conductivity.

3.1. Nitroxide Radicals

Nitroxide radicals are named for containing a nitroxide radical motif (N-O·). TEMPO-based materials exhibit intrinsic bipolar characteristics, making them particularly suitable for use as cathode materials due to their high redox potential, typically around 3.6 V vs. Li/Li^+. The electrochemical stability of nitroxide radicals primarily arises from the nitrogen–oxygen bond (N-O·) within the molecule and the effect of intramolecular electron delocalization. Their electrochemical stability and conductivity can be further enhanced by introducing π-conjugated structures (such as aromatic rings) into the nitroxide radicals to modify their molecular structure or combining them with conductive materials like MXene and porous carbon [92–94]. Additionally, nitroxide radicals can be produced from renewable biomass-derived materials. This process enables controlled polymerization with reduced byproducts and waste.

3.1.1. PTMA

The synthesis of PTMA begins with the radical polymerization of the precursor monomer, 2,2,6,6-tetramethylpiperidinyl methyl acrylate (TMPMA), followed by a chemical oxidation step that converts the piperidine ring into a stable nitrogen–oxygen radical. This process endows PTMA with excellent chemical stability and unique electronic properties, making it suitable as a positive electrode material in applications requiring high-rate performance, such as small energy storage devices and fast-charging batteries [95,96]. When used alongside conventional $LiFePO_4$ or NCM cathodes, PTMA can serve as an additive to optimize conductive networks, thereby enhancing electrochemical performance and prolonging cycling life. Furthermore, PTMA delivers a high output voltage of approximately 3.5 V, which is comparable to that of traditional cathode materials like $LiFePO_4$. It also offers additional capacity and specific energy density, particularly without the expansion and contraction issues associated with conventional inorganic cathode materials during lithiation and delithiation [97,98].

Zhang et al. developed a layered composite material composed of PTMA and reduced graphene oxide (rGO) through non-covalent π-π stacking, leveraging the advantages of PTMA and the exceptional conductivity and structural stability of rGO. This innovative approach significantly enhanced the cycling performance of lithium batteries at high rates [99]. As illustrated in Figure 6a, PTMA served as the polymer matrix, and the introduction of pyrene groups via chemical modification strengthened its interaction with rGO. This led to the formation of a stable and ordered layered structure, which improved ion transport and cycling stability. Additionally, the nitrogen oxide radicals present in the PTMA chains contributed to the energy storage capacity of the batteries. Li et al. reported the preparation of a composite material, P(TMA-co-AQ), by grafting anthraquinone (AQ) units onto TEMPO polymer chains through a polymerization reaction [100]. The modification of AQ occurred when the quinone groups (C=O) on the chain segments received electrons from reductants, forming a semiquinone radical intermediate (AQ^-). This intermediate then acted as an electron donor, transferring electrons to TEMPO molecules to accelerate their reduction. As a result, the radical electron structure in TEMPO can stably and persistently accept or transfer electrons, making it less prone to degradation. The P(TMA-co-AQ) composite with multi-walled carbon nanotubes (MWCNTs) as the electrode material exhibited rapid and reversible redox cycling. This grafting structure not only enhanced the stability of TEMPO but also facilitated electron transfer between P(TMA-co-AQ) and the carbon nanotubes. In half-cell tests, AQ-functionalized PTMA demonstrated an initial capacity of 174 $mAh \cdot g^{-1}$ with a capacity loss of 0.18% per cycle, while the discharge capacity based on the TEMPO pair was approximately 85 $mAh \cdot g^{-1}$ (Figure 6b).

3.1.2. Polynorbornene (PNB)

PNB, as a binder, represents a promising approach to enhancing the adhesion and dispersion of electrode components. It is utilized to strengthen the bonding between active material particles. Additionally, PNB's unique molecular structure provides exceptional mechanical support and chemical stability for the electrodes, alongside its electronic conductivity.

Figure 6c illustrates that Daun Jeong et al. [101] designed a poly (norbornene-co-norbornene dicarboxylic acid-co-heptafluorobutyl norbornene imide) (PNCI)-based binder for nickel-rich layered oxide $LiNi_xCo_yMn_zO_2$ (NCM, $x > 0.8$) electrodes. Norbornene served as the backbone of the main chain, providing rigidity and mechanical strength, while its fluorinated structure imparted strong hydrophobicity, low surface energy, and high chemical stability. Additionally, the molar composition of the PNCI binder was systematically adjusted to optimize structural integrity, minimizing material loss during

charging and discharging. Kan Hatakeyama-Sato et al. [103] synthesized a novel free radical polymer with PNB as the backbone and 2,2,5,5-tetramethyl-1-pyrrolidinyl-N-oxyl (PROXYL) as the side group of unsaturated derivatives. This composite polymer combined a rigid backbone chain with stable nitroxide radical side groups, resulting in a high modulus and good flexibility. These properties enabled the polymer to maintain structural integrity during electrode expansion or contraction. Furthermore, the composite polymer exhibited stable redox capacity as a cathode material, owing to the reversible conversion of the nitroxide radical structure of PROXYL to its reduced state (imine, N-OH).

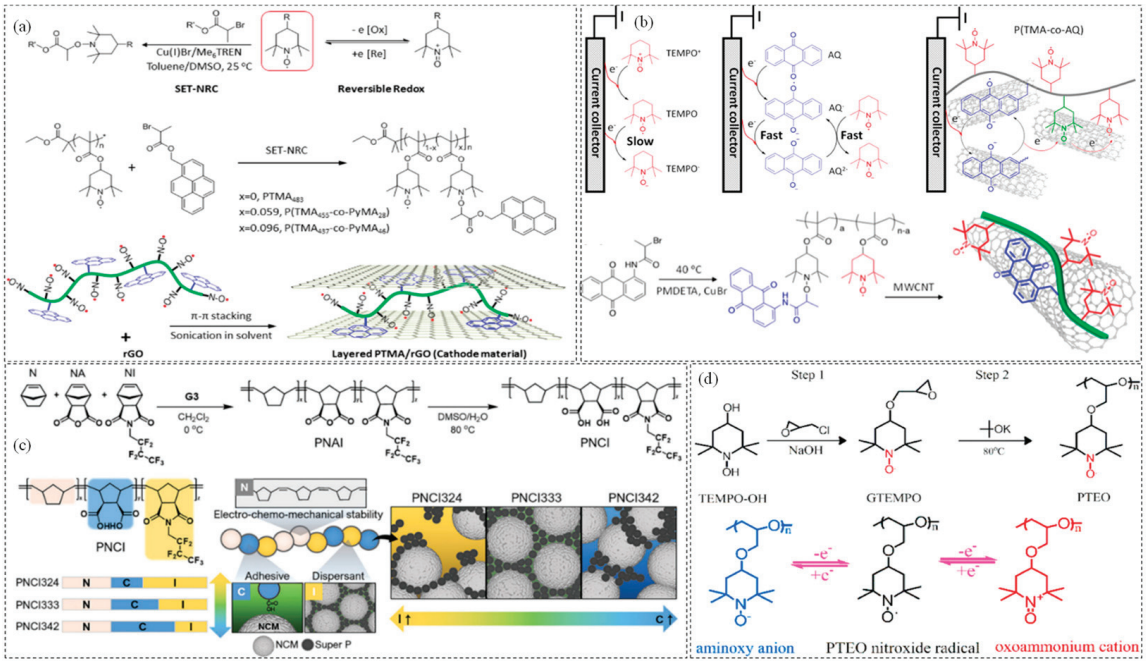

Figure 6. (**a**) Preparation process of PTMA/rGO composites [99]; copyright 2017, American Chemical Society. (**b**) P(TMA–co–AQ) and copolymer/multi–wall carbon nanotube composite electrode [100]; copyright 2022, American Chemical Society. (**c**) Synthesis of PNCI terpolymers and the functional contributions of the PNCI binder [101]; copyright 2023, John Wiley and Sons. (**d**) Synthetic route of PTEO [102]. Copyright 2020, Elsevier.

3.1.3. Poly(tempo-ether-oxetane) (PTEO)

PTEO is a novel organic radical polymer used as a composite electrode material, primarily prepared by incorporating TEMPO with flexible ether chains or oxetane. The nitroxide radicals in PTEO exhibit high efficiency in electron transfer reactions, providing excellent redox activity and high reversibility. The introduction of oxetane or ether groups into the polymer enhances its flexibility and stress resistance, improving the electrode's adaptability. During the charging process, the nitroxide radical is oxidized, losing electrons to form the oxidation state (N^+=O). Conversely, during discharging, the nitroxide group is reduced to imine (N-OH) by capturing electrons and lithium ions. Deng et al. incorporated a silica skeleton into the PTEO backbone to construct a highly rigid 3D network structure [102]. As an organic positive electrode, this material can withstand volumetric stresses under high pressure and repeated electrochemical changes. The nitrogen and oxygen radicals in PTEO serve as active centers for energy storage, enabling efficient redox reactions (Figure 6d). The modified PTEO exhibited an electrical conductivity of 0.13 $S \cdot m^{-1}$, surpassing that of other organic cathode materials used in lithium-ion batteries. In performance tests, the PTEO-based lithium-ion battery achieved a capacity of up to 220 $mAh \cdot g^{-1}$ at 0.2 °C, while maintaining capacities of 165 $mAh \cdot g^{-1}$ at 1 °C and 95 $mAh \cdot g^{-1}$ at 8 °C.

3.2. Phenoxyl Radicals

Phenoxyl radicals are characterized by extensive conjugated aromatic structures, and their highly efficient reversible transformation between neutral phenoxyl radicals (R-O·) and phenoxyl anions ($R\text{-}O^-$) plays a crucial role in the energy storage processes of rechargeable batteries. The electrochemical stability of phenoxyl radicals is influenced by molecular structure, electrochemical environment, and substituent effects. For instance, the phenoxenium cation of α-tocopherol exhibits enhanced stability due to intramolecular hydrogen bonding and electron delocalization. Through rational molecular design and optimization of electrochemical conditions, the electrochemical stability of phenoxyl radicals can be significantly improved.

The preparation of phenoxy free radicals involves two main steps: free radical polymerization and chemical oxidation. Specifically, hydrogen galvinoxyl styrene is used as a monomer, which is initiated to generate free radicals at a specific temperature. These free radicals then react with styrene groups to form either dendritic or linear polymers. Subsequently, the hydroxyl group in the hydrogen galvinoxyl group is oxidized to form a free radical (R-O) through chemical oxidation [104,105]. From a green development perspective, phenoxyl radicals can be derived from natural phenolic compounds, such as those extracted from lignin or other plant secondary metabolites. The preparation process can incorporate green chemistry methods, such as aqueous phase systems or photocatalytic processes, to reduce energy and solvent consumption, thereby minimizing environmental pollution.

N-type polymers are polymers that gain electrons during a redox reaction (undergo reduction) and typically function as electron acceptors. These polymers generally exhibit low LUMO (Lowest Unoccupied Molecular Orbital) energy levels, making them suitable candidates for anode materials in batteries. Common examples of n-type polymers include those based on naphthalene diimide (NDI), perylene diimide (PDI), and fullerene derivatives [106]. In contrast, p-type polymers are polymers that lose electrons during a redox reaction (undergo oxidation). These polymers typically possess high HOMO (Highest Occupied Molecular Orbital) energy levels and are commonly used as electron donors and cathode materials in batteries. Common examples of p-type polymers include those based on thiophene (P3HT), benzodithiophene (BDT), and carbazole [107].

As depicted in Figure 7a,b, Takeo Suga et al. investigated the reversible and rapid one-electron redox reaction between phenoxyl radicals and phenoxyl anions [108]. They explored an n-type and redox-active radical polymer with galvinoxyl as the anode active material. Building on this, a totally organic radical battery was developed with the n-type redox-active radical polymer as the anode and a p-type radical polymer as the cathode [109]. Li et al. [110] reported the synthesis of two stable bifunctional radicals prepared through C-C coupling of redox-active phenoxyl radicals with perylene diimides (PDIs) or benzo perylene triimides (BPTIs). Incorporating electron-deficient PDIs or BPTIs into phenoxyl radicals increased the density of redox-active groups per molecule, elevated the redox potential, and enhanced the stability of the phenoxyl radicals.

3.3. Hydrazyl Radicals

Hydrazyl radicals are a class of organic free radicals centered around nitrogen, characterized by the presence of hydrazine groups (-N•-N=). These radicals are typically generated through the oxidation or dehydrogenation of hydrazine compounds (R-NH-NR′). The general formula for hydrazyl radicals is R-N•-NR′ or $R_2N\text{-}N\bullet\text{-}R$, where at least one nitrogen atom carries an unpaired electron. The electrochemical stability of hydrazyl radicals can be significantly enhanced by introducing specific electron-withdrawing groups or by designing particular molecular structures, such as bulky substituents or conjugated

systems. Experimentally, their electrochemical stability is typically characterized using cyclic voltammetry (CV) and electron paramagnetic resonance (EPR) [111]. Hydrazyl radicals are generally synthesized from hydrazine and aromatic compounds, involving organic hydrazine derivatives that usually rely on petrochemical resources. Recently, the synthesis process has been optimized to reduce byproducts or select alternative reagents. Hydrazyl radicals exhibit high reactivity, which can lower catalyst requirements and improve chemical conversion efficiency, highlighting their potential as green chemistry candidates.

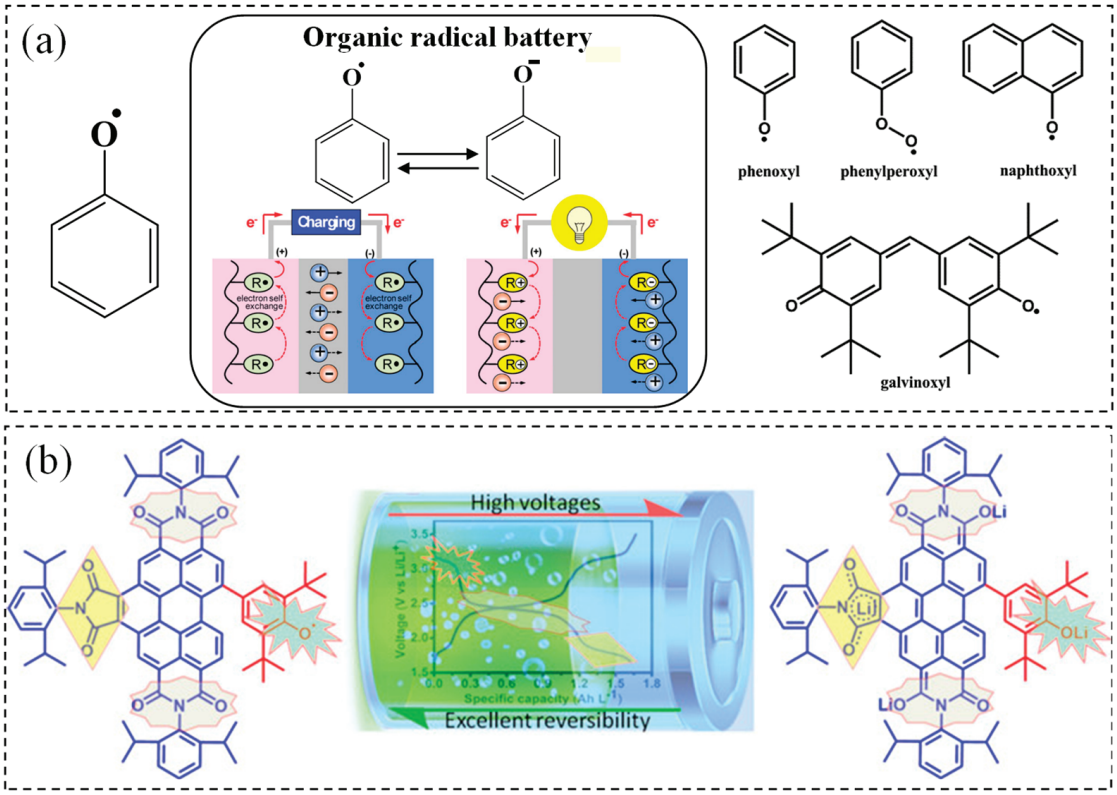

Figure 7. (**a**) The derivatives and applications of phenoxy radicals [109]; copyright 2009, John Wiley and Sons. (**b**) Stable radical preparation process by C–C coupling of phenoxy radical with PDI or BPTIs [110]. Copyright 2018, John Wiley and Sons.

Lee et al. [112] reported the synthesis and characterization of stable triazenyl radicals, which were obtained through the single-electron reduction of the corresponding triazenyl cations using potassium metal (Figure 8a). Among these, the triazine radical with a hydrazine structure can be oxidized to form a triazine cation. When treated with a transition metal source or an electrophilic reagent, these radicals reversibly oxidize back into cations while extracting a hydrogen atom from heteranthrene, forming an N-H bond at the central nitrogen atom [113]. Additionally, due to their aromaticity and conjugated systems, triazenyl radicals exhibit high chemical stability and can undergo multiple redox reactions. Furthermore, lightweight triazenyl radicals delivered a theoretical specific capacity of up to 200 $mAh \cdot g^{-1}$ as positive active materials in lithium-ion batteries. Triazenyl radicals can also serve as redox media to promote the oxidation of Li_2O_2 particles, reducing the overpotential in lithium–oxygen batteries. In Figure 8b, Bai et al. [114] designed a redox medium utilizing the nitrogen-containing free radical 1,1-diphenyl-2-pyridine hydrazyl radical 2,2-diphenyl-1-(2,4,6-trinitrobenzene) hydrazyl (DPPH). DPPH significantly enhanced the solubility and migration rate of oxygen, improved charge transport, and facilitated the decomposition of Li_2O_2. Consequently, lithium–oxygen batteries incorporating DPPH as an intermediate molecule achieved a low terminal charge voltage of 4.12 V and maintained

stable performance over 80 cycles at a high current density of 400 $mA \cdot g^{-1}$ with a fixed capacity of 1000 $mAh \cdot g^{-1}$.

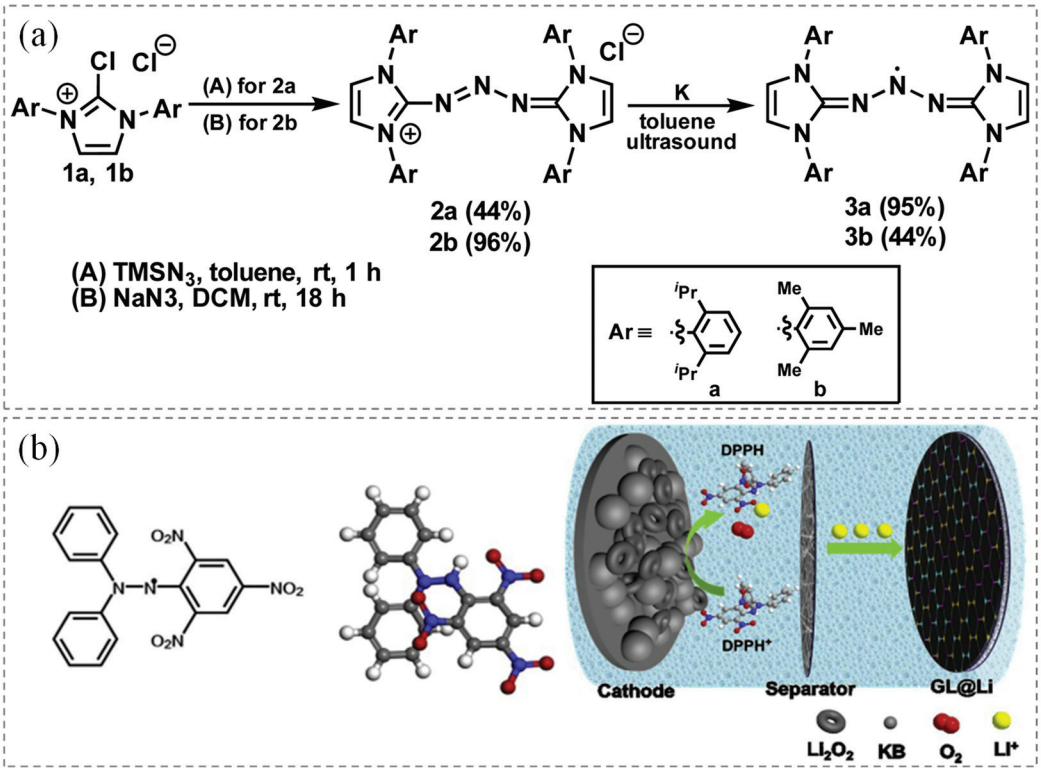

Figure 8. (**a**) Synthesis of N–heterocyclic carbenes supported triazenyl radicals [112]. Copyright 2017, American Chemical Society. (**b**) Molecular structure of DPPH and its charging reaction mechanism in Li–O_2 batteries [114]. Copyright 2020, Elsevier.

In this part, the application and progress of several radical polymers, including nitroxide free radicals, phenoxy free radicals, and hydrazine free radicals, in lithium batteries are reviewed. Their synthesis methods, electrochemical properties, and strategies for functional improvement are discussed in detail. These polymers are composed of flexible scaffolds and side groups bearing free radicals with highly localized electrons, enabling them to exhibit excellent electron transport kinetics and electrochemical performance.

PTMA is a typical nitroxide radical polymer known for its excellent chemical stability and electron transport capabilities, making it a suitable candidate for use as an electrode material. However, its higher molecular weight and fewer active sites limit its stability in higher voltage ranges. Another nitroxide radical polymer, PNB, exhibits adhesive properties and can serve as a binder for electrode materials. It is crucial to note that the incorporation level of PNB significantly influences the electrochemical performance of the electrodes. Therefore, its large-scale application still depends on further research, including the optimization of adhesion behavior in solutions and improvement of compatibility with existing electrode systems. Composite electrodes combining NCM with PNB demonstrate outstanding mechanical properties, chemical stability, and conductivity, enhancing energy density and cycling stability. Furthermore, phenoxy radicals prepared through free radical polymerization and chemical oxidation possess efficient reversible electron transfer capabilities. Research indicates that binding with electron-deficient molecules, such as perylene diimides or benzo perylene triimides, is one of the most effective strategies for improving the cycling life of batteries based on phenoxy free radicals.

Additionally, some free radical polymers, such as hydrocarbon radicals and halogen radicals, have been reported to exhibit high redox reaction activity. However, when utilized

as electrode active materials in lithium batteries, hydrocarbon radicals can induce the decomposition of organic electrolytes, significantly compromising the cycling lifespan and safety of the batteries. Although this issue can be mitigated through the design of radical scavengers or reactive additives, it remains a considerable challenge. In contrast, halogen radicals readily react with organic electrolytes and electrode materials, leading to unstable side reactions. To address this, research has focused on chemical modification or doping to adjust the reactivity of halogen radicals, thereby reducing their adverse impact on the electrochemical properties of batteries.

4. Conclusions and Outlook

ECFPs have emerged as a promising class of materials for advanced energy storage applications, combining electron transport capabilities, lithium storage reactivity, structural flexibility, and molecular design versatility. This review focuses on two major categories of ECFPs: conjugated polymers and free radical polymers.

For conjugated polymers, the molecular design and structural optimization of the π-conjugated skeleton can significantly enhance electron transport capacity and electrochemical performance. Specific strategies include main-chain extension, side-chain modification, orientation control, doping, and composite formation. Main-chain extension aims to reduce the π-π stacking distance and lower the energy band gap, which decreases the resistance to electron and hole mobility, thereby improving conductivity. Orientation control involves aligning polymer segments using external forces, promoting the orderly arrangement of molecular chains and enhancing charge carrier mobility. Side-chain engineering often incorporates functional groups, such as electron donors (D) and electron acceptors (A), to improve charge separation and transport characteristics. Additionally, doping with protonic acids, oxidants, ionic liquids, or carbon nanotubes can significantly enhance charge transport efficiency. Composite formation with materials such as graphene or carbon nanotubes is a widely accepted strategy to improve electrical conductivity, mechanical properties, and electrode stability. The applications of conjugated polymers in energy storage systems have garnered significant attention. For instance, PANI- and PPy-based materials demonstrate exceptional polysulfide capture ability and high-rate performance in lithium–sulfur batteries.

On the other hand, radical polymers achieve enhanced stability and electrochemical performance through rational molecular design. This includes the strategic incorporation of stable radical moieties (e.g., hydroxylamine radicals, enoxy radicals, and nitrogen–sulfur radicals), main/side-chain engineering to optimize radical density and electronic structure, and flexible chain integration (e.g., ether/oxetane segments in PTEO) for improved volume adaptability. By compositing with conductive materials such as reduced graphite oxide or multi-walled carbon nanotubes, free radical polymers can build conductive networks, significantly enhancing electron transport capacity. Additionally, the development of multifunctional binder systems, such as adhesive PNB derivatives, demonstrates dual benefits: enhanced interparticle adhesion in composite electrodes and improved mechanical strength and chemical stability.

In the future, the development of ECFPs will focus on three critical areas: synthetic innovation, multifunctional integration, and system optimization. Synthetic innovation will prioritize eco-friendly and scalable synthesis methodologies. For example, the development of water-based polymer systems or biocatalytic synthesis pathways for the preparation of PANI aims to replace traditional toxic solvents, such as NMP. Similarly, enzyme-catalyzed polymerization or photoinitiated polymerization for PPY preparation can reduce residues of oxidants like $FeCl_3$. Multifunctional integration will involve designing adaptive architectures for diverse energy storage platforms. PANI/PEDOT:PSS heterojunctions can be

developed by utilizing the pseudo-capacitance of PANI alongside the high conductivity of PEDOT:PSS. Furthermore, the synergy between redox activity and conductivity allows for the incorporation of nitroxide radicals onto the PPY backbone. The optimization of the system will focus on balancing energy density, rate capability, and cycling durability through hierarchical structural design, interface engineering, and the development of advanced binders. For instance, nanotube arrays combined with microporous carbon can optimize the ionic/electronic transport pathways of PANI. Gradient-doped multilayer films can effectively balance the surface conductivity of PEDOT:PSS with adhesion to underlying layers. Porous frameworks loaded with radical molecules can enhance the utilization of active sites in radical materials. Furthermore, temperature-sensitive or light-responsive adhesives based on PBI or PEDOT:PSS can enable the dynamic regulation of electrode structures. The continued evolution of ECFPs in molecular design, performance optimization, and sustainable manufacturing positions these materials as pivotal components in next-generation energy storage and conversion technology, offering wide-ranging prospects for their applications in energy storage and conversion devices.

Author Contributions: Z.H. and M.L.: writing—original draft, investigation, resources; J.C. and C.X.: resource collection; N.M.: conceptualization, review and editing. F.L.: writing—review and editing, funding acquisition, project administration, supervision. All authors have read and agreed to the published version of the manuscript.

Funding: This work was financially supported by the National Natural Science Foundation of China (No. 52172180).

Data Availability Statement: No new data were created or analyzed in this study.

Conflicts of Interest: The authors declare no conflicts of interest.

Abbreviations

The following abbreviations are used in this manuscript:

ECFPs	Electrically conductive functional polymers
PANI	Polyanilines
PEDOT	Poly(3,4-ethylenedioxythiophene)
PSS	Polystyrene sulfonic acid
PBI	Polybenzimidazole
PPy	Polypyrroles
PVA	Polyvinyl alcohol
PTH	Polythiophene
TA	Tannic acid
PEO	Polyethylene oxide
PEI	Polyethylene imine
COF	Covalent organic skeletons
TEMPO	2,2,6,6-tetramethylpiperidinyl-n-oxyl
PTEO	Poly (tempo-ether-oxetane)
AQ	Anthraquinone
PNB	Polynorbornene
PROXYL	2,2,5,5-tetramethyl-1-pyrrolidinyl-N-oxyl
PPD	polyaniline diamine
MEH-PPV	Poly[(2-ethylhexyl) phenylene vinylene)]
PBTTT	Poly[2,5-bis(3-hexylthiophene-2-yl) thiophene]
PTAA	Poly(triaryl amine)
BBL	Poly(benzimidazobenzophenanthroline)

References

1. Shirakawa, H.; Louis, E.J.; MacDiarmid, A.G.; Chiang, C.K.; Heeger, A.J. Synthesis of electrically conducting organic polymers: Halogen derivatives of polyacetylene, (CH)x.J. *Chem. Soc. Chem. Commun.* **1977**, *16*, 578–580. [CrossRef]
2. Kim, J.; Lee, J.; You, J.; Park, M.-S.; Al Hossain, S.M.; Yamauchi, Y.; Kim, J.H. Conductive polymers for next-generation energy storage systems: Recent progress and new functions. *Mater. Horiz.* **2016**, *3*, 517–535. [CrossRef]
3. Otero, T.F. Biomimetic conducting polymers: Synthesis, materials, properties, functions, and devices. *Polym. Rev.* **2013**, *53*, 311–351. [CrossRef]
4. Deng, H.; Lin, L.; Ji, M.; Zhang, S.; Yang, M.; Fu, Q. Progress on the morphological control of conductive network in conductive polymer composites and the use as electroactive multifunctional materials. *Prog. Polym. Sci.* **2014**, *39*, 627–655. [CrossRef]
5. Huang, H.; Cong, H.T.; Lin, Z.; Liao, L.; Shuai, C.X.; Qu, N.; Luo, Y.; Guo, S.; Xu, Q.C.; Bai, H.; et al. Manipulation of conducting polymer hydrogels with different shapes and related multifunctionality. *Small* **2024**, *20*, e2309575. [CrossRef]
6. Unnikrishnan, V.; Zabihi, O.; Ahmadi, M.; Li, Q.; Blanchard, P.; Kiziltas, A.; Naebe, M. Metal–organic framework structure–property relationships for high-performance multifunctional polymer nanocomposite applications. *J. Mater. Chem. A* **2021**, *9*, 4348–4378. [CrossRef]
7. Zhuang, X.; Wang, F.; Hu, X. Biodegradable polymers: A promising solution for green energy devices. *Eur. Polym. J.* **2024**, *204*, 112696. [CrossRef]
8. Numazawa, H.; Sato, K.; Imai, H.; Oaki, Y. Multistage redox reactions of conductive-polymer nanostructures with lithium ions: Potential for high-performance organic anodes. *NPG Asia Mater.* **2018**, *10*, 397–405. [CrossRef]
9. Xie, Y.; Zhang, K.; Yamauchi, Y.; Oyaizu, K.; Jia, Z. Nitroxide radical polymers for emerging plastic energy storage and organic electronics: Fundamentals, materials, and applications. *Mater. Horiz.* **2021**, *8*, 803–829. [CrossRef]
10. Majeed, A.H.; Mohammed, L.A.; Hammoodi, O.G.; Sehgal, S.; Alheety, M.A.; Saxena, K.K.; Dadoosh, S.A.; Mohammed, I.K.; Jasim, M.M.; Salmaan, N.U.; et al. A review on polyaniline: Synthesis, properties, nanocomposites, and electrochemical applications. *Int. J. Polym. Sci.* **2022**, *2022*, 9047554. [CrossRef]
11. McGraw, M.; Kolla, P.; Yao, B.; Cook, R.; Quiao, Q.; Wu, J.; Smirnova, A. One-step solid-state in-situ thermal polymerization of silicon-PEDOT nanocomposites for the application in lithium-ion battery anodes. *Polymers* **2016**, *99*, 488–495. [CrossRef]
12. Choudhary, R.B.; Ansari, S.; Purty, B. Robust electrochemical performance of polypyrrole (PPy) and polyindole (PIn) based hybrid electrode materials for supercapacitor application: A review. *J. Energy Storage* **2020**, *29*, 101302. [CrossRef]
13. Charkhesht, V.; Yürüm, A.; Alkan Gürsel, S.; Yarar Kaplan, B. Titania-based freestanding electronically conductive electrospun anodes with enhanced performance for Li-Ion batteries. *ACS Appl. Energy Mater.* **2021**, *4*, 13922–13931. [CrossRef]
14. Chen, R.; Li, Q.; Yu, X.; Chen, L.; Li, H. Approaching practically accessible solid-state batteries: Stability issues related to solid electrolytes and interfaces. *Chem. Rev.* **2019**, *120*, 6820–6877. [CrossRef]
15. Nasreldin, M.; Delattre, R.; Calmes, C.; Ramuz, M.; Sugiawati, V.A.; Maria, S.; Tocnaye, J.-L.d.B.d.l.; Djenizian, T. High performance stretchable Li-ion microbattery. *Energy Storage. Mater.* **2020**, *33*, 108–115. [CrossRef]
16. Wang, Z.; Pan, R.; Xu, C.; Ruan, C.; Edström, K.; Strømme, M.; Nyholm, L. Conducting polymer paper-derived separators for lithium metal batteries. *Energy Storage. Mater.* **2018**, *13*, 283–292. [CrossRef]
17. Guo, X.; Facchetti, A. The journey of conducting polymers from discovery to application. *Nat. Mater.* **2020**, *19*, 922–928. [CrossRef]
18. Gao, H.; Xue, L.; Xin, S.; Goodenough, J.B. A high-energy-density potassium battery with a polymer-gel electrolyte and a polyaniline cathode. *Angew. Chem. Int. Ed.* **2018**, *57*, 5449–5453. [CrossRef]
19. Zhang, Y.; Gou, B.; Li, Y.; Liao, Y.; Lu, J.; Wu, L.; Zhang, W.; Xu, H.; Huang, Y. Integration of gel polymer electrolytes with dry electrodes for quasi-solid-state batteries. *Chem. Eng. J.* **2024**, *498*, 155544. [CrossRef]
20. Baker, C.O.; Huang, X.; Nelson, W.; Kaner, R.B. Polyaniline nanofibers: Broadening applications for conducting polymers. *Chem. Soc. Rev.* **2017**, *46*, 1510–1525. [CrossRef]
21. Beygisangchin, M.; Abdul Rashid, S.; Shafie, S.; Sadrolhosseini, A.R.; Lim, H.N. Preparations, properties, and applications of polyaniline and polyaniline thin films—A review. *Polymers* **2021**, *13*, 2003. [CrossRef]
22. Joo, Y.; Agarkar, V.; Sung, S.H.; Savoie, B.M.; Bryan, W. Boudouris. A nonconjugated radical polymer glass with high electrical conductivity. *Science* **2018**, *359*, 1391–1395. [CrossRef]
23. Wingate, A.J.; Boudouris, B.W. Recent advances in the syntheses of radical-containing macromolecules. *J. Polym. Sci. Pol. Chem.* **2016**, *54*, 1875–1894. [CrossRef]
24. Rousseau, R.; Glezakou, V.-A.; Selloni, A. Theoretical insights into the surface physics and chemistry of redox-active oxides. *Nat. Rev. Mater.* **2020**, *5*, 460–475. [CrossRef]
25. Kim, J.; Kim, J.H.; Ariga, K. Redox-active polymers for energy storage nano architectonics. *Joule* **2017**, *1*, 739–768. [CrossRef]
26. Kaiser, J.M.; Long, B.K. Recent developments in redox-active olefin polymerization catalysts. *Coord. Chem. Rev.* **2018**, *372*, 141–152. [CrossRef]
27. Luppi, B.T.; Muralidharan, A.V.; Ostermann, N.; Cheong, I.T.; Ferguson, M.J.; Siewert, I.; Rivard, E. Redox-active heteroatom-functionalized polyacetylenes. *Angew. Chem. Int. Ed.* **2021**, *61*, e202114586. [CrossRef]

28. Lutkenhaus, J. A radical advance for conducting polymers. *Science* **2018**, *359*, 1334–1335. [CrossRef]
29. Tang, H.; Liang, Y.; Liu, C.; Hu, Z.; Deng, Y.; Guo, H.; Yu, Z.; Song, A.; Zhao, H.; Zhao, D.; et al. A solution-processed n-type conducting polymer with ultrahigh conductivity. *Nature* **2022**, *611*, 271–277. [CrossRef]
30. Shi, Y.; Peng, L.; Ding, Y.; Zhao, Y.; Yu, G. Nanostructured conductive polymers for advanced energy storage. *Chem. Soc. Rev.* **2015**, *44*, 6684–6696. [CrossRef]
31. Li, X.; Wang, Y.; Lv, L.; Zhu, G.; Qu, Q.; Zheng, H. Electroactive organics as promising anode materials for rechargeable lithium ion and sodium ion batteries. *Energy Mater.* **2022**, *2*, 200014. [CrossRef]
32. Xie, J.; Gu, P.; Zhang, Q. Nanostructured conjugated polymers: Toward high-performance organic electrodes for rechargeable batteries. *ACS Energy Lett.* **2017**, *2*, 1985–1996. [CrossRef]
33. Kashyap, Y.; Pandey, R.R.; Andola, A.; Nagaraju, D.H.; Pandey, R.K. Solid-state responses of electrochemically deposited polyaniline and polypyrrole-based symmetric supercapacitors in different pH conditions. *J. Solid-State Electrochem.* **2024**, *28*, 3357–3365. [CrossRef]
34. Liao, G.; Li, Q.; Xu, Z. The chemical modification of polyaniline with enhanced properties: A review. *Prog. Org. Coat.* **2019**, *126*, 35–43. [CrossRef]
35. Chen, X.; Zhao, C.; Yang, K.; Sun, S.; Bi, J.; Zhu, N.; Cai, Q.; Wang, J.; Yan, W. Conducting polymers meet lithium–sulfur batteries: Progress, challenges, and perspectives. *Energy Environ. Mater.* **2023**, *6*, e12483. [CrossRef]
36. Zhao, R.; Chang, Z.; Fu, X.; Xu, M.; Ai, X.; Qian, J. Revisit of polyaniline as a high-capacity organic cathode material for Li-ion batteries. *Polymers* **2024**, *16*, 1401. [CrossRef]
37. Guo, Z.; Wang, J.; Yu, P.; Li, M.; Huang, L.; Hu, Z.; Wang, Y.; Song, Z. Toward full utilization and stable cycling of polyaniline cathode for nonaqueous rechargeable batteries. *Adv. Energy Mater.* **2023**, *13*, 2301520. [CrossRef]
38. Zou, R.; Liu, W.; Ran, F. Selenium-doped cathode materials with polyaniline skeleton for lithium-organosulfur batteries. *J. Energy Chem.* **2023**, *79*, 148–157. [CrossRef]
39. Wang, Z.L.; Sun, K.; Henzie, J.; Hao, X.; Li, C.; Takei, T.; Kang, Y.M.; Yamauchi, Y. Spatially confined assembly of monodisperse ruthenium nanoclusters in a hierarchically ordered carbon electrode for efficient hydrogen evolution. *Angew. Chem. Int. Ed.* **2018**, *57*, 5848–5852. [CrossRef]
40. Zhou, J.; Qian, T.; Xu, N.; Wang, M.; Ni, X.; Liu, X.; Shen, X.; Yan, C. Selenium-doped cathodes for lithium–organosulfur batteries with greatly improved volumetric capacity and coulombic efficiency. *Adv. Mater.* **2017**, *29*, 1701294. [CrossRef]
41. Chen, X.; Li, C.; Tang, Y.; Li, L.; Du, Y.; Li, L. Integrated optimization of cutting tool and cutting parameters in face milling for minimizing energy footprint and production time. *Energy* **2019**, *175*, 1021–1037. [CrossRef]
42. Fu, H.; Gao, B.; Qiao, Y.; Zhu, W.; Liu, Z.; Wei, G.; Feng, Z.; Kamali, A.R. Graphene nanonetwork embedded with polyaniline nanoparticles as anode of Li-ion battery. *Chem. Eng. J.* **2023**, *477*, 146936. [CrossRef]
43. Li, J.; Li, X.; Fan, X.; Tang, T.; Li, M.; Zeng, Y.; Wang, H.; Wen, J.; Xiao, J. Holey graphene anchoring of the monodispersed nano-sulfur with covalently-grafted polyaniline for lithium sulfur batteries. *Carbon* **2022**, *188*, 155–165. [CrossRef]
44. Zhang, J.; Yang, C.P.; Yin, Y.X.; Wan, L.J.; Guo, Y.G. Sulfur encapsulated in graphitic carbon nanocages for high-rate and long-cycle lithium–sulfur batteries. *Adv. Mater.* **2016**, *28*, 9539–9544. [CrossRef]
45. Xu, L.; Daphne Ma, X.Y.; Wang, W.; Liu, J.; Wang, Z.; Lu, X. Polymeric one-side conductive Janus separator with preferably oriented pores for enhancing lithium metal battery safety. *J. Mater. Chem. A* **2021**, *9*, 3409–3417. [CrossRef]
46. Chen, Q.; Wang, X.; Chen, F.; Zhang, N.; Ma, M. Extremely strong and tough polythiophene composite for flexible electronics. *Chem. Eng. J.* **2019**, *368*, 933–940. [CrossRef]
47. Gueye, M.N.; Carella, A.; Faure-Vincent, J.; Demadrille, R.; Simonato, J.-P. Progress in understanding structure and transport properties of PEDOT-based materials: A critical review. *Prog. Mater. Sci.* **2020**, *108*, 100616. [CrossRef]
48. Kayser, L.V.; Lipomi, D.J. Stretchable conductive polymers and composites based on PEDOT and PEDOT: PSS. *Adv. Mater.* **2019**, *31*, e1806133. [CrossRef]
49. Li, J.; Cao, J.; Lu, B.; Gu, G. 3D-printed PEDOT: PSS for soft robotics. *Nat. Rev. Mater.* **2023**, *8*, 604–622. [CrossRef]
50. Ouyang, J.; Xu, Q.; Chu, C.-W.; Yang, Y.; Li, G.; Shinar, J. On the mechanism of conductivity enhancement in poly(3,4-ethylenedioxythiophene): Poly (styrene sulfonate) film through solvent treatment. *Polymers* **2004**, *45*, 8443–8450. [CrossRef]
51. Park, S.; Lee, C.W.; Kim, J.-M. Highly conductive PEDOT: PSS patterns based on photo-crosslinkable and water-soluble diacetylene diol additives. *Org. Electron.* **2018**, *58*, 1–5. [CrossRef]
52. Adilbekova, B.; Scaccabarozzi, A.D.; Faber, H.; Nugraha, M.I.; Bruevich, V.; Kaltsas, D.; Naphade, D.R.; Wehbe, N.; Emwas, A.H.; Alshareef, H.N.; et al. Enhancing the Electrical Conductivity and Long-Term Stability of PEDOT: PSS Electrodes through Sequential Treatment with Nitric Acid and Cesium Chloride. *Adv. Mater.* **2024**, *36*, e2405094. [CrossRef]
53. Zhang, M.; Meng, Q.; Ahmad, A.; Mao, L.; Yan, W.; Wei, Z. Poly(3,4-ethylenedioxythiophene)-coated sulfur for flexible and binder-free cathodes of lithium–sulfur batteries. *J. Mater. Chem. A* **2017**, *5*, 17647–17652. [CrossRef]
54. Chen, B.; Xu, D.; Chai, S.; Chang, Z.; Pan, A. Enhanced silicon anodes with robust SEI formation enabled by functional conductive binder. *Adv. Funct. Mater.* **2024**, *34*, 2401794. [CrossRef]

55. Li, S.; Zhang, X.; Chen, B.; Shi, Z.; Wu, S.; Wang, C.; Tong, Q.; Zhu, M.; Weng, J. Improving $LiFePO_4$ cathode stability in lithium-ion batteries by hybridizing activated tannic with PEDOT: PSS binders. *Electrochim. Acta* **2024**, *483*, 144037. [CrossRef]
56. Sarang, K.T.; Li, X.; Miranda, A.; Terlier, T.; Oh, E.-S.; Verduzco, R.; Lutkenhaus, J.L. Tannic acid as a small-molecule binder for silicon anodes. *ACS Appl. Energy Mater.* **2020**, *3*, 6985–6994. [CrossRef]
57. Zeng, W.; Wang, L.; Peng, X.; Liu, T.; Jiang, Y.; Qin, F.; Hu, L.; Chu, P.K.; Huo, K.; Zhou, Y. Enhanced ion conductivity in conducting polymer binder for high-performance silicon anodes in advanced lithium-ion batteries. *Adv. Energy Mater.* **2018**, *8*, 1702314. [CrossRef]
58. Geng, W.; Hu, X.; Zhou, Q.; Zhang, Y.; He, B.; Liu, Z.; Xiao, K.; Cai, D.; Yang, S.; Nie, H.; et al. Rational design of trifunctional conductive binder for high-performance Si anodes in lithium-ion batteries. *J. Power. Sources* **2024**, *601*, 234285. [CrossRef]
59. Gao, C.; Cui, X.; Wang, C.; Wang, M.; Wu, S.; Quan, Y.; Wang, P.; Zhao, D.; Li, S. 3D-printed hierarchical porous and multidimensional conductive network based on conducting polymer/graphene oxide. *J. Mater.* **2024**, *10*, 234–244. [CrossRef]
60. Li, H.; Lian, F.; Meng, N.; Xiong, C.; Wu, N.; Xu, B.; Li, Y. Constructing electronic and ionic dual conductive polymeric interface in the cathode for high-energy-density solid-state batteries. *Adv. Funct. Mater.* **2020**, *31*, 2008487. [CrossRef]
61. Cao, J.; Wang, L.; Li, D.; Yuan, Z.; Xu, H.; Li, J.; Chen, R.; Shulga, V.; Shen, G.; Han, W. $Ti_3C_2T_x$ MXene conductive layers supported bio-derived $Fe_{x-1}Se_x$/MXene/carbonaceous nanoribbons for high-performance half/full sodium-ion and potassium-ion batteries. *Adv. Mater.* **2021**, *33*, e2101535. [CrossRef] [PubMed]
62. He, F.; Tang, C.; Liu, Y.; Li, H.; Du, A.; Zhang, H. Carbon-coated MoS_2 nanosheets@CNTs-Ti_3C_2 MXene quaternary composite with the superior rate performance for sodium-ion batteries. *J. Mater. Sci. Technol.* **2022**, *100*, 101–109. [CrossRef]
63. Chen, J.; Chen, H.; Chen, M.; Zhou, W.; Tian, Q.; Wong, C.-P. Nacre-inspired surface-engineered MXene/nanocellulose composite film for high-performance supercapacitors and zinc-ion capacitors. *Chem. Eng. J.* **2022**, *428*, 131380. [CrossRef]
64. Cong, S.; Wang, J.; Wang, Z.; Liu, X. Polybenzimidazole (PBI) and benzimidazole-linked polymer (BILP) membranes. *Green Che. Eng.* **2021**, *2*, 44–56. [CrossRef]
65. Cruz-Arzon, A.J.; Serrano-Garcia, W.; Pinto, N.J.; Gupta, N.; Johnson, A.T.C. Temperature dependent charge transport in electrostatically doped poly[benzimidazobenzophenanthroline] thin films. *J. Appl. Polym. Sci.* **2022**, *140*, e53470. [CrossRef]
66. Wang, M.; Wang, G.; Naisa, C.; Fu, Y.; Gali, S.M.; Paasch, S.; Wang, M.; Wittkaemper, H.; Papp, C.; Brunner, E.; et al. Poly(benzimidazobenzophenanthroline)-ladder-type two-dimensional conjugated covalent organic framework for fast proton storage. *Angew. Chem. Int. Ed.* **2023**, *62*, e202310937. [CrossRef]
67. Kandambeth, S.; Dey, K.; Banerjee, R. Covalent organic frameworks: Chemistry beyond the structure. *J. Am. Chem. Soc.* **2018**, *141*, 1807–1822. [CrossRef]
68. Roy, A.; Mondal, S.; Halder, A.; Banerjee, A.; Ghoshal, D.; Paul, A.; Malik, S. Benzimidazole linked arylimide based covalent organic framework as gas adsorbing and electrode materials for supercapacitor application. *Eur. Polym. J.* **2017**, *93*, 448–457. [CrossRef]
69. Deng, Y.; Hussain, A.; Raza, W.; Cai, X.; Liu, D.; Shen, J. Review on current development of polybenzimidazole membrane for lithium battery. *J. Energy Chem.* **2024**, *91*, 579–608. [CrossRef]
70. Jalees, S.; Hussain, A.; Iqbal, R.; Raza, W.; Ahmad, A.; Saleem, A.; Majeed, M.K.; Faheem, M.; Ahmad, N.; Rehman, L.N.U.; et al. Functional PBI membrane based on polyimide covalent organic framework for durable lithium metal battery. *J. Energy Storage* **2024**, *101*, 113985. [CrossRef]
71. Liu, X.; Cheng, M.; Zhao, Y.; Qiu, Y. Theoretical Studies on the Chemical Degradation and Proton Dissociation Property of PBI used in High-Temperature Polymer Electrolyte Membrane Fuel Cells. *J. Phys. Chem. B* **2024**, *128*, 6167–6177. [CrossRef] [PubMed]
72. Ren, S.; Meng, L.; Ma, C.; Yu, Y.; Lou, Y.; Zhang, D.; Han, Y.; Shi, Z.; Feng, S. Synthesis of a microporous poly-benzimidazole as high-performance anode materials for lithium-ion batteries. *Chem. Eng. J.* **2021**, *405*, 126621. [CrossRef]
73. Nie, P.; Liu, X.; Fu, R.; Wu, Y.; Jiang, J.; Dou, H.; Zhang, X. Mesoporous silicon anodes by using polybenzimidazole derived pyrrolic N-enriched carbon toward high-energy Li-ion batteries. *ACS Energy Lett.* **2017**, *2*, 1279–1287. [CrossRef]
74. Balan, B.K.; Manissery, A.P.; Chaudhari, H.D.; Kharul, U.K.; Kurungot, S. Polybenzimidazole mediated n-doping along the inner and outer surfaces of a carbon nanofiber and its oxygen reduction properties. *J. Mater. Chem. C* **2012**, *22*, 23668–23679. [CrossRef]
75. Xiang, H.; Deng, N.; Zhao, H.; Wang, X.; Wei, L.; Wang, M.; Cheng, B.; Kang, W. A review on electronically conducting polymers for lithium-sulfur battery and lithium-selenium battery: Progress and prospects. *J. Energy Chem.* **2021**, *58*, 523–556. [CrossRef]
76. Xie, Y.; Zhao, H.; Cheng, H.; Hu, C.; Fang, W.; Fang, J.; Xu, J.; Chen, Z. Facile large-scale synthesis of core–shell structured sulfur@polypyrrole composite and its application in lithium–sulfur batteries with high energy density. *Appl. Energy* **2016**, *175*, 522–528. [CrossRef]
77. Chi, M.; Shi, L.; Wang, Z.; Zhu, J.; Mao, X.; Zhao, Y.; Zhang, M.; Sun, L.; Yuan, S. Excellent rate capability and cycle life of Li metal batteries with ZrO_2/POSS multilayer-assembled PE separators. *Nano Energy* **2016**, *28*, 1–11. [CrossRef]
78. Zhang, D.; Huang, W.; Li, Z.; Li, Y.; Xiang, C.; Chen, M.; Wang, X.; Wang, X. Core–shell structure S@PPy/CB with high electroconductibility to effective confinement polysulfide shuttle effect for advanced lithium-sulfur batteries. *Energy Fuels* **2021**, *35*, 10181–10189. [CrossRef]

79. Jiang, H.; Liu, X.C.; Wu, Y.; Shu, Y.; Gong, X.; Ke, F.S.; Deng, H. Metal–Organic frameworks for high charge–discharge rates in lithium–sulfur batteries. *Angew. Chem. Int. Ed.* **2018**, *130*, 3980–3985. [CrossRef]
80. Yi, Y.; Hai, F.; Tian, X.; Wu, Z.; Zheng, S.; Guo, J.; Chen, W.; Hua, W.; Qu, L.; Li, M. A novel sulfurized polypyrrole composite for high-performance lithium-sulfur batteries based on solid-phase conversion. *Chem. Eng. J.* **2023**, *466*, 143303. [CrossRef]
81. Kang, B.-H.; Shin, S.; Nam, K.; Bae, J.; Oh, J.-M.; Koo, S.-M.; Sohn, H.; Park, S.-H.; Shin, W.H. Exfoliated $NbSe_2$ nanosheet@polypyrrole hybrid nanocomposites as a high-performance anode of lithium-ion batteries. *J. Mater. Chem. A* **2023**, *11*, 19083–19090. [CrossRef]
82. Xu, Z.; Zheng, E.; Xiao, Z.; Shao, H.; Liu, Y.; Wang, J. Photo-initiated in situ synthesis of polypyrrole Fe-coated porous silicon microspheres for high-performance lithium-ion battery anodes. *Chem. Eng. J.* **2023**, *459*, 141543. [CrossRef]
83. Xia, T.; Xu, C.; Dai, P.; Li, X.; Lin, R.; Tang, Y.; Zhou, Y.; Wu, P. Interpenetrating gels as conducting/adhering matrices enabling high-performance silicon anodes. *J. Mater. Chem. A* **2021**, *9*, 12003–12008. [CrossRef]
84. Lv, Y.; Shang, M.; Chen, X.; Nezhad, P.S.; Niu, J. Largely improved battery performance using a micro sized silicon skeleton caged by polypyrrole as anode. *ACS Nano* **2019**, *13*, 12032–12041. [CrossRef]
85. Mao, J.; Iocozzia, J.; Huang, J.; Meng, K.; Lai, Y.; Lin, Z. Graphene aerogels for efficient energy storage and conversion. *Energy Environ. Sci.* **2018**, *11*, 772–799. [CrossRef]
86. Wang, S.; Li, F.; Easley, A.D.; Lutkenhaus, J.L. Real-time insight into the doping mechanism of redox-active organic radical polymers. *Nat. Mater.* **2018**, *18*, 69–75. [CrossRef]
87. Xiong, Y.; Wang, Z.; Li, Y.; Chen, Y.; Dong, L. Conjugated nitroxide radical polymer with low temperature tolerance potential for high-performance organic polymer cathode. *J. Am. Chem. Soc.* **2024**, *146*, 22777–22786. [CrossRef]
88. Chen, Y.; Chen, L.; Jiang, L.; Zhu, X.; Li, F.; Liu, X.; Mai, K.; Zhang, Z.; Fan, X.; Lv, X. Multifunctional radical polymers-enabled rapid charge/discharge and high capacity for flexible self-standing $LiFePO_4$/PETM/SWNT hybrid electrodes. *Chem. Eng. J.* **2024**, *482*, 149008. [CrossRef]
89. Nakahara, K.; Iwasa, S.; Satoh, M.; Morioka, Y.; Iriyama, J.; Suguro, M.; Hasegawa, E. Rechargeable batteries with organic radical cathodes. *Chem. Phys. Lett.* **2002**, *359*, 351–354. [CrossRef]
90. Rostro, L.; Baradwaj, A.G.; Boudouris, B.W. Controlled radical polymerization and quantification of solid-state electrical conductivities of macromolecules bearing pendant stable radical groups. *ACS Appl. Mater. Interfaces* **2013**, *5*, 9896–9901. [CrossRef]
91. Lee, S.; Kwon, G.; Ku, K.; Yoon, K.; Jung, S.K.; Lim, H.D.; Kang, K. Recent progress in organic electrodes for Li and Na rechargeable batteries. *Adv. Mater.* **2018**, *30*, e1704682. [CrossRef] [PubMed]
92. Kim, J.; Kim, Y.; Yoo, J.; Kwon, G.; Ko, Y.; Kang, K. Organic batteries for a greener rechargeable world. *Nat. Rev. Mater.* **2022**, *8*, 54–70. [CrossRef]
93. Jiang, S.; Xie, Y.; Xie, Y.; Yu, L.-J.; Yan, X.; Zhao, F.-G.; Mudugamuwa, C.J.; Coote, M.L.; Jia, Z.; Zhang, K. Lewis Acid-Induced Reversible Disproportionation of TEMPO Enables Aqueous Aluminum Radical Batteries. *J. Am. Chem. Soc.* **2023**, *145*, 14519–14528. [CrossRef]
94. Chen, B.; Lu, Z.; Feng, S.; Zhou, Z.; Lu, C. Redox-active nitroxide radicals grafted onto MXene: Boosting energy storage via improved charge transfer and surface capacitance. *ACS Energy Lett.* **2023**, *8*, 1096–1106. [CrossRef]
95. Bugnon, L.; Morton, C.J.; Novak, P.; Vetter, J.; Nesvadba, P. Synthesis of poly(4-methacryloyloxy-TEMPO) via group-transfer polymerization and its evaluation in organic radical battery. *Chem. Mater.* **2007**, *19*, 2910–2914. [CrossRef]
96. Nakahara, K.; Iriyama, J.; Iwasa, S.; Suguro, M.; Satoh, M.; Cairns, E.J. High-rate capable organic radical cathodes for lithium rechargeable batteries. *J. Power Sources* **2007**, *165*, 870–873. [CrossRef]
97. Nakahara, K.; Iriyama, J.; Iwasa, S.; Suguro, M.; Satoh, M.; Cairns, E.J. Cell properties for modified PTMA cathodes of organic radical batteries. *J. Power Sources* **2007**, *165*, 398–402. [CrossRef]
98. Chen, H.; Wang, C.; Dai, Y.; Ge, J.; Lu, W.; Yang, J.; Chen, L. In-situ activated polycation as a multifunctional additive for Li-S batteries. *Nano Energy* **2016**, *26*, 43–49. [CrossRef]
99. Zhang, K.; Hu, Y.; Wang, L.; Monteiro, M.J.; Jia, Z. Pyrene-functionalized PTMA by NRC for Greater π–π stacking with rGO and enhanced electrochemical properties. *ACS Appl. Mater. Interfaces* **2017**, *9*, 34900–34908. [CrossRef]
100. Li, W.; Jiang, S.; Xie, Y.; Yan, X.; Zhao, F.; Pang, X.; Zhang, K.; Jia, Z. Anthraquinone-catalyzed TEMPO reduction to realize two-electron energy storage of poly (TEMPO-methacrylate). *ACS Energy Lett.* **2022**, *7*, 1481–1489. [CrossRef]
101. Jeong, D.; Kwon, D.S.; Kim, H.J.; Shim, J. Striking a balance: Exploring optimal functionalities and composition of highly adhesive and dispersing binders for high-nickel cathodes in lithium-ion batteries. *Adv. Energy Mater.* **2023**, *13*, 2302845. [CrossRef]
102. Deng, W.; Shi, W.; Liu, Q.; Jiang, J.; Wang, Q.; Guo, C. Conductive nonconjugated radical polymer as high-capacity organic cathode material for high-energy Li/Na ion batteries. *J. Power Sources* **2020**, *479*, 228796. [CrossRef]
103. Hatakeyama-Sato, K.; Matsumoto, S.; Takami, H.; Nagatsuka, T.; Oyaizu, K. A PROXYL-type norbornene polymer for high-voltage cathodes in lithium batteries. *Macromol. Rapid Commun.* **2021**, *42*, 2100374. [CrossRef]

104. Yoshida, L.; Hakari, T.; Matsui, Y.; Deguchi, M.; Yamamoto, H.; Inoue, M.; Ishikawa, M. Understanding the improved performances of Lithium–Sulfur batteries containing oxidized microporous carbon with an affinity-controlled interphase as a sulfur host. *J. Power Sources* **2024**, *624*, 235572. [CrossRef]
105. Jähnert, T.; Hager, M.D.; Schubert, U.S. Assorted phenoxyl-radical polymers and their application in lithium-organic batteries. macromol. *Rapid Commun.* **2016**, *37*, 725–730. [CrossRef]
106. Facchetti, A. π-conjugated polymers for organic electronics and photovoltaic cell applications. *Chem. Mater.* **2010**, *23*, 733–758. [CrossRef]
107. Heeger, A.J. Semiconducting and metallic polymers: The fourth generation of polymeric materials. *J. Phys. Chem. B* **2001**, *105*, 8475–8491. [CrossRef]
108. Suga, T.; Ohshiro, H.; Sugita, S.; Oyaizu, K.; Nishide, H. Emerging n-type redox-active radical polymer for a totally organic polymer-based Rechargeable Battery. *Adv. Mater.* **2009**, *21*, 1627–1630. [CrossRef]
109. Jahnert, T.; Hager, M.D.; Schubert, U.S. Application of phenolic radicals for antioxidants, as active materials in batteries, magnetic materials and ligands for metal-complexes. *J. Mater. Chem. A* **2014**, *2*, 15234–15251. [CrossRef]
110. Li, L.; Gong, H.X.; Chen, D.Y.; Lin, M.J. Stable bifunctional perylene imide radicals for high-performance organic–lithium redox-flow batteries. *Chem. Eur. J.* **2018**, *24*, 13188–13196. [CrossRef]
111. Gu, S.; Chen, J.; Hussain, I.; Wang, Z.; Chen, X.; Ahmad, M.; Feng, S.P.; Lu, Z.; Zhang, K. Modulation of radical intermediates in rechargeable organic batteries. *Adv. Mater.* **2023**, *36*, e2306491. [CrossRef] [PubMed]
112. Back, J.; Park, J.; Kim, Y.; Kang, H.; Kim, Y.; Park, M.J.; Kim, K.; Lee, E. Triazenyl radicals stabilized by n-heterocyclic carbenes. *J. Am. Chem. Soc.* **2017**, *139*, 15300–15303. [CrossRef] [PubMed]
113. Chen, Z.X.; Li, Y.; Huang, F. Persistent and stable organic radicals: Design, synthesis, and applications. *Chem* **2021**, *7*, 288–332. [CrossRef]
114. Bai, W.-L.; Zhang, Z.; Chen, X.; Wei, X.; Zhang, Q.; Xu, Z.-X.; Liu, Y.-S.; Chang, B.; Wang, K.-X.; Chen, J.-S. Boosting the electrochemical performance of Li–O_2 batteries with DPPH redox mediator and graphene-luteolin-protected lithium anode. *Energy Storage Mater.* **2020**, *31*, 373–381. [CrossRef]

polymers

MDPI

Article

Enhanced Piezoelectric Performance of Highly-Aligned ZnO Nanorods Embedded in P(VDF-TrFE) Nanofiber Membranes

Xingjia Li [1,†], Zhongbo Zhang [2,†], Jianjun Ye [1], Yuan Li [3], Qichao Li [3], Han Wang [2], Xiuli Zhang [1,*] and Yiping Guo [3,*]

[1] School of Mathematics, Physics and Statistics, Shanghai University of Engineering Science, Shanghai 201620, China; xjli@sues.edu.cn (X.L.); jjye@sues.edu.cn (J.Y.)
[2] School of Chemistry and Chemical Engineering, Shanghai University of Engineering Science, Shanghai 201620, China; zhangzhongbo@sues.edu.cn (Z.Z.); wanghan@sues.edu.cn (H.W.)
[3] State Key Laboratory of Metal Matrix Composites, School of Materials Science and Engineering, Shanghai Jiao Tong University, Shanghai 200240, China; yuan.li@sjtu.edu.cn (Y.L.); liqichao@sjtu.edu.cn (Q.L.)
* Correspondence: xlzhang@sues.edu.cn (X.Z.); ypguo@sjtu.edu.cn (Y.G.)
† These authors contributed equally to this work.

Abstract: Flexible and wearable electronics often rely on piezoelectric materials, and Poly(vinylidene fluoride-trifluoroethylene) (P(VDF-TrFE)) membranes are popular for this application. However, their electromechanical performance is limited due to a relatively low piezoelectric coefficient. To address this, this study investigates the incorporation of zinc oxide (ZnO) nanorods (NRs) into a P(VDF-TrFE) nanofiber membrane matrix. ZnO NRs were synthesized and doped into well-aligned P(VDF-TrFE) nanofibers using electrospinning with a high-speed rotating drum. The impact of ZnO NRs' mass fraction on the piezoelectric properties of the membranes was evaluated. Results show that a maximum piezoelectric coefficient (d_{33}) of −62.4 pC/N, 9.5 times higher than neat P(VDF-TrFE), was achieved. These enhanced membranes demonstrated excellent performance in finger-tapping and bending detection, making them promising for large-scale flexible sensor applications in wearable electronics. This approach offers a simple and effective route to improve the performance of piezoelectric materials in flexible devices.

Keywords: P(VDF-TrFE)/ZnO nanocomposite; P(VDF-TrFE) nanofibers; ZnO nanorods; piezoelectricity; flexible electromechanical sensors

1. Introduction

Rapid advancements in science and technology have increased the demand for portable and wearable electronic devices. These devices are used in diverse sectors, including healthcare [1], motion monitoring [2], environmental monitoring [3], and data transmission and processing [4]. Traditional battery-based power sources have several limitations. These include their large size, short lifespan, limited integration capabilities, environmental impact, and poor biocompatibility [5]. These challenges underscore the need for alternative, clean, and sustainable power solutions that are portable and flexible. Many wearable electronics have low energy consumption. As a result, harvesting energy from the environment—such as solar, thermal, and mechanical sources—presents a promising solution [6]. Among the various energy harvesting technologies developed, including photovoltaics [7], thermoelectrics [8], magnetoelectrics [9], piezoelectric nanogenerators (PENGs) [10], and frictional nanogenerators [11], PENGs stand out for their ability to provide flexible, lightweight, and sustainable power [12]. These advantages make PENGs

ideal for a wide range of applications, including electronic skin [13], healthcare [14], gesture recognition [15], and artificial synapses [16].

Piezoelectric materials are a class of materials capable of converting mechanical energy into electrical energy. These materials are broadly categorized into inorganic piezoelectric materials and piezoelectric polymers [17–21]. Inorganic piezoelectric materials typically exhibit higher electrical activity compared to polymers, offering greater sensitivity to external mechanical stimuli and the ability to generate higher power density [22,23]. However, their intrinsic brittleness and lack of flexibility limit their applicability, particularly in flexible electronic devices. In contrast, poly(vinylidene fluoride) (PVDF) and its copolymer, poly(vinylidene fluoride-trifluoroethylene) (P(VDF-TrFE)), have been widely employed in PENGs, especially when integrated into small-scale electronics. This is due to their flexibility, biocompatibility, chemical resistance, environmental friendliness, and ease of fabrication [24–28].

The piezoelectric performance of P(VDF-TrFE) is closely related to its crystalline structure, which varies based on the orientation of the fluorine atoms along the polymer backbone. The material can crystallize into different phases, such as the trans–gauche–trans–gauche (TGTG) configuration (α-phase) and the all-trans (TTTT) configuration (β-phase). Among these, the β-phase exhibits the highest piezoelectric performance and is the primary contributor to P(VDF-TrFE)'s piezoelectricity [29,30]. Compared to PVDF homopolymers, P(VDF-TrFE) copolymers have a stronger tendency to crystallize into the β-phase. This is attributed to the steric effects of the third fluorine atom in the TrFE monomer units. These effects inhibit the formation of the TGT conformation [31]. These unique structural properties make P(VDF-TrFE) a promising material for flexible piezoelectric applications.

To further improve the piezoelectric properties of P(VDF-TrFE) copolymers, a commonly employed strategy is the introduction of an additional phase, such as lead zirconate titanate (PZT) [32], barium titanate (BTO) [33], graphene, metal electrodes [34], or zinc oxide (ZnO) [34–36]. These additives can significantly enhance the electrical response of the polymer matrix [37]. Among these materials, ZnO is a notable lead-free piezoelectric material. It is known for its high thermal stability, favorable piezoelectric and dielectric properties, and environmental compatibility [38–41].

Electrospinning offers several distinct advantages over conventional methods for fabricating flexible sensor membranes, particularly in the context of nanomaterial-based sensors. One of the primary benefits is its ability to produce highly flexible membranes with fine, continuous nanofibers that are not achievable with traditional fabrication techniques. The nanoscale fibers produced via electrospinning exhibit excellent flexibility, allowing the sensor membranes to conform to complex surfaces, which is essential for wearable or flexible sensor applications.

Another key advantage of electrospinning is its ability to generate membranes with a high surface area-to-volume ratio. This large surface area enhances the sensor's sensitivity and responsiveness to target analytes, improving detection limits and allowing for more accurate measurements. This is particularly important for flexible sensors, where high sensitivity is required to detect small changes in the surrounding environment.

Moreover, electrospinning allows for precise control over the morphology of the fibers, including their diameter, alignment, and porosity. This level of control is crucial for optimizing the mechanical and electrical properties of the sensor membrane. The flexibility and tensile strength of electrospun fibers can be tailored to ensure that the membranes remain functional under various mechanical deformations, such as bending or stretching, which is often required in flexible electronics and wearable sensor applications.

Electrospinning also offers the capability to incorporate a wide variety of functional materials into the nanofibers, such as conductive polymers, metal nanoparticles, or

biomolecules. This versatility allows the creation of multifunctional sensor membranes with enhanced properties, such as increased electrical conductivity, catalytic activity, or specific interaction with analytes, which can further improve sensor performance in diverse sensing environments.

In this study, we employ a high-speed electrospinning technique to fabricate highly aligned P(VDF-TrFE) nanofibers doped with oriented ZnO NRs. Due to their high aspect ratio, the ZnO NRs align along the direction of the P(VDF-TrFE) nanofibers during the electrospinning process. This dual alignment of nanofibers and ZnO NRs enhances the piezoelectric properties of the resulting nanocomposite membranes, which is crucial for the advancement of efficient nanogenerators. Moreover, we investigate the expanded potential applications of these optimized materials in sensing technologies. Notably, the membranes exhibit the capability to detect finger bending and tapping, demonstrating their high sensitivity and versatility. These results lay a solid foundation for the development of advanced energy harvesting systems and flexible sensing devices, underscoring the potential of this approach for next-generation wearable and self-powered electronics.

2. Materials and Methods

2.1. Materials

The 70/30 P(VDF-TrFE) powders were obtained from Kunshan Hisense Electronics, Suzhou, China. Zinc acetate dihydrate [$Zn(CH_3COO)_2 \cdot 2H_2O$] was supplied by Shanghai Macklin Biochemical Co., Ltd., Shanghai, China. N,N-dimethylformamide (DMF), acetone, sodium hydroxide (NaOH), and ethanol were purchased from Shanghai Reagents Co., Ltd., Shanghai, China. All chemicals and materials were used as received without any further purification.

2.2. Methods

2.2.1. Synthesis of ZnO NRs

Zinc oxide nanorods (ZnO NRs) were synthesized using a hydrothermal method, as illustrated in Figure 1a. Initially, 0.88 g of $Zn(CH_3COO)_2 \cdot 2H_2O$ was dissolved in 40 mL of ethanol at a concentration of 0.1 mol/L. Separately, 3.2 g of NaOH was dissolved in 80 mL of ethanol at a concentration of 1 mol/L. Both solutions were stirred at room temperature for 2.5 h. Subsequently, the two solutions were mixed and stirred continuously for an additional 3 h. The resulting mixture was then transferred into a 250 mL Teflon-lined autoclave, which was tightly sealed and placed in an oven for hydrothermal treatment at 145 °C for 24 h. After the reaction, the autoclave was allowed to cool to room temperature naturally. The solution was then filtered and washed several times with deionized water and ethanol to remove impurities. Finally, the ZnO powder was obtained by drying the product in an oven at 75 °C for 12 h.

2.2.2. Fabrication of ZnO/P(VDF-TrFE) Nanocomposite Films

The ZnO/P(VDF-TrFE) film was fabricated using an electrospinning method, as illustrated in Figure 1b. First, an appropriate amount of ZnO NRs was dispersed in 10 mL of a mixed solvent of DMF and acetone (60:40 *w*/*w*). The suspension was stirred for 30 min and subsequently subjected to ultrasonic treatment for an additional 30 min. Following this, 1.6 g of P(VDF-TrFE) was added to the ZnO suspension, and the mixture was vigorously stirred at 40 °C for 24 h until a uniform and transparent solution was obtained.

For the electrospinning process, as shown in Figure 1b, the prepared solution was loaded into a 5 mL plastic syringe equipped with a 24 G needle. The electrospinning parameters were set as follows: the applied voltage was 20 kV, the distance between the needle tip and the collector was 20 cm, and the solution flow rate was 1.32 mL/h. A

rotating drum covered with aluminum foil was used as the collector, with a rotation speed of 1500 rpm to ensure fiber alignment. The temperature and relative humidity during electrospinning were maintained at 24 °C and 50%, respectively.

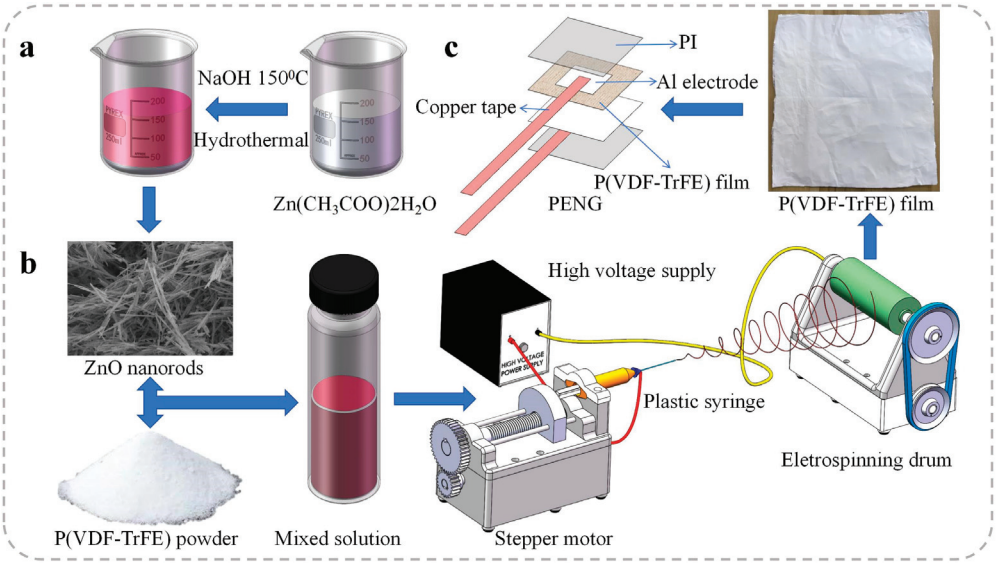

Figure 1. Schematic illustrations of the fabrication processes: (**a**) Synthesis of ZnO NRs using the hydrothermal method. (**b**) Fabrication of P(VDF-TrFE) fibers via the electrospinning method. (**c**) Assembly process of PENGs.

After electrospinning, the collected films were dried overnight at 70 °C to remove residual organic solvents. Finally, the dried membranes were annealed in a drying oven at 140 °C for 6 h and then cooled to room temperature to complete the fabrication process.

2.2.3. Fabrication of PENGs

A photograph and schematic diagram of a typical nanofiber membrane device are presented in Figure 1c. The complete device, with an effective electrode area of 4 cm^2, consists of the following layers arranged from top to bottom: a PI encapsulation layer, a top copper tape, an aluminum (Al) top electrode, the nanofiber membrane (the thickness of all the samples is 20 μm), an Al bottom electrode, a bottom copper tape, and a PI substrate.

2.2.4. Characterizations

The morphologies of the ZnO NRs and ZnO/P(VDF-TrFE) films were characterized using a scanning electron microscope (SEM, model S4700, Hitachi, Tokyo, Japan). The crystal structures were analyzed by X-ray diffraction (XRD, model D/max-2200/PC, Rigaku, Wako, Japan) diffractometer with Cu Kα radiation (λ = 0.154056 nm). XRD patterns were recorded in the 2θ range of 5° to 75° with a scanning rate of 3°/min at room temperature. Fourier transform infrared (FTIR) spectra were collected using a Microscopic Infrared Spectrometer (FTIR, model 760, Nicolet, Rhinelander, WI, USA) in the wavenumber range of 4000–500 cm^{-1}. The length and diameter distributions of the nanofibers were analyzed using the Nano-measurer (Nano Measurer 1.2.5) software.

In the piezoelectric performance testing, due to the inherent variability in sample preparation, we conducted multiple tests for each data point, using five identical samples per measurement. The best performance result from each group was recorded as the experimental outcome. The β-phase content was calculated using FTIR data from films of the same batch. The analysis followed a standard method, ensuring the accuracy and consistency of the results.

The electrical measurements, including the open-circuit voltage (V_{OC}) and short-circuit current (I_{SC}), were recorded using a precision source meter (2612B, Keithley, Cleveland, OH, USA). The vertical piezoelectric performance of the PENGs was evaluated using a custom-designed piezoelectric measurement system, as illustrated in Figure 2a. The piezoelectric signals generated by the nanofiber membrane were captured and recorded using an oscilloscope.

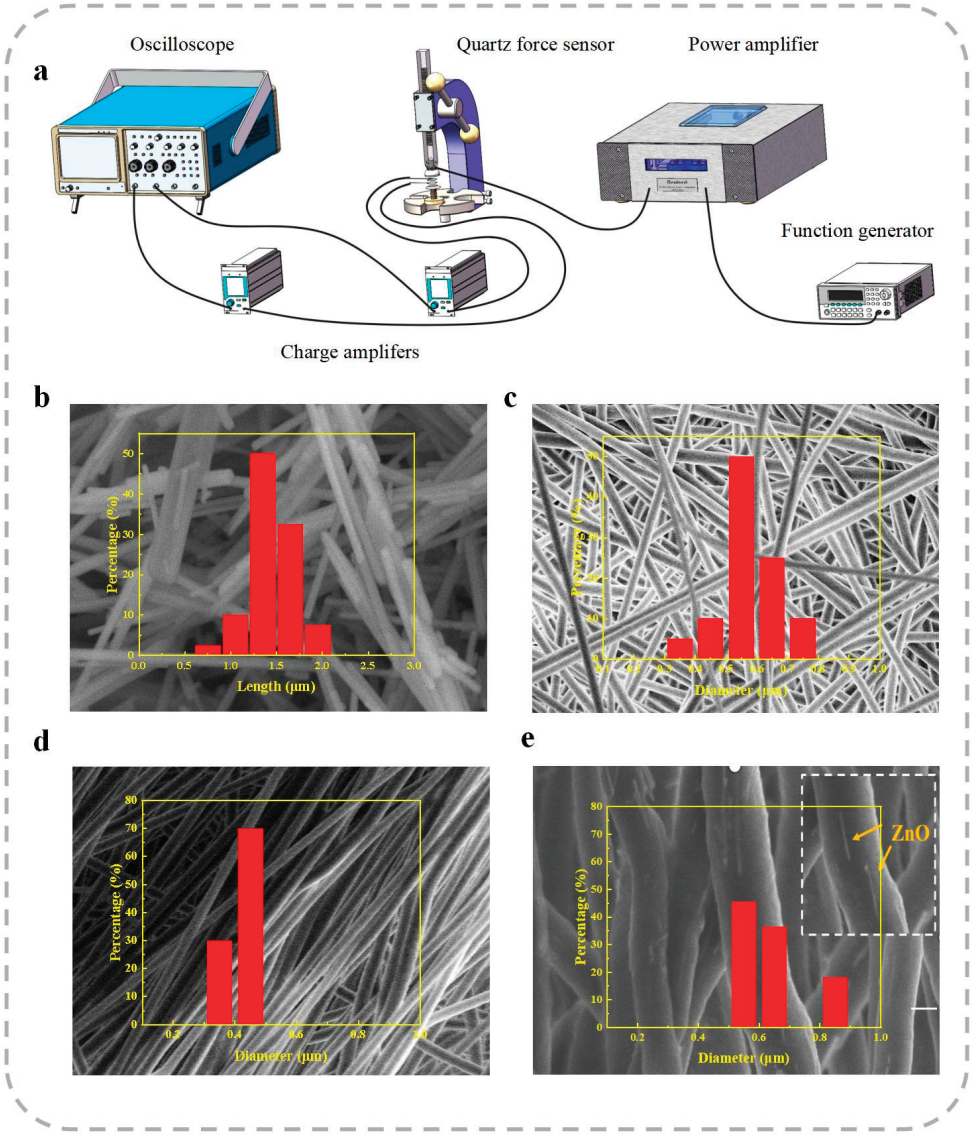

Figure 2. (**a**) Schematic diagram of the self-assembled vertical piezoelectric experimental setup. SEM images of (**b**) ZnO NRs, (**c**) neat P(VDF-TrFE) nanofibers collected at a rotating speed of 300 rpm on the electrospinning drum, (**d**) neat P(VDF-TrFE) nanofibers collected at a rotating speed of 1500 rpm on the electrospinning drum, and (**e**) P(VDF-TrFE) nanofibers doped with ZnO NRs at a mass fraction of 9 wt%, collected at a rotating speed of 1500 rpm on the electrospinning drum.

3. Results

3.1. Microstructures of ZnO NRs

The incorporation of ZnO, in various morphologies, into piezoelectric polymers has shown promise in fabricating biocompatible, high-performance piezoelectric nanofiber membranes. ZnO NRs, in particular, offer notable advantages due to their high aspect ratio and piezoelectric characteristics. Unlike non-piezoelectric high-aspect-ratio fillers, ZnO NRs can synergistically enhance the piezoelectric performance of polymer matrices. Their

unique morphology allows for improved mechanical–electrical energy conversion, making them suitable for generating high-performance piezoelectric nanocomposites [42,43].

The morphologies of the ZnO NRs were analyzed using scanning electron microscopy (SEM), as shown in Figure 2b. The as-synthesized ZnO NRs exhibited a uniform morphology with a high aspect ratio. The average length of the ZnO NRs was approximately 1.4 μm, with an average diameter of around 47 nm. The X-ray diffraction (XRD) patterns of the ZnO NRs, presented in Figure 3a, display distinct diffraction peaks corresponding to the hexagonal wurtzite structure of ZnO, which are consistent with the standard data from JCPDS Card No. 75-0576.

3.2. Aligned Neat P(VDF-TrFE) Fibers

Electrospinning is a versatile and widely used template-free technique for fabricating piezoelectric polymer fibers. This method enables the production of large-scale, self-polarized piezoelectric polymer nanofiber membranes by applying a high voltage to drive a jet of charged polymer droplets through a metal nozzle. During the fabrication process, polymer nanofibers are formed through mechanical stretching as the charged droplets travel toward a rotating collector. However, this liquid-to-solid transition process often results in randomly distributed fibers, which exhibit suboptimal electrical properties and limited sensitivity to mechanical stimuli. The alignment of electrospun fibers has been demonstrated to significantly enhance their piezoelectric performance. Aligned fibers can be fabricated through post-electrospinning mechanical stretching or by using a collector oriented parallel to the spinning axis during the electrospinning process [44–48]. While these methods improve the alignment of fibers and their piezoelectric properties to some extent, challenges remain in achieving high electrical responses from the resulting fiber membranes. Furthermore, there is a growing demand for the scalable fabrication of biocompatible, high-performance, and well-aligned nanofiber membranes to meet the requirements of advanced applications. Despite ongoing efforts, progress in this area has been limited, highlighting the need for improved strategies to enhance the performance and scalability of aligned piezoelectric nanofiber membranes.

Figure 2c,d depicts neat P(VDF-TrFE) nanofibers collected at rotating speeds of 300 and 1500 rpm on the electrospinning drum, respectively. It can be clearly observed that the nanofibers collected at a rotating speed of 1500 rpm exhibit an oriented arrangement. To further enhance the piezoelectric properties of the fiber films, varying contents of ZnO nanorods (NRs) were used for doping. The doped P(VDF-TrFE) nanofibers were collected at a rotating speed of 1500 rpm on the electrospinning drum. Figure 2e shows a closer examination of the SEM images and reveals that the nanofibers in the region are well-formed, with ZnO NRs aligning along the in-plane direction within the P(VDF-TrFE) polymer matrix, showing good dispersion.

3.3. Doped ZnO/P(VDF-TrFE) Fibers

The morphologies of the electrospun ZnO/P(VDF-TrFE) fibers are shown in Figure 2e. It is evident that the ZnO NRs are well-aligned along the axis of the P(VDF-TrFE) fibers and are evenly dispersed within the polymer matrix. Moreover, the interfaces between the ZnO NRs and the P(VDF-TrFE) fibers exhibit strong interfacial bonding, indicating efficient integration of the nanorods into the polymer fibers.

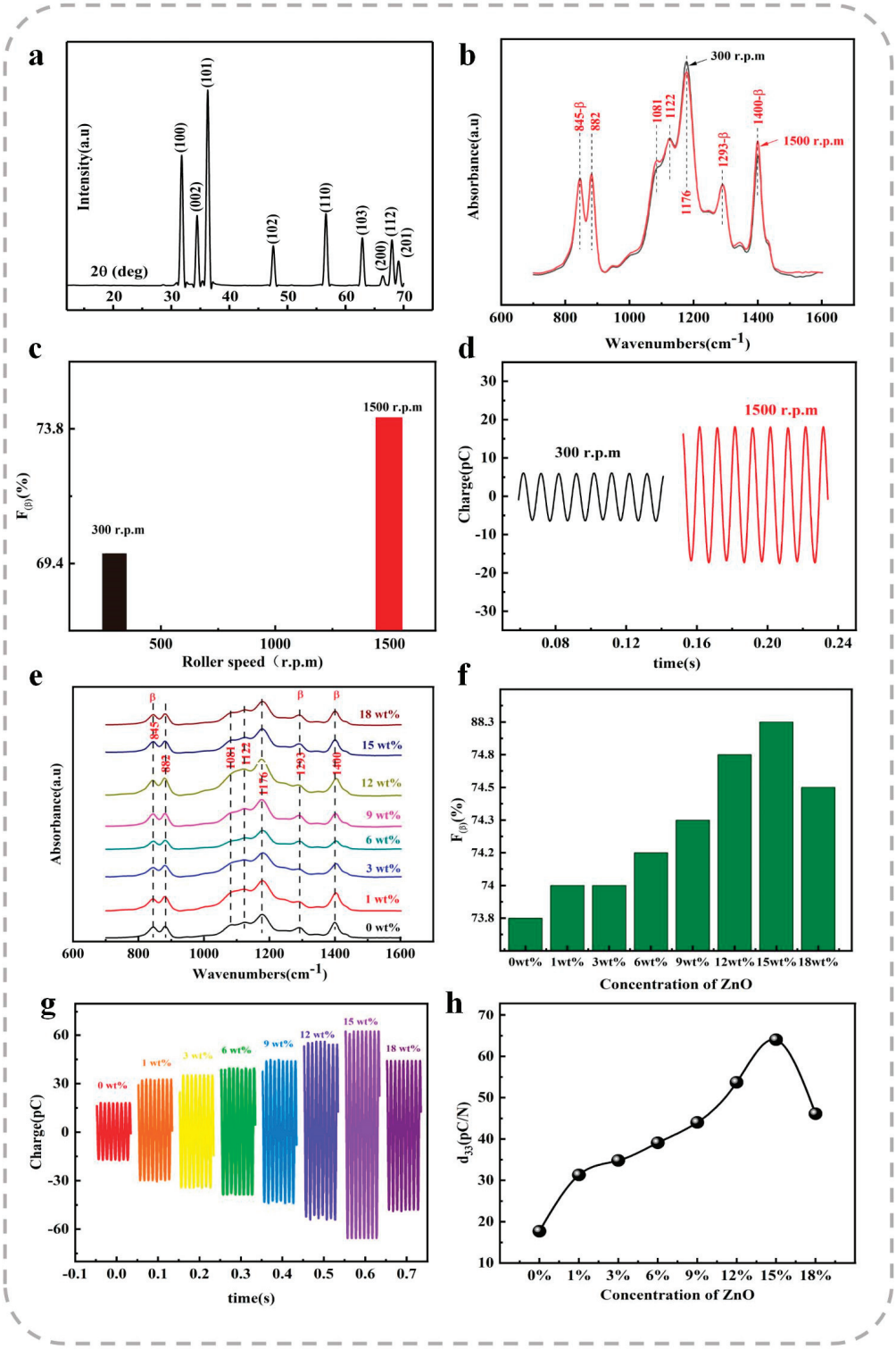

Figure 3. (**a**) XRD patterns of the ZnO NRs. (**b**) FTIR spectra of P(VDF-TrFE) fibers collected at rotating speeds of 300 and 1500 rpm on the electrospinning drum. (**c**) Corresponding β-phase content of P(VDF-TrFE) fibers. (**d**) Induced charges of neat P(VDF-TrFE) films collected at rotating speeds of 300 and 1500 rpm on the electrospinning drum. (**e**) FTIR spectra of P(VDF-TrFE)/ZnO fiber composites with varying doping contents of ZnO NRs. (**f**) Corresponding β-phase content of P(VDF-TrFE)/ZnO fiber composites. (**g**) Induced charges of P(VDF-TrFE) composites with different doping contents of ZnO NRs. (**h**) d_{33} values of P(VDF-TrFE) composite films with varying doping contents of ZnO NRs.

Upon doping P(VDF-TrFE) nanofibers with ZnO NRs, an increase in the fiber diameter was observed. Specifically, the average diameter of the fibers increased from approximately 450 nm for neat fibers to about 600 nm for ZnO doped fibers. This increase in diameter is attributed to the high aspect ratio of the ZnO NRs. During the electrospinning process, the ZnO NRs are aligned along the direction of the P(VDF-TrFE) fibers, which disrupts the typical fiber formation mechanism. The presence of these elongated nanorods facilitates the formation of thicker fibers as the nanorods act as a structural support, preventing the fibers from shrinking to their original dimensions. This interaction between the ZnO NRs and the polymer matrix effectively alters the electrospinning dynamics, leading to an increase in the fiber diameter. Additionally, the incorporation of ZnO NRs into the fiber matrix also influences the overall material structure, contributing to changes in fiber morphology and porosity.

Our findings reveal that increasing the rotational speed of the electrospinning drum to 1500 rpm effectively promotes the overall alignment of the nanofibers [49]. Simultaneously, the incorporated ZnO NRs become oriented along the axis of the nanofibers during the fabrication process. This dual orientation—of both the nanofibers and the ZnO NRs—significantly enhances the piezoelectric performance in both the perpendicular and transverse directions.

4. Discussion

4.1. Microstructure and Crystallization Behavior of ZnO/P(VDF-TrFE) Nanocomposites

To further examine the effects of the electrospinning drum's rotating speed and the doping of ZnO nanorods (NRs) on the crystalline structure of P(VDF-TrFE) nanofibers, Fourier transform infrared spectroscopy (FTIR) analysis was performed on both neat P(VDF-TrFE) fibers and ZnO NRs-doped P(VDF-TrFE) fibers. For the neat P(VDF-TrFE) fibers collected at different rotating speeds of the electrospinning drum, multiple characteristic peaks were observed, as shown in Figure 3a. The infrared spectra revealed vibrational bands in the frequency range of 700–1600 cm^{-1}. Three characteristic peaks corresponding to the β-crystalline phase were identified at 845 cm^{-1}, 1293 cm^{-1}, and 1400 cm^{-1}. Specifically, the absorption peaks at 845 cm^{-1} and 1293 cm^{-1} were attributed to the symmetric stretching vibrations of -CF_2 and C–C, respectively, while the peak at 1400 cm^{-1} was associated with -CH_2 oscillations and the antisymmetric stretching of C–C. Notably, no significant absorption peak corresponding to the α-crystalline phase was detected at 760 cm^{-1}, indicating that the electrospun fiber membrane predominantly consists of the β-crystalline phase.

When the rotating speed of the electrospinning drum was increased from 300 rpm to 1500 rpm, the collected nanofibers exhibited a transition from a random arrangement to an oriented alignment, as illustrated in Figure 2c,d. Additionally, the average diameter of the nanofibers decreased from 0.55 μm to 0.45 μm. This transition can be attributed to the enhanced mechanical stretching exerted by the higher rotating speed of the electrospinning drum. As shown in Figure 3b, the absorption peak at 1400 cm^{-1} became more prominent, while the peak at 1176 cm^{-1} was significantly diminished. These findings indicate a gradual transformation of the non-polar phase in P(VDF-TrFE) into the electroactive β-phase. The axial stretching of the fibers during the electrospinning process facilitates the alignment of polar molecules in the polymer chains at specific angles, thereby increasing polarization and enhancing the β-crystalline phase content.

To precisely evaluate the influence of the rotating speed of the electrospinning drum on the crystalline structure of P(VDF-TrFE), the content of the electroactive β-phase was calculated using the infrared spectral data and Equation (1):

$$F_\beta = \frac{A_\beta}{\left[\left(\frac{K_\beta}{K_\alpha}\right)A_\alpha + A_\beta\right]}, \quad (1)$$

where A_α and A_β represent the absorbance of the α-phase and β-phase at 766 cm^{-1} and 840 cm^{-1}, respectively, and K_α and K_β are the absorption coefficients of the α-phase and β-phase, with values of 6.1×10^4 and 7.7×10^4 cm^2/mol, respectively. As shown in Figure 3c, the β-phase content of the fibers collected at a rotating speed of 1500 rpm was 73.8%, compared to 69.4% for the fibers collected at 300 rpm. This result indicates that the oriented fiber films exhibit higher crystallinity than their disordered counterparts due to increased molecular alignment induced by the higher rotating speed of the drum.

The β-phase content was further calculated for P(VDF-TrFE) nanofibers doped with varying concentrations of ZnO NRs and collected using the high-speed electrospinning drum, as presented in Figure 3f. The results demonstrate that the incorporation of ZnO NRs significantly enhances the β-phase content of the P(VDF-TrFE) nanofibers. A maximum β-phase content of 88.3% was achieved at a doping concentration of 15 wt% ZnO NRs. The initial increase in β-phase content with increasing ZnO NR doping can be attributed to the stronger intermolecular interactions exerted by the ZnO NRs, which promote molecular alignment of the P(VDF-TrFE) polymer chains and improve crystallinity. However, when the ZnO NR doping concentration reached 18 wt%, a noticeable decline in β-phase content was observed. This reduction is likely due to the dominant positive piezoelectric effect of ZnO NRs, which counteracts part of the negative piezoelectric effect inherent to P(VDF-TrFE). This counteraction diminishes the overall piezoelectric performance of the composite film, thereby reducing crystallinity and electroactivity in the fiber membrane.

This observation highlights the critical importance of optimizing the ZnO NR doping concentration to achieve a balance between the alignment forces induced by ZnO NRs and the structural integrity of the polymer matrix. Such optimization is essential for maximizing the piezoelectric performance and preserving the crystalline properties of the composite nanofibers.

4.2. Electromechanical Conversion Performance of ZnO/P(VDF-TrFE) Nanocomposites

Piezoelectric materials, owing to their mechanical-to-electrical energy conversion characteristics, hold significant potential for applications in energy harvesting, pressure sensing, and bio-sensing. To effectively serve these purposes, it is essential for piezoelectric materials to exhibit excellent piezoelectric properties. In this study, PENGs were fabricated using a simple sandwich structure, as illustrated in Figure 1c, to facilitate the measurement of their piezoelectric performance.

The vertical piezoelectric characteristics were evaluated by applying mechanical excitation along the thickness direction of the film and recording the resulting electrical response along the same direction. Conversely, the transverse piezoelectric characteristics were assessed by applying mechanical stress along the surface direction of the film and measuring the corresponding electrical response along the film's thickness direction.

The excitation frequency of 100 Hz was chosen based on prior research which showed that a variation in frequency (between 100, 200, and 300 Hz) did not significantly affect the piezoelectric performance of the material. Therefore, 100 Hz was selected to ensure that the results were consistent and did not introduce unnecessary complexity. This frequency is likely optimal for capturing the material's response under typical conditions.

It is important to note that all measurements were conducted under relatively low applied strain levels, which were insufficient to induce any observable plastic deformation in the material. This ensured that the observed electrical responses were attributed solely to the piezoelectric behavior of the material, rather than any structural changes or damage. These results provide a clear understanding of the piezoelectric performance of the fabricated PENGs and their suitability for various applications requiring efficient mechanical-to-electrical energy conversion.

The 2 N amplitude was chosen as it provided the most stable output for the material's piezoelectric performance. In previous tests, it was observed that at this level of excitation force, the sample produced the most reliable and consistent piezoelectric output. The elastic modulus of the sample also played a role here, as the material's deformation behavior under this force led to the most stable measurements, making it an ideal choice for this experiment.

The vertical piezoelectric properties of the PENGs were evaluated using a custom-designed piezoelectric performance testing system. This system comprised a vibrator, a power amplifier, a function generator, a commercial quartz force sensor, and a charge amplifier, as illustrated in Figure 2a. Both the PENG and the quartz force sensor were placed on the vibrator. The vibrator was driven by a voltage signal generated by the function generator, which was pre-amplified using the power amplifier. By adjusting the amplitude, frequency, and waveform of the excitation voltage, mechanical forces with specific characteristics could be applied to the nanofiber membranes and the quartz sensor.

The induced charges generated in the P(VDF-TrFE) nanofiber membrane under a sinusoidal mechanical excitation frequency of 100 Hz and an amplitude of 2 N are presented in Figure 3d. For the aligned neat P(VDF-TrFE) fiber film collected at an electrospinning drum rotating speed of 1500 rpm, the induced charge was measured to be 35.4 pC, which is 187.8% higher than that of the randomly distributed fibers collected at a drum rotating speed of 300 rpm. This improvement can be attributed to the increased mechanical stretching forces exerted by the high-speed electrospinning drum, which enhance the alignment of the fibers. Additionally, the higher degree of alignment leads to improved crystallinity of the nanofiber films, thereby increasing their piezoelectric responses.

For composite films with different doping contents of ZnO NRs (0–18 wt%) collected at a drum rotating speed of 1500 rpm, the maximum induced charge was observed at a doping content of 15 wt%. At this doping level, the induced charge reached a peak value of 124.8 pC under a cyclic pressure of 2 N and a frequency of 100 Hz. Correspondingly, the d_{33} value was calculated to be -62.4 pC/N, which is 252.5% higher than that of PENGs fabricated from neat P(VDF-TrFE). This d_{33} value also exceeds the values reported in previous studies (d_{33}), ranging from -21.0 to -52.0 pC/N [50–54]. Figure 3g,h illustrates the induced charges and the d_{33} values of the composite films with varying ZnO NR doping contents, respectively.

The doping range of 0–18 wt% was selected based on observed trends in our experiments where increasing the doping concentration of ZnO NRs initially enhanced piezoelectric performance but after a certain threshold, the performance began to decline. At 0–18 wt%, both the transverse and longitudinal piezoelectric performance showed a clear increase and subsequent decrease, allowing for a full characterization of the doping effect. Beyond 18 wt%, the piezoelectric properties were found to worsen, hence the range was capped at 18 wt% for this study.

A comparison between Figures 3f and 3g reveals that the trend in β-phase content aligns closely with the trend in induced charges as the doping content of ZnO NRs varies. This suggests that the piezoelectric properties of the polymer in the vertical piezoelectric test are predominantly influenced by the β-phase content. The enhanced β-phase content in the composite films with optimized ZnO NR doping contributes significantly to their superior piezoelectric performance.

The transverse piezoelectric properties are particularly critical for PENGs in specific application scenarios, such as wearable sensors for human motion gesture recognition, arterial pulse monitoring, and eye fatigue detection. The experimental setup for transverse piezoelectric characterization is schematically illustrated in Figure 3a. In this system, the nanofiber membranes are fixed onto a linear motor, and the movement of the motor induces compression and stretching of the membranes. The resulting electrical responses

are recorded using a source meter. The strain applied to the membranes and the frequency (f) of the bending–releasing process are controlled by adjusting the final displacement (Δd) and the speed (v) of the motor's slider.

During the measurements, the bottom electrode of the nanofiber membrane is electrically grounded, and the nanofibers are bent upward to perform the transverse piezoelectric tests. Additionally, the test specimen was straightened before initiating the bending operation. The initial distance (d_0) between the slider and the fixed end of the setup is set to 35 mm.

The difference in optimal ZnO concentrations for the transverse and vertical piezoelectric responses is a complex phenomenon related to the anisotropic nature of the composite material. The alignment of the ZnO nanoparticles within the polymer matrix can vary depending on the direction of the applied stress. In the vertical configuration, where the stress is applied perpendicular to the film, the alignment of the particles may differ from that in the transverse configuration, where the stress is applied parallel to the surface. As a result, the ZnO nanoparticles may interact differently with the polymer matrix in these two orientations, leading to variations in the optimal concentration for each type of response. This behavior is influenced by both the mechanical properties of the matrix and the piezoelectric properties of the ZnO nanoparticles themselves.

The typical V_{OC} responses of all membranes under a slider speed of v = 9.5 mm/s and a displacement of d = 20 mm are shown in Figure 4b,d. A negative V_{OC} output is observed during the bending half-cycle, while a positive V_{OC} response is detected during the releasing half-cycle. These alternating outputs confirm the piezoelectric behavior of the membranes under transverse mechanical deformation. Furthermore, the I_{SC} outputs of the composite membranes are presented in Figure 4c,e. The consistent I_{SC} signals further demonstrate the effective transverse piezoelectric response of the membranes.

These results highlight the potential of the P(VDF-TrFE)-based nanofiber membranes, with or without ZnO NR doping, for applications requiring transverse piezoelectric energy conversion or sensing, particularly in wearable and flexible electronic devices.

As presented in Figure 4b,c, the transverse piezoelectric properties of the fiber films were investigated to further evaluate the effect of increasing the rotation speed of the electrospinning drum. The fiber films collected at a drum rotating speed of 1500 rpm demonstrated superior electrical output performance compared to those collected at lower speeds. Specifically, the V_{OC} and I_{SC} of the neat P(VDF-TrFE) fiber film collected at 1500 rpm reached 12.0 V and 16.7 nA, respectively. In contrast, the V_{OC} and I_{SC} of the P(VDF-TrFE) fiber film prepared at a lower drum rotating speed of 300 rpm were 8.8 V and 6.8 nA, respectively. These results indicate that the use of a high-speed electrospinning drum effectively enhances the transverse piezoelectric properties of the fiber films due to improved fiber alignment and crystallinity.

The transverse piezoelectric properties of composite fiber films doped with varying mass fractions of ZnO nanorods (NRs) and prepared at a drum rotating speed of 1500 rpm are shown in Figure 4d,e. As the ZnO NR doping content increased, the V_{OC} and I_{SC} of the composite films initially increased and subsequently decreased. The maximum V_{OC} and I_{SC} were observed at a ZnO NR doping content of 9 wt%, reaching 42.6 V and 138.8 nA, respectively. These values represent significant enhancements of 255.0% and 731.1%, respectively, compared to the neat P(VDF-TrFE) fiber film.

The enhanced performance observed at the optimal ZnO NR doping level can be attributed to the incorporation of ZnO NRs into the P(VDF-TrFE) matrix, which promotes an increase in the electroactive β-phase content and enhances the overall crystallinity of the fiber membrane. This improvement leads to a higher proportion of the effective piezoelectric β-phase, a critical factor in improving piezoelectric performance.

As ZnO NRs are introduced into the P(VDF-TrFE) matrix, they could influence the polymer's crystallization behavior by altering the local electrostatic fields or the molecular orientation of the polymer chains. This can be used to explain the initial increasing of the β-phase. In the case of PDMS-based composites, the reduction in piezoelectric response has indeed been linked to the hardening of the polymer matrix [55], which restricts the mobility of dipoles and limits the piezoelectric effect. In our study, while there is no β-phase in the ZnO itself, the interaction between the ZnO nanoparticles and the polymer may result in a similar phenomenon, specifically as the concentration of ZnO increases. This hardening effect could explain the reduction in β-phase at higher ZnO concentrations, similar to what is observed in PDMS-based composites, leading to its reduction at higher concentrations of ZnO NRs. Similarly, a decline in piezoelectric performance is observed at higher ZnO NR doping levels. This phenomenon can be explained by the positive piezoelectric effect of ZnO NRs, which counteracts the intrinsic negative piezoelectric effect of P(VDF-TrFE). This counteraction reduces the overall piezoelectric response of the composite film.

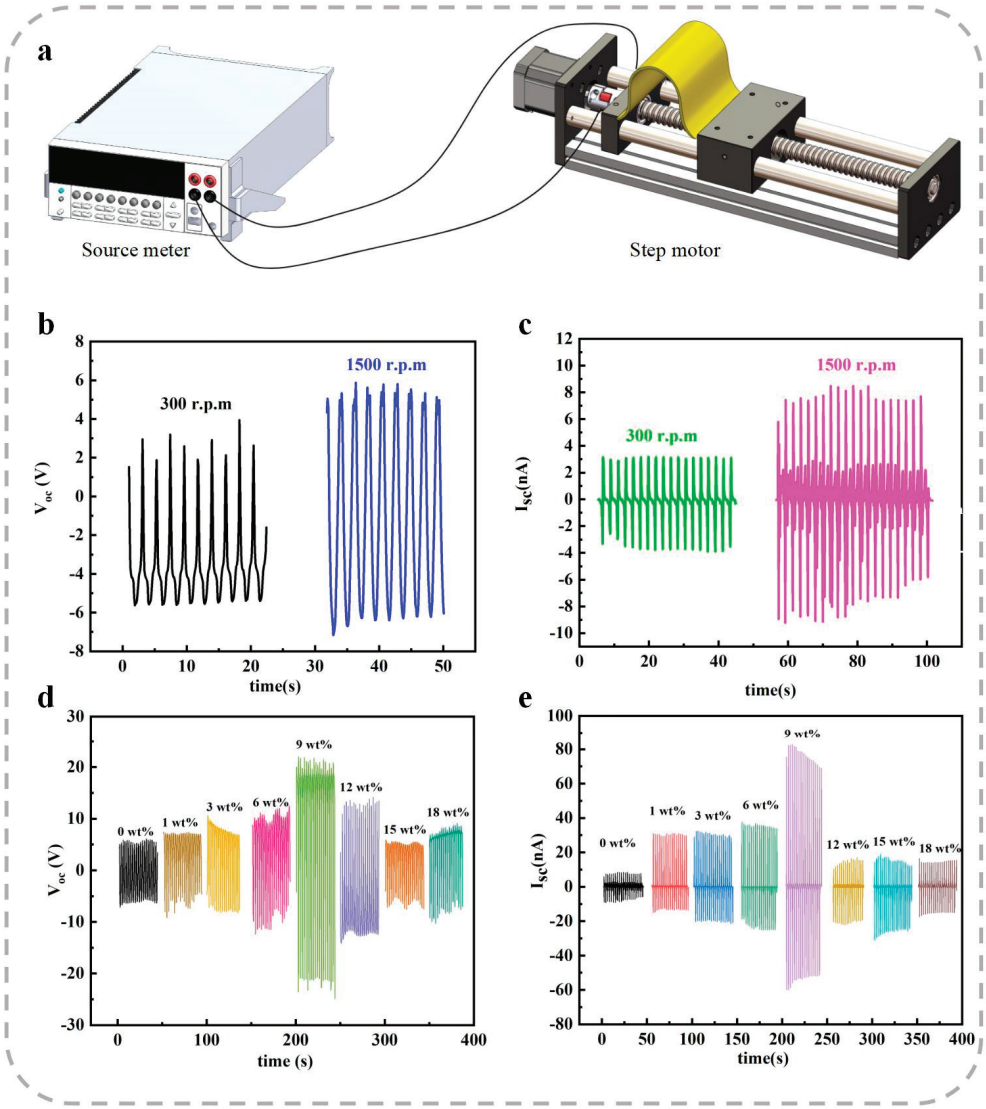

Figure 4. Measurement of transverse piezoelectric properties. (**a**) Schematic diagram of the measurement system. (**b**) V_{OC} and (**c**) I_{SC} of neat P(VDF-TrFE) fiber films collected at electrospinning drum rotating speeds of 300 rpm and 1500 rpm. (**d**) V_{OC} and (**e**) I_{SC} of P(VDF-TrFE) composite films with varying ZnO NR doping contents.

As a result, the piezoelectric performance of the composite fiber membranes decreases when the ZnO NR doping content exceeds the optimal level. These results highlight the necessity of optimizing ZnO NR doping content to achieve superior transverse piezoelectric properties in P(VDF-TrFE)-based fiber films. This optimization is essential for maximizing the piezoelectric output and ensuring the effective integration of ZnO NRs into the P(VDF-TrFE) matrix.

The piezoelectric nanofiber membrane capacitor was further optimized for mechanical energy harvesting applications. As illustrated in Figure 5a, the energy harvester was electrically connected in parallel with a variable resistor to evaluate the optimal external load and determine the maximum power density generated. A source meter was employed to measure the current drop across the variable resistor, which was induced by the movement of a linear motor.

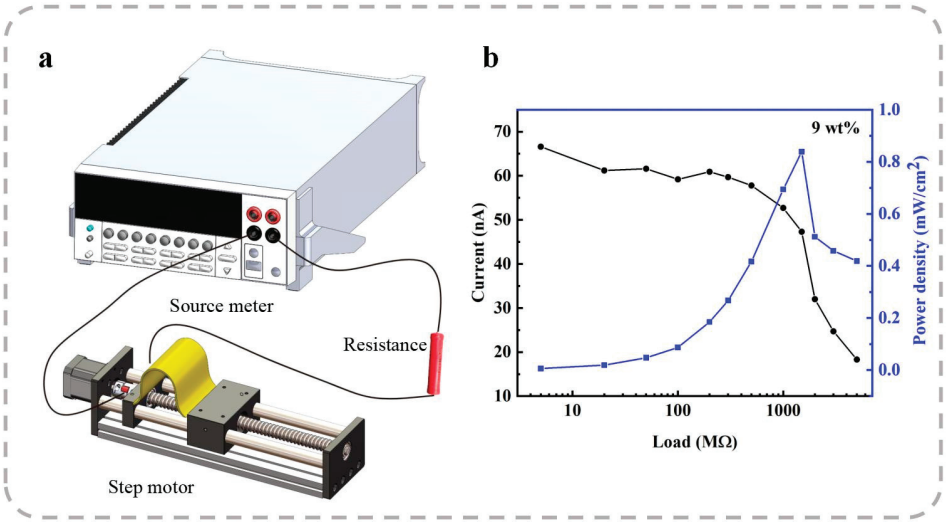

Figure 5. Mechanical energy harvesting from nanofiber membranes. (**a**) Schematic diagram of the measurement system used for mechanical energy harvesting. (**b**) Peak current outputs and the corresponding peak power density values as a function of the external resistance load.

Figure 6 presents the current responses of the 9 wt% ZnO-doped nanofiber membrane under different external resistance loads (R_{var}). The results indicate that the current response increases proportionally with the external resistance for the tested nanofiber membranes. To further analyze the output performance, the peak current outputs (I_{peak}) were extracted from Figure 6 and plotted as a function of the external resistance in Figure 5b. The corresponding peak electrical power density (P_{peak}) generated per unit area for each external resistance load was calculated using Equation (2):

$$P_{peak} = \frac{I_{peak}^2 R_{\mathrm{var}}}{A}, \tag{2}$$

where A represents the effective electrode area (4 cm^2). The peak power density (P_{peak}) for each nanogenerator initially increases as the external resistance (R_{var}) rises from 5 MΩ to 1.5 GΩ, and subsequently decreases beyond this value. As a result, an optimal external resistance of 1.5 GΩ yields a maximum P_{peak} value of 0.84 μW/cm^2 for the 9 wt% ZnO-doped P(VDF-TrFE) membranes. This achieved maximum power density is notably higher than the 0.53 μW/cm^2 reported for $BaSrTiO_3$-doped P(VDF-TrFE) membranes [56]. These findings highlight the enhanced energy harvesting performance of ZnO-doped P(VDF-TrFE) membranes over other doped systems, making them promising candidates for high-performance piezoelectric energy harvesters.

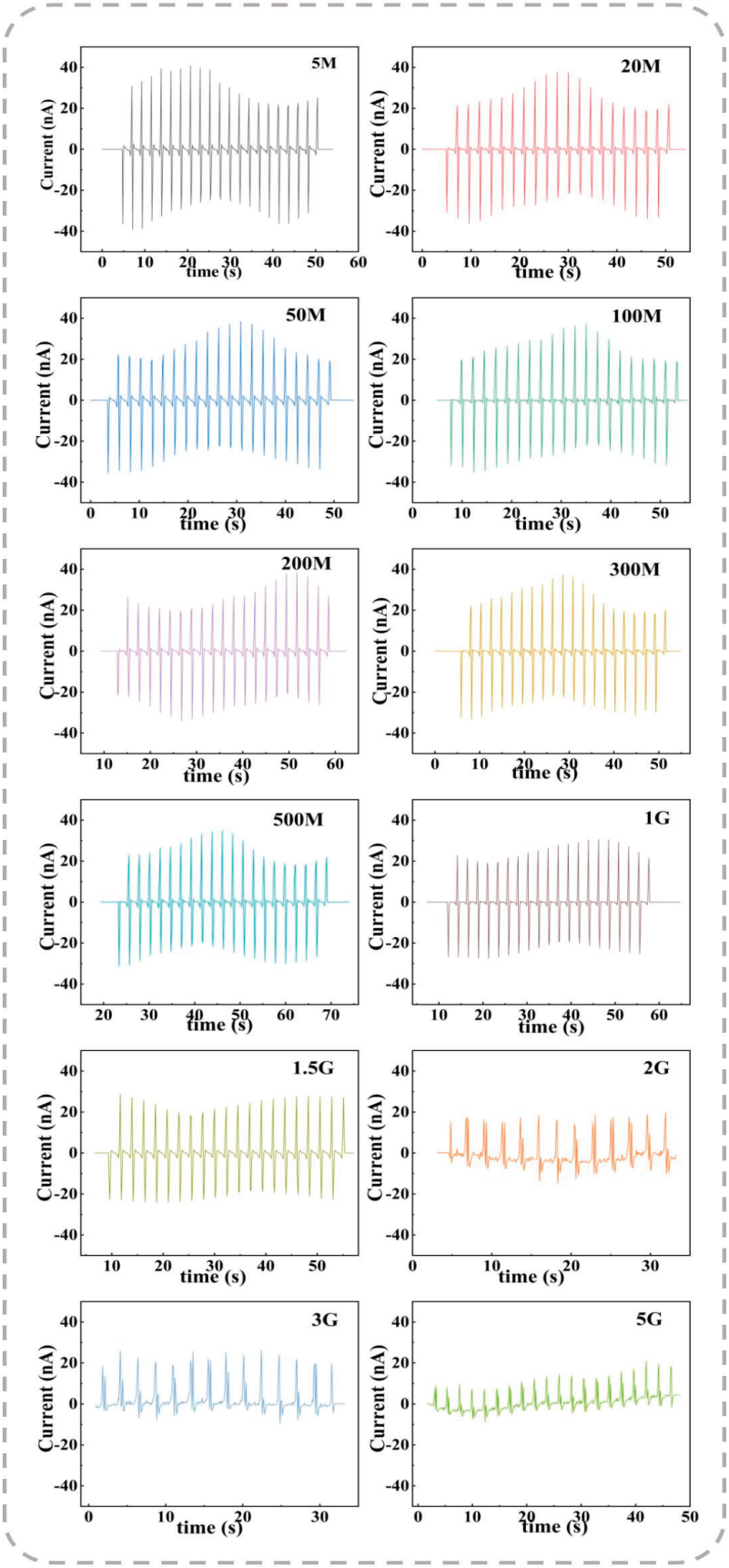

Figure 6. Current responses of 9 wt% ZnO-doped P(VDF-TrFE) membranes under repeated bending operations with varying external resistance loads.

Finally, to evaluate the potential application of the ZnO-doped nanofiber membrane as a wearable sensor, a series of tests involving finger tapping, bending, and releasing were conducted. As shown in Figure 7, the sensor exhibited distinct V_{OC} responses of approximately 20 V for finger tapping and 60 V for bending and releasing.

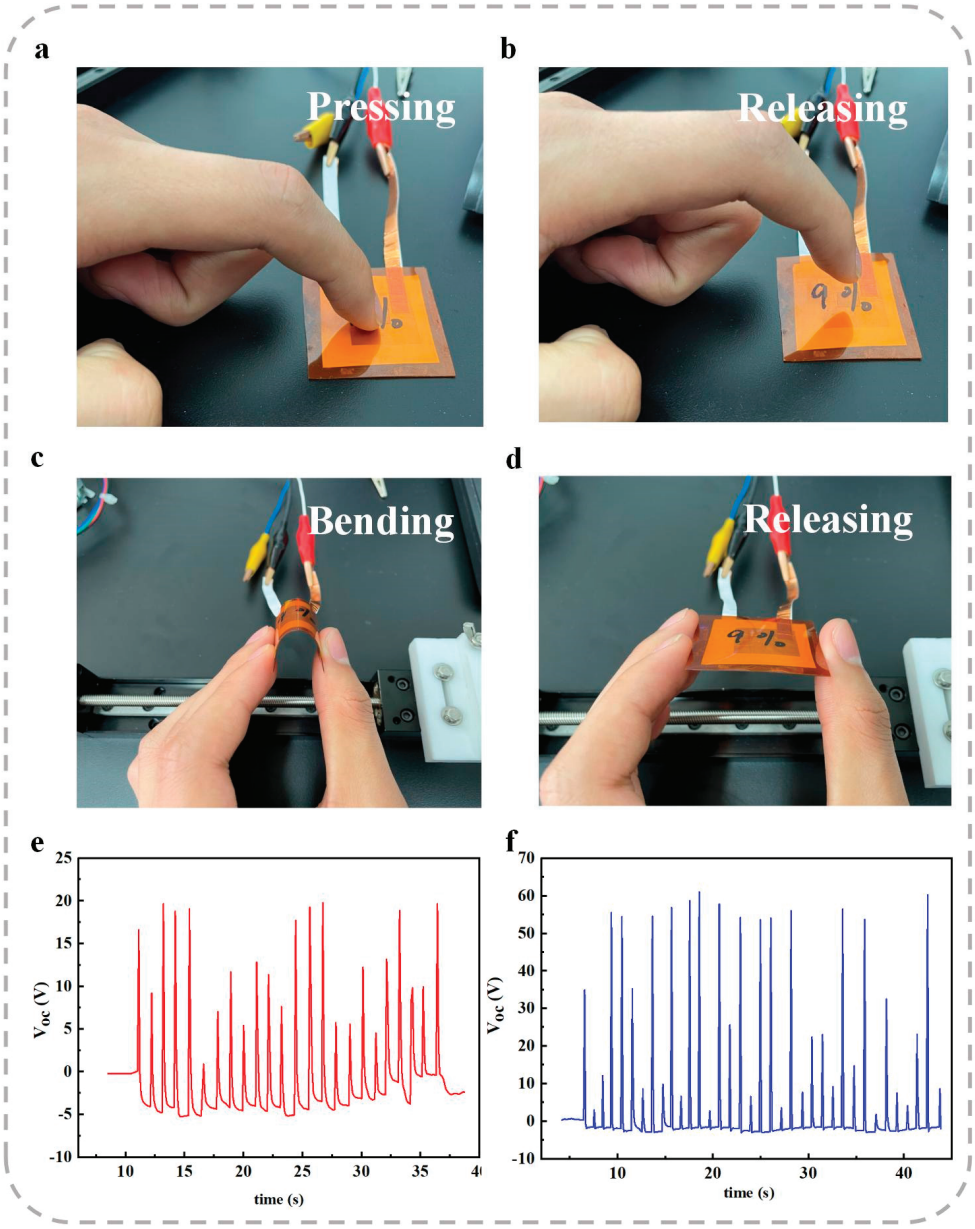

Figure 7. Application of the 9 wt% ZnO-doped nanofiber membrane as a wearable sensor for the detection of (**a**,**b**) finger tapping and (**c**,**d**) bending and releasing of the sensor. (**e**) V_{OC} response to finger tapping. (**f**) V_{OC} response to bending and releasing of the sensor.

These results demonstrate the significant sensitivity and responsiveness of the sensor, suggesting its strong potential for further development in various applications, particularly in the field of human physiological monitoring. This highlights the versatility and practicality of the ZnO-doped nanofiber membrane for wearable sensing technologies.

5. Conclusions

In this study, highly aligned P(VDF-TrFE) nanofiber membranes were successfully fabricated using the electrospinning technique. The incorporation of ZnO nanorods (NRs)

into the fiber membranes resulted in preferential alignment of the ZnO NRs along the fiber direction, enhancing the overall structural and piezoelectric properties of the membranes.

The alignment of the P(VDF-TrFE) nanofibers significantly improved their piezoelectric performance. The d_{33} of the aligned fibers increased by 187.8% compared to randomly oriented fibers. In transverse measurements, the V_{OC} and I_{SC} of the aligned membranes exhibited enhancements of 36.4% and 145.6%, respectively.

The addition of ZnO further augmented the piezoelectric properties. At a ZnO doping level of 15 wt%, the vertical d_{33} value increased by 252.5%, while the transverse V_{OC} and I_{SC} exhibited dramatic improvements of 255.0% and 731.1%, respectively, at a doping content of 9 wt%.

Moreover, the optimized nanofiber membranes demonstrated a peak power density of 0.84 $\mu W/cm^2$ at an optimal load resistance, confirming their potential for energy harvesting applications. Additionally, the ZnO-doped P(VDF-TrFE) nanofiber membranes were successfully applied as wearable sensors, effectively detecting finger tapping, bending, and releasing motions, with corresponding V_{OC} responses of approximately 20 V and 60 V.

These results highlight the significant enhancement of piezoelectric and power generation properties in ZnO-doped P(VDF-TrFE) nanofiber membranes. The findings validate the potential of these materials for advanced applications in wearable and flexible electronics, paving the way for future developments in this field.

There are several avenues for potential future work that could further enhance the practical applications of this technology:

Optimization of ZnO Doping Levels: While this study explored doping at various concentrations, further research could focus on fine-tuning the optimal doping levels for different applications, balancing performance with material stability over long-term use.

Scalability and Fabrication Methods: Scaling up the electrospinning process for large-area, high-throughput production while maintaining the alignment of nanofibers could be a critical next step. This would help in addressing the manufacturing challenges associated with deploying these materials in mass-market wearable and flexible devices.

Human-Body Interface and Health Monitoring: Further studies could focus on expanding the range of human physiological signals that can be captured by these sensors, such as muscle movement, heart rate, or even respiration patterns. Incorporating additional sensor modalities could lead to more comprehensive health monitoring solutions.

By pursuing these research directions, future work could lead to the refinement and broader adoption of ZnO-doped P(VDF-TrFE) nanofiber membranes in advanced wearable and flexible electronics, making them more efficient, versatile, and reliable for a range of applications in healthcare and energy harvesting.

Author Contributions: Conceptualization, X.L., Z.Z., H.W., X.Z. and Y.G.; methodology, X.L., Z.Z. and J.Y.; software, X.L.; validation, Z.Z., J.Y. and Y.L.; formal analysis, Z.Z., J.Y. and Q.L.; investigation, X.L., Y.L. and Q.L.; writing—original draft preparation, X.L. and Z.Z.; writing—review and editing, H.W., X.Z. and Y.G.; visualization, Y.L. and Q.L.; supervision, H.W., X.Z. and Y.G.; project administration, H.W., X.Z. and Y.G.; funding acquisition, X.L., X.Z. and Y.G. All authors have read and agreed to the published version of the manuscript.

Funding: This research was funded by the National Key Research and Development Program of China, grant numbers 2022YFA1205300 and No. 2022YFA1205304, And the National Natural Science Foundation of China, grant numbers 12304310 and 52272109.

Institutional Review Board Statement: Not applicable.

Data Availability Statement: All the data of this study are included in the manuscript.

Acknowledgments: The authors would like to express their gratitude to the School of Mathematics, Physics and Statistics, Shanghai University of Engineering Science, School of Chemistry and Chemical

Engineering, Shanghai University of Engineering Science, and the State Key Laboratory of Metal Matrix Composites, School of Materials Science and Engineering, Shanghai Jiao Tong University.

Conflicts of Interest: The authors declare no conflicts of interest.

Abbreviations

P(VDF-TrFE)	Poly(vinylidene fluoride-trifluoroethylene)
ZnO	Zinc oxide
NRs	Nanorods
LD	Linear dichroism
PENGs	Piezoelectric nanogenerators
PVDF	Poly(vinylidene fluoride)
TGTG	Trans–gauche–trans–gauche configuration
TTTT	All-trans configuration
PZT	Lead zirconate titanate
BTO	Barium titanate
$Zn(CH_3COO)_2{\cdot}2H_2O$	Zinc acetate dihydrate
DMF	N, N-dimethylformamide
NaOH	Sodium hydroxide
FTIR	Fourier transform infrared spectra
V_{OC}	Open-circuit voltage
I_{SC}	Short-circuit current
d_{33}	Vertical piezoelectric coefficient
I_{peak}	Peak current outputs
P_{peak}	Peak power density
R_{var}	External resistance

References

1. Cui, X.N.; Zhang, C.; Liu, W.H.; Zhang, Y.; Zhang, J.H.; Li, X.; Geng, L. Pulse sensor based on single-electrode triboelectric nanogenerator. *Sens. Actuators A Phys.* **2018**, *280*, 326–331. [CrossRef]
2. Li, N.; Yi, Z.Y.; Ma, Y.; Xie, F.; Huang, Y.; Tian, Y.W.; Dong, X.X.; Liu, Y.; Shao, X.; Li, Y.; et al. Direct Powering a Real Cardiac Pacemaker by Natural Energy of a Heartbeat. *ACS Nano* **2019**, *13*, 2822–2830. [CrossRef] [PubMed]
3. Fuh, Y.K.; Ye, J.C.; Chenc, P.C.; Huang, Z.M. A highly flexible and substrate-independent self-powered deformation sensor based on massively aligned piezoelectric nano-/microfibers. *J. Mater. Chem. A* **2014**, *2*, 16101–16161. [CrossRef]
4. Wu, H.; Huang, Y.A.; Xu, F.; Duan, Y.Q.; Yin, Z.P. Energy Harvesters for Wearable and Stretchable Electronics: From Flexibility to Stretchability. *Adv. Mater.* **2016**, *28*, 9881–9919. [CrossRef]
5. Wang, Z.L. Entropy theory of distributed energy for internet of things. *Nano Energy* **2019**, *58*, 669–672. [CrossRef]
6. Proto, A.; Penhaker, M.; Conforto, S.; Schmid, M. Nanogenerators for Human Body Energy Harvesting. *Trends Biotechnol.* **2017**, *35*, 610–624. [CrossRef]
7. Wang, R.; Mujahid, M.; Duan, Y.; Wang, Z.K.; Xue, J.J.; Yang, Y. A Review of Perovskites Solar Cell Stability. *Adv. Funct. Mater.* **2019**, *29*, 1808843. [CrossRef]
8. Haras, M.; Skotnicki, T. Thermoelectricity for IoT—A review. *Nano Energy* **2018**, *54*, 461–476. [CrossRef]
9. Khan, F.U.; Qadir, M.U. State-of-the-art in vibration-based electrostatic energy harvesting. *J. Micromech. Microeng.* **2016**, *26*, 103001. [CrossRef]
10. Zhu, G.; Peng, B.; Chen, J.; Jing, Q.S.; Wang, Z.L. Triboelectric nanogenerators as a new energy technology: From fundamentals, devices, to applications. *Nano Energy* **2015**, *14*, 126–138. [CrossRef]
11. Liu, H.C.; Zhong, J.W.; Lee, C.K.; Lee, S.W.; Lin, L.W. A comprehensive review on piezoelectric energy harvesting technology: Materials, mechanisms, and applications. *Appl. Phys. Rev.* **2018**, *5*, 041306. [CrossRef]
12. Lee, S.H.; Jeong, C.K.; Hwang, G.T.; Lee, K.J. Self-powered flexible inorganic electronic system. *Nano Energy* **2015**, *14*, 111–125. [CrossRef]
13. Lei, Y.Z.; Zhao, T.M.; He, H.X.; Zhong, T.Y.; Xue, X.Y. A self-powered electronic-skin for detecting CRP level in body fluid based on the piezoelectric-biosensing coupling effect of GaN nanowire. *Smart Mater. Struct.* **2019**, *28*, 105001. [CrossRef]
14. Deng, C.R.; Tang, W.; Liu, L.; Chen, B.D.; Li, M.C.; Wang, Z.L. Self -Powered Insole Plantar Pressure Mapping System. *Adv. Funct. Mater.* **2018**, *28*, 1801606. [CrossRef]

15. Chen, Q.; Cao, Y.Y.; Lu, Y.; Akram, W.; Ren, S.; Niu, L.; Sun, Z.; Fang, J. Hybrid Piezoelectric/Triboelectric Wearable Nanogenerator Based on Stretchable PVDF−PDMS Composite Films. *ACS Appl. Mater. Interfaces* **2024**, *16*, 6239–6249. [CrossRef]
16. Liu, Y.Q.; Zhong, J.F.; Li, E.L.; Yang, H.H.; Wang, X.M.; Lai, D.X.; Chen, H.P.; Guo, T.L. Self-powered artificial synapses actuated by triboelectric nanogenerator. *Nano Energy* **2019**, *60*, 377–384. [CrossRef]
17. Takahashi, H.; Numamoto, Y.; Tani, J.J.; Tsurekawa, S. Piezoelectric Properties of $BaTiO_3$ Ceramics with High Performance Fabricated by Microwave Sintering. *Jpn. J. Appl. Phys.* **2006**, *45*, 7405–7408. [CrossRef]
18. Chen, B.; Li, H.M.; Tian, W.; Zhou, C.G. PZT Based Piezoelectric Sensor for Structural Monitoring. *J. Electron. Mater.* **2019**, *48*, 2916–2923. [CrossRef]
19. Jiang, L.M.; Yang, Y.; Chen, Y.; Zhou, Q.F. Ultrasound-induced wireless energy harvesting: From materials strategies to functional applications. *Nano Energy* **2020**, *77*, 105131. [CrossRef]
20. Sabolsky, E.M.; James, A.R.; Kwon, S.; T-McKinstry, S.; Messing, G.L. Piezoelectric properties of <001> textured $Pb(Mg_{1/3}Nb_{2/3})O_3$–$PbTiO_3$ ceramics. *Appl. Phys. Lett.* **2001**, *78*, 2551–2553. [CrossRef]
21. Bunde, R.L.; Jarvi, E.J.; Rosentreter, J.J. Piezoelectric quartz crystal biosensors. *Talanta* **1998**, *46*, 1223–1236. [CrossRef]
22. Jia, N.; He, Q.; Sun, J.; Xia, G.M.; Song, R. Crystallization behavior and electroactive properties of PVDF, P(VDF-TrFE) and their blend films. *Polym. Test.* **2017**, *57*, 302–306. [CrossRef]
23. Yachi, Y.; Yoshimura, T.; Fujimura, N. Effect of the Annealing Temperature of P(VDF-TrFE) Thin Films on Their Ferroelectric Properties. *J. Korean Phys. Soc.* **2013**, *62*, 1065–1068. [CrossRef]
24. Du, M.Y.; Zu, G.Q.; Sun, C.Y.; Ye, F.; Yang, X.J. All-fiber wearable energy harvesting and storage system based on lamellar structural MXene. *J. Alloys Compd.* **2024**, *1005*, 176069. [CrossRef]
25. Mokhtari, F.; Usman, K.A.S.; Zhang, J.Z.; Komljenovic, R.; Simon, Z.; Dharmasiri, B.; Rezk, A.; Sherrell, P.C.; Henderson, L.C.; Varley, R.J.; et al. Enhanced Acoustoelectric Energy Harvesting with $Ti_3C_2T_x$ MXene in an All-Fiber Nanogenerator. *ACS Appl. Mater. Interfaces* **2025**, *17*, 3214–3228. [CrossRef]
26. Zhang, H.; Zhang, X.S.; Cheng, X.L.; Liu, Y.; Han, M.D.; Xue, X.; Wang, S.F.; Yang, F.; Smitha, A.S.; Zhang, H.X.; et al. A flexible and implantable piezoelectric generator harvesting energy from the pulsation of ascending aorta: In vitro and in vivo studies. *Nano Energy* **2015**, *12*, 296–304. [CrossRef]
27. Zhang, C.; Fan, Y.J.; Li, H.Y.; Li, Y.Y.; Zhang, L.; Cao, S.B.; Kuang, S.Y.; Zhao, Y.B.; Chen, A.H.; Zhu, G.; et al. Fully Rollable Lead-Free Poly(vinylidene fluoride)-Niobate-Based Nanogenerator with Ultra-Flexible Nano-Network Electrodes. *ACS Nano.* **2018**, *12*, 4803–4811. [CrossRef]
28. Ma, S.Y.; Ye, T.; Zhang, T.; Wang, Z.; Li, K.W.; Chen, M.; Zhang, J.; Wang, Z.X.; Ramakrishna, S.; Wei, L. Highly Oriented Electrospun P(VDF-TrFE) Fibers via Mechanical Stretching for Wearable Motion Sensing. *Adv. Mater. Technol.* **2018**, *3*, 1800033. [CrossRef]
29. Augustine, A.; Augustine, R.; Hasan, A.; Raghuveeran, V.; Rouxel, D.; Kalarikkal, N.; Thomas, S. Development of titanium dioxide nanowire incorporated poly(vinylidene fluoride–trifluoroethylene) scaffolds for bone tissue engineering applications. *J. Mater. Sci.-Mater. Med.* **2019**, *30*, 96. [CrossRef]
30. Peter, C.; Kliem, H. Ferroelectric imprint and polarization in the amorphous phase in P(VDF-TrFE). *J. Appl. Phys.* **2019**, *125*, 174107. [CrossRef]
31. Baltá, C.F.J.; Arche, A.G.; Ezquerra, T.A.; Cruz, C.S.; Batallan, F.; Frick, B.; López Cabarcos, E. Structure and properties of ferroelectric copolymers of poly(vinylidene fluoride). In *Structure in Polymers with Special Properties*; Zachmann, H.G., Ed.; Springer: Berlin, Germany, 1993; pp. 1–48.
32. Ting, Y.; Sofi, M.A.; Joo, M.Y.; Simanullang, R.; Lu, P.C. Fabrication of PZT/PVDF composite film and the influence of homogeneity to dielectric constant. *J. Appl. Polym. Sci.* **2024**, *141*, e55893. [CrossRef]
33. Cao, C.; Zhou, P.; Qin, W.C.; Wang, J.Q.; Liu, M.X.; Wang, P.; Zhang, T.J.; Qi, Y.J. Enhanced sensing performance of piezoelectric pressure sensors via integrated nanofillers incorporated with P(VDF-TrFE) composites. *Appl. Surf. Sci.* **2025**, *685*, 162028. [CrossRef]
34. Park, S.; Kim, Y.; Jung, H.; Park, J.Y.; Lee, N.; Seo, Y. Energy harvesting efficiency of piezoelectric polymer film with graphene and metal electrodes. *Sci. Rep.* **2017**, *7*, 17290. [CrossRef]
35. Kumar, M.; Kumari, P. P(VDF-TrFE)/ZnO nanocomposite synthesized by electrospinning: Effect of ZnO nanofiller on physical, mechanical, thermal, rheological and piezoelectric properties. *Polym. Bull.* **2023**, *80*, 4859–4878. [CrossRef]
36. Sahoo, R.; Mishra, S.; Unnikrishnan, L.; Mohanty, S.; Mahapatra, S.; Nayak, S.K.; Anwar, A.; Ramadoss, A. Enhanced dielectric and piezoelectric properties of Fe-doped ZnO/PVDF-TrFE composite films. *Mater. Sci. Semicond. Process.* **2020**, *117*, 105173. [CrossRef]
37. Chen, S.; Lou, Z.; Chen, D.; Chen, Z.J.; Jiang, K.; Shen, G.Z. Highly flexible strain sensor based on ZnO nanowires and P(VDF-TrFE) fibers for wearable electronic device. *Sci. China Mater.* **2016**, *59*, 173–181. [CrossRef]
38. Yu, J.R.; Yang, X.X.; Sun, Q.J. Piezo/Tribotronics Toward Smart Flexible Sensors. *Adv. Intell. Syst.* **2020**, *2*, 1900175. [CrossRef]

39. Yang, R.S.; Qin, Y.; Dai, L.M.; Wang, Z.L. Power generation with laterally packaged piezoelectric fine wires. *Nat. Nanotechnol.* **2009**, *4*, 34–39. [CrossRef]
40. Wang, Z.L.; Zhu, G.; Yang, Y.; Wang, S.H.; Pan, C.F. Progress in nanogenerators for portable electronics. *Mater. Today* **2012**, *15*, 532–543. [CrossRef]
41. Xu, S.; Qin, Y.; Xu, C.; Wei, Y.G.; Yang, R.S.; Wang, Z.L. Self-powered nanowire devices. *Nat. Nanotechnol.* **2010**, *5*, 366–373. [CrossRef] [PubMed]
42. Zhao, G.D.; Sun, M.L.; Liu, X.L.; Xuan, J.Y.; Kong, W.C.; Zhang, R.N.; Sun, Y.P.; Jia, F.C.; Yin, G.C.; Liu, B. Fabrication of CdS quantum dots sensitized ZnO nanorods/TiO_2 nanosheets hierarchical heterostructure films for enhanced photoelectrochemical performance. *Electrochim. Acta* **2019**, *304*, 334–341. [CrossRef]
43. Nguyena, V.S.; Rouxel, D.; Vincent, B.; Badiec, L.; Domingues, F.; Santos, D.; Lamourouxc, E.; Fort, Y. Influence of cluster size and surface functionalization of ZnO nanoparticles on the morphology, thermomechanical and piezoelectric properties of P(VDF-TrFE) nanocomposite films. *Appl. Surf. Sci.* **2013**, *279*, 204–211. [CrossRef]
44. Chen, K.; Zhang, S.C.; Liu, B.W.; Mao, X.; Sun, G.; Yu, J.Y.; Al-Deyabc, S.S.; Ding, B. Large-scale fabrication of highly aligned poly(mphenylene isophthalamide) nanofibers with robust mechanical strength. *RSC Adv.* **2014**, *4*, 45760–45767. [CrossRef]
45. Heidari, I.; Mashhadi, M.M.; Faraji, G. A novel approach for preparation of aligned electrospun polyacrylonitrile Nanofibers. *Chem. Phys. Lett.* **2013**, *590*, 231–234. [CrossRef]
46. Erickson, A.E.; Edmondson, D.; Chang, F.-C.; Wood, D.; Gong, A.; Levengood, S.L.; Zhang, M.Q. High-throughput and high-yield fabrication of uniaxially-aligned chitosan-based nanofibers by centrifugal electrospinning. *Carbohyd. Polym.* **2015**, *134*, 467–474. [CrossRef] [PubMed]
47. Cai, X.M.; Zhu, P.; Lu, X.Z.; Liu, Y.F.; Lei, T.P.; Sun, D.H. Electrospinning of very long and highly aligned fibers. *J. Mater. Sci.* **2017**, *52*, 14004–14010. [CrossRef]
48. Hu, S.Y.; Li, H.P.; Su, Z.; Yan, Y.W. Parallel patterning of SiO_2 wafer via near-field electrospinning of metallic salts and polymeric solution mixtures. *Nanotechnology* **2017**, *28*, 415301. [CrossRef]
49. Prabhakaran, M.P.; Vatankhah, E.; Ramakrishna, S. Electrospun Aligned PHBV/Collagen Nanofibers as Substrates for Nerve Tissue Engineering. *Biotechnol. Bioeng.* **2013**, *110*, 2775–2784. [CrossRef]
50. Bhavanasi, V.; Kusuma, D.Y.; Lee, P.S. Polarization Orientation, Piezoelectricity, and Energy Harvesting Performance of Ferroelectric PVDF-TrFE Nanotubes Synthesized by Nanoconfinement. *Adv. Energy Mater.* **2014**, *4*, 1400723. [CrossRef]
51. Yuan, X.T.; Gao, X.Y.; Shen, X.Y.; Yang, J.K.; Li, Z.M.; Dong, S.X. A 3D-printed, alternatively tilt-polarized PVDF-TrFE polymer with enhanced piezoelectric effect for self-powered sensor application. *Nano Energy* **2021**, *85*, 105985. [CrossRef]
52. Yang, L.; Liu, C.S.; Yuan, W.J.; Meng, C.Z.; Dutta, A.; Chen, X.; Guo, L.G.; Niu, G.Y.; Cheng, H.Y. Fully stretchable, porous MXene-graphene foam nanocomposites for energy harvesting and self-powered sensing. *Nano Energy* **2022**, *103*, 107807. [CrossRef]
53. Chai, B.; Shi, K.M.; Wang, Y.L.; Liu, Y.J.; Liu, F.; Jiang, P.K.; Sheng, G.H.; Wang, S.J.; Xu, P.; Xu, X.Y.; et al. Modulus-Modulated All-Organic Core−Shell Nanofiber with Remarkable Piezoelectricity for Energy Harvesting and Condition Monitoring. *Nano Lett.* **2023**, *23*, 1810–1819. [CrossRef]
54. Shepelin, N.A.; Sherrell, P.C.; Skountzos, E.N.; Goudeli, E.; Zhang, J.Z.; Lussini, V.C.; Imtiaz, B.; Usman, K.A.S.; Dicinoski, G.W.; Shapter, J.G.; et al. Interfacial piezoelectric polarization locking in printable $Ti_3C_2T_x$ MXene-fluoropolymer Composites. *Nat. Commun.* **2021**, *12*, 3171. [CrossRef]
55. Meisak, D.; Plyushch, A.; Kinka, M.; Balciunas, S.; Kalendra, V.; Schaefer, S.; Zarkov, A.; Selskis, A.; Banys, J.; Fierro, V.; et al. Effect of Particle Size on the Origin of Electromechanical Response in $BaTiO_3$/PDMS Nanogenerators. *ACS Appl. Electron. Mater.* **2024**, *6*, 7464–7474. [CrossRef]
56. An, S.; Jo, H.S.; Li, G.; Samuel, E.; Yoon, S.S.; Yarin, A.L. Sustainable Nanotextured Wave Energy Harvester Based on Ferroelectric Fatigue-Free and Flexoelectricity-Enhanced Piezoelectric P(VDF-TrFE) Nanofibers with $BaSrTiO_3$ Nanoparticles. *Adv. Funct. Mater.* **2020**, *30*, 2001150. [CrossRef]

polymers

MDPI

Article

Poly(amic acid)-Polyimide Copolymer Interfacial Layers for Self-Powered $CH_3NH_3PbI_3$ Photovoltaic Photodiodes

Wonsun Kim [1], JaeWoo Park [2,3], HyeRyun Jeong [1], Kimin Lee [1], Sui Yang [3], Eun Ha Choi [1,2] and Byoungchoo Park [1,2,*]

[1] Department of Electrical and Biological Physics, Kwangwoon University, Wolgye-Dong, Seoul 01897, Republic of Korea; dnjsun21@naver.com (W.K.); skad10004@naver.com (H.J.); dlrlals1123@naver.com (K.L.); choipdp@gmail.com (E.H.C.)

[2] Department of Plasma-Bio Display, Kwangwoon University, Wolgye-Dong, Seoul 01897, Republic of Korea; jpark441@asu.edu

[3] Materials Science and Engineering, School for Engineering of Matter Transport and Energy, Arizona State University, Tempe, AZ 85287, USA; suiyang@asu.edu

* Correspondence: bcpark@kw.ac.kr; Tel.: +82-2-940-5237

Abstract: Hybrid organohalide perovskites have received considerable attention due to their exceptional photovoltaic (PV) conversion efficiencies in optoelectronic devices. In this study, we report the development of a highly sensitive, self-powered perovskite-based photovoltaic photodiode (PVPD) fabricated by incorporating a poly(amic acid)-polyimide (PAA-PI) copolymer as an interfacial layer between a methylammonium lead iodide ($CH_3NH_3PbI_3$, $MAPbI_3$) perovskite light-absorbing layer and a poly(3,4-ethylenedioxythiophene)-poly(styrene sulfonate) (PEDOT: PSS) hole injection layer. The PAA-PI interfacial layer effectively suppresses carrier recombination at the interfaces, resulting in a high power conversion efficiency (*PCE*) of 11.8% compared to 10.4% in reference devices without an interfacial layer. Moreover, applying the PAA-PI interfacial layer to the $MAPbI_3$ PVPD significantly improves the photodiode performance, increasing the specific detectivity by 49 times to 7.82×10^{10} Jones compared to the corresponding results of reference devices without an interfacial layer. The PAA-PI-passivated $MAPbI_3$ PVPD also exhibits a wide linear dynamic range of ~103 dB and fast response times, with rise and decay times of 61 and 18 μs, respectively. The improved dynamic response of the PAA-PI-passivated $MAPbI_3$ PVPD enables effective weak-light detection, highlighting the potential of advanced interfacial engineering with PAA-PI interfacial layers in the development of high-performance, self-powered perovskite photovoltaic photodetectors for a wide range of optoelectronic applications.

Keywords: photodetector; poly(amic acid)-polyimide copolymer; polymeric interfacial layer; organic/inorganic hybrid perovskite

1. Introduction

In recent years, organohalide perovskites have emerged as promising materials for energy harvesting devices, largely due to their solution-processable fabrication methods and exceptional optoelectronic properties, especially in terms of the photon-to-electricity conversion efficiency [1–7]. Perovskites, with the general chemical formula of ABX_3 (where A is a monovalent organic cation such as methylammonium (MA^+) or formamidinium (FA^+), B is a metal cation such as Pb^{2+} or Sn^{2+}, and X is a halide anion such as Cl^-, Br^-, or I^-), have enabled remarkable advances in photovoltaic (PV) performance, with power conversion efficiencies (*PCE*s) exceeding 26.7% [7–11]. These high efficiencies of perovskite

PV devices are attributed to their strong optical absorption, high carrier mobility, ambipolar charge transport, and tunable bandgaps, which collectively support the development of efficient, scalable optoelectronic devices [7,9,11–14]. Beyond PV applications, organohalide perovskites have also shown strong potential in photodetectors, achieving impressive metrics such as responsivity (R) values between 360 and 470 mA/W and specific detectivity (D^*) values ranging from 2.1×10^{11} to 7.8×10^{12} Jones, comparable to those of conventional silicon-based detectors [15–18].

Despite these advances, challenges remain in the fabrication of high-quality, stable perovskite-based devices. Defects and distortions within the perovskite lattice, both in the bulk and at the surface, present significant obstacles to achieving consistent and stable performance [19–23]. Furthermore, the sensitivity of perovskites to environmental factors such as heat and humidity can lead to the degradation and loss of device performance over time [20,24]. In addition, grain boundaries, pinholes, and surface defects in the perovskite layer often lead to recombination losses, further reducing device efficiency [20–23,25]. Weak interfacial interactions between the perovskite layer and adjacent charge transport layers, such as hole transport layers (HTLs) and electron transport layers (ETLs), further limit charge separation and transport efficiency, reducing the overall device performance and stability [20–23].

In order to address these issues, interfacial engineering has emerged as a critical strategy for optimizing the performance and stability of perovskite-based devices, including PV cells [11,12,26–29] and photodetectors [23,30–35]. Recent advancements have demonstrated that interfacial layers with tailored physical and electronic properties can effectively address challenges such as energy level misalignment [7,12,23,28], charge recombination [11,21,23,30,34], and suboptimal charge extraction efficiency [22,28,29,33,35]. Various polymers, including polystyrene [21,27], poly(4-vinylpyridine) [21,36], and poly(methyl methacrylate) [21,24,34,35,37–41], have been employed as interfacial passivation layers, reportedly achieving *PCE*s of approximately 15–20% [20,26]. Furthermore, molecular interfacial engineering using small molecular layers has shown significant improvements in carrier dynamics and device stability [28,31]. Additionally, strategies focusing on dual interfacial optimization and additive engineering have also been highlighted for their role in enhancing photoresponsivity and device longevity [32,35].

Compared to these advancements in perovskite PV cells, the application of interfacial layers in perovskite photodetectors remains relatively underexplored. This gap presents an important opportunity to address persistent limitations, including grain boundary defects [28,29], dark leakage currents [32], and noise [31,33], all of which adversely affect R and D^* [30,34,35]. Moreover, the poor interfacial quality between the perovskite light-absorbing layer and the charge transport layers frequently results in increased recombination losses and suboptimal charge extraction, ultimately hindering device performance [41].

In this regard, we explore the use of a poly(amic acid)-polyimide (PAA-PI) copolymer interfacial layer, which has previously demonstrated significant performance improvements in organic light-emitting diodes (OLEDs) [42]. The PAA-PI interfacial layer, known for its excellent film-forming properties, high hole transport capabilities, and effective passivation, has shown promise in mitigating problems such as grain boundaries, surface defects, and weak interfacial interactions in perovskite devices. In OLEDs, the incorporation of PAA-PI layers resulted in significant performance improvements, with peak brightness values of approximately 100,000 cd/m^2 and efficiencies exceeding 90 cd/A, significantly outperforming reference OLEDs without a PAA-PI layer [42]. These improvements were attributed to the capability of the PAA-PI interfacial layer to enhance energy level alignment, promote hole transport, and block electron diffusion. Given the demonstrated benefits of PAA-PI interfacial layers in OLEDs, it is plausible that such layers could enhance the

performance capabilities of perovskite photodetectors by improving the interfacial quality between the perovskite layer and the charge transport layers, thereby mitigating defect-related problems, recombination losses, and dark leakage currents. This approach offers straightforward integration into the fabrication of high-performance, stable, and low-cost photodetectors without the need for complex processing techniques.

In this study, we systematically investigate the incorporation of a PAA-PI interfacial layer into methylammonium lead iodide ($CH_3NH_3PbI_3$, $MAPbI_3$)-based perovskite photovoltaic photodiodes (PVPDs). We evaluate the effect of the PAA-PI interfacial layer on the optoelectronic properties of the device, specifically the external quantum efficiency (*EQE*), *R*, *D**, and the linear dynamic range (*LDR*) under self-powered (zero bias) conditions. Moreover, we evaluate the temporal photoresponse, in this case the rise and decay times, and signal spectra, with a reference PVPD without a PAA-PI interfacial layer tested for comparison. Our results demonstrate that the incorporation of the PAA-PI interfacial layer significantly improves device performance, exceeding that of similar devices reported in the literature.

2. Materials and Methods

2.1. Materials

N,*N*-dimethylformamide (DMF), anhydrous dimethyl sulfoxide (DMSO), anhydrous chlorobenzene (CB), anhydrous isopropyl alcohol (IPA), and a poly(amic acid) (PAA) solution of poly(pyromellitic dianhydride-*co*-4,4′-oxydianiline) (PMDA-ODA) were purchased from Sigma-Aldrich (St. Louis, MO, USA). Methylammonium iodide (MAI) and lead(II) iodide (PbI_2), used as the perovskite precursors here, were sourced from Greatcell Solar (Queanbeyan, Australia) and Alfa Aesar (Haverhill, MA, USA), respectively. Phenyl-C_{61}-butyric acid methyl ester ($PCBM_{60}$) was purchased from Nano-C (Westwood, MA, USA), and the colloidal zinc oxide (ZnO) nanoparticle suspension (N-10) used in this study was supplied by Avantama (Stäfa, Switzerland). Bathocuproine (BCP) was procured from Tokyo Chemical Industry Co., Ltd (Tokyo, Japan). The poly(3,4-ethylenedioxythiophene) polystyrene sulfonate (PEDOT:PSS) aqueous solution (Clevios P-VP-AI-4083) was purchased from H.C. Starck (Leverkusen, Germany). All chemicals were used as received without further purification.

2.2. Methods

A pre-patterned 80 nm thick indium tin oxide (ITO, 20 Ω/sq) layer on a glass substrate served as the transparent anode. Prior to device fabrication, the ITO substrates were ultrasonically cleaned in ethyl alcohol, a detergent, and deionized water, followed by drying with N_2 gas and a treatment with ultraviolet ozone for five minutes. To form a 30 nm thick PEDOT:PSS hole injection layer (HIL), the PEDOT:PSS solution was spin-coated onto the ITO substrate at 4000 rpm for 35 s, and the thus-coated substrate was annealed at 120 °C for 20 min. For the PAA-PI interfacial layer, the synthesis method employed in this study followed the protocol described in our previous work [42] to optimize the device architecture performance. Specifically, a precursor solution containing PAA in N-methyl-2-pyrrolidone (NMP) (1:20 volume ratio) was spin-coated onto a PEDOT:PSS-coated ITO substrate at 2000 rpm for 35 s. The resulting PAA precursor layer was pre-baked at 80 °C for 30 min and subsequently annealed at 180 °C for 1 h to form a 6 nm thick PAA-PI interfacial layer [42].

Next, the substrate coated with the PAA-PI interfacial layer was transferred into a nitrogen-filled glovebox. To prepare the perovskite precursor solution, PbI_2 and MAI were mixed at a 1:1 molar ratio in a solvent mixture of DMF and DMSO (8:2 volume ratio) and stirred overnight. The perovskite precursor solution was spin-coated onto the substrate at

3800 rpm for 30 s in the glovebox. During this spin coating process, anhydrous CB was dropped as an antisolvent onto the spinning substrate after a delay of 5–10 s to promote the formation of a uniform film. Following the spin coating step, the perovskite film was allowed to dry at room temperature for 5 min and was then annealed at 100 °C for 20 min to crystallize the $MAPbI_3$ layer, resulting in a 250 nm thick $MAPbI_3$ perovskite film.

Subsequently, the $MAPbI_3$ perovskite-coated substrates were spin-coated with a 50 nm thick $PCBM_{60}$ ETL from a 20 mg/mL solution in CB and a 20 nm thick ZnO ETL from a colloidal nanoparticle suspension. Finally, a 12 nm thick BCP hole-blocking layer and a 70 nm thick Al cathode were thermally evaporated onto the ZnO layer at a base pressure of less than 2×10^{-6} Torr. The resulting $MAPbI_3$ perovskite PVPD device structure was [ITO/PEDOT:PSS/PAA-PI/$MAPbI_3$/$PCBM_{60}$/ZnO/BCP/Al], with an active area of 6 mm^2.

2.3. Characterization

The surface morphology of each functional layer was analyzed using scanning electron microscopy (SEM; Inspect F50, FEI, Philips, Eindhoven, The Netherlands), and the grain size distribution was quantified from SEM images using ImageJ software (version 1.53t). The surface roughness of the layers was assessed using atomic force microscopy (AFM; FlexAFM, Nanosurf AG, Liestal, Switzerland) and simultaneous Kelvin probe force microscopy (KPFM), with morphological profiles obtained using Gwyddion software (version 2.62). Ultraviolet photoelectron spectroscopy (UPS; PHI 5000 Versa Probe, ULVAC-PHI Inc., Chigasaki, Japan) was employed to analyze the electronic structures and properties of the layers, while their optical properties were examined using ultraviolet–visible (UV–visible) spectrometry (Cary 1E, Varian, Agilent, Santa Clara, CA, USA). To minimize sample degradation in ambient air, all measurements were conducted within 1–2 h of fabrication.

The PV performance of the fabricated devices was evaluated under simulated solar illumination (100 mW/cm^2) using an AM 1.5G light source (96000 Solar Simulator, Newport, Irvine, CA, USA), with calibration performed using a reference PV cell (BS-520, Bunkoh-Keiki Co., Ltd., Tokyo, Japan). Current–voltage (*J-V*) characteristics were measured using source meters (Keithley 2400, 2636, Tektronix, Beaverton, OR, USA). The *EQE* spectra and spectral responsivity (R_λ) were obtained using an incident photon-to-current efficiency measurement system (IQE-200 EQE/IQE, Newport, Irvine, CA, USA).

To evaluate the performance of the photodiode (PD), a monochromatic light source (λ = 637 nm) from a diode laser (COMPACT-100G-637-A, World Star Tech, Markham, ON, Canada) with a maximum modulation frequency of 50 kHz and output power of 100 mW was utilized. The noise current (i_n) level was determined via a fast Fourier transform (*FFT*) analysis of the dark current (I_{dark}), measured without external bias using a source meter (Keithley 2636, Tektronix, Beaverton, OR, USA), with data acquisition at a sampling rate of 1 kHz. The 3 dB cutoff frequencies were extracted through logarithmic transformation of the normalized photoresponses, which were modulated using the aforementioned 637 nm laser system and analyzed as a function of the modulation frequency.

3. Results and Discussion

3.1. Characteristics of PAA-PI Interfacial Layers

Before investigating the impact of the PAA-PI interfacial layer on the performance of $MAPbI_3$ perovskite PVPDs, we first characterized the properties of the PAA-PI interfacial layers. Figure 1a shows the molecular structure of the PAA-PI copolymer, which consists of two components: one derived from PAA, formed by polymerizing PMDA with carbonyl groups and ODA containing nitrogen atoms, and the other from imidized PI. This copolymer serves as the interfacial layer between the $MAPbI_3$ active layer and the HIL of

PEDOT:PSS. To achieve a thin and homogeneous PAA-PI interfacial layer, a PAA precursor solution was spin-coated onto the PEDOT:PSS substrate and then annealed at 180 °C to imidize the PAA, forming the PAA-PI copolymer (imidization degree ~46%) following previously reported synthesis routes [43].

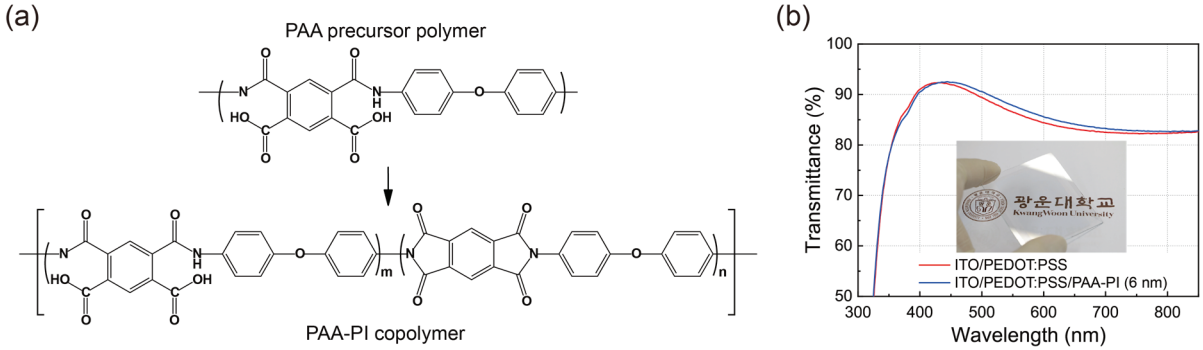

Figure 1. (**a**) Molecular structure of the PAA-PI copolymer based on PMDA-ODA PAA used in this study. (**b**) UV–visible optical transmission spectra of 6 nm thick (Sample) and 0 nm thick (Reference) PAA-PI interfacial layers on a PEDOT:PSS HIL, deposited on an ITO electrode. The inset shows a photograph of the Sample with a 6 nm thick PAA-PI layer on a 5.5 × 5.5 cm^2 substrate [42].

The optical properties of the PAA-PI layers were initially investigated. Optical images and transmission spectra of the PAA-PI layers deposited on ITO/PEDOT:PSS substrates are shown in Figure 1b. The results demonstrate that the PAA-PI copolymer-coated substrates maintain high optical transparency, which is essential for their application in optoelectronic devices. For instance, the average optical transmittance of the ITO/PEDOT:PSS/PAA-PI (6 nm) layer in the visible range (400–700 nm) is approximately 88%, slightly higher than the transmittance of 87% observed for the Reference ITO/PEDOT:PSS layer. This improvement is accompanied by a minor redshift in the transmission peak, attributed to optical interference effects. Therefore, the addition of the PAA-PI layer does not significantly affect the optical transparency of the ITO/PEDOT:PSS substrate.

We investigated the surface morphology of the PAA-PI layers in more detail using AFM. Figure 2a presents the AFM topography of a 6 nm thick PAA-PI layer deposited on an ITO/PEDOT:PSS substrate. The root mean square (RMS) roughness of the Reference ITO/PEDOT:PSS layer is approximately 0.80 nm, while that of the PAA-PI layer increases to approximately 1.54 nm. These values indicate that the PAA-PI layers form smooth and homogeneous surfaces on PEDOT:PSS, free from needle-like defects or pinholes.

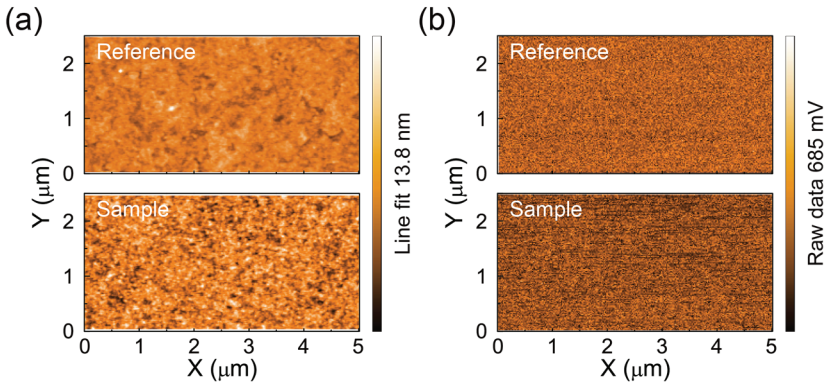

Figure 2. (**a**) AFM topography images and (**b**) corresponding KPFM potential maps of ITO/PEDOT:PSS (30 nm)/PAA-PI layers with PAA-PI thicknesses of 0 nm (Reference, top) and 6 nm (Sample, bottom) [42].

To investigate the surface properties further, we conducted KPFM measurements to assess the surface potentials of the PAA-PI interfacial layer. The KPFM surface potential maps in Figure 2b confirm the uniformity of the PAA-PI layer. The contact potential difference (CPD) values were measured, with $V_{CPD(PEDOT:PSS)}$ equal to approximately −84 mV for the Reference ITO/PEDOT:PSS layer and $V_{CPD(PAA\text{-}PI)}$ equal to approximately 335 mV for the 6 nm thick PAA-PI layer. These results indicate a significant increase in the surface potential upon the formation of the PAA-PI interfacial layer. This increased surface potential can be attributed to a surface dipole moment in the PAA-PI layer, which is composed of strong polar groups, in this case carboxyl (-COOH) and amide (-CONH) functionalities [44–46]. These dipoles likely align with their moments pointing away from the underlying PEDOT:PSS layer, resulting in the observed increase in the CPD value. These changes in the surface potential can significantly affect the electronic properties of both the interfacial layer and the adjacent functional layers [47].

3.2. Characteristics of $MAPbI_3$ Layers on PAA-PI Interfacial Layers

An ultrathin, homogeneous PAA-PI interfacial layer was deposited on the PEDOT:PSS HIL, followed by the deposition of a $MAPbI_3$ perovskite active layer using an antisolvent-assisted rapid crystallization method to achieve a uniform, continuous film structure [30, 34]. During the spin coating of the $MAPbI_3$ layer, a CB antisolvent was applied to the spinning perovskite layer to facilitate the formation of a homogeneous $MAPbI_3$ film. Thus, the investigated film structure includes an ITO/PEDOT:PSS HIL/PAA-PI interfacial layer/$MAPbI_3$ perovskite layer configuration, as shown in Figure 3a. The functional groups within the PAA-PI interfacial layer can interact with the $MAPbI_3$ active layer and affect the film quality, as discussed below.

In order to evaluate the effects of the PAA-PI interfacial layer on the morphology and quality of the $MAPbI_3$ layers, SEM was used. Comparative SEM images of the $MAPbI_3$ layers fabricated with (Sample) and without (Reference) the PAA-PI interfacial layer, as shown in Figure 3b, indicate that the presence of the PAA-PI layer leads to a clear increase in the grain size and fewer film defects in the $MAPbI_3$ layer. This SEM analysis confirms that the $MAPbI_3$ films fabricated with the PAA-PI interfacial layer exhibit a more uniform and smoother morphology.

For a quantitative assessment of the grain size distributions in the $MAPbI_3$ films (Figure 3b), ImageJ software was used to estimate the domain sizes. The average grain size of the Reference $MAPbI_3$ layer was approximately 71 nm, whereas the Sample $MAPbI_3$ layer showed an increased average grain size of approximately 80 nm. This increase in the grain size is attributable to the inhibition of nucleation sites [35,48], allowing the growth of larger $MAPbI_3$ grains to be promoted by the PAA-PI interfacial layer. The PAA-PI interfacial layer facilitates larger $MAPbI_3$ grains while mitigating defects such as spikes and pinholes, potentially reducing carrier recombination losses at the perovskite interface and improving charge extraction and transfer from the perovskite layer to adjacent functional layers.

To investigate the electronic structures and properties imparted by the PAA-PI films more concisely, UPS was employed. Figure 3c,d show the UPS spectra (He I) of the PAA-PI-modified ITO/PEDOT:PSS layers, highlighting the photoemission threshold energy and the energy difference between the Fermi level (E_F) and the valence band maximum (E_{VBM}) or highest occupied molecular orbital (HOMO) level (E_{HOMO}). The UPS analysis shows that the work function and E_{HOMO}s of the unmodified Reference ITO/PEDOT:PSS layer are approximately 5.02 eV and 5.20 eV, respectively, in agreement with previously reported UPS data [49]. In contrast, the work function for the ITO/PEDOT:PSS/PAA-PI layer is reduced to approximately 4.35 eV for a 6 nm thick PAA-PI layer on ITO/PEDOT:PSS (Figure 3c).

This reduction in the work function suggests that the dipole moment of the PAA-PI layer is oriented away from the PEDOT:PSS layer [50], confirming the results obtained from the KPFM surface potential measurements. Furthermore, the estimated E_{HOMO} for the ITO/PEDOT:PSS/PAA-PI layers is around 4.97 eV for a 6 nm thick PAA-PI layer, indicating that the PAA-PI layer effectively modulates both the work function and E_{HOMO} (~5.20 eV) of the ITO/PEDOT:PSS layers.

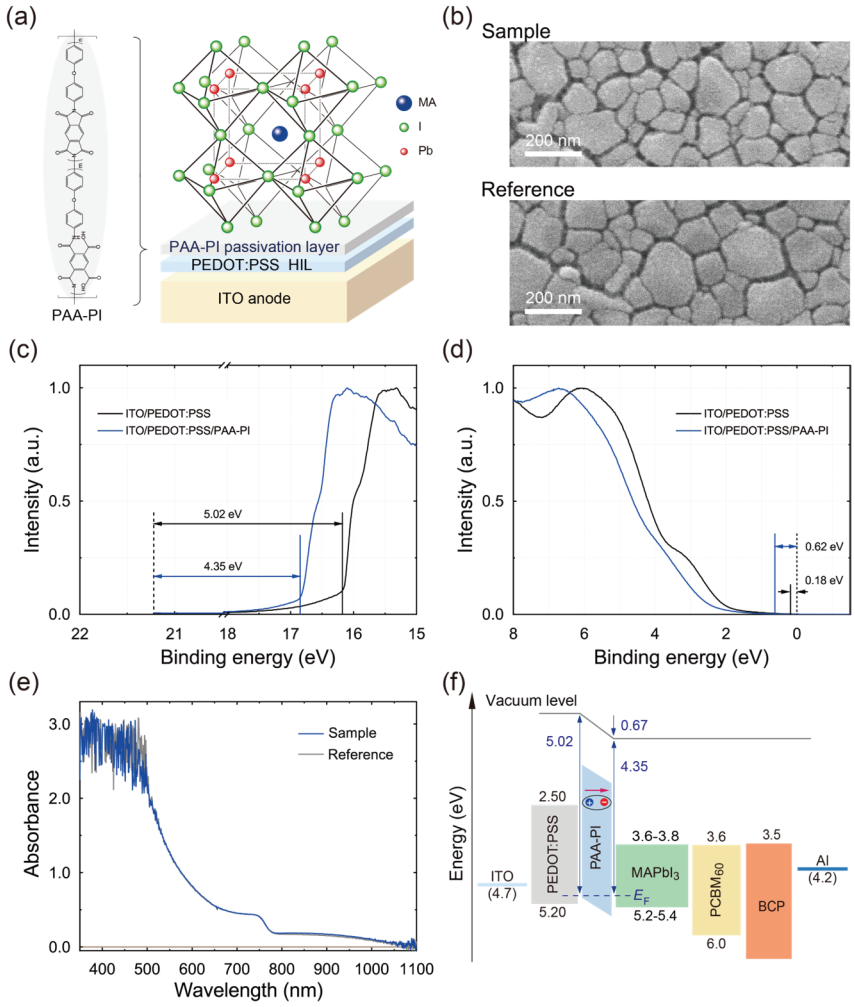

Figure 3. (**a**) Schematic illustration of the $MAPbI_3$ perovskite layer with a polymer interfacial layer (PAA-PI) on a PEDOT:PSS HIL on an ITO electrode, resulting in the ITO/PEDOT:PSS/PAA-PI/$MAPbI_3$ configuration. (**b**) High-magnification SEM images comparing the top-view morphologies of $MAPbI_3$ perovskite layers without (Reference: ITO/PEDOT:PSS/$MAPbI_3$) and with (Sample: ITO/PEDOT:PSS/PAA-PI/$MAPbI_3$) a PAA-PI interfacial layer on PEDOT:PSS. (**c**) UPS spectra of the Reference and Sample layers used to determine their respective work functions [42]. (**d**) VBM values derived for the Reference and Sample layers [42]. (**e**) UV–visible absorption spectra of the $MAPbI_3$ Reference and Sample layers illustrating their optical absorption characteristics. (**f**) Energy level diagram illustrating the Sample layer (ITO/PEDOT:PSS/PAA-PI/$MAPbI_3$) with the addition of thin $PCBM_{60}$ and BCP ETLs and an Al cathode, highlighting the alignment of the energy levels across the layers.

The UV–visible absorption spectra of the Reference and Sample $MAPbI_3$ layers, shown in Figure 3e, show strong absorption in the visible wavelength range of 450–700 nm. Notably, the optical absorption of the Sample $MAPbI_3$ layer is nearly identical to that of the Reference layer, indicating that the PAA-PI interfacial layer does not affect the optical absorption properties of the $MAPbI_3$ perovskite layer. Together with the energy levels

estimated for the $MAPbI_3$ and $PCBM_{60}$ functional layers, an energy level diagram was constructed for $MAPbI_3$ devices with and without a PAA-PI interfacial layer (Figure 3f). In the sample layer, the introduction of a PAA-PI interfacial layer between the PEDOT:PSS HIL and the $MAPbI_3$ active layer results in an E_{HOMO} value of approximately 5.0 eV for the PAA-PI interfacial layer while also inducing a significant vacuum level (E_{vac}) downshift of approximately 0.67 eV, as estimated from UPS measurements (Figure 3c,d). This substantial E_{vac} downshift confirms the formation of a dipolar interfacial layer, with the negative end oriented toward the perovskite and the positive end facing outward, as mentioned above. The dipole formation, therefore, significantly alters the interfacial energy band structure, leading to a downshift in the HOMO level of $MAPbI_3$ and a reduced hole collection barrier [47]. Consequently, the enhanced interfacial dipole of the PAA-PI layer may improve charge collection, contributing to a considerably higher *PCE*.

Notably, in the Sample layer with the PAA-PI interfacial layer, a substantial energy barrier (~2.1 eV) exists between the lowest unoccupied molecular orbital (LUMO) levels of the PAA-PI interfacial layer and the $MAPbI_3$ active layer, potentially allowing the PAA-PI layer to function as an electron-blocking layer. These results suggest that the physical and electronic properties of the PAA-PI interfacial layer play an important role in overall device performance.

3.3. PV Performance of $MAPbI_3$ PVPDs with PAA-PI Interfacial Layers

Given the observed properties of the $MAPbI_3$ layer, as described above, the introduction of a PAA-PI interfacial layer appears to improve the interfacial quality between the $MAPbI_3$ active layer and the adjacent HIL effectively without altering the optical properties of the $MAPbI_3$ layer. This interface improvement is expected to reduce i_n and increase the photocurrent, thereby potentially improving the performance of $MAPbI_3$ perovskite PVPDs [35].

To investigate the PV performance of $MAPbI_3$ PVPDs with and without PAA-PI interfacial layers, a schematic of the $MAPbI_3$ PVPD structure was devised, as shown in Figure 4a. In this configuration, ITO serves as the anode, PEDOT:PSS acts as the HIL, PAA-PI acts as the interfacial layer, and $MAPbI_3$ is the perovskite light-absorbing layer. ETLs consisting of $PCBM_{60}$ and BCP were subsequently deposited onto the $MAPbI_3$ layer, and an Al cathode completed the device structure.

The device performance of the $MAPbI_3$ PVPDs without (Reference) and with the PAA-PI interfacial layer (Sample) was evaluated by measuring the dark current densities (J_{dark}s) as a function of the applied voltage (J_{dark}-V), as shown in Figure 4b. The results show diodic behavior and high rectification ratios (*RR*s) under dark conditions, indicating sufficient perovskite layer coverage. However, there was a noticeable difference between the PVPDs; the Reference device exhibited an *RR* of approximately 0.02×10^3 at 1.0 V, while the Sample device showed a significantly increased *RR* of 1.59×10^3, higher than previously reported values (~0.75×10^3) for devices with PEDOT:PSS [18]. This increase is attributed to the reduction in the leakage current, likely due to the improved interfacial quality between the $MAPbI_3$ active layer and the PEDOT:PSS HIL. In addition, the Sample device exhibited a lower J_{dark} of close to 8.15×10^{-6} mA/cm^2 at zero voltage compared to ~2.18×10^{-4} mA/cm^2 for the Reference device. This reduction in I_{dark}, combined with the increased *RR*, highlights the effective interfacial benefits conferred by the PAA-PI layer [14,18].

To examine the effect of the PAA-PI interfacial layers on trap states within the light-absorbing layers more closely, the J_{dark}-V curves of the perovskite PVPDs were replotted on a logarithmic scale, enabling the determination of the trap-filling limit voltages (V_{TFL}), as shown in the panel at the bottom of Figure 4b [7,40,51,52]. The V_{TFL} values for the Reference and Sample PVPDs were approximately 0.67 V and 0.40 V, respectively. Using the space charge limited current (SCLC) model, the trap state density (N_{trap}) was calculated using the

equation $N_{trap} = (2\varepsilon\varepsilon_0 V_{TFL})/(eL^2)$, where ε is the relative permittivity of $MAPbI_3$, ε_0 is the vacuum permittivity, e is the elementary charge (1.6×10^{-19} C), and L is the perovskite film thickness [7,40,51]. The calculated N_{trap} values were approximately 1.78×10^{15} cm^{-3} for the Reference device and 1.06×10^{15} cm^{-3} for the Sample device, indicating significant defect passivation at the $MAPbI_3$ interfaces in the Sample device.

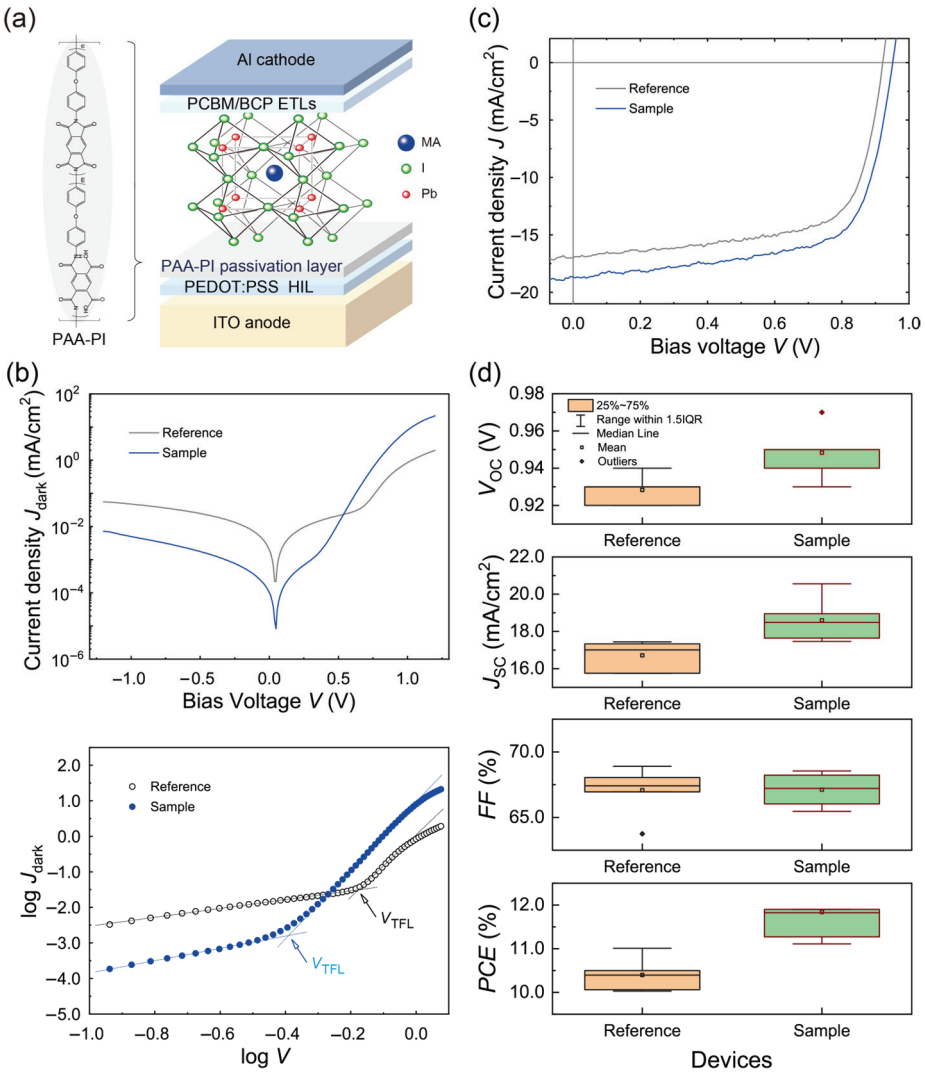

Figure 4. (**a**) Schematic illustration of a planar $MAPbI_3$ perovskite PVPD with a PAA-PI interfacial layer. (**b**) J_{dark}-V characteristics of $MAPbI_3$ PVPDs without (Reference) and with (Sample) a PAA-PI interfacial layer, presented on a semi-logarithmic scale (top panel) and a log-logarithmic scale (bottom panel). (**c**) J-V characteristics of $MAPbI_3$ PVPDs during backward scanning under AM 1.5G illumination. (**d**) Comparison of PV performance parameters—V_{OC}, J_{SC}, *FF*, and *PCE*—for the Reference and Sample $MAPbI_3$ PVPDs.

Next, the PV performance of the $MAPbI_3$ PVPDs was evaluated under AM 1.5G illumination, as shown in Figure 4c. The Reference device exhibited a *PCE* of 10.4%, with a short-circuit current density (J_{SC}) of 16.7 mA/cm^2, an open-circuit voltage (V_{OC}) of 0.93 V, and a fill factor (*FF*) of 67.1%, consistent with previously reported values for solution-processed $MAPbI_3$ devices [18,35]. In contrast, the Sample device showed a significant improvement, achieving a *PCE* of 11.8%, with J_{SC} = 18.6 mA/cm^2, V_{OC} = 0.95 V, and *FF* = 67.1%. The improved J_{SC} in the Sample device is attributed to increased photo-generated charge carriers, supported by the larger grain sizes and fewer defect sites in the homogeneous $MAPbI_3$ layer, which allow for efficient charge separation under the

high built-in potential (V_{bi}) of the heterostructure [18,34]. In addition, the observed shunt resistance (R_{Shunt}) and series resistance (R_{Series}) of the Sample device were found to be nearly identical to those of the Reference device. The high R_{Shunt} value observed in the Sample device indicates that the PAA-PI interfacial passivation layer effectively suppresses non-radiative recombination losses and minimizes leakage pathways [53]. This optimized interfacial quality directly contributes to the enhanced overall device performance, as evidenced by the improved *PCE* values and increased stability (see Appendix A). The PV performance metrics of the $MAPbI_3$ PVPDs are summarized in Table 1. Notably, deviations from the optimal deposition conditions, particularly for the PAA-PI interfacial layer, resulted in a significant decrease in the performance of the Sample PVPDs.

Table 1. Summary of PV performance parameters of $MAPbI_3$-based PVPDs with PAA-PI interfacial layers during backward scanning under AM 1.5G illumination (100 mW/cm^2).

PVPDs	Interfacial Layers	V_{OC} (V)	J_{SC} (mA/cm^2)	*FF* (%)	*PCE* (%) *	R_{Shunt} (Ω cm^2)	R_{Series} (Ω cm^2)
Reference	None	0.93 ± 0.01	16.71 ± 0.76	67.08 ± 1.77	10.40 ± 0.36	359.19 ± 69.37	4.60 ± 0.31
Sample	PAA-PI	0.95 ± 0.01	18.60 ± 1.12	67.12 ± 1.23	11.84 ± 0.70	359.55 ± 74.50	4.67 ± 0.39

* The reported values represent the average results obtained from multiple (at least eight) individual devices.

While the *PCE* value of the Sample device in this study is relatively low compared to that reported in our previous work [35], this difference primarily stems from the single-sided passivation strategy employed here, in contrast to the double-sided passivation approach combined with nickel oxide (NiO_x) as the HTL in the previous study. This combination effectively mitigated surface and interface defects, minimized non-radiative recombination losses, and enhanced the charge extraction efficiency, resulting in higher *PCE* values. In this study, we focused on implementing an insoluble bottom-side passivation layer of PAA-PI, which serves as a crucial prerequisite for successfully achieving an advanced double-sided passivation strategy in future developments. Additionally, we employed PEDOT:PSS as the HIL, offering distinct advantages, including lower processing temperatures, better mechanical flexibility, and improved scalability, making it highly suitable for flexible device architectures. This contrasts with conventional NiO_x-based HTLs, which, despite their high efficiency, are limited by higher processing temperatures, mechanical brittleness, and challenges in achieving compatibility with flexible substrates. Therefore, the findings of this study establish an optimized foundation for bottom-interface passivation using PAA-PI on PEDOT:PSS, representing a significant step toward the development of advanced, flexible, and highly efficient double-sided passivation architectures in future investigations.

3.4. Photodetection Performance of $MAPbI_3$ PVPDs with PAA-PI Interfacial Layers

The *EQE* spectra of the $MAPbI_3$ PVPDs at zero applied voltage were evaluated, as shown in Figure 5a. The Sample device exhibited significantly higher *EQE* values compared to the Reference device, with a maximum *EQE* of approximately 64.5%, exceeding the maximum *EQE* of the Reference device, which was close to 64.1%. The improved *EQE* in the Sample device is attributable to the PAA-PI interfacial layers, which enhance carrier extraction and reduce recombination losses by reducing the charge trap density within the $MAPbI_3$ layer, as discussed previously.

To evaluate the PD performance of the $MAPbI_3$ PVPDs under self-powered conditions, the R_λ value was calculated from the *EQE* spectra (Figure 5a) using the following formula:

$$R_\lambda = EQE \cdot \frac{e\lambda}{hc}, \quad (1)$$

where h is the Planck constant (6.63×10^{-34} J·s) and c is the speed of light (3.0×10^{8} m/s). The R_λ spectra shown in Figure 5b indicate that the Sample device achieves significantly higher sensitivity at zero bias voltage compared to the Reference device. The peak R_λ value for the Sample device is approximately 343 mA/W at 660 nm, whereas the Reference device shows a peak value of approximately 325 mA/W at 630 nm. This improvement in R_λ is primarily attributed to the enhanced photocurrent generation resulting from the improved charge collection efficiency and reduced recombination losses. Notably, the high peak R_λ value observed in the Sample device is competitive with previously reported values for $MAPbI_3$-based PDs [18,30].

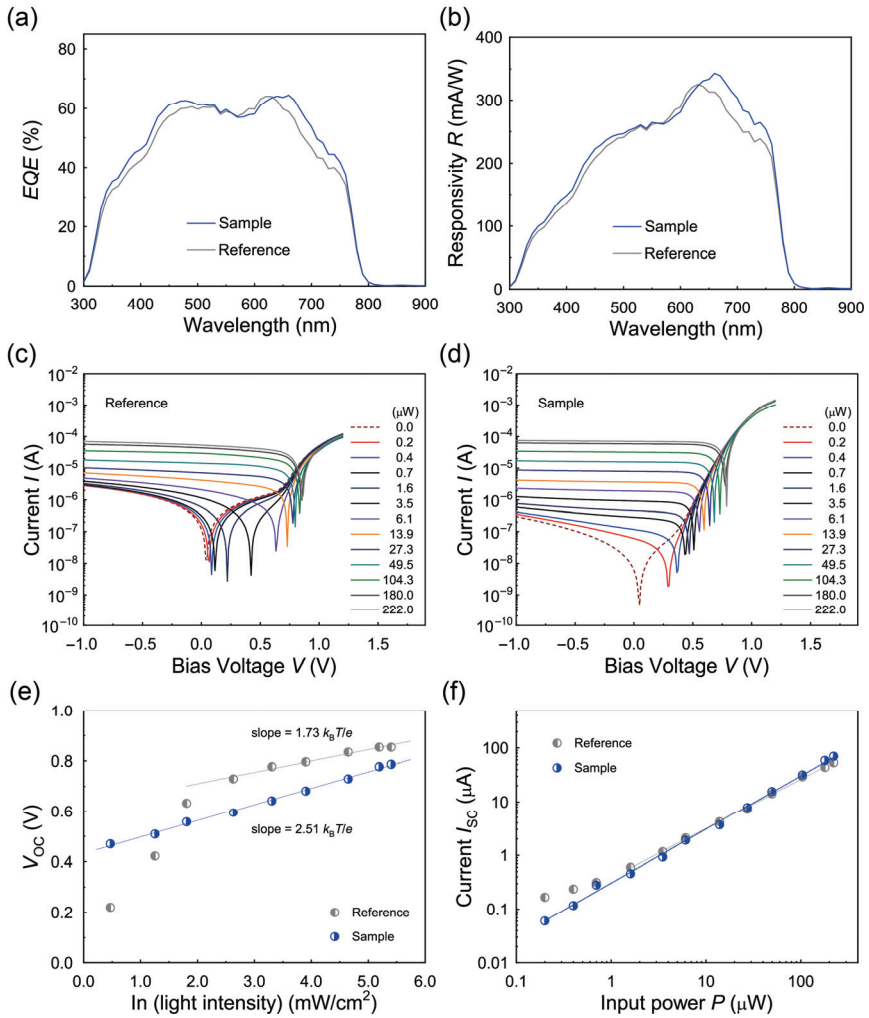

Figure 5. (**a**) *EQE* spectra of $MAPbI_3$ PVPDs without (Reference) and with (Sample) a PAA-PI interfacial layer. (**b**) R_λ at zero bias voltage for the Reference and Sample devices, comparing the $MAPbI_3$ PVPDs. (**c**,**d**) Photo *I-V* characteristics for the Reference device (**c**) and Sample device (**d**) under different intensity levels of 637 nm irradiation. (**e**) V_{OC} versus P (637 nm) for the Reference and Sample PVPDs. (**f**) I_{SC} as a function of P (637 nm) for the Reference and Sample devices.

The photocurrent characteristics of the PVPDs were further analyzed as a function of the applied bias voltage under varying incident light power levels (P) at a wavelength of λ = 637 nm. The results are presented in Figure 5c for the Reference device and in Figure 5d for the Sample device. Both V_{OC} and the short-circuit current (I_{SC}) increased with an increase in P. The relationship between V_{OC} and P, derived from the photocurrent versus applied bias voltage (photo *I-V*) curves and plotted on a semi-logarithmic scale in Figure 5e, was analyzed using the equation $V_{OC} \propto (nk_BT/e)\ln(P)$ to investigate trap-assisted recombination in the devices [54]. Here, k_B is the Boltzmann constant, T is the

temperature, and n is the ideality factor. Linear fitting of the V_{OC} data yielded an ideality factor of 1.73 for the Reference device, which is lower than the value of 2.51 for the Sample device. Typically, an n of 1.0 indicates bimolecular bulk recombination dominance, while $1.0 < n < 2.0$ suggests the presence of carrier-limited or trap-assisted recombinations, and $n > 2.0$ is associated with Shockley–Read–Hall (SRH) recombinations, often occurring in the bulk or at interfaces [18,55,56]. This analysis suggests that the Reference PVPD is governed by charge-carrier-limited recombinations, whereas the Sample device is primarily influenced by SRH recombinations. The PAA-PI interfacial layer in the Sample device effectively reduces hole-limited recombination pathways by enhancing the interfacial quality and facilitating a more efficient charge extraction process. The V_{bi} values of the PVPDs were then estimated using the coupled charge transport model with the equation $V_{bi} = -(nk_BT/e)\ln(J_0)$, where J_0 is the reverse saturation current density [11,18,57,58]. The V_{bi} value of the Sample device under P = 222 μW was approximately 0.61 V, much larger than that of 0.42 V for the Reference device, indicating effective charge selectivity by the PAA-PI-passivated PEDOT:PSS HIL and $PCBM_{60}$ ETL.

The dependence of I_{SC} on P was also extracted from the photo I-V curves (Figure 5d), and this relation is shown in Figure 5f. Here, I_{SC} increased linearly with a higher P due to the efficient charge separation and collection under the high-V_{bi} condition, even at zero bias. The Sample device exhibited higher I_{SC} and lower I_{dark} values than the Reference device due to the enhanced photo-excited carrier collection, which is critical for achieving high PD sensitivity [59]. Using these photocurrent data, R_λ at λ = 637 nm (R_{637}) under zero bias was re-estimated via

$$R_\lambda = \left(\frac{I_{PH}}{P}\right), \tag{2}$$

where $I_{PH} = I_{light} - I_{dark}$ is the net photocurrent. The estimated R_{637} for the Sample device was approximately 371 mA/W, significantly higher than that (~348 mA/W) of the Reference device, similar to the results for R_λ (Figure 5b), further confirming the superior PD performance of the Sample device with the PAA-PI interfacial layer.

Subsequently, the linearity of I_{SC} with P in the investigated PVPDs (Figure 5f) was analyzed using the power law $I_{SC} = \kappa \cdot P^\theta$, where κ is a proportional constant and θ is the power-law index [11,18,23,60]. Here, θ was estimated to be 0.997 for the Sample device, nearly ideal ($\theta \approx 1.0$) and higher than that (0.855) of the Reference device. The near-ideal θ for the Sample device indicates excellent linearity and underscores the high photosensitivity of the Sample device and the effective collection of photo-excited carriers, which are essential for high-performance photodetectors.

For broader practical applications in image sensors and photometers, achieving a large *LDR* is essential for photodetectors so that they can accurately detect light across a wide intensity spectrum. In this study, the *LDR* of the $MAPbI_3$ PVPDs was determined using the photocurrent data presented in Figure 5f and calculated based on the following relationship [17,23,59,61–63]:

$$LDR = 20\log\left(\frac{I_{PH}}{I_{dark}}\right) \tag{3}$$

At zero bias, the *LDR* value for the Sample device was approximately 103 dB, significantly surpassing the 72 dB observed for the Reference device. This result highlights the superior photoelectric conversion capability of the Sample device, along with excellent linearity across a wide range of incident light intensity levels. Furthermore, the *LDR* of the Sample device exceeds previously reported values (~90–120 dB) for $MAPbI_3$ perovskite photodetectors and even approaches those of commercial silicon photodetectors [16,17]. This improvement in the *LDR* performance demonstrates the beneficial role of the PAA-PI interfacial layer between the $MAPbI_3$ layer and the PEDOT:PSS HIL.

Another critical parameter in the evaluation of photodetectors is i_n. To estimate i_n, the I_{dark} value was measured at room temperature as a function of time under zero bias, with the i_n values subsequently extracted by means of an *FFT* analysis of the I_{dark} data [16,59,64–66]. Figure 6a displays the frequency-dependent i_n values for the Reference and Sample devices, revealing dominant frequency-independent white noise across the observed range. At a 1 Hz bandwidth (Δf), the i_n value for the Sample device was approximately 1.07 pA/Hz$^{1/2}$, significantly lower than the value of 43.5 pA/Hz$^{1/2}$ observed in the Reference device. This substantial reduction in i_n underscores the effective suppression of dark leakage and noise currents by the PAA-PI interfacial layers, emphasizing their potential for use in high-performance perovskite photodetectors.

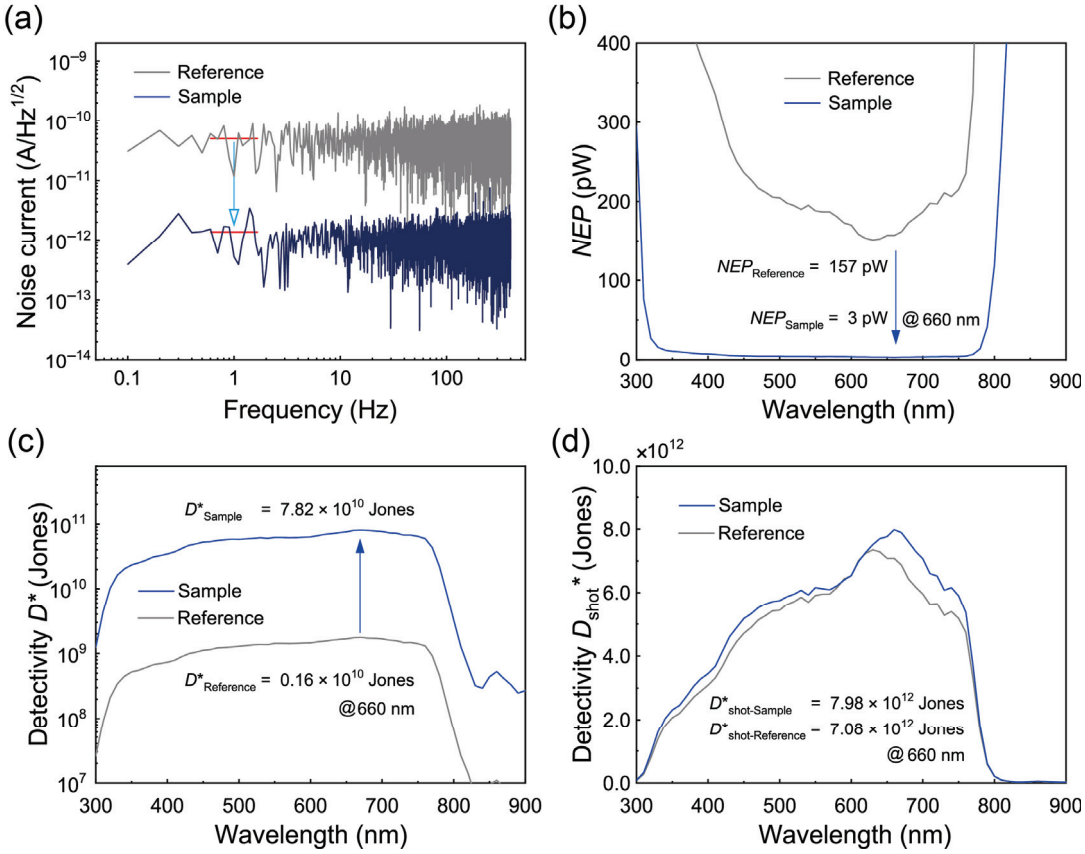

Figure 6. (**a**) Frequency-dependent i_n characteristics derived from the *FFT* analysis of I_{dark} measurements for the Reference and Sample devices, showing dominant frequency-independent white noise behavior. (**b**) Comparison of *NEP* spectra between the Sample and Reference devices. (**c**) D^* spectra calculated from zero-bias i_n measurements for the $MAPbI_3$ PVPDs. (**d**) D^*_{shot} spectra derived from zero-bias I_{dark} data for the Reference and Sample devices.

For a further comparison, the shot noise levels ($i_{n,s}$) caused by thermal agitation were estimated for each device using the relationship $i_{n,s} = \sqrt{2eI_{dark}}$ [63,65,66]. The calculated value of $i_{n,s}$ for the Sample device was 10.5 fA/Hz$^{1/2}$, slightly lower than the value of 10.8 fA/Hz$^{1/2}$ observed in the Reference device. These $i_{n,s}$ values were two orders of magnitude lower than the observed i_n values, suggesting that other thermal noise sources, as opposed to shot noise, are the dominant contributors to the overall noise characteristics in these PVPDs [64].

The noise-equivalent power (*NEP*), which quantifies the minimum detectable optical power, was then determined for the PVPDs as $NEP = i_n / R_\lambda$ (Figure 6b) [16–18,59,61,63,67]. At zero bias, the *NEP* for the Sample device was approximately 3 pW at approximately 660 nm compared to 157 pW for the Reference device, confirming the improved sensitivity

of the Sample device for low-power signal detection. Based on the *NEP* values, D^* was evaluated to assess the ability of the PVPDs to detect weak signals. This parameter was calculated as follows:

$$D^* = \frac{\sqrt{A \cdot B}}{NEP} = R_\lambda \cdot \frac{\sqrt{A \cdot B}}{i_n}, \quad (4)$$

where A is the effective area and B is the bandwidth (1 Hz) [16–18,23,59,61–63,65–68]. Figure 6c shows the D^* spectra, revealing a peak D^* of nearly 0.16×10^{10} Jones for the Reference device and a significantly higher value of approximately 7.82×10^{10} Jones for the Sample device. This represents a 49-fold increase, demonstrating the exceptional ability of the Sample device to detect weak signals. Notably, the D^* value of the Sample device exceeds typical values reported for self-powered $MAPbI_3$ perovskite PVPDs and is comparable to those of commercial silicon photodetectors [30,65,66,68].

In addition, previous studies have conventionally assumed that $i_{n,s}$ is the dominant noise source, leading to the calculation of specific detectivity based on J_{dark} and R_λ (D^*_{shot}) with the relationship $D^*_{shot} \sim \frac{R_\lambda}{\sqrt{2eJ_{dark}}}$ [59,62,63,65]. Using this approach, the estimated D^*_{shot} for the Sample device was approximately 7.98×10^{12} Jones, significantly higher than the value of 7.08×10^{12} Jones observed for the Reference device. Furthermore, this detectivity value surpasses those previously reported for self-powered PDs utilizing $MAPbI_3$ as the light-absorbing layer with a PEDOT:PSS HIL [18], underscoring the critical role of the PAA-PI interfacial layer in enhancing device detectivity capabilities. These results indicate that the PAA-PI interfacial layer significantly improves the interfacial quality and charge collection, providing a basis for further advances in perovskite PVPDs and high-sensitivity photodetectors.

The D^*_{shot} value of our $MAPbI_3$-based Sample PD, incorporating the PAA-PI interfacial layer, reached 7.98×10^{12} Jones, surpassing or matching recently reported values for similar self-powered perovskite PDs, as shown in Table 2. Compared to previously reported devices using a PEDOT:PSS-based HIL, such as PEDOT:PSS/$MAPbI_xBr_{1-x}$:RhB (6.7×10^{11} Jones) and PEDOT:PSS/SnPb perovskite (1.6×10^9 Jones), our approach demonstrates superior performance. Furthermore, when compared to devices utilizing a NiO_x-based HTL, such as NiO_x/PMMA/$MAPbI_3$ (4.5×10^{13} Jones) and NiO_x/PbI_2/Perovskite (4.0×10^{12} Jones), our Sample device achieves slightly lower but comparable detectivity levels. These results emphasize the significant role of the PAA-PI interfacial layer in enhancing the hole extraction efficiency, reducing recombination losses, and facilitating improved PD performance.

Table 2. Comparison of the critical parameters of various recent self-powered perovskite PDs.

Interfacial Layer	Device Configuration	Wavelength (nm)	R_λ (mA/W)	D^*_{shot} (Jones)	Rise/Decay Time	Ref.
None	ITO/$MAPbI_3$/P3HT/Ni/Au	532	6.6	5×10^9	35/36 ms	[69]
None	ITO/PEDOT:PSS/$MAPbI_xBr_{1-x}$/PCBM/C_{60}/LiF/Al	665	7.6	6.7×10^{11}	140/190 ms	[70]
None	ITO/NiO/$CH_3NH_3PbI_3$/PCBM/ZnO NPs/ BCP/Al	594	360	2.0×10^{11}	0.9/1.8 ms	[18]
Bottom	ITO/NiO_x/Nb_2CT_x/$MAPbI_3$/PCBM/BCP/Ag	656	860	1.58×10^{12}	29.2/98.2 µs	[71]
Bottom	ITO/NiO_x/PbI_2/Perovskite/ C_{60}/BCP/Ag	-	360	4.0×10^{12}	-	[72]
Top	ITO/SnO/Perovskite/P3HT/ spiro-OMeTAD/Ag	700	410	0.61×10^{12}	0.19/0.21 ms	[23]
Top	ITO/NiO_x/$MAPbI_3$/PMMA/$PCBM_{60}$/ZnO/BCP/Al	637	401	4.5×10^{13}	50/17 µs	[34]
Both	ITO/NiO_x/PMMA/$MAPbI_3$/PMMA/$PCBM_{60}$/ ZnO/BCP/Al	637	401	1.0×10^{14}	57/18 µs	[35]
Bottom	ITO/PEDOT:PSS/PAA-PI/$MAPbI_3$/$PCBM_{60}$/BCP/Ag	660	343	7.98×10^{12}	61/18 µs	This work

3.5. Dynamic Characteristics of $MAPbI_3$ PVPDs with PAA-PI Interfacial Layers

To investigate the dynamic characteristics of the PVPDs, we measured their temporal photoresponses at zero bias voltage under incident monochromatic light (λ = 637 nm, P = 190 μW) modulated at a frequency of 2 kHz, as shown in Figure 7a. The Sample device exhibited a notably stronger photocurrent response compared to the Reference device. The rise (τ_r) and decay (τ_d) response times of the devices were determined by measuring the time required for the photocurrent signal amplitude to transition between 10% and 90% of its peak value during the rising and decaying edges, respectively. The response times for the Sample device were approximately 61 μs for τ_r and 18 μs for τ_d, similar to the values of approximately 67 μs and 20 μs observed for the Reference device. Notably, these response times are shorter than those typically reported for $MAPbI_3$-based PDs [23]. The decay-time-based bandwidth (f_B) was also estimated using the relationship $f_B = 0.443/\tau_d$ [64], resulting in comparable frequency-based bandwidths of approximately 24.6 kHz for the Sample device and 22.2 kHz for the Reference device.

Subsequently, the −3 dB cutoff bandwidth (f_{-3dB}) was measured, yielding values of 10.7 kHz for the Reference device and 12.9 kHz for the Sample device, as shown in Figure 7c. These f_{-3dB} and f_B values indicate that the PAA-PI interfacial layer slightly but clearly affects the dynamic properties of the perovskite layer. Thus, further optimization of the Sample device architecture may improve the response speed of Sample $MAPbI_3$ PVPDs.

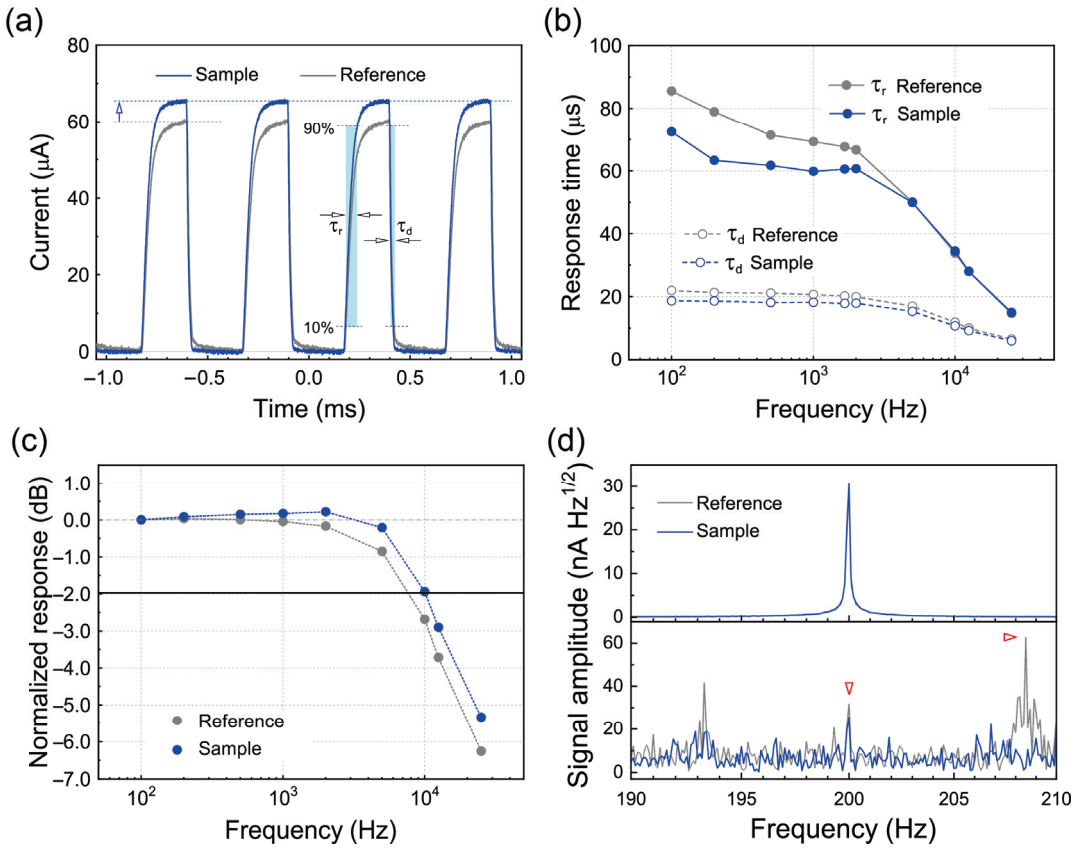

Figure 7. (**a**) Temporal photoresponses of the Reference and Sample devices at zero bias during on/off cycling of incident light (λ = 637 nm, P = 190 μW) at a frequency of 2 kHz. (**b**) τ_r and τ_d as a function of the modulation frequency for the $MAPbI_3$ PVPDs. (**c**) Normalized response as a function of the incident light modulation frequency (λ = 637 nm, P = 190 μW). (**d**) Signal spectra of the Reference and Sample devices at zero bias during on/off cycling of weak incident light (λ = 637 nm) at 200 Hz, displayed for illumination power levels of P = 20 W (top panel) and P = 2 W (bottom panel).

Finally, we evaluated the weak-light detection capabilities of the $MAPbI_3$ PVPDs by measuring the signal spectra of the Reference and Sample devices under self-powered conditions with low-intensity illumination. In these measurements, the 637 nm illumination was modulated at 200 Hz at a specific power level, and representative signal spectra are shown in Figure 7d. At an input power P of 20 nW, both devices showed a clear response to the modulated light, with the Sample device producing a stronger output signal than the Reference device. However, at a lower power level of 2 nW, only the Sample device showed a detectable response above the background noise, while the Reference device did not show a signal response comparable to or lower than the background noise signals, as shown in the panel at the bottom of the figure. These results clearly demonstrate that the PAA-PI interfacial layer significantly enhances the weak-light detection capability of the $MAPbI_3$ PVPD compared to the Reference device. Future investigations will focus on optimizing this weak-light detection performance further by improving the ETL and other functional layers of $MAPbI_3$ PVPDs with PAA-PI interfacial layers.

Thus, the results presented here demonstrate that PAA-PI interfacial layers significantly enhance the film quality of solution-processed $MAPbI_3$ perovskite films, offering a promising pathway for further improvement of the performance of PVPDs. The exceptional sensitivity and performance achieved with the PAA-PI interfacial layers establish a robust foundation for developing highly sensitive, self-powered perovskite photodetectors.

While this study provides substantial evidence of the improved performance of perovskite PDs incorporating a PAA-PI interfacial layer, impedance spectroscopy (IS) measurements were not performed. An IS analysis would offer valuable insights into the charge transfer resistance, recombination dynamics, and interfacial capacitance [73]. Future studies will incorporate an IS analysis to provide a more comprehensive understanding of the interfacial charge transfer mechanisms and their impact on device performance. Future advancements can be realized through targeted material optimization of both the organohalide perovskite layer and other functional layers. In particular, double-sided passivation strategies present significant potential for further improving device performance. Unlike single-sided passivation, which primarily addresses defects and trap states at the bottom interface between the perovskite active layer and the HIL (or HTL), double-sided approaches can simultaneously suppress surface trap states, reduce non-radiative recombination losses, and improve the charge extraction efficiency. The effective implementation of double-sided passivation using insoluble PAA-PI layers can address challenges such as maintaining layer stability during subsequent deposition processes. The rational design and optimization of polymeric interfacial layers, particularly those resistant to perovskite precursor inks, will be essential for achieving reliable double-sided passivation. Future studies will build upon the insights gained from this single-sided passivation approach to optimize device performance and long-term stability levels further, paving the way for next-generation perovskite photodetectors.

4. Conclusions

In summary, this study demonstrates the enhanced performance of solution-processed, self-powered $MAPbI_3$ perovskite PVPDs achieved by incorporating PAA-PI interfacial layers at the interface between the PEDOT:PSS HIL and the $MAPbI_3$ active layer. The PAA-PI interfacial layer significantly improves the quality of the $MAPbI_3$ interface, resulting in larger grain sizes, a smoother surface morphology, and fewer film defects. These improvements ultimately reduce non-radiative recombination losses, lower the dark leakage current, and suppress i_n. Compared to conventional devices lacking interfacial layers, $MAPbI_3$ PVPDs with a PAA-PI interfacial layer exhibit enhanced charge extraction and collection efficiencies, achieving an increased *PCE* of 11.8%. Additionally, the self-powered $MAPbI_3$

PVPD demonstrates outstanding photodetector characteristics, including an exceptionally high peak D^* of 7.98 × 10^{12} Jones (derived from I_{dark}) and 7.82 × 10^{10} Jones (derived from i_n), a significantly reduced *NEP* of ~3 pW, a high peak R_λ of 343 mA/W, and an extensive *LDR* of ~103 dB. Furthermore, the devices exhibit fast photoresponse dynamics, with τ_r and τ_d values of ~61 μs and ~18 μs, respectively. These results underscore the critical role of the PAA-PI interfacial layer in enhancing both optoelectronic and noise suppression properties, establishing a robust foundation for high-performance, self-powered $MAPbI_3$ PVPDs. The successful integration of PAA-PI interfacial layers also paves the way for advanced interfacial-engineered hybrid organohalide perovskite heterostructures, with broad applicability in next-generation optoelectronic and photodetection systems. These include high-sensitivity, low-power photodetectors, waveguide-integrated PDs, imaging sensors, and optical nanophotodetectors.

Author Contributions: Conceptualization, W.K. and J.P.; Methodology, W.K. and J.P.; Formal analysis and data curation, W.K., H.J., J.P., and K.L.; Writing—original draft preparation, W.K. and J.P.; Writing—review and editing, W.K., J.P., H.J., K.L., S.Y., E.H.C. and B.P.; Project administration, B.P. and E.H.C. All authors have read and agreed to the published version of the manuscript.

Funding: This research was funded by the National Research Foundation of Korea (RS-2024-00350044, 2021R1A6A1A03038785) and by the Excellent Researcher Support project of Kwangwoon University (2024). J.P. and S.Y. acknowledge support from the Office of Naval Research (ONR) (N00014-23-1-2659).

Institutional Review Board Statement: Not applicable.

Data Availability Statement: The original contributions presented in this study are included in the article. Further inquiries can be directed to the corresponding author.

Conflicts of Interest: The authors declare no conflicts of interest.

Appendix A

Figure A1 shows the normalized *PCE* characteristics of $MAPbI_3$ perovskite devices without (Reference) and with a PAA-PI interfacial layer (Sample) over different storage times. The *PCE* of the Reference device decreases significantly as the storage time increases, while the Sample device shows comparatively smaller decreases even after prolonged storage, indicating improved stability. The decreases in the *PCE* shown in Figure A1 were analyzed using the stretched exponential decay function [74]: $y = \mathrm{Exp}[-(t/\tau)^{\beta}]$, where τ and β are the characteristic time and exponent, respectively. The dashed lines in the figure represent theoretical curves based on the best-fit parameters: for the Reference device, τ = 962 h and β = 1.00, whereas for the Sample device, τ = 3357 h and β = 0.72. This analysis shows that the PAA-PI interfacial layer significantly improves the storage stability of the Sample device, resulting in a 3.5-fold increase in the characteristic time τ compared to the Reference device.

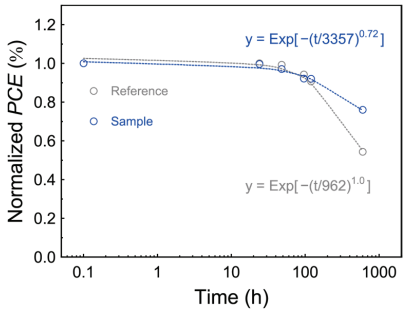

Figure A1. Decreases in normalized *PCE* values for the Reference and Sample $MAPbI_3$ PVPD devices as a function of the storage time. The dashed curves represent theoretical fits derived from the best-fit parameters of the stretched exponential function.

References

1. Kojima, A.; Teshima, K.; Shirai, Y.; Miyasaka, T. Organometal Halide Perovskites as Visible-Light Sensitizers for Photovoltaic Cells. *J. Am. Chem. Soc.* **2009**, *131*, 6050–6051. [CrossRef] [PubMed]
2. Lee, M.M.; Teuscher, J.; Miyasaka, T.; Murakami, T.N.; Snaith, H.J. Efficient Hybrid Solar Cells Based on Meso-Superstructured Organometal Halide Perovskites. *Science* **2012**, *338*, 643–647. [CrossRef]
3. Bi, C.; Wang, Q.; Shao, Y.; Yuan, Y.; Xiao, Z.; Huang, J. Non-wetting surface-driven high-aspect-ratio crystalline grain growth for efficient hybrid perovskite solar cells. *Nat. Commun.* **2015**, *6*, 7747. [CrossRef]
4. Momblona, C.; Gil-Escrig, L.; Bandiello, E.; Hutter, E.M.; Sessolo, M.; Lederer, K.; Blochwitz-Nimoth, J.; Bolink, H.J. Efficient vacuum deposited p-i-n and n-i-p perovskite solar cells employing doped charge transport layers. *Energy Environ. Sci.* **2016**, *9*, 3456–3463. [CrossRef]
5. Eperon, G.E.; Leijtens, T.; Bush, K.A.; Prasanna, R.; Green, T.; Wang, J.T.-W.; McMeekin, D.P.; Volonakis, G.; Milot, R.L.; May, R.; et al. Perovskite-perovskite tandem photovoltaics with optimized bandgaps. *Science* **2016**, *354*, 861–865. [CrossRef]
6. Yang, W.S.; Park, B.-W.; Jung, E.H.; Jeon, N.J.; Kim, Y.C.; Lee, D.U.; Shin, S.S.; Seo, J.; Kim, E.K.; Noh, J.H.; et al. Iodide management in formamidinium-lead-halide–based perovskite layers for efficient solar cells. *Science* **2017**, *356*, 1376–1379. [CrossRef] [PubMed]
7. Choi, K.; Choi, H.; Min, J.; Kim, T.; Kim, D.; Son, S.Y.; Kim, G.-W.; Choi, J.; Park, T. A Short Review on Interface Engineering of Perovskite Solar Cells: A Self-Assembled Monolayer and Its Roles. *Sol. RRL* **2020**, *4*, 1900251. [CrossRef]
8. NREL. Best Research-Cell Efficiency Chart. National Renewable Energy Laboratory. Available online: https://www.nrel.gov/pv/cell-efficiency.html/ (accessed on 8 December 2024).
9. Saliba, M.; Matsui, T.; Seo, J.-Y.; Domanski, K.; Correa-Baena, J.-P.; Nazeeruddin, M.K.; Zakeeruddin, S.M.; Tress, W.; Abate, A.; Hagfeldt, A.; et al. Cesium-containing triple cation perovskite solar cells: Improved stability, reproducibility and high efficiency. *Energy Environ. Sci.* **2016**, *9*, 1989–1997. [CrossRef]
10. Cheng, J.; Zhang, H.; Zhang, S.; Ouyang, D.; Huang, Z.; Nazeeruddin, M.K.; Hou, J.; Choy, W.C.H. Highly efficient planar perovskite solar cells achieved by simultaneous defect engineering and formation kinetic control. *J. Mater. Chem. A* **2018**, *6*, 23865–23874. [CrossRef]
11. Cao, Q.; Li, Y.; Zhang, H.; Yang, J.; Han, J.; Xu, T.; Wang, S.; Wang, Z.; Gao, B.; Zhao, J.; et al. Efficient and stable inverted perovskite solar cells with very high fill factors via incorporation of star-shaped polymer. *Sci. Adv.* **2021**, *7*, eabg0633. [CrossRef]
12. Vasilopoulou, M.; Fakharuddin, A.; Coutsolelos, A.G.; Falaras, P.; Argitis, P.; Yusoff, A.R.B.M.; Nazeeruddin, M.K. Molecular materials as interfacial layers and additives in perovskite solar cells. *Chem. Soc. Rev.* **2020**, *49*, 4496–4526. [CrossRef] [PubMed]
13. He, M.; Li, B.; Cui, X.; Jiang, B.; He, Y.; Chen, Y.; O'Neil, D.; Szymanski, P.; El-Sayed, M.A.; Huang, J.; et al. Meniscus-assisted solution printing of large-grained perovskite films for high-efficiency solar cells. *Nat. Commun.* **2017**, *8*, 16045. [CrossRef] [PubMed]
14. Bae, I.-G.; Park, B. All-self-metered solution-coating process in ambient air for the fabrication of efficient, large-area, and semitransparent perovskite solar cells. *Sustain. Energy Fuels* **2020**, *4*, 3115–3128. [CrossRef]
15. Shen, L.; Fang, Y.; Wang, D.; Bai, Y.; Deng, Y.; Wang, M.; Lu, Y.; Huang, J. A Self-Powered, Sub-nanosecond-Response Solution Processed Hybrid Perovskite Photodetector for Time-Resolved Photoluminescence-Lifetime Detection. *Adv. Mater.* **2016**, *28*, 10794–10800. [CrossRef]
16. Fang, Y.; Huang, J. Resolving Weak Light of Sub-picowatt per Square Centimeter by Hybrid Perovskite Photodetectors Enabled by Noise Reduction. *Adv. Mater.* **2015**, *27*, 2804–2810. [CrossRef]
17. Zhao, Y.; Li, C.; Shen, L. Recent advances on organic-inorganic hybrid perovskite Photodetectors with fast response. *InfoMat* **2019**, *1*, 164–182. [CrossRef]
18. Afzal, A.M.; Bae, I.-G.; Aggarwal, Y.; Park, J.; Jeong, H.-R.; Choi, E.H.; Park, B. Highly efficient self-powered perovskite photodiode with an electron-blocking hole-transport NiO_x layer. *Sci. Rep.* **2021**, *11*, 169. [CrossRef]
19. Bi, D.; Tress, W.; Dar, M.I.; Gao, P.; Luo, J.; Renevier, C.; Schenk, K.; Abate, A.; Giordano, F.; Baena, J.-P.C.; et al. Efficient luminescent solar cells based on tailored mixed-cation perovskites. *Sci. Adv.* **2016**, *2*, e1501170. [CrossRef]
20. Zheng, X.; Chen, B.; Dai, J.; Fang, Y.; Bai, Y.; Lin, Y.; Wei, H.; Zeng, X.C.; Huang, J. Defect passivation in hybrid perovskite solar cells using quaternary ammonium halide anions and cations. *Nat. Energy* **2017**, *2*, 17102. [CrossRef]
21. Aydin, E.; De Bastiani, M.; De Wolf, S. Defect and Contact Passivation for Perovskite Solar Cells. *Adv. Mater.* **2019**, *31*, 1900428. [CrossRef]
22. Cai, F.; Cai, J.; Yang, L.; Li, W.; Gurney, R.S.; Yi, H.; Iraqi, A.; Liu, D.; Wang, T. Molecular engineering of conjugated polymers for efficient hole transport and defect passivation in perovskite solar cells. *Nano Energy* **2018**, *45*, 28–36. [CrossRef]
23. Wang, D.; Xu, W.; Min, L.; Tian, W.; Li, L. Interfacial Passivation and Energy Level Alignment Regulation for Self-Powered Perovskite Photodetectors with Enhanced Performance and Stability. *Adv. Mater. Interfaces* **2022**, *9*, 2101766. [CrossRef]
24. Taguchi, M.; Suzuki, A.; Ueoka, N.; Oku, T. Effects of poly(methyl methacrylate) addition to perovskite photovoltaic devices. *AIP Conf. Proc.* **2019**, *2067*, 020018.
25. Son, D.-Y.; Lee, J.-W.; Choi, Y.J.; Jang, I.-H.; Lee, S.; Yoo, P.J.; Shin, H.; Ahn, N.; Choi, M.; Kim, D.; et al. Self-formed grain boundary healing layer for highly effcient $CH_3NH_3PbI_3$ perovskite solar cells. *Nat. Energy* **2016**, *1*, 16081. [CrossRef]

26. Piao, C.; Xi, J.; Choi, M. Directionally Selective Polyhalide Molecular Glue for Stable Inverted Perovskite Solar Cells. *Sol. RRL* **2020**, *4*, 2000244. [CrossRef]
27. Kim, M.; Motti, S.G.; Sorrentino, R.; Petrozza, A. Enhanced solar cell stability by hygroscopic polymer passivation of metal halide perovskite thin film. *Energy Environ. Sci.* **2018**, *11*, 2609–2619. [CrossRef]
28. Wang, K.; Yu, B.; Lin, C.; Yao, R.; Yu, H.; Wang, H. Synergistic Passivation on Buried Interface for Highly Efficient and Stable p-i-n Perovskite Solar Cells. *Small* **2024**, *20*, 42. [CrossRef]
29. Li, L.; Wei, M.; Carnevali, V.; Zeng, H.; Zeng, M.; Liu, R.; Lempesis, N.; Eickemeyer, F.T.; Luo, L.; Agosta, L.; et al. Buried-Interface Engineering Enables Efficient and 1960-Hour ISOS-L-2I Stable Inverted Perovskite Solar Cells. *Adv. Mater.* **2024**, *36*, 2303869. [CrossRef]
30. Park, J.; Aggarwal, Y.; Kim, W.; Sharma, S.; Choi, E.H.; Park, B. Self-powered $CH_3NH_3PbI_3$ perovskite photodiode with a noise-suppressible passivation layer of poly(methyl methacrylate). *Opt. Express* **2023**, *31*, 1202–1213. [CrossRef]
31. Chang, A.-C.; Wu, Y.-S.; Chen, W.-C.; Weng, Y.-H.; Lin, B.-H.; Chueh, C.-C.; Lin, Y.-C.; Chen, W.-C. Modulating the Photoresponsivity of Perovskite Photodetectors through Interfacial Engineering of Self-Assembled Monolayers. *Adv. Opt. Mater.* **2024**, *12*, 2301789. [CrossRef]
32. Zhao, Y.; Jiao, S.; Yang, S.; Wang, D.; Gao, S.; Wang, J. Achieving Low-Cost and High-Performance Flexible $CsPbIBr_2$ Perovskite Photodetectors Arrays with Imaging System via Dual Interfacial Optimization and Structural Design. *Adv. Opt. Mater.* **2024**, *12*, 2400019. [CrossRef]
33. Khan, A.A.; Kumar, N.; Jung, U.; Heo, W.; Tan, Z.; Park, J. Performance and Stability Enhancement of Perovskite Photodetectors by Additive and Interface Engineering using a Dual-Functional PPS Zwitterion. *Nanoscale Horiz.* **2023**, *8*, 1577–1587. [CrossRef] [PubMed]
34. Kim, W.; Park, J.; Aggarwal, Y.; Sharma, S.; Choi, E.H.; Park, B. Highly Efficient and Stable Self-Powered Perovskite Photodiode by Cathode-Side Interfacial Passivation with Poly(Methyl Methacrylate). *Nanomaterials* **2023**, *13*, 619. [CrossRef]
35. Aggarwal, Y.; Park, J.; Kim, W.; Sharma, S.; Jeong, H.; Kim, M.G.; Kil, J.; Choi, E.H.; Park, B. Highly efficient self-powered $CH_3NH_3PbI_3$ perovskite photodiode with double-sided poly(methyl methacrylate) passivation layers. *Sol. Energy Mater. Sol. Cells* **2024**, *270*, 112815. [CrossRef]
36. Chaudhary, B.; Kulkarni, A.; Jena, A.K.; Ikegami, M.; Udagawa, Y.; Kunugita, H.; Ema, K.; Miyasaka, T. Poly(4-Vinylpyridine)-Based Interfacial Passivation to Enhance Voltage and Moisture Stability of Lead Halide Perovskite Solar Cells. *ChemSusChem* **2017**, *10*, 2473. [CrossRef]
37. Yang, F.; Lim, H.E.; Wang, F.; Ozaki, M.; Shimazaki, A.; Liu, J.; Mohamed, N.B.; Shinokita, K.; Miyauchi, Y.; Wakamiya, A.; et al. Roles of Polymer Layer in Enhanced Photovoltaic Performance of Perovskite Solar Cells via Interface Engineering. *Adv. Mater. Interfaces* **2018**, *5*, 1701256. [CrossRef]
38. Peng, J.; Khan, J.I.; Liu, W.; Ugur, E.; Duong, T.; Wu, Y.; Shen, H.; Wang, K.; Dang, H.; Aydin, E.; et al. A Universal Double-Side Passivation for High Open-Circuit Voltage in Perovskite Solar Cells: Role of Carbonyl Groups in Poly(methyl methacrylate). *Adv. Energy Mater.* **2018**, *8*, 1801208. [CrossRef]
39. Kim, H.; Lee, K.S.; Paik, M.J.; Lee, D.Y.; Lee, S.-U.; Choi, E.; Yun, J.S.; Seok, S.I. Polymethyl Methacrylate as an Interlayer Between the Halide Perovskite and Copper Phthalocyanine Layers for Stable and Efficient Perovskite Solar Cells. *Adv. Funct. Mater.* **2022**, *32*, 2110473. [CrossRef]
40. Jo, B.; Han, G.S.; Yu, H.M.; Choi, J.; Zhu, J.; Ahn, T.K.; Namkoong, G.; Jung, H.S. Composites of cross-linked perovskite/polymer with sodium borate for efficient and stable perovskite solar cells. *J. Mater. Chem. A* **2022**, *10*, 14884–14893. [CrossRef]
41. Peng, J.; Wu, Y.; Ye, W.; Jacobs, D.A.; Shen, H.; Fu, X.; Wan, Y.; Duong, T.; Wu, N.; Barugkin, C.; et al. Interface passivation using ultrathin polymer–fullerene films for high-efficiency perovskite solar cells with negligible hysteresis. *Energy Environ. Sci.* **2017**, *10*, 1792–1800. [CrossRef]
42. Park, J.; Kim, W.; Aggawal, Y.; Shin, K.; Choi, E.H.; Park, B. Highly Efficient and Stable Organic Light-Emitting Diodes with Inner Passivating Hole-Transfer Interlayers of Poly(amic acid)-Polyimide Copolymer. *Adv. Sci.* **2022**, *9*, 2105851. [CrossRef] [PubMed]
43. Ji, D.; Li, T.; Zou, Y.; Chu, M.; Zhou, K.; Liu, J.; Tian, G.; Zhang, Z.; Zhang, X.; Li, L.; et al. Copolymer dielectrics with balanced chain-packing density and surface polarity for high-performance flexible organic electronics. *Nat. Commun.* **2018**, *9*, 2339. [CrossRef] [PubMed]
44. He, J.-J.; Yang, H.-X.; Zheng, F.; Yang, S.-Y. Dielectric Properties of Fluorinated Aromatic Polyimide Films with Rigid Polymer Backbones. *Polymers* **2022**, *14*, 649. [CrossRef]
45. Ji, D.; Xu, X.; Jiang, L.; Amirjalayer, S.; Jiang, L.; Zhen, Y.; Zou, Y.; Yao, Y.; Dong, H.; Yu, J.; et al. Surface polarity and self-structured nanogrooves collaborative oriented molecular packing for high crystallinity towards efficient charge transport. *J. Am. Chem. Soc.* **2017**, *139*, 2734–2740. [CrossRef]
46. Zhang, K.; Yu, Q.; Zhu, L.; Liu, S.; Chi, Z.; Chen, X.; Zhang, Y.; Xu, J. The Preparations and Water Vapor Barrier Properties of Polyimide Films Containing Amide Moieties. *Polymers* **2017**, *9*, 677. [CrossRef]

47. Zhang, M.; Chen, Q.; Xue, R.; Zhan, Y.; Wang, C.; Lai, J.; Yang, J.; Lin, H.; Yao, J.; Li, Y.; et al. Reconfiguration of interfacial energy band structure for high-performance inverted structure perovskite solar cells. *Nat. Commun.* **2019**, *10*, 4593. [CrossRef]
48. Muscarella, L.A.; Hutter, E.M.; Sanchez, S.; Dieleman, C.D.; Savenije, T.J.; Hagfeldt, A.; Saliba, M.; Ehrler, B. Crystal Orientation and Grain Size: Do They Determine Optoelectronic Properties of $MAPbI_3$ Perovskite? *J. Phys. Chem. Lett.* **2019**, *10*, 6010–6018. [CrossRef]
49. Sun, W.; Peng, H.; Li, Y.; Yan, W.; Liu, Z.; Bian, Z.; Huang, C. Solution-Processed Copper Iodide as an Inexpensive and Effective Anode Buffer Layer for Polymer Solar Cells. *J. Phys. Chem. C* **2014**, *118*, 16806–16812. [CrossRef]
50. Chen, Q.; Wang, C.; Li, Y.; Chen, L. Interfacial Dipole in Organic and Perovskite Solar Cells. *J. Am. Chem. Soc.* **2020**, *142*, 18281–18292. [CrossRef]
51. Bube, R.H. Trap Density Determination by Space-Charge-Limited Currents. *J. Appl. Phys.* **1962**, *33*, 1733–1737. [CrossRef]
52. Sworakowski, J.; Ferreira, G.F.L. Space-charge-limited currents and trap-filled limit in one-dimensional insulator. *J. Phys. D Appl. Phys.* **1984**, *17*, 135–139. [CrossRef]
53. Tvingstedt, K.; Escrig, L.G.; Momblona, C.; Rieder, P.; Kiermasch, D.; Sessolo, M.; Baumann, A.; Bolink, H.J.; Dyakonov, V. Removing Leakage and Surface Recombination in Planar Perovskite Solar Cells. *ACS Energy Lett.* **2017**, *2*, 424–430. [CrossRef]
54. Fu, J.; Yang, Q.; Huang, P.; Chung, S.; Cho, K.; Kan, Z.; Liu, H.; Lu, X.; Lang, Y.; Lai, H.; et al. Rational molecular and device design enables organic solar cells approaching 20% efficiency. *Nat. Commun.* **2024**, *15*, 1830. [CrossRef] [PubMed]
55. Courtier, N.E. Interpreting Ideality Factors for Planar Perovskite Solar Cells: Ectypal Diode Theory for Steady-State Operation. *Phys. Rev. Appl.* **2020**, *14*, 024031. [CrossRef]
56. Sarritzu, V.; Sestu, N.; Marongiu, D.; Chang, X.; Masi, S.; Rizzo, A.; Colella, S.; Quochi, F.; Saba, M.; Mura, A.; et al. Optical determination of Shockley-Read-Hall and interface recombination currents in hybrid perovskites. *Sci. Rep.* **2017**, *7*, 44629. [CrossRef]
57. Speirs, M.J.; Dirin, D.N.; Abdu-Aguye, M.; Balazs, D.M.; Kovalenko, M.V.; Loi, M.A. Temperature dependent behaviour of lead sulfide quantum dot solar cells and films. *Energy Environ. Sci.* **2016**, *9*, 2916–2924. [CrossRef]
58. Ryu, S.; Nguyen, D.C.; Ha, N.Y.; Park, H.J.; Ahn, Y.H.; Park, J.-Y.; Lee, S. Light Intensity-dependent Variation in Defect Contributions to Charge Transport and Recombination in a Planar $MAPbI_3$ Perovskite Solar Cell. *Sci. Rep.* **2019**, *9*, 19846. [CrossRef]
59. Dou, L.; Yang, Y.; You, J.; Hong, Z.; Chang, W.-H.; Li, G.; Yang, Y. Solution-processed hybrid perovskite photodetectors with high detectivity. *Nat. Commun.* **2014**, *5*, 5404. [CrossRef]
60. Lu, H.; Tian, W.; Cao, F.; Ma, Y.; Gu, B.; Li, L. A Self-Powered and Stable All-Perovskite Photodetector–Solar Cell Nanosystem. *Adv. Funct. Mater.* **2016**, *26*, 1296–1302. [CrossRef]
61. Veeramalai, C.P.; Feng, S.; Zhang, X.; Pammi, S.V.N.; Pecunia, V.; Li, C. Lead–halide perovskites for next-generation self powered photodetectors: A comprehensive review. *Photonics Res.* **2021**, *9*, 968–991. [CrossRef]
62. Gong, X.; Tong, M.; Xia, Y.; Cai, W.; Moon, J.S.; Cao, Y.; Yu, G.; Shieh, C.-L.; Nilsson, B.; Heeger, A.J. High-Detectivity Polymer Photodetectors with Spectral Response from 300 nm to 1450 nm. *Science* **2009**, *325*, 1665–1667. [CrossRef] [PubMed]
63. Wang, Y.; Liu, Y.; Cao, S.; Wang, J. A review on solution-processed perovskite/ organic hybrid photodetectors. *J. Mater. Chem. C* **2021**, *9*, 5302–5322. [CrossRef]
64. Xue, J.; Zhu, Z.; Xu, X.; Gu, Y.; Wang, S.; Xu, L.; Zou, Y.; Song, J.; Zeng, H.; Chen, Q. Narrowband Perovskite Photodetector-Based Image Array for Potential Application in Artificial Vision. *Nano Lett.* **2018**, *18*, 7628–7634. [CrossRef]
65. Wang, S.; Li, T.; Li, Q.; Zhao, H.; Zheng, C.; Li, M.; Li, J.; Zhang, Y.; Yao, J. Inhibition of buried cavities and defects in metal halide perovskite photodetectors via a two-step spin-coating method. *J. Mater. Chem. C* **2022**, *10*, 7886–7895. [CrossRef]
66. Guo, F.; Yang, B.; Yuan, Y.; Xiao, Z.; Dong, Q.; Bi, Y.; Huang, J. A nanocomposite ultraviolet photodetector based on interfacial trap-controlled charge injection. *Nat. Nanotechnol.* **2012**, *7*, 798–802. [CrossRef]
67. Li, C.; Wang, H.; Wang, F.; Li, T.; Xu, M.; Wang, H.; Wang, Z.; Zhan, X.; Hu, W.; Shen, L. Ultrafast and broadband photodetectors based on a perovskite/organic bulk heterojunction for large-dynamic-range imaging. *Light Sci. Appl.* **2020**, *9*, 31. [CrossRef]
68. Li, T.; Li, Q.; Tang, X.; Chen, Z.; Li, Y.; Zhao, H.; Wang, S.; Ding, X.; Zhang, Y.; Yao, J. Environment-friendly antisolvent tert-amyl alcohol modified hybrid perovskite photodetector with high responsivity. *Photonics Res.* **2021**, *9*, 781–791. [CrossRef]
69. Yang, Z.; Li, X.; Gao, L.; Zhang, W.; Wang, X.; Liu, H.; Wang, S.; Pan, C.; Guo, L. Ferro-pyro-phototronic effect enhanced self-powered, flexible and ultra-stable photodetectors based on highly crystalized 1D/3D ferroelectric perovskite film. *Nano Energy* **2022**, *102*, 107743. [CrossRef]
70. Fan, Q.; Zhang, H.; Li, K.; Jin, Z.; Zhang, T.; Wan, C.; Liu, X.; Li, S.; Huang, J. Narrowband and Broadband Dual-Mode Perovskite Photodetector for RGB Detection Application. *Adv. Opt. Mater.* **2023**, *11*, 2300272. [CrossRef]
71. Shafique, S.; Qadir, A.; Iqbal, T.; Sulaman, M.; Yang, L.; Hou, Y.; Miao, Y.; Wu, J.; Wang, Y.; Zheng, F.; et al. High-performance self-powered perovskite photodetectors enabled by Nb_2CT_x-passivated buried interface. *J. Alloys Compd.* **2024**, *1004*, 175903. [CrossRef]

72. Zhu, H.L.; Cheng, J.; Zhang, D.; Liang, C.; Reckmeier, C.J.; Huang, H.; Rogach, A.L.; Choy, W.C.H. Room-Temperature Solution-Processed NiO_x:PbI_2 Nanocomposite Structures for Realizing High-Performance Perovskite Photodetectors. *ACS Nano* **2016**, *10*, 6808–6815. [CrossRef] [PubMed]
73. Contreras-Bernal, L.; Ramos-Terrón, S.; Riquelme, A.; Boix, P.P.; Idígoras, J.; Mora-Seró, I.; Anta, J.A. Impedance analysis of perovskite solar cells: A case study. *J. Mater. Chem. A* **2019**, *7*, 12191–12200. [CrossRef]
74. Féry, C.; Racine, B.; Vaufrey, D.; Doyeux, H.; Cinà, S. Physical mechanism responsible for the stretched exponential decay behavior of aging organic light-emitting diodes. *Appl. Phys. Lett.* **2005**, *87*, 213502. [CrossRef]

polymers

MDPI

Article

Exploring the Impact of Structural Modifications of Phenothiazine-Based Novel Compounds for Organic Solar Cells: DFT Investigations

Walid Taouali [1,*], Amel Azazi [2,*], Rym Hassani [3], Entesar H. EL-Araby [2] and Kamel Alimi [1]

[1] Research Laboratory of Asymmetric Synthesis and Molecular Engineering of Materials for Organic Electronic (LR18ES19), Department of Physics, Faculty of Sciences of Monastir, University of Monastir, Avenue of Environment, Monastir 5019, Tunisia; kamel.alimi@fsm.rnu.tn
[2] Department of Physical Sciences, Physics Division, College of Science, Jazan University, P.O. Box 114, Jazan 45142, Saudi Arabia; eelaraby@jazanu.edu.sa
[3] Environment and Nature Research Centre, Jazan University, P.O. Box 114, Jazan 45142, Saudi Arabia; rhassani@jazanu.edu.sa
* Correspondence: tawali_walid@yahoo.fr (W.T.); aazazi@jazanu.edu.sa (A.A.)

Abstract: This paper explores a novel group of D-π-A configurations that has been specifically created for organic solar cell applications. In these material compounds, the phenothiazine, the furan, and two derivatives of the thienyl-fused IC group act as the donor, the π-conjugated spacer, and the end-group acceptors, respectively. We assess the impact of substituents by introducing bromine atoms at two potential substitution sites on each end-group acceptor (EG1 and EG2). With the donor and π-bridge held constant, we have employed density functional theory and time-dependent DFT simulations to explore the photophysical and optoelectronic properties of tailored compounds (M1–M6). We have demonstrated how structural modifications influence the optoelectronic properties of materials for organic solar cells. Moreover, all proposed compounds exhibit a greater V_{oc} exceeding 1.5 V, a suitable HOMO-LUMO energy gap (2.14–2.30 eV), and higher dipole moments (9.23–10.90 D). Various decisive key factors that are crucial for exploring the properties of tailored compounds—frontier molecular orbitals, transition density matrix, electrostatic potential, open-circuit voltage, maximum absorption, reduced density gradient, and charge transfer length (D_{index})—were also explored. Our analysis delivers profound insights into the design principles of optimizing the performance of organic solar cell applications based on halogenated material compounds.

Keywords: density functional theory; reduced density gradient; open-circuit voltage; charge transfer length; transition density matrix

1. Introduction

Over recent years, organic photovoltaic (OPV) devices have attracted a lot of attention because of their promise to provide lightweight, flexible, and semitransparent nature, and inexpensive solar energy solutions [1–3]. The development in molecular design strategies and efficiency enhancement in OPVs have been thoroughly collected in recent works [4–7], which offer a detailed background for comprehending updates of the field and highlight important limits that still need to be addressed. Non-fullerene acceptors (NFAs) progress has drawn considerable interest in the sector of organic photovoltaic applications in light of their advanced properties exceeding the limitations of traditional fullerene acceptor material [8–11]. The donor–spacer–acceptor (D-π-A) structure has attracted a

lot of interest among different molecular configurations because it can improve light absorption, speed up charge transfer procedures, and adjust electrical characteristics. Within the diverse NFAs, end-groups (EGs) of the fused-ring electron acceptors (FREAs) are the source of improving the overall performance of these materials [12–14]. Their tunable planarity and strong electron-withdrawing ability provide a major influence on the optical and electronic properties of NFAs [15,16]. These properties allow for fine-tuning of charge transfer properties and absorption spectra and facilitate intermolecular π-π stacking. Consequently, understanding the effect of EG modifications on the photophysical and opto-electronic properties of FREAs is crucial for the rational design of high-performance NFAs. Several types of innovative building materials, including cyanide (CN), 1-dicyanomethylene-3-indanone (IC), malononitrile, diketopyrrolopyrrole (DPP), and rhodamine, have been exploited as EGs for FREAs [17–19]. The most efficient end-group in these compounds is the IC group and its derivatives. Since the discovery of the IC group, more than fifty IC derivatives designed to enhance the performance properties of NFAs [20,21].

Among the derivatives of IC groups, thienyl-fused IC group compounds are especially notable due to their wide-ranging applications in organic electronics [22–24]. The optoelectronic properties of FREAs can be affected by thienyl positions. Studying substituent effects on molecular systems plays a decisive role in modulating and predicting their chemical properties and reactivity. The introduction of halogens such as chlorine and bromine into these systems can alter their electronic distribution, intermolecular interactions, and overall stability, consequently influencing their optoelectronic properties.

On the other hand, phenothiazine (PTZ) and the materials derived from it have gained popularity in a number of optoelectronic applications in recent years, due to their distinct optical and electrical properties, flexibility in functionalization, affordability, and commercial availability [25–28]. Moreover, it was demonstrated by the evaluation of organic photovoltaic performance that adding a spacer does not always result in higher power conversion efficiency. However, it was found that polymers possessing a furan π-spacer were somewhat more effective than their thiophene counterparts and more potent than those without a π-spacer [29–31].

Hence, in this study, phenothiazine as the donor material (D) bridged with furan π-spacer to thienyl-fused IC end-groups (A) was used to give D-π-A type of chromophores configuration as mentioned in Figure 1. It is expected that the suggested compound will have good solubility in common organic solvents, including toluene, chloromethane, and chloroform, based on the structural properties of the designed molecules and similar systems documented in the literature [32–35]. The aromatic framework, combined with heteroatoms like sulfur and oxygen in the fused system, enhances its compatibility with these solvents. Furthermore, methods like adding alkyl groups are well-established for enhancing solubility even more, when necessary, without affecting the electronic properties of these compounds [36,37]. In this perspective, we have highlighted how structural change, such as bromine atom substituents and the change inthienyl positions of the fused-ring electron acceptors, influences the optoelectronic properties. This work notably explores the influence of bromine (Br) substitution on two thienyl-fused (IC) derivatives denoted EG1 and EG2. EG1 and EG2 contain identical atoms but differ in the positions of their thienyl group. Each molecule of them presents two potential substitution sites 1 and 2 (see Supplementary Figure S1).With the substitution of bromine (Br) atoms at these sites, our goal is to clarify how structural modifications influence the optoelectronic properties of the D-π-A configurations. Our results will offer deeper understanding into the design strategies for enhancing the performance of novel compounds in advanced organic electronic applications.

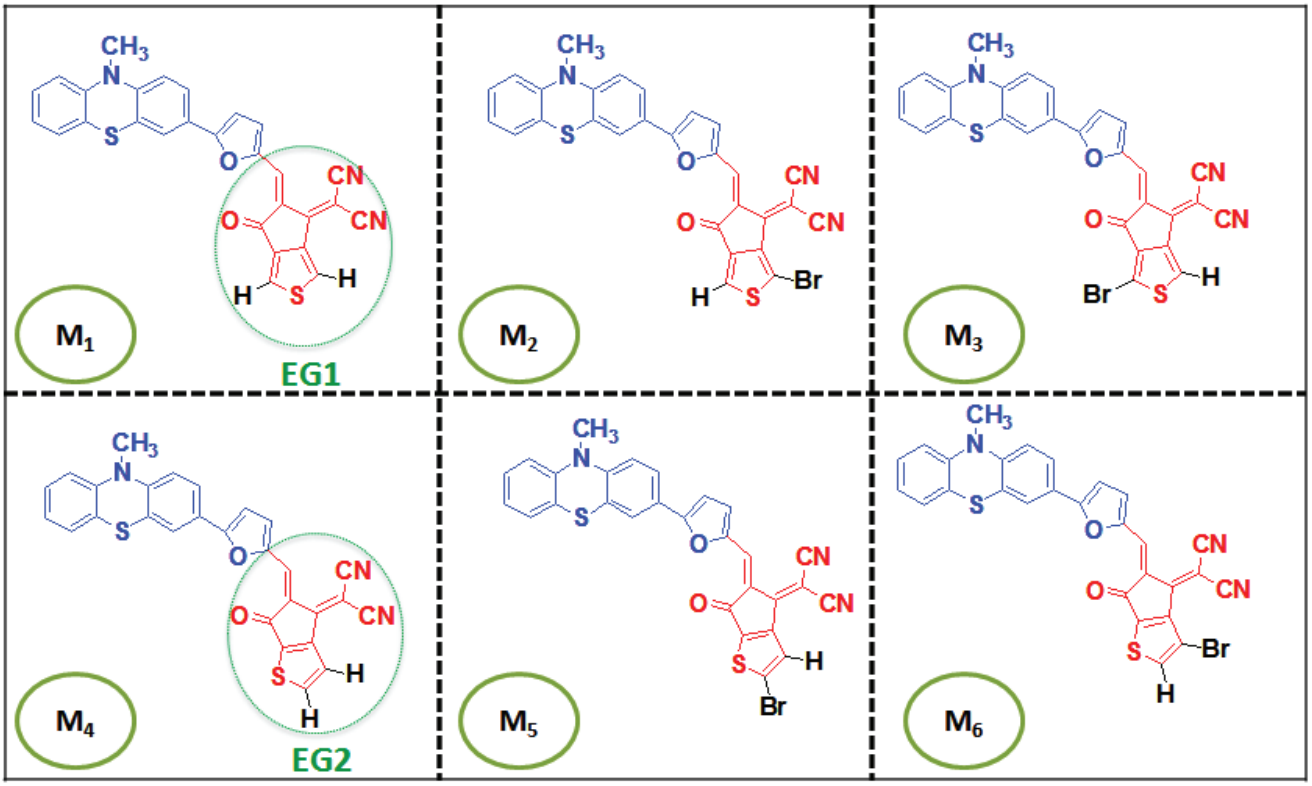

Figure 1. Two-dimensional molecular geometries of all tailored compounds.

2. Computational Methodology

Gaussian 09 software [38] was used to carry out calculation approaches employing density functional theory (DFT) and time-dependent density functional theory (TD-DFT). The optimization of molecular geometries was performed through the B3LYP/6-311G(d,p) level of theory [39,40], focusing on studying energies and electronic structures of proposed molecules M1–M6. Electronic excitations and absorption spectra were assessed through the TD-DFT B3LYP/6-311G(d,p) level of theory [41]. B3LYP functional was chosen for the theoretical simulations due to its demonstrated accuracy in predicting the optoelectronic characteristics and geometries of various organic compound. Properties of charge transport and distribution of all substituted molecules were simulated according to results derived from DFT simulations. Fundamental parameters derived from DFT simulations, including electron localization function (ELF) maps, transition density matrix, molecular orbitals, electronic transitions, Δr index, D index, and dipole moment, were carefully analyzed for the tailored molecules, and examined and presented using the software packages Gauss View 5 [42], Swizard [43], VMD 1.9 [44],and Multiwfn [45].

3. Results

3.1. Geometry Optimization

We created six new structures in our study by changing the terminal acceptors labeled as M1 to M6, which are divided into two distinct compounds based on the position of the sulfur (S) atom. Compound group 1 includes M1, M2, and M3, while compound group 2 consists of M4, M5, and M6. However, within each group of compounds, every structure under investigation has a unique terminal acceptor that differs by the position of the bromine (Br) substituent. All tailored compounds share the identical donor phenothiazine (PTZ) linked with the furan π-spacer.

In order to carry out structural optimization of the recently tailored compounds, the functional B3LYP was utilized with basis set 6-311G(d,p). To proceed with additional com-

putations in subsequent molecular simulations, it is imperative to optimize the molecular configurations. Figure 1 shows the graphic representation of every derived structure from unsubstituted structures (M1 and M4). The scrutinized compounds are divided into two fragments: a newly substituted acceptor (red) characterized by low electron density and a donor (blue) with high electron density.

The ground state structures of the molecules have a close relationship with the opto-electronic properties. The bond lengths (L_{c-c}) and dihedral angle (θ) of designed structures were determined using geometry optimizations. These parameters are shown in Figure 2. Table 1 tabulates these computationally produced results of investigated parameters. The bond length between the donor and acceptor of designed structures fluctuates between 1.405 and 1.411 Å, falling between the L_{c-c} of double bond C=C (1.34 Å) and the L_{c-c} of carbon–carbon single bond (1.54 Å). This demonstrates considerable π-electron conjugation between the donor unit and the terminal acceptors [46,47]. The degree of conjugation determines the structural characteristics of all compounds.

Table 1. Assessment of planarity of all studied compounds: bond length (L_{c-c}), dihedral angle (θ), MPP, and SDP.

Compounds	Bond Length L_{c-c} (Å)	Dideral Angle θ (°)	Molecular Planarity Parameter (Å)	Span of Deviation (Å)
M1	1.406	0.032	0.437	1.980
M2	1.405	0.390	0.454	2.091
M3	1.408	2.253	0.770	2.786
M4	1.410	0.053	0.433	1.970
M5	1.409	0.064	0.435	1.980
M6	1.411	1.458	0.479	2.110

Computationally created molecules have dihedral angles that range from 0.032° to 2.253°. This reveals molecular planarity, leading to increased resonance and faster charge transfer. The donor and acceptor can rotate freely with less obstruction and prominent planarity when the dihedral angle (θ) is minimal. Planarity is represented by both of these parameters (L_{c-c} and θ), and strong conjugation may enhance the optoelectronic properties of these compounds.

The planarity of the structures under study was evaluated by looking at the molecular planarity parameter (MPP) and the span of deviation from the plane (SDP) utilizing Multiwfn 3.8 and VMD 1.9.3 [48]. As seen in Table 1, the molecular coplanar behavior is indicated by the MPP, although the degree of molecular component divergence from the fitted plane is revealed by the SDP. Planarity and MPP exhibit an inverse correlation. The MPP values for investigated compounds (M1 to M6) range between 0.433 and 0.777, indicating a moderate to high degree of planarity. It is clear that M1 and M4, which lack of bromination, exhibit higher planarity compared to brominated molecules. Consequently, bromination at specific sites, as observed in M2, M3, M4, and M5, may generate steric hindrances that marginally reduce the planarity.

Moreover, the SDP values of generated structures are ranging from 1.970 to 2.110 Å, and the lowest SDP values are attributed to the compounds without bromine atoms (M1 and M4), which predict the critical coherence between the SDP and MPP values.

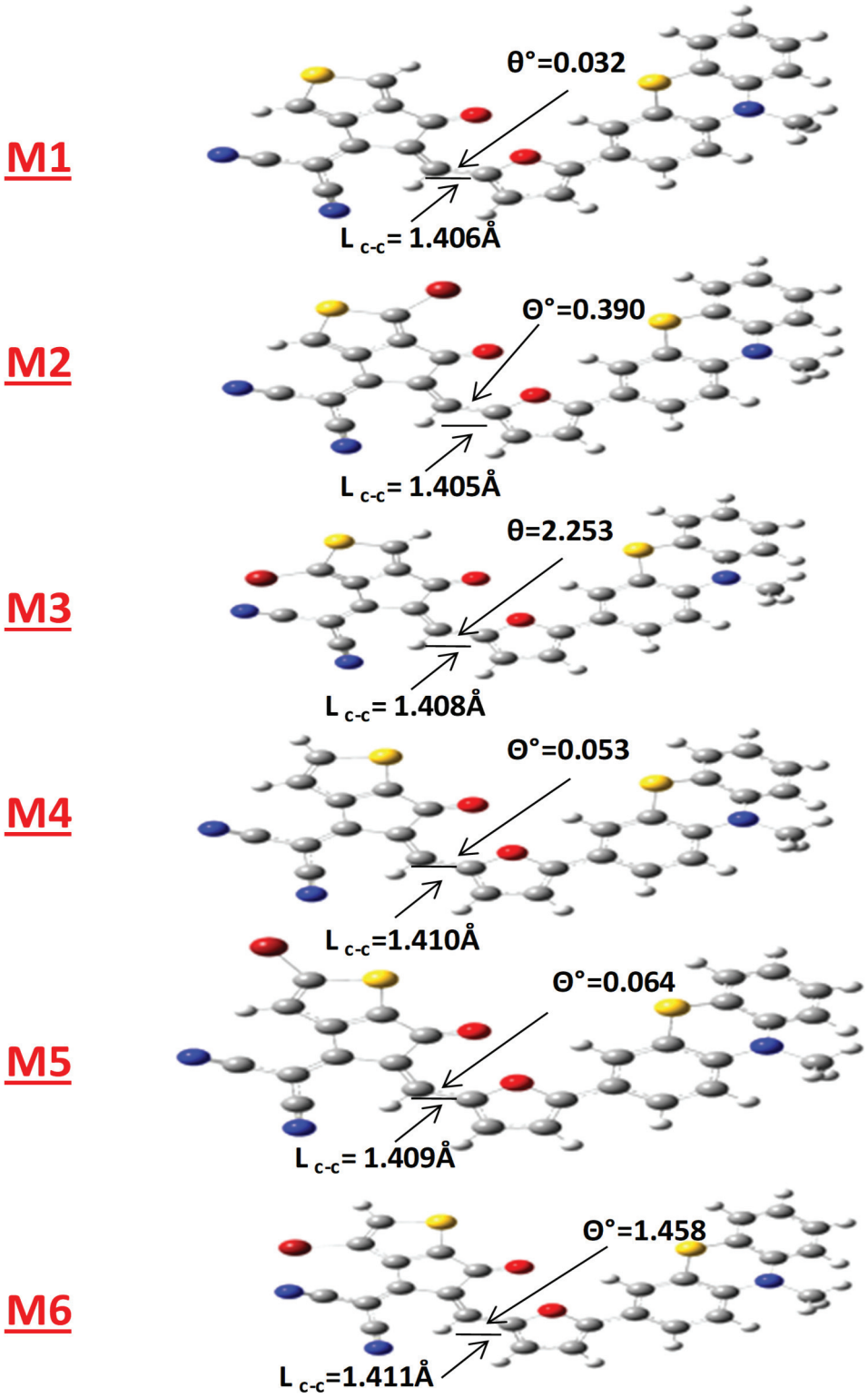

Figure 2. The optimized configurations of tailored compounds illustrating bond lengths (L_{c-c}) and dihedral angle (θ) between the π-spacer and the end-group acceptor.

3.2. Frontier Molecular Orbitals

The energy levels of molecular orbitals have a great impact on organic solar cells (OSCs) because they affect the way charges are transported from the donor unit to the acceptor unit. The redistribution of charge density between the ground and excited state energy levels is represented by frontier molecular orbitals (FMOs). When an electron is excited, it effectively moves from the highest occupied molecular orbital (HOMO) to the lowest

unoccupied molecular orbital (LUMO) state. Figure 3 demonstrates that the LUMO energy level is located in the acceptor fragment of the studied compounds and the HOMO energy level is located in the donor fragment. The HOMO-LUMO energy difference presents a crucial parameter, which controls the material's ability to absorb light and exerts an effect on charge mobility as well as solar cell efficiency. Supplementary Table S1 demonstrates how variations in the positions of bromine (Br) atoms directly affect the dipole moment of the end-group, consequently affecting the LUMO electron distribution of the non-fullerene acceptor (NFA). Moreover, the electron localization function (ELF) maps furnish a detailed visualization of electron density distribution and localization within each atom of the end-group molecule. It is widely employed in computational molecular science to provide additional information beyond conventional bonding descriptors derived from electron density [49–51]. As seen in Supplementary Figure S2, the color red signifies increased electron density localization, whereas blue color indicates a decreased concentration of localized electron density. On the ELF map, the bromine atom in tailored compounds is surrounded by a noticeable blue ring, indicating a considerable degree of electron delocalization. The electron cloud arrangement of adjacent atoms in substituted structures at position 1 presented in 1Br-EG1 and 1Br-EG2 structures closely resembles that observed in molecules EG1 and EG2. However, there is a slight difference observed in the malonitrile region of molecules EG1 and EG2 when the brome was substituted at position 2. Thus, our design strategy begins with optimizing the dipole moment and elevating the LUMO energy levels of the end-groups, which effectively suppresses the V_{oc} loss in organic solar cells (OSCs). This approach serves as an initial hypothesis for enhancing the photovoltaic properties of NFAs.

The FMOs of the developed compounds are shown in Figure 3, with colors according to the strength of charge distribution. Areas of high potential are indicated by red colors, whereas low-potential orbitals are indicated by blue colors. Higher solar cell efficiency and quick excitation are generally linked to a LUMO positioned at a low energy level and a HOMO found at a high energy level. As seen in Figure 3, the energy levels of the HOMO are essentially located in the donor areas of all tailored structures. The electron density of the LUMO is found on both the acceptor and donor units. However, in contrast to the HOMO, the LUMO electron density of all designed compounds was redistributed toward the end-group acceptors. All studied compounds exhibit a charge shift from donor fragment to end-group acceptor areas, indicating the occurrence of intermolecular charge transfer. This property enables these materials to function as effective OSCs. The arrangement of the HOMO-LUMO gap values across all tailored compounds ranks in the following orders: M4 (2.30 eV) > M6 (2.29 eV) > M5 (2.24 eV) and M1 (2.20 eV) > M3 (2.16 eV) > M2 (2.14 eV). These results predict that all designed compounds possessed narrower HOMO-LUMO energy gaps around 2.2 eV. Organic materials used in optoelectronic devices, such as organic solar cells, typically include these energy gaps; a smaller gap can improve light absorption and charge transport. The change in the energy gap shows how structural elements like sulfur positioning and bromination affect the electronic properties of the compound. The position of the sulfur atom significantly affects the energy gap, leading to a reduction of approximately 0.1 eV depending on its location. A notable difference of 0.16 eV in the HOMO-LUMO energy gap can be observed with Br substitution along with the modification of the sulfur atom position.

Moreover, Koopman's theorem states that overall reactivity features of the studied compounds are primarily analyzed in order to determine their stability and reactivity. The parameters that are described using the energy gap E_g, include the ionization potential ($IP = -E_{HOMO}$), electron affinity ($EA = -E_{LUMO}$), chemical potential (μ), electrophilicity

index (ω), and global hardness (η) [52–54]. Equations (1)–(3) are used to calculate the above mentioned parameters.

$$\mu = -X = \frac{E_{CV\ HOMO} - E_{CV\ LUMO}}{2} \tag{1}$$

$$\eta = E_{CV\ LUMO} - E_{CV\ HOMO} \tag{2}$$

$$\omega = \frac{\mu^2}{2\eta} \tag{3}$$

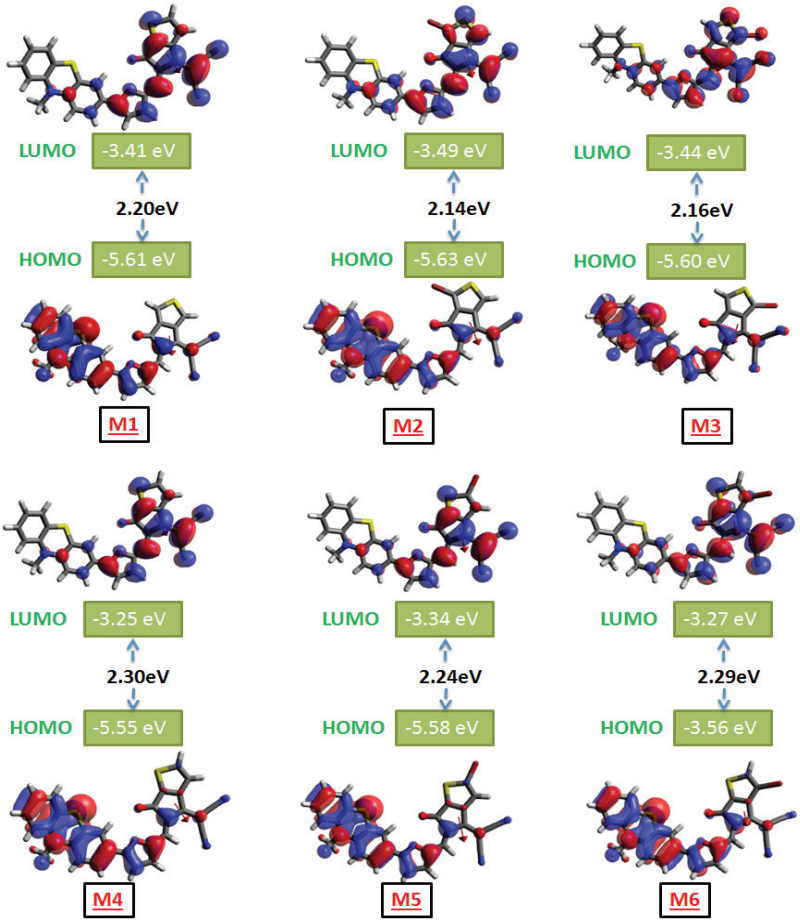

Figure 3. FMOs of all studied compounds associated with their HOMO-LUMO energy gap.

The reactivity parameter values are tabulated in Table 2. It is clear that the substitution of bromine in position 1 leads M2 and M5 to have the largest negative chemical potential (μ) values, at −4.56 eV and −4.46 eV, respectively, indicating their highest stability. Moreover, these structures M2 and M5 have the lowest values of hardness, 1.07 eV and 1.12 eV, respectively, relative to their primary compounds M1 and M4 (1.10 eV and 1.15 eV, respectively), which indicates that these compounds do not resist electron transfer. A molecule's electrophilicity value reveals its ability to draw electrons and function as an electrophile, where a lower number denotes its ability to donate electrons and function as a nucleophile. It is remarkable that all of the substituted structures have more electrophilicity than their primary structures due to the substituent of bromine. Moreover, one of the most intriguing characteristics of OSCs is drawn in the higher value of dipole moment (ϱ), which enhances the stability of these compounds and results in superior charge transfer CT. All

tailored compounds exhibited a higher value of dipole moment exceeding 9 Debye, which confirm their stability. It is clear from this table that halogenated structures possess greater dipole moments than unsubstituted structures.

Table 2. Chemical reactivity parameters of all studied compounds (M1–M6).

Compound	HOMO (eV)	LUMO (eV)	E_g (eV)	η (eV)	μ (eV)	ω (eV)	ϱ (Debye)
M1	−5.61	−3.41	2.20	1.10	−4.51	9.25	10.56
M2	−5.63	−3.49	2.14	1.07	−4.56	9.72	10.65
M3	−5.60	−3.44	2.16	1.08	−4.52	9.46	10.90
M4	−5.55	−3.25	2.30	1.15	−4.40	8.42	9.23
M5	−5.58	−3.34	2.24	1.12	−4.46	8.88	9.94
M6	−5.56	−3.27	2.29	1.14	−4.41	8.53	10.25

3.3. Analysis of Electrostatic Potential (MEP)

The molecular electrostatic potential (MEP) surface has been created to estimate both nucleophilic and electrophilic areas of chemical attack on the designed compounds. The interaction zones can be found on these sites [55,56]. As seen in Figure 4, the nucleophilic reactive attack sites are indicated by blue dots with positive electrostatic potential values, while electrophilic reactive attack sites are indicated by red dots with negative electrostatic potential values. Green dots represent the neutral zone of electrostatic potential. Figure 4 clearly shows the total electron density on which the MEP mapping was performed of all designed compounds. It also demonstrates the relative reactivity of the atoms and chemically active places. At every structure under investigation, the atoms with the highest electron densities are the nitrogen and oxygen ones at the terminal acceptor groups. Given the large charge dispersion with separate zones of all tailored compounds, it can be assumed that they are all great candidates for high-efficiency organic solar cells.

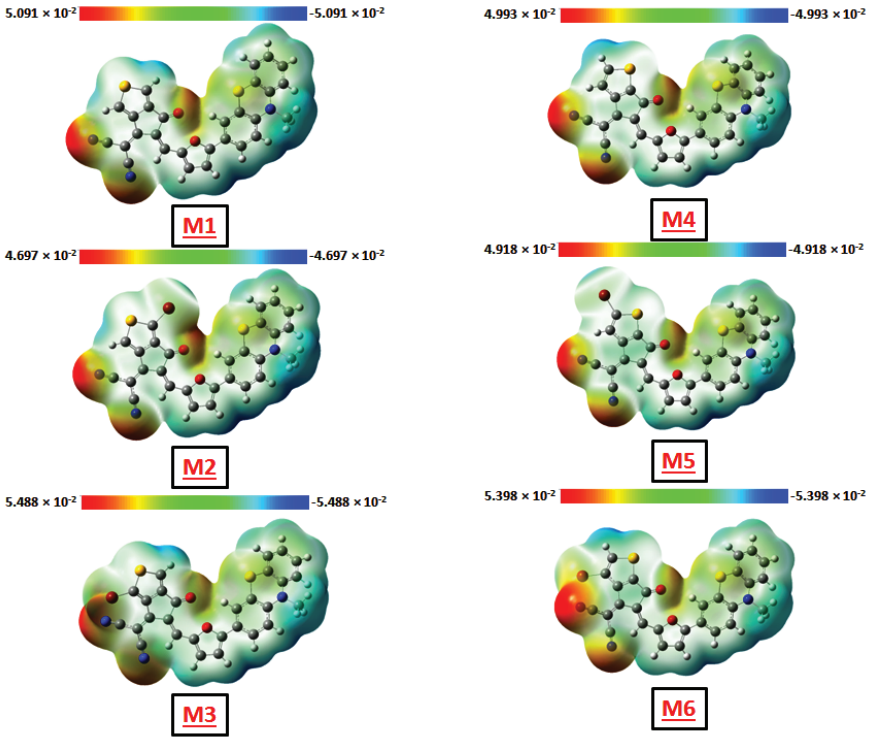

Figure 4. Molecular electrostatic potential of all designed compounds (M1–M6).

3.4. Reduced Density Gradient

Reduced density gradient (RDG) calculations based on the examination of non-covalent interactions (NCI) can be used to identify weak intramolecular or intermolecular interactions found in our study [57–59]. These interactions can contribute to the stability of the molecular structure. The NCI-RDG methods for all studied compounds were carried through an isosurface value of 0.3, and their results are displayed in Figure 5. The RDG isosurface around their real space can be used to identify the different types of interaction; the blue, green, and red regions, respectively, represent the steric effect, vdW interactions, and H-bond interactions. The strongest non-covalent interactions are represented by the peaks. All of the graphs demonstrate that van der Waals and attractive forces predominate steric force, indicating that all of these tailored compounds are stable, precisely structures substituted by bromine in position 2.

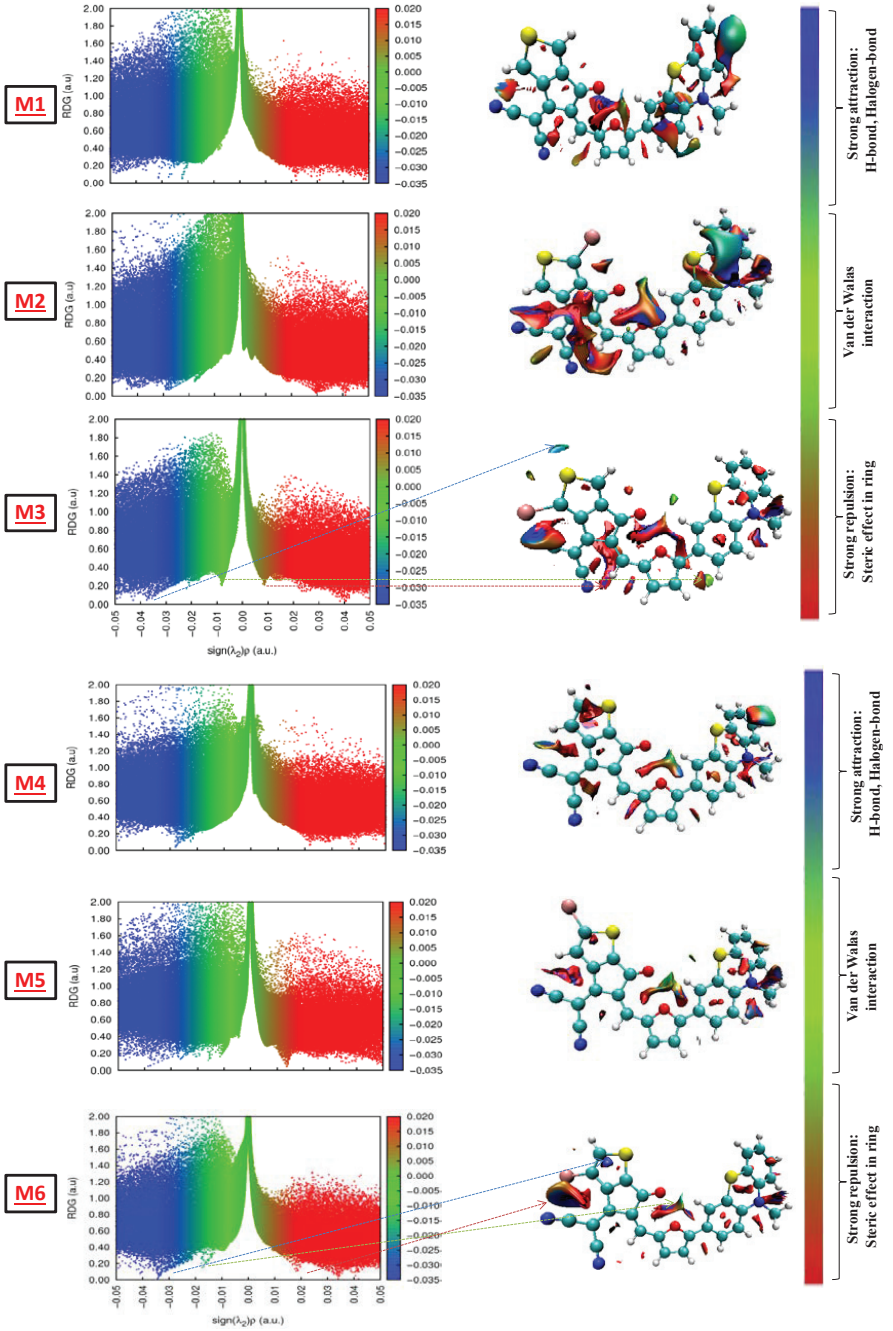

Figure 5. NCI-RDG and interaction types of all tailored compounds.

3.5. Optical Properties

Modification of the optical and electrical characteristics of polymers can either greatly accelerate or profoundly slow down their photovoltaic properties. Lower excitation energy, increased oscillator strength, and a wide absorption spectrum are necessary to create an OSC with exceptional performance. All of the designed structures showed an impressive ability to absorb energy in the visible and near-IR regions, which is stated from 400 nm to nearly 950 nm, as shown by the graph in Figure 6. Table 3 provides an overview of the studied compounds, as well as the excitation energy, oscillator strength, maximum absorption, and intramolecular charge transfer contribution. The computed results indicate that the main peak corresponds to the singlet HOMO→LUMO transition with a contribution exceeding 90%. It is observed that the substitution of compounds M1 and M3 with bromine atoms does not have a significant effect on the oscillator strength values f. The simulated λ_{max} values of proposed compounds are increasing in the following trends: M4 (620.47 nm) < M6 (626.49 nm) < M5 (639.12 nm) and M1 (638.10 nm) < M3 (648.88 nm) < M2 (654.02). It is evident that all of the substituted structures with bromine substituent atoms enhance their primary compound absorptions (M1 and M4), which indicates improved light absorption. Since M2 has the smallest HOMO-LUMO energy gap (2.14 eV), it showed the highest λ_{max} value, which is advantageous for enhancing solar energy conversion efficiency.

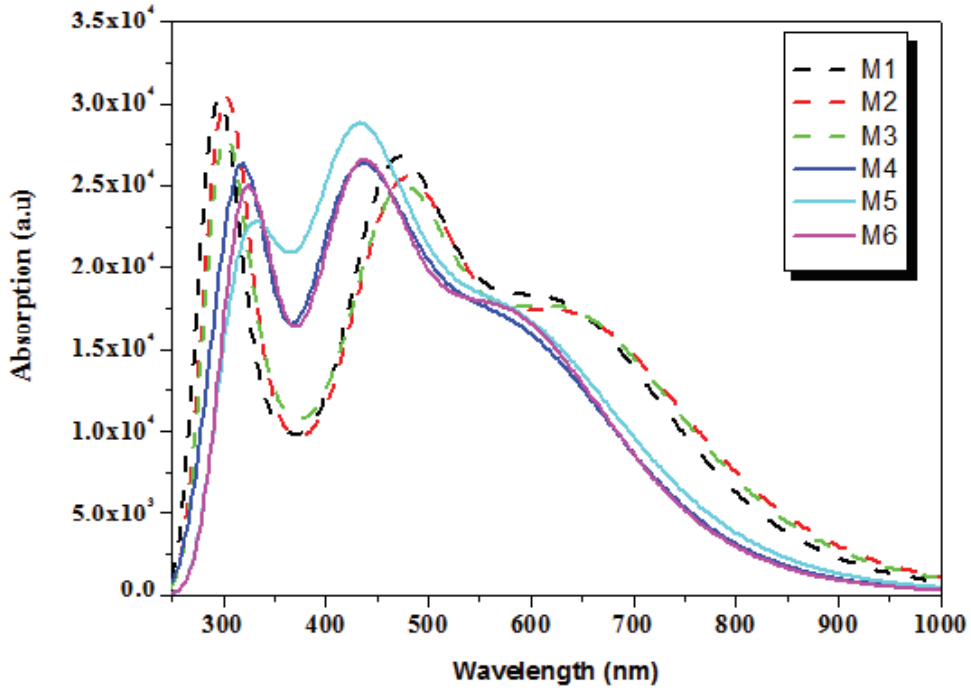

Figure 6. Absorption spectra of all proposed compounds (M1–M6).

Table 3. Simulated values of optical parameters:λ_{max}, energy excitation (E), oscillator strength (f), and electronic transition contributions.

Compounds	λ_{max} (nm)	Energy E (cm^{-1})	Oscillator Strength f	Contribution
M1	638.10	15,671.46	0.41	HOMO → LUMO (98%)
M2	654.02	15,289.95	0.39	HOMO → LUMO (98%)
M3	648.88	15,410.94	0.40	HOMO → LUMO (98%)
M4	620.47	16,116.68	0.25	HOMO → LUMO (96%)
M5	639.12	15,646.45	0.20	HOMO → LUMO (95%)
M6	626.49	15,961.82	0.16	HOMO → LUMO (92%)

Determining the excited state characteristic is crucial to understanding the electrical configuration and properties of these compounds. Numerous indices such as D_{index}, S_r, t_{index}, and Δr have been calculated to depict the first excited state.

The distance between the hole centroid and the electron centroid is known as the D_{index}. Δr index of these compounds was computed at the same theoretical level, which may be used to evaluate the average hole–electron distance upon photo-excitation, in order to verify the accuracy of the computed D_{index}. The Δr index provides a quantitative assessment for accessing the charge transfer length (D_{index}) of electron excitation; a larger Δr index correlates with a longer CT distance. The overlap distance between the centroid of the hole and the electron is expressed by the overlap integral Sr. Efficient exciton dissociation enhances charge transfer in the photo-electric conversion process of organic solar cells. For the purpose of comparing the exciton separation ability of studied compounds, the key parameters of electron excitation of the first five excitations were computed and tabulated in Table 4. From this table, the Δr indices of all proposed compounds suggest that the excitations from ground state (S_0) to excited state (S_1) acquire strong charge transfer excitations because their Δr indices are sufficiently large (2.0 Å serves as a criterion for discerning between local excitation (LE) and charge transfer excitations (CT) [60,61]). After looking at the Sr index, it was found that substituted compounds with bromine have smaller Sr indices than their primary structures, mostly because of their elevated D_{index} value. In particular, M6 possesses a minimal Sr value of 0.321, which suggests that there may be an overlap between the hole and electron in the first excited state. The t_{index} values of all studied compounds exhibit positive values, indicating that in their first excited state, holes, and electrons are significantly separated from one another [62].

Table 4. Simulated results of the first excited state for all proposed compounds including the centroid distance (D_{index}), electron–hole overlap (S_r), degree of separation (t), and charge transfer length (Δr).

Compound	D_{index} (Å)	S_r	t_{index} (Å)	Δr (Å)
M1	6.243	0.456	3.165	6.242
M2	6.282	0.454	3.169	6.281
M3	6.427	0.446	3.356	6.423
M4	7.338	0.370	4.511	7.007
M5	7.507	0.352	4.725	7.143
M6	7.713	0.321	5.074	7.244

3.6. Transition Density Matrix

The electronic excitation, acceptor-donor interactions, and electron–hole localization are all examined by the transition density matrix (TDM) [63,64]. The electron coherence and donor connection of each structure are most clearly depicted in TDM maps. Because of their minimal impact on significant transitions, the hydrogen atoms are excluded from our analysis. The identification of electron–hole pair delocalization is aided by the first excited state S_1. Each compound is separated into donor and acceptor parts as shown in Figure 1. As shown in Figure 7, TDM maps for every tailored compound are obtained using Multiwfn 3.8, which is useful in some of the previously described parameters. A closer examination reveals that the acceptor's area of M3 and M6 compounds had more brilliant fringes. Fringes in diagonal positions manifest the extent of localization of electron density, while those in off-diagonal positions refer to the charge transfer process in these structures. Moreover, it is observed that the acceptor portions of these two structures exhibit noticeably reduced dark spot areas, suggesting that in the aforementioned compounds, the ratio of excited electrons that moved from the donor to the acceptor region is quite high. The hole–electron coherence in the tailored compounds obeys the subse-

quent order M3 (2.91) > M1 (0.72) > M2 (0.66) > M6 (1.15) > M4 (0.44) > M5 (0.39), which is determined by the coefficient interactions between the donor and acceptor portions. This interaction order shows that M3 exhibits a weak hole–electron coupling, which results in an efficient exciton dissociation. These results support the finding of higher D_{index} and Δr values obtained for compound M3.

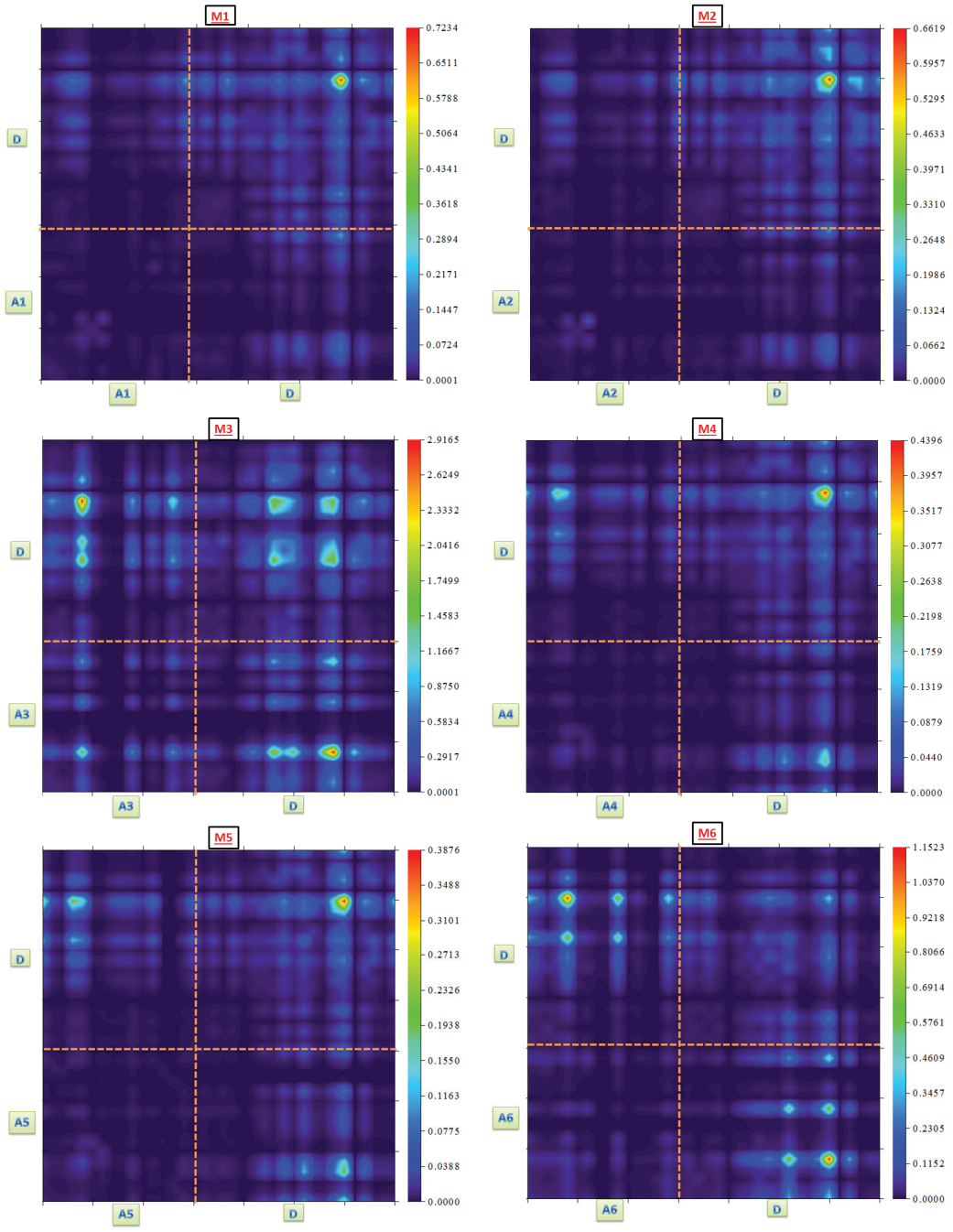

Figure 7. TDM plots showing electron density distribution across A–D fragments of all compounds. (D: Donor + π spacer; A: end-group acceptor).

3.7. Exciton Binding

An OSC device's productivity is regulated by exciton binding energy (E_b), which is the minimal amount of energy required for exciton dissociation. Electrical energy is produced when specific radiation is absorbed because the excitons become separated and are drawn to the electrodes in which they are located. The enhanced charge separation is stimulated

by the lowest E_b, which increases charge mobility. The next equation is utilized to calculate the E_b values of all tailored compounds [65]:

$$E_b(M) = E_g(M) - E_{opt}(M) \quad (4)$$

The energy of the HOMO-LUMO gap is represented by the term $E_g(M)$, and E_{opt} represents the excitation energy for the first state S1. Table 5 summarizes the quantitative results of all designed compounds. The ranking of E_b for all designed compounds is listed as follows: M6 (0.31 eV) > M6 = M5 (0.30 eV) > M1(0.26 eV) > M3 (0.25 eV) > M2 (0.24 eV). According to the binding energy results, M3 exhibits the lowest value, indicating higher and easier electron–hole pair dissociation in the excited state.

Table 5. Simulated exciton binding energy for all proposed compounds.

Compound	E_g (eV)	E_{opt} (eV)	E_b (eV)
M1	2.20	1.94	0.26
M2	2.14	1.90	0.24
M3	2.16	1.91	0.25
M4	2.30	2.00	0.30
M5	2.24	1.94	0.30
M6	2.29	1.98	0.31

3.8. Open-Circuit Voltage (V_{oc}) and Fill Factor

The open-circuit voltage (V_{oc}) parameter is significant in organic solar cells since it is used to measure the working capabilities and performance of OSCs. If the HOMO value of the donor is lower and the LUMO value of the acceptor is higher in energy, an increased value of V_{oc} can be reached. The following expression can be used to produce V_{oc} values:

$$V_{oc} = \left(\frac{1}{e}\right) \quad \left[\left|E_{HOMO}^{Donor}\right| - \left|E_{LUMO}^{Acceptor}\right|\right] - 0.3 \quad (5)$$

where "e" represents the electron charge and 0.3 represents the empirical factors [66,67]. The primary goal of V_{oc} is to match the HOMO of the recognized PBDB-T donor with the LUMO of designed compounds. PBDB-T polymer offers a high-performance donor with HOMO and LUMO energy levels of −5.33 eV and −2.92 eV, respectively, based on available resources [68]. Then, we have evaluated the difference between the LUMO energy levels of our proposed compounds and the HOMO energy level of donor polymer (PBDB-T). Figure 8 lists the assembled results, and the descending order of V_{oc} is M4 (1.78 V) > M6 (1.76 V) > M5 (1.69 V) > M1 (1.62 V) > M3 (1.59 V) > M2 (1.54 V). The alignment of the donor (PBDB-T) and the acceptor (M1–M6) energy levels predicts a high open-circuit voltage V_{oc}; a significant overlap between the HOMO of the donor and the LUMO of the acceptor suggests a high V_{oc}. Organic compounds having a relatively moderate optical band gap have been discovered to have high V_{oc} values, which is consistent with previous studies [69–72]. Nevertheless, despite their potential, these theoretical forecasts include inherent uncertainties. They should therefore be regarded as first estimates, and experimental validation is necessary to verify the anticipated values. It should be mentioned that bromine substitution combined with positional change of the sulfur atom, leads to a 0.24 V difference in V_{oc} values. It is therefore possible to successfully improve organic solar cells by employing these recently suggested molecules with V_{oc} values exceeding 1.5 V.

Effective dissociation of the exciton requires the electron to move from the LUMO of the donor to the LUMO of the acceptor. As seen in Figure 8, the energy difference between

the LUMOs of the PBDB-T and designed compounds denoted $LUMO_{offset}$ is greater than 0.3 eV, which ensures charge transfer in organic photovoltaic devices.

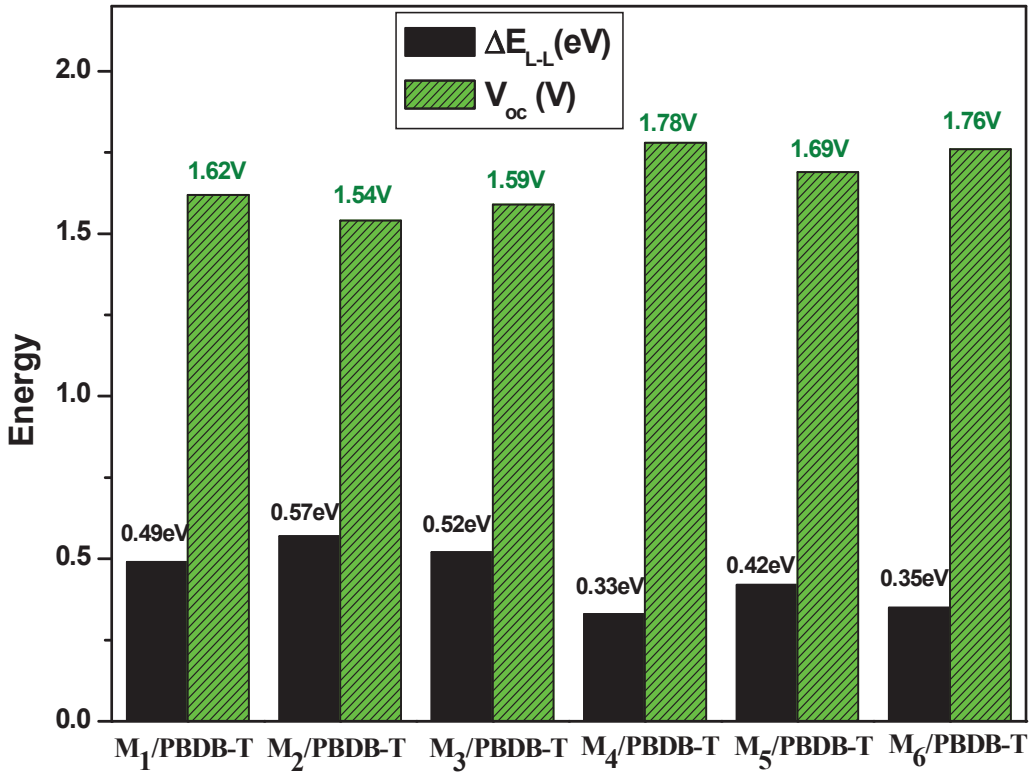

Figure 8. Open-circuit voltage (V_{oc}) and LUMO $_{offset}$ ($\Delta E_{L\text{-}L}$)for all studied molecules.

Higher fill factor (FF) and V_{oc} are necessary for higher power conversion efficiency (PCE). The expected values for fill factor are typically larger than they are in reality since shunt and series resistances are ignored. However, it continues to be a significant element influencing the effectiveness of a device's photovoltaic efficiency. The following equation can be used to compute the fill factor.

$$FF = \frac{\frac{e\,V_{oc}}{K_B\,T} - \ln\left(\frac{e\,V_{oc}}{K_B\,T} + 0.72\right)}{\frac{e\,V_{oc}}{K_B\,T} + 1} \quad (6)$$

The normalized V_{oc} is represented by the formula above as (eV_{oc}/K_BT) [73,74]. While K_B is the Boltzmann constant, T is the temperature (300 K), and e is the electron charge. As seen in Table 6, M4 and M6 molecules showed the highest fill factor values of 0.925 and 0.924, respectively. This demonstrates the amazing ability of the M6 molecule to efficiently convert solar sunlight into electrical energy, increasing photovoltaic efficiency.

Table 6. Calculated normalized V_{oc} and fill factor (FF) of all proposed structures.

Compound	V_{oc} (V)	Normalized V_{oc} (V)	FF
M1	1.62	62.69	0.919
M2	1.54	59.59	0.916
M3	1.59	61.53	0.918
M4	1.78	68.88	0.925
M5	1.69	65.40	0.922
M6	1.76	68.11	0.924

4. Conclusions

In summary, the theoretical investigations of the six designed phenothiazine-based novel material compounds, which were classified into two groups based on the thienyl position of the fused-ring electron acceptor, show that bromination significantly affects the optoelectronic properties of these compounds. We have employed density-functional theory (DFT) and time-dependent DFT to explore the impact of structural modifications on the optoelectronic properties of newly designed D-π-A material compounds (M1–M6). With the donor (phenothiazine) and π-bridge (furan) held constant, we assessed the impact of bromine atom substituents and the change of sulfur atom positions on the optoelectronic properties of the tailored compounds. Substituting the bromine atom and repositioning the thienyl group within the fused IC terminal acceptor reduced the energy gap from 2.30 to 2.14 eV due to their planar geometries. We demonstrated that all of the designed compounds showed an impressive ability to absorb energy in the visible and near-IR regions, which is stated from 400 nm to nearly 950 nm. Brominated structures showed a slight red shift in the maximum absorption as compared to non-substituted compounds. Moreover, the energy levels of all proposed compounds align well with those of the PBDB-T polymer donor, resulting in a V_{oc} value between 1.54 V and 1.78 V, which is crucial for achieving optimal performance in photovoltaic devices. Through an extensive analysis of the electron localization function, reactivity parameter values, transition density matrix, reduced density gradient, optical properties, charge transfer length, overlap integral, and HOMO-LUMO energy gap, we have revealed pivotal information about these novel proposed compounds. The results suggest that substituting bromine atoms in our studied molecules improves their efficiency as materials for transporting holes. These results show how combining the change of sulfur atom position of the end-group associated with bromine substitution can significantly enhance the performance of novel material compounds, providing valuable guidance for the design of more efficient organic photovoltaic devices.

Supplementary Materials: The following supporting information can be downloaded at: https://www.mdpi.com/article/10.3390/polym17010115/s1, Figure S1: Optimized molecular structures of EG1 and EG2 and their monobrominated isomers; Figure S2: Electron Localization Function (ELF) map for EG1 and EG2 and their monobrominated structures; Table S1: Calculated HOMO (eV), LUMO (eV), and dipole moment (Debye) of the monobrominated isomers of end groups (EG1 and EG2).

Author Contributions: Conceptualization, W.T.; Methodology, W.T. and A.A.; Validation, W.T., A.A. and R.H.; Formal Analysis, W.T. and A.A.; Investigation, W.T., A.A., R.H. and E.H.E.-A.; Writing—Original Draft Preparation, W.T. and A.A.; Writing—Review and Editing, W.T., A.A., R.H., E.H.E.-A. and K.A.; Visualization, W.T., A.A. and K.A.; Supervision, K.A. All authors have read and agreed to the published version of the manuscript.

Funding: The authors gratefully acknowledge the funding of the Deanship of Graduate Studies and Scientific Research, Jazan University, Saudi Arabia, through project number (RG24-M08).

Institutional Review Board Statement: Not applicable.

Data Availability Statement: The original contributions presented in this study are included in the article/Supplementary Materials. Further inquiries can be directed to the corresponding author(s).

Acknowledgments: The authors would like to extend their sincere appreciation to the Deanship of Graduate Studies and Scientific Research, Jazan University, Saudi Arabia, for funding this work (RG24-M08).

Conflicts of Interest: The authors declare no conflict of interest.

References

1. Zhou, Q.; Yan, C.; Li, H.; Zhu, Z.; Gao, Y.; Xiong, J.; Tang, H.; Zhu, C.; Yu, H.; Lopez, S.P.G.; et al. Polymer Fiber Rigid Network with High Glass Transition Temperature Reinforces Stability of Organic Photovoltaics. *Nano-Micro Lett.* **2024**, *16*, 224. [CrossRef] [PubMed]
2. Li, Y.; Wang, J.; Yan, C.; Zhang, S.; Cui, N.; Liu, Y.; Li, G.; Cheng, P. Optical and electrical losses in semitransparent organic photovoltaics. *Joule* **2024**, *8*, 527–541. [CrossRef]
3. He, W.; Li, H.; Ma, R.; Yan, X.; Yu, H.; Hu, Y.; Hu, D.; Qin, J.; Cui, N.; Wang, J.; et al. In Situ Self-Assembly of Trichlorobenzoic Acid Enabling Organic Photovoltaics with Approaching 19% Efficiency. *Adv. Funct. Mater.* **2024**, *34*, 2313594. [CrossRef]
4. Yu, H.; Wang, J.; Zhou, Q.; Qin, J.; Wang, Y.; Lu, X.; Cheng, P. Semi-transparent organic photovoltaics. *Chem. Soc. Rev.* **2023**, *52*, 4132–4148. [CrossRef]
5. Kong, W.; Wang, J.; Hu, Y.; Cui, N.; Yan, C.; Cai, X.; Cheng, P. P-type Polymers in Semitransparent Organic Photovoltaics. *Angew. Chem. Int. Ed.* **2023**, *62*, e202307622. [CrossRef] [PubMed]
6. Taouali, W.; Alimi, k.; Nangraj, A.S.; Casida, M.E. Density-functional theory (DFT) and time-dependent DFT study of the chemical and physical origins of key photoproperties of end-group derivatives of a nonfullerene acceptor molecule for bulk heterojunction organic solar cells. *J. Comput. Chem.* **2023**, *44*, 2130–2148. [CrossRef]
7. Taouali, W.; Casida, M.E.; Darghouth, A.; Alimi, K. Theoretical design of new small molecules with a low band-gap for organic solar cell applications: DFT and TD-DFT study. *Comput. Mater. Sci.* **2018**, *150*, 54–61. [CrossRef]
8. Wang, J.; Xie, Y.; Chen, K.; Wu, H.; Hodgkiss, J.M.; Zhan, X. Physical insights into non-fullerene organic photovoltaics. *Nat. Rev. Phys.* **2024**, *6*, 365–381. [CrossRef]
9. Sun, Y.; Wang, L.; Guo, C.; Xiao, J.; Liu, C.; Chen, C.; Xia, W.; Gan, Z.; Cheng, J.; Zhou, J.; et al. π-Extended Nonfullerene Acceptor for Compressed Molecular Packing in Organic Solar Cells to Achieve over 20% Efficiency. *J. Am. Chem. Soc.* **2024**, *146*, 12011–12019. [CrossRef]
10. Xu, R.; Jiang, Y.; Liu, F.; Ran, G.; Liu, K.; Zhang, W.; Zhu, Z. High Open-Circuit Voltage Organic Solar Cells with 19.2% Efficiency Enabled by Synergistic Side-Chain Engineering. *Adv. Mater.* **2024**, *36*, 2312101. [CrossRef]
11. Kacimi, R.; Ali, U.; Azaid, A.; Sarfaraz, S.; Raftani, M.; Bejjit, L.; Bouachrine, M. Quantum chemical study of symmetrical non-fullerene acceptor chromophores for organic photovoltaics. *Comput. Theor. Chem.* **2024**, *1233*, 114475. [CrossRef]
12. Zubair, H.; Akhter, M.S.; Waqas, M.; Ishtiaq, M.; Bhatti, I.A.; Iqbal, J.; Skawky, A.M.; Khera, R.A. A computational insight into enhancement of photovoltaic properties of non-fullerene acceptors by end-group modulations in the structural framework of INPIC molecule. *J. Mol. Graph. Model.* **2024**, *126*, 108664. [CrossRef] [PubMed]
13. Zhang, Y.; Li, Y.; Peng, R.; Qiu, Y.; Shi, J.; Chen, Z.; Ge, J.; Zhang, C.; Tang, Z.; Ge, Z. End-group modulation of phenazine based non-fullerene acceptors for efficient organic solar cells with high open-circuit voltage. *J. Energy Chem.* **2024**, *88*, 461–468. [CrossRef]
14. Alam, S.; Yang, S.; Jeong, Y.; Li, M.Q.; Park, G.Y.; Kim, M.; Lee, J. Critical role of the end-group acceptor in enhancing the efficiency of indacenodithiophene-benzothiadiazole-linked nonfullerene organic solar cells through morphology optimization. *Synth. Met.* **2024**, *305*, 117605. [CrossRef]
15. Mo, D.; Chen, H.; Zhou, J.; Han, L.; Zhu, Y.; Chao, P.; Zheng, N.; Xie, Z.; He, F. Isomeric effects of chlorinated end groups on efficient solar conversion. *J. Mater. Chem. A* **2020**, *8*, 23955–23964. [CrossRef]
16. Sadiq, S.; Waqas, M.; Zahoor, A.; Mehmood, R.F.; Essid, M.; Aloui, Z.; Khera, R.A.; Akram, S.J. Synergistic modification of end groups in Quinoxaline fused core-based acceptor molecule to enhance its photovoltaic characteristics for superior organic solar cells. *J. Mol. Graph. Model.* **2023**, *123*, 108518. [CrossRef]
17. Liu, F.; Zhou, Z.; Zhang, C.; Vergote, T.; Fan, H.; Liu, F.; Zhu, X. A thieno[3,4-b]thiophene-based non-fullerene electron acceptor for high-performance bulk-heterojunction organic solar cells. *J. Am. Chem. Soc.* **2016**, *138*, 15523–15526. [CrossRef] [PubMed]
18. Vartanian, M.; Singhal, R.; Cruz, P.; Biswas, S.; Sharma, G.D.; Langa, F. Low energy loss of 0.57 eV and high efficiency of 8.80% in porphyrin-based BHJ solar cells. *ACS Appl. Mater. Interfaces* **2018**, *1*, 1304–1315. [CrossRef]
19. Wang, H.; Zhao, C.; Burešová, Z.; Bureš, F.; Liu, J. Cyano-capped molecules: Versatile organic materials. *J. Mater. Chem. A* **2023**, *11*, 3753–3770. [CrossRef]
20. Zhang, Y.; Lang, Y.; Li, G. Recent advances of non-fullerene organic solar cells: From materials and morphology to devices and applications. *EcoMat* **2023**, *5*, 12281. [CrossRef]
21. Huang, J.; Tang, H.; Yan, C.; Li, G. 1,1-Dicyanomethylene-3-Indanone End-Cap Engineering for Fused-Ring Electron Acceptor-Based High-Performance Organic Photovoltaics. *Cell Rep. Phys. Sci.* **2021**, *2*, 100292. [CrossRef]
22. Zhang, J.; Li, Y.; Hu, H.; Zhang, G.; Ade, H.; Yan, H. Chlorinated Thiophene End Groups for Highly Crystalline Alkylated Non-Fullerene Acceptors toward Efficient Organic Solar Cells. *Chem. Mater.* **2019**, *31*, 6672–6676. [CrossRef]
23. Luo, Z.; Yan, H.; Yang, C. End-Group Engineering of Nonfullerene Acceptors for High-Efficiency Organic Solar Cells. *Acc. Mater. Res.* **2023**, *4*, 968–981. [CrossRef]

24. Zhang, G.; Wu, Q.; Duan, Y.; Liu, W.; Zou, M.; Zhou, H.; Cao, J.; Li, R.; Xu, X.; Yu, L.; et al. Simultaneously improved Jsc and Voc achieving 19.15% efficiency in ternary blend polymer solar cell containing a Y-type acceptor with thiophene based end groups. *Chem. Eng. J.* **2023**, *476*, 146538. [CrossRef]
25. Badgurjar, D.; Duvva, N.; Pooja, A.P.; Gahlot, S.; Pawar, R.; Singh, S.P.; Garg, A.; Giribabu, L.; Chitta, R. Phenothiazine functionalized fulleropyrrolidines: Synthesis, charge transport and applications to organic solar cells. *Photochem. Photobiol. Sci.* **2023**, *22*, 379–393. [CrossRef] [PubMed]
26. Al-Marhabi, A.; El-Shishtawy, R.; Bouzzine, M.; Hamidi, M.; Al-Ghamdi, H.; Al-Footy, K. D-D-π-A-π-A-based quinoxaline dyes incorporating phenothiazine, phenoxazine and carbazole as electron donors: Synthesis, photophysical, electrochemical, and computational investigation. *J. Photochem. Photobiol. A Chem.* **2023**, *436*, 114389. [CrossRef]
27. Amin, M.F.; Anwar, A.; Gnida, P.; Jarząbek, B. Polymers Containing Phenothiazine, Either as a Dopant or as Part of Their Structure, for Dye-Sensitized and Bulk Heterojunction Solar Cells. *Polymers* **2024**, *16*, 2309. [CrossRef] [PubMed]
28. Dhivya, K.S.; Senthilkumar, C.; Karthika, K.; Srinivasan, P. Structural, electrical, optical, and DFT studies of phenothiazine-based D–π–A frameworks for dye-sensitized solar cell applications. *Struct. Chem.* **2024**, *35*, 1843–1863. [CrossRef]
29. Buene, A.; Uggerud, N.; Economopoulos, S.; Gautun, O.; Helge, B. Effect of π-linkers on phenothiazine sensitizers for dye-sensitized solar cells. *Dye. Pigment.* **2018**, *151*, 263–271. [CrossRef]
30. Folabi, S.; Semire, B.; Idowu, M. Electronic and optical properties' tuning of phenoxazine-based D-A2-π-A1 organic dyes for dye-sensitized solar cells. DFT/TDDFT investigations. *Heliyon* **2021**, *7*, e06827. [CrossRef] [PubMed]
31. Nitha, P.; Soman, S.; John, J. Indole fused heterocycles as sensitizers in dye-sensitized solar cells: An overview. *Mater. Adv.* **2021**, *2*, 6136–6168. [CrossRef]
32. Nhari, L.M.; El-Shishtawy, R.M.; Bouzzine, M.; Hamidi, M.; Asiri, A.M. Phenothiazine-based dyes containing imidazole with π-linkers of benzene, furan and thiophene: Synthesis, photophysical, electrochemical and computational investigation. *J. Mol. Struct.* **2022**, *1251*, 131959. [CrossRef]
33. Al-Ghamdi, S.N.; Al-Ghamdi, H.A.; El-Shishtawy, R.M.; Asiri, A.M. Advances in phenothiazine and phenoxazine-based electron donors for organic dye-sensitized solar cells. *Dye. Pigment.* **2021**, *194*, 109638. [CrossRef]
34. Qian, X.; Wang, X.; Shao, L.; Li, H.; Yan, R.; Hou, L. Molecular engineering of D–D–π–A type organic dyes incorporating indoloquinoxaline and phenothiazine for highly efficient dye-sensitized solar cells. *J. Power Sources.* **2016**, *326*, 129–136. [CrossRef]
35. Zhang, Z.; Feng, L.; Xu, S.; Yuan, J.; Zhang, Z.; Peng, H.; Li, Y.; Zou, Y. Achieving over 10% efficiency in a new acceptor ITTC and its blends with hexafluoroquinoxaline based polymers. *Mater. Chem. A* **2017**, *5*, 11286–11293. [CrossRef]
36. Yao, X.; Shao, W.; Xiang, X.; Xiao, W.; Liang, L.; Zhao, F.; Ling, J.; Lu, Z.; Li, J.; Li, W. Side chain engineering on a small molecular semiconductor: Balance between solubility and performance by choosing proper positions for alkyl side chains. *Org. Electron.* **2018**, *61*, 56–64. [CrossRef]
37. Mooney, M.; Wang, Y.; Nyayachavadi, A.; Zhang, S.; Gu, X.; Rondeau-Gagné, S. Enhancing the Solubility of Semiconducting Polymers in Eco-Friendly Solvents with Carbohydrate-Containing Side Chains. *ACS Appl. Mater. Interfaces* **2021**, *13*, 25175–25185. [CrossRef]
38. Frisch, M.J.; Trucks, G.W.; Schlegel, H.B.; Scuseria, G.E.; Robb, M.A.; Cheeseman, J.R.; Scalmani, G.; Barone, V.; Mennucci, B.; Petersson, G.A.; et al. *Gaussian09 Revision D.01*; Gaussian Inc.: Wallingford, CT, USA, 2013.
39. Becke, A.D. Density-functional exchange-energy approximation with correct asymptotic behavior. *Phys. Rev. A* **1988**, *38*, 3098–3100. [CrossRef] [PubMed]
40. Lee, C.; Yang, W.; Parr, R.G. Development of the Colle-Salvetti correlation-energy formula into a functional of the electron density. *Phys. Rev. B* **1988**, *37*, 785–789. [CrossRef] [PubMed]
41. Yanai, T.; Tew, D.; Handy, N. A new hybrid exchange-correlation functional using the Coulomb-attenuating method (CAM-B3LYP). *Chem. Phys. Lett.* **2004**, *393*, 51–57. [CrossRef]
42. Dennington, R.; Keith, T.; Millam, J. *Gauss View*, version 5; Semichem Inc.: Shawnee, KS, USA, 2009.
43. Gorelsky, S.I. *SWizard Program*; University of Ottawa: Ottawa, ON, Canada, 2013. Available online: http://www.sg-chem.net/ (accessed on 1 January 2024).
44. Humphrey, W.; Dalke, A.; Schulten, K. VMD: Visual molecular dynamics. *J. Mol. Graph.* **1996**, *14*, 33–38. [CrossRef]
45. Lu, T.; Chen, F. Multiwfn: A multifunctional wavefunction analyzer. *J. Comput. Chem.* **2012**, *33*, 580–592. [CrossRef] [PubMed]
46. Waqas, M.; Hadia, N.; Shawky, A.; Mahmood, R.; Essid, M.; Aloui, Z.; Alatawi, N.; Iqbal, J.; Khera, R. Theoretical framework for achieving high Voc in non-fused non-fullerene terthiophene-based end-capped modified derivatives for potential applications in organic photovoltaics. *RSC Adv.* **2023**, *13*, 7535–7553. [CrossRef] [PubMed]
47. Saeed, U.; Bousbih, R.; Mahal, A.; Majdi, H.; Jahan, N.; Jabir, M.; Soliman, M.; Ayub, A.; Elsayed, N.; Ali, S.; et al. Engineering of asymmetric A1-D1-A2-D2-A1 type non-fullerene acceptors of 4T2CSi–4F derivatives to enhance photovoltaic properties: A DFT study. *J. Phys. Chem. Solids* **2024**, *192*, 112094. [CrossRef]
48. Lu, T. Simple, reliable, and universal metrics of molecular planarity. *J. Mol. Model.* **2021**, *27*, 263. [CrossRef] [PubMed]

49. Chamorro, E.; Guerra, C.; Henríquez, L.A.; Duque, M.; Pérez, P.; Rincón, E. Chapter 16—New insights from a bonding evolution theory based on the topological analysis of the electron localization function. *Chem. React.* **2023**, *1*, 465–481. [CrossRef]
50. Moztarzadeh, O.; Jamshidi, M.; Taherpour, A.; Babuska, V. Molecular modeling of fullerene C60 functionalized by nitric oxide for use in biological environment. *Sci. Rep.* **2024**, *14*, 2565. [CrossRef]
51. Lu, T.; Chen, Q. A simple method of identifying π orbitals for non-planar systems and a protocol of studying π electronic structure. *Theor. Chem. Acc.* **2020**, *139*, 25. [CrossRef]
52. Parr, R.G.; Szentpaly, L.V.; Liu, S. Electrophilicity Index. *J. Am. Chem. Soc.* **1999**, *121*, 1922–1924. [CrossRef]
53. Bourass, M.; Benjelloun, A.T.; Benzakour, M.; Mcharfi, M.; Hamidi, M.; Bouzzine, S.M.; Bouachrine, M. DFT and TD-DFT calculation of new thienopyrazine-based small molecules for organic solar cells. *BMC Chem.* **2016**, *10*, 67. [CrossRef] [PubMed]
54. Bavadi, M.; Niknam, K.; Shahraki, O. Novel pyrrole derivatives bearing sulfonamide groups: Synthesis invitro cytotoxicity evaluation, molecular docking and DFT study. *J. Mol. Struct.* **2017**, *1146*, 242–253. [CrossRef]
55. Ali, S.; Akhter, M.; Waqas, M.; Zubair, H.; Bhatti, H.; Mahal, A.; Shawky, A.; Alkhouri, A.; Khera, R. End-capped engineering of Quinoxaline core-based non-fullerene acceptor materials with improved power conversion efficiency. *J. Mol. Graph. Model.* **2024**, *127*, 108699. [CrossRef]
56. Chemek, M.; Rhouma, F.; Chemek, M.; Safi, Z.; Kadi, A.; Naili, S.; Wazzan, N.; Kamel, A. Impact of the chemical insertion of the dimethylamino group on the electronic and optical properties of the 4-(methoxyphenyl acetonitrile) monomer (MPA): A DFT theoretical investigation. *J. Mol. Model.* **2024**, *30*, 271. [CrossRef] [PubMed]
57. Ltayef, M.; Mbarek, M.; Almoneef, M.M.; Alimi, K. Modeling of the photophysical and photovoltaic properties of an active layer based on the organic composite poly(2-methoxy-5-(2-ethyl-hexyloxy)-1,4-phenylene-vinylene) (MEH-PPV)–poly(3-hexylthiophene) (P3HT): (6,6)-phenyl C61 butyric acid methyl ester (PCBM). *Int. J. Quantum Chem.* **2023**, *123*, e27204. [CrossRef]
58. Saleh, G.; Gatti, C.; Presti, L.; García, J. Revealing Non-covalent Interactions in Molecular Crystals through their Experimental Electron Densities. *Chem. Eur. J.* **2012**, *18*, 15523–15536. [CrossRef] [PubMed]
59. García, J.; Johnson, E.R.; Keinan, S.; Chaudret, R.; Piquemal, J.P.; Beratan, D.N.; Yang, W. NCIPLOT: A Program for Plotting Noncovalent Interaction Regions. *J. Chem. Theory Comput.* **2011**, *7*, 625–632. [CrossRef] [PubMed]
60. Danish, I.A.; Kores, J.; Sasitha, T.; Jebaraj, J.W. DFT, NBO, HOMO-LUMO, NCI, stability, Fukui function and hole-Electron analyses of tolcapone. *Comput. Theor. Chem.* **2021**, *1202*, 113296. [CrossRef]
61. Antony, D.I.; Jebasingh, K.J.; Abiya, C.D.; Bala, S.T.; Winfred, J.J. In silico analyses of solvent effects, toxicity, NBO, homo-lumo and hole-electron transfer of 7-hydroxy-2-nitrofluoranthene. *J. Indian Chem. Soc.* **2024**, *101*, 101147. [CrossRef]
62. Liu, X.; Wang, Y.; Liu, J.; Tian, J.; Fei, X. A High Performance 2-Hydroxynaphthalene Acylhydrazone Fluorescent Chemosensor for Detection of Al3+ Ions Through ESIPT and PET Signalling Mechanism. *J. Clust. Sci.* **2023**, *34*, 813–822. [CrossRef]
63. Li, S.; Zhang, Y.; Xu, Y.; Li, L.; Liu, J.; Quan, H.; Zhang, W.; Li, A. Design and modification thienonaphthalimides based non-fullerene acceptors for organic solar cells with high photovoltaic performance in visible light absorption range. *Comput. Theor. Chem.* **2024**, *1240*, 114832. [CrossRef]
64. UrRehman, S.; Laraib, M.; Shahzadi, T.; Bibi, S.; Khan, S.; Ran, J. Designation of efficient diketopyrrolopyrrole based non-fullerene acceptors for OPVs: DFT Study. *Mater. Chem. Phys.* **2024**, *327*, 129871. [CrossRef]
65. Xiong, C.; Sun, J.; Cai, C.; Caiyang, W.; Zhu, Y. Disclosing exciton binding energy of organic materials from absorption spectrum. *J. Sol. Energy.* **2020**, *240*, 155–160. [CrossRef]
66. Aboulouard, A.; Mtougui, S.; Demir, N.; Moubarik, A.; El idrissi, M.; Can, M. New non-fullerene electron acceptors-based on quinoxaline derivatives for organic photovoltaic cells: DFT computational study. *Synth. Met.* **2021**, *279*, 116846. [CrossRef]
67. Aboulouard, A.; Can, M.; El Azze, S.; El Baz, M.; Elhadadi, B.; El idrissi, M.; Laasri, S. A computational study of thiophene containing small-molecule electron acceptors for non-fullerene organic photovoltaic cells. *Mater. Sci. Energy Technol.* **2023**, *6*, 137–144. [CrossRef]
68. Jin, F.; Yuan, J.; Guo, W.; Xu, Y.; Zhang, Y.; Sheng, C.; Ma, W.; Zhao, H. Improved Charge Generation via Ultrafast Effective Hole-Transfer in All-Polymer Photovoltaic Blends with Large Highest Occupied Molecular Orbital (HOMO) Energy Offset and Proper Crystal Orientation. *Adv. Funct. Mater.* **2018**, *28*, 1801611. [CrossRef]
69. Liu, W.; Li, S.; Huang, J.; Yang, S.; Chen, J.; Zuo, L.; Shi, M.; Zhan, X.; Li, C.; Chen, H. Nonfullerene Tandem Organic Solar Cells with High Open-Circuit Voltage of 1.97 V. *Adv. Mater.* **2016**, *28*, 9729–9734. [CrossRef]
70. Akram, S.J.; Hadia, N.M.A.; Shawky, A.M.; Iqbal, J.; Khan, M.I.; Alatawi, N.S.; Ibrahim, M.A.A.; Ans, M.; Khera, R.A. Designing of Thiophene [3, 2-b] Pyrrole Ring-Based NFAs for High-Performance Electron Transport Materials: A DFT Study. *ACS Omega* **2023**, *8*, 11118–11137. [CrossRef] [PubMed]
71. Tang, A.; Xiao, B.; Chen, F.; Zhang, J.; Wei, Z.; Zhou, E. The Introduction of Fluorine and Sulfur Atoms into Benzotriazole-Based p-Type Polymers to Match with a Benzotriazole-Containing n-Type Small Molecule: "The Same-Acceptor-Strategy" to Realize High Open-Circuit Voltage. *Adv. Energy Mater.* **2018**, *8*, 1801582. [CrossRef]

72. Rehman, F.; Waqas, M.; Imran, M.; Ibrahim, M.A.A.; Iqbal, J.; Khera, R.M.; Hadia, N.M.A.; Al-Saeedi, S.I.; Shaban, M. Approach toward Low Energy Loss in Symmetrical Nonfullerene Acceptor Molecules Inspired by Insertion of Different π-Spacers for Developing Efficient Organic Solar Cells. *ACS Omega* **2023**, *8*, 43792–43812. [CrossRef]
73. Green, M.A. Solar cell fill factors: General graph and empirical expressions. *Solid-State Electron.* **1981**, *24*, 788–789. [CrossRef]
74. Lu, Q.; Qiu, M.; Zhao, M.; Li, Z.; Li, Y. Modification of NFA-Conjugated Bridges with Symmetric Structures for High-Efficiency Non-Fullerene PSCs. *Polymers* **2019**, *11*, 958. [CrossRef] [PubMed]

polymers

MDPI

Article

Exploring Crystal Structure Features in Proton Exchange Membranes and Their Correlation with Proton and Heat Transport

Cong Feng [1,*], Cong Luo [1], Pingwen Ming [2] and Cunman Zhang [2]

[1] College of Materials Science and Engineering, Tongji University, Shanghai 201804, China; 2130588@tongji.edu.cn
[2] School of Automotive Studies, Tongji University, Shanghai 201804, China; pwming@tongji.edu.cn (P.M.); zhangcunman@tongji.edu.cn (C.Z.)
* Correspondence: fengcong@tongji.edu.cn

Abstract: Proton exchange membranes (PEMs) are dominated by semicrystalline structures because highly pure crystals are still challenging to produce and control. Currently, the development and application of PEMs have been hindered by a lack of understanding regarding the effects of microstructure on proton and heat transport properties. Based on an experimentally characterized perfluoro sulfonic acid membrane, the corresponding semicrystalline model and the crystal model contained therein were constructed. The water distribution, proton, and heat transport in the crystal, amorphous, and semicrystalline regions were examined using molecular dynamics simulations and energy-conserving dissipative particle dynamics simulations. The crystal structure had pronounced water connection pathways, a proton transport efficiency 5–10 times higher than that of the amorphous structure, and an in-plane covalent bonding that boosted the thermal diffusion coefficient and thermal conductivity by more than 1–3 times. The results for the semicrystalline structure were validated by the corresponding experiments. In addition, a proportionality coefficient that depended on both temperature and water content was proposed to explain how vehicle transport contributed to the proton conductivities, facilitating our understanding of the proton transport mechanism. Our findings enhance our theoretical understanding of PEMs in proton and heat transport, considering both the semicrystalline and crystalline regions. Additionally, the research methods employed can be applied to the study of other semicrystalline polymers.

Keywords: semicrystalline structure; multiscale simulations; proton conductivity; thermal properties; characterization tests

1. Introduction

Proton exchange membranes (PEMs), with their potential to address pressing energy and environmental challenges, are critical components of fuel cells and water electrolysis systems [1–4]. Despite significant advances in research, development, and practical applications, the widespread commercialization of PEMs remains hindered by various technical and economic obstacles. Among the primary concerns are the challenges of balancing chemical and thermal stability, high proton conductivity, and cost-effectiveness [5–7]. Currently, perfluorosulfonic acid (PFSA) is the dominant material used in commercial PEMs, with newly developed membranes often being compared with the performance of Nafion, a widely-used PFSA-based membrane. Consequently, understanding the nanostructure of Nafion and its correlation with its properties is crucial for evaluating novel PEM materials. However, the molecular-level nanostructure of Nafion and its conductive properties remain areas of uncertainty. Specifically, the configuration, distribution, and volume occupancy of crystal regions within Nafion and their effects on proton conduction and thermal properties are critical factors influencing PEM functionality.

In recent years, single-crystal proton-conducting materials, such as metal–organic frameworks (MOFs) [8–10], hydrogen-bonded organic frameworks [11,12], and polyoxometalates (POMs) [13], have garnered considerable attention due to their well-defined structures and distinguishable proton transmission pathways. For example, the POM crystal material discovered by Wang et al. exhibited high proton conductivity, reaching 0.19 S/cm along the [001] direction at 85 °C and 98% relative humidity. When processed into a composite membrane, it demonstrated peak proton conductivity of 5.31×10^{-2} S/cm [13]. These findings suggest that the conductivity of the crystal segments within PEMs significantly influences their overall conductivity. Similarly, Nafion membranes, with their semicrystalline nanostructure, typically achieve proton conductivities of 0.1 S/cm under comparable temperature and humidity conditions. This raises the question of how increasing the grain size and crystallinity of Nafion membranes might affect proton conductivity.

Studies on the microstructures of Nafion have been conducted using small-angle X-ray scattering (SAXS), wide-angle X-ray scattering (WAXS), and X-ray diffraction (XRD). The SAXS profile reveals two peaks: one corresponding to ionic clusters and the other to the hydrophobic matrix [14,15]. The first peak is attributed to ionic clusters, while the second is associated with lamellar tetrafluoroethylene crystallites. In the WAXS plots, the observed peak indicates the crystalline phase, and both crystallite size and crystallinity generally increase with heating cycles from 40 to 250 °C [16]. However, the crystallinity of Nafion can vary depending on the preparation method, fabrication process, and testing techniques. For example, the crystallinity of Nafion with an equivalent weight (EW) of 1100 was 23% in its nonionic form and 18–14% in its carboxylated form, with crystallinity increasing as the EW value increased [17]. For the untreated commercial Nafion 117 membrane, XRD measurements typically showed a crystallinity between 27% and 30% [18,19].

Simulation is another effective method of investigating the microstructural characteristics of Nafion membranes. For example, all-atom molecular dynamics simulations, due to molecular vibrations and transport occurring on a picosecond timescale, offer significant advantages in studying the structural characteristics and dynamic properties of PFSA membranes [20–22]. Short side-chain ionomers, such as Aquivion, exhibit higher diffusion coefficients for water molecules and hydronium ions compared with Nafion systems [21]. This is attributed to the shorter side chains, which facilitate the movement of hydronium ions among host groups, enhancing chain adsorption [22]. Dissipative particle dynamics simulation has the advantage of reconstructing the water-phase structure and analyzing the diffusion of particles and tortuosity of the hydrated membrane at a mesoscopic scale [23–25]. Furthermore, two-dimensional pattern simulations, through calculated electron density maps, can approximate SAXS curves, optimizing the distribution and characteristics of crystalline, semicrystalline, and amorphous regions, thus explaining the structural features of Nafion [26]. While these investigations provide valuable insights into the nanostructure and its associated particle transport properties, the atomistic arrangement in crystalline regions and their contribution to particle transport and heat transport have been less reported.

In addition to proton conduction, efficient heat transfer is another essential property of PEMs, as thermal management is crucial for the performance of PEM fuel cell (PEMFC) stacks [27,28]. Various studies have focused on improving system structures, enhancing heat transfer efficiency, and boosting the thermal properties of key materials [29–31]. Early investigations have shown that the thermal conductivity of Nafion ranges from 0.2 to 0.4 W/(m·K), increasing with water content and varying with temperature [32–36]. However, the thermal properties of single-crystal or semicrystalline PEM materials differ significantly from their amorphous counterparts due to in-plane covalent bonding. Factors such as phonon collision probability, transmission, and diffusivity—crucial for heat transfer—are notably different between these material phases [37–39].

This study aims to determine the nanostructural characteristics of PEM materials, particularly the crystal regions, such as lattice structure, grain size, and volume occupancy ratio. Through a combination of experimental and simulation methods, we seek to establish

a relationship between the semicrystalline microstructure of PEMs and their macroscopic properties related to proton and heat transport.

2. Research Methods

2.1. Microstructure Characterization

The semicrystalline morphology of Nafion was characterized using high-resolution transmission electron microscopy (HR-TEM) (JEM-2100F, JEOL, Tokyo, Japan). A Nafion D2020 resin solution with an initial concentration of 20 wt% was diluted to 1 wt% using isopropyl alcohol to prepare the sample. The crystal characteristics of the commercial Nafion 117 membrane were then analyzed via XRD (DX-2700BH, HAOYUAN, Fuyang, China) at room temperature.

The HR-TEM image of Nafion's semicrystalline nanostructure is presented in Figure 1a, where crystal regions (dark zones) appear as approximately 4 nm circular spots, randomly dispersed within the amorphous matrix. The XRD pattern for Nafion 117 (Figure 1b) showed a sharp peak at $2\theta = 17.89°$, corresponding to an interplanar crystal spacing of $d = 4.95$ Å. These data suggest a crystallinity of 28% and a grain size of 4.41 nm, consistent with findings in the literature [18,19,40]. A second broad peak around $2\theta = 38°$ was attributed to intra-chain spacing, likely resulting from overlapping diffraction along the polymer chain axis due to intramolecular correlations in both amorphous and crystal phases [41,42].

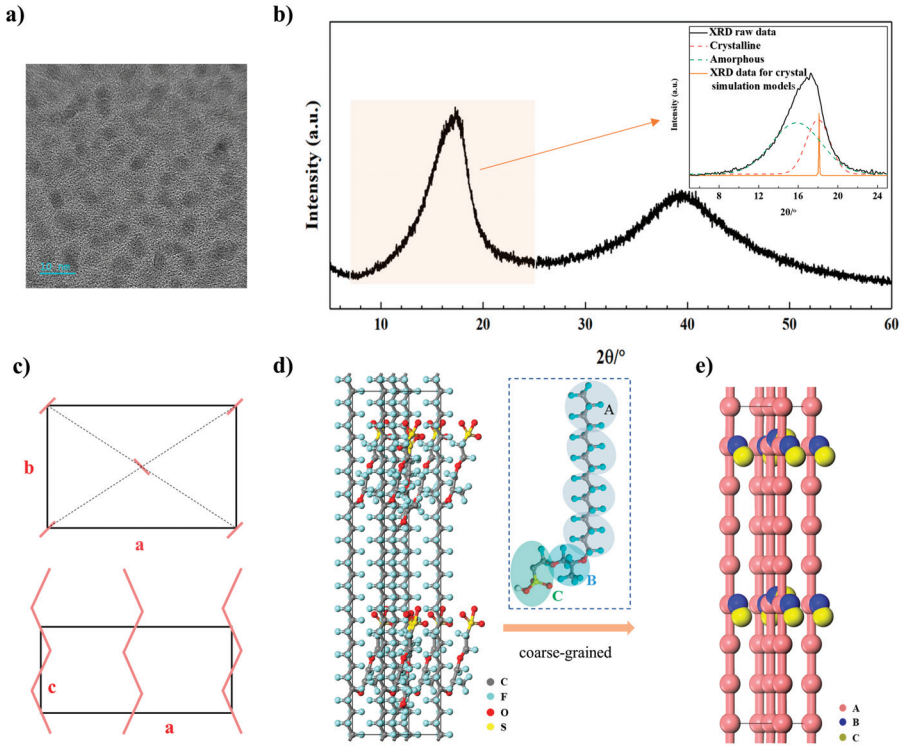

Figure 1. Characterization and modeling of the crystal structure. (**a**) HR-TEM and (**b**) XRD patterns of Nafion 117, and the inset shows the crystal and amorphous peaks of XRD, as well as the crystal peak of molecular modeling. (**c**) Schematic representative, (**d**) all-atom model, and (**e**) coarse-grained model of the crystal structure.

2.2. Modeling and Validation of Crystal Structure

By integrating the XRD data and HR-TEM images, it was deduced that Nafion possesses an orthorhombic crystal structure with unit cell dimensions of $a = 9.9$ Å, $b = 5.6$ Å and $c = 2.8$ Å (Figure 1c). These results align with those reported by Heijden et al. [42]. Using this information, an all-atom molecular model was constructed to represent the crystal structure (Figure 1d), and the XRD intensity for this model was calculated. The calculated

XRD results closely matched the experimental Nafion XRD pattern (inset in Figure 1b), particularly at the peak corresponding to the (2 0 0) crystal plane, confirming the accuracy of the model.

Since the real membrane scale is much larger than that of the all-atom model, a coarse-grained model was developed to extend the simulation scales. In the coarse-grained model, each particle represents a collection of atoms. For instance, four water molecules are grouped into a bead (W), with the radius R_c = 7.82 Å, derived from water's mass and density. Three hydrated protons form a bead (P). The Nafion backbone is divided into beads (A) comprising 12 atoms (-CF2-CF2-CF2-CF2-), while the side chain is represented by bead B (-O-CF3-CF-CF2-O-) and bead C (-CF2-CF2-SO3-) (Figure 1e).

2.3. Semicrystalline and Amorphous Structures

For semicrystalline structures, larger coarse-grained models were constructed to encompass multiple crystal and amorphous regions. Crystal models were randomly placed in a simulation box, followed by the addition of amorphous polymer chains to match the observed crystallinity of 28%. This semicrystalline unit cell (Figure S1) was then enlarged by a factor of three along the x, y, and z axes, resulting in a final model size of 30–40 nm.

Amorphous structures were created by randomly arranging polymer chains in a periodic box. The size of these boxes and the number of molecular chains were kept identical to those used in the crystal structures, ensuring that the comparison focused solely on structural effects without introducing other variables.

2.4. Simulation Details

To investigate proton transport and thermal properties, energy-conserving dissipative particle dynamics (eDPDs) and all-atom molecular dynamics (AAMDs) simulations were employed. These simulations were conducted using the large-scale atomic/molecular massively parallel simulator (LAMMPS) [43]. The two simulation methods complement each other, as eDPDs enable analysis on larger time and size scales, while AAMDs provide detailed insights into atomic-level interactions in both crystal and amorphous regions.

In the AAMD simulations, interactions between water molecules were modeled using the TIP3P water model, while the perfluorosulfonic acid system was described using the DREIDING force field. This force field was validated by comparing calculated energy values with those obtained from the commercial software Materials Studio 6.0. Specific parameters and validation results are provided in Tables S1–S5. For eDPD simulations, derived parameters and equations are detailed in the Supplementary Material (Note S3).

Periodic boundary conditions were applied to all models. To investigate proton transport under the vehicle mechanism, a constant electric field of 1×10^3 V/m was applied along one direction of the PEM model, simulating the potential difference typical of PEMFC conditions. The hydronium ion diffusion coefficient (D) was calculated using Einstein's diffusion law, based on the mean square displacement (MSD) curves (Figure S2a). Proton conductivity (σ_V) was then derived from the diffusion coefficient [44]. Heat transport simulations were performed along the Z-axis of the models. Heat was applied to the top and removed from the bottom of the simulation box over 50,000 time steps to reach thermal equilibrium (Figure S2b). The final 20,000 steps were used to monitor temperature gradients across 1 nm slices along the Z-axis (Figure S2c).

2.5. Thermal Performance Testing

The thermal properties of Nafion 117, including thermal diffusivity and thermal conductivity, were experimentally measured to validate the simulation results. The thermal diffusivity was determined using a laser thermal conductivity instrument (LFA 467, HyperFlash, NETZSCH, Sable, Germany). Four identical samples were tested, with each sample coated with carbon to enhance measurement accuracy. Thermal conductivity measurements were conducted using a thermal conductivity analyzer (TPS3500, Hot Disk, Uppsala, Sweden), which calculates conductivity by monitoring voltage shifts during heat

transfer. Three samples were tested at each temperature to ensure the reproducibility and consistency of the data.

3. Results and Discussion

3.1. Water Distribution

Understanding water distribution within the proton exchange membrane (PEM) is essential for analyzing both proton and heat transport mechanisms. In this study, water distribution was examined under three hydration levels (denoted as λ = 3, 11, and 21) across a temperature range of 300 to 360 K, reflecting typical operating conditions of fuel cells. The water distribution patterns within both the crystal and amorphous structures were simulated using AAMD and eDPD, showing consistent results (Figure S3).

The simulations revealed that the morphology of water channels was influenced by both temperature and hydration levels. As shown in Figure 2a, in the crystal regions, a layered water distribution was observed, where water molecules were concentrated between adjacent polymer backbone chains. This layering effect arose from the regular arrangement of hydrophilic groups within the crystal domains, which promoted the formation of connected water channels adjacent to the ionomer side chains. However, at the lowest hydration level (λ = 3), the structure lacked pronounced layering due to insufficient water content. As the water content increased (λ = 11), a partially delaminated structure emerged, while at the highest hydration level (λ = 21), the structure became more well-defined and ordered.

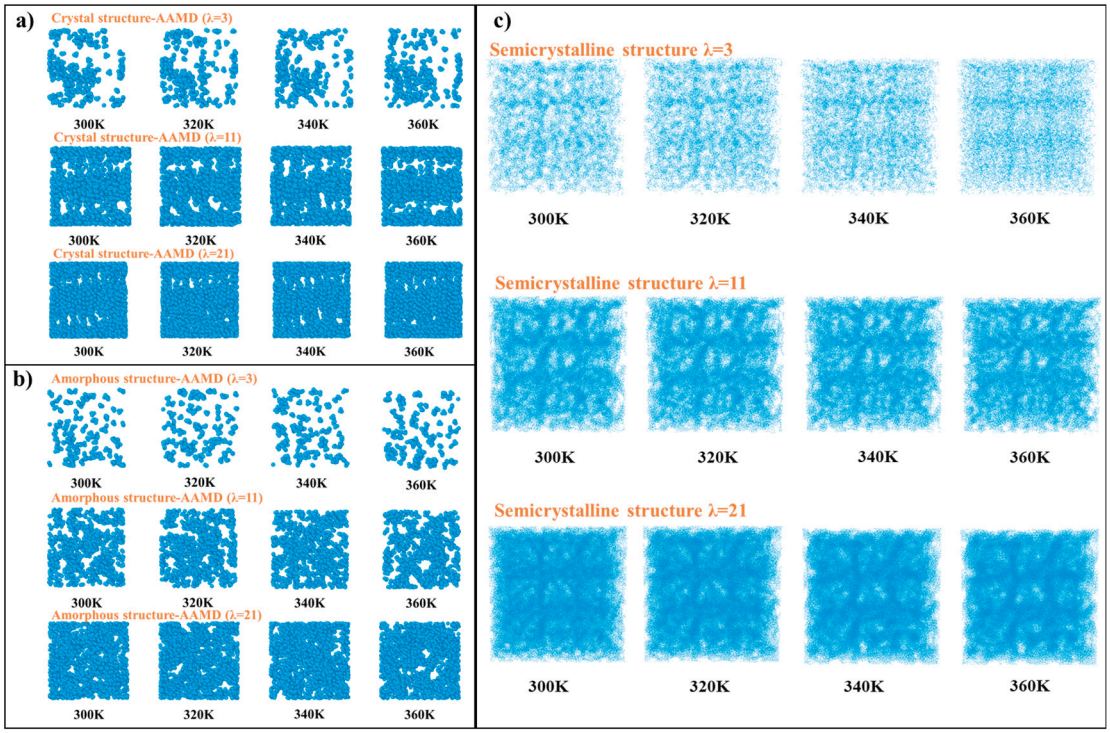

Figure 2. Distribution of water molecules in (**a**) crystal, (**b**) amorphous, and (**c**) semicrystalline structures.

In contrast, the water distribution within amorphous regions showed no specific regular structure (Figure 2b). Water molecules were more randomly dispersed, lacking the organization seen in the crystal regions. Nevertheless, the semicrystalline structure, which contained both crystal and amorphous domains, exhibited a more ordered water distribution than the fully amorphous structure (Figure 2c). This was because the crystal regions helped to organize the water channels. Interestingly, temperature appeared to have

a lesser impact on water distribution than hydration level, as the water molecules were primarily influenced by structural arrangements, rather than thermal fluctuations.

3.2. Proton-Conducting Properties

3.2.1. Influence Factors

The parameter σ_V, which is governed by the vehicle transport mechanism of PEMs, was investigated in detail. Given the anisotropic nature of crystal structures, special attention was paid to how proton conductivity changes with respect to the orientation of the electric field relative to the polymer backbone. Figure 3a illustrates this setup, where $\theta = 0°$ represents a field direction parallel to the backbone chain.

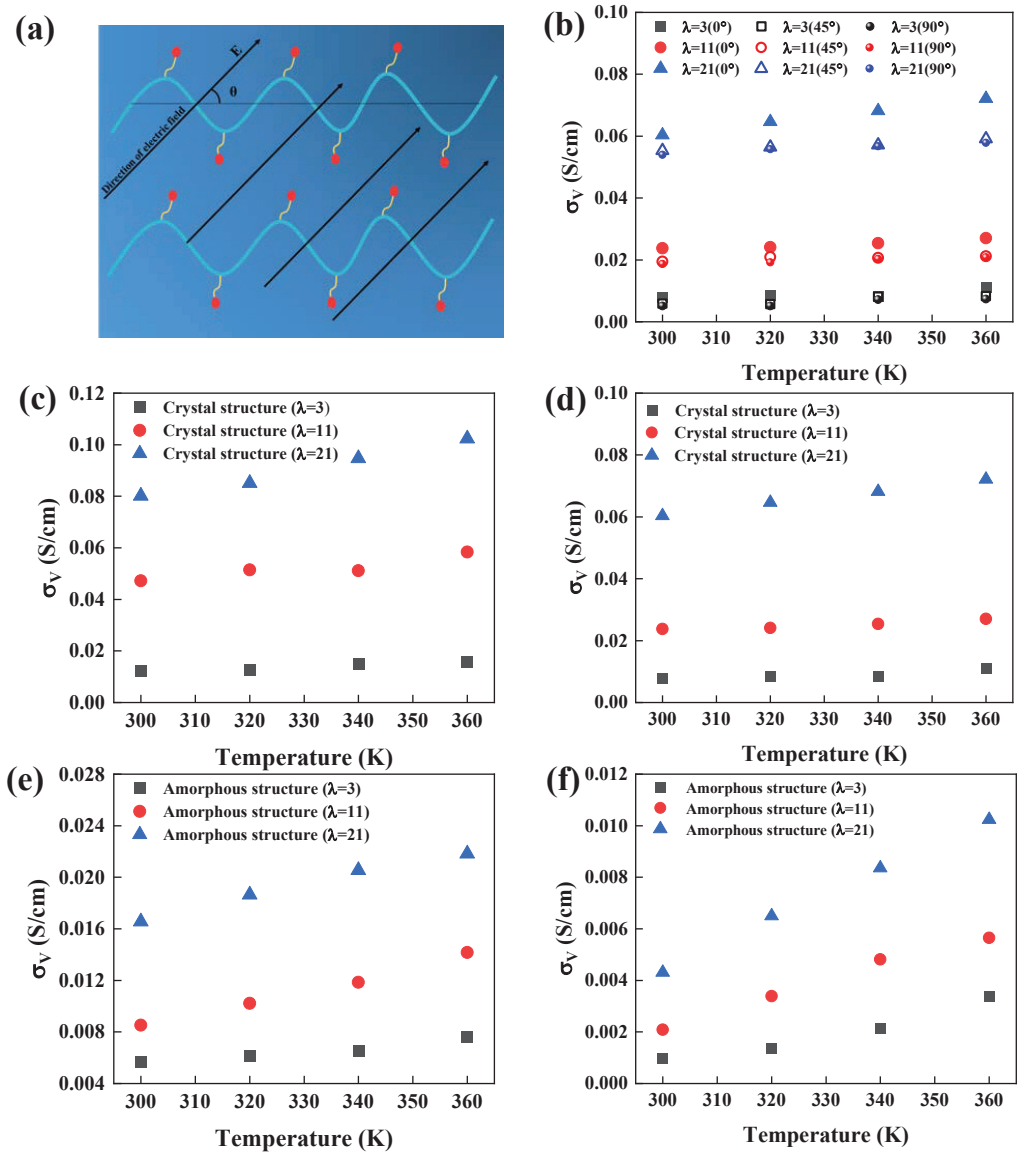

Figure 3. (**a**) Schematic of the direction of the electric field and the structure of the backbone chain arrangement. (**b**) Proton conductivity in different electric field directions. (**c**–**f**) Proton conductivity in crystal and amorphous structures from AAMD and eDPD simulations.

In crystal structures, proton transport is facilitated by the presence of continuous hydrophilic channels running parallel to the backbone. When the electric field is applied along this direction ($\theta = 0°$), proton conductivity is highest. However, as the field angle increases, conductivity decreases significantly (Figure 3b). Proton transport is least efficient when the electric field is applied perpendicular to the proton-conducting channels ($\theta = 90°$),

but even under these conditions, proton conductivity in the crystal regions is still notably higher than that of amorphous regions. This highlights the critical role that regularly arranged crystal structures play in enhancing proton transport.

The simulations (Figure 3c,d) further demonstrated that crystal structures exhibited proton conductivities that are five to ten times higher than those of amorphous structures. Both temperature and water content positively influenced conductivity by increasing the fluidity of the water channels and the thermal motion of atoms, thereby accelerating proton transport. In contrast, in amorphous regions, the entangled polymer chains obstructed the water channels, leading to slower proton transport. Additionally, the proton conductivity from eDPD simulations was slightly higher than that obtained from AAMD simulations, likely due to the larger time and system scales accessible in eDPD (Figure 3e,f). Semicrystalline structures, owing to their mixed composition, exhibited intermediate conductivity between fully crystal and amorphous structures (Figure S4). As a result, the proton conductivity exhibited a progressive decrease in crystal, semicrystalline, and amorphous structures, and were primarily determined by crystallinity, with less influence from other factors like temperature, water content, and electric field direction.

3.2.2. Relationship Between Microstructure and Macroscopic Properties

Controlling the macroscopic properties of PEMs through their microstructural design is crucial for optimizing proton conductivity. It is well-known that periodic boundary conditions (PBCs) in molecular simulations can introduce boundary effects, leading to deviations in particle transport compared to macroscopic models. To address this, an empirical relationship was applied to calculate the correlation of the diffusion coefficient under PBC conditions (D_{PBC}) with the diffusion coefficient in an infinite system (D_0) using the equation $D_{PBC} = D_0 - h/LD_{PBC}$, where L is the box length and h is a constant [45–48]. This approach allowed us to account for system size effects and calculate proton conductivity more accurately for semicrystalline structures (Figure 4a–c).

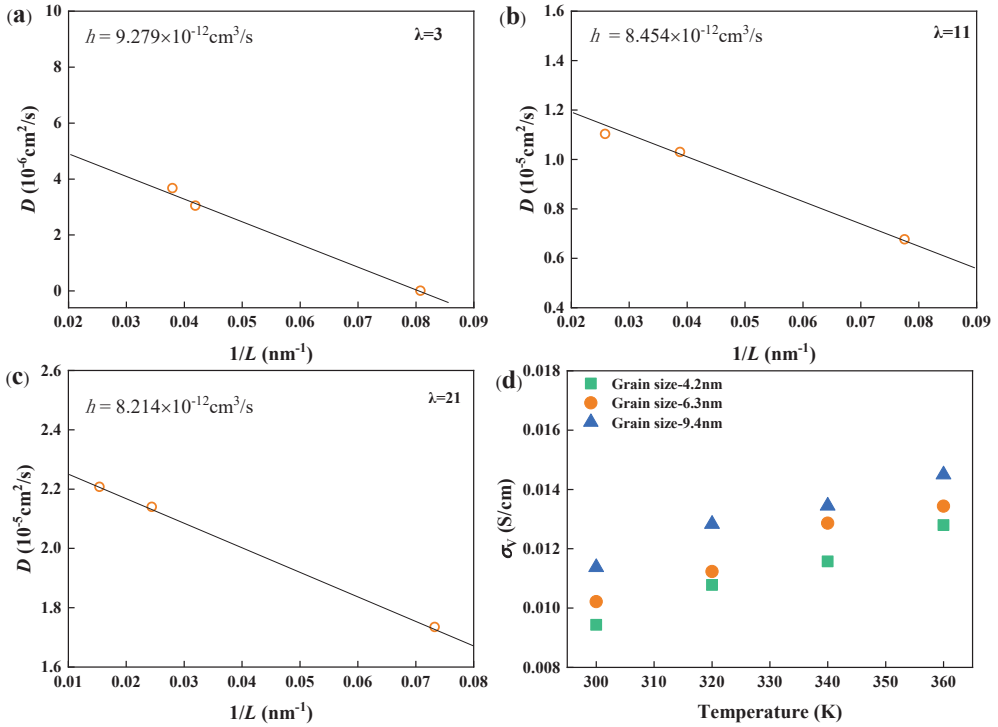

Figure 4. Proton diffusion coefficients of semicrystalline structures as a function of 1/L at (**a**) λ = 3, (**b**) λ = 11, and (**c**) λ = 21. (**d**) Proton conductivity in the same semicrystalline structure with different grain sizes.

Next, the effect of grain size on proton conductivity was explored in semicrystalline structures at λ = 3 with a constant crystallinity of 28%. As shown in Figure 4d, larger grain sizes resulted in higher proton transport due to the improved connectivity of water channels. This suggests that increasing the crystallinity or grain size of PEM materials could enhance proton transport efficiency.

3.2.3. Proportionality Coefficient σ_E/σ_V

Electrochemical impedance spectroscopy (EIS) was used to determine the total proton conductivity (σ_E) and compare it with the vehicle transport conductivity (σ_V). The proportionality coefficient $N = \sigma_E/\sigma_V$ was calculated, which provides insight into the relative contributions of the Vehicle and Grotthuss mechanisms to overall proton transport. Here, σ_V was derived from our semicrystalline model, which represented a real Nafion membrane, as both shared similar structural properties, such as crystallinity, crystal size and structural parameters. It had the following fitted expression under different environmental conditions:

$$\sigma_V = (3.906\lambda + 1)exp\left(-5.737 - \frac{379.978}{T}\right) \quad (1)$$

Using the proton conductivity σ_E of Nafion 117, proposed in a previous study [49] as a function of temperature (T) and water content (λ), the proportionality coefficient N can be expressed as follows

$$\frac{\sigma_E}{\sigma_V} = N = (0.01\lambda + 1)exp\left(2.853 - \frac{817.653}{T}\right) \quad (2)$$

Figure S4 presents the specific values of σ_V and σ_E at different temperatures and water contents. N increased with both temperature and water content, as shown in Figure 5, indicating that the Grotthuss mechanism became increasingly dominant under these conditions.

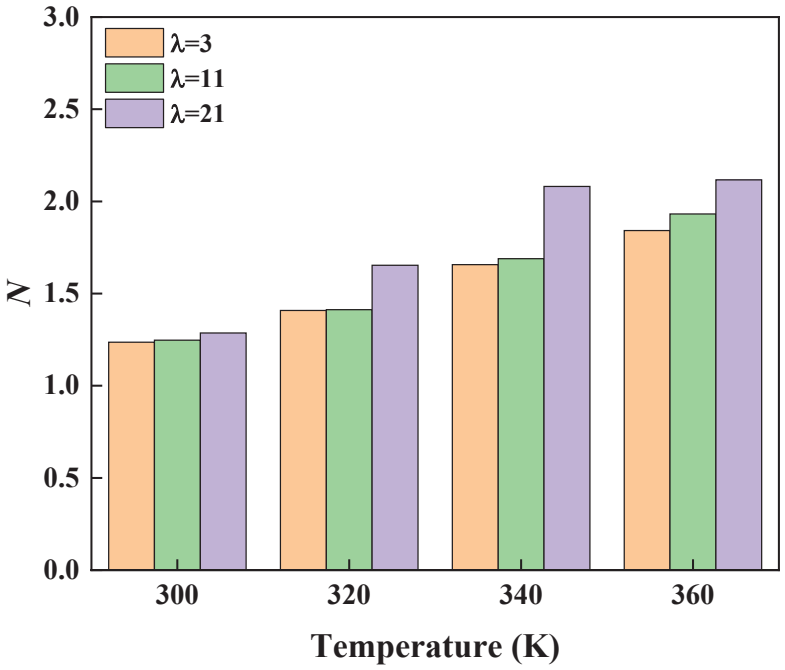

Figure 5. Proportionality coefficient N versus temperature and water content.

3.3. Thermal Properties

The thermal properties of Nafion, including thermal diffusivity, specific heat capacity, and thermal conductivity, were investigated through both simulations and experiments. The simulated system included three different water contents (λ = 3, 11, and 21). In contrast, due to the uncontrollable humidity conditions in the chamber of the experimental apparatus, only

samples with humidity levels similar to those of the surrounding atmosphere were measured, corresponding to λ values of 4–5. These thermal properties were primarily determined by the atomic molar heat capacity of the system, which was analyzed in detail (Figure S5). A periodic heat conduction simulation was conducted by applying a non-contact heat source to each coarse-grained particle in the eDPD model [50] (Figure S2b).

3.3.1. Thermal Diffusion Coefficients

The thermal diffusion coefficients for crystal, amorphous, and semicrystalline structures are presented in Figure 6a–c. In crystal structures, phonon mobility is enhanced due to the reduced probability of phonon collisions, resulting in a higher thermal diffusion coefficient compared with amorphous structures. Water, with a higher thermal diffusion coefficient than Nafion, further increased the overall thermal diffusivity as water content increased between 30 and 360 K. However, temperature had a relatively minor effect on thermal diffusion coefficients within the studied range. The comparison between the simulation and experimental results (Figure 6d) showed good agreement, though the simulated values were slightly higher, likely due to the smaller time and system scales used in the simulations.

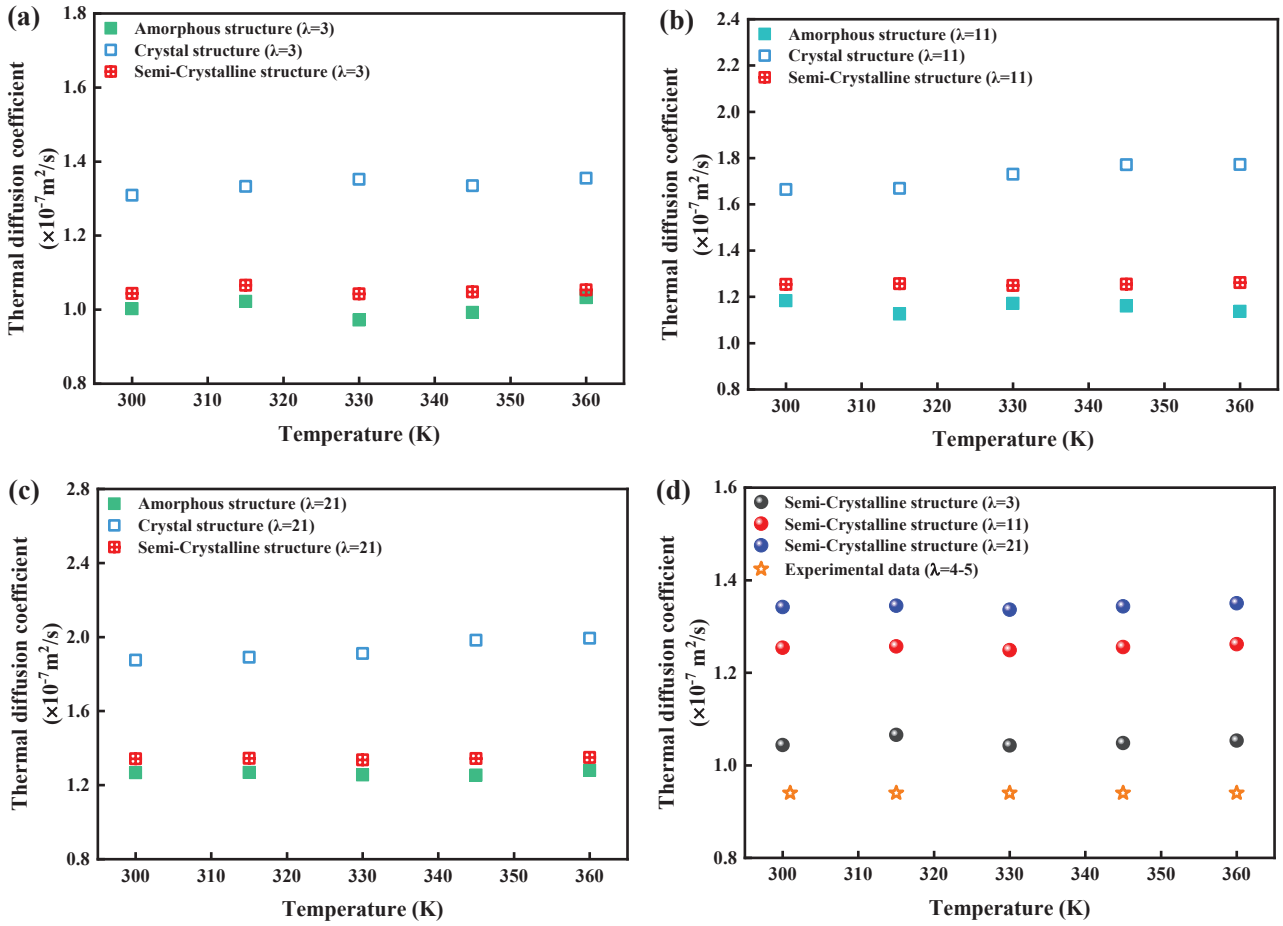

Figure 6. Thermal diffusion coefficient of crystal, amorphous and semicrystalline structures at (**a**) λ = 3, (**b**) λ = 11, and (**c**) λ = 21. (**d**) Comparison of simulation and experimental results.

3.3.2. Specific Heat Capacity

The specific heat capacities of the crystal, semicrystalline, and amorphous structures are illustrated in Figure 7. Specific heat capacity increased with both temperature and water content. Crystal structures, due to their denser atomic packing and restricted atomic vibrations, exhibited lower specific heat capacities than amorphous structures. Additionally, because water has a higher specific heat capacity than Nafion, increasing water content in-

creased the overall heat capacity. The simulation results aligned well with the experimental data, particularly for hydration levels $\lambda = 3$ and $\lambda = 11$, as shown in Figure 7d.

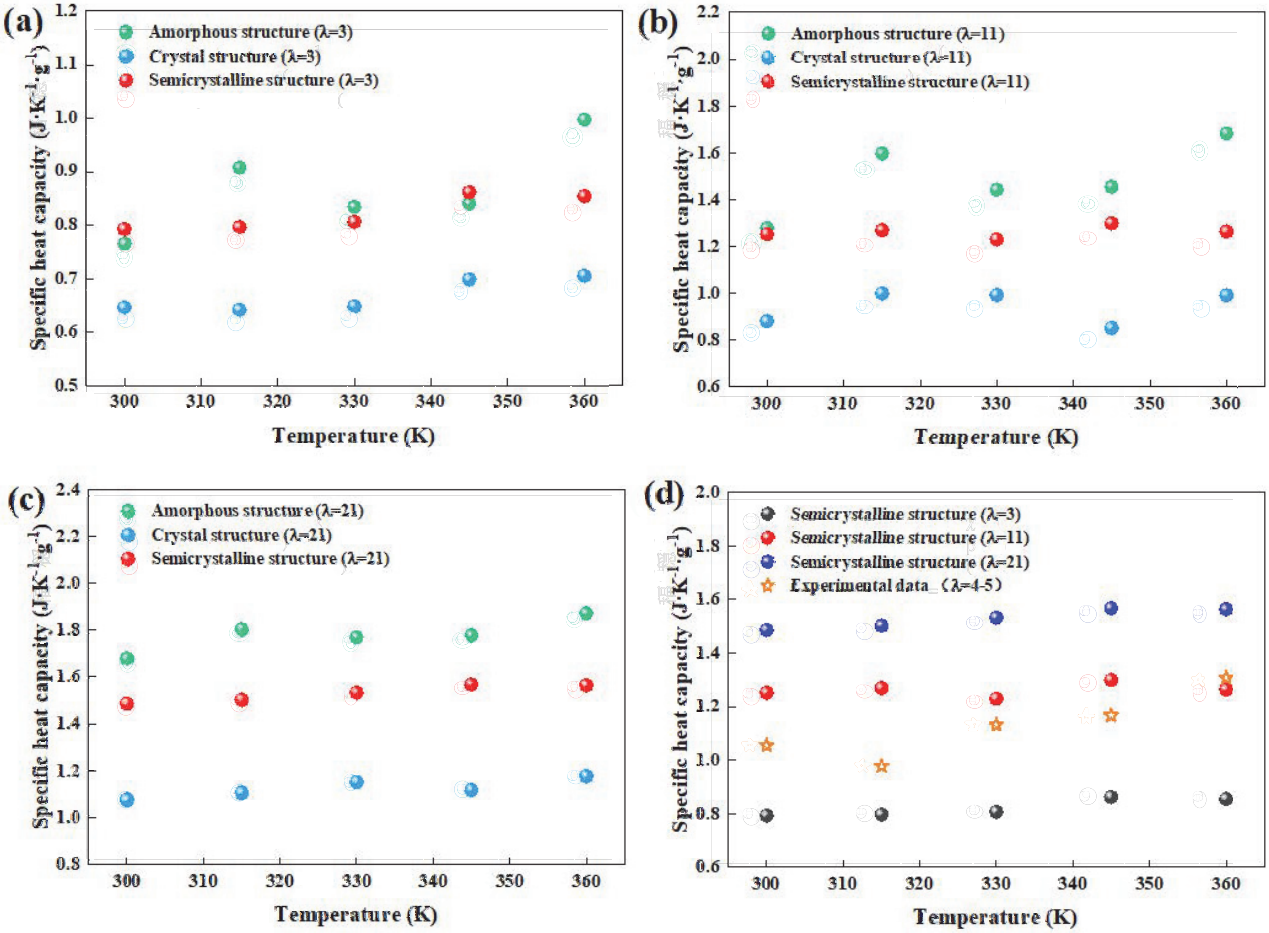

Figure 7. Specific heat capacity of crystal, amorphous, and semicrystalline structures at (**a**) $\lambda = 3$, (**b**) $\lambda = 11$, and (**c**) $\lambda = 21$. (**d**) Comparison of simulation and experimental results.

3.3.3. Thermal Conductivity

Thermal conductivity (κ) was calculated using the relationship between thermal diffusivity (α), specific heat capacity (C), and density (ρ), where $\kappa = \alpha \times \rho \times C$. As seen in Figure 8, thermal conductivity increased with temperature, driven by the increase in specific heat capacity, while thermal diffusivity remained relatively constant. Crystal structures had higher thermal conductivity (about 1.3 times) compared with amorphous structures due to their longer phonon mean free paths, with semicrystalline structures displaying intermediate values. The simulation results agreed well with experimental data for Nafion 117 (Figure 8d). Therefore, thermal conductivity was primarily influenced by the structural organization and water content of the material, with crystal structures outperforming amorphous regions. These results provide valuable insights into the thermal management of PEMs in fuel cell applications.

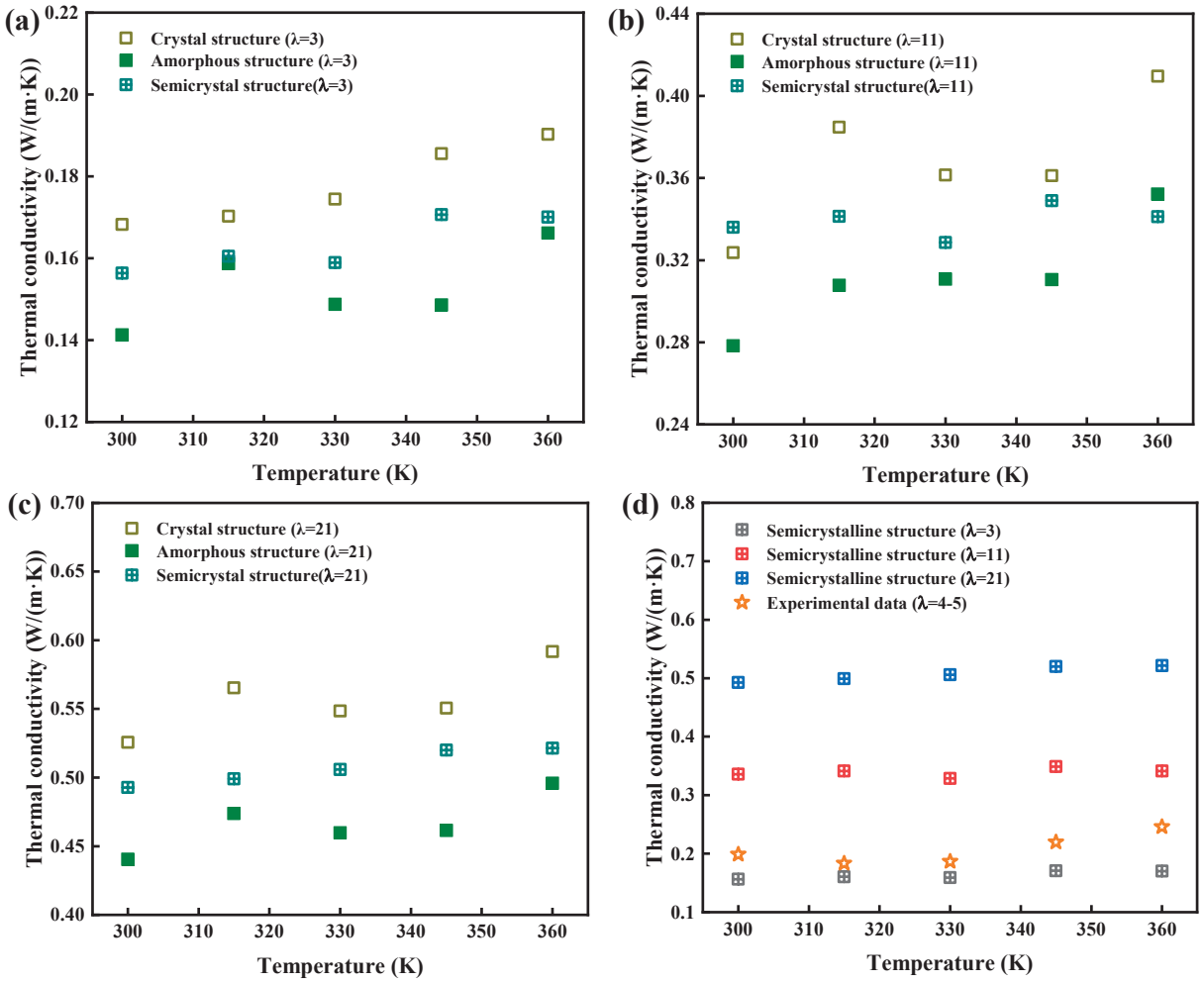

Figure 8. Thermal conductivity of crystal, amorphous, and semicrystalline structures, as calculated from eDPD simulations, for (**a**) λ = 3, (**b**) λ = 11, and (**c**) λ = 21; and (**d**) a comparison of Nafion membrane's thermal conductivity, measured experimentally and calculated from eDPD simulations, for semicrystalline structures. The hollow, solid, hollow with cross, and pentagram symbols represent the thermal conductivity of the crystal, amorphous, and semicrystalline structures and Nafion 117 membrane, respectively.

4. Conclusions

In conclusion, molecular simulations and experimental characterizations were employed to establish and validate a crystal structure model of the Nafion membrane. The regular arrangement of side chains in the crystal structure facilitated a smoother and more connected distribution of water molecules, enabling efficient proton transport with minimal dependence on the direction of the electric field. This behavior contrasted with that observed in amorphous and semicrystalline structures. Specifically, for a given crystallinity and environmental conditions, an increase in grain size led to enhanced proton conductivity. The diffusion coefficient was extrapolated from periodic boundary systems to macroscopic systems using a scaling factor h, and the contribution of vehicle transport to proton conductivity was quantified through the proportionality coefficient N.

Additionally, thermal properties, such as the thermal diffusion coefficient, specific heat capacity, and thermal conductivity of PEMs, were determined and confirmed through experimentation. At the same temperature and water content, the crystal structure exhibited the highest thermal conductivity and diffusion coefficient, while the amorphous structure exhibited the lowest. This study provides valuable insights into the relationship between the microstructural features of semicrystalline PEMs and their proton and heat transport

properties. These findings will not only contribute to the development of novel PEM materials and inform technical applications based on molecular interaction mechanisms, but also serve as a methodological reference for exploring other semicrystalline polymer materials.

Supplementary Materials: The following supporting information can be downloaded at: https://www.mdpi.com/article/10.3390/polym16233250/s1.

Author Contributions: C.F.: Writing—original draft, Investigation, Conceptualization, Validation, Supervision. C.L.: Visualization, Methodology, Software, Formal analysis, Data curation. P.M.: Writing—review & editing, Conceptualization. C.Z.: Resources, Project administration. All authors have read and agreed to the published version of the manuscript.

Funding: This research was funded by the National Key Research and Development Program of China (2021YFB4001701) and the Natural Science Foundation of Shanghai (21ZR1465300).

Institutional Review Board Statement: Not applicable.

Data Availability Statement: The original contributions presented in the study are included in the article/Supplementary Materials, further inquiries can be directed to the corresponding author.

Acknowledgments: The authors gratefully acknowledge the financial support provide by the National Key Research and Development Program of China (2021YFB4001701) and the Natural Science Foundation of Shanghai (21ZR1465300).

Conflicts of Interest: The authors declare that they have no known competing financial interests or personal relationships that could have appeared to influence the work reported in this paper.

References

1. Haider, R.; Wen, Y.; Ma, Z.F.; Wilkinson, D.P.; Zhang, L.; Yuan, X.; Song, S.; Zhang, J. High temperature proton exchange membrane fuel cells: Progress in advanced materials and key technologies. *Chem. Soc. Rev.* **2021**, *50*, 1138–1187. [CrossRef] [PubMed]
2. Fang, W.; Guo, W.; Lu, R.; Yan, Y.; Liu, X.; Wu, D.; Li, F.M.; Zhou, Y.; He, C.; Xia, C.; et al. Durable CO_2 conversion in the proton-exchange membrane system. *Nature* **2024**, *626*, 86–91. [CrossRef] [PubMed]
3. Jiao, K.; Xuan, J.; Du, Q.; Bao, Z.; Xie, B.; Wang, B.; Zhao, Y.; Fan, L.; Wang, H.; Hou, Z.; et al. Designing the next generation of proton-exchange membrane fuel cells. *Nature* **2021**, *595*, 361–369. [CrossRef] [PubMed]
4. Suter, T.A.M.; Smith, K.; Hack, J.; Rasha, L.; Rana, Z.; Angel, G.M.A.; Shearing, P.R.; Miller, T.S.; Brett, D.J.L. Engineering catalyst layers for next-generation polymer electrolyte fuel cells: A review of design, materials, and methods. *Adv. Energy Mater.* **2021**, *11*, 2101025. [CrossRef]
5. Liu, R.T.; Xu, Z.L.; Li, F.M.; Chen, F.Y.; Yu, J.Y.; Yan, Y.; Chen, Y.; Xia, B.Y. Recent advances in proton exchange membrane water electrolysis. *Chem. Soc. Rev.* **2023**, *52*, 5652–5683. [CrossRef]
6. Zhang, G.; Qu, Z.; Tao, W.Q.; Mu, Y.; Jiao, K.; Xu, H.; Wang, Y. Advancing next-generation proton-exchange membrane fuel cell development in multi-physics transfer. *Joule* **2024**, *8*, 45–63. [CrossRef]
7. Tan, H.; Zhao, S.; Ali, S.E.; Zheng, S.; Alanazi, A.K.; Wang, R.; Zhang, H.; Abo-Dief, H.M.; Xu, B.B.; Algadi, H.; et al. Perfluorosulfonic acid proton exchange membrane with double proton site side chain for high-performance fuel cells at low humidity. *J. Mater. Sci. Technol.* **2023**, *166*, 155–163. [CrossRef]
8. Lim, D.W.; Kitagawa, H. Rational strategies for proton-conductive metal–organic frameworks. *Chem. Soc. Rev.* **2021**, *50*, 6349–6368. [CrossRef]
9. Wei, Y.S.; Hu, X.P.; Han, Z.; Dong, X.Y.; Zang, S.Q.; Mak, T.C.W. Unique proton dynamics in an efficient MOF-based proton conductor. *J. Am. Chem. Soc.* **2017**, *139*, 3505–3512. [CrossRef]
10. Mahalingam, A.; Pushparaj, H. Synthesis, characterization, and fabrication of nickel metal–organic framework-incorporated polymer electrolyte membranes for fuel-cell applications. *ACS Appl. Mater. Interfaces* **2024**, *16*, 31145–31157. [CrossRef]
11. Sun, Y.; Wei, J.; Fu, Z.; Zhang, M.; Zhao, S.; Xu, G.; Li, C.; Zhang, J.; Zhou, T. Bio-inspired synthetic hydrogen-bonded organic frameworks for efficient proton conduction. *Adv. Mater.* **2023**, *35*, 2208625. [CrossRef] [PubMed]
12. Zhao, F.; Cao, L.H.; Bai, X.T.; Chen, X.Y.; Yin, Z. Application of ionic hydrogen-bonded organic framework materials in hybrid proton exchange membranes. *Cryst. Growth Des.* **2023**, *23*, 1798–1804. [CrossRef]
13. Wang, M.; Cai, J.; Lun, H.; Lv, M.; Zhang, J.; Andra, S.; Li, B.; Dang, D.; Bai, Y.; Li, Y. Design and analysis of POM-guanidine compounds: Achieving ultra-high single-crystal proton conduction. *Adv. Funct. Mater.* **2024**, *34*, 2311912. [CrossRef]
14. Mensharapov, R.M.; Ivanova, N.A.; Spasov, D.D.; Grigoriev, S.A.; Fateev, V.N. SAXS investigation of the effect of freeze/thaw cycles on the nanostructure of Nafion® membranes. *Polymers* **2022**, *14*, 4395. [CrossRef]
15. Ren, X.; Gobrogge, E.; Beyer, F.L. States of water in recast Nafion® films. *J. Membr. Sci.* **2021**, *637*, 119645. [CrossRef]

16. da Silva, J.S.; Carvalho, S.G.; da Silva, R.P.; Tavares, A.C.; Schade, U.; Puskar, L.; Matos, B.R. SAXS signature of the lamellar ordering of ionic domains of perfluorinated sulfonic-acid ionomers by electric and magnetic field-assisted casting. *Phys. Chem. Chem. Phys.* **2020**, *22*, 13764–13779. [CrossRef]
17. Mauritz, K.A.; Moore, R.B. State of understanding of Nafion. *Chem. Rev.* **2004**, *104*, 4535–4586. [CrossRef]
18. Kim, H.; Lee, S.; Kim, S.; Oh, C.; Ryu, J.; Kim, J.; Park, E.; Hong, S.; No, K. Membrane crystallinity and fuel crossover in direct ethanol fuel cells with Nafion composite membranes containing phosphotungstic acid. *J. Mater. Sci.* **2017**, *52*, 2400–2412. [CrossRef]
19. Park, Y.S.; Yamazaki, Y. Novel Nafion/Hydroxyapatite composite membrane with high crystallinity and low methanol crossover for DMFCs. *Polym. Bull.* **2005**, *53*, 181–192. [CrossRef]
20. Tajima, N.; Nara, J.; Ozawa, T.; Nitta, H.; Ohata, K.; Ohno, T. Interface of hydrated perfluorosulfonic acid electrolyte with a platinum catalyst: Structural analyses with dissipative particle dynamics simulations. *J. Electrochem. Soc.* **2020**, *167*, 064513. [CrossRef]
21. Malek, A.; Sadeghi, E.; Jankovic, J.; Eikerling, M.; Malek, K. Aquivion ionomer in mixed alcohol–water solution: Insights from multiscale molecular modeling. *J. Phys. Chem. C* **2020**, *124*, 3429–3438. [CrossRef]
22. Cha, J. Morphological effect of side chain on H_3O^+ transfer inside polymer electrolyte membranes across polymeric chain via molecular dynamics simulation. *Sci. Rep.* **2020**, *10*, 22014. [CrossRef] [PubMed]
23. Sengupta, S.; Lyulin, A. Dissipative particle dynamics modeling of polyelectrolyte membrane–water interfaces. *Polymers* **2020**, *12*, 907. [CrossRef]
24. Johansson, E.O.; Yamada, T.; Sundén, B.; Yuan, J. Dissipative particle dynamics approach for nano-scale membrane structure reconstruction and water diffusion coefficient estimation. *Int. J. Hydrogen Energy* **2015**, *40*, 1800–1808. [CrossRef]
25. Sen, U.; Ozdemir, M.; Erkartal, M.; Kaya, A.M.; Manda, A.A.; Oveisi, A.R.; Aboudzadeh, M.A.; Tokumasu, T. Mesoscale morphologies of Nafion-based blend membranes by dissipative particle dynamics. *Processes* **2021**, *9*, 984. [CrossRef]
26. Bordín, S.P.F.; Andrada, H.E.; Carreras, A.C.; Castellano, G.E.; Oliveira, R.G.; Josa, V.M.G. Nafion membrane channel structure studied by small-angle X-ray scattering and Monte Carlo simulations. *Polymer* **2020**, *155*, 58–63. [CrossRef]
27. Wang, Y.; Diaz, D.F.R.; Chen, K.S.; Wang, Z.; Adroher, X.C. Materials, technological status, and fundamentals of PEM fuel cells—A review. *Mater. Today* **2020**, *32*, 178–203. [CrossRef]
28. Xu, J.; Zhang, C.; Wan, Z.; Chen, X.; Chan, S.H.; Tu, Z. Progress and perspectives of integrated thermal management systems in PEM fuel cell vehicles: A review. *Renew. Sust. Energ. Rev.* **2022**, *155*, 111908. [CrossRef]
29. Wang, Q.; Tang, F.; Li, B.; Dai, H.; Zheng, J.P.; Zhang, C.; Ming, P. Study on the thermal transient of cathode catalyst layer in proton exchange membrane fuel cell under dynamic loading with a two-dimensional model. *Chem. Eng. J.* **2022**, *433*, 133667. [CrossRef]
30. Zhang, G.; Qu, Z.; Wang, Y. Full-scale three-dimensional simulation of air-cooled proton exchange membrane fuel cell stack: Temperature spatial variation and comprehensive validation. *Energy Convers. Manag.* **2022**, *270*, 116211. [CrossRef]
31. Chen, Q.; Zhang, G.; Zhang, X.; Sun, C.; Jiao, K.; Wang, Y. Thermal management of polymer electrolyte membrane fuel cells: A review of cooling methods, material properties, and durability. *Appl. Energy* **2021**, *286*, 116496. [CrossRef]
32. Wang, W.; Qu, Z. Molecular dynamics simulation of the mechanical properties and thermal conductivity of aromatic electrolytes in proton exchange membrane fuel cells. *J. Power Sources* **2023**, *585*, 233622. [CrossRef]
33. Zheng, J.; Feng, C.; Ming, P.; Zhang, C. Effect of microstructural damage on the thermomechanical properties of electrodes in proton exchange membrane fuel cells. *ACS Appl. Mater. Interfaces* **2022**, *14*, 2918–2929. [CrossRef]
34. Khandelwal, M.; Mench, M.M. Direct measurement of through-plane thermal conductivity and contact resistance in fuel cell materials. *J. Power Sources* **2006**, *161*, 1106–1115. [CrossRef]
35. Zheng, C. Proton mobility and thermal conductivities of fuel cell polymer membranes: Molecular dynamics simulation. *Comp. Mater. Sci.* **2017**, *132*, 55–61. [CrossRef]
36. Burheim, O.; Vie, P.J.S.; Pharoah, J.G.; Kjelstrup, S. Ex situ measurements of through-plane thermal conductivities in a polymer electrolyte fuel cell. *J. Power Sources* **2010**, *195*, 249–256. [CrossRef]
37. Germann, L.S.; Carlino, E.; Taurino, A.; Magdysyuk, O.V.; Voinovich, D.; Dinnebier, R.E.; Bučar, D.; Hasa, D. Modulating thermal properties of polymers through crystal engineering. *Angew. Chem. Int. Edit.* **2023**, *62*, e202212688. [CrossRef] [PubMed]
38. Meirzadeh, E.; Evans, A.M.; Rezaee, M.; Milich, M.; Dionne, C.J.; Darlington, T.P.; Bao, S.T.; Bartholomew, A.K.; Handa, T.; Rizzo, D.J.; et al. A few-layer covalent network of fullerenes. *Nature* **2023**, *613*, 71–76. [CrossRef]
39. Zhu, L.; Zhang, M.; Zhou, G.; Hao, T.; Xu, J.; Wang, J.; Qiu, C.; Prine, N.; Ali, J.; Feng, W.; et al. Efficient organic solar cell with 16.88% efficiency enabled by refined acceptor crystallization and morphology with improved charge transfer and transport properties. *Adv. Energy Mater.* **2020**, *10*, 1904234. [CrossRef]
40. Park, Y.S.; Yamazaki, Y. Low water/methanol permeable Nafion/CHP organic–inorganic composite membrane with high crystallinity. *Eur. Polym. J.* **2006**, *42*, 375–387. [CrossRef]
41. Mendil-Jakani, H.; Pouget, S.; Gebel, G.; Pintauro, P.N. Insight into the multiscale structure of pre-stretched recast Nafion® membranes: Focus on the crystallinity features. *Polymer* **2015**, *63*, 99–107. [CrossRef]
42. Van Der Heijden, P.C.; Rubatat, L.; Diat, O. Orientation of drawn Nafion at molecular and mesoscopic scales. *Macromolecules* **2004**, *37*, 5327–5336. [CrossRef]

43. Thompson, A.P.; Aktulga, H.M.; Berger, R.; Bolintineanu, D.S.; Brown, W.M.; Crozier, P.S.; Veld, P.J.I.; Kohlmeyer, A.; Moore, S.G.; Nguyen, T.D.; et al. LAMMPS-a flexible simulation tool for particle-based materials modeling at the atomic, meso, and continuum scales. *Comput. Phys. Commun.* **2022**, *271*, 108171. [CrossRef]
44. Luo, C.; Guo, Q.; Feng, C.; Wang, Y.; Ming, P.; Zhang, C. Proton transport, electroosmotic drag and oxygen permeation in polytetrafluoroethylene reinforced ionomer membranes and their effects on fuel cell performance. *J. Electrochem. Soc.* **2024**, *171*, 034513. [CrossRef]
45. Linke, M.; Köfinger, J.; Hummer, G. Rotational diffusion depends on box size in molecular dynamics simulations. *J. Phys. Chem. Lett.* **2018**, *9*, 2874–2878. [CrossRef]
46. Yeh, I.-C.; Hummer, G. System-size dependence of diffusion coefficients and viscosities from molecular dynamics simulations with periodic boundary conditions. *J. Phys. Chem. B* **2004**, *108*, 15873–15879. [CrossRef]
47. Dünweg, B.; Kremer, K. Molecular dynamics simulation of a polymer chain in solution. *J. Chem. Phys.* **1993**, *99*, 6983–6997. [CrossRef]
48. Vögele, M.; Köfinger, J.; Hummer, G. Hydrodynamics of diffusion in lipid membrane simulations. *Phys. Rev. Lett.* **2018**, *120*, 268104. [CrossRef]
49. Springer, T.E.; Zawodzinski, T.A.; Gottesfeld, S. Polymer electrolyte fuel cell model. *J. Electrochem. Soc.* **1991**, *138*, 2334–2342. [CrossRef]
50. Li, Z.; Tang, Y.H.; Lei, H.; Caswell, B.; Karniadakis, G.E. Energy-conserving dissipative particle dynamics with temperature-dependent properties. *J. Comput. Phys.* **2014**, *265*, 113–127. [CrossRef]

polymers

MDPI

Review

Unraveling the Electrochemical Insights of Cobalt Oxide/Conducting Polymer Hybrid Materials for Supercapacitor, Battery, and Supercapattery Applications

Annu *, Sang-Shin Park, Md Najib Alam *, Manesh Yewale and Dong Kil Shin *

School of Mechanical Engineering, Yeungnam University, 280 Daehak-ro, Gyeongsan 38541, Republic of Korea
* Correspondence: drannu@yu.ac.kr or annuchem92@gmail.com (A.) mdnajib.alam3@gmail.com (M.N.A.) dkshin@yu.ac.kr (D.K.S.)

Abstract: This review article focuses on the potential of cobalt oxide composites with conducting polymers, particularly polypyrrole (PPy) and polyaniline (PANI), as advanced electrode materials for supercapacitors, batteries, and supercapatteries. Cobalt oxide, known for its high theoretical capacitance, is limited by poor conductivity and structural degradation during cycling. However, the integration of PPy and PANI has been proven to enhance the electrochemical performance through improved conductivity, increased pseudocapacitive effects, and enhanced structural integrity. This synergistic combination facilitates efficient charge transport and ion diffusion, resulting in improved cycling stability and energy storage capacity. Despite significant progress in synthesis techniques and composite design, challenges such as maintaining structural stability during prolonged cycling and scalability for mass production remain. This review highlights the synthesis methods, latest advancements, and electrochemical performance in cobalt oxide/PPy and cobalt oxide/PANI composites, emphasizing their potential to contribute to the development of next-generation energy storage devices. Further exploration into their application, especially in battery systems, is necessary to fully harness their capabilities and meet the increasing demands of energy storage technologies.

Keywords: polypyrrole; polyaniline; conducting polymers; air batteries; pseudocapacitance; ion transport

1. Introduction

In the quest to meet the ever-increasing global demand for energy, scientists and engineers are turning towards innovative energy storage solutions, particularly supercapacitors and batteries, due to their ability to deliver high power density and rapid energy release [1]. Unlike traditional capacitors and batteries, supercapacitors store and release electrical energy through electrostatic principles at the electrode–electrolyte interface, enabling them to store a significant amount of charge. This characteristic results in a high power density and rapid charge-discharge capability, making them suitable for applications requiring quick energy delivery [2]. Additionally, supercapacitors and batteries offer numerous advantages, including a wide operational temperature range, long cycle life, and high energy conversion efficiency, making them an attractive option for future energy storage technologies [1–4]. The basic hierarchy of electrochemical energy storage devices is presented in Figure 1, with the inset showing basic electrochemical characteristics of supercapacitors, batteries, and supercapatteries.

Transition metal oxide has a high energy density and better chemical stability [5]. The purpose of choosing cobalt oxide is mainly because of the recent advancements focused on cobalt oxide and its hybrid materials for electrochemical applications. While other transition metals such as nickel (Ni), iron (Fe), molybdenum (Mo), and manganese (Mn) also exhibit promising features, cobalt oxide (CoO, Co_3O_4) presents a series of advantages that justify its prioritization in this context. Table 1 shows a comparative discussion to

substantiate the choice of cobalt oxide. Over the past five years, significant progress has been made in fabricating cobalt oxide nanostructures with various dimensionalities for applications in rechargeable batteries, supercapacitors, and electrocatalysis [6,7]. Cobalt oxide is gaining attention as a promising electrode material for next-generation electrochemical energy devices due to its favorable properties, such as low cost, abundance, high theoretical capacity and capacitance, excellent electrochemical activity, and robust chemical and mechanical stability. These characteristics make cobalt oxide an attractive alternative to other metal oxides in energy storage applications [8].

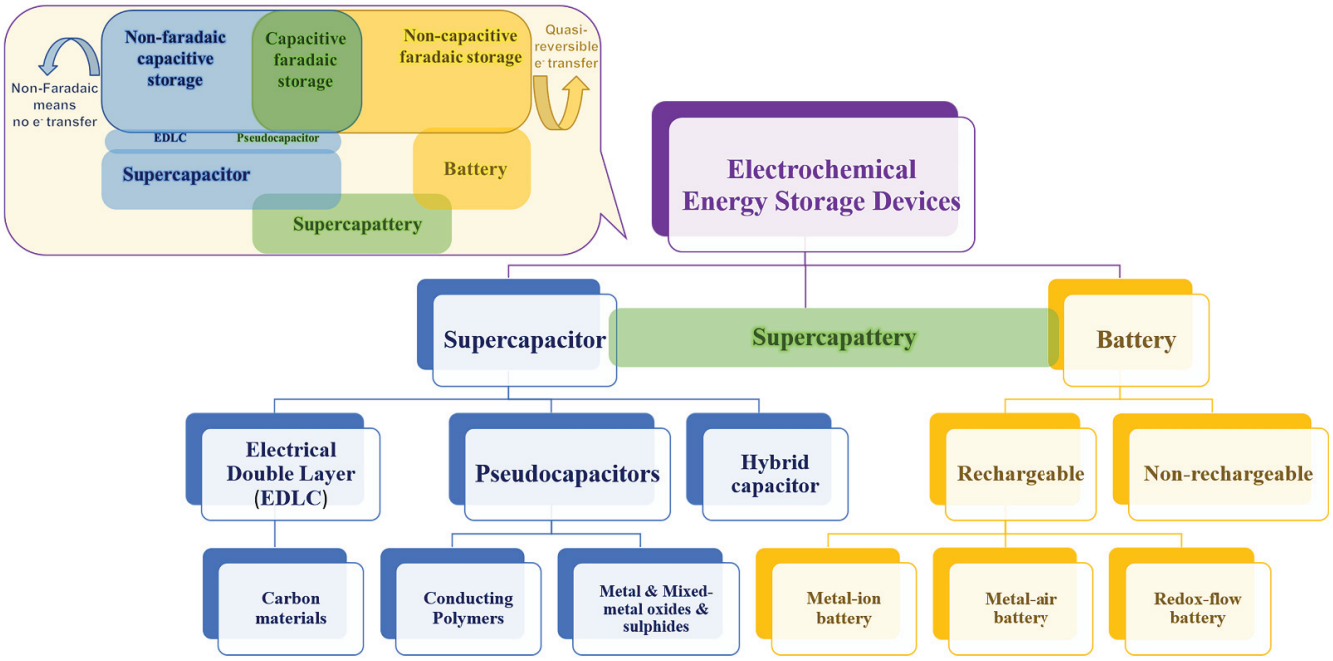

Figure 1. Hierarchical illustration of electrochemical energy storage devices.

Sustainable methods have been developed recently to produce cobalt oxide nanoarchitectures. Raimundo et al. [9] explored the synthesis of a Co_3O_4-CoO nanocomposite using agar-agar through a two-step biogenic process for oxygen evolution reaction (OER) [10]. Natural lemon extract was employed for cobalt oxide nanoparticles (NPs) formation for an LPG gas sensor application [11]. Edison et al. [12] synthesized carbon-supported cobalt oxide NPs, which led to the best specific capacitance, which was calculated to be 642 Fg^{-1} at 1 Ag^{-1} in 2 M KOH solution. The green Co_3O_4@C NPs synthesized using *T. chebula* fruit shows good pseudocapacitance activity. The milk sap of *Calotropis procera* was also utilized for the synthesis of cobalt oxide NPs by the chemical growth method, and their supercapacitor application was reported by Bhatti et al. [13]. The supercapacitor efficiency of cobalt oxide NPs synthesized using marine red algae (*Grateloupia sparsa*) was recently investigated. The algae's carbohydrates and polyphenols aided in reducing and stabilizing the NPs. The study found that the activated carbon/cobalt oxide nanocomposite had a significantly higher specific capacitance than raw activated carbon. Electrochemical analysis showed a specific capacitance of 125 Fg^{-1} for the cobalt oxide electrode in a 1M Na_2SO_4 electrolyte, with 93.75% capacity retention after 8000 cycles [14]. Huang et al. [15] investigated the supercapacitor performance of biogenic cobalt oxide NPs through *Bacillus pasteurii* bacteria in aqueous KOH by using the MIP (microbial-induced precipitation) process and showed a specific capacitance of about 162.78 Fg^{-1} at a current density of 1 mA cm^{-2} with a power density and an energy density as 64.29 W· and 4.58 Wh·kg^{-1}, respectively. Srivastava et al. [5] investigated the biogenic production of cobalt oxide NPs via *Citrus reticulata* (Mandarin oranges) fruit extract, and the specific capacitance was calculated to be 90 Fg^{-1} at 1 Ag^{-1} in electrolyte/solution. Shim et al. [16] proposed the synthesis of cobalt oxide

NPs by using *Micrococcus lylae* bacteria and showed its supercapacitor performance. The electrochemical studies revealed a specific capacitance of 214 Fg^{-1} at 2 A g^{-1} for the cobalt oxide electrode, with a remarkable cyclic stability in aqueous electrolyte solution (3 M KOH) and 95% capacity retention after 4000 cycles at 5 $mAcm^{-2}$ current density. All such studies prove that cobalt oxide not only has the ability to mitigate with minimal toxicity but is also significant in energy storage technologies.

Table 1. Comparison of electrochemical behavior of cobalt oxide and other transition metals.

Material	Specific Capacitance	Current Density/Scan Rate	Energy Density	Power Density	Ref.
Co_3O_4@$Co(OH)_2$	1164 F g^{-1}	1.2 A g^{-1}	9.4 mWh cm^{-3}	354 mW cm^{-3}	[17]
Co-NiO@ carbon textile	106 F g^{-1}	10 mA cm^{-2}	52 Wh kg^{-1}	1206 W kg^{-1}	[18]
Co_2O_4@Zn-CuO	890 F g^{-1}	1 A g^{-1}	36 Wh kg^{-1}	4800 W kg^{-1}	[19]
CuO nanowires	594 F g^{-1}	0.71 A g^{-1}	35 Wh kg^{-1}	520 W kg^{-1}	[20]
CuO@Ni foam	431 F g^{-1}	3.5 mA cm^{-2}	19.7 Wh kg^{-1}	7 kW kg^{-1}	[21]
CuO nanoflowers	612 F g^{-1}	1 A g^{-1}	27 Wh kg^{-1}	800 W kg^{-1}	[22]
$FeCo_2O_4$	231 C g^{-1}	1 A g^{-1}	400 Wh kg^{-1}	930 W kg^{-1}	[23]
$LaMnO_3$-$NiCo_2O_4$@NF	811 C g^{-1}	0.5 A g^{-1}	37 Wh kg^{-1}	800 W kg^{-1}	[24]
NiO flakes	574 F g^{-1}	0.1 mA cm^{-2}	11 Wh kg^{-1}	124 W kg^{-1}	[25]
$NiCo_2O_4$@$MnMoO_4$	1118 F g^{-1}	1 A g^{-1}	237 Wh kg^{-1}	700 W kg^{-1}	[26]
$ZnCo_2O_4$@$Ni(OH)_2$	4.6 F cm^{-2}	2 mA cm^{-2}	49 Wh kg^{-1}	428 W kg^{-1}	[27]
MoS_2@Ti_3C_2Tx	1022.7 F/g	1 A g^{-1}	54.7 Wh kg^{-1}	1601.3 W kg^{-1}	[28]
Bi_2O_3-Sb_2O_4-ZrO	441 F/g	1 A g^{-1}	18 Wh/kg	-	[29]
MoS_2/N-rGO	539.5 F g^{-1}	1 A g^{-1}	71.5 Wh kg^{-1}	25.4 kW kg^{-1}	[30]

However, the pristine forms of cobalt oxide still face challenges, such as poor electrical conductivity, slow reaction kinetics, and significant morphological and volume changes during electrochemical reactions. These intrinsic drawbacks often lead to rapid performance degradation, poor structural stability, limited cycling performance, and slow activation processes. To overcome these limitations, researchers have been exploring cobalt oxide-based hybrids that combine the unique advantages of each component, resulting in synergistic effects that improve electronic conductivity, enhance reaction kinetics, and buffer volume changes during repeated charge-discharge cycles. These hybrid materials, compared to pristine cobalt oxide nanostructures, demonstrate enhanced rate capability, improved cycling stability, reduced overpotential, and overall better electrochemical properties, making them more suitable for energy-related applications. Despite these advances, challenges remain in optimizing cobalt oxide-based composites for practical electrochemical energy storage applications.

Conducting polymers have also emerged as a significant class of materials in the development of supercapacitor electrodes. Among them, conductive polymers such as polyaniline (PANI) and polypyrrole (PPy) are frequently used to hybridize with metal oxides such as TiO_2 and cobalt oxide nanostructures to enhance their electrical conductivity, improve adhesion, and facilitate rapid charge transfer [31,32]. The strategy to incorporate polymers in the electrode material assembly is sustainable compared to other metal incorporation. Besides, the storage mechanism of these conductive polymers primarily relies on redox reactions. During oxidation, ions are incorporated into the polymer backbone and subsequently released into the electrolyte during reduction, enabling efficient charge storage and release [33,34]. The integration of cobalt oxides with conductive polymers can greatly enhance the reaction rate and improve the ion-storage performance, resulting in superior electrochemical properties [35] (Figure 2).

Recent advancements in electrode materials for supercapacitors emphasize the synergy between multiple components to enhance electrochemical performance. Dongxian et al. synthesized a ternary composite (rGO/NiCo/PPy) with a sea urchin-like structure using a combination of Hummer's and hydrothermal methods, followed by in-situ polymerization. This composite achieved a high specific capacitance of 333.2 F/g at 1 A/g and retained 94% capacitance after 7000 cycles. The assembled asymmetric supercapacitor displayed

superior performance, reaching a specific capacitance of 253 F/g at a power density of 1250 W/kg [35].

Similarly, Ishaq et al. presented a one-step method to create binary (rGO/$CoFe_2O_4$) and ternary (rGO/$CoFe_2O_4$/PPy) nanocomposites. The ternary composite showed significantly enhanced performance, with a specific capacitance of 164 F/g and energy density of 22.8 Wh/kg, thanks to the conductive properties of PPy. This method offers advantages in terms of simplicity, cost-efficiency, and sustainability compared to more complex approaches [36].

Zhou et al. developed a supercapacitor electrode comprising CoO nanowires on 3D nickel foam with a PPy coating. This architecture leverages the high electrochemical activity of CoO and the conductivity of PPy, achieving a specific capacitance of 2223 F g^{-1}, 99.8% retention after 2000 cycles, and high energy and power densities in an asymmetric supercapacitor device, which efficiently powered LEDs and a mini motor [37]. Nayak et al. used a chitosan biopolymer binder for supercapattery electrodes to create a silver-zirconia composite. This material demonstrated an energy density of 31.94 Wh/kg at a power density of 500.86 W/kg and retained 89% of its capacity after 2500 cycles at 10 A/g [38]. Among various conducting polymers, polyaniline (PANI) is the most extensively studied due to its variable oxidation states, which allow for tunable pseudocapacitive performance. Its high conductivity and ease of synthesis further add to its appeal. PANI has been widely used not only as a standalone supercapacitor electrode but also as a conductive additive to enhance the electrochemical performance of other materials. Recently, Kuchena and Wang demonstrated that an ammonium-ion battery cell utilizing an emeraldine salt (ES-PANI) cathode material achieved a commendable discharge capacity of 160 mAh g^{-1} at a current of 1 A g^{-1}. Additionally, the battery exhibited strong capacity retention, maintaining 82% of its capacity after 100 cycles at a higher current of 5 A g^{-1}, along with excellent rate capability [39]. As a result, it has been successfully integrated with cobalt oxides, mixed-metal oxides, carbon materials, and metal sulfides to develop advanced supercapacitor electrodes with enhanced performance. For instance, Hai et al. synthesized core–shell structured PANI-Co_3O_4 nanocomposites using a carbon-assisted in-situ polymerization method, achieving high specific capacitance and excellent cycling stability, with 84.9% capacity retention after 1000 charge-discharge cycles [40].

This review explores the sustainable perspectives of cobalt oxide/polymer nanocomposites for supercapacitor, battery, and supercapattery applications, highlighting the synthesis of electrode materials, their electrochemical performance associated with recent advancements, current challenges, and future directions in this rapidly evolving field. The amalgamation of cobalt oxides with conducting polymers, especially PPy and PANI, presents a promising avenue for developing high-performance, durable, and environmentally friendly energy storage devices, offering significant potential for meeting future energy demands. Moreover, we present focused data on green synthesized cobalt oxide, highlighting its potential to create sustainable electrode materials. This information aims to guide researchers in the development of environmentally friendly supercapacitors and batteries. The general electrochemical differences between supercapacitors, batteries, and supercapatteries are discussed in Table 2.

Table 2. General differences between supercapacitors, batteries, and supercapatteries.

Parameter	Supercapacitors	Batteries	Supercapatteries
Energy storage mechanism	Electrostatic (capacitive)	Electrochemical (faradaic)	Hybrid: capacitive + faradaic reactions
Energy density	Low (1–10 Wh/kg)	High (100–265 Wh/kg, for LIB)	Moderate (between supercapacitors and batteries, 20–100 Wh/kg)
Power density	Very High (>10,000 W/kg)	Moderate to Low (200–2000 W/kg)	High (closer to supercapacitors, 1000–10,000 W/kg)
Charge-discharge speed	Very fast (seconds to minutes)	Slow (hours)	Fast (minutes to tens of minutes)
Cycle life	Long (up to 1,000,000 GCD cycles)	Shorter (500–3000 cycles)	Long (10,000–100,000 cycles)
Voltage window	2.5–2.7 V per cell	3.6–4.2 V per cell	2.5–4.0 V (material dependent)
Response time	Instantaneous	Slow	Fast (intermediate between the two)
Self-discharge	Quickly when not in use	Low	Moderate (lower than supercapacitors but higher than batteries)
Cost	Lower per unit of power	Higher per unit of energy	Moderate
Application	High-power applications (e.g., regenerative braking)	Energy storage applications (e.g., mobile phones, EVs)	Hybrid applications (e.g., electric vehicles, power grids)

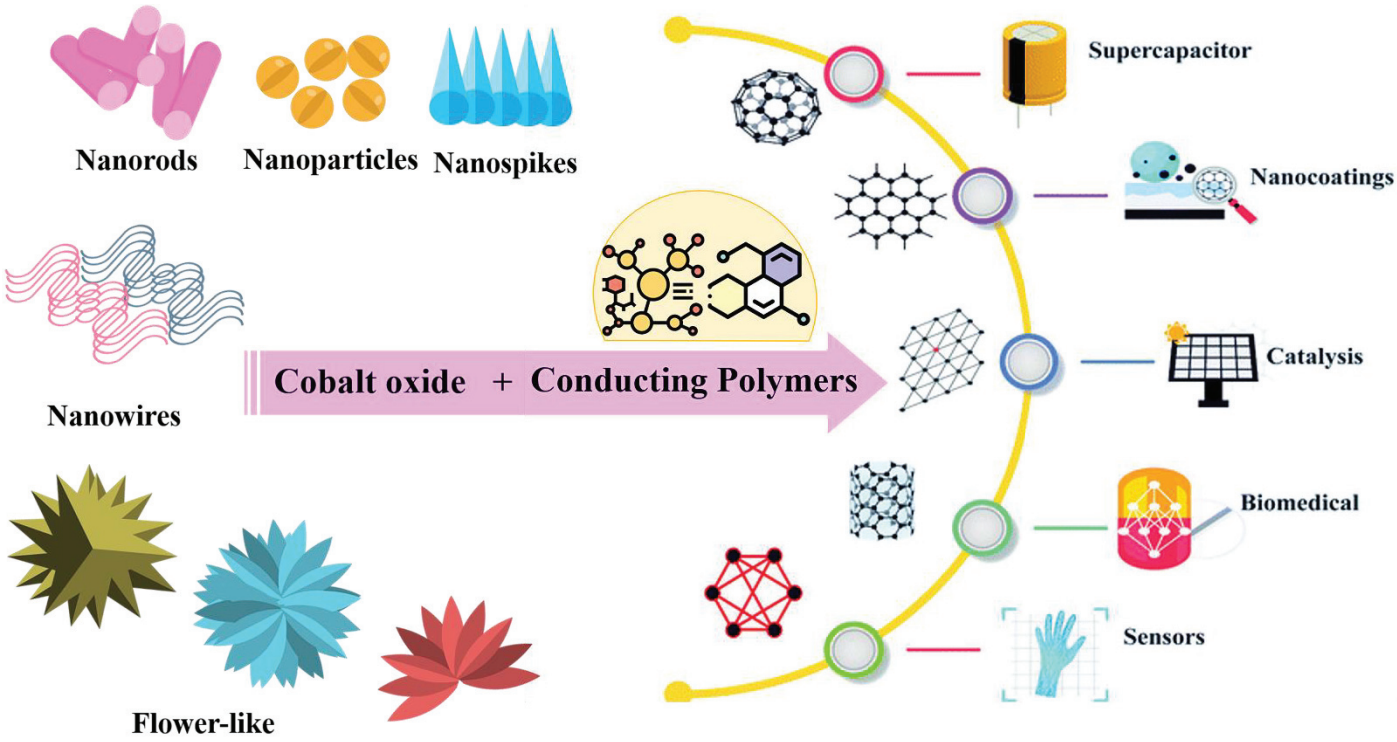

Figure 2. Representation of different morphologies of cobalt oxide for cobalt oxide/polymer nanocomposites and their possible applications [41].

2. Cobalt Oxide/Polymer Nanocomposites

The integration of cobalt oxide with conducting polymers like polypyrrole (PPy) and polyaniline (PANI) has gained significant attention in the field of energy storage, particularly for supercapacitor applications. The combination of these materials leverages the high pseudocapacitance of cobalt oxide with the excellent conductivity and flexibility of conducting polymers, resulting in enhanced electrochemical performance. The crystal lattice structural representation of cobalt oxide spinels and different types of conducting polymers are depicted in Figure 3. This section delves into the synthesis methods, roles, and factors influencing the performance of cobalt oxide/PPy and cobalt oxide/PANI nanocomposites for supercapacitors.

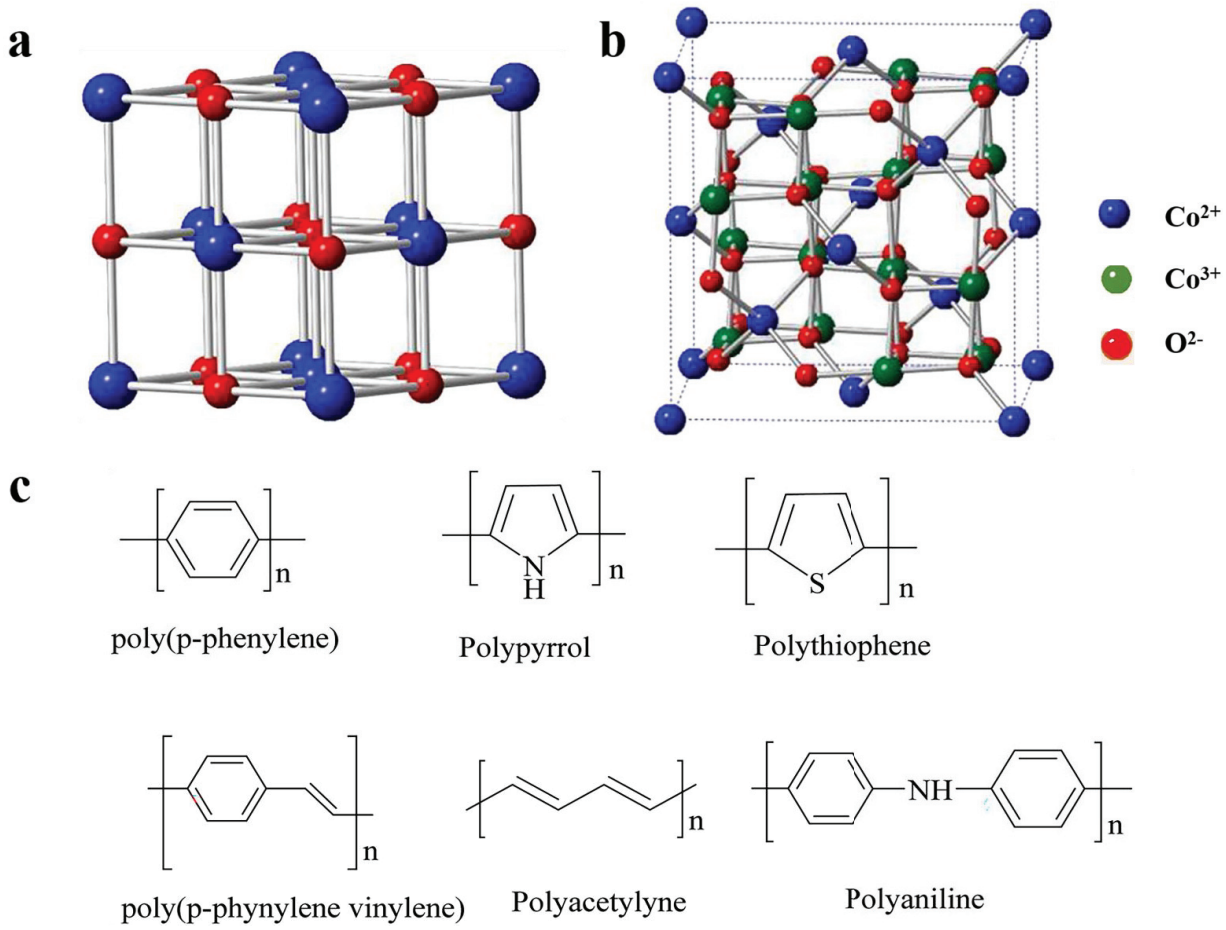

Figure 3. (**a**) Structure of cobalt oxide spinels CoO and (**b**) Co_3O_4 [8] and (**c**) different conducting polymers [41].

3. Cobalt Oxide/PPy Nanocomposites for Supercapacitors

The cobalt oxide/PPy nanocomposites combine the high theoretical capacitance of cobalt oxide with the excellent electrical conductivity and flexibility of PPy, resulting in enhanced electrochemical performance beneficial for supercapacitors. Table 3 depicts the electrochemical properties of different cobalt oxide/PPy electrodes used in fabricating high-energy supercapacitors.

3.1. Synthesis of Cobalt Oxide/PPy Nanocomposites

Cobalt oxide/PPy nanocomposites are typically synthesized using methods that ensure uniform distribution of PPy over cobalt oxide nanostructures [42–44]. Common synthesis techniques include:

In-situ polymerization: In this method, pyrrole monomers are polymerized in the presence of pre-synthesized cobalt oxide NPs or nanostructures. The cobalt oxide acts as a template and provides a site for pyrrole polymerization, ensuring a uniform coating of PPy over the cobalt oxide surface.

Electrochemical polymerization: This technique involves the electrochemical deposition of PPy onto cobalt-oxide-coated electrodes. The electrochemical process facilitates the formation of a conformal PPy layer on cobalt oxide, enhancing the composite's electrical conductivity and mechanical stability.

Chemical oxidation polymerization: In this method, cobalt oxide is mixed with pyrrole monomers in the presence of an oxidizing agent, leading to the polymerization of pyrrole and the formation of a cobalt oxide/PPy composite. This method allows for the fine

tuning of the composite's morphology by adjusting the concentration of the monomers and oxidizing agents.

3.2. Advantages of PPy in Supercapacitors

PPy enhances the performance of cobalt-oxide-based supercapacitors through several mechanisms, such as by increasing conductivity, pseudocapacitance, and structural stability. *Improved conductivity*: PPy is a highly conductive polymer that increases the overall electrical conductivity of the composite. This enhances the charge transfer between the electrode and the electrolyte, improving the rate capability and specific capacitance. *Pseudocapacitance contribution*: PPy contributes to the pseudocapacitance through its redox-active nature. The oxidation and reduction of PPy during charging and discharging cycles provide additional capacitance, complementing the pseudocapacitance of cobalt oxide. *Structural stability*: The flexibility of PPy helps in accommodating the volume changes of cobalt oxide during the charge-discharge cycles, thereby enhancing the cycling stability of the supercapacitor [43].

3.3. Electrochemical Performance of Cobalt Oxide/PPy Nanocomposites in Supercapacitors

Electrochemical Mechanism: Cobalt oxide/PPy nanocomposites exhibit enhanced electrochemical performance due to the synergistic effects of cobalt oxide and PPy. The electrochemical behavior of these nanocomposites is primarily governed by two key mechanisms:

(i) *Faradaic redox reactions of cobalt oxide*: Cobalt oxide, particularly in its spinel form Co_3O_4, undergoes reversible redox reactions during the charging and discharging process. These reactions involve the oxidation and reduction of cobalt ions, contributing significantly to the pseudocapacitance. These reactions are facilitated by the high surface area of the nanostructured cobalt oxide, which provides a large number of active sites for redox reactions. The typical reactions are (Equations (1) and (2)):

$$Co_3O_4 + OH^- + H_2O \rightarrow 3CoOOH + e^- \quad (1)$$

$$CoOOH + OH^- \rightarrow CoO_2 + H_2O + e^- \quad (2)$$

(ii) *Capacitive behavior of PPy*: PPy contributes to the overall capacitance of the nanocomposite through its capacitive properties, which arise from the doping and dedoping processes. During charging, PPy undergoes oxidation, where it accepts electrons, and during discharging, it is reduced, releasing electrons. This redox process is accompanied by the exchange of ions (usually Cl^- or $SO_4{}^{2-}$) between the PPy matrix and the electrolyte. The reaction can be represented as (Equation (3)):

$$PPy^0 + Cl^- \rightarrow PPy^+Cl^- + e^- \quad (3)$$

The high conductivity of PPy facilitates fast electron transfer, enhancing the overall charge-discharge rates and cyclic stability of the nanocomposite.

Recent studies focused on improving synthesis methods and structural design demonstrated the superior electrochemical performance of cobalt oxide/PPy nanocomposites to optimize their performance. For example, Ramesh et al. synthesized Co_3O_4/PPy@N-MWCNT via an ultrasonication-mediated solvothermal method, yielding impressive results for both supercapacitors and glucose sensors. The composite exhibited a capacitance of ~872 F/g at 0.5 A/g with excellent cycling stability (96.8% retention after 10,000 cycles) alongside superior glucose-sensing performance. These studies highlight the potential of cobalt oxide/polymer composites in energy storage and sensing applications [45]. Zhou et al. synthesized a Co_3O_4/PPy nanocomposite that showed a specific capacitance of 2223 F g^{-1}, approaching the theoretical value for supercapacitors. The enhanced performance was attributed to the well-aligned Co_3O_4 nanowire array on a 3D nickel foam substrate, which was uniformly coated with PPy. This architecture allowed for a short ion diffusion pathway and efficient electron transfer, resulting in a high power density of

5500 W kg^{-1} and an outstanding cycling stability with 99.8% capacitance retention after 2000 cycles [37].

Table 3. Electrochemical behavior of different cobalt oxide/PPy electrodes for energy storage applications.

Electrode Material	Enhancement	Morphology	Synthesis Method	Specific Capacitance (F g^{-1})	Application	Ref.
CoO/PPy	-	Nanowires	Hydrothermal + chemical polymerization	2223 at 1 mA cm^{-2}	Supercapacitor	[37]
PPy/Co_3O_4/Carbon paper	Carbon paper	Composite	Hydrothermal + electrodeposition	398.4 at 1 A g^{-1}	Supercapacitor	[42]
Co_3O_4@PPy/MWCNT	MWCNT	Composite	Chemical polymerization + hydrothermal	609 at 3 A g^{-1}	Supercapacitor	[44]
Co_3O_4/PPy/MnO_2	MnO_2	Core–shell	Hydrothermal + chemical polymerization	780 at 0.5 A g^{-1}	Supercapacitor	[46]
Co_3O_4/AuPPy	Au	Nanowires	Hydrothermal + chemical polymerization	2062 at 5 mA cm^{-2}	Supercapacitor	[47]
AC//Co_3O_4/PPy/MnO_2	Activated carbon, MnO_2	Nanowires	Hydrothermal + electrodeposition	629 at 1.2 mA cm^{-2}	Supercapacitor	[48]
$NiCo_2O_4$/PPy/Carbon textiles	Carbon textiles	Nanowires	Hydrothermal + chemical polymerization	2244.5 at 1 A g^{-1}	Supercapacitor	[49]

In a study, a novel electrode material composed of $NiCo_2O_4$ nanowire arrays (NWAs) on carbon textiles with a PPy nanosphere shell layer was reported by Kong et al. to significantly enhance pseudocapacitive performance. The highly conductive nature of PPy, combined with the short ion transport channels within the ordered mesoporous $NiCo_2O_4$ nanowire arrays, along with the synergistic interaction between $NiCo_2O_4$ and PPy, contributed to an impressive specific capacitance of 2244 F g^{-1}. The material also exhibited excellent rate capability and notable cycling stability. Specifically, the $NiCo_2O_4$/PPy electrode retained around 89.2% of its capacitance after 5000 cycles.

Moreover, a lightweight and flexible asymmetric supercapacitor (ASC) was assembled using $NiCo_2O_4$/PPy NWAs as the positive electrode and activated carbon (AC) as the negative electrode. The ASC device demonstrated remarkable electrochemical performance, achieving a high energy density of 58.8 W h kg^{-1} at a power density of 365 W kg^{-1}, as well as a peak power density of 10.2 kW kg^{-1} at an energy density of 28.4 W h kg^{-1}, showcasing the material's ability to deliver energy rapidly. Additionally, the cycling stability of the ASC device was excellent, retaining ~89.2% of its initial capacitance after 5000 charge-discharge cycles in a gel electrolyte (KOH/PVA). In Figure 4a,b, a schematic illustration of the fabrication process for the hierarchical mesoporous Co/Au-PPy and $NiCo_2O_4$/PPy hybrid nanowires on carbon textiles is provided, highlighting the structure of the electrode material. Figure 4b(b,c) shows the cyclic voltammetry (CV) curves of the $NiCo_2O_4$/PPy NWAs and AC half cells measured in 3 M KOH solution at a scan rate of 10 mV s^{-1}. It indicates that when the voltage is 1.0 V, two weak symmetric broad redox peaks can be observed, which indicate that the pseudocapacitive properties of the ASC device is derived from the positive electrode ($NiCo_2O_4$/PPy NWAs). It is evident that $NiCo_2O_4$/PPy NWAs exhibited superior electrochemical performance. Figure 4b(b) presents the CV curves of the $NiCo_2O_4$/PPy/AC ASC measured at different potential windows and a scan rate of 150 mV s^{-1}. The results demonstrate the ASC's wide operating voltage window and robust charge storage capabilities. The CV curves exhibited a quasi-rectangular shape, indicative of EDLC behavior, along with weak redox peaks, suggesting the presence of pseudocapacitive (PC) reactions. This combination of EDLC and PC contributions ensured that the device effectively stores energy. Even at a high scan rate of 500 mV s^{-1}, the CV curve maintained its shape, demonstrating the good rate capability of the device, meaning it can handle fast charge-discharge cycles without significant degradation in performance. This

retention of shape indicates strong electrochemical stability, even under rapid operation (Figure 4b(c)). Meanwhile, the charge-discharge profiles (Figure 4b(d)) as galvanostatic charge-discharge (GCD) curves were highly symmetric at all current densities, which signifies good Coulombic efficiency, meaning that the amount of charge stored during charging is almost equal to the amount of charge released during discharging. Even at the high current density of 30 mA cm^{-2}, the device maintained excellent performance, with minimal voltage drop and well-preserved charge-discharge symmetry. This suggests that the ASC device exhibited outstanding electrochemical performance, fast charge transfer, and stable cycling behavior, even under high current stress, which is critical for applications requiring rapid energy storage and discharge. The specific and volumetric capacitance is depicted as a function of current density, showing the stable capacitance performance even at higher current densities (Figure 4b(e)). The cycling performance of the ASC devices, measured at a scan rate of 10 mA cm^{-2} over 5000 cycles, is depicted in Figure 4b(f), showing minimal capacitance degradation, as the inset compares the charge-discharge curves of the 1st and 5000th cycles as depicted in the Nyquist plots (Figure 4b(g)) for the ASC device, indicating low charge-transfer resistance, further confirming the device's superior long-term electrochemical stability [49]. Similarly, the Nyquist plot and cycle stability of two different electrodes provided significant reliability in terms of their electrochemical advancements (Figure 4c,d).

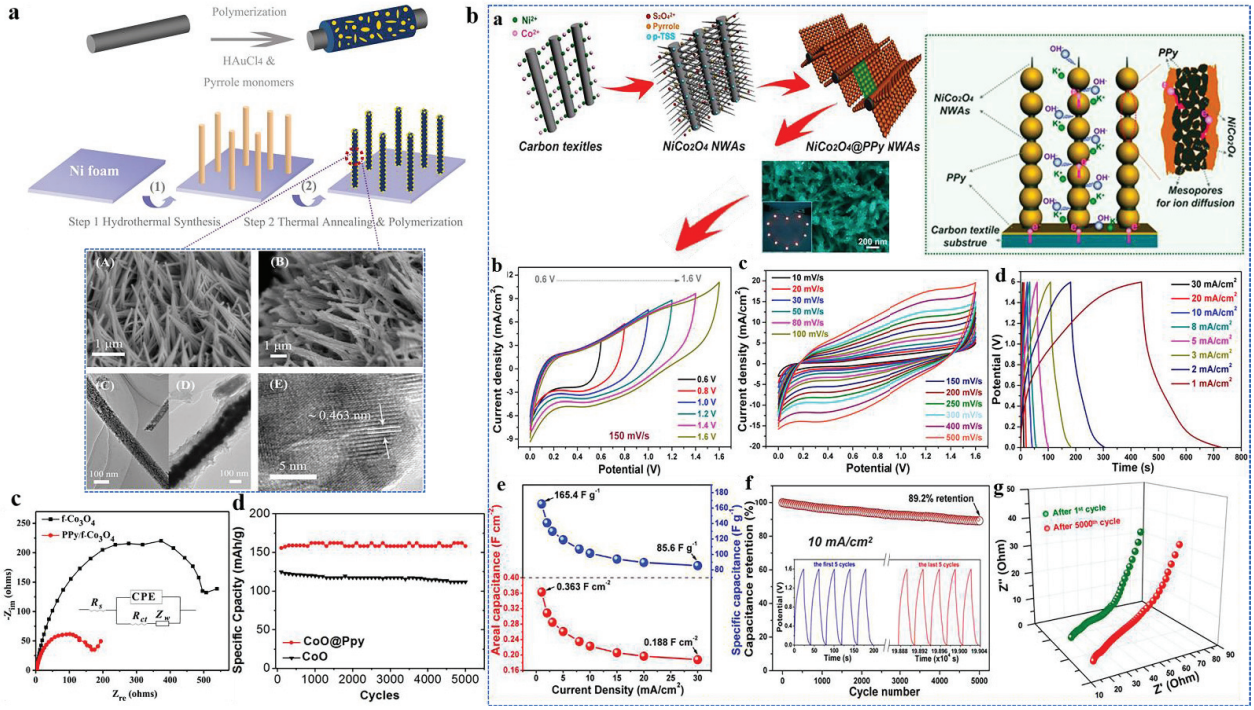

Figure 4. (**a**) Synthesis of cobalt oxide/PPy nanowires by hydrothermal followed by chemical polymerization [47]. (**b**) The charge transfer mechanism and electrochemical performance via CV curves at different potential windows (150 mV s^{-1}) and different scan rates (0–1.6 V), GCD curves at different current densities, specific and volumetric capacitance and cycling performance of ASC device (10 mA cm^{-2}) with Nyquist plots for the $NiCo_2O_4$/PPy/AC device (reprinted with permission from [49]; copyright 2015 American Chemical Society). (**c**) Nyquist plot of electropolymerized cobalt oxide/PPy/CP electrode [42] and (**d**) cycle stability of hydrothermally and electrodeposition polymerized CoO/Ppy nanoarrays [43].

3.4. Factors Influencing the Electrochemical Performance of Supercapacitors

Several factors influence the electrochemical performance of cobalt oxide/PPy nanocomposites and hence the supercapacitor, such as [42–44]:

Morphology and porosity: The nanostructure of cobalt oxide (e.g., nanowires, NPs, nanosheets) significantly affects the composite's surface area and porosity, which are crucial for ion diffusion and charge storage. The morphology of the PPy coating also plays a role; a porous and uniform PPy layer facilitates efficient ion transport and enhances the electrode's capacitance.

Polymer content: The amount of PPy relative to cobalt oxide is a critical parameter. An optimal PPy content maximizes conductivity and pseudocapacitance without compromising the active surface area of cobalt oxide. Excessive PPy can block active sites and reduce the overall capacitance.

Electrode configuration: The method of electrode fabrication, such as drop-casting or spin-coating of the composite onto current collectors, can affect the uniformity and adhesion of the composite layer, impacting the overall electrochemical performance.

4. Cobalt Oxide/PANI Nanocomposites for Supercapacitors

4.1. Synthesis of Cobalt Oxide/PANI Nanocomposites

The synthesis of cobalt oxide/PANI nanocomposites generally involves techniques that promote strong interaction between polyaniline and cobalt oxide nanostructures. The common synthesis methods include [40,50,51]:

In-situ chemical oxidation polymerization: This method involves the polymerization of aniline monomers in the presence of cobalt oxide particles using an oxidizing agent. The process results in the formation of a uniform PANI coating on cobalt oxide, enhancing the composite's electrical properties (Figure 5c).

Hydrothermal synthesis followed by polymerization: This is the most common method of fabricating electrode materials for supercapacitors. Cobalt oxide nanostructures are first synthesized via a hydrothermal method, followed by the oxidative polymerization of aniline (Figure 5a,b). This sequential approach allows for better control over the size and distribution of PANI on cobalt oxide

Layer-by-layer assembly: In this method, thin layers of cobalt oxide and PANI can be alternately deposited onto a substrate, creating a well-defined multilayer structure as done by Zhang et al. in the case of SnO_2 nanosheets [52]. This technique allows for precise control over the thickness and composition of each layer, optimizing the electrochemical properties.

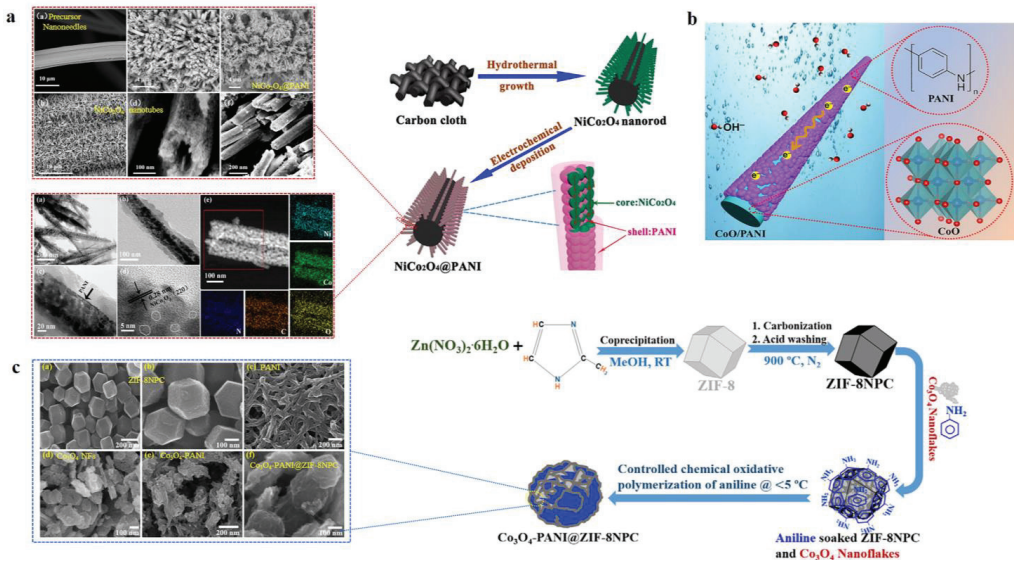

Figure 5. Synthesis methods: (**a**) hydrothermal followed by electrodeposition, (**b**) structural representation of CoO/PANI nanowires showing electron and electrolyte transport [53], and (**c**) in-situ chemical oxidative polymerization for $NiCo_2O_4$/PANI nanotubes [54] (reprinted with permission from [54]; copyright 2019 American Chemical Society), nanorods (reprinted with permission from [55]; copyright 2016 American Chemical Society), and a Co_3O_4-PANI/ZIF-8 nanoporous carbon (NPC) nanocomposite [56].

4.2. Advantages of PANI in Supercapacitors

PANI enhances the performance of cobalt-oxide-based supercapacitors by the following. *Increasing electrical conductivity*: PANI, like PPy, is a conductive polymer that significantly enhances the electrical conductivity of the composite, facilitating faster charge and discharge rates. *Enhancing pseudocapacitance*: PANI exhibits high pseudocapacitance due to its multiple oxidation states. The redox transitions of PANI contribute additional capacitance, complementing the faradaic reactions of cobalt oxide, thus improving the overall energy storage capacity. *Mechanical flexibility*: PANI's flexibility helps to accommodate the volume changes of cobalt oxide during the charge-discharge cycles, thereby improving the durability and cycling stability of the composite electrode [31,51].

4.3. Electrochemical Performance of Cobalt Oxide/PANI Nanocomposites in Supercapacitors

Electrochemical Mechanism: Cobalt oxide/PANI nanocomposites demonstrate significant electrochemical performance enhancements due to the combination of the pseudocapacitive properties of cobalt oxide and the redox-active, conductive nature of PANI [40]. The electrochemical properties of different cobalt oxide/PANI electrodes for high-energy supercapacitors are depicted in Table 4.

(i) *Faradaic redox reactions of cobalt oxide*: Similar to the cobalt oxide/PPy nanocomposite, the cobalt oxide in the cobalt oxide/PANI composite also undergoes reversible oxidation and reduction reactions. The redox reactions of Co^{2+}/Co^{3+} and Co^{3+}/Co^{4+} contribute to the overall pseudocapacitance. These reactions benefit from the high surface area provided by the nanostructured cobalt oxide, leading to enhanced redox activity. The reactions can be represented as (Equations (4) and (5)):

$$Co_3O_4 + OH^- + H_2O \rightarrow 3CoOOH + e^- \quad (4)$$

$$CoOOH + OH^- \rightarrow CoO_2 + H_2O + e^- \quad (5)$$

(i) *Pseudocapacitive and conductive properties of PANI*: PANI contributes to the electrochemical performance through its pseudocapacitive properties, which are derived from its multiple redox states (leucoemeraldine, emeraldine, and pernigraniline). The redox transitions involve the transfer of protons (H^+) and electrons (e^-) and are represented as (Equation (6)):

$$PANI^0 + 2H^+ + 2e^- \rightarrow PANI^{2+}(\text{Emeraldine}) \quad (6)$$

The ability of PANI to undergo such redox transitions at various oxidation states contributes to its high capacitance. Furthermore, the conductive backbone of PANI facilitates rapid electron transport, enhancing the overall charge storage and discharge capabilities of the nanocomposite.

Recent research has shown significant improvements in the electrochemical performance of cobalt oxide/PANI nanocomposites (Table 3). Hai et al. synthesized a core–shell structured Co_3O_4/PANI nanocomposite via a carbon-assisted in-situ polymerization method, achieving a high specific capacitance of 854 F g^{-1}. The composite exhibited excellent cycling stability, with 84.9% retention of capacity after 1000 galvanostatic charge-discharge cycles. The improved performance was attributed to the unique core–shell architecture, which provided a large surface area for redox reactions and improved ion diffusion pathways [40].

Recently, a study on PANI/CoO nanowires grown on Ni foam (PCN) demonstrated a significantly enhanced electrochemical performance when used as a binder-free supercapacitor electrode. The core–shell structure of the PANI/CoO nanowires exhibited a high specific capacitance of 2473 F g^{-1} at a current density of 3 A g^{-1}, with an excellent cycling stability of 86.3% after 10,000 charge-discharge cycles. The optimized design resulted in substantial synergistic effects between PANI and CoO, contributing to the high specific en-

ergy of 35.8 Wh kg^{-1}, making the PCN2 electrode a highly promising candidate for future supercapacitors (Figure 6). Figure 6a(a) demonstrates that while the conductive emeraldine salt form of PANI was successfully produced in both PCN2 and PCN3, the capacitive performance of PCN3 was lower compared to PCN2. This reduction in performance is attributed to the excessive polymer coating in PCN3, which resulted in a thicker layer around the CoO nanowire arrays. The thicker polymer coating hindered the rate of ion transport, leading to a decreased specific capacitance (Figure 6a(b)). This is very important to be noted. The electrochemical analysis of PCN2 and PCN3 revealed distinct performance differences. PCN2 exhibited the lowest equivalent series resistance (ESR) at 0.39 Ω, with the ESR trend closely following the specific capacitance results (Figure 6a(c)). The lower ESR in PCN2 suggests improved conductivity, which facilitates efficient electron and charge transfer during the electrochemical process. This enhancement was further supported by the Nyquist plot in the low-frequency region, where PCN2 demonstrated a more vertical profile compared to other electrode materials, indicating faster electrode kinetics and reduced resistance. In Figure 6a(d), the nonlinear charge-discharge profiles of PCN2 at different current densities point to the occurrence of faradaic reactions, confirming the electrochemical activity of the material during cycling. This behavior is indicative of the faradaic process driving the charge storage mechanism in PCN2. Figure 6a(e) shows a significant improvement in cycling stability, with the coulombic efficiency increasing from 92.3% to 98.1% over 10,000 cycles. This remarkable cycling stability can be attributed to the porous structure of the electrode, which allowed for better accommodation of the volume changes during charge-discharge cycling. Additionally, the presence of PANI helped to mitigate volumetric expansion and compression, ensuring that the electrode maintained structural integrity throughout prolonged cycling. As a result, PCN2 outperformed other Co-based electrodes in terms of long-term stability and electrochemical performance. Moreover, an asymmetric supercapacitor based on these PANI/CoO nanowire arrays demonstrated the capability to power 19 red LEDs [53]. Similarly, the ZIF-67 templates with the Co_3O_4/PANI nanocomposite synthesized by hydrothermal and chemical in-situ polymerization showed high specific capacitance (Figure 6b(a)) attributing to the high surface area and the short transport path for ions and electrons due to the hierarchically hollow structured Co_3O_4 and the highly conductive PANI layer. Moreover, the study revealed good cycle stability with 90% retention after 2000 cycles (Figure 6b(b)), which indicates the ability of such polymeric hybrid electrodes in enhancing the conductivity, pseudocapacitance, and stability (Figure 6b(c)) [57].

Chhetri et al. reported an advanced composite material for supercapacitors combining Zeolitic Imidazolate Framework-8 (ZIF-8)-derived nanoporous carbons (NPCs) with Co_3O_4 nanoflakes and PANI. The Co_3O_4-PANI@ZIF-8NPC nanocomposite was synthesized through controlled in-situ polymerization of PANI on the surface of ZIF-8NPC, with Co_3O_4 nanoflakes providing additional pseudocapacitive behavior. This unique nanostructure yielded a specific capacitance of 1407 F g^{-1} at a current density of 1 A g^{-1}, demonstrating both remarkable rate capability and cyclic stability. The enhanced electrochemical performance was attributed to the combination of the high conductivity provided by PANI, the increased number of redox-active sites from Co_3O_4, and the high surface area and suitable pore size distribution of ZIF-8NPC. Furthermore, an ASC was assembled using Co_3O_4-PANI@ZIF-8NPC as the positive electrode and ZIF-8NPC as the negative electrode. This ASC exhibited outstanding energy storage capabilities, achieving energy densities of 52.81 Wh kg^{-1} at a power density of 751.51 W kg^{-1} and 18.75 Wh kg^{-1} at a power density of 7500 W kg^{-1}. The ASC also demonstrated excellent cycling stability, retaining 88.43% of its initial capacitance after 10,000 cycles at a high current density of 10 A g^{-1} [56].

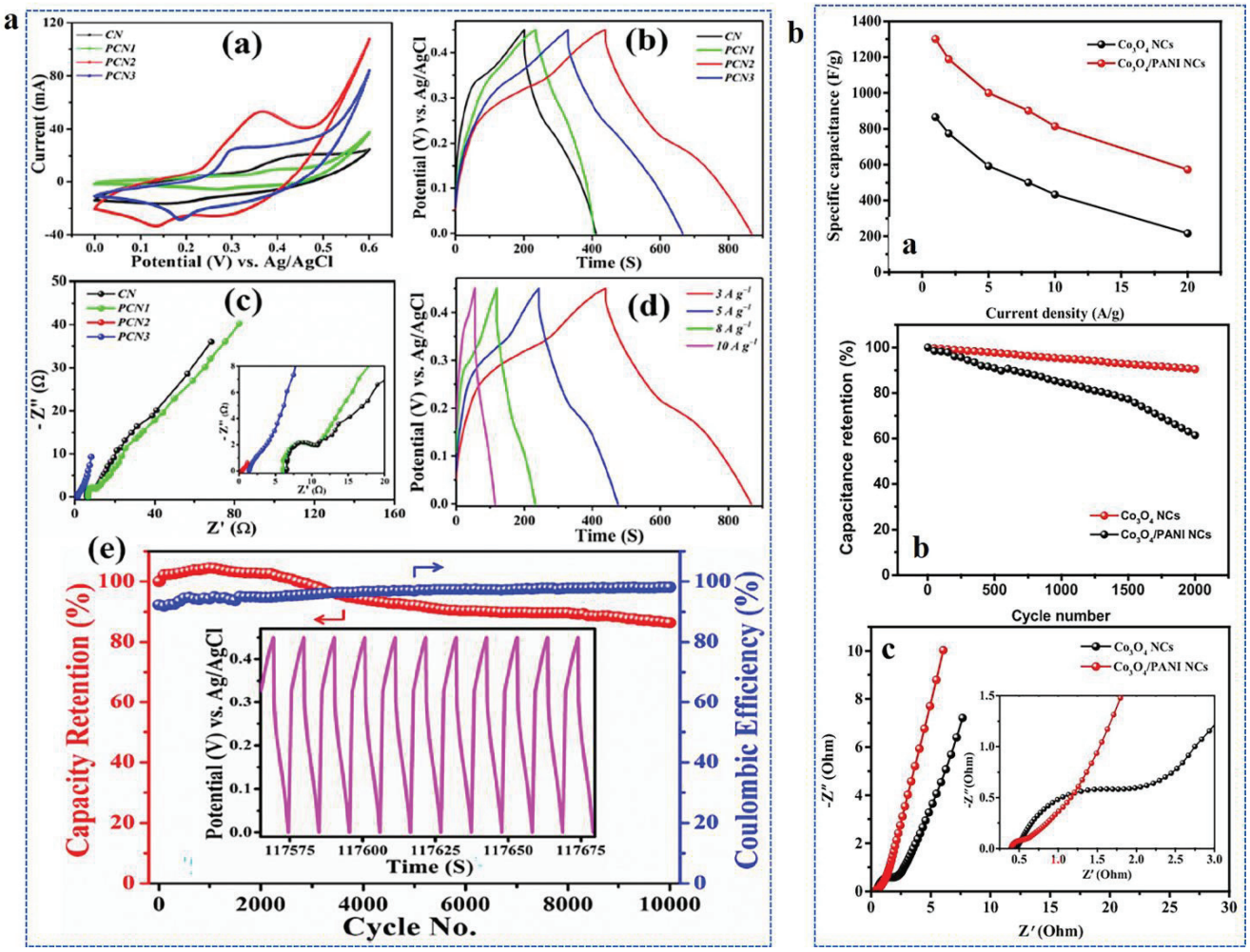

Figure 6. (**a**) Electrochemical performance of CoO/PANI nanowires: a—CV curves (scan rate 5 mV/s), b—charge-discharge profiles at 3 A/g, c—Nyquist plots, d—charge-discharge profiles at different current densities, and e—cycling stability curve of optimized PCN2, inset showing last few cycles [53]. (**b**) a—Specific capacitance, b—cycling stability at 10 A/g current density, and c—EIS spectra and Nyquist plot of Co_3O_4 and Co_3O_4/PANI nanocomposite, respectively [57].

Another study by Jabeen et al. focused on addressing the structural instability of PANI, which often limits its cycle life. The researchers developed a $NiCo_2O_4$@PANI core–shell nanorod array as an electrode material for supercapacitors. This hybrid structure, with highly porous $NiCo_2O_4$ serving as the conductive core and PANI as the active pseudocapacitive material, achieved a high specific capacitance of 901 F g^{-1} at 1 A g^{-1} in 1 M H_2SO_4. Notably, the electrode demonstrated excellent cycling stability with a capacitance retention of 91% after 3000 cycles at 10 A g^{-1}, which is a significant improvement compared to most reported PANI-based pseudocapacitors [55].

Similarly, $NiCo_2O_4$ has emerged as a promising supercapacitor material, though it requires improvement in capacitance and cycle stability for practical use. A $NiCo_2O_4$@PANI nanotube array on carbon textiles was synthesized via a two-step process, which resulted in a specific capacity of 720.5 C g^{-1} at 1 A g^{-1}. The introduction of a PANI layer significantly improved the cycle stability, with 99.64% capacity retention after 10,000 cycles. The PANI coating not only provided additional pseudocapacitance but also protected the tubular $NiCo_2O_4$ structure from deformation, further enhancing its electrochemical performance. Detailed analyses revealed reduced charge transfer resistance and faster charge storage kinetics, indicating the superior performance of the $NiCo_2O_4$@PANI composite as a supercapacitor electrode [54].

Rajkumar et al. also reported the synthesis of $FeCo_2O_4$/PANI nanocomposites via an in-situ polymerization method. The resulting material exhibited an impressive specific capacity of 940 C g^{-1} at 1 A g^{-1}, as measured by galvanostatic charge-discharge tests. The enhanced capacitive behavior was attributed to the nanorod-like structure of the composite, which provided a large surface area and a significant number of active sites, facilitating efficient ion and electron transport [58].

A recent study reported the synthesis of a ternary composite consisting of PANI, Co_3O_4 nanoparticles, and chitosan via an in-situ chemical oxidation method. The Co_3O_4 nanoparticles were uniformly coated with layers of chitosan and PANI, forming a core/double-shell nanostructure. The ternary composite demonstrated significantly improved specific capacitance compared to binary PANI/Co_3O_4 or PANI/CS composites. The optimal nanocomposite, with 40% Co_3O_4 nanoparticles, achieved a specific capacitance of 687 F g^{-1}, along with an energy density of 95.42 Wh kg^{-1} at 1 A g^{-1} and a power density of 1549 W kg^{-1} at 3 A g^{-1}. Additionally, the composite exhibited excellent cycling stability, retaining 91% of its capacitance after 5000 charge-discharge cycles. The synergistic effect between PANI, Co_3O_4, and CS contributed to the enhanced electrochemical performance [59].

These studies collectively demonstrate the effectiveness of incorporating PANI with metal oxides to enhance the electrochemical performance of supercapacitors. The synergistic effects between the metal oxides and PANI contribute to improved capacitance, cycling stability, and rate capability, making these nanocomposites highly promising candidates for advanced energy storage systems.

4.4. Factors Influencing the Electrochemical Performance of Supercapacitors

The performance of cobalt oxide/PANI nanocomposites is affected by several factors:

Morphology and nanostructure: The shape and size of cobalt oxide nanostructures (e.g., NPs, nanoflakes) determine the surface area and active sites available for redox reactions. The morphology of PANI, whether it forms a fibrous, tubular, or granular structure, influences the ion diffusion pathways and overall capacitance.

PANI loading and distribution: The amount and distribution of PANI in the composite are crucial for balancing conductivity and capacitance. Adequate PANI content ensures high conductivity and pseudocapacitance, but excess PANI can lead to a decrease in the active surface area and hinder ion transport.

Porosity and surface area: A high surface area and porosity of the composite facilitate better electrolyte penetration and ion diffusion, which are crucial for achieving high capacitance and fast charge-discharge cycles. The porosity of both the cobalt oxide and the PANI layers needs to be optimized for maximum performance.

Table 4. Electrochemical behavior of different cobalt oxide/PANI electrodes for energy storage applications.

Electrode Material	Enhancement	Morphology	Synthesis Method	Specific Capacitance (F g^{-1})	Application	Ref.
PANI-Co_3O_4	-	Core–shell	Hydrothermal + chemical polymerization	1184 at 1.25 A g^{-1}	Supercapacitor	[40]
PANI/CoO/NF	Ni foam	Nanowires	Hydrothermal + electrodeposition	2473 at 3 A g^{-1}	Supercapacitor	[53]
$NiCo_2O_4$/PANI carbon textiles	Carbon textiles	Nanotubes	Hydrothermal + chemical polymerization	720 C g^{-1}	Supercapacitor	[54]
$NiCo_2O_4$/PANI/CC	Ni, Carbon cloth	Nanorods	Hydrothermal + electrodeposition	901 at 1 A g^{-1}	Supercapacitor	[55]

Table 4. *Cont.*

Electrode Material	Enhancement	Morphology	Synthesis Method	Specific Capacitance ($F\ g^{-1}$)	Application	Ref.
carbon, Co_3O_4, and PANI	Carbon	Nanocomposite	Hydrothermal + Chemical oxidative polymerization	1407 at 1 A g^{-1}	Supercapacitor	[56]
Graphene/PANI/Co_3O_4	Graphene	Nanocomposite	Chemical polymerization + hydrothermal	789.7 at 1 A g^{-1}	Supercapacitor	[60]
$FeCo_2O_4$ and PANI	Fe	Nanorods	Hydrothermal + Chemical oxidative polymerization	940 C g^{-1}	Supercapacitor	[58]
Co^{2+} doped PANI	-	Films	Electrodeposition	736 at 3 mA cm^{-2}	Supercapacitor	[61]
Graphene/PANI/Co_3O_4 aerogel	Graphene	Aerogels	Chemical polymerization + hydrothermal	1247 at 1 A g^{-1}	Supercapacitor	[62]
PANI/Co_3O_4/CS	Chitosan	Nanocomposite	In-situ chemical oxidation polymerization	687 at 1 A g^{-1}	Supercapacitor	[59]
PANI/CoO/ZT	Zeolite	Composite	Co-precipitation + Chemical oxidative polymerization	1282 at 1 A g^{-1}	Supercapacitor	[63]
Co_3O_4/PANI	ITO	Nanoshrubs	Sol-gel + Emulsion polymerization	1151 at 3 A g^{-1}	Supercapacitor	[64]
Co_3O_4/PANI	ZIF-67	Nanocage	Precipitation + Chemical polymerization	1301 at 1 A g^{-1}	Supercapacitor	[57]

5. Cobalt Oxide/PPy Nanocomposites for Batteries

The application of cobalt oxide/conducting polymer nanocomposites as electrode materials in batteries remains largely underexplored compared to their use in supercapacitors and hybrid supercapatteries. We have come across only a limited number of studies of cobalt oxide/PPy and cobalt oxide/PANI for battery applications. While these materials have shown promising electrochemical performance, further research is needed to fully understand their potential in battery applications. Expanding studies in this area will help optimize their structural, electrochemical, and cycling properties, paving the way for broader utilization in advanced battery technologies. The electrochemical performance of cobalt oxide-based nanocomposites combined with conducting polymers like PPy and PANI extends beyond supercapacitors to rechargeable battery applications, including lithium-ion batteries (LIBs), sodium-ion batteries (SIBs), and other emerging air battery systems [65].

5.1. Synthesis Strategies of Cobalt Oxide/PPy Nanocomposites for Batteries

Focusing on achieving uniform distribution, optimal morphology, and enhanced interface interactions between cobalt oxide and PPy, several synthesis methods have been employed to fabricate cobalt oxide/PPy nanocomposites. Common synthesis strategies include [66,67]:

In-situ polymerization: In this method, cobalt oxide NPs are first synthesized through a hydrothermal or sol-gel method. The pyrrole monomer is then added to the Cobalt oxide dispersion, and polymerization is initiated using an oxidizing agent (e.g., ammonium

persulfate) under controlled conditions. This process allows PPy to form uniformly on the surface of cobalt oxide NPs, ensuring intimate contact and a robust composite structure.

Electrochemical polymerization: This method involves depositing cobalt oxide onto a substrate followed by electrochemical polymerization of pyrrole in a suitable electrolyte solution. The applied potential drives the polymerization, forming a PPy coating on the cobalt oxide NPs. This technique offers precise control over the thickness and uniformity of the PPy layer, which is crucial for optimizing electrochemical performance.

Solvothermal and co-precipitation methods: Cobalt oxide NPs are synthesized via solvothermal methods, followed by the addition of a pyrrole monomer. Polymerization is induced by temperature or chemical initiators. Coprecipitation of cobalt precursors with pyrrole ensures simultaneous formation of cobalt oxide and PPy, leading to a homogeneous nanocomposite structure.

5.2. Role of PPy in Enhancing Battery Performance

Similar to supercapacitors, in the case of batteries, PPy plays a critical role in improving the electrochemical performance of cobalt-oxide-based batteries with [4,65]:

Enhanced conductivity: PPy is an intrinsically conductive polymer that forms a continuous conductive network within the composite. This network facilitates efficient electron transport, which is vital for high-rate charge and discharge processes in batteries.

Buffering effect: PPy provides a flexible matrix that buffers the volumetric expansion and contraction of Cobalt oxide during the lithiation/delithiation or sodiation/desodiation cycles, thereby enhancing the structural stability of the electrode.

Additional pseudocapacitive contribution: PPy contributes to the overall capacity through its redox-active sites, which can store and release charge, thereby improving the specific capacity of the electrode.

5.3. Electrochemical Performance of Cobalt Oxide/PPy Nanocomposites in Batteries

Electrochemical Mechanism: Cobalt oxide is a well-known anode material for lithium-ion and sodium-ion batteries due to its high theoretical capacity and multiple oxidation states that facilitate reversible redox reactions. The integration of PPy enhances the electrochemical performance through the following mechanisms [66–68]:

(i) Lithium-ion batteries (LIBs): In LIBs, cobalt oxide undergoes conversion and alloying reactions during lithiation and delithiation processes. The electrochemical reactions can be summarized as in Equations (7) and (8):

$$Co_3O_4 + 8Li^+ + 8e^- \rightarrow 3Co + 4Li_2O \quad (7)$$

The reaction involves the conversion of cobalt oxide to metallic Co and Li_2O during lithiation, and the reverse reaction occurs during delithiation. The Co NPs formed during this process act as active sites for the further reduction of lithium ions, contributing to the high capacity of the electrode.

Role of PPy: PPy serves as a conductive matrix, enhancing the electronic conductivity of the composite and buffering the volume changes associated with the redox reactions of cobalt oxide. PPy also provides a pathway for rapid electron transport, which is crucial for maintaining the structural integrity and high rate capability of the electrode.

(ii) Sodium-ion batteries (Na-ion batteries):

Cobalt oxide redox reactions: The electrochemical behavior in Na-ion batteries is similar to that in Li-ion batteries, with the conversion of cobalt oxide into Na_2O and Co during the sodiation process:

$$Co_3O_4 + 8Na^+ + 8e^- \rightarrow 3Co + 4Na_2O \quad (8)$$

Role of PPy: PPy enhances the sodium storage capacity by providing a conductive network that supports the redox reactions of cobalt oxide. Moreover, the flexible nature of

PPy accommodates the strain from the volume changes during sodiation and desodiation, improving cycling stability.

Recent studies have explored novel nanocomposites involving PPy and cobalt-based compounds for advanced energy storage applications, including lithium-ion and sodium-ion batteries. Guo et al. synthesized a polypyrrole–cobalt–oxygen (PPy-Co-O) coordination complex, which demonstrated excellent lithium storage capacity and stability. Using extended X-ray absorption fine structure (EXAFS) and Raman spectroscopy, they revealed that this complex form when PPy-coated Co_3O_4 is cycled between 0.0 V and 3.0 V versus Li^+/Li. DFT calculations suggested that each cobalt atom coordinates with two nitrogen atoms in the PPy-Co structure, while oxygen atoms link the layers. This coordination weakens C-H bonds in PPy, resulting in a high-capacity, long-lasting lithium-storage material [68].

Similarly, Hou et al. developed a Co_3O_4/PPy nanohybrid through a hydrothermal process, optimized for bifunctional catalysis in lithium-oxygen (Li-O_2) batteries (Figure 7a). The Co_3O_4/PPy hybrid material enhanced both oxygen reduction reaction (ORR) and oxygen evolution reaction (OER) performance, yielding a discharge capacity of 3585 mAh g^{-1} and a charge capacity of 2784 mAh g^{-1} at 100 mA g^{-1}. The improved electrochemical performance was attributed to the synergy between the conductive PPy nanoweb structure and the high catalytic activity of Co_3O_4 nanoparticles [69]. Figure 7b demonstrates the enhanced electrochemical performance of the Co_3O_4/PPy hybrid due to synergistic effects between Co_3O_4 and PPy, contributing to its promising application in lithium-oxygen batteries. The study revealed the initial charge-discharge profiles of the nanofibrous Co_3O_4/PPy hybrid and pristine PPy cathodes in lithium-oxygen batteries. These curves were recorded at a current density of 100 mA g^{-1} in a 1 M $LiCF_3SO_3$/TEGDME electrolyte (operating between 2.0 and 4.4 V vs. Li^+/Li) (Figure 7b(a)). The distinct profiles highlighted the superior capacity and energy efficiency of the Co_3O_4/PPy hybrid compared to the pristine PPy. The electrochemical impedance spectroscopy (EIS) plots compared the impedance of the Co_3O_4/PPy hybrid and the pristine PPy cathodes before and after the first recharge. The lower impedance of the Co_3O_4/PPy hybrid indicated better charge transfer kinetics and reduced resistance (Figure 7b(b)). Figure 7b(c,d) shows the charge-discharge curves and cycling performance of the Co_3O_4/PPy hybrid electrode, tested at a capacity limit of 500 mAh g^{-1} and a current density of 100 mA g^{-1}, indicating stable cycling over multiple cycles. The performance highlights the hybrid's ability to sustain capacity over prolonged use. Furthermore, the charge-discharge profiles and cycling performance of the pristine PPy cathode under the same testing conditions revealed a rapid decline in capacity with increasing cycle number. This suggests the superior stability and cycling retention of the Co_3O_4/PPy hybrid compared to the pristine PPy (Figure 7b(e,f)) [69].

In a recent study, cobalt-based binary sulfides were investigated for sodium-ion batteries (SIBs). The high abundance and cost-effectiveness of sodium make SIBs an attractive alternative for energy storage. However, challenges such as high-volume expansion and limited cycle life persist. A novel PPy/ZnCoS@CC nanocomposite, where zinc cobalt sulfide nanosheets were coated with PPy, was synthesized via a hydrothermal process. The PPy coating helped mitigate volume expansion and enhanced cycling stability, achieving an aerial capacity of 2.33 mAh cm^{-2}, with 75% retention after 100 cycles. The study also utilized the galvanic intermittent titration technique (GITT) to measure the diffusion coefficient, showing that the conductive polymer coating played a crucial role in stabilizing the electrode during charge-discharge cycles [70].

These findings underscore the potential of PPy/cobalt nanocomposites for enhancing energy storage devices by addressing key limitations such as cycle stability, volume expansion, and electrochemical performance.

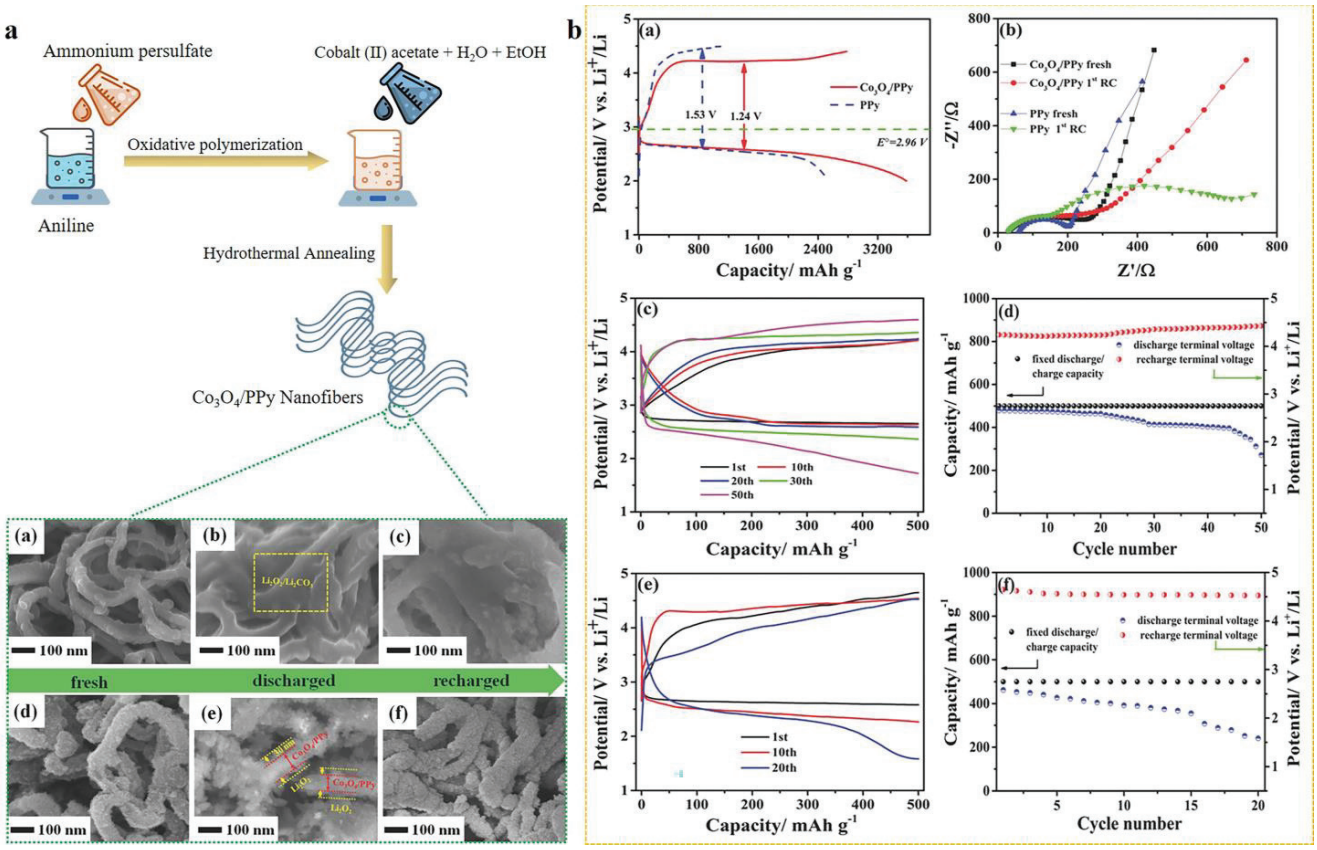

Figure 7. (**a**) Preparation method of Co_3O_4/PPy nanohybrid for batteries showing their SEM images. (**b**) Electrochemical performance of Co_3O_4/PPy nanofibers for LiO_2 battery applications [69].

5.4. Factors Influencing the Electrochemical Performance of Batteries

The cobalt oxide/PPy nanocomposites used in batteries can be affected by different factors, which in turn influence the electrochemical performance of the batteries [4], such as:

Morphology and porosity: The porous structure of cobalt oxide/PPy nanocomposites provides a larger surface area for electrochemical reactions and facilitates ion diffusion, enhancing the battery's capacity and rate capability.

Polymer content: The ratio of PPy to cobalt oxide is crucial; excessive PPy may lead to a reduction in specific capacity due to its lower theoretical capacity compared to cobalt oxide, while insufficient PPy might not provide adequate conductivity or structural support.

Particle size distribution: Uniform distribution of cobalt oxide particles within the PPy matrix ensures consistent electrochemical performance and prevents agglomeration, which can degrade the battery's capacity and stability.

6. Cobalt Oxide/PANI Nanocomposites for Batteries

6.1. Synthesis Strategies of Cobalt Oxide/PANI Nanocomposites for Batteries

The synthesis of cobalt oxide/PANI nanocomposites involves similar strategies to those used for cobalt oxide/PPy composites, with a focus on achieving optimal polymerization and composite formation [71,72]:

In-situ oxidative polymerization: This method involves dispersing cobalt oxide NPs in an aniline monomer solution, followed by the addition of an oxidizing agent (e.g., ammonium persulfate). Polymerization occurs on the surface of cobalt oxide, forming a PANI coating. This method ensures strong interfacial bonding and uniform distribution of PANI on cobalt oxide.

Template-assisted synthesis: Cobalt oxide is synthesized using a template that provides a specific morphology (e.g., nanorods, nanowires). Aniline is then polymerized on the cobalt oxide template, producing a PANI-coated cobalt oxide nanocomposite. This method allows control over the morphology and surface area, which are crucial for enhancing electrochemical performance.

Electrospinning and chemical vapor deposition (CVD): Electrospinning can be used to create a fibrous network of cobalt oxide embedded within a PANI matrix, providing a high surface area and porous structure. Alternatively, CVD allows for the precise deposition of PANI onto cobalt oxide NPs, enhancing uniformity and composite stability.

6.2. Role of PANI in Enhancing Battery Performance

PANI enhances the performance of cobalt-oxide-based batteries through several mechanisms:

Improved electrical conductivity: PANI is a highly conductive polymer that forms a continuous pathway for electron transport, reducing internal resistance and enhancing charge-discharge rates.

Pseudocapacitive behavior: PANI provides additional pseudocapacitive storage through its redox transitions (emeraldine to leucoemeraldine and pernigraniline states), which contribute to the overall charge storage capacity of the electrode.

Mechanical flexibility and stability: The flexible nature of PANI helps to accommodate the volumetric changes in cobalt oxide during cycling, reducing mechanical stress and improving the cycling stability of the composite.

6.3. Electrochemical Performance of Cobalt Oxide/PANI Nanocomposites in Batteries

Electrochemical Mechanism: The integration of cobalt oxide with PANI in the most common battery electrodes leads to enhanced electrochemical performance due to the following mechanisms:

(i) Lithium-ion batteries (LIBs):

Cobalt oxide (Co_3O_4) redox reactions: Similar to the cobalt oxide/PPy system, cobalt oxide in cobalt oxide PANI nanocomposites undergoes a conversion reaction where cobalt oxide is reduced to Co and Li_2O during lithiation. The delithiation process involves the oxidation of Co and the release of Li^+ (Equation (9)).

$$Co_3O_4 + 8Na^+ + 8e^- \rightarrow 3Co + 4Na_2O \quad (9)$$

Reaction with PANI: PANI not only enhances the electronic conductivity but also provides pseudocapacitive contributions from its redox-active sites. PANI can undergo reversible redox transitions between its leucoemeraldine, emeraldine, and pernigraniline states, contributing to the overall capacity. These transitions allow for additional charge storage and improve the rate capability of the electrode (Equation (10)).

$$PANI^0 + 2Li^+ + 2e^- \rightarrow PANI^{2+}(\text{Emeraldine}) \quad (10)$$

(ii) Sodium-ion batteries (Na-ion batteries):

Cobalt oxide redox reactions: In Na-ion batteries, Co_3O_4 undergoes a similar conversion reaction as in Li-ion batteries (Equation (11)):

$$Co_3O_4 + 8Na^+ + 8e^- \rightarrow 3Co + 4Na_2O \quad (11)$$

Reaction with PANI: PANI enhances the sodium storage capacity by providing a conductive network and additional pseudocapacitance from its redox-active sites. The flexibility of PANI also helps to accommodate the volume expansion associated with sodium insertion, which is more pronounced than lithium insertion, thereby improving the cycling stability.

Recently, Kuchena and Wang synthesized an ammonium-ion battery cell utilizing an emeraldine salt (ES-PANI) cathode material that exhibited a high discharge capacity of

160 mAh g^{-1} at 1 A g^{-1} in Li-ion batteries. The composite showed excellent rate capability, with a capacity retention of 82% after 100 cycles at 5 A g^{-1}. The improved performance was attributed to the synergistic effects of ES-PANI, which enhanced electron transport and provided additional charge storage through the redox activity of PANI [39]. Qi et al. presented a novel approach for constructing advanced anode materials by fabricating Co_3O_4/polyaniline (PANI) core–shell arrays (CSAs). Using chemical bath deposition (CBD) followed by electrodeposition, they achieved a highly conductive and stress-buffering PANI shell intimately coating Co_3O_4 nanorods. The resulting Co_3O_4/PANI CSAs demonstrated significantly improved electrochemical performance, with a reversible capacity of 787 mAh g^{-1} and enhanced cycle stability compared to the unmodified Co_3O_4 counterpart (Figure 8a). The core–shell design, which merges the high conductivity of PANI with the energy storage capability of Co_3O_4, opens up new possibilities for fabricating inorganic–organic composite electrodes for energy storage [73].

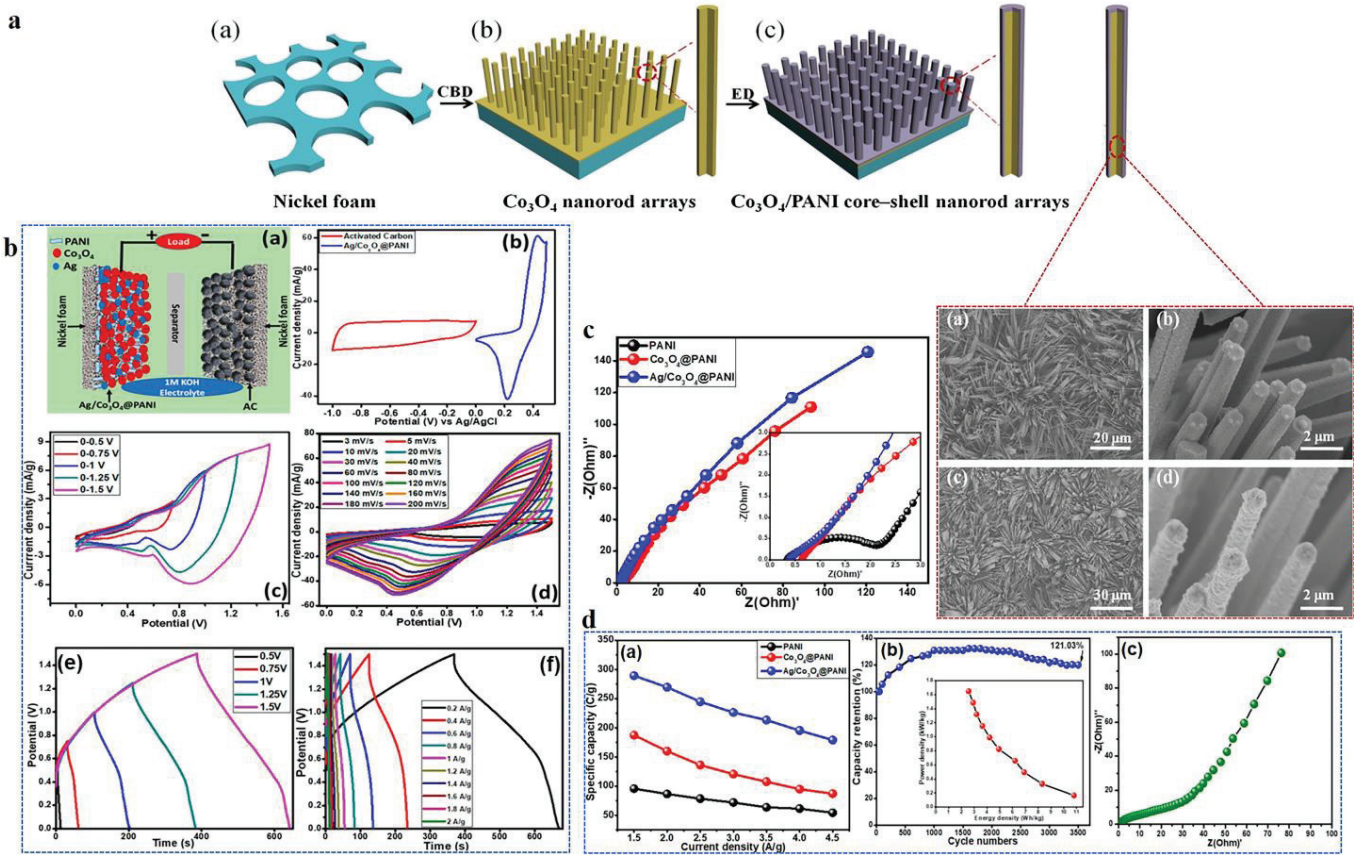

Figure 8. (**a**) Synthesis of Co_3O_4/PANI nanorods as an anode material by chemical bath deposition (CBD) followed by electrodeposition (ED) and its impedance spectra for Li-ion batteries [73]. (**b**) Supercapattery device fabrication by Ag/Co_3O_4/PANI nanocomposites as battery-type positive electrode material, showing its CV curves at different potential and scan rates, and charge-discharge at different potentials and current densities. Comparative analysis by (**c**) Nyquist plot and (**d**) specific capacity and current density of Ag/Co_3O_4/PANI nanocomposite along with the cycle stability and energy and power densities of the fabricated device [71].

Gu et al. tackled the major challenges in lithium-sulfur (Li-S) batteries, such as the shuttle effect of lithium polysulfides (LiPS), poor conductivity, and volume expansion during charge-discharge cycles, by designing $CoFe_2O_4$ nanotubes decorated with polyaniline (PANI). The $CoFe_2O_4$ nanotubes provided void space to accommodate sulfur and mitigate volume changes, while PANI enhanced the overall conductivity and LiPS retention. This smart design resulted in a S/$CoFe_2O_4$@PANI electrode with a high initial capacity of

864.1 mAh g^{-1} and a reversible capacity of 582.6 mAh g^{-1} after 500 cycles at 2 C, marking a significant improvement in cycling stability for Li-S batteries [74].

6.4. Factors Influencing the Electrochemical Performance of Batteries

Regarding the battery material, cobalt oxide/PANI nanocomposites can be affected by different factors that influence the electrochemical performance of the batteries [4], such as:

Morphology and structural integrity: The morphology of cobalt oxide/PANI composites, such as core–shell or nanofiber structures, influences ion diffusion and electron transport, directly impacting battery performance.

Polymer content: The content of PANI in the composite should be optimized to balance between providing sufficient conductivity and maintaining a high specific capacity. An optimal balance ensures enhanced electrochemical performance without compromising capacity.

Interfacial interactions: Strong interfacial interactions between cobalt oxide and PANI are essential for efficient charge transfer and maintaining structural integrity during cycling. Weak interactions can lead to detachment or degradation of the composite, adversely affecting performance.

7. Supercapattery: Basic Concept, Comparison, and How It Works

Supercapatteries are the hybrid energy storage devices that combine the properties of both supercapacitors and batteries. They aim to bridge the gap between these two technologies, offering the fast charge-discharge rates of supercapacitors and the high energy density typical of batteries.

Driving force for its origin: Supercapacitors are known for high power density, meaning they can deliver energy quickly, but they have relatively low energy storage capacity (energy density). Furthermore, batteries are known for their high energy density, meaning they store a large amount of energy, but their power density (ability to release energy quickly) is lower compared to supercapacitors. This has resulted in the goal to develop supercapatteries. Supercapatteries usually involve a hybrid structure, which may consist of battery-type and capacitive-type electrode materials:

Battery-type materials: Electrodes made from materials with faradaic (battery-like) behavior, such as transition metal oxides or conducting polymers.

Capacitor-type materials: Electrodes that use materials with electrostatic storage, such as carbon-based materials (graphene, activated carbon).

Characteristics of supercapatteries:

Energy density: Supercapatteries have higher energy density than traditional supercapacitors, closer to that of batteries.

High Power Density: They retain a higher power density, allowing for rapid charge and discharge, more typical of supercapacitors.

Lifespan: Like supercapacitors, supercapatteries have longer cycle lives than conventional batteries, as they can handle more charge-discharge cycles without significant degradation.

Applications: These devices are particularly useful in applications requiring both quick energy delivery and reasonable storage capacity, such as in electric vehicles, renewable energy systems, and portable electronics.

The electrochemical performance of energy storage devices like supercapacitors, batteries, and supercapatteries can be clearly distinguished by analyzing their cyclic voltammetry (CV) and galvanostatic charge-discharge (GCD) profiles. CV and GCD are used to assess the redox behavior and charge/discharge under constant current, respectively. The electrochemical difference between supercapacitors, batteries, and supercapatteries in terms of their CV and GCD curves are provided in Table 5 and Figure 9.

Table 5. Comparison of CV and GCD of supercapacitors, batteries, and supercapatteries.

Device	CV	GCD
Supercapacitors		
EDLCs	Rectangular	Linear (symmetric)
Pseudocapacitors	Oval with redox peaks	Slightly non-linear (asymmetric)
Hybrid capacitors	Rectangular with redox peaks (mixed)	Combination of linear and non-linear
Batteries	Sharp redox peaks	Non-linear with distinct plateaus
Supercapatteries	Quasi-rectangular with broad redox peaks	Quasi-linear with slight curvature

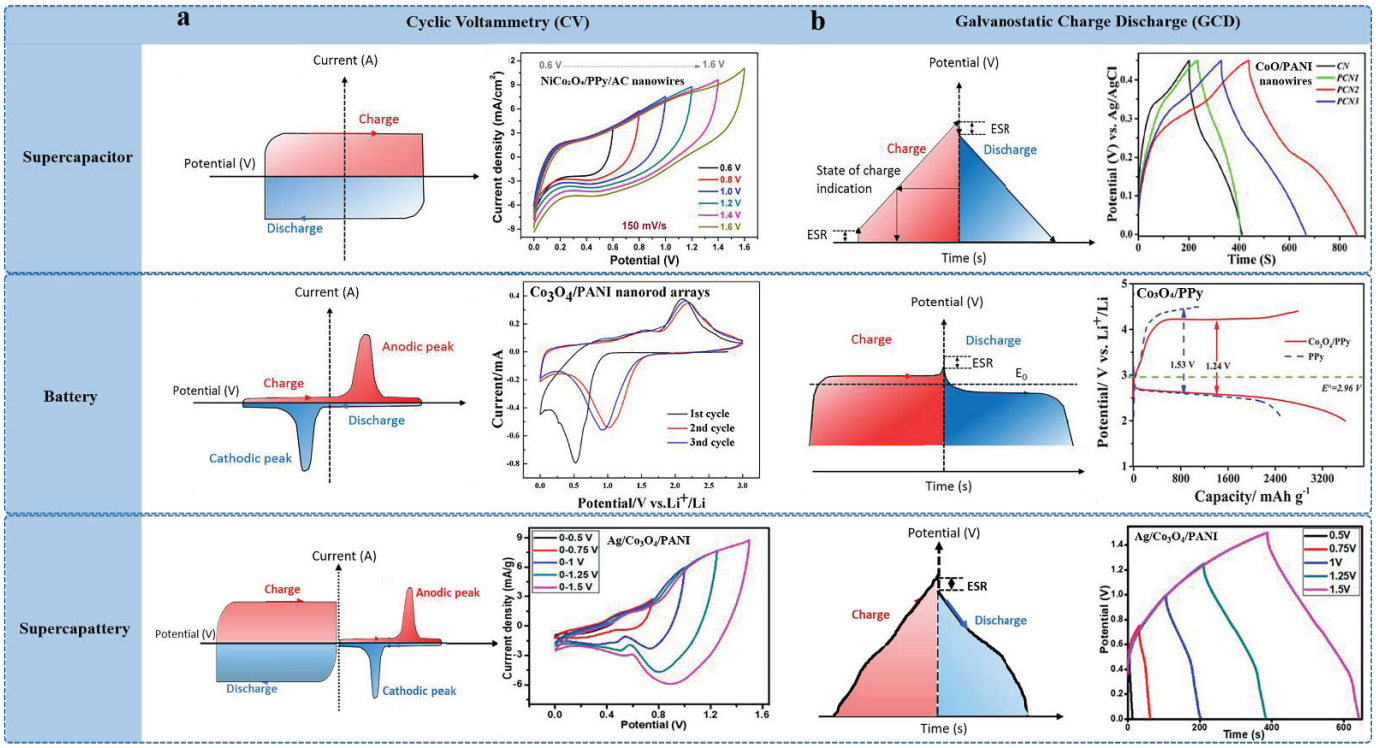

Figure 9. Comparative electrochemical differences in (**a**) CV and (**b**) GCD curves of cobalt oxide/conducting polymer (PPy and PANI)-based electrode materials for supercapacitor, battery, and supercapattery applications (ESR is equivalent series resistance) [1,49,53,69,71,73] (*reprinted with permission from* [1]; *copyright 2018 American Chemical Society*).

8. Cobalt Oxide/PPy and Cobalt Oxide/PANI Nanocomposites for Supercapatteries

8.1. Synthesis Strategies

The synthesis strategies for cobalt oxide nanocomposites with PPy and PANI for supercapatteries include:

In-situ polymerization: Pyrrole or aniline monomers are polymerized in the presence of pre-synthesized cobalt oxide nanoparticles, leading to the formation of the Co_3O_4/conducting polymer composite.

Electrochemical deposition: Cobalt oxide is electrodeposited onto a conductive substrate, followed by electropolymerization of pyrrole or aniline to form PPy or PANI on the cobalt oxide surface.

Hydrothermal synthesis: Cobalt oxide is synthesized via hydrothermal methods, and the conducting polymer is subsequently polymerized in-situ on the cobalt oxide.

Sol-gel method with polymerization: Cobalt oxide is synthesized using the sol-gel method, followed by in-situ oxidative polymerization of pyrrole or aniline to form the composite.

Template-assisted synthesis: A hard or soft template is used to create nanostructured cobalt oxide, followed by the deposition of a conducting polymer.

Mechanical mixing and coating: Pre-synthesized cobalt oxide nanoparticles are physically mixed with the conducting polymer, often followed by oxidative polymerization.

Co-precipitation with pyrrole polymerization: Co-precipitation of cobalt oxide is combined with the polymerization of pyrrole or aniline to form the nanocomposite.

8.2. Role of PPY and PANI in Enhancing Supercapattery Performance

PPy and PANI enhance the performance of cobalt-oxide-based supercapatteries in several ways:

High Conductivity: Cobalt oxide alone has moderate electrical conductivity. PPy and PANI, as conducting polymers, enhance the composite's electrical conductivity, allowing for faster electron transport during charge-discharge processes. This improved conductivity increases the power density of the supercapattery.

Pseudocapacitance: PPy and PANI contribute to pseudocapacitance due to their ability to undergo fast and reversible redox reactions during charge-discharge. This pseudocapacitive behavior enhances the overall capacitance of the composite, boosting energy storage capacity.

Structural Flexibility: PPy and PANI provide mechanical flexibility to the composite, accommodating volume changes in cobalt oxide during cycling. This reduces structural degradation and enhances cycle stability.

Synergistic Effect: The combination of capacitive properties of PPy or PANI and cobalt oxide's faradaic behavior results in a synergistic effect, improving both energy and power density.

8.3. Electrochemical Performance of Cobalt Oxide/PANI Nanocomposites in Supercapatteries

There are a limited number of studies exploring the interaction between cobalt oxide and conducting polymers, such as PPy and PANI, to form electrode materials for supercapattery applications. Addressing this research gap presents a valuable opportunity to make significant advancements in the fabrication of energy storage devices.

In a recent study on supercapatteries, Iqbal et al. fabricated silver (Ag)- and Co_3O_4-decorated PANI fibers by a combination of in-situ aniline oxidative polymerization and hydrothermal synthesis. The structural and morphological analyses revealed that PANI fibers were uniformly coated with Ag and Co_3O_4 nanograins, forming a fibrous nanocomposite with high purity and crystallinity. Electrochemical evaluations revealed that the incorporation of Ag and Co_3O_4 significantly enhanced the electrochemical properties of the PANI matrix (Figure 8b). The synergistic effect of these materials provided additional active sites for faradaic reactions, leading to a higher specific capacity. The Ag/Co_3O_4/PANI ternary nanocomposite exhibited a remarkable specific capacity of 262.62 C g^{-1} at a scan rate of 3 mV s^{-1}. Furthermore, the material depicted high energy and power densities, reaching 14.01 Wh kg^{-1} and 165.00 W kg^{-1}, respectively. The cycling stability of the supercapattery, consisting of Ag/Co_3O_4/PANI as the battery-type electrode and activated carbon as the counterpart, was notably impressive. The specific capacity initially increased during the first 1000 cycles and remained stable up to 2500 cycles. After 3500 cycles, the supercapattery retained 121.03% of its initial capacity, reflecting its excellent long-term stability (Figure 8c,d). This study underscores the potential of metal-doped Ag/Co_3O_4/PANI nanocomposites in advanced energy storage applications due to their enhanced electrochemical performance and durability [71].

Together, such studies highlight the importance of cobalt oxide in combination with conductive polymers like PANI in advancing battery and supercapacitor technologies. The core–shell structures, synergistic effects, and tailored composites are crucial for enhancing

electrochemical performance, including capacity retention, conductivity, and cycle stability, making these materials highly promising for next-generation energy storage systems.

8.4. Factors Influencing the Electrochemical Performance of Supercapatteries

Morphology of cobalt oxide: The surface area, shape, and size of cobalt oxide nanostructures influence ion diffusion and electron transfer, directly affecting the overall performance. Nanostructures like nanowires or nanosheets offer a high surface area and improve charge storage.

Loading amount of conducting polymer: The amount of PPy or PANI influences the balance between capacitive and faradaic charge storage. Excess polymers may block active sites on cobalt oxide, while insufficient polymers reduce conductivity.

Composite conductivity: The overall conductivity of the composite impacts the charge transfer resistance and the charge-discharge rates. Highly conductive polymers and well-distributed cobalt oxide nanoparticles improve electron transport.

Electrolyte choice: The electrolyte determines the ion transport rate and the operating voltage window. Aqueous electrolytes (e.g., H_2SO_4 or KOH) provide fast ion transport, while organic electrolytes enable a higher voltage window but may limit ion mobility.

Synthesis temperature: High synthesis or annealing temperatures can enhance crystallinity and conductivity but may also degrade the polymer, reducing its performance.

Cobalt oxide–polymer interaction: Strong interfacial bonding between cobalt oxide and PPy ensures better charge transfer and structural stability, which is crucial for long-term cycling.

9. Effect of Electrolytes on Supercapacitors, Batteries, and Supercapatteries

Electrolytes play a crucial role in determining the overall performance of energy storage devices such as supercapacitors, batteries, and supercapatteries. They influence the ion transport, electrochemical stability, operating voltage window, and charge storage mechanism, all of which affect the device's energy and power densities, cycle life, and efficiency. Table 6 illustrates the effects of electrolytes on the electrochemical performance of supercapacitors, batteries, and supercapatteries.

Table 6. Effects of electrolytes on the electrochemical performance of supercapacitors, batteries, and supercapatteries.

Parameter	Supercapacitors	Batteries	Supercapatteries
Energy density	Higher with organic and ionic liquids; lower with aqueous electrolytes	Higher in organic/solid electrolytes, liquid electrolytes (e.g., lithium-ion systems)	Balanced; depends on electrolyte selection (aqueous for power, organic for energy)
Power density	Higher with aqueous electrolytes due to fast ion transport	Moderate to low due to solid-state diffusion limits	Higher with aqueous electrolytes; organic provides balanced performance
Cycle life	Aqueous and ionic liquids can provide excellent stability; organic electrolytes have moderate stability	Longer with solid-state or stable liquid electrolytes; dendrite formation is a risk with liquid	Long-term stability depends on electrolyte–electrode compatibility
Rate capability	Aqueous electrolytes provide superior rate capability	Lower in solid-state, moderate in liquid systems	Aqueous electrolytes provide faster charge-discharge; organic is slower
Safety	Aqueous and ionic electrolytes are safer (non-flammable)	Solid-state offers better safety than liquid; organic is flammable	Solid-state or aqueous electrolytes offer enhanced safety

In supercapacitors, electrolytes facilitate the movement of ions between the electrodes during charging and discharging. The performance of a supercapacitor is highly dependent on the nature of the electrolyte, which impacts its specific capacitance, rate capability, and voltage range. Energy density is directly related to the voltage window ($E = \frac{1}{2} CV^2$). Organic (e.g., $TEABF_4$ in acetonitrile, propylene carbonate) and ionic liquid (e.g., $EMIMBF_4$) electrolytes provide higher energy densities due to their wider voltage windows compared to aqueous (e.g., KOH, H_2SO_4, Na_2SO) electrolytes. Aqueous electrolytes offer higher ionic conductivity, leading to faster ion movement and higher power density. Electrolytes' chemical stability and reactivity with electrode materials impact the cycle life. Aqueous electrolytes may cause electrode corrosion over time, while organic and ionic liquids typically offer better long-term stability [75].

In batteries, electrolytes enable the movement of ions between the cathode and anode during charge and discharge. The choice of electrolyte significantly influences the ionic conductivity, chemical stability, and electrochemical window, which in turn affect the battery's capacity, voltage, efficiency, and lifespan. The energy density of a battery depends on the capacity of the electrodes and the voltage window provided by the electrolyte. Liquid electrolytes (e.g., $LiPF_6$ in organic solvents like EC, DMC) in lithium-ion batteries offer high voltage ranges (3.6–4.2 V), enabling high energy density. Solid-state electrolytes (e.g., $Li_7La_3Zr_2O_{12}$, sulfide-based solid electrolytes) enhance battery safety by reducing risks related to leakage and flammability. Additionally, they provide better stability against dendrite formation, which is critical in lithium-based systems. Additionally, for safety and stability concerns, polymer electrolytes, such as PEO-based electrolytes, are fabricated for their flexibility, light weight, and wearability, as they are safer than liquid electrolytes. Electrolytes' chemical stability ensures minimal side reactions with electrodes, reducing capacity fading and improving cycling life. High-purity, stable electrolytes minimize self-discharge and internal resistance [75].

Supercapatteries combine the characteristics of both supercapacitors and batteries, and the choice of electrolyte has a profound impact on their hybrid performance. The electrolyte must balance high energy density (from battery-like faradaic processes) and high power density (from capacitor-like electrostatic processes). The electrolyte determines how well the supercapattery can balance energy density (from battery-like electrodes) and power density (from supercapacitor-like electrodes). Organic (e.g., $LiPF_6$ in organic solvents) and ionic liquid electrolytes offer higher energy density, but aqueous electrolytes provide superior power density due to faster ion transport. Electrolyte stability is critical for maintaining long-term cycle life in supercapatteries. Organic electrolytes offer better voltage stability, while aqueous electrolytes, though faster, may cause electrode corrosion over extended cycling. Ionic liquid electrolytes provide excellent stability but can suffer from poor rate capability [75].

10. Other Miscellaneous Electrochemical Studies and Applications

With the individual combination of cobalt oxide, PPy and PANI, there are a plethora of studies which state their application in energy-related fields such as electrocatalysis, photocatalytic degradation of dyes, sensing, and so on. A few of them are mentioned in Table 7.

Table 7. Miscellaneous combinations of cobalt oxide, PPy, and PANI for different electrochemical studies and their applications.

Composite	Cobalt as	Polymer	Material	Application	Ref.
Co–iron oxide/PANI (CFOP)	Co metal	PANI	Separator	Li-S batteries	[76]
PPN-CoO	CoO	PPy	Anode	Electrocatalytic water splitting	[77]
Co_3O_4/Ppy/MWCNT	Co_3O_4	PPy	Electrode	Electrocatalytic water splitting	[78]
ChGP/Co_3O_4	Co_3O_4	Chitosan, PANI	Nanocomposite	Photocatalytic dye degradation	[79]
Co_3O_4/PVA/PVP	Co_3O_4	Poly(vinyl alcohol), poly(vinyl pyrolidone)	Nanocomposite	Supercapacitor	[80]
$NiCo_2O_4$/PVA	CoO	Poly(vinyl alcohol)	Electrode	Supercapacitor	[81]
$LiCoO_2$ (MLCO)	CoO	Poly[N,N-bis(2-cryano-ethyl)-acrylamide]	Cathode	Li-ion batteries	[82]
[Co(tfbdc)(4,40-bpy)(H2O)2] Co-LCP	Co metal	Coordination polymer	Anode	Li-ion batteries	[83]
PDs-CoO	CoO	Polyethylene glycol diacid	Nanocomposite	Supercapacitor	[84]
Mg/SPE/Co_3O_4	Co_3O_4	Methyl cellulose	Electrolyte films	Batteries	[85]
Phosphene-PANI	-	PANI	Cathode	Zn-ion batteries	[72]
Co_3O_4/CoO/Co/C	Co_3O_4, CoO, Co metal	-	Electrode	Li-ion batteries, supercapacitors, and OER	[86]
rGO/Co_3O_4/Ag/ activated carbon	Co_3O_4	-	Anode	Supercapatteries	[87]
Co/C_2N	Cobalt oxide	C_2N network	Catalyst	HER	[88]

11. Current Challenges

Despite significant advancements in cobalt-oxide-based nanomaterials and their hybrids with conductive polymers for energy storage applications such as supercapacitors, batteries, and supercapatteries, several critical challenges remain. These challenges must be addressed to fully harness their potential in high-performance electrochemical devices.

Agglomeration and structural degradation

One of the foremost challenges faced by cobalt-oxide-based nanomaterials is the agglomeration of low-dimensional nanostructures. Agglomeration leads to a reduction in the active surface area, diminishing the number of available electrochemically active sites. Moreover, repeated charge-discharge cycles cause mechanical stress, leading to structural pulverization and cracks in the electrode materials. This degradation is a key factor in the rapid decay of performance in supercapacitors and batteries, particularly under long-term cycling.

Synthesis and material uniformity

While numerous synthesis methods for cobalt-oxide-based nanostructures have been developed, achieving reproducible, property-on-demand materials remains a major challenge. The trade-off between uniformity, size control, and large-scale production complicates the design of cobalt oxide nanomaterials with consistent electrochemical properties. This variability can lead to uneven electrochemical performance, making it difficult to optimize for large-scale practical applications.

Side reactions in electrochemical devices

Cobalt-oxide-based materials are prone to side reactions when used in electrochemical energy storage devices, which can negatively impact performance. In real-world systems,

factors such as electrode–electrolyte interactions, the stability of the electrolyte, and electrode degradation contribute to undesirable side reactions. These side reactions can lead to irreversible capacity loss and affect the overall efficiency of the system, particularly in the complex operating conditions of supercapacitors, batteries, and hybrid devices like supercapatteries.

Polymer degradation in hybrids

The integration of cobalt oxide with conductive polymers such as PANI or PPy has shown promise due to the enhanced redox reactions and conductivity these hybrids offer. However, one of the main issues with these polymer-based nanostructures is their mechanical degradation over extended cycling. Conductive polymers often suffer from volumetric expansion and contraction during the charge-discharge process, leading to cracks and a reduction in mechanical integrity. This degradation causes a loss in electrochemical performance, especially in long-term cycling, limiting the lifespan of energy storage devices.

Electrochemical pathways and reaction mechanisms

Although there have been significant efforts to understand the reaction mechanisms of cobalt oxide during ion storage and electrocatalysis, the exact pathways remain incompletely understood. Electrochemical reactions are complex, and multiple variables—such as the type of electrolyte, separator, and external environmental conditions—affect performance. Continued theoretical and experimental studies are required to uncover the detailed mechanisms governing these materials to improve their performance predictability and optimize their electrochemical behavior.

12. Future Outlook

Significant strides have been made in the development of cobalt oxide/conducting polymer nanocomposites for energy storage devices like supercapacitors, batteries, and supercapatteries. These materials demonstrate impressive electrochemical properties, including high capacitance, energy density, and conductivity. However, overcoming current limitations will lead to even broader practical applications. Future work is likely to focus on several key areas:

Deepening understanding of reaction mechanisms: Continued exploration of the fundamental electrochemical processes, especially the interaction between cobalt oxides and conducting polymers, will enhance the stability and efficiency of these materials. This includes studying ion transport, charge transfer, and the redox reactions that occur during cycling.

Advanced material design: The next phase of development will likely focus on the rational design of novel cobalt oxide/polymer hybrids. The integration of theoretical modeling and simulations will aid in predicting structure–property relationships, which is essential for optimizing the performance of these materials in energy storage systems. Simulations can guide the fabrication of hybrid structures with controlled porosity, particle size, and conductivity.

Enhancing durability and conductivity: The development of composites that incorporate reinforcing agents like carbon nanotubes, graphene, or metallic nanoparticles (e.g., silver) will address issues of mechanical degradation and enhance conductivity. Such hybrid materials could offer better cycling stability and prevent the volume expansion that often plagues cobalt oxide/polymer systems.

Innovative synthesis techniques: To facilitate large-scale commercialization, scalable and eco-friendly synthesis methods such as hydrothermal, electrochemical deposition, and sol-gel techniques will be further refined. These processes will enable the mass production of uniform cobalt oxide/polymer nanostructures with consistent electrochemical performance.

Integration with next-gen devices: The application of cobalt oxide/conducting polymer nanocomposites is poised to expand beyond traditional supercapacitors and batteries. With innovations in device architecture, such materials may play a key role in next-generation

energy storage systems, such as flexible and wearable electronics or hybrid supercapatteries that bridge the gap between capacitors and batteries.

Promising breakthrough: Minimizing side reactions and their mechanisms could enhance the electrochemical performance of the electrode material.

Overall, future research will be geared towards optimizing the stability, conductivity, and scalability of cobalt oxide/conducting polymer hybrids. As theoretical understanding grows and synthesis techniques improve, these materials are expected to become central to the advancement of high-performance energy storage technologies.

13. Critical Thinking Insights and Recommendations

As electrode material for supercapacitors, the combination of cobalt oxide's pseudocapacitive behavior with the high conductivity of PPy/PANI enhances energy storage, but challenges remain in optimizing cycling stability. For batteries, cobalt oxide's high theoretical capacity pairs well with PPy/PANI's flexibility, but side reactions and poor long-term stability need further investigation. For supercapatteries, the hybrid device benefits from cobalt oxide's energy density and PPy/PANI's fast charge transport, though achieving a balance between energy and power density is still a key challenge.

The critical analysis revealed that the focus should be on minimizing side reactions, enhancing cycling stability, and resolving conductivity challenges in cobalt oxide/PPy and cobalt oxide/PANI systems. The strength signifies that the cobalt oxide combined with PPy/PANI offers high energy and power densities with good flexibility, while the limitations include poor long-term stability, side reactions, and suboptimal performance at high rates.

Our unique perspective emphasizes the role of hybrid mechanisms in supercapatteries as a novel and underexplored area, offering insights into potential breakthroughs in energy density improvements. Furthermore, we recommend exploring advanced synthesis methods to improve interface stability and develop more robust electrolytes to mitigate side reactions.

14. Conclusions

In summary, cobalt-oxide-based nanocomposites, particularly those incorporating conducting polymers like polypyrrole (PPy) and polyaniline (PANI), hold great promise as high-performance electrode materials for supercapacitors, batteries, and supercapatteries. These materials benefit from the complementary properties of cobalt oxide's excellent capacitance and the conductive polymers' enhanced electron transport and pseudocapacitive behavior. Factors like morphology optimization, interfacial bonding, and controlled porosity significantly influence their performance in energy storage. While advances have been made, further exploration is needed, especially for battery applications, to unlock their full potential and ensure scalability for practical use in next-generation energy devices.

Author Contributions: Conceptualization, A.; methodology, A.; formal analysis, A., S.-S.P., M.N.A., and M.Y.; investigation, A.; resources, D.K.S.; writing—original draft preparation, A.; writing—review and editing, A., S.-S.P., and M.N.A.; visualization, A., M.N.A., and M.Y.; supervision, D.K.S. All authors have read and agreed to the published version of the manuscript.

Funding: This work was supported by the Technology Innovation Program (#20010170) funded by the Ministry of Trade, Industry and Energy (MOTIE), Republic of Korea.

Institutional Review Board Statement: Not applicable.

Data Availability Statement: No other data are available for this work.

Conflicts of Interest: The authors declare no conflicts of interest.

References

1. Shao, Y.; El-Kady, M.F.; Sun, J.; Li, Y.; Zhang, Q.; Zhu, M.; Wang, H.; Dunn, B.; Kaner, R.B. Design and Mechanisms of Asymmetric Supercapacitors. *Chem. Rev.* **2018**, *118*, 9233–9280. [CrossRef] [PubMed]

2. Kumar, N.; Kim, S.-B.; Lee, S.-Y.; Park, S.-J. Recent Advanced Supercapacitor: A Review of Storage Mechanisms, Electrode Materials, Modification, and Perspectives. *Nanomaterials* **2022**, *12*, 3708. [CrossRef] [PubMed]
3. Chatterjee, D.P.; Nandi, A.K. A Review on the Recent Advances in Hybrid Supercapacitors. *J. Mater. Chem. A* **2021**, *9*, 15880–15918. [CrossRef]
4. Njema, G.G.; Ouma, R.B.O.; Kibet, J.K. A Review on the Recent Advances in Battery Development and Energy Storage Technologies. *J. Renew. Energy* **2024**, *2024*, 2329261. [CrossRef]
5. Srivastava, R.; Bhardwaj, S.; Kumar, A.; Singhal, R.; Scanley, J.; Broadbridge, C.C.; Gupta, R.K. Waste Citrus Reticulata Assisted Preparation of Cobalt Oxide Nanoparticles for Supercapacitors. *Nanomaterials* **2022**, *12*, 4119. [CrossRef]
6. Nare, R.K.; Ramesh, S.; Basavi, P.K.; Kakani, V.; Bathula, C.; Yadav, H.M.; Dhanapal, P.B.; Kotanka, R.K.R.; Pasupuleti, V.R. Sonication-Supported Synthesis of Cobalt Oxide Assembled on an N-MWCNT Composite for Electrochemical Supercapacitors via Three-Electrode Configuration. *Sci. Rep.* **2022**, *12*, 1998. [CrossRef]
7. Ma, J.; Wei, H.; Liu, Y.; Ren, X.; Li, Y.; Wang, F.; Han, X.; Xu, E.; Cao, X.; Wang, G.; et al. Application of Co_3O_4-Based Materials in Electrocatalytic Hydrogen Evolution Reaction: A Review. *Int. J. Hydrogen Energy* **2020**, *45*, 21205–21220. [CrossRef]
8. Mei, J.; Liao, T.; Ayoko, G.A.; Bell, J.; Sun, Z. Cobalt Oxide-Based Nanoarchitectures for Electrochemical Energy Applications. *Prog. Mater. Sci.* **2019**, *103*, 596–677. [CrossRef]
9. Raimundo, R.A.; Silva, J.N.; Silva, T.R.; Araújo, A.J.M.; Oliveira, J.F.G.A.; de Lima, L.C.; Morales, M.A.; Soares, M.M.; Macedo, D.A. Green Chemistry Synthesis of Co_3O_4-CoO Nanocomposite and Electrochemical Assessment for Oxygen Evolution Reaction. *Mater. Lett.* **2023**, *341*, 134196. [CrossRef]
10. Laghari, A.J.; Aftab, U.; Shah, A.A.; Solangi, M.Y.; Abro, M.I.; Al-Saeedi, S.I.; Naeim, N.; Nafady, A.; Vigolo, B.; Emo, M.; et al. Surface Modification of Co_3O_4 Nanostructures Using Wide Range of Natural Compounds from Rotten Apple Juice for the Efficient Oxygen Evolution Reaction. *Int. J. Hydrogen Energy* **2023**, *48*, 15447–15459. [CrossRef]
11. Poonguzhali, R.V.; Kumar, E.R.; Srinivas, C.; Alshareef, M.; Aljohani, M.M.; Keshk, A.A.; El-Metwaly, N.M.; Arunadevi, N. Natural Lemon Extract Assisted Green Synthesis of Spinel Co_3O_4 Nanoparticles for LPG Gas Sensor Application. *Sens. Actuators B Chem.* **2023**, *377*, 133036. [CrossRef]
12. Edison, T.N.J.I.; Atchudan, R.; Sethuraman, M.G.; Lee, Y.R. Supercapacitor Performance of Carbon Supported Co_3O_4 Nanoparticles Synthesized Using Terminalia Chebula Fruit. *J. Taiwan Inst. Chem. Eng.* **2016**, *68*, 489–495. [CrossRef]
13. Bhatti, A.L.; Tahira, A.; Kumar, S.; Ujjan, Z.A.; Bhatti, M.A.; Kumar, S.; Aftab, U.; Karsy, A.; Nafady, A.; Infantes-Molina, A.; et al. Facile Synthesis of Efficient Co_3O_4 Nanostructures Using the Milky Sap of Calotropis Procera for Oxygen Evolution Reactions and Supercapacitor Applications. *RSC Adv.* **2023**, *13*, 17710–17726. [CrossRef] [PubMed]
14. Al Jahdaly, B.A.; Abu-Rayyan, A.; Taher, M.M.; Shoueir, K. Phytosynthesis of Co_3O_4Nanoparticles as the High Energy Storage Material of an Activated Carbon/Co_3O_4Symmetric Supercapacitor Device with Excellent Cyclic Stability Based on a Na_2SO_4Aqueous Electrolyte. *ACS Omega* **2022**, *7*, 23673–23684. [CrossRef]
15. Hsu, C.M.; Huang, Y.H.; Chen, H.J.; Lee, W.C.; Chiu, H.W.; Maity, J.P.; Chen, C.C.; Kuo, Y.H.; Chen, C.Y. Green Synthesis of Nano-Co_3O_4 by Microbial Induced Precipitation (MIP) Process Using Bacillus Pasteurii and Its Application as Supercapacitor. *Mater. Today Commun.* **2018**, *14*, 302–311. [CrossRef]
16. Shim, H.W.; Lim, A.H.; Kim, J.C.; Jang, E.; Seo, S.D.; Lee, G.H.; Kim, T.D.; Kim, D.W. Scalable One-Pot Bacteria-Templating Synthesis Route toward Hierarchical, Porous-Co_3O_4 Superstructures for Supercapacitor Electrodes. *Sci. Rep.* **2013**, *3*, 1–9. [CrossRef]
17. Pang, H.; Li, X.; Zhao, Q.; Xue, H.; Lai, W.-Y.; Hu, Z.; Huang, W. One-Pot Synthesis of Heterogeneous Co_3O_4-Nanocube/Co $(OH)_{2-}$ Nanosheet Hybrids for High-Performance Flexible Asymmetric All-Solid-State Supercapacitors. *Nano Energy* **2017**, *35*, 138–145. [CrossRef]
18. Gao, Z.; Song, N.; Li, X. Microstructural Design of Hybrid CoO@NiO and Graphene Nano-Architectures for Flexible High Performance Supercapacitors. *J. Mater. Chem. A* **2015**, *3*, 14833–14844. [CrossRef]
19. Zhou, S.; Ye, Z.; Hu, S.; Hao, C.; Wang, X.; Huang, C.; Wu, F. Designed Formation of Co_3O_4/$ZnCo_2O_4$/CuO Hollow Polyhedral Nanocages Derived from Zeolitic Imidazolate Framework-67 for High-Performance Supercapacitors. *Nanoscale* **2018**, *10*, 15771–15781. [CrossRef]
20. Liu, Y.; Cao, X.; Jiang, D.; Jia, D.; Liu, J. Hierarchical CuO Nanorod Arrays in Situ Generated on Three-Dimensional Copper Foam via Cyclic Voltammetry Oxidation for High-Performance Supercapacitors. *J. Mater. Chem. A* **2018**, *6*, 10474–10483. [CrossRef]
21. Moosavifard, S.E.; El-Kady, M.F.; Rahmanifar, M.S.; Kaner, R.B.; Mousavi, M.F. Designing 3D Highly Ordered Nanoporous CuO Electrodes for High-Performance Asymmetric Supercapacitors. *ACS Appl. Mater. Interfaces* **2015**, *7*, 4851–4860. [CrossRef] [PubMed]
22. Mishra, A.K.; Nayak, A.K.; Das, A.K.; Pradhan, D. Microwave-Assisted Solvothermal Synthesis of Cupric Oxide Nanostructures for High-Performance Supercapacitor. *J. Phys. Chem. C* **2018**, *122*, 11249–11261. [CrossRef]
23. Li, S.; Wang, Y.; Sun, J.; Xu, C.; Chen, H. Simple Preparation of Porous $FeCo_2O_4$ Microspheres and Nanosheets for Advanced Asymmetric Supercapacitors. *ACS Appl. Energy Mater.* **2020**, *3*, 11307–11317. [CrossRef]
24. Tian, H.; Lang, X.; Nan, H.; An, P.; Zhang, W.; Hu, X.; Zhang, J. Nanosheet-Assembled $LaMnO_3$@$NiCo_2O_4$ Nanoarchitecture Growth on Ni Foam for High Power Density Supercapacitors. *Electrochim. Acta* **2019**, *318*, 651–659. [CrossRef]
25. Goel, S.; Tomar, A.K.; Sharma, R.K.; Singh, G. Highly Pseudocapacitive NiO Nanoflakes through Surfactant-Free Facile Microwave-Assisted Route. *ACS Appl. Energy Mater.* **2018**, *1*, 1540–1548. [CrossRef]

26. Gu, Z.; Zhang, X. $NiCo_2O_4$@$MnMoO_4$ Core–Shell Flowers for High Performance Supercapacitors. *J. Mater. Chem. A* **2016**, *4*, 8249–8254. [CrossRef]
27. Pan, Y.; Gao, H.; Zhang, M.; Li, L.; Wang, G.; Shan, X. Three-Dimensional Porous $ZnCo_2O_4$ Sheet Array Coated with Ni $(OH)_2$ for High-Performance Asymmetric Supercapacitor. *J. Colloid Interface Sci.* **2017**, *497*, 50–56. [CrossRef]
28. Ali, S.; Sufyan Javed, M.; Umer, K.; Wang, J.; Fu, Y.; Kong, S.; Khan, S.; Ahmad, A.; Parkash, A.; Albaqami, M.D.; et al. MoS_2@$Ti_3C_2T_x$ Heterostructure: A New Negative Electrode Material for Li-Ion Hybrid Supercapacitors. *Chem. Eng. J.* **2024**, *498*, 155330. [CrossRef]
29. Azhar, S.; Al-Hawadi, J.S.; Annu; Ahmad, K.S.; Abrahams, I.; Lin, W.; Gupta, R.K.; Majid, S.; Abdel-Maksoud, M.A.; Malik, A. Sustainable Synthesis of Facile Bi_2O_3-Sb_2O_4-ZrO. Nanocomposite as Electrode Material for Energy Storage and Bifunctional Electrocatalyst for Energy Generation. *J. Energy Storage* **2024**, *98*, 113161. [CrossRef]
30. Bokhari, S.W.; Ellis, A.V.; Uceda, M.; Wei, S.; Pope, M.; Zhu, S.; Gao, W.; Sherrell, P.C. Nitrogen-Doped Reduced Graphene Oxide/MoS_2 'Nanoflower' Composites for High-Performance Supercapacitors. *J. Energy Storage* **2022**, *56*, 105935. [CrossRef]
31. Li, Z.; Gong, L. Research Progress on Applications of Polyaniline (PANI) for Electrochemical Energy Storage and Conversion. *Materials* **2020**, *13*, 548. [CrossRef] [PubMed]
32. Liu, Y.; Xie, L.; Zhang, W.; Dai, Z.; Wei, W.; Luo, S.; Chen, X.; Chen, W.; Rao, F.; Wang, L.; et al. Conjugated System of PEDOT: PSS-Induced Self-Doped PANI for Flexible Zinc-Ion Batteries with Enhanced Capacity and Cyclability. *ACS Appl. Mater. Interfaces* **2019**, *11*, 30943–30952. [CrossRef] [PubMed]
33. Elumalai, P.; Charles, J.; Senthil Kumar, P.; Uma Shankar, V. Fabrication of Ternary Polyaniline-Titanium Dioxide-Polypyrrole (PANI-TiO-PPy) Nanocomposite as an Efficient Polymer Electrode for Supercapacitors. *J. Appl. Polym. Sci.* **2023**, *140*, e54478. [CrossRef]
34. Naik, Y.V.; Kariduraganavar, M.; Srinivasa, H.T.; Siddagangaiah, P.B.; Naik, R. Influence of TiO_2 Nanoparticles during In-Situ Polymerization of TiO_2/PANI Nanocomposites and Its Supercapacitor Properties. *J. Energy Storage* **2024**, *97*, 112874. [CrossRef]
35. Yan, D.; Qin, L.; Fan, X.; Zhang, X.; Pang, S. Fabrication of RGO/Cobalt-Nickel Oxide/Polypyrrole Composites and Their Electrochemical Performance. *Optoelectron. Adv. Mater. Commun.* **2024**, *18*, 66–75.
36. Ishaq, S.; Moussa, M.; Kanwal, F.; Ayub, R.; Van, T.N.; Azhar, U.; Losic, D. One Step Strategy for Reduced Graphene Oxide/Cobalt-Iron Oxide/Polypyrrole Nanocomposite Preparation for High Performance Supercapacitor Electrodes. *Electrochim. Acta* **2022**, *427*, 140883. [CrossRef]
37. Zhou, C.; Zhang, Y.; Li, Y.; Liu, J. Construction of High-Capacitance 3D CoO@Polypyrrole Nanowire Array Electrode for Aqueous Asymmetric Supercapacitor. *Nano Lett.* **2013**, *13*, 2078–2085. [CrossRef]
38. Nayak, S.; Kittur, A.A.; Nayak, S. Green Synthesis of Silver-Zirconia Composite Using Chitosan Biopolymer Binder for Fabrication of Electrode Materials in Supercapattery Application for Sustainable Energy Storage. *Curr. Res. Green Sustain. Chem.* **2022**, *5*, 100292. [CrossRef]
39. Kuchena, S.F.; Wang, Y. Superior Polyaniline Cathode Material with Enhanced Capacity for Ammonium Ion Storage. *ACS Appl. Energy Mater.* **2020**, *3*, 11690–11698. [CrossRef]
40. Hai, Z.; Gao, L.; Zhang, Q.; Xu, H.; Cui, D.; Zhang, Z.; Tsoukalas, D.; Tang, J.; Yan, S.; Xue, C. Facile Synthesis of Core–Shell Structured PANI-Co_3O_4 Nanocomposites with Superior Electrochemical Performance in Supercapacitors. *Appl. Surf. Sci.* **2016**, *361*, 57–62. [CrossRef]
41. Namsheer, K.; Rout, C.S. Conducting Polymers: A Comprehensive Review on Recent Advances in Synthesis, Properties and Applications. *RSC Adv.* **2021**, *11*, 5659–5697. [CrossRef]
42. Wei, H.; He, C.; Liu, J.; Gu, H.; Wang, Y.; Yan, X.; Guo, J.; Ding, D.; Shen, N.Z.; Wang, X.; et al. Electropolymerized Polypyrrole Nanocomposites with Cobalt Oxide Coated on Carbon Paper for Electrochemical Energy Storage. *Polymer* **2015**, *67*, 192–199. [CrossRef]
43. Yang, C.; Chen, H.; Guan, C. Hybrid CoO Nanowires Coated with Uniform Polypyrrole Nanolayers for High-Performance Energy Storage Devices. *Nanomater* **2019**, *9*, 586. [CrossRef]
44. Ramesh, S.; Haldorai, Y.; Kim, H.S.; Kim, J.-H. A Nanocrystalline Co_3O_4@polypyrrole/MWCNT Hybrid Nanocomposite for High Performance Electrochemical Supercapacitors. *RSC Adv.* **2017**, *7*, 36833–36843. [CrossRef]
45. Ramesh, S.; Karuppasamy, K.; Haldorai, Y.; Sivasamy, A.; Kim, H.-S.; Kim, H.S. Hexagonal Nanostructured Cobalt Oxide @ Nitrogen Doped Multiwalled Carbon Nanotubes/Polypyyrole Composite for Supercapacitor and Electrochemical Glucose Sensor. *Colloids Surf. B Biointerfaces* **2021**, *205*, 111840. [CrossRef]
46. Wang, B.; He, X.; Li, H.; Liu, Q.; Wang, J.; Yu, L.; Yan, H.; Li, Z.; Wang, P. Optimizing the Charge Transfer Process by Designing Co_3O_4@PPy@MnO_2 Ternary Core–Shell Composite. *J. Mater. Chem. A* **2014**, *2*, 12968–12973. [CrossRef]
47. Hong, W.; Wang, J.; Li, Z.; Yang, S. Hierarchical Co_3O_4@Au-Decorated PPy Core/Shell Nanowire Arrays: An Efficient Integration of Active Materials for Energy Storage. *J. Mater. Chem. A* **2015**, *3*, 2535–2540. [CrossRef]
48. Han, L.; Tang, P.; Zhang, L. Hierarchical Co_3O_4@PPy@MnO_2 Core–Shell–Shell Nanowire Arrays for Enhanced Electrochemical Energy Storage. *Nano Energy* **2014**, *7*, 42–51. [CrossRef]
49. Kong, D.; Ren, W.; Cheng, C.; Wang, Y.; Huang, Z.; Yang, H.Y. Three-Dimensional $NiCo_2O_4$@Polypyrrole Coaxial Nanowire Arrays on Carbon Textiles for High-Performance Flexible Asymmetric Solid-State Supercapacitor. *ACS Appl. Mater. Interfaces* **2015**, *7*, 21334–21346. [CrossRef]

50. Abbas, Q.; Khurshid, H.; Yoosuf, R.; Lawrence, J.; Issa, B.A.; Abdelkareem, M.A.; Olabi, A.G. Engineering of Nickel, Cobalt Oxides and Nickel/Cobalt Binary Oxides by Electrodeposition and Application as Binder Free Electrodes in Supercapacitors. *Sci. Rep.* **2023**, *13*, 15654. [CrossRef]
51. Majeed, A.H.; Mohammed, L.A.; Hammoodi, O.G.; Sehgal, S.; Alheety, M.A.; Saxena, K.K.; Dadoosh, S.A.; Mohammed, I.K.; Jasim, M.M.; Salmaan, N.U. A Review on Polyaniline: Synthesis, Properties, Nanocomposites, and Electrochemical Applications. *Int. J. Polym. Sci.* **2022**, *2022*, 9047554. [CrossRef]
52. Xiang, Y.; Liu, Y.; Chen, K.; Tian, Q. Hierarchical Structure Assembled from In-Situ Carbon-Coated Porous Tin Dioxide Nanosheets towards High Lithium Storage. *J. Electroanal. Chem.* **2019**, *847*, 113204. [CrossRef]
53. Sahoo, S.; Dhakal, G.; Kim, W.K.; Lee, Y.R.; Shim, J.-J. Unidirectional Growth of Polyaniline on 3D CoO Nanowires for Aqueous Asymmetric Supercapacitors. *J. Energy Storage* **2023**, *73*, 109061. [CrossRef]
54. Pan, C.; Liu, Z.; Li, W.; Zhuang, Y.; Wang, Q.; Chen, S. $NiCo_2O_4$@Polyaniline Nanotubes Heterostructure Anchored on Carbon Textiles with Enhanced Electrochemical Performance for Supercapacitor Application. *J. Phys. Chem. C* **2019**, *123*, 25549–25558. [CrossRef]
55. Jabeen, N.; Xia, Q.; Yang, M.; Xia, H. Unique Core–Shell Nanorod Arrays with Polyaniline Deposited into Mesoporous $NiCo_2O_4$ Support for High-Performance Supercapacitor Electrodes. *ACS Appl. Mater. Interfaces* **2016**, *8*, 6093–6100. [CrossRef]
56. Chhetri, K.; Tiwari, A.P.; Dahal, B.; Ojha, G.P.; Mukhiya, T.; Lee, M.; Kim, T.; Chae, S.-H.; Muthurasu, A.; Kim, H.Y. A ZIF-8-Derived Nanoporous Carbon Nanocomposite Wrapped with Co_3O_4-Polyaniline as an Efficient Electrode Material for an Asymmetric Supercapacitor. *J. Electroanal. Chem.* **2020**, *856*, 113670. [CrossRef]
57. Ren, X.; Fan, H.; Ma, J.; Wang, C.; Zhang, M.; Zhao, N. Hierarchical Co_3O_4/PANI Hollow Nanocages: Synthesis and Application for Electrode Materials of Supercapacitors. *Appl. Surf. Sci.* **2018**, *441*, 194–203. [CrossRef]
58. Rajkumar, S.; Elanthamilan, E.; Princy Merlin, J.; Sathiyan, A. Enhanced Electrochemical Behaviour of $FeCo_2O_4$/PANI Electrode Material for Supercapacitors. *J. Alloys Compd.* **2021**, *874*, 159876. [CrossRef]
59. Vellakkat, M.; Hundekkal, D. Chitosan Mediated Synthesis of Core/Double Shell Ternary Polyaniline/Chitosan/Cobalt Oxide Nano Composite-as High Energy Storage Electrode Material in Supercapacitors. *Mater. Res. Express* **2016**, *3*, 15502. [CrossRef]
60. Wang, H.; Guo, Z.; Yao, S.; Li, Z.; Zhang, W. Design and Synthesis of Ternary Graphene/Polyaniline/Co_3O_4 Hierarchical Nanocomposites for Supercapacitors. *Int. J. Electrochem. Sci.* **2017**, *12*, 3721–3731. [CrossRef]
61. Xu, H.; Wu, J.; Li, C.; Zhang, J.; Wang, X. Investigation of Polyaniline Films Doped with Co_{2+} as the Electrode Material for Electrochemical Supercapacitors. *Ionics* **2015**, *21*, 1163–1170. [CrossRef]
62. Lin, H.; Huang, Q.; Wang, J.; Jiang, J.; Liu, F.; Chen, Y.; Wang, C.; Lu, D.; Han, S. Self-Assembled Graphene/Polyaniline/Co_3O_4 Ternary Hybrid Aerogels for Supercapacitors. *Electrochim. Acta* **2016**, *191*, 444–451. [CrossRef]
63. Belardja, M.S.; Dahou, F.Z.; Djelad, H.; Benyoucef, A. Adsorption and Supercapacitor Applications of CoO-Zeolite Decorated Conducting Polymer Nanocomposite. *Int. J. Environ. Anal. Chem.* **2014**, 1–14. [CrossRef]
64. Sandya, C.P.; Rishad Baig, E.; Pillai, S.; Molji, C.; Aravind, A.; Devaki, S.J. Polyaniline-Cobalt Oxide Nano Shrubs Based Electrodes for Supercapacitors with Enhanced Electrochemical Performance. *Electrochim. Acta* **2019**, *324*, 134876.
65. Blinova, N.V.; Stejskal, J.; Trchová, M.; Prokeš, J.; Omastová, M. Polyaniline and Polypyrrole: A Comparative Study of the Preparation. *Eur. Polym. J.* **2007**, *43*, 2331–2341. [CrossRef]
66. Zhang, X.X.; Xie, Q.S.; Yue, G.H.; Zhang, Y.; Zhang, X.Q.; Lu, A.L.; Peng, D.L. A Novel Hierarchical Network-like Co_3O_4 Anode Material for Lithium Batteries. *Electrochim. Acta* **2013**, *111*, 746–754. [CrossRef]
67. Liang, X.; Gao, G.; Jiang, X.; Zhang, W.; Bi, W.; Wang, J.; Du, Y.; Wu, G. Preparation of Hydrophobic PPy Coated V_2O_5 Yolk–Shell Nanospheres-Based Cathode Materials with Excellent Cycling Performance. *ACS Appl. Energy Mater.* **2020**, *3*, 2791–2802. [CrossRef]
68. Guo, B.; Kong, Q.; Zhu, Y.; Mao, Y.; Wang, Z.; Wan, M.; Chen, L. Electrochemically Fabricated Polypyrrole–Cobalt–Oxygen Coordination Complex as High-Performance Lithium-Storage Materials. *Chem. A Eur. J.* **2011**, *17*, 14878–14884. [CrossRef]
69. Liu, L.; Hou, Y.; Wang, J.; Chen, J.; Liu, H.-K.; Wu, Y.; Wang, J. Nanofibrous Co_3O_4/PPy Hybrid with Synergistic Effect as Bifunctional Catalyst for Lithium-Oxygen Batteries. *Adv. Mater. Interfaces* **2016**, *3*, 1600030. [CrossRef]
70. Xiao, C.-Y.; Kubendhiran, S.; Wang, G.-B.; Kongvarhodom, C.; Chen, H.-M.; Yougbaré, S.; Saukani, M.; Wu, Y.-F.; Lin, L.-Y. Innovative Design of Dual Functional Polypyrrole-Coated Zinc Cobalt Sulfide Nanosheets on Carbon Cloth as a Binder-Free Anode of Sodium-Ion Batteries. *J. Energy Storage* **2024**, *91*, 112012. [CrossRef]
71. Iqbal, J.; Numan, A.; Omaish Ansari, M.; Jafer, R.; Jagadish, P.R.; Bashir, S.; Hasan, P.M.Z.; Bilgrami, A.L.; Mohamad, S.; Ramesh, K.; et al. Cobalt Oxide Nanograins and Silver Nanoparticles Decorated Fibrous Polyaniline Nanocomposite as Battery-Type Electrode for High Performance Supercapattery. *Polymers* **2020**, *12*, 2816. [CrossRef] [PubMed]
72. Gao, X.; Shi, T.; Zu, L.; Lian, H.; Cui, X.; Wang, X. Highly Stable Polyaniline-Based Cathode Material Enabled by Phosphorene for Zinc-Ion Batteries with Superior Specific Capacity and Cycle Life. *ACS Appl. Mater. Interfaces* **2024**, *16*, 24781–24795. [CrossRef] [PubMed]
73. Qi, M.; Xie, D.; Zhong, Y.; Chen, M.; Xia, X. Smart Construction of Polyaniline Shell on Cobalt Oxides as Integrated Core-Shell Arrays for Enhanced Lithium Ion Batteries. *Electrochim. Acta* **2017**, *247*, 701–707. [CrossRef]
74. Gu, L.-L.; Wang, C.; Qiu, S.-Y.; Wang, K.-X.; Gao, X.-T.; Zuo, P.-J.; Sun, K.-N.; Zhu, X.-D. Cobalt-Iron Oxide Nanotubes Decorated with Polyaniline as Advanced Cathode Hosts for Li-S Batteries. *Electrochim. Acta* **2021**, *390*, 138873. [CrossRef]

75. Pal, B.; Yang, S.; Ramesh, S.; Thangadurai, V.; Jose, R. Electrolyte Selection for Supercapacitive Devices: A Critical Review. *Nanoscale Adv.* **2019**, *1*, 3807–3835. [CrossRef]
76. Li, Z.; Cong, Y.; Zhao, J.; Su, H.; Shang, Y.; Liu, H. Polyaniline-Coated Cobalt–Iron Oxide Composites Modified Separator for High Performance Lithium–Sulfur Batteries. *ACS Appl. Electron. Mater.* **2024**, *6*, 3780–3789. [CrossRef]
77. Morales, D.V.; Astudillo, C.N.; Anastasoaie, V.; Dautreppe, B.; Urbano, B.F.; Rivas, B.L.; Gondran, C.; Aldakov, D.; Chovelon, B.; André, D.; et al. A Cobalt Oxide–Polypyrrole Nanocomposite as an Efficient and Stable Electrode Material for Electrocatalytic Water Oxidation. *Sustain. Energy Fuels* **2021**, *5*, 4710–4723. [CrossRef]
78. Jayaseelan, S.S.; Bhuvanendran, N.; Xu, Q.; Su, H. Co_3O_4 Nanoparticles Decorated Polypyrrole/Carbon Nanocomposite as Efficient Bi-Functional Electrocatalyst for Electrochemical Water Splitting. *Int. J. Hydrogen Energy* **2020**, *45*, 4587–4595. [CrossRef]
79. Shahabuddin, S.; Sarih, N.M.; Ismail, F.H.; Shahid, M.M.; Huang, N.M. Synthesis of Chitosan Grafted-Polyaniline/Co_3O_4 Nanocube Nanocomposites and Their Photocatalytic Activity toward Methylene Blue Dye Degradation. *RSC Adv.* **2015**, *5*, 83857–83867. [CrossRef]
80. Muthumari, P.; Siva, V.; Murugan, A.; Shameem, A.; Bahadur, S.A.; Thangarasu, S. Hydrothermally Synthesized Cobalt Oxide Embedded Polymer Nanocomposites as Efficient Electrode Material for Asymmetric Supercapacitors. *J. Mater. Sci. Mater. Electron.* **2023**, *34*, 1491. [CrossRef]
81. Siwatch, P.; Sharma, K.; Manyani, N.; Kang, J.; Tripathi, S.K. Characterization of Nanostructured Nickel Cobalt Oxide-Polyvinyl Alcohol Composite Films for Supercapacitor Application. *J. Alloys Compd.* **2021**, *872*, 159409. [CrossRef]
82. Yang, Z.; Li, R.; Deng, Z. A Deep Study of the Protection of Lithium Cobalt Oxide with Polymer Surface Modification at 4.5 V High Voltage. *Sci. Rep.* **2018**, *8*, 863. [CrossRef] [PubMed]
83. Shi, C.; Xia, Q.; Xue, X.; Liu, Q.; Liu, H.-J. Synthesis of Cobalt-Based Layered Coordination Polymer Nanosheets and Their Application in Lithium-Ion Batteries as Anode Materials. *RSC Adv.* **2016**, *6*, 4442–4447. [CrossRef]
84. Alimola, F.; Arsalani, N.; Ahadzadeh, I. Facile Fabrication of a New Nanocomposite Based on Cobalt Oxide and a New Polymer Dots Derived from Polyethylene Glycol Diacid as a High Performance, Ultra-Stable Symmetric Supercapacitor. *Electrochim. Acta* **2022**, *417*, 140283. [CrossRef]
85. Jayalakshmi, K.; Ismayil; Hegde, S.; Sanjeev, G.; Murari, M.S. Improving Electrolyte Performance: Nanocomposite Solid Polymer Electrolyte Films with Cobalt Oxide Nanoparticles. *Polym. Compos.* **2024**, *45*, 137–150. [CrossRef]
86. Xu, D.; Mu, C.; Xiang, J.; Wen, F.; Su, C.; Hao, C.; Hu, W.; Tang, Y.; Liu, Z. Carbon-Encapsulated Co_3O_4@CoO@Co Nanocomposites for Multifunctional Applications in Enhanced Long-Life Lithium Storage, Supercapacitor and Oxygen Evolution Reaction. *Electrochim. Acta* **2016**, *220*, 322–330. [CrossRef]
87. Iqbal, J.; Numan, A.; Jafer, R.; Bashir, S.; Jilani, A.; Mohammad, S.; Khalid, M.; Ramesh, K.; Ramesh, S. Ternary Nanocomposite of Cobalt Oxide Nanograins and Silver Nanoparticles Grown on Reduced Graphene Oxide Conducting Platform for High-Performance Supercapattery Electrode Material. *J. Alloys Compd.* **2020**, *821*, 153452. [CrossRef]
88. Mahmood, J.; Jung, S.-M.; Kim, S.-J.; Park, J.; Yoo, J.-W.; Baek, J.-B. Cobalt Oxide Encapsulated in C2N-H2D Network Polymer as a Catalyst for Hydrogen Evolution. *Chem. Mater.* **2015**, *27*, 4860–4864. [CrossRef]

polymers

MDPI

Article

Synthesis of Cellulose Acetate Butyrate Microspheres as Precursor for Hard Carbon-Based Electrodes in Symmetric Supercapacitors

Johanna Fischer [1,2,*], Katrin Thümmler [1], Igor Zlotnikov [3], Daria Mikhailova [2] and Steffen Fischer [1,*]

[1] Institute of Plant and Wood Chemistry, TUD Dresden University of Technology, Pienner Str. 19, 01737 Tharandt, Germany; katrin.thuemmler@tu-dresden.de
[2] Leibniz Institute for Solid State and Material Research (IFW) Dresden e.V., Institute for Materials Chemistry (IMC), Helmholtzstraße 20, 01069 Dresden, Germany; d.mikhailova@ifw-dresden.de
[3] B CUBE—Center for Molecular Bioengineering, TUD Dresden University of Technology, Tatzberg 41, 01307 Dresden, Germany; igor.zlotnikov@tu-dresden.de
* Correspondence: johanna.fischer1@tu-dresden.de (J.F.); steffen.fischer@tu-dresden.de (S.F.)

Abstract: Cellulose microspheres have a wide range of applications due to their unique properties and versatility. Various preparation methods have been explored to tailor these microspheres for specific applications. Among these methods, the acetate method using cellulose acetate is well known. However, replacement of the acetate group through the butyrate group significantly extends the variety of morphological properties. In the present work, microspheres based on cellulose acetate butyrate are being developed with modified characteristics in terms of particle size, porosity, surface morphology and the inner structure of the microspheres. While the inner structure of cellulose acetate microspheres is predominantly porous, microspheres prepared from cellulose acetate butyrate are mainly filled or contain several smaller microspheres. Carbon materials from cellulose acetate butyrate microspheres exhibit a high specific surface area of 567 m^2 g^{-1}, even without further activation. Activation processes can further increase the specific surface area, accompanied by an adaptation of the pore structure. The prepared carbons show promising results in symmetrical supercapacitors with aqueous 6 M KOH electrolytes. Activated carbons derived from cellulose acetate butyrate microspheres demonstrate an energy density of 12 Wh kg^{-1} at a power density of 0.9 kW kg^{-1}.

Keywords: cellulose microspheres; cellulose acetate butyrate; activated carbons; electrochemical energy storage

1. Introduction

For the preparation of cellulose-based microspheres, a variety of preparation methods are known, resulting in a wide range of particle sizes from 1 µm to 3 mm. In this work, the acetate method [1,2] is used to obtain homogeneous particles with a particle size less than 5 µm and a very narrow particle size distribution. The cellulose microspheres have high and controllable porosity in combination with high mechanical strength and chemical reactivity. Further, they possess a good hydrophilicity and are insoluble in most organic solvents. The many possibilities for functionalisation allow an optimal adaption of the spherical particles to the respective application [3–5].

Cellulose microspheres can be used in a wide range of applications, from pharmacy to chromatography and water purification. In the pharmaceutical sector, the beads function as adsorbents in extracorporeal blood purification or for the controlled release of active ingredients [3,6–9]. For the purification of water, functionalised beads are used to adsorb metals from aqueous solutions [3,4,7,8]. Commercially available cellulose microspheres such as Cellufine® with a particle size of 40–130 µm, or Cytopore™ with a particle size of

200–280 µm, are used for chromatography or in suspension culture systems to support cell growth, respectively [10,11].

The two cellulose esters used in this work, cellulose-2.5-acetate and cellulose acetate butyrate, differ primarily in terms of their substituents (Figure 1). The properties of cellulose esters are significantly influenced by the type of substituent, the degree of substitution and the distribution of the functional groups along the chain [12].

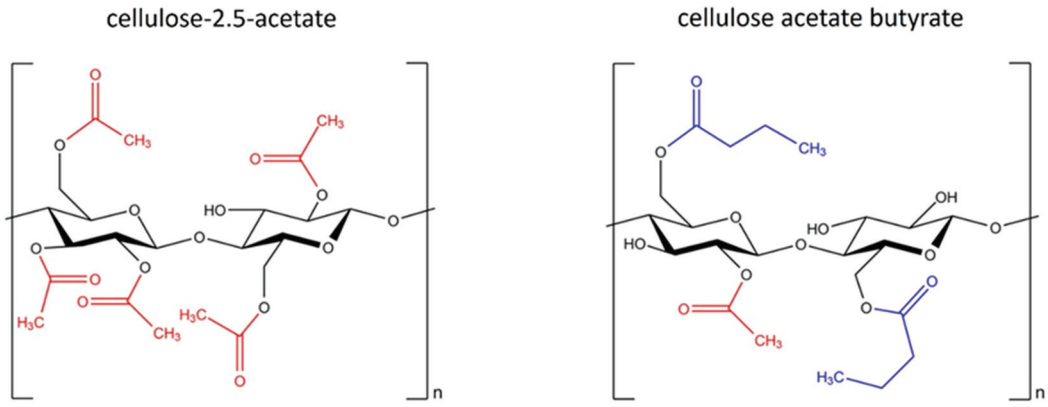

Figure 1. Structural formula of cellulose-2.5-acetate and cellulose acetate butyrate.

Cellulose acetate butyrate (CAB) is currently used mainly either in the pharmaceutical sector for the encapsulation of active ingredients such as repaglinide or ketoprofen, or as a coating material. CAB is the most commonly used cellulose ester for encapsulation due to its high UV stability, good film forming properties and good tolerability. They are usually prepared by the emulsion–solvent evaporation method, which results in particle sizes in the range of 100 to 600 µm, depending on the active ingredient contained. Another method to obtain more homogeneous and smaller particles < 10 µm is spray drying [13–16].

In this work, microspheres with cellulose acetate butyrate or a mixture of cellulose acetate and cellulose acetate butyrate using the acetate method are prepared in order to obtain relatively homogeneous microspheres with a particle size < 5 µm. We have investigated how the physical characteristics as morphology, particle size, porosity and thermal behaviour can be varied with the use of cellulose acetate butyrate. In addition, the first orientation studies on the inner structure of the microspheres are performed.

Electrochemical energy storage systems are very important for the reliable availability of electrical energy. In the past years, electrochemical capacitors, also known as supercapacitors, have come into research focus. Supercapacitors offer extremely high power densities combined with short charging and discharging processes in the range of seconds, and a long cycle life [17–19]. Due to their high power density and the fast available energy, supercapacitors are mainly used for uninterruptible power supplies as well as in fire and emergency systems or for regenerative braking [18,20]. Supercapacitors can be divided into two categories, electrical double layer capacitors (EDLC) and pseudocapacitors, which differ in the type of energy storage mechanisms. The choice of the electrode material depends mainly on the type of storage mechanism. For the EDLCs, activated carbons with a high specific surface area are the most commonly used electrode materials. A variety of carbonaceous precursor materials can be used to prepare activated carbons. Thereby, the demand for more sustainable materials is constantly increasing [19,21]. Also, carbon doping with various heteroatoms such as phosphorous, nitrogen or oxygen is investigated to improve the electrochemical performance through functional groups on the surface of carbons [22].

Our previous works have shown that carbons derived from cellulose acetate microspheres are promising as electrode materials in symmetrical supercapacitors with aqueous electrolytes [23,24] and as anode materials in Li-Ion batteries [25]. In this work, carbons from the prepared cellulose acetate butyrate microspheres were also tested as electrode

materials in supercapacitors. It is assumed that the advantages over cellulose acetate microspheres are due to the modified surface functionality, the higher carbon amount and the changed morphology of the microspheres. The relationship between the properties and the structure of the microspheres and the properties of the resulting carbons was investigated.

2. Materials and Methods

2.1. Preparation of Cellulose Acetate Butyrate Microspheres

First, solutions of cellulose acetate and cellulose acetate butyrate as well as methylcellulose (Methocel, viscosity 1200–1800 mPas) as protective colloid were prepared in order to produce microspheres by the acetate process [1]. Both cellulose-2.5-acetate (Aceplast, Acetati SpA, Verbania, Italy) and cellulose acetate butyrate (Sigma Aldrich, St. Louis, MO, USA, 180963) were dissolved in ethyl acetate and methanol under stirring, while methylcellulose was dissolved in water. For the preparation, different ratios of cellulose acetate (CA) and cellulose acetate butyrate (CAB) solutions were mixed. The microspheres are labelled with the amount of CAB used, e.g., the microspheres made entirely of CAB are named CAB100, while the mixed product of 25% CA and 75% CAB solution is named as CAB75. The dissolved methylcellulose was mixed with salt (sodium acetate trihydrate, Roth) and surfactant (Triton X-100, Sigma Aldrich), and afterwards the CA/CAB solution was added. In order to form microspheres, the emulsion was dispersed by an inline Turrax, and the solvents were evaporated. This process, schematically depicted in Figure 2, is a further development of the acetate process elaborated by Thümmler et al. [2]. The samples were washed several times by centrifugation and resuspension in water. For further characterisation and carbonisation steps the samples were freeze-dried.

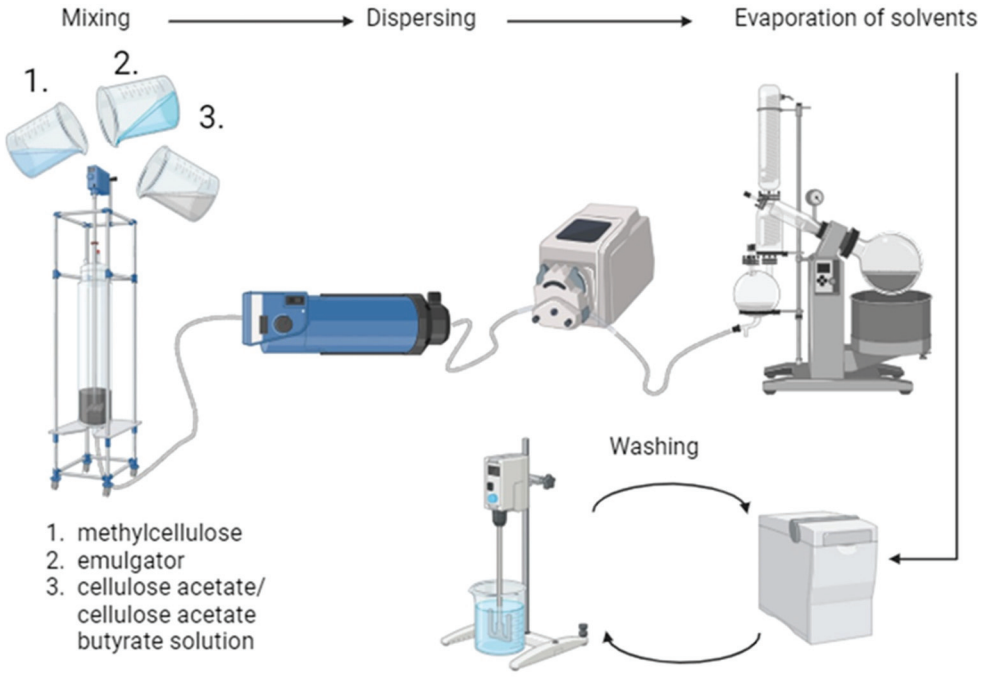

Figure 2. Schematic illustration of the preparation process of cellulose acetate (butyrate) microspheres. Created with BioRender.com.

2.2. Carbonisation and Activation

The prepared microspheres were carbonised for 2 h at 800 °C with a heating rate of 300 K h^{-1} in an argon atmosphere (argon flow with 0.2 L min^{-1}). For CAB100, an activation step with potassium hydroxide was performed. The precursor material was mixed with a KOH solution with a cellulose/KOH mass ratio of 1:1. The suspension was dried at 80 °C for 24 h and afterwards carbonised at 800 °C as described above for the carbonisation process. Afterwards, the activated carbon was washed with distilled water.

2.3. Materials Characterisation

The particle size distributions of the microspheres were measured using a Mastersizer 3000 laser diffraction particle analyser (Malvern), and the data were analysed using the Mie model [26]. Raman measurements to characterise the microspheres were performed using a MultiRam (Bruker Optik GmbH, Ettlingen, Germany) with a laser power of 100 mW and a wavelength of 1064 nm. To investigate the morphology, SEM images of the microspheres were recorded with a FEI Quanta FEG 650 microscope at an accelerating voltage of 5 kV using a SE detector. FIB/SEM measurements were carried out at a Scios LoVac Dual Beam FIB/SEM (FEI/ThermoFisher, Waltham, MA, USA) device at an acceleration voltage of 5 kV. The porosity of the beads was determined by investigations on the sedimentation volume and the packing density using a Universal 320 R centrifuge (Hettich, Kirchlengern, Germany). Further, the carbon and nitrogen contents were determined by a Vario EL III (Elementar, Langenselbold, Germany) in accordance with DIN 51721 [27] and the thermal behaviour of the particles was investigated using an STA 449 F5 Jupiter (Netzsch, Selb, Germany) analysing system under Ar atmosphere with a heating rate of 5 K min^{-1} up to 1200 °C.

The specific surface area, pore size distribution and pore volume of precursors and carbons were determined by nitrogen physisorption experiments using a Quadrasorb SI (Quantachrome Instruments,) at 77 K. Prior to the measurements, the samples were outgassed in a FloVac degasser for 24 h in a dynamic vacuum at 70 °C and 150 °C for cellulosic materials (about 200 mg) and carbons (about 25 mg), respectively. The specific surface area was calculated using the Brunauer-Emmett-Teller (BET) method at relative pressures of p/p_0 = 0.1–0.3 [28]. The t-plot method was used to calculate the micropore surface area [29]. The total pore volumes were calculated using the Gurvich rule at a relative pressure of p/p_0 = 0.9, while the pore size distribution was evaluated using the quenched solid density functional theory (QSDFT) for slit and cylindrical pores of carbons [30–32]. For the calculations, the software Quadrawin 5.11 (Quantachrome Instruments) was used. Furthermore, the graphitic and disordered parts of the carbons were investigated using a DXR SmartRaman (Thermo Scientific) spectrometer with a wavelength of 532 nm and a laser power of 9 mW; the spectra were analysed using Lorentzian fitting models. SEM images of the carbons were recorded using an LEO Gemini 1530 (Zeiss, Jena, Germany) at an accelerating voltage of 20 kV. An SE2 detector was used. Powder X-ray diffraction (XRD) experiments were carried out in transmission mode on a STOE STADI P powder diffractometer with a curved Ge(111) crystal monochromator using a Dectris 1 K detector. The samples were tested with Cu $K\alpha_1$ radiation of 1.54056 Å wavelength, a scan range of $5° < 2\theta < 100°$, and a step size of $\Delta 2\theta = 0.01°$. For the preparation, powder samples were glued as a thin layer between acetate films. X-ray photoelectron spectroscopy (XPS) measurements were performed using a PHI 5600 CI (Physical Electronics, Chanhassen, MN, USA) spectrometer. A non-monochromated Al Kα radiation (200 W) was used at a pass energy of 29.35 eV.

2.4. Electrochemical Measurements

The electrodes for the electrochemical measurements were prepared from a mixture of 95% carbon material and 5% binder solution (PVDF in acetone) and homogenised in an ultrasonic bath. The electrode mass was then dropped onto steel current collectors with a diameter of 12 mm, the mass loading per electrode was about 5 mg. A symmetrical two-electrode configuration in Swagelok cells was used. Whatman glass fibre was used as a separator between the electrodes, and 250 µL of 6 M KOH solution was used as the electrolyte. The measurements were carried out at 25 °C in a climatic chamber using a multichannel potentiostat from BioLogic. Cells were tested by cyclic voltammetry (CV) at scan rates ranging from 2 to 500 mV s^{-1} and by galvanostatic cycling with potential limitations at current rates ranging from 1 to 10 A g^{-1}. The potential window for measurements was fixed between 0 and 0.8 V.

The specific capacitances (C_{spec}) for the electrodes of the supercapacitor were calculated as follows (1):

$$C_{spec} = \frac{I_{spec}}{\frac{\Delta U}{\Delta t}} \quad (1)$$

I_{spec} (A g^{-1}) is the applied current per mass, and $\Delta U/\Delta t$ is the slope of the galvanostatic discharge curve, excluding the iR drop. The energy (E, Wh kg^{-1}) and power (P, W kg^{-1}) densities were calculated using Equations (2) and (3):

$$\text{Energy density}: \ E = 0.5 \times C_{spec} * U2 \quad (2)$$

$$\text{Power density}: \ P = \frac{E}{\Delta t} \quad (3)$$

3. Results

3.1. Cellulose Acetate Butyrate Microspheres

Figure 3a shows Raman spectra of the microspheres prepared with different amounts of CAB for characteristic bands of cellulose acetate and cellulose acetate butyrate. The complete Raman spectra of the microspheres with different CAB amounts as well as the Raman spectra of the raw materials CA2.5 and CAB powder, for comparison, are shown in Figure S1, Supplementary Material.

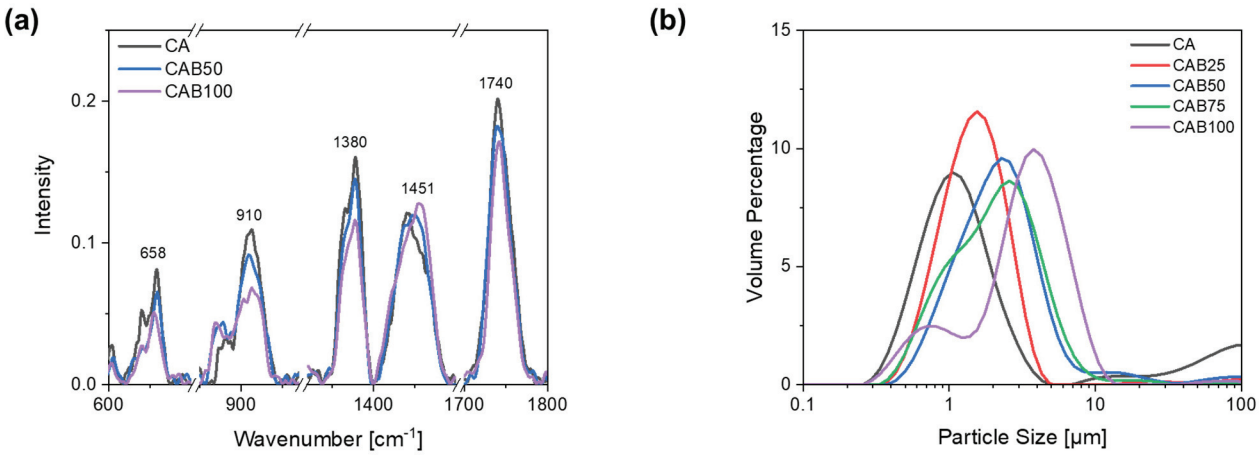

Figure 3. (**a**) Raman spectra for characteristic bands and (**b**) particle size distribution of microspheres with different amounts of CAB.

All materials have a strong band at a wavenumber of 1740 cm^{-1}, which is typical for esters and is caused by C=O stretching vibrations of the acetyl group. The band at 1380 cm^{-1} is also present in all prepared materials as well as in the raw material, which can be attributed to various deformation vibrations of the cellulose structure as δ(CH2), δ(HCC), δ(HCO), δ(COH). Other bands, which are caused by signals from the cellulose backbone, are in the range of 1200–1000 cm^{-1}. The band at a wavenumber of 658 cm^{-1} indicates signals from the acetyl group, in particular deformation vibrations of the C=O bonds in ester groups. Cellulose acetate has a characteristic band at 1437 cm^{-1}, which can be attributed to deformation vibrations of the CH_3 group. In contrast, cellulose acetate butyrate has a characteristic band at 1451 cm^{-1}, which is assigned to the amorphous phase. In addition, another typical band is seen for cellulose acetate butyrate at 866 cm^{-1}, caused by deformation vibrations of the C-O-O-H and O-C-O bonds in the molecular plane [33–36].

With the Raman spectra we confirmed that the prepared microspheres contain cellulose acetate butyrate, depending on the amount. The two bands at a wavenumber of 866 cm^{-1} and 1451 cm^{-1}, which are typical for cellulose acetate butyrate, show a clear differentiation

to the cellulose acetate microspheres. The band at 1451 cm^{-1} is slightly shifted depending on the CAB amount of the microspheres. In contrast, the band at 1740 cm^{-1}, which is caused by C=O stretching vibrations of the acetyl group, decreases with an increasing amount of CAB. The intensity of the bands typical for cellulose (1380, 1200–1000, 910, 658 cm^{-1}) also decreases with a higher amount of CAB in the microspheres.

For the CA microspheres, it is known from other studies that it is possible to obtain particle sizes below 5 µm with a narrow particle size distribution [2,23]. As the amount of cellulose acetate butyrate in the microspheres increases, the particle size rises and the particle size distribution becomes wider, as shown in Figure 3b. The particles with 0% CAB (CA) have a median d_{50} value of 1.3 µm, whereas those with 50% and 100% CAB have values of 2.2 µm and 3.4 µm, respectively. The particle size distribution for the microspheres containing 75% CAB shows a shoulder at about 1 µm, indicating the beginning of particle segregation. When the amount of CAB is further increased to 100%, two fractions of different particle sizes are recognisable. There are very small particles with an average diameter of 0.8 µm and larger particles with an average diameter of 4.2 µm.

The different particle sizes as well as the morphology of the microspheres and their surface structure were investigated by scanning electron microscopy, shown in Figure 4. The CA microspheres without CAB are relatively homogeneous in terms of particle size and structure, in agreement with other studies [2,23]. The microspheres have a netlike structure at the surface and appear to be highly porous. By adding CAB solution in the preparation process of the microspheres, the particle sizes become larger and the distribution in the particle size significantly wider, in accordance with the particle size measurements. In addition, the two fractions of different particle sizes for CAB100 with the very small and large particles are depicted.

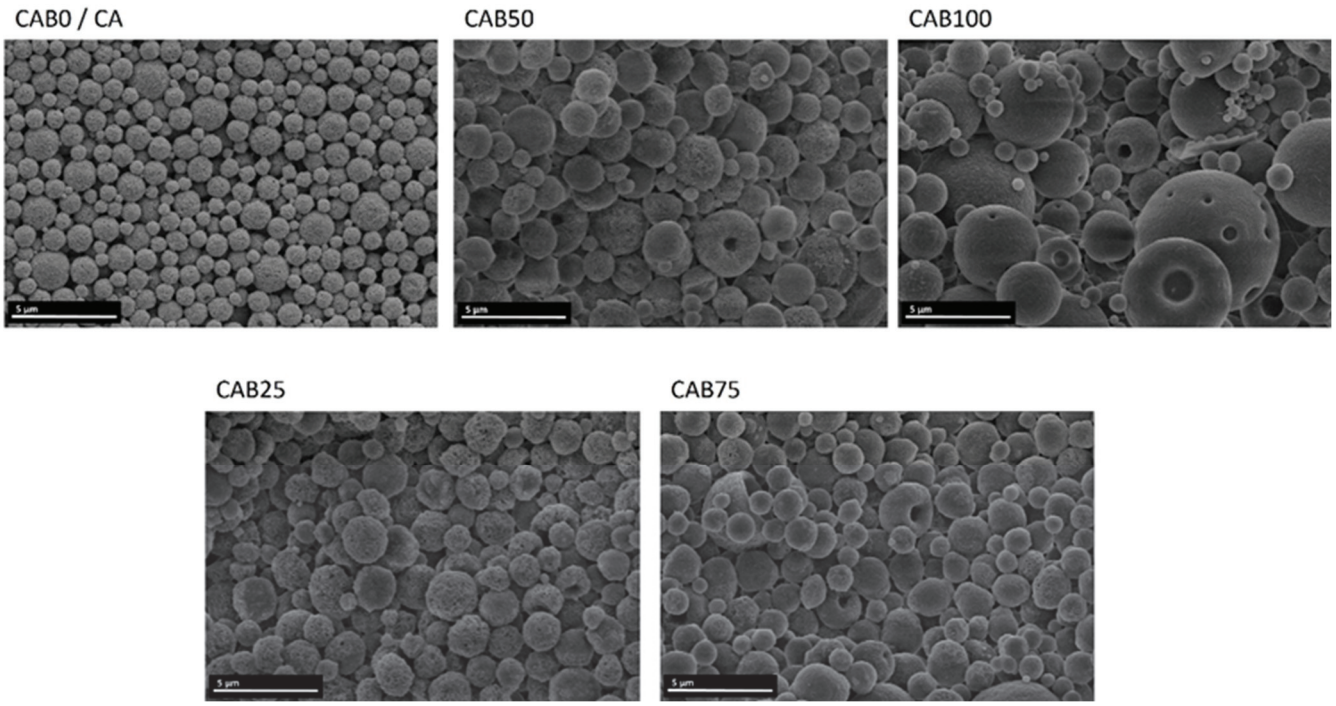

Figure 4. SEM images of the microspheres with various CAB amounts.

The SEM images of the particles with different amounts of CAB show that for all amounts spherical particles are created, but the structure of the microspheres changes (Figure 4). As the amount of CAB increases, the surface of the microspheres becomes smoother and the microspheres appear to be "filled", instead of the porous structure with a netlike surface of the CA microspheres. For some of the microspheres, which seem to be filled and have a relatively smooth surface, dents appear at the surface. These holes might

arise through an increase in internal pressure within the microspheres, caused by the filling. The microspheres CAB25 and CAB50 show two different structures and sometimes both structures coexist together on the same particle. One half is rather porous and has a netlike structure, while the other half has a smooth surface. The differences in the formation of the microspheres between cellulose acetate and cellulose acetate butyrate are very evident in these microspheres, which show both structures simultaneously. Accordingly, CAB25, CAB50 and CAB75, which were prepared from a mixture of the two solutions (CA and CAB), contain individual microspheres of CA and CAB, as well as mixed microspheres, depending on the amount of CAB.

SEM measurements of Focused Ion Beam (FIB)-sliced samples enabled for the first time analysis of the inner structure of the microspheres (Figure 5). The CA microspheres have, as shown before by the SEM images, a porous and netlike structure on the surface, which also extends into the inner part of the microspheres. This results in a high porosity of the CA microspheres. The inner structure of the CAB100 microspheres differs significantly from that of CA. For the cellulose acetate butyrate microspheres, two types can be detected in relation to the inner structure. In some cases, it was found that several smaller microspheres are enclosed within a larger microsphere, while in others the microspheres are almost completely filled. Up to now, it was not possible to clarify when the formation of the microspheres leads to a complete filling and when it leads to the inclusion of smaller microspheres. Furthermore, it is not clear what the proportion of each type of the microspheres (filled or enclosed microspheres) is. Possible influencing factors are the choice of surfactant and the temperature during the preparation process. However, a number of further investigations are required to clarify this phenomenon and to identify the key components influencing the process. The different inner structures of the microspheres have a major impact on the subsequent formation of the carbons in terms of the specific surface area and pore structure.

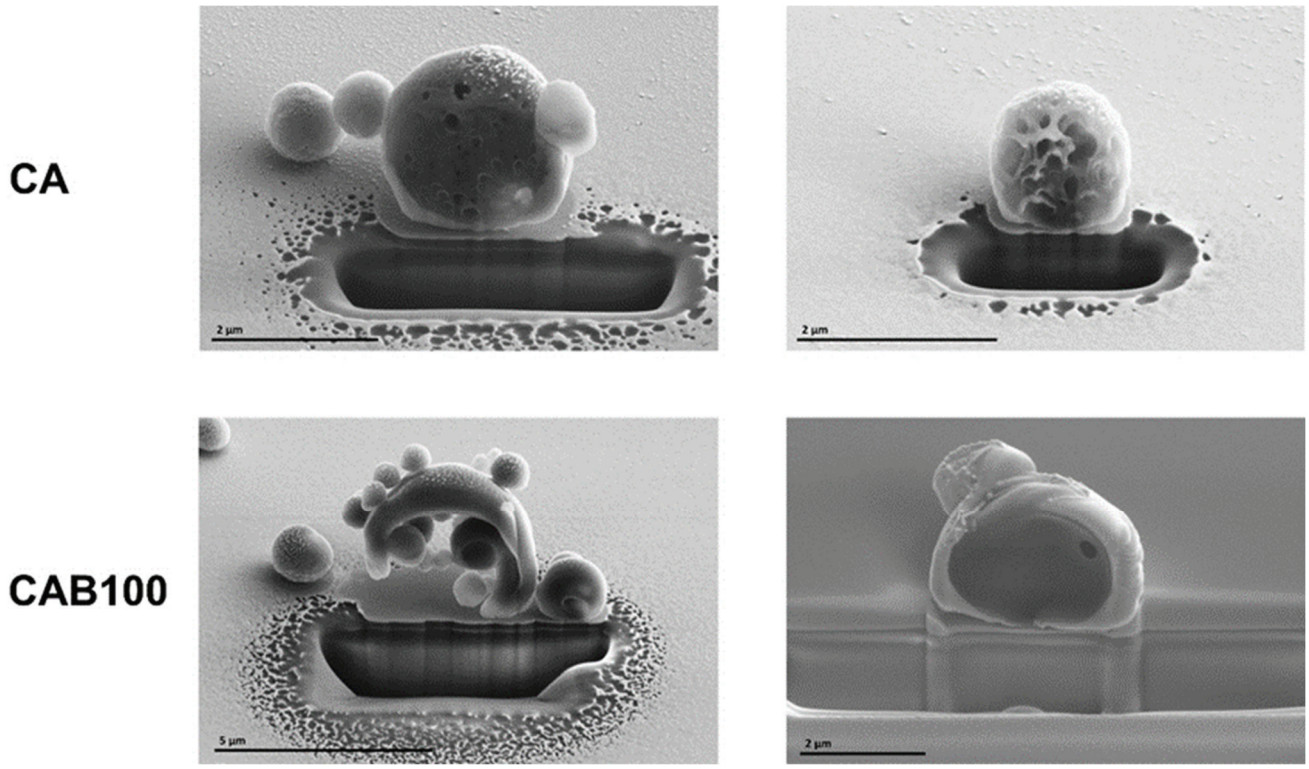

Figure 5. SEM images of CA and CAB100 microspheres sliced using a Focused Ion Beam (FIB).

The porosity of the cellulose acetate (butyrate) microspheres was determined from the sedimentation volume and the packing density of the beads according to the method

of Thümmler et al. [2]. The microspheres were dispersed in water and then centrifuged at 4500 rpm for 30 min. Afterwards, the sedimentation volume V_{Sed} is calculated from the difference between the total volume V_{tot} and the volume of the water supernatant V_{WS}, w_{CA} is the solid content of the microspheres. For the calculation it is assumed that the density of the microspheres is ρ = 1.25 g cm^{-3}. Further, the packing density PD (4) and the porosity ε (5) are calculated as follows:

$$PD = 10 * \frac{w_{CA} * V_{tot}}{V_{Sed}} \quad (4)$$

$$\varepsilon = 100 * \left(1 - \frac{4}{3} * \frac{PD}{\rho}\right) \quad (5)$$

As shown in Table 1 and Figure 6a, the porosity of the microspheres decreases with a higher amount of cellulose acetate butyrate. While pure cellulose acetate microspheres have a porosity of 62.1%, the porosity drops to 55.5% with the addition of 25% CAB. Afterwards, the porosity decreases a bit more slightly and the CAB100 microspheres have a porosity of only 46.7%. The large differences between the CAB microspheres and the CA microspheres are probably due to the significantly larger particle sizes of the microspheres and, therefore, a smaller void space between the microspheres. Furthermore, the SEM images show that the porous structure on the surface of CA microspheres changes to a smoother surface with an increasing amount of CAB. With a smoother surface, water adsorption in the pores probably decreases and, therefore, the "inner" porosity of the microspheres becomes smaller. These results are also consistent with the FIB/SEM measurements, which provide information on the inner structure of the microspheres. While the CA microspheres have a relatively porous structure, the CAB100 microspheres are either completely filled or contain several small microspheres. With the porosity determined by measuring the difference between the total volume and the sedimentation volume, the total empty space within and between the microspheres is measured and it contains no reliable information about the pore volume and the pore size distribution of the microspheres [3].

For the further preparation of carbons, the amount of carbon in the cellulose acetate (butyrate) microspheres is an important parameter. The carbon content in the raw (purchased) materials CA2.5 and CAB is 48.0% and 51.8%, respectively. The microspheres from cellulose acetate have a slightly higher carbon content of 49.4% compared to the raw material, probably due to the preparation process of the microspheres, such as the use of methylcellulose. With the addition of cellulose acetate butyrate in the preparation process, the amount of carbon in the microspheres increases slightly and the carbon content of CAB100 (51.3%) is very similar to the raw material of cellulose acetate butyrate.

Table 1. Characteristics of the prepared microspheres.

CAB Amount [%]	Average Particle Size [µm]	Porosity [%]	Specific Surface Area [m^2 g^{-1}]	C Amount [%]	Decomposition Temperature [°C]
0	1.3	62.1	4.9	49.4	327.4
25	1.5	55.5	6.4	49.6	-
50	2.2	51.6	4.4	50.8	333.2
75	2.2	49.6	3.6	52.0	-
100	3.4	46.7	4.6	51.3	320.9
CA2.5 powder	-	-	15.4	48.0	336.0
CAB powder	-	-	3.7	51.8	340.3

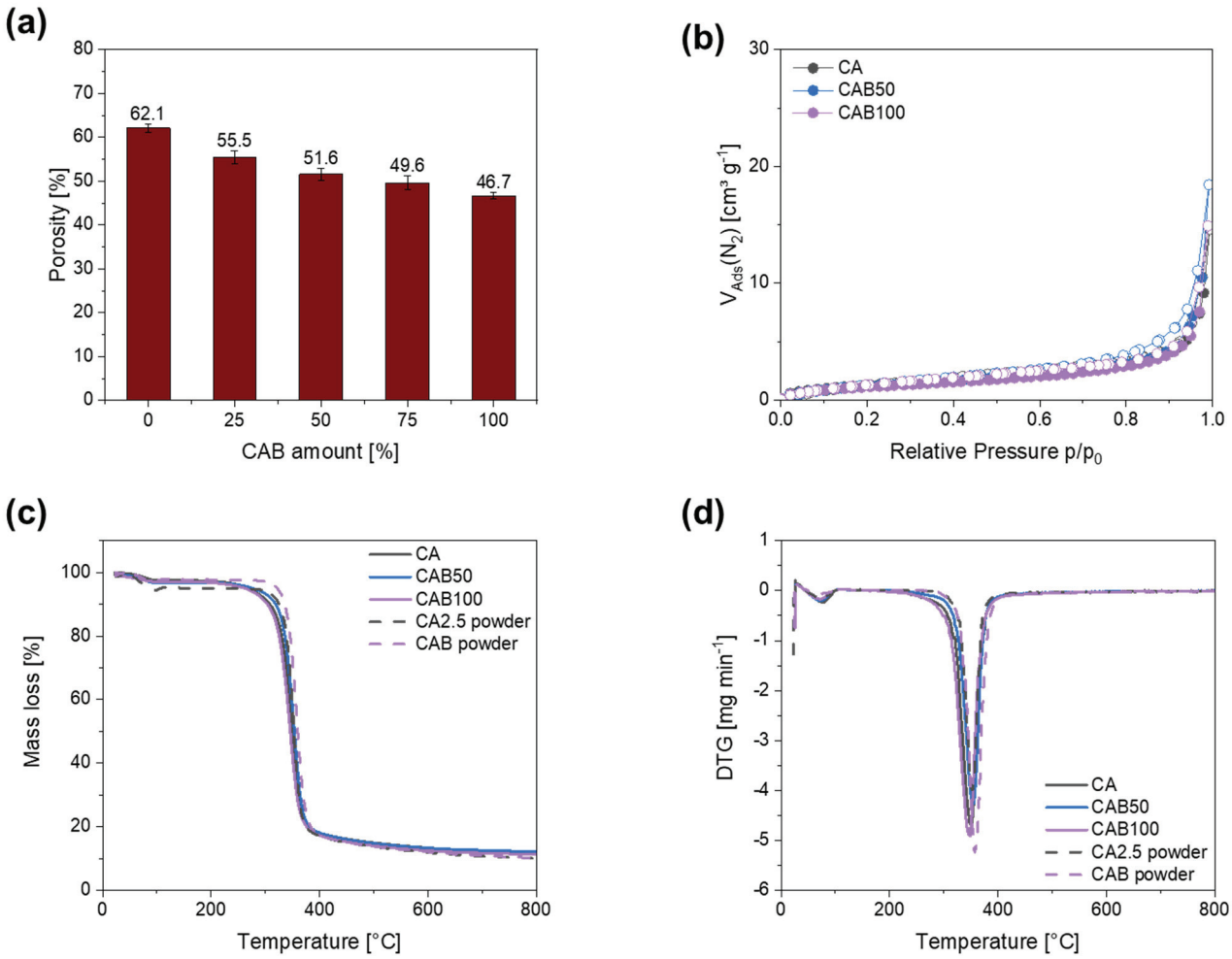

Figure 6. (**a**) Porosity depending on the CAB amount, (**b**) nitrogen physisorption isotherms, (**c**) mass loss and (**d**) DTG for several microspheres.

Nitrogen physisorption measurements were carried out to obtain information about the specific surface area. The nitrogen physisorption isotherms as well as their hysteresis forms are assigned according to IUPAC [37]. The nitrogen physisorption isotherms for the prepared microspheres (Figure 6b and Figure S2) are very similar and can be assigned to type III without hysteresis. Characteristic for type III is that there is no identifiable monolayer and the interactions between the adsorbents and adsorptive are very weak. The specific surface area does not differ significantly, ranging from 4.4 to 4.9 m^2 g^{-1} for CA, CAB50 and CAB100. Therefore, the different particle sizes, morphologies and porosities of the microspheres have no influence on their specific surface area.

Furthermore, the decomposition behaviour of the microspheres and the raw materials was investigated using thermogravimetric analysis (Figure 6c,d). The decomposition temperature for the microspheres varies between 320 and 330 °C and is slightly higher for the raw materials CA2.5 and CAB powder with 336 and 340 °C, respectively. For all samples, the residual mass at a temperature of 800 °C is 14.5–15% with a slightly increased value for a higher amount of CAB in the samples. As the decomposition process is very similar, the same carbonisation conditions are used for CAB and CA microspheres.

3.2. Carbons from the Prepared Microspheres

An important method for characterising the carbons is the nitrogen physisorption, also used in the previous part to characterise the microspheres. In addition to the specific surface area, it also provides information about pore structure, pore volume and the microporosity of the carbons (Table 2).

Table 2. Characteristics of non-activated (c) and activated (ac) carbons from CA and CAB microspheres compared to carbons from the CAB raw material.

	Specific Surface Area [m^2 g^{-1}]	S_{micro} [m^2 g^{-1}]	Average Pore Width [nm]	Pore Volume [cm^3 g^{-1}]	Pore Volume Micro [cm^3 g^{-1}]	I_D/I_G
cCA	448.6	268.8 (60%)	3.9	0.34	0.15 (43%)	1.7
cCAB50	435.0	290.7 (67%)	4.1	0.30	0.16 (53%)	1.9
cCAB100	566.7	318.4 (56%)	6.7	0.54	0.17 (32%)	1.7
cCAB powder	114.0	35.7 (31%)	-	-	-	1.9
ac CAB100	948.7	813.1 (86%)	3.0	0.58	0.44 (76%)	1.4
ac CA	1197.6	1015.6 (85%)	2.1	0.69	0.55 (80%)	1.4

The specific surface area of the carbons changes only slightly for microspheres containing a mixture of cellulose acetate and cellulose acetate butyrate (CAB50) compared to carbons from cellulose acetate microspheres, with values of 448.6 m^2 g^{-1} for cCA and 435.0 m^2 g^{-1} for cCAB50. However, it is interesting to note that the proportion of the specific surface area due to micropores is significantly higher for cCAB50 (67%) than for cCA (60%) (Figure 7c). In contrast, the specific surface area of the carbons prepared from microspheres entirely from cellulose acetate butyrate (CAB100) is significantly higher, with a value of 566.7 m^2 g^{-1}. The higher surface area of the carbons from cellulose acetate butyrate microspheres compared to cellulose acetate microspheres is probably related to their inner structure. As shown before, some of the larger cellulose acetate butyrate microspheres additionally contain small microspheres which are released during the decomposition to carbon, thus providing additional surface area. The filled microspheres might also lead to an increased surface area, since the structure is destroyed during carbonisation. The proportion of the specific surface area related to micropores decreases again to 56.2%. For comparison, cellulose acetate butyrate powder was carbonised under the same conditions. The specific surface area of this carbon of 114.0 m^2 g^{-1} is significantly lower in contrast to carbon prepared from the spherical particles of CAB100. Additionally, the proportion of micropores contributing to the specific surface area is only 31.4%.

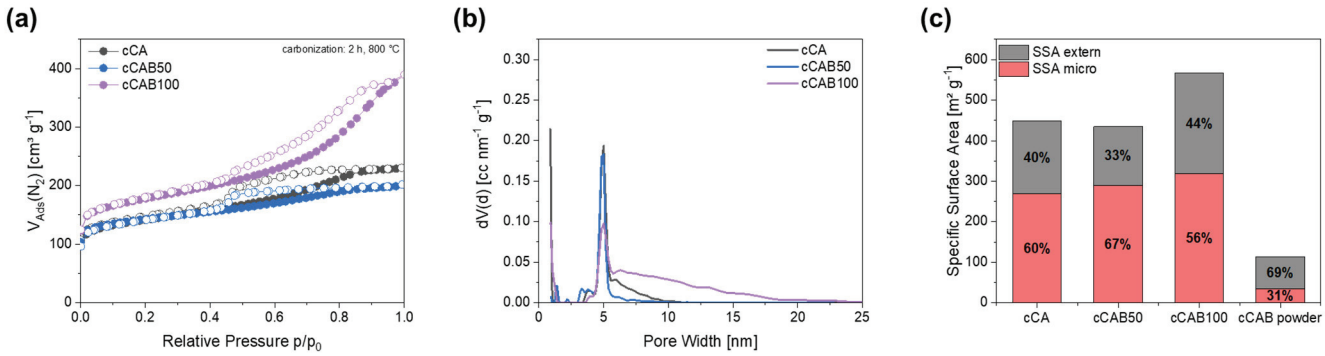

Figure 7. (**a**) Nitrogen physisorption isotherms with (**b**) corresponding pore size distribution and (**c**) classification into extern and micro specific surface area of carbons from microspheres with different amounts of CAB as well as carbonised CAB powder.

The sorption isotherms of all carbons without activation (Figure 7a) show a type IV shape, whereby the type of hysteresis depends on the amount of CAB. For cCA and cCAB50, the hysteresis has a type 2 form, whereas cCAB100 shows a type 4 shape. Characteristic for the type IV isotherm is the occurrence of a turning point located at low relative pressure ($p/p_0 < 0.1$), which is related to the filling of the first monolayer. Type IV is typical for mesoporous materials, and after the filling of the first monolayer pore condensation takes place. At a relative pressure of $p/p_0 > 0.9$, a saturation plateau is reached, whereby this plateau becomes smaller as the amount of CAB increases. In addition, the slope of the isotherm for cCAB100 is significantly steeper in the range of $0.4 < p/p_0 < 0.9$, indicating a larger volume of mesopores filled in this relative pressure range.

The hysteresis type contains further information about the structure of the carbon, but both the type 2 and type 4 shapes assigned to the carbons from the respective microspheres imply complex pore structures. Type 2 is typical for a variety of network effects such as pore blocking and ink bottle-shaped pores, whereas type 4 has a complex network containing micropores and mesopores [31]. This is also confirmed by the pore size distribution in Figure 7b, where all carbons show a mixture of micro- and mesopores with a peak < 1 nm and a peak around 5 nm. The proportion of mesopores with a pore diameter > 5 nm increases significantly with a higher CAB content, resulting in a higher mean pore diameter of 6.7 nm for cCAB100. In contrast, cCA and cCAB50 have smaller mean pore diameters of 3.9 nm and 4.1 nm.

Raman spectra of the prepared carbons from the microspheres show intense D and G bands, pointing to the existence of both graphitic and disordered regions (Figure 8a). The D band, located at 1350–1355 cm^{-1}, arises from the disordered parts, whereas the G band, located at 1580–1600 cm^{-1}, arises from the graphitic parts. The intensity ratio I_D/I_G between the both integrated peaks is used to obtain information about the degree of graphitisation. As the intensity of the D band increases, the proportion of disordered carbon parts gets higher and the crystallite size of graphite decreases [38,39].

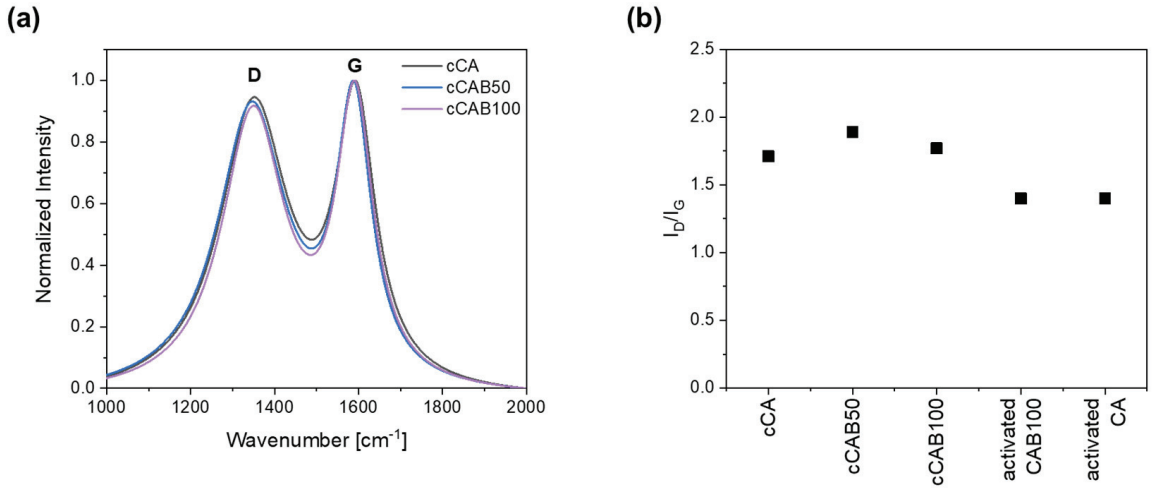

Figure 8. (**a**) Raman spectra and (**b**) I_D/I_G ratio for non-activated and activated carbons from microspheres with different CAB amounts.

The degree of graphitisation initially decreases slightly with the introduction of CAB components with an I_D/I_G value of 1.7 for cCA to 1.9 for cCAB50 (Figure 8b). With a further increase in the CAB amount (cCAB100), the I_D/I_G value rises again to 1.9. Overall, however, the values are within a very narrow range of 1.7 to 1.9, so that no clear effect can be established by changing the cellulose acetate butyrate content on the degree of graphitisation. With the activation of the carbons, the degree of graphitisation increases, giving the I_D/I_G value of 1.4 for both the activated CA and CAB100.

The SEM images in Figure 9 show the morphology of carbon particles prepared from the microspheres with different amounts of CAB as well as the carbon from the raw material.

In general, all the carbons have a relatively smooth surface, although the particle sizes vary considerably. With a higher amount of CAB, the particles generally become a bit smaller. It is also noticeable that the proportion of very small carbon particles increases and thus the particle size distribution becomes wider. The higher number of these very small particles is probably responsible for the higher specific surface area of cCAB100 compared to cCA. The carbon from the CAB powder has a very smooth surface and comparatively large particles of about 100 µm. These results in a much lower specific surface area and a smaller pore volume compared to the carbons from the microspheres.

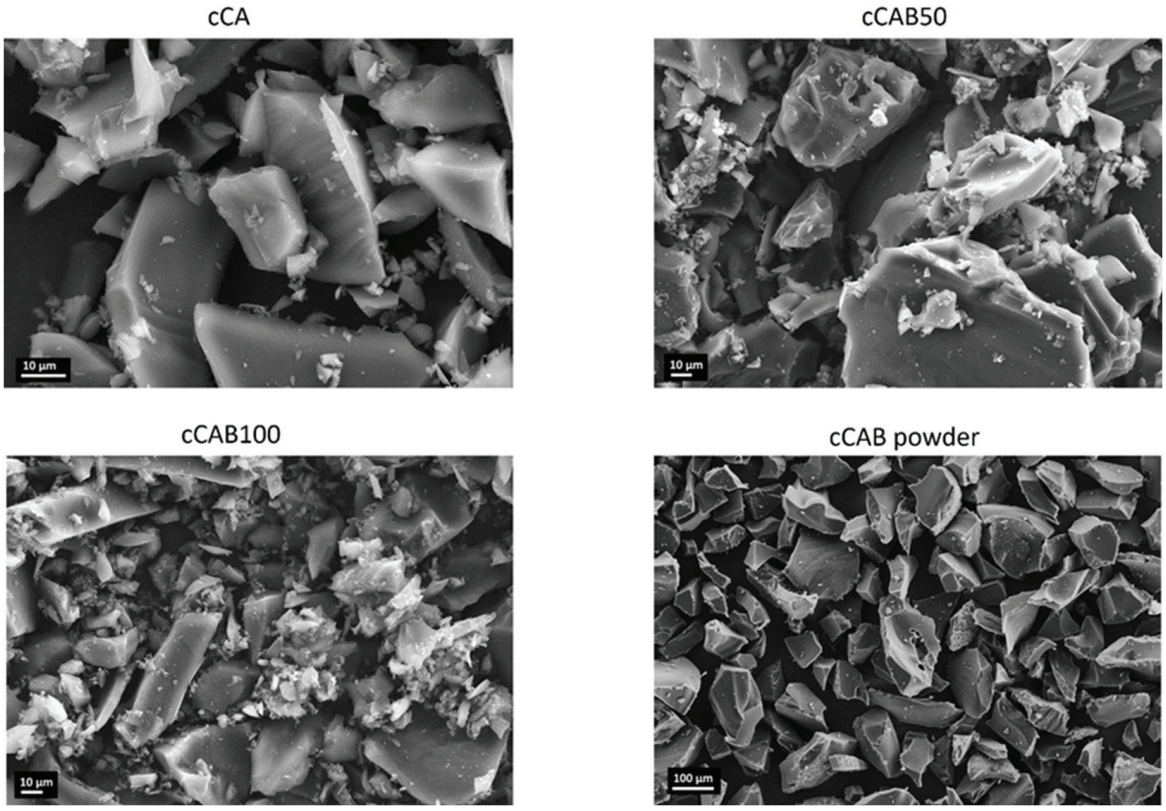

Figure 9. SEM images of carbons from microspheres with different CAB amounts as well as from CAB powder.

Irrespective of the CAB amount of the microspheres, none of the carbons show any sharp reflections in the X-ray diffraction pattern (Figure 10a), which would indicate crystalline phases. The broad reflections at about 23° and 50° can be assigned to the (002) and (100) planes, which are typical for graphitic and amorphous carbons [40,41]. XPS measurements show that the elemental concentrations of C and O at the surface depend on the CAB content of the carbons (Table 3). The carbon concentration increases from 90.0% for cCA to 95.6% for cCAB100, while the oxygen concentration decreases with an increasing CAB content of the carbons. The C 1s spectra in Figure 10b are relatively similar and do not show any clear differences with regard to the distribution of functional groups on the surface of the carbons. All carbons show a distinct peak at a binding energy of 284.8 eV, which can be attributed to the carbon bonds C=C, C-C and C-H. It can also be assumed that each carbon has a small proportion of bonds with oxygen in the form of alcohols (286–287 eV) and carbonates (289–291 eV) [42].

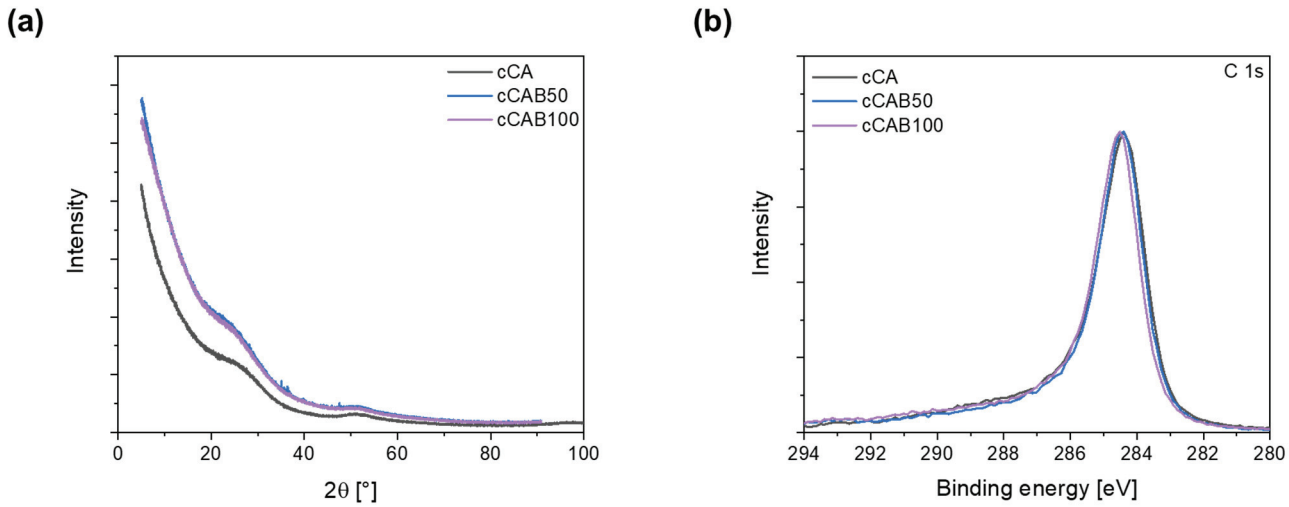

Figure 10. (**a**) X-ray diffraction patterns (Cu Kα_1 radiation, λ = 1.54056 Å) and (**b**) XPS spectra for carbons from microspheres with different CAB amounts.

Table 3. Atomic concentrations of carbon and oxygen on the surface for carbons obtained from microspheres with different CAB amounts.

	C 1s [%]	**O 1s [%]**
cCA	90.0	10.0
cCAB50	92.3	7.7
cCAB100	95.6	4.4

In contrast to the non-activated carbons, the activated carbon derived from CAB100 has a type I-shaped isotherm with a rapid increase at low pressures $p/p_0 < 0.1$, caused by the filling of the micropores (Figure 11a). In general, type I isotherms are typical for microporous materials. Furthermore, a minimal hysteresis of type 4 can be observed for the activated carbon, indicating a small proportion of mesopores. Activation with KOH, therefore, results in a higher specific surface area of 948.7 $m^2\ g^{-1}$ and in a change from a more mesoporous to a microporous structure, which is also reflected in the pore size distribution as well as in a higher proportion of the specific surface area caused by micropores (86%). The pore size distribution of the non-activated carbon shows a high proportion of mesopores with a peak at 5 nm (Figure 11b). After activation, the proportion of micropores < 1 nm is generally slightly larger and the proportion of mesopores decreases. Furthermore, an additional peak at 2.2 nm occurs during activation. This results in a smaller average pore diameter of the activated CAB100 carbon of 3.0 nm in contrast to the non-activated carbon with a pore diameter of 6.7 nm. The combination of numerous micropores with smaller mesopores appears to be advantageous for the accessibility of the electrolyte ions for subsequent use as electrode material in supercapacitors. The specific surface area of the activated carbon derived from cellulose acetate microspheres is slightly higher and the average pore diameter is smaller than that of the activated CAB100. A detailed description of the characteristics of the activated CA carbon is given in further studies [23]. The larger specific surface area of activated carbons from CA microspheres compared to CAB100 microspheres could be due to a more effective activation of the material with KOH due to the higher porosity of the CA microspheres. The SEM images of the activated carbons derived from CAB100 microspheres in Figure S3 also show a significantly altered surface structure compared to the non-activated carbons. The surface of the individual particles is attacked by the activation with KOH and many small particles and increased pores are formed resulting in an increased specific surface area.

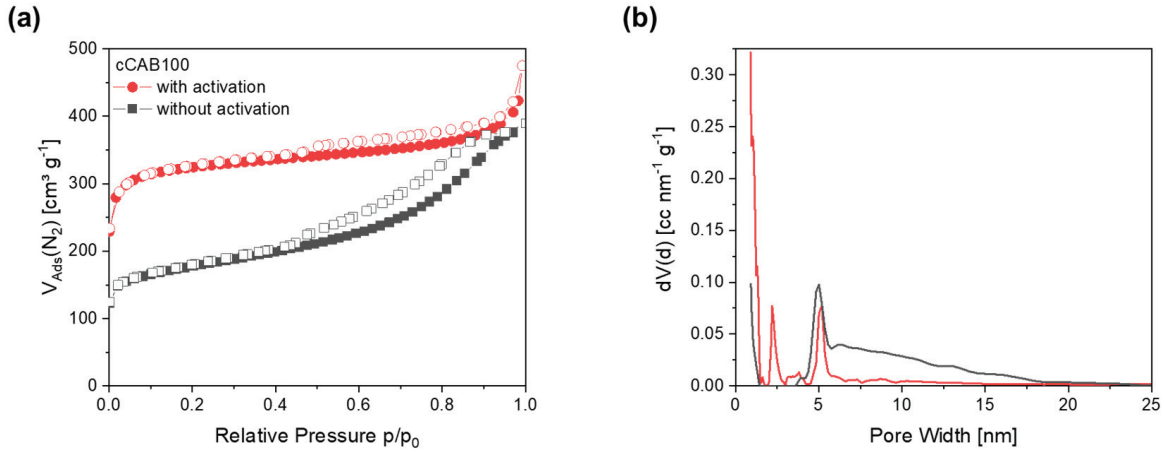

Figure 11. (**a**) Nitrogen physisorption isotherms and (**b**) corresponding pore size distributions for activated and non-activated carbons prepared from CAB100 microspheres.

3.3. Electrochemical Measurements

By adding cellulose acetate butyrate during the preparation of the microspheres, carbons can be produced which achieve higher specific capacitances compared to carbons from CA microspheres (Figure 12a). The electrochemical performance depends on the amount of CAB used. The higher the amount of CAB in the microspheres used as precursors, the higher the specific capacitances that can be achieved in both cyclic voltammetry and GCPL tests. Thus, at a scan rate of 10 mV s^{-1}, the capacitance can be increased from 46.0 F g^{-1} for cCA to 74.1 F g^{-1} at a CAB amount of 50% (cCAB50) and further to 93.6 F g^{-1} for cCAB100. In contrast, the carbon from the CAB raw material (cCAB powder) leads to very low capacities of 5.1 F g^{-1} at a scan rate of 10 mV s^{-1}. Therefore, the conversion of CAB or CA precursors into the spherical form is crucial for the suitability of the resulting carbons as electrode materials for electrochemical applications. The cyclic voltammogram at a scan rate of 10 mV s^{-1} in Figure 12b shows an almost ideal rectangular shape for cCAB100, which deviates only slightly for lower amounts of CAB in the carbons. The rectangular shape is typical for an ideal electrochemical double layer capacitor, which has no redox reaction or any noticeable resistance within the cell. For carbons from CAB powder, the curve is rather slit-like, indicating high internal resistances in the cell. However, at higher scan rates, the capacitances drop for all materials and reach values between 12 and 40 F g^{-1} at a fast scan rate of 500 mV s^{-1} (charge/discharge time 3.2 s).

The results of the CV measurements with higher capacitances for carbons, prepared from precursors with a higher CAB amount, can also be confirmed by GCPL tests (Figure 12c). At a current rate of 1 A g^{-1}, a comparatively high specific capacitance of 84.2 F g^{-1} is achieved for cCAB100, while cCA shows a value of only 29.4 F g^{-1}. In addition, cCAB100 shows good stability at higher current densities compared to the carbons produced from precursors with a lower amount of CAB with a specific capacitance of 62.8 F g^{-1} at 10 A g^{-1}. The GCPL curves at a current density of 1 A g^{-1} in Figure 12d show a triangular shape with a small iR drop for cCAB100, whereas the shape deviates slightly with lower amounts of CAB and the iR drop, which indicates inner resistances in the cell, becomes larger.

The charging/discharging at a current rate of 1 A g^{-1} requires about 63 s for cCAB100 and is, therefore, more than twice as fast as the CV measurements at a scan rate of 10 mV s^{-1} with a charging/discharging time of about 160 s.

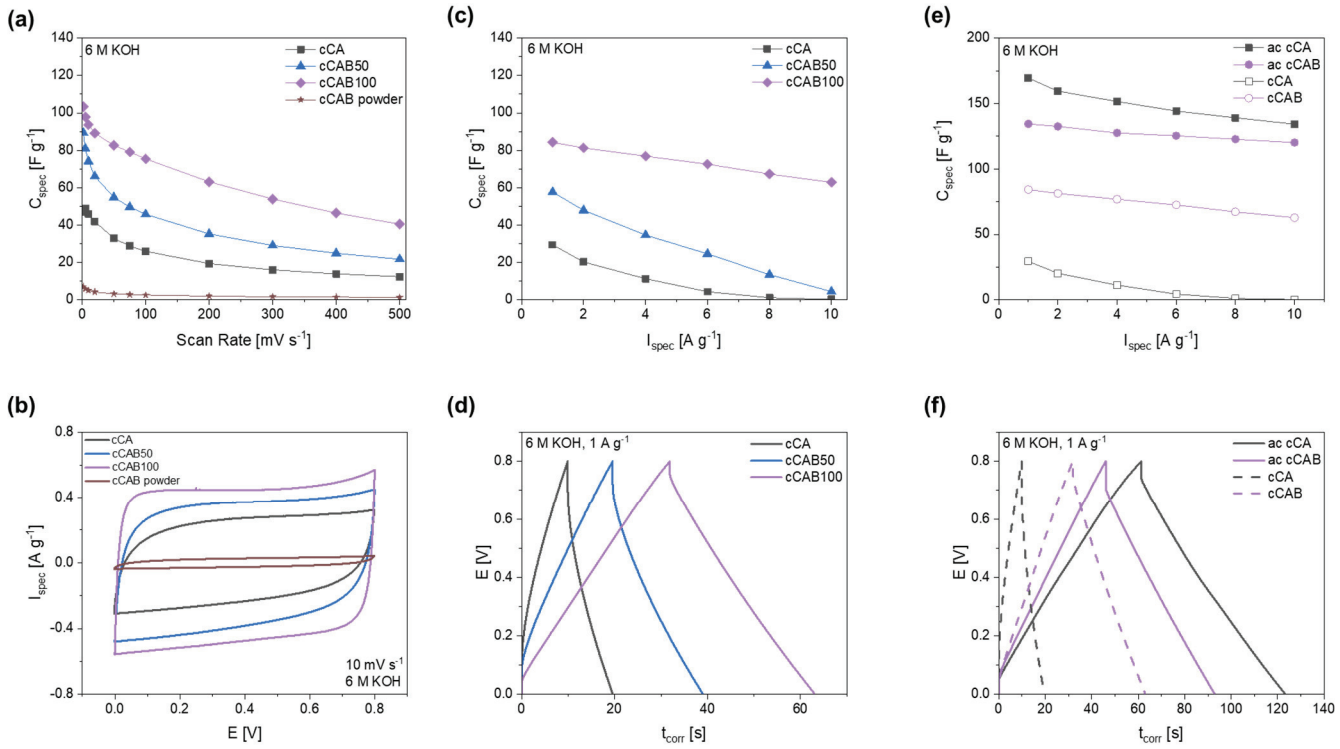

Figure 12. (**a**) Specific capacitances depending on the scan rate with (**b**) corresponding cyclic voltammograms at a scan rate of 10 mV s^{-1}, (**c**) specific capacitances depending on the current rate with (**d**) corresponding GCPL curves at 1 A g^{-1} for carbons prepared from microspheres with different CAB amounts, as well as (**e**) specific capacitances of activated and non-activated carbons from CA and CAB100 microspheres with (**f**) corresponding GCPL curves at 1 A g^{-1}.

Promising specific capacitances have already been achieved with carbon from cellulose acetate butyrate microspheres without activating the material. For further improving the performance for the use as electrode material in supercapacitors, the CAB100 microspheres were activated with KOH in a mass ratio of 1:1. However, in contrast to the non-activated carbons, the activated carbons from CAB100 microspheres achieve lower specific capacitances in the CGPL measurements in Figure 12e compared to the activated carbons from CA microspheres. At a current rate of 1 A g^{-1}, the activated CAB100 has a specific capacitance of 134.4 F g^{-1}, whereas the activated CA achieves 169.5 F g^{-1}. The activated carbons of CA and CAB100 differ primarily in their specific surface area, which is, at 1197.6 m^2 g^{-1}, significantly larger for CA than for CAB100, with a value of 948.7 m^2 g^{-1}. Both surfaces are mostly caused by micropores (about 85%). The larger specific surface area of activated CA is probably the reason for the higher specific capacitance compared to CAB100. Also, the iR drop in the GCPL curve at 1 A g^{-1} in Figure 12f is significantly larger for activated CAB100, indicating possible resistances within the cell influencing the specific capacitance and the electrochemical stability.

The specific energy and power densities, shown in the Ragone plot in Figure 13, are an important characteristic for comparing the performance of supercapacitors. The higher the amount of CAB of the microspheres used as precursor for the carbons, the higher the energy density when used as electrode material. At 1 A g^{-1}, the energy densities for cCA, cCAB50 and cCAB100 are 2.6, 5.1 and 7.5 Wh kg^{-1}, respectively. While the energy density for cCA and cCAB50 decreases sharply at higher current rates, it remains relatively stable for cCAB100. A higher proportion of CAB therefore contributes to stability and better performance.

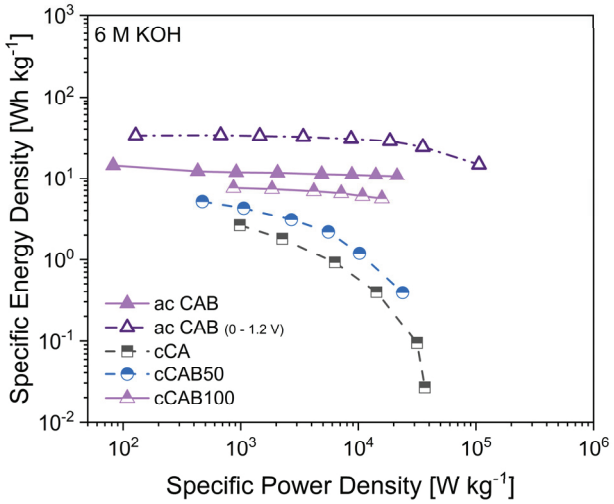

Figure 13. Ragone plot of supercapacitors with carbon electrodes derived from microspheres with different amount of CAB.

In order to achieve higher specific capacitances and thus higher energy densities, activated carbons from microspheres of CA and CAB were used. The energy densities of the supercapacitors with activated carbons are 12 Wh kg^{-1} for CAB microspheres and 15 Wh kg^{-1} for CA microspheres with comparable power densities of 0.9 kW kg^{-1} at a current density of 1 A g^{-1} in a potential window of 0–0.8 V. By extending the potential window during cycling from 0–0.8 V to 0–1.2 V, both the energy and power densities of the supercapacitor can be further optimised. At 1 A g^{-1}, the energy density reaches 33 Wh kg^{-1} at a power density of 1.5 kW kg^{-1}. However, a prerequisite for extending the potential range is the stability of the electrolyte, which for aqueous electrolytes is limited by the decomposition of water at a potential > 1.23 V [43]. In addition, a good long-term stability over 2000 cycles can be shown for electrodes with activated carbon from CAB microspheres when cycled in a potential window of 0–1.2 V (Figure S4, Supplementary Material).

4. Conclusions

In conclusion, the acetate method represents a viable approach for obtaining microspheres with a particle size of less than 5 µm, even when cellulose acetate butyrate instead of cellulose acetate is used as a precursor. The substitution of cellulose acetate with cellulose acetate butyrate during the preparation process significantly changes the structure and properties of the microspheres. This substitution results in smoother surfaces with some dents and a less porous inner structure, leading to reduced porosity and increased particle size with a broader particle size distribution as the amount of CAB in the microspheres increases. After carbonisation, the microspheres derived from CAB have a notably higher specific surface area of 567 m^2 g^{-1} compared to those derived from CA with 449 m^2 g^{-1}, indicating the potential for improved electrochemical performance. The activation of the cellulose acetate butyrate microspheres with KOH can further increase the specific surface area and change the pore structure of the carbons, resulting in a higher proportion of micropores. These prepared carbons show promising results as electrode materials in symmetrical supercapacitors with 6 M KOH aqueous electrolytes. Carbons derived from CAB100 exhibit a specific capacitance of 84.2 F g^{-1} at 1 A g^{-1} and show stable performance at higher current densities with 62.8 F g^{-1} at 10 A g^{-1}, too. Activation with KOH further enhances the performance leading to a specific capacitance of 134.4 F g^{-1} at a current density of 1 A g^{-1}. In addition, the conversion of cellulose-derivative precursors into a spherical structure positively effects the structure of the carbons and, therefore, their electrochemical performance. Carbons derived solely from CAB powder exhibit a lower specific surface area of 114 m^2 g^{-1} and inferior electrochemical performance when used as electrode materials.

Overall, these results highlight the potential of carbons from CAB-derived microspheres as promising candidates for high performance supercapacitor electrodes, especially when optimised by activation processes. Furthermore, the preparation of spherical microspheres with cellulose acetate butyrate can serve as a basis for the preparation of microspheres with other cellulose derivatives. The changed properties and surface functionalities compared to the cellulose microspheres may also have advantages for other applications besides electrochemical energy storage.

Supplementary Materials: The following supporting information can be downloaded at https://www.mdpi.com/article/10.3390/polym16152176/s1, Figure S1: Raman spectroscopy of (a) microspheres with different amounts of CAB and (b) the raw materials CA2.5 powder and CAB powder, Figure S2: nitrogen physisorption isotherms of CAB25 and CAB75, Figure S3: SEM images of activated carbon derived from CAB100 microspheres, Figure S4: long-term electrochemical performance for activated carbons from CAB microspheres at 1 A g^{-1} for 2000 cycles using 6 M KOH electrolyte.

Author Contributions: J.F.: conceptualization, methodology, investigation, analysis, writing—original draft; K.T.: methodology, analysis, writing—review and editing; I.Z.: methodology, investigation; D.M.: methodology, analysis, writing—review and editing, supervision, project administration, funding acquisition; S.F.: conceptualization, methodology, analysis, supervision, project administration, funding acquisition. All authors have read and agreed to the published version of the manuscript.

Funding: This research was funded by the German Research Foundation (DFG) in the project Cellstor, grant number 511521214 (FI755/16-1, MI945/8-1).

Institutional Review Board Statement: Not applicable.

Data Availability Statement: The original contributions presented in the study are included in the article/supplementary material; further inquiries can be directed to the corresponding authors.

Acknowledgments: The authors would like to thank Björn Günther (Institute of Soil Science and Site Ecology, TU Dresden, Germany) for the SEM measurements of the microspheres as well as Martin Hantusch (Leibniz Institute for Solid State and Material Research (IFW), Dresden e.V,) for the XPS measurements of the carbons.

Conflicts of Interest: The authors declare no conflicts of interest.

References

1. Wagenknecht, W.; Fanter, C.; Loth, F. Process for Producing Spherical Microparticles on the Basis of Cellulose Acetate. European Patent EP0750007, 18 June 1996.
2. Thümmler, K.; Fischer, S.; Feldner, A.; Weber, V.; Ettenauer, M.; Loth, F.; Falkenhagen, D. Preparation and characterization of cellulose microspheres. *Cellulose* **2011**, *18*, 135–142. [CrossRef]
3. Gericke, M.; Trygg, J.; Fardim, P. Functional Cellulose Beads: Preparation, Characterization, and Applications. *Chem. Rev.* **2013**, *113*, 4812–4836. [CrossRef]
4. Stamberg, J. Bead Cellulose. *Sep. Purif. Methods* **1988**, *17*, 155–183. [CrossRef]
5. Luo, X.; Zhang, L. Creation of regenerated cellulose microspheres with diameter ranging from micron to millimeter for chromatography applications. *J. Chromatogr. A* **2010**, *1217*, 5922–5929. [CrossRef]
6. Weber, V.; Ettenauer, M.; Linsberger, I.; Loth, F.; Thümmler, K.; Feldner, A.; Fischer, S.; Falkenhagen, D. Functionalization and Application of Cellulose Microparticles as Adsorbents in Extracorporeal Blood Purification. *Macromol. Symp.* **2010**, *294*, 90–95. [CrossRef]
7. Carvalho, J.P.F.; Silva, A.C.Q.; Silvestre, A.J.D.; Freire, C.S.R.; Vilela, C. Spherical Cellulose Micro and Nanoparticles: A Review of Recent Developments and Applications. *Nanomaterials* **2021**, *11*, 2744. [CrossRef] [PubMed]
8. Trygg, J.; Fardim, P.; Gericke, M.; Mäkilä, E.; Salonen, J. Physicochemical design of the morphology and ultrastructure of cellulose beads. *Carbohydr. Polym.* **2013**, *93*, 291–299. [CrossRef] [PubMed]
9. Volkert, B.; Wolf, B.; Fischer, S.; Li, L.; Lou, C. Application of Modified Bead Cellulose as a Carrier of Active Ingredients. *Macromol. Symp.* **2009**, *280*, 130–135. [CrossRef]
10. Cellufine. Cellufine Chromatography Media. Available online: https://cdn.shopify.com/s/files/1/0250/3553/8495/files/CA_general_N1_V30_E.pdf?v=1636966080 (accessed on 21 May 2024).
11. Cytiva. Cytopore 1 Microcarriers (Dry Powder). Available online: https://www.cytivalifesciences.com/en/dk/shop/cell-culture-and-fermentation/microcarriers/cytopore-1-microcarriers-dry-powder-p-05928#tech-spec-table (accessed on 21 May 2024).
12. Zugenmaier, P. Characteristics of cellulose acetates—Characterization and physical properties of cellulose acetates. *Macromol. Symp.* **2004**, *208*, 81–166. [CrossRef]

13. Rokhade, A.P.; Patil, S.A.; Belhekar, A.A.; Halligudi, S.B.; Aminabhavi, T.M. Preparation and evaluation of cellulose acetate butyrate and poly(ethylene oxide) blend microspheres for gastroretentive floating delivery of repaglinide. *J. Appl. Polym. Sci.* **2007**, *105*, 2764–2771. [CrossRef]
14. Obeidat, W.M.; Price, J.C. Preparation and in vitro evaluation of propylthiouracil microspheres made of Eudragit RL 100 and cellulose acetate butyrate polymers using the emulsion-solvent evaporation method. *J. Microencapsul.* **2005**, *22*, 281–289. [CrossRef]
15. Giunchedi, P.; Conti, B.; Maggi, L.; Conte, U. Cellulose Acetate Butyrate and Polyaprolactone for Ketoprofen Spray-Dried Microsphere Preparation. *J. Microencapsul.* **1994**, *11*, 381–393. [CrossRef]
16. Huang, A.; Li, X.; Liang, X.; Zhang, Y.; Hu, H.; Yin, Y.; Huang, Z. Solid-Phase Synthesis of Cellulose Acetate Butyrate as Microsphere Wall Materials for Sustained Release of Emamectin Benzoate. *Polymers* **2018**, *10*, 1381. [CrossRef]
17. Simon, P.; Gogotsi, Y. Materials for electrochemical capacitors. *Nat. Mater.* **2008**, *7*, 845–854. [CrossRef]
18. Béguin, F.; Frackowiak, E. *Supercapacitors—Materials, Systems, and Applications*; WILEY-VCH Verlag GmbH & Co KGaA: Weinheim, Germany, 2013.
19. Mensah-Darkwa, K.; Zequine, C.; Kahol, P.K.; Gupta, R.K. Supercapacitor Energy Storage Device Using Biowastes: A Sustainable Approach to Green Energy. *Sustainability* **2019**, *11*, 414. [CrossRef]
20. Wei, L.; Yushin, G. Nanostructured activated carbons from natural precursors for electrical double layer capacitors. *Nano Energy* **2012**, *1*, 552–565. [CrossRef]
21. Frackowiak, E. Carbon materials for supercapacitor application. *Phys. Chem. Chem. Phys.* **2007**, *9*, 1774–1785. [CrossRef]
22. Minakshi, M.; Samayamanthry, A.; Whale, J.; Aughterson, R.; Shinde, P.A.; Ariga, K.; Shrestha, L.K. Phosphorous—Containing Activated Carbon Derived from Natural Honeydew Peel Powers Aqueous Supercapacitors. *Chem. Asian J.* 2024, *in press*. [CrossRef]
23. Fischer, J.; Thümmler, K.; Fischer, S.; Martinez, I.G.G.; Oswald, S.; Mikhailova, D. Activated Carbon Derived from Cellulose and Cellulose Acetate Microspheres as Electrode Materials for Symmetric Supercapacitors in Aqueous Electrolytes. *Energy Fuels* **2021**, *35*, 12653–12665. [CrossRef]
24. Fischer, J.; Pohle, B.; Dmitrieva, E.; Thümmler, K.; Fischer, S.; Mikhailova, D. Symmetric supercapacitors with cellulose-derived carbons and Na2SO4 electrolytes operating in a wide temperature range. *J. Energy Storage* **2022**, *55*, 105725. [CrossRef]
25. Fischer, J.; Wolfram, L.; Oswald, S.; Fischer, S.; Mikhailova, D. Carbons Derived from Regenerated Spherical Cellulose as Anodes for Li-Ion Batteries at Elevated Temperatures. *ChemPhysChem* **2024**, *25*, e202300833. [CrossRef]
26. Mie, G. Beiträge zur Optik trüber Medien, speziell kolloidaler Metallösungen. *Ann. Phys.* **1908**, *330*, 377–445. [CrossRef]
27. *DIN 51721:2001-08*; Prüfung Fester Brennstoffe, Bestimmung des Gehaltes an Kohlenstoff und Wasserstoff, Verfahren nach Radmacher-Hoverath. Deutsches Institut für Normung: Berlin, Germany, 2001.
28. Brunaer, S.; Emmett, P.; Teller, E. Adsorption of Gases in Multimolecular Layers. *J. Am. Chem. Soc.* **1938**, *60*, 309–319. [CrossRef]
29. Magee, R.W. Evaluation of the External Surface Area of Carbon Black by Nitrogen Adsorption. *Rubber Chem. Technol.* **1995**, *68*, 590–600. [CrossRef]
30. Ravikovitch, P.I.; Neimark, A.V. Density Functional Theory Model of Adsorption on Amorphous and Microporous Silica Materials. *Langmuir* **2006**, *22*, 11171–11179. [CrossRef]
31. Thommes, M. Physical Adsorption Characterization of Nanoporous Materials. *Chem. Ing. Tech.* **2010**, *82*, 1059–1073. [CrossRef]
32. Gurvich, L. Physio-Chemical Attractive Force. *J. Russ. Phys. Chem. Soc.* **1915**, *47*, 805–827.
33. Socrates, G. *Infrared and Raman Characteristic Group Frequencies: Tables and Charts*; John Wiley & Sons: Chichester, UK, 2001.
34. Marlina, D.; Novita, M.; Anwar, M.T.; Kusumo, H.; Sato, H. Raman spectra of polyethylene glycol/cellulose acetate butyrate biopolymer blend. *J. Phys. Conf. Ser.* **2021**, *1869*, 012006. [CrossRef]
35. Zhang, K.; Feldner, A.; Fischer, S. FT Raman spectroscopic investigation of cellulose acetate. *Cellulose* **2011**, *18*, 995–1003. [CrossRef]
36. Firsov, S.P.; Zhbankov, R.G. Raman spectra and physical structure of cellulose triacetate. *J. Appl. Spectrosc.* **1982**, *37*, 940–947. [CrossRef]
37. Sing, K.S.W.; Everett, D.H.; Haul, R.A.W.; Moscou, L.; Pierotti, R.A.; Rouquérol, J.; Siemieniewska, T. Reporting physisorption data for gas/solid systems with special reference to the determination of surface area and porosity (Recommendations 1984). *Pure Appl. Chem.* **1985**, *57*, 603–619. [CrossRef]
38. Ferrari, A.C.; Robertson, J. Interpretation of Raman spectra of disordered and amorphous carbon. *Phys. Rev. B* **2000**, *61*, 14095–14107. [CrossRef]
39. Tuinstra, F.; Koenig, J.L. Raman Spectrum of Graphite. *J. Chem. Phys.* **1970**, *53*, 1126–1130. [CrossRef]
40. Zhang, X.; Zhao, M.; Chen, Z.; Yan, T.; Li, J.; Ma, Y.; Ma, L. The application of biomass-based carbon materials in flexible all-solid supercapacitors. *J. Mater. Sci. Mater. Electron.* **2022**, *33*, 15422–15432. [CrossRef]
41. Narayanan, A.; Siddiqa, A.; Kodihalli, N.K.; Hegde, G.; Nagaraju, D.H.; Padaki, M. Designing of a Free-Standing Flexible Symmetric Electrode Material for Capacitive Deionization and Solid-State Supercapacitors. *ACS Sustain. Chem. Eng.* **2023**, *11*, 3750–3759. [CrossRef]

42. Moulder, J.F.; Stickle, W.F.; Sobol, P.E.; Bomben, K.D. *Handbook of X-ray Photoelectron Spectroscopy*; Physical Electronics: Eden Prairie, MN, USA, 1995.
43. Wan, F.; Zhu, J.; Huang, S.; Niu, Z. High-Voltage Electrolytes for Aqueous Energy Storage Devices. *Batter. Supercaps* **2020**, *3*, 323–330. [CrossRef]

MDPI AG
Grosspeteranlage 5
4052 Basel
Switzerland
Tel.: +41 61 683 77 34

Polymers Editorial Office
E-mail: polymers@mdpi.com
www.mdpi.com/journal/polymers

Academic Open
Access Publishing

mdpi.com

ISBN 978-3-7258-6002-9